Isotopic constraints on the origin and nature of primitive material in the Solar System and on early Earth

David V. Bekaert

UNIVERSITE DE LORRAINE

Ecole doctorale SIReNa

Centre de Recherches Pétrographiques et Géochimiques

THESE DE DOCTORAT

présentée et soutenue publiquement le 24 janvier 2020 pour l'obtention du titre de Docteur de l'Université de Lorraine (spécialité Géosciences)

par David V. Bekaert

Isotopic constraints on the origin and nature of primitive material in the Solar System and on early Earth.

Contraintes isotopiques sur l'origine et la nature de la matière primitive dans le Systeme Solaire et sur la Terre jeune.

Composition du Jury

Directeurs de thèse

Prof. Bernard Marty, Université de Lorraine, Centre de Recherches Pétrographiques et Géochimiques (France)

Dr. Laurent Tissandier, Centre de Recherches Pétrographiques et Géochimiques (France)

Rapporteurs

Prof. Jamie Gilmour, Department of Earth and Environmental Sciences, University of Manchester (UK)

Prof. Chrystèle Sanloup, Sorbonne Universités, UPMC Université Paris 06, Institut des Sciences de la Terre (France)

Examinateurs

Dr. Rita Parai, Department of Earth and Planetary Sciences, Washington University in St. Louis (MO, USA)

Dr. Jessica Barnes, Lunar and Planetary Laboratory, The University of Arizona in Tucson (AZ, USA)

Invités

Dr. Laurent Rémusat, Institut de minéralogie, de physique des matériaux et de cosmochimie, UPMC/MNHN (France)

Prof. Nathalie Carrasco, Université Versailles Saint Quentin, UPMC Université Paris 06, LATMOS/IPSL (France)

Remerciements

De nombreuses personnes m'ont aidé et/ou soutenu au cours de ce travail de thèse, et je vais essayer de ne pas trop en oublier. C'est parti.

Tout d'abord, je tiens à remercier Bernard pour sa confiance, son enthousiasme, et pour l'ensemble des opportunités qui m'ont été données pendant cette thèse. On a fait quelques découvertes, passé de longs moments à tordre les isotopes du xénon dans tous les sens. Mais plus important encore, on s'est bien marrés. MERCI.

Ensuite, un grand merci à Tix pour son soutien et ses conseils toujours avisés sur le Nébulotron et ses bizarreries. C'était un plaisir de t'avoir en co-directeur.

Je tiens à remercier Chrystèle Sanloup, Jamie Gilmour, Rita Parai, Jessica Barnes, Nathalie Carrasco et Laurent Rémusat d'avoir accepté de faire partie de mon jury de thèse.

Ma seconde maison au cours de ces dernières années se trouve au second étage côté Sud du CRPG. Le labo gaz rare représente pour moi un environnement de travail idéal, où on peut faire de la science, tout en mangeant des pâtés lorrains ("due to their inertness, noble gases do not react with pâtés lorrains"). J'y ai trouvé des gens formidables, dont l'inévitable Laurent, le grand manitou des gaz rares avec toujours ce sourire en coin du mec qui va sortir une connerie. Et le pire, c'est qu'il la sort toujours. Sa connerie. J'ai aussi beaucoup apprécié les interactions scientifiques que j'ai pu avoir avec Evelyn, P-H, et Pete, lors de mes premières années au CRPG. Merci à Bouch pour son aide et ses conseils avec le détecteur de fuites invisibles. Bien plus que des collègues, j'ai aussi trouvé de vrais amis, avec Dave, Matthieu, à qui je souhaite bonne chance pour la suite de Photonis, ainsi que plein de bières et de parties de billards, où Matthieu gagnera même si tout le monde sait que c'est Dave le meilleur. Et bien sûr, Michael, en compagnie duquel vous m'aurez peut-être aperçu une fois ou deux au cours de cette thèse. Merci de ton soutien et de ta bienveillance. Tu as beaucoup contribué à mon bien-être au cours de ces trois dernières années, ainsi qu'à la réussite de cette thèse. Bravo bro, et fuck you. FYOTOS.

Merci à tous les gens que j'ai pu fréquenter, de près ou de loin, au CRPG, et qui ont contribué à rendre ma vie au labo si agréable. Un grand merci à l'équipe administrative, Aurélie, Isabelle, Corine, Cathy, Joëlle, pour leur travail en sous-marin, qui fait tourner le CPRG. Promis Isa, je te rends Spatule bientôt. Je voudrais aussi tout particulièrement remercier les chercheurs du 4e, Yves, Johan, Guillaume, Camille, Laurette, avec qui j'ai

partagé de super moments, et pas seulement au labo. Un merci tout particulier à Yves, pour m'avoir impliqué aussi généreusement dans ses travaux, et à Laurette, pour m'avoir appris à faire du snowboard :) Merci à Delphine et Lucile du sous-sol pour m'avoir aidé avec le fameux Nébulotron, ainsi qu'à Pierre le mécano pour son travail impeccable. Bien évidemment, un énorme merci à mes co-bureaux préférés, Apo, Marine et Guillaume. Merci de votre gentillesse, et d'avoir toujours assuré la présence de gâteaux dans l'armoire du bureau.

Merci à toutes les personnes hors-CRPG avec lesquelles j'ai pu collaborer au cours de ces dernières années, au Muséum (Adriana, F. Robert, L. Rémusat), à l'IPGP (S. Charnoz), au LATMOS (N. Carasco, J. Bourgalais, L. Vettier), à Métis (S. Derenne, C. Anquetil, F. Delarue), à l'ISMO (B. Gans). Un énorme merci tout particulier à Guillaume Avice, qui a énormément contribué à ma formation, et à qui j'enverrai toujours des mails improbables avec des questions obscures sur le xénon.

Je remercie du fond du coeur tous les copains de Nancy, Quentin, Ben, Marin, Somfy, la Reine de la Bringue, Just', Titi, Pierre, Gaël, OPH, Simon... J'ai tellement de chance de vous avoir dans ma vie ! Merci pour toutes les larmes de sang partagées ensemble.

Merci à Dan (Kikito !!) et Margot pour leur accueil toujours chaleureux à Paris.

Merci Nini et Julien pour tous ces bons moments passés ensemble.

Merci à ma famille pour leur soutien et leur amour.

Merci à Béton et Pentouky pour leur patience, leur tendresse,
et tout ce qui fait ce quotidien que je ne saurai plus aimer.

A mon père,

Jean-Paul Bekaert.

Résumé en français

Ce travail de thèse questionne l'origine des éléments très volatils (ou atmophiles, c'est-à-dire concentrés dans l'atmosphère et l'hydropshère: eau, carbone, azote, halogènes, gaz nobles) sur Terre. Déterminer quand, et sous quelle(s) forme(s) ceux-ci ont été mis à disposition à la surface de la Terre est crucial pour mieux comprendre l'évolution de l'atmosphère, et la mise en place de conditions favorables au développement de la vie. Notre planète est un système dynamique, animé de flux de matière et de chaleur entre sa surface et son intérieur. Au travers du volcanisme, des gaz primordiaux retenus dans les profondeurs de la Terre depuis sa formation sont continuellement transférés vers l'atmosphère. D'autre part, certains éléments volatils de surface sont recyclés dans le manteau terrestre par subduction de croûte océanique hydratée. Cet équilibre entre dégazage et "regazage" de la Terre a contrôlé l'établissement de l'atmosphère et une partie de son évolution au cours des temps géologiques. Dans cette thèse, j'ai utilisé les gaz nobles comme traceurs de l'origine et de l'évolution des éléments volatils dans les réservoirs terrestres. De part leur caractère inerte, les gaz nobles ne participent pas à des réactions chimiques qui pourraient affecter leur composition isotopique et/ou élémentaire. La signature portée par un échantillon donné dépend ainsi (i) de la composition initiale/héritée (source), (ii) de contributions secondaires de réactions nucléaires (radioactivité, fission, spallation), et/ou (iii) de fractionnements potentiels liés à des processus physiques (diffusion, évaporation, condensation). En déconvoluant les signatures associées à chacun de ces aspects, il est possible de renseigner l'origine, la nature et le timing des processus ayant contrôlé le budget en éléments volatils d'un réservoir géologique donné.

L'étude comparative de la composition de l'atmosphère et de celle du manteau terrestre permet de tester leur lien génétique. Une vision simplifiée du manteau terrestre le subdivise en deux grands réservoirs: le manteau supérieur, convectif, source des basaltes de rides médio-céaniques (*Mid Ocean Ridge Basalts*, ou MORB), et le manteau inférieur, moins chimiquement évolué, source des basaltes d'îles océaniques (*Oceanic Island Basalts* ou OIBs). Ce dernier, échantillonné par les panaches volcaniques, préserve l'empreinte du gaz de la nébuleuse protosolaire qui se serait directement dissout dans l'océan magmatique à la surface de la Terre en formation (e.g., Yokochi & Marty 2004; Williams and Mukhopadhyay, 2019). Ce gaz "solaire" du disque protoplanétaire (DPP) s'est ensuite dissipé, soit vers le milieu interstellaire soit par accrétion sur l'étoile centrale (le Soleil), avec seulement une fraction résiduelle restée piégée dans les corps rocheux du Système solaire en formation, notamment implantée et/ou incorporée dans les poussières constitutives des astéroïdes et des météorites primitives. Pour le néon par exemple, ce processus d'implantation - combiné à l'érosion partielle des grains de poussière - induit un fractionnement isotopique favorisant la préservation des isotopes lourds, résultants ainsi en un rapport $^{20}Ne/^{22}Ne$ moins élevé dans la

signature chondritique (i.e. des météorites) que dans le gaz solaire initial (Moreira and Charnoz, 2016). Pour les gaz nobles lourds, l'incorporation de krypton et de xénon dans la matière organique des météorites induit un fractionnement isotopique dépendant de la masse, favorisant les isotopes lourds (Marrocchi et al. 2011; Kuga et al. 2016). Ainsi, la signature des gaz nobles portés par les météorites est fondamentalement différente de celle du gaz accrété par le Soleil. Alors que du néon d'origine "solaire" a été détecté dans le manteau source des OIBs, la signature primordiale (héritée) de l'argon, du krypton et du xénon dans des échantillons du manteau est chondritique (Holland and Ballentine, 2009; Caracausi et al. 2016; Péron and Moreira 2018), attestant ainsi du caractère hétérogène des sources d'éléments volatils sur Terre.

L'établissement de l'atmosphère terrestre n'a pas été un processus simple et linéaire. De fait, la fin de l'accrétion de la Terre fut marquée par un impact géant avec un corps planétaire de la taille de Mars, ayant notamment provoqué l'éjection de matériel en orbite de la proto-Terre et ainsi mené à la formation de la Lune. Cet épisode d'une extrême violence aurait eu lieu ≥ 40 Ma après la naissance du Système Solaire, lorsque la proto-Terre commençait à peine à se refroidir et à se solidifier (Kleine et al. 2005). Au cours de sa formation, la Terre a probablement connu plusieurs impacts géants similaires à celui qui a formé la Lune, celui-ci représentant le dernier en date. A chacun de ces épisodes, l'atmosphère en place était (au moins en partie) balayée, puis le manteau terrestre refondu et dégazé vers la surface. Au sein d'un océan magmatique, les matériaux les plus denses (e.g., Fe, Ni, éléments du groupe du platine) plongent et contribuent à former le noyau, tandis que les phases moins denses migraient vers la surface: on parle de différenciation planétaire. A la suite de l'impact géant ayant généré la Lune, l'atmosphère a continué à être affectée par de plus petits impacts, contribuant simultanément à son érosion et à son réapprovisionnement. La trace de ces impacts tardifs se reflète notamment dans la présence d'éléments sidérophiles (denses) en abondances relatives chondritiques dans le manteau de la Terre. Si ces éléments avaient déjà été présents sur Terre au moment de l'épisode d'océan magmatique ayant suivi le dernier impact géant, ils auraient naturellement plongé vers le noyau. Leur présence dans le manteau témoigne d'un "vernis tardif", correspondant à l'apport de matériaux chondritiques à une Terre déjà - au moins partiellement - solidifiée (Morbidelli and Wood 2015).

Les rôles respectifs de ce vernis tardif et du dégazage mantellique lors de la formation de la Terre ne sont pas bien compris. Le manteau source des MORBs présente un degré de dégazage largement supérieur à celui du manteau inférieur. Pourtant, le simple dégazage du manteau supérieur ne permettrait pas de reproduire le budget et la composition des gaz présents dans l'atmosphère. Notamment, la signature isotopique du xénon de l'atmosphère présente une anomalie nucléosynthétique (un déficit en isotopes produits par des processus de nucléosynthèse rapides, r-process) ne correspondant à aucun des réservoirs connus du Système solaire (le Soleil ou les chondrites; Pepin 1994). Cette particularité requiert donc la contribution d'un composant exotique, étranger au réservoir à partir duquel les planètes et

astéroïdes se sont formés. Pendant des décennies, les comètes ont été présentées comme les meilleurs candidats potentiels. Seulement, la caractérisation d'échantillons cométaires s'est longtemps limitée à leur analyse à distance, par spectroscopie, et à l'étude de poussières cométaires (collectées en Antarctique ou lors de missions spatiales - cf. the Stardust mission, NASA) contenant trop peu de Xe pour permettre une mesure isotopique. Les estimations de la potentielle contribution cométaire à l'atmosphère terrestre se sont donc basées sur des analogues de rapports élémentaires de gaz nobles dans la glace cométaire, issus d'expériences de laboratoire cherchant à reproduire le comportement des gaz nobles dans la glace d'eau à basse température et basse pression (Owen et al. 1992).

Les modèles de formation et d'évolution précoce de l'atmosphère ont longtemps expliqué sa composition actuelle, élémentaire et isotopique, en gaz nobles par des processus de fractionnement lors d'épisodes d'échappement hydrodynamique (pertes atmosphériques) dues aux impacts géants (Pepin 2003). Cependant, des travaux plus récents ont montré que des caractéristiques phares de l'atmosphère (telles que le rapport $^{20}Ne/^{22}Ne$ et $^{36}Ar/^{22}Ne$) pouvaient plus simplement être expliquées par un mélange bimodal entre un réservoir de composition solaire et une composante chondritique (de type chondrites carbonées, Marty 2012). De plus, l'analyse de la composition isotopique des gaz nobles dans des gaz de l'atmosphère ancienne piégés dans des barytines et quartz d'âges archéens ont montré que l'évolution isotopique du xénon atmosphérique, depuis sa composante primordiale jusqu'à une composition moderne, s'est étalée sur 2.5 Ga (Avice et al. 2018). En d'autres termes, le fractionnement isotopique du xénon atmosphérique, initialement incorporé dans le modèle d'évolution précoce de l'atmosphère par échappement hydrodynamique, serait finalement le résultat d'un processus d'évolution lente de l'atmosphère au cours des temps géologiques.

Le xénon de l'atmosphère moderne présente une troisième particularité: il est sous-abondant par rapport aux gaz nobles plus légers, d'un facteur 10 à 20, comparé aux rapports élémentaires typiquement mesurés dans les chondrites. Ce déficit pourrait avoir résulté d'une fuite atmosphérique ayant également fractionné ses isotopes; seulement, les autres gaz nobles, plus légers, auraient alors dû être également affectés, ce qui n'est pas le cas. Ainsi, soit cette fuite n'était pas thermique (non dépendante de la masse), soit il existe un processus insoupçonné qui aurait appauvri le Xe atmosphérique. Ce problème, connu depuis plusieurs décennies, a été appelé le "paradoxe du xénon manquant". Au cours de ces dernières années, de nombreuses études expérimentales ont proposé que le xénon "manquant" pourrait être piégé dans des réservoirs géochimiques (noyau, manteau, croûte). Dans ce cas, la sous-abondance de Xe dans l'atmosphère s'expliquerait par la séquestration de celui-ci dans des réservoirs cachés, inaccessibles à l'échantillonnage. Etant donné que la définition même du Xe manquant repose sur la comparaison de rapports élémentaires entre l'atmosphère et les météorites (e.g., Ar/Xe, Kr/Xe), un tel scénario requiert cependant la vérification que les gaz nobles plus légers ne subissent pas le même sort que le Xe en se retrouvant aussi séquestrés dans ces réservoirs cachés. Un tel piégeage doit aussi permettre de fractionner les isotopes du

Xe de l'ordre de 3-4 ‰/u, ce qui est considérable (voir invraisemblable) pour un élément inerte et lourd. La résolution du problème du xénon manquant par piégeage dans un reservoir terrestre solide doit aujourd'hui également prendre en compte l'aspect isotopique du paradoxe du Xe manquant. De récents modèles numériques montrent que l'échappement sélectif de Xe ionisé dans la haute atmosphère terrestre pourrait être à l'origine de l'évolution isotopique du Xe atmosphérique observée au cours de l'Archéen (Zahnle 2015; Zahnle et al. 2019). Ce mécanisme, reposant sur l'échappement d'hydrogène ionisé, entrainant le Xe^+ jusqu'à l'exobase de l'atmosphère où il pourrait alors s'échapper vers l'espace, pourrait (au moins en partie) expliquer le paradoxe du Xe manquant (Avice et al. 2018).

Une fois formée, l'atmosphère terrestre a évolué au cours des temps géologiques, offrant des conditions environnementales devenues progressivement propices à l'émergence de la vie. La Grande Oxygénation (GO; Holland, 2006), correspondant à une crise écologique majeure provoquée par la hausse du niveau d'oxygène dans l'atmosphère autour de 2.4 Ga, suscite un intérêt particulier. Elle marque la transition d'une atmosphère plutôt réduite, avec potentiellement du CH_4 et/ou H_2, à une atmosphère oxydante. Les causes exactes de ce bouleversement sont discutées. Par exemple, l'oxygène produit par photosynthèse oxygénique de cyanobactéries pourrait s'être accumulé dans les océans, avec une abondance initialement tamponnée par réaction avec le carbone organique, ou encore par le fer dissous (à l'origine des gisements de fer rubané, comme à Pilbara, en Australie de l'Ouest). Une fois ces puits d'oxygène saturés dans l'océan, l'oxygène aurait commencé à s'accumuler dans l'atmosphère, menant à terme au développement de la vie basée sur le métabolisme aérobie que nous connaissons aujourd'hui.

L'échappement d'hydrogène vers l'espace, par photolyse du CH_4 ou par photodissociation de H_2O dans la haute atmosphère, pourrait aussi avoir joué un rôle prépondérant dans l'oxydation progressive de la surface de la Terre (Zahnle et al. 2013). C'est ce même processus d'échappement d'hydrogène qui a été proposé pour permettre la fuite du Xe atmosphérique conduisant à son fractionnement isotopique (Zahnle et al. 2019). La GO semble notamment être contemporaine avec la fin de l'évolution du fractionnement isotopique du Xe atmosphérique (Avice et al. 2018). Aussi, avant la GO, les signatures isotopiques du soufre atmosphérique montrent des fractionnements isotopiques indépendants de la masse (FIM-S), liés à des réactions photochimiques n'ayant pu avoir eu lieu qu'en absence d'oxygène. Aucun FIM-S n'a été reporté à ce jour pour des échantillons plus récents que 2.4 Ga. La GO marque enfin, peut-être par coïncidence, le début du "regazage" de la Terre. Des traces de FIM-S de l'atmosphère archéenne retrouvées dans des basaltes des îles Cook (au Sud de l'Océan Pacifique) échantillonnant un réservoir profond influencé par le recyclage de croute océanique ancienne témoignent du fait que la subduction a débuté avant la GO (Cabral et al. 2013). Mais pour d'autres éléments volatils tels que l'eau et les gaz nobles, il semble que le "regazage" efficace de la Terre n'ait pu commencer qu'il y a environ 2.5 Ga. Avant cette date la subduction était essentiellement "sèche" (Parai et Mukhopadhyay 2018).

Aujourd'hui, les proportions de gaz nobles lourds atmosphériques recyclés dans les réservoirs source des MORB et OIB sont relativement similaires, avec ~ 80% du Kr et Xe présent dans le manteau qui proviendrait de la surface de la Terre (Parai et Mukhopadhyay 2015).

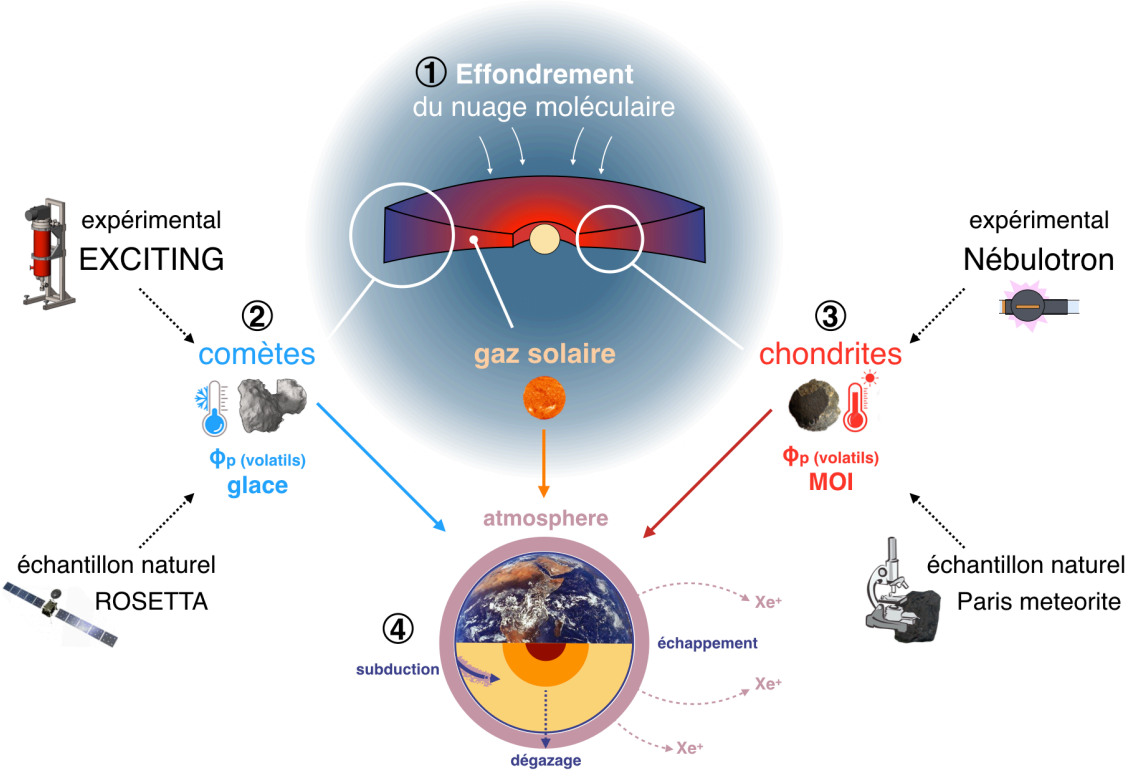

Fig. 1. Plan général de cette thèse mettant en lien les différents études sur (1) la distribution des solides et éléments volatils dans le disque d'accrétion, (2) la nature et composition des corps cométaires occupant les environnements froids du Système Solaire externe, (3) l'origine de la matière organique et des gaz rares dans les chondrites, (4) la formation et l'évolution de l'atmosphère en lien avec la Terre solide. Les trois sources principales d'éléments volatils pour la Terre sont les comètes, le gaz solaire, et les chondrites. ϕ_p(volatils) indique la phase porteuse principale des éléments volatils dans les corps célestes considérés (glace pour les comètes, MOI pour les chondrites). La caractérisation de ces derniers nécessite la combinaison des approches expérimentales à l'analyse d'échantillons naturels. Une fois la Terre et son atmosphère formées (4), nous discutons les processus d'interaction manteau-surface via dégazage et subduction, ainsi que les mécanismes de perte vers l'espace par échappement (comme invoqué pour l'évolution isotopique du Xe atmosphérique par exemple).

Dans cette thèse, je me suis intéressé à l'origine et à l'évolution des éléments volatils terrestres en adoptant une approche globale, dans le temps et dans l'espace. La première étape de ce travail a été de replacer la formation de la Terre dans son contexte astrophysique, en tentant de répondre à une première question: quelle est la nature des briques élémentaires ayant formé la Terre, et quelle fraction de l'atmosphère moderne pourrait avoir été héritée de cette accrétion primordiale? En effet, les matériaux constitutifs de la Terre portaient probablement en eux des gaz chondritiques et/ou solaires, qui pourraient avoir été en partie dégazés vers l'atmosphère au cours des épisodes d'océan magmatique et/ou par volcanisme.

Cette thèse s'interroge ensuite sur la contribution des apports tardifs (de type chondritique et/ou cométaire) à la surface de la Terre, après formation de la Lune. S'agissait-il principalement de matériaux pauvres en eau, formés proches du soleil? Ou alors de matière riche en éléments volatils, provenant du Système Solaire externe? Quelle est la contribution des matériaux de type cométaire? Répondre à ces questions implique, dans un premier temps, de connaitre la composition (et variabilité associée) en éléments volatils des corps chondritiques et cométaires. Pour cela, j'ai adopté, pour chacun de ces deux pôles, une approche expérimentale couplée à l'analyse d'échantillons naturels.

Concernant le pôle cométaire, cette thèse s'inscrit directement dans le cadre de la mission Rosetta (ESA, NASA) qui, pour la première fois, a permis l'analyse *in-situ* de la composition isotopique et élémentaire d'éléments volatils (incluant les gaz rares) cométaires (comète 67P/Churyumov–Gerasimenko; 67P/C-G). En particulier, nous avons montré dans une publication à *Science* (Marty et al. 2017) que l'anomalie nucléosynthétique si caractéristique du précurseur du Xe atmosphérique était liée à la contribution de ~20% de Xe cométaire portant cette même anomalie (déficit relatif en isotopes produits par processus rapide). L'ensemble des données gaz rare obtenues sur la comète remet en question la représentativité des expériences de laboratoire visant à simuler le comportement des gaz rares dans la glace amorphe, analogue cométaire, requérant ainsi de nouvelles investigations. Pour cela, j'ai construit un système expérimental nommé EXCITING (pour ***E****xploring* ***X****enon in* ***C****ometary* ***I****ce by* ***T****rapping and* ***I****rradiating* ***N****oble* ***G****ases*) permettant de former et de faire évoluer des glaces amorphes porteuses de gaz rares, de 20 K à 300 K, sous irradiation UV. Des résultats préliminaires obtenus au Laboratoire de Spectroscopie des Glaces (Jet Propulsion Laboratory, JPL, NASA) en collaboration avec le Dr. Murthy S. Gudipati suggèrent qu'une partie du Xe retenue dans la glace d'eau au delà de la température de sublimation du Xe (~65 K) pourrait être fractionnée en faveur des isotopes lourds par rapport à la composition isotopique du gaz initialement piégé. La ligne EXCITING a été construite pour pouvoir tester ces résultats préliminaires, dont les implications sont brièvement discutées dans ce manuscrit.

Concernant le pôle chondritique, j'ai pu analyser au cours de cette thèse la composition en gaz rares de la météorite carbonée la plus primitive qui soit à ce jour à notre disposition sur Terre, la météorite de Paris. Les résultats de cette étude sont reportés dans un papier publié en 2018 à *Meteoritics and Planetary Science*, discutant notamment l'origine de la phase Q qui, ubiquiste dans tous les types de chondrites, est la principale phase porteuse des gaz rares lourds dans les météorites. Cependant, la nature même de la phase Q est mal comprise, bien qu'elle semble être intimement liée à la matière organique insoluble (MOI). Des expériences de plasma (Nébulotron) conduites par Maia Kuga au CRPG pendant sa thèse (2015) ont démontré que des composés organiques formés par dissociation et ionisation de CO, dans des conditions analogues à celles du DPP, pouvaient piéger les gaz rares avec des abondances, rapports élémentaires et rapports isotopiques similaires à ce qui est observé dans

la phase Q par rapport à la composition initiale du gaz solaire. Combinée avec d'autres analyses moléculaires et isotopiques de la MOI des météorites, ces résultats suggèrent une origine nébulaire de la matière carbonée présente dans les météorites. Cette dernière est généralement composée à 80% de MOI, les 20% restants étant constitués de matière organique soluble (MOS), dont la diversité chimique présente un intérêt prébiotique tout particulier. Je me suis intéressé à la caractérisation moléculaire et isotopique de la MOI et MOS produite par des expériences de Nébulotron, avec différentes conditions expérimentales - notamment en faisant varier la proportion de H_2 dans la décharge, de $< 1\%$ à $> 60\%$. Ceci a requis le développement d'un Nébulotron nouvelle génération, atteignant un vide poussé (10^{-7} mbar) et permettant de travailler avec des mélanges gazeux haute pureté. La comparaison de nos résultats avec l'analyse des phases organiques retrouvées dans les météorites suggère que le processus de synthèse organique dans les régions ionisées du disque d'accrétion permet d'expliquer une partie des caractéristiques de la MOS et MOI des météorites (Bekaert et al. 2018a, *The Astrophysical Journal*). La MOI produite dans le Nébulotron ne présente pas un degré d'aromatisation suffisant par rapport aux échantillons naturels. Ceci peut être expliqué soit par (i) des rapports H/C plus importants dans le disque d'accrétion que dans nos expériences, soit (ii) par des processus de maturation secondaire liés à l'altération aqueuse et/ou thermique des composés organiques sur leur corps parent (astéroïde). De même, la MOS synthétisée ne présente pas une diversité chimique comparable à celle des météorites. D'autres sources de MOS, notamment par photochimie des glaces du Système Solaire externe et/ou altération aqueuse astéroïdale, ont probablement contribué au produit final de la MOS extraterrestre. Enfin, la matière organique des météorites présente de larges variations isotopiques de l'azote, avec des enrichissements en ^{15}N qui ne sont pas reproduits dans le Nébulotron. Cette signature pourrait indiquer l'effet de réactions photochimiques ayant eu lieu dans le DPP, hypothèse qui pourrait être testée par de nouvelles simulations de photochimie organique en phase gazeuse.

Une des questions centrales concernant la distribution des solides et des éléments volatils dans le Système Solaire jeune concerne les processus d'homogénéisation/séparation des poussières du DPP. Dans l'introduction de ce manuscrit, j'insiste sur l'état d'avancement de notre connaissance concernant le taux de mélange des différents réservoirs du disque, et les implications quant à la nature des matériaux constitutifs de la Terre. La turbulence du gaz constitue le principal processus menant à l'homogénéisation des poussières du DPP. Dans cette thèse, je présente des résultats de simulations numériques de transport de poussières et de particules organiques produites dans les régions ionisées du DPP, pour proposer un modèle unificateur de l'origine de la matière organique extraterrestre. Le code numérique utilisé permet de simuler l'évolution dynamique du DPP, avant la formation précoce des planètes géantes. Ces dernières auraient joué un rôle majeur dans la structuration dynamique du disque, et potentiellement mené à l'établissement d'une dichotomie nucléosynthétique entre deux grandes familles de météorites (les carbonées et les non-carbonées), séparées

spatialement par une barrière physique matérialisée par l'orbite de Jupiter (Kruijer et al. 2017). C'est précisément l'analyse de ces anomalies nucléosynthétiques et leur comparaison avec des échantillons terrestres qui permet de retracer l'évolution de la nature des matériaux chondritiques ayant formé la Terre (Dauphas 2017).

En combinant nos données et celles de la littérature pour définir les compositions élémentaires et isotopiques des pôles chondritiques et cométaires, nous proposons un modèle de mélange permettant de reconstituer la composition théorique de l'atmosphère primitive de la Terre (Bekaert et al. en révision à *Scientific Reports*). Ce modèle est basé sur les contraintes isotopiques des gaz rares de l'atmosphère, et notamment la quantité de Xe cométaire nécessaire pour former le précurseur du Xe atmosphérique (Marty et al. 2017). Nous déterminons ainsi que les comètes, ayant contribué à hauteur de 20% au Xe et au Kr atmosphérique, n'auraient apporté que quelques pourcents tout au plus de l'eau, du carbone, des halogènes et de l'azote terrestres. Le principal de ces derniers proviendrait de matériaux chondritiques, potentiellement de type chondrites à enstatite - notre meilleur analogue des briques élémentaires constitutives de la Terre (Dauphas 2017). Ces dernières appartiennent à la famille des chondrites non carbonées, formées relativement proche du Soleil dans le Système Solaire interne. Aucun scénario ne semble cependant satisfaire toutes les contraintes isotopiques et élémentaires de l'atmosphère, avec par exemple le néon, qui requiert une large contribution de chondrites carbonées (formées dans le Système Solaire externe) pour former l'atmosphère (Marty 2012).

Ainsi, le dégazage de la Terre solide, les apports tardifs à l'atmosphère, le recyclage des réservoirs du surface par subduction dans le manteau terrestre, et les processus d'échappement vers l'espace ont conjointement façonné l'atmosphère que nous connaissons aujourd'hui, et rendu la surface de la Terre habitable. Le timing exact de l'émergence et du développement de la vie est cependant mal contraint. L'identification des plus anciennes traces de vie (stromatolithes, microfossiles, carbone biogénique) est sujette à controverse (Javaux, 2019). Ces témoins potentiels de la vie primitive sont souvent altérés, partiellement métamorphisés et/ou ont été contaminés par des sources de matière organique plus récente au cours des temps géologiques. Pour pouvoir identifier un composé organique ancien comme témoin de vie primitive, il est nécessaire de s'assurer de sa biogénécité (i.e., du fait qu'il ait bien été produit par des processus biologiques et non abiotiques) et de sa syngénécité (i.e. qu'il est bien aussi ancien que sa roche hôte). Ce dernier point est crucial étant donné que des générations plus récentes de matière carbonée pourraient avoir contaminé les échantillons organiques anciens, biaisant ainsi notre détermination de l'évolution temporelle des différentes formes de vie. Comme observé dans les météorites, les gaz rares lourds peuvent être trouvés en grande abondance dans la MOI terrestre (appelée kérogène une fois isolée de la roche hôte). Dans cette thèse, nous proposons de combiner notre connaissance de l'évolution isotopique du Xe atmosphérique avec l'analyse de kérogènes archéens: si les kérogènes sont capables de piéger et de conserver une composante du Xe atmosphérique de l'époque à

laquelle ils se sont formés, le degré de fractionnement isotopique de celui-ci par rapport à l'atmosphère moderne permettrait de donner un âge modèle de formation du kérogène. Le premier échantillon que nous avons testé pour cette méthode a permis de démontrer que les kérogènes anciens pouvaient préserver du Xe de l'atmosphère archéenne, et que le kérogène étudié était probablement syngénétique de sa roche hôte (âges de la roche hôte et âge modèle concordants; Bekaert et al. 2018c, *Science Advances*). L'analyse de davantage de kérogènes archéens, âgés de 3.5 Ga à 1.8 Ga, a cependant montré que la méthode de datation basée sur les isotopes du Xe ne pouvait pas s'appliquer de façon systématique, et qu'en cas de non-correspondance entre l'âge modèle et l'âge de la roche hôte, il était difficile d'apporter des contraintes sur la syngénécité de l'échantillon (Bekaert et al. 2020, *Precambrian Research*).

Ce travail de thèse s'inscrit donc dans le contexte général de l'origine et de l'évolution des éléments volatils sur Terre, soulevant un certain nombre de problèmes encore non résolus à ce jour. Parmi eux, se pose la question de la répartition des éléments volatils dans le Système Solaire. En collaboration avec Yves Marrocchi (Marrocchi et al. 2018, *Earth and Planetary Sciences*), nous avons estimé l'origine et l'abondance de l'eau dans différents corps parents des chondrites carbonées. Ces résultats semblent en apparente contradiction avec le scénario des chondrites carbonées ayant accrété au delà de l'orbite de Jupiter, les signatures isotopiques et concentrations en eau correspondant davantage à une composition locale, dérivée du Système Solaire interne. De même, les témoins de contribution cométaire au réservoir d'accrétion des chondrites et planètes sont limités, requérant potentiellement l'intervention d'une barrière physique (Saturne?) entre ces deux réservoirs (comètes et chondrites). La nature et l'origine des composés organiques observés dans les comètes sont aussi inconnues. S'agit-il du même matériel que celui présent dans les météorites? La MOI cométaire porte-t-elle aussi la signature Q si ubiquiste dans le réservoir chondritique? Seule l'analyse en laboratoire de suffisamment (quelques mg) de matériel cométaire, dans le cadre d'une mission spatiale de retour d'échantillon, nous le dira. Ce travail de thèse confirme enfin qu'aucun processus connu ne permet aujourd'hui d'expliquer toutes les caractéristiques (isotopiques, structurales et moléculaires) des composés organiques trouvés dans les météorites, suggérant une multiplicité des sources et processus secondaires.

Comme je l''expose dans l'introduction de cette thèse, la nature des matériaux chondritiques ayant formé la Terre au cours de ses différentes phases d'accrétion (accrétion principale, impact géant ayant formé la Lune, vernis tardif) est débattue. Chaque phase d'accrétion pourrait, suivant les modèles, avoir peu ou largement contribué à l'apport des volatils terrestres. Comment réconcilier les différents traceurs géochimiques de la nature des briques constitutives de la Terre et de son atmosphère représente un enjeu majeur qui nécessitera de mieux contraindre l'effet des processus géologiques (impacts géants, océans magmatiques, subduction, échappement atmosphérique) sur la composition de l'atmosphère terrestre. Ce travail de thèse s'inscrit dans un projet de financement européen (European Research Council, bourse PHOTONIS 695618 octroyée à B. Marty).

Table of abbreviations

^{13}C-NMR: ^{13}C Nuclear Magnetic Resonance spectroscopy
67P/C-G: 67P/Churyumov–Gerasimenko
amu: atomic mass unit
Ar: Argon
CC: Carbonaceous Chondrites
DFMS: Double Focusing Mass Spectrometer
EC: Enstatite Chondrites
EUV: Enhanced Ultra Violet
eV: electron volt
FTIR: Fourier Transform Infrared Spectroscopy
FT-Raman: Fourier Transform Raman Spectroscopy
Ga: billion years ago
GC-MS: Gas Chromatography Mass Spectrometry
Py GC-MS: Curie point pyrolysis Gas Chromatography Mass Spectrometry
GOE: Great Oxidation Event
Gyr: billion years
He: Helium
IOM: Insoluble Organic Matter
ISM: InterStellar Medium
Kr: Krypton
LHB: Late Heavy Bombardment
Ma: million years ago
MCC: Metal-rich Carbonaceous Chondrites
MDF: Mass Dependent Fractionation
MIF-S: Mass Independently Fractionated Sulphur
MO: Magma Ocean
MORB: Mid-Ocean Ridge Basalt
Myr: million years
Ne: Neon
OC: Ordinary Chondrites
OIB: Ocean Island Basalt
PPD: ProtoPlanetary disk
PSN: ProtoSolar Nebula
ROSINA: Rosetta Orbiter Spectrometer for Ion and Neutral Analysis
SIMS: Secondary Ion Mass Spectrometry
SOM: Soluble Organic Matter
UPB: Ureilite Parent Body
UV: Ultra Violet
and last but not least **Xe:** Xenon

Abstract

The Earth was likely formed from the heterogeneous accretion of solid materials originating from various heliocentric distances in the Solar System. Depending on their origin in the Solar System, the rocky building blocks from which our planet formed comprised variable amounts of volatile elements that were subsequently reshuffled through geological processes to shape the Earth's surface into the unique habitat for life we see today. The compositional variability of Earth's accreting materials therefore reflects the heterogeneous distribution of volatile elements in the early Solar System. The extent of volatile element incorporation into growing planetesimals was controlled by their location with respect to the different snow lines (e.g., water, CO). Within the inner region of the protoplanetary disk (PPD), planetary bodies were probably more reduced, drier, and exposed to higher temperatures and irradiation doses than those accreting outwith the orbit of Jupiter. Further out in the Solar System, cometary bodies would have been limitedly processed within the protosolar nebula, therefore representing the most pristine materials. Their remoteness has however hampered precise analysis of their composition, especially for isotopic ratios, making their potential contribution to the volatile inventory of terrestrial planets difficult to substantiate.

From the analysis of mantle-derived samples, it is possible to probe the accretion and degassing history of the Earth, therefore investigating the potential for accretionary volatiles within different mantle reservoirs to have contributed to form the atmosphere. Uncertainties regarding the initial composition of the Earth surface reservoir however preclude accurate determination of how it evolved over geological periods of time. Nonetheless, geochemical witnesses of major changes in the composition of the atmosphere, such as the Great Oxidation event some 2.5 Ga, are preserved in the geological records. Their analysis can provide insights into the timing of life's emergence and evolution, but significant challenges remain regarding the identification of life's oldest remnants due to poor preservation rates.

If there is one fundamental question that this PhD tries to tackle, it could be formulated as follows: how did the Earth's atmosphere form and evolve through time to produce a unique habitat in the Solar System that is sustainable for life? This manuscript is split into six main sections. The first one constitutes a broad bibliographical review presenting the main concepts and outstanding questions that motivated this work. It is itself divided into nine sections that cover a wide range of themes going from stellar nucleosynthesis processes to the distribution of solids and volatile elements in the PPD, from the composition of comets and chondrites to the formation of the solid Earth and its atmosphere, broaching the different scenarios that have been advocated regarding the source(s) of volatile elements on Earth.

Chapter 1 presents the methods for noble gas analysis. It summarises the main noble gas components in geological samples and processes of elemental and isotopic fractionation,

before introducing, for each element, some of the main applications in geo- and cosmochemistry. I then detail the procedures dor analysing the noble gases, from the extraction, separation and purification procedures, to the analysis. I provide some information regarding the specifications of the Helix MC Plus mass spectrometer used during this thesis, including the tunings of the source and performances of the machine. Finally, I detail the data reduction and error propagation procedure. The general organization of this manuscript then follows the flowchart presented Fig. 1:

- **Chapter 2** presents the results obtained on the Xe isotopic composition of 67P/C-G, and their implications for (i) the origin of the atmospheric Xe progenitor (U-Xe) and (i) closure age of the mantle-atmosphere system. Based on the volatile element isotopic composition of comet 67/C-G, I discuss the potential for it to be of presolar origin. Finally, I present our current understanding of the indigenous volatile element inventory of the Moon and its role as a witness to the late volatile contributions to the Earth.

- **Chapter 3** presents a series of experiments that I carried out at the Ice Spectroscopy Laboratory (Jet Propulsion Laboratory, Pasadena, USA) to investigate the potential for Xe-bearing chemical compounds to form within cometary water ice analogues upon photo-irradiation. The detection of mass-dependently fractionated Xe signatures in these cometary ice analogues motivated the conception and setting up of a new experimental system at the noble gas platform of CPRG. This setup, called EXCITING, allows for noble gas-bearing cometary ice analogues to be condensed under high vacuum, heated and/or irradiated with an ultra-violet lamp. Released noble gases can then be analysed by static mass spectrometry for high precision isotopic measurements. As I am finalizing my PhD, Matthieu Almayrac, new PhD student with Prof. Bernard Marty, is carrying out the first, promising measurements on EXCITING.

- **Chapter 4** discusses the main noble gas components in chondritic materials, emphasizing the cryptic origin of the ubiquitous phase Q. This component corresponds to the main carrier of heavy noble gases in primitive chondrites, and appears to be intimately linked with insoluble organic materials. We present the noble gas analysis of bulk and insoluble organic matter samples from the least altered carbonaceous chondrite known so far, the Paris meteorite. Previous analysis of this meteorite demonstrated the potential occurrence of interstellar-/cometary-like water in its matrix, but we found no evidence for it from our noble gas isotopic analyses. Our results however support the proposal that variable amounts of Xe-HL in chondrites are required to account for the intrinsic variability of Xe-Q.

- **Chapter 5** presents the isotopic and molecular characterization of organic materials produced by plasma experiments relevant to the process of organosynthesis in the ionised

regions of the protosolar nebula. A new, high-vacuum and high-purity Nebulotron was built for the purpose of this study. We show that organosynthesis can account for most, but not all, of the features of chondritic organics (soluble and insoluble fractions), pointing towards a complex and probably multistage origin of organic materials in meteorites. Based on a numerical model of dust transport by turbulent diffusion in PPDs, we propose that organic materials produced within ionised environments could have been transported throughout the disk and served as precursor for organic materials in any chondritic type.

- **Chapter 6** presents a new recipe to form the terrestrial atmosphere from chondritic and cometary precursors. Through mixing calculations between cometary and chondritic end-members, we propose a scenario accounting for the heavy noble gas signature of the atmosphere, including the missing Xe paradox. We estimate the cometary contribution to carbon, nitrogen, water and halogens within the Earth surface resevoir to be low, a few percent at most. Finally, by computing the present-day noble gas to water ratio of the atmosphere and considering how geological processes affecting the Earth surface reservoir (giant impact, magma ocean, subduction, escape to space) could have changed this ratio through time, we infer that the planetary bodies that supplied most of the volatiles in the atmosphere were presumably dry (similar to enstatite chondrites).

- **Chapter 7** discusses the temporal evolution of the terrestrial atmosphere, exposing the main issues related to determining the timing of life's emergence and development. I present a new method that has the potential to set constraints on the syngenetic origin of Archean organic materials (related papers presented in appendix). This relies on the facts that the isotopic composition of atmospheric Xe evolved through time, and that organic materials have a tendency to trap and preserve heavy noble gases from their formation environment. Hence, we propose to use the isotopic composition of potentially trapped Xe in Archean organic materials to provide them with model ages and test on their syngenetic origin. This method is applied to one sample with success, but appears to require additional analytical development to potentially deconvolute (and allow interpretation of) disrupted signals.

This manuscript contains four papers (published or under review) that are reported within the associated chapters (Marty et al. 2017 *Science*; Bekaert et al. 2019a *MAPS*; Bekaert et al. 2018a *APJ*; Bekaert et al. *under review at Scientific Reports*). Two additional papers are appended in the Supplementary materials (Bekaert et al. 2019c *EPSL*; Bekaert et al. 2020 *Precambrian Research*), and are briefly discussed in the main text of this manuscript.

Table of contents

Bibliographical review

Distribution of volatile elements in the Solar System and on Earth

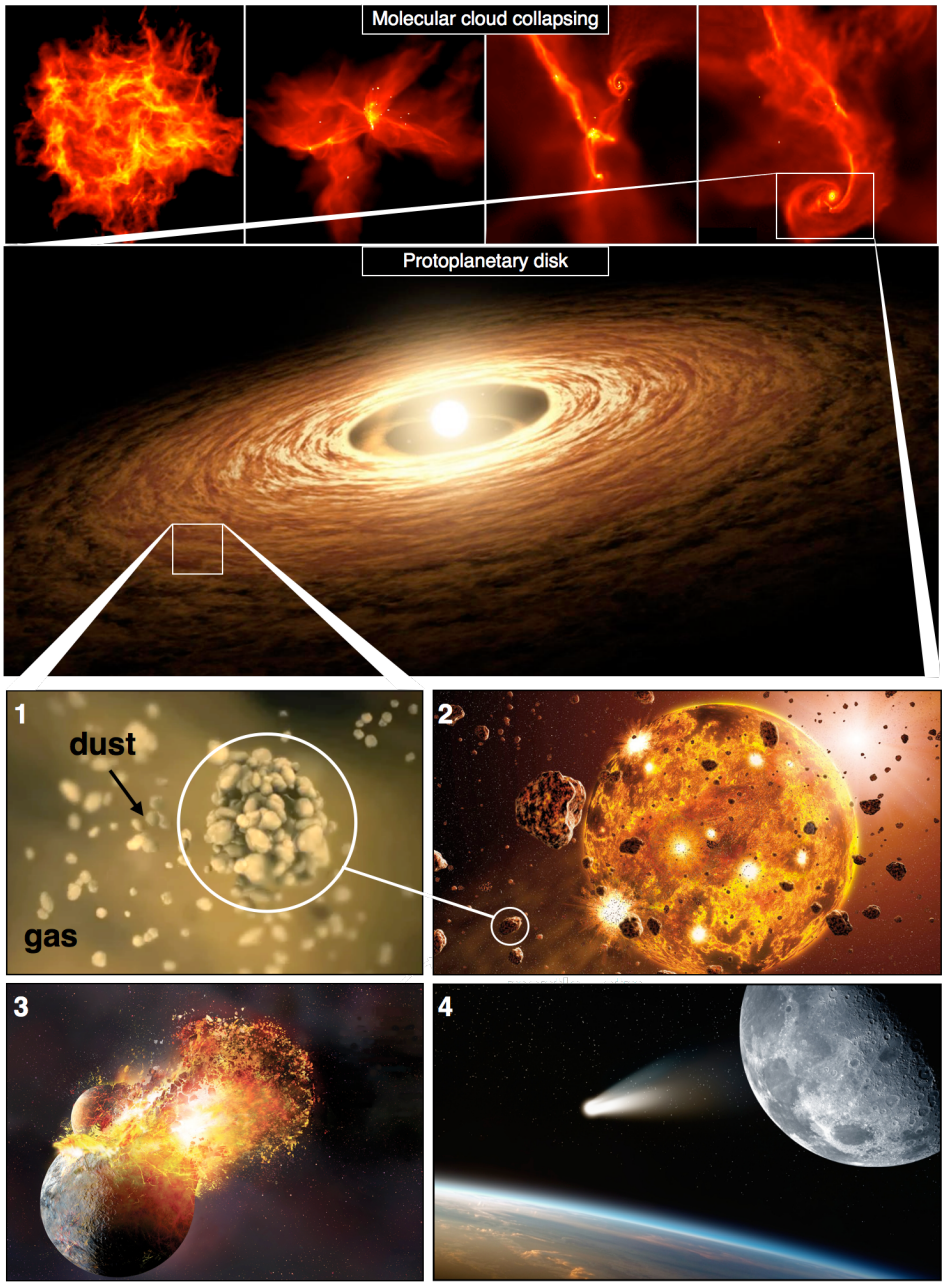

Fig. 2. Graphical abstract representating the main steps of planetary formation, from the collapse of the molecular cloud to the agglomeration of dust particles (1) into planetary embryos (2). At this stage, the two main sources of terrestrial volatile elements consist in the gas phase of the protosolar nebula, and solid materials (dust, pebbles, boulders, planetesimals) carrying trapped volatiles. The last stage of Earth's main accretion was marked by a giant impact with a Mars-sized object (3), which resulted in the formation of the Moon (4). Late supplies of cometary and/or chondritic materials to the Earth surface (4) are thought to have contributed a significant amount of volatile elements to form the terrestrial atmosphere, which happened to provide a unique habitat for the blossoming of life. Each fundamental step in the process of building a habitable Earth will be discussed in the following bibliographic review.

1. Formation of the Solar System

Ordinary atomic matter in the universe (referred to as "baryonic" matter by astronomers) originates from the primordial nucleosynthesis of H, He and Li some 13.8 Ga, and subsequent production of heavier elements in stars (stellar nucleosynthesis). Newly formed generations of stars therefore inherit starting compositions reflecting that of the parental molecular clouds from which they formed by gravitational collapse. During the first stages of stellar formation, protoplanetary disks (PPDs) of gas and dust orbiting around stars naturally form as a consequence of the conservation of angular momentum during collapse (Fig. 2). An accretionary disk is characterised by the outward transport of angular momentum, with significant inward mass transport to the protostar and/or loss by photo-evaporation processes (Williams and Cieza, 2011). Within PPDs, solid materials may condense from the gas phase on the timescale of a few Myr, and agglomerate to form increasingly larger bodies such as asteroids and planets (Fig. 2). Further out in the PPD, pristine bodies (e.g., comets) may form from the accretion of significant fractions of interstellar matter, with limited to no processing within the PPD. From the inner edge of the Solar System to its most remote outer reaches, asteroidal and cometary materials therefore inform us on the origin and evolution of matter from which planets formed.

Planetary objects that accreted (i) early enough to contain large amounts of now-extinct radioactive elements (e.g., ^{26}Al), and/or (ii) to a sufficiently large size to accumulate significant quantities of accretionary and radioactive heat, would have experienced early planetary differentiation (Kleine et al. 2002). Such planetary bodies would thus have developed compositionally distinct layers, whereby elements such as Fe and Ni would sink to form the metallic core, leaving behind a predominantly silicate mantle and crust. Conversely, some of the most pristine meteorites collected on Earth, known as chondrites, have not been modified due to melting or differentiation processes. Their major constituent materials formed at different times and locations within the PPD, from hot and ionised environments close to the star to colder environments in the outer Solar System (see section 3). As such, the analysis of chondrites provides a temporal and spatial record of the matter that formed our Solar System, yielding unique insights into the structure and composition of the PPD. In addition, a small fraction of primitive chondrites preserves inheritance of presolar material that was delivered to the PPD and incorporated into their parent bodies with little modification. These grains, which have not been homogenised with the bulk material of the Solar System, preserve the isotopic compositions of their stellar sources, which can be extremely anomalous with respect to the bulk Solar System composition (section 4). Nucleosynthetic anomalies in meteorites reflect compositional heterogeneities in the material that was inherited from the parental molecular cloud. Over the last decade, the study of nucleosynthetic anomalies in meteorites has greatly improved our understanding of the dynamical organization of the PPD and provenance of meteorites (section 6).

2. Dust growth processes and volatile element distribution in the PPD

In two dimensions, PPD are classically represented with a triangular shape, with the height of the disk increasing with heliocentric distance (Fig. 3). The motion of small dust particles is tightly coupled to that of the gas, which is controlled by turbulence (Charnoz et al. 2011). Small particles may therefore be transported throughout the disk by turbulent diffusion (typical initial dust-to-gas ratios in PPD is ~10^{-2}), until they reach a sufficient size by coagulation to decouple from the gas motion. The motion of large particles in the disk is then controlled by gravitational processes, starting with their settling to the midplane and radial inward drift towards the central star (Fig. 3).

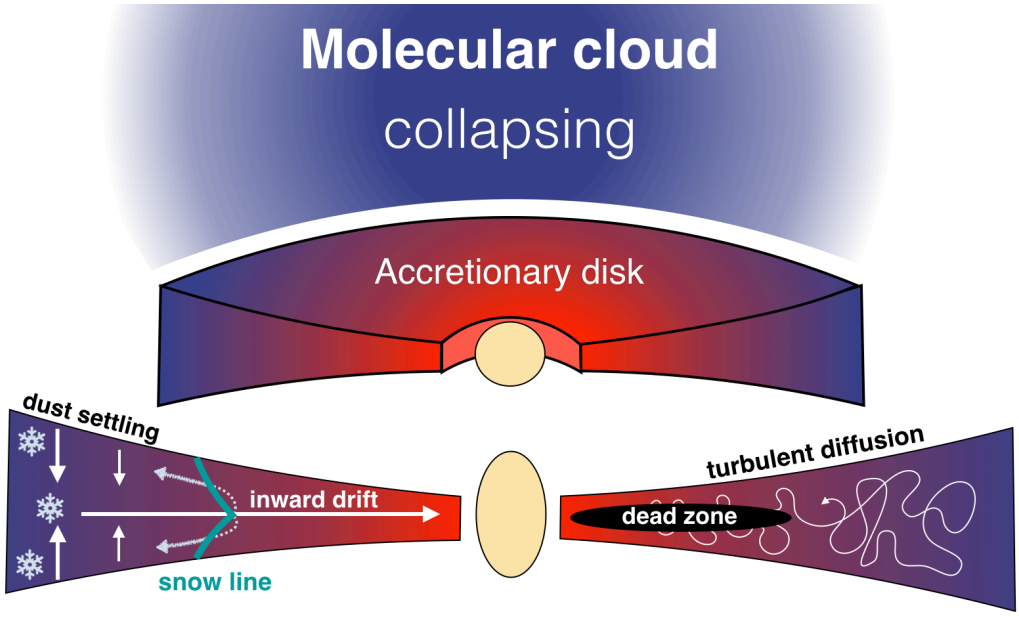

Fig. 3. Dust motion in an accretionary disk. Grain size evolution through fragmentation/coagulation leads to the formation of larger and larger particles that then settle to the midplane and experience radial drift to the central star. When icy particles cross the snow line, their water contents evaporate and are transported backward to the outer Solar System, where they recondense. Small particles remain coupled to the turbulent motion of the gas and can be transported throughout the PPD. The dead zone region, where turbulence significantly drops, represents a preferential location for dust growth into larger objects, potentially up to planetesimal-sized objects (Charnoz et al. 2012, 2019; Misener et al. 2019).

The PPD is intrinsically heterogeneous, in the sense that it is characterised by extreme temperature, pressure and compositional gradients related to the presence of a growing star at its centre, and a cold interstellar medium at the edges. Close to the star and at the surface of the disk, the gas is exposed to ultra-violet (UV) and X-ray irradiation by the central star, therefore reaching high temperatures and high degrees of ionization (Fig. 4; Chapter 5). At the midplane of the disk, temperature drops significantly from a few hundred K to a few tens of K, with much higher gas densities. This region is shielded from the stellar irradiation, and the

main source of heat corresponds to viscous heating. At sufficient heliocentric distance from the central star, the temperature may be low enough for the gas to condense in the form of ice.

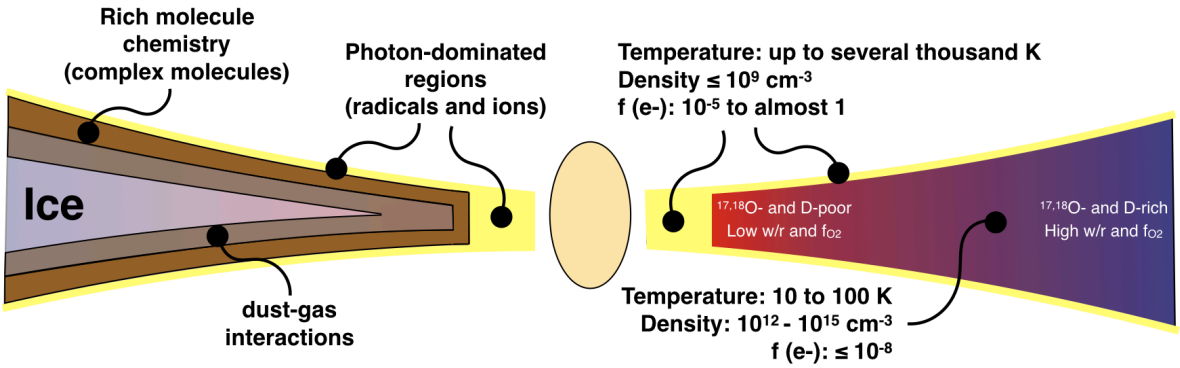

Fig. 4. Schematic representation of the chemical structure of the PPD. On the left, are represented the photon-dominated regions, warm molecular layer (with a rich molecule chemistry) and dust-gas interaction region. On the right, are reported indicative temperatures, density and fractional abundances of electrons (adapted from Walsh et al. 2012).

The distance from a central protostar at which water ice grains can form corresponds to temperatures ≤ 150-170 K, which is signified by the "snow line". The position of the snow line is crucial for the repartition of water in the Solar System. Inward from the snow line, water exists as vapour, and cannot therefore be efficiently accreted onto planetary bodies (low water to rock ratios; w/r, Fig. 4). Beyond the snow line, significant amounts of water ice can be accreted onto planetary bodies (high w/r; Fig. 4). Overall, reducing conditions are thought to prevail within the inner parts of the disk (low f_{O2}; Fig. 4), whilst the outermost environments of the PPD would be oxidised (high f_{O2}; Fig. 4). From an isotopic perspective, outer Solar System water (sometimes referred to - perhaps misleadingly - as interstellar water, Vacher et al. 2016) is richer in heavier isotopes (^{17,18}O, D), compared to the inner, ^{16}O-rich Solar System (Marrocchi et al. 2018). Such a gradient in hydrogen and oxygen isotopes can be accounted for by either self-shielding of ^{16}O-rich nebular CO gas by UV light (Yurimoto and Kuramoto, 2004), or the outermost parts of the disk being significantly influenced by unprocessed molecular cloud material with high D/H and ^{17,18}O/^{16}O ratios due to ion-molecule reactions at low temeprature (Sakamoto et al. 2007).

The analysis of the grain size profiles in PPD, as inferred from optical depth profiles, suggests more than one order of magnitude increase in particle sizes when moving in from r ~ 100 AU to ~ 10AU scales (where AU corresponds to the Astronomical Unit, i.e. the distance between the Sun and the Earth; Testi et al. 2014; Fig. 5a). However, there are two main barriers that impede dust growth in a PPD: bouncing and fragmentation of colliding particles. The first one can be overcome by taking into account the presence of ice and organic materials coating the surface of dust particles and largely enhancing their sticking probabilities, therefore resulting in their rapid growth to decimetre-sized objects (Ros and Johansen, 2013). The second barrier, also known as the "meter-sized barrier", is related to the fact that the speed of

large particles in the disk is a function of their size, and is maximal (~100 $m.s^{-1}$) for meter-sized objects, therefore resulting in their rapid radial drift to the central star and efficient destruction in case of a collision.

Several models advocating local fluid instabilities in the disk have been proposed to overcome this barrier. For instance, "streaming instabilities" can be triggered at particular disk locations where the local volume density of solids exceeds that of the gas (Simon et al. 2016; Fig. 5b). In this case, the drag felt by solid particles orbiting in a gas disk can lead to they spontaneously group into clumps, which then gravitationally collapse and rapidly form planetesimals through the efficient accretion of inward drifting pebbles (pebble accretion; Johansen & Lambrechts 2017). Runaway growth can then occur, when gravitational focusing enhances the accretion cross-section of protoplanets. At the same time, growth by accretion of planetesimals is self-limited as the growing planetesimal excites the random velocities of nearby planetesimals, therefore decreasing the efficiency of gravitational focusing (Kokubo and Ida 2000; Leinhardt and Richardson 2005).

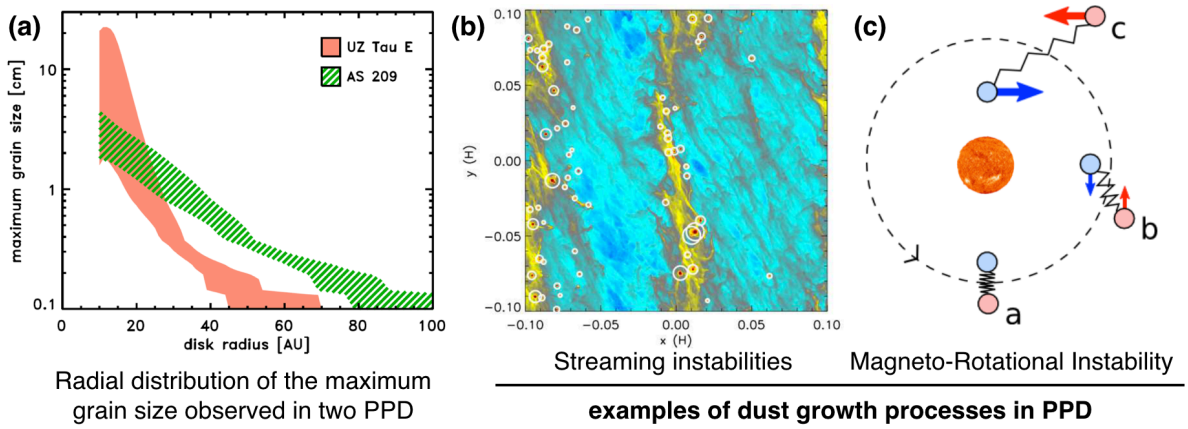

Fig. 5. Processes of dust accretion in PPD. (a) Radial distribution of the maximum dust size for two PPD (AS 209 and UZ Tau E) from resolved continuum emission measurements at 9 mm (Testi et al. 2014). (b) Caption of streaming instabilities in MHD simulations (Simon et al. 2016). (c) Schematic representation of the Magneto-Rotational Instabilities.

Alternatively, Magneto-Rotational Instabilities (MRI) may arise within the ionised regions of the disk, from the action of the magnetic field: when the angular velocity of the gas decreases with heliocentric distance, magnetic tensions between neighbouring particles, subject to differential rotation, cause the extraction of angular momentum from the disk and allow rapid accretion to take place (Bai 2011; Fig. 5c). Models of PPD structure consider a turbulent envelope of plasma (the ‘active zone’, where MRI take place; Fig. 4) encasing an extensive body of quiescent gas (the "dead zone"; Fig. 3-4; Chapter 5). Within the dead zone, the effective viscosity (i.e., turbulence) is greatly reduced due to the disc self-shielding against stellar radiation. As a consequence, mass accumulation is greatly enhanced near the outer edge of the dead zone, where the inward migration of planetary cores is considerably slowed down

(the so-called "planet trap" mechanism; Morbidelli et al. 2007), enabling their further growth and runaway gas accretion. In particular, accretion of planetesimals is enhanced around the snow line (Hyodo et al. 2019), where (i) water evaporation changes the mass and sticking efficiency between grains of the drifting pebbles, therefore slowing drift and increasing local mass, and (ii) ice evaporation and retro-diffusion of water that recondenses just outside of the snow line (Fig. 3) locally concentrates icy pebbles, therefore triggering planetesimal formation via streaming instability (Drazkowska & Alibert 2017).

Dust growth processes in PPDs, from micron-sized particles to pebbles, planetesimals and planets, therefore arise from non-linear processes that mainly take place at the midplane of the disk. Planet migration and gas accretion onto large (at least Mars-sized) planetary embryos - as witnessed by the presence of solar nebula-derived Ne in the lower mantle of the Earth (Williams and Mukhopadhyay 2019) or presence of solar-derived Xe on Mars (Matthew and Marti, 2001)-, are consequences of gravitational interactions between growing planets and the gas phase of the PPD. Importantly, the dispersal of the gaseous disk in a few Myr is a natural trigger for dynamical instabilities, yielding a debris disk characterised by a protracted phase (~100 Myr) of destructive collisions among residual planetesimals (Gilmour and Filtness, 2019).

Meteorites are the remnants of planetary formation and, as such, their study provides crucial information regarding early processes taking place in the PPD. For instance, iron meteorites consist overwhelmingly of an iron-nickel alloys that originate from the cores of planetesimals that were disrupted by large collisions in the early Solar System (Kleine et al. 2005). Some other meteorites (e.g., angrites and ureilites) represent the old partially melted mantles that belonged to large, differentiated planetesimals in the inner Solar System (Goodrich et al. 1987). Chondrites have been subject to limited processing since their "sedimentation" in the disk and therefore represent direct snapshots of the environmental conditions prevailing in the region of their accretion. Further out in the Solar System, icy objects referred to as comets appear to also be extremely pristine, but their relation to the PPD and bulk Solar System material is not clear as they could originate from the interstellar medium, with little relation to the disk's materials. The next sections detail the main constituents and types of meteorites and comets, discussing their implications for the distribution of volatile elements and processes of dust transport within the PPD.

3. Meteorites and their constituents

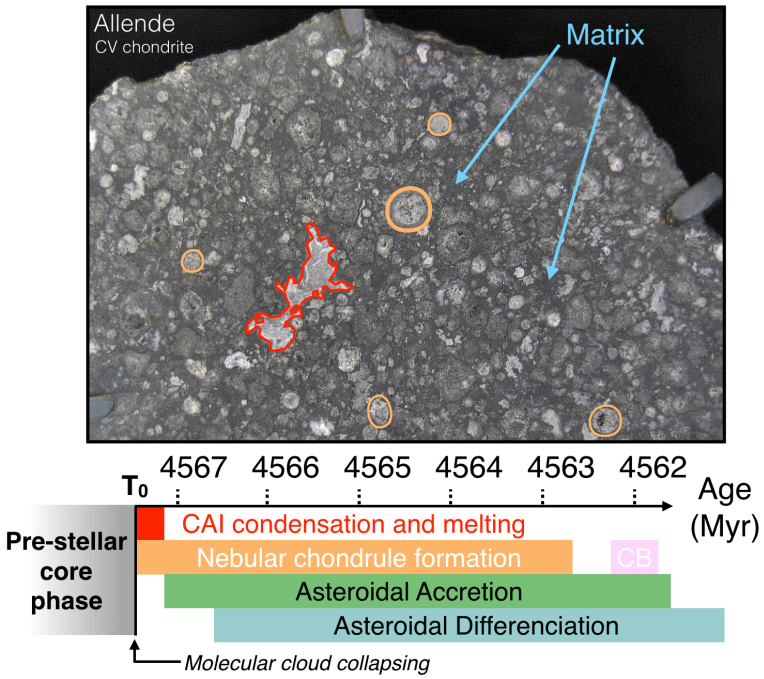

Fig. 6. Main constituents of meteorites as seen from a section of the Allende meteorite (CAI, chondrules, matrix), with the timescales of formation of CAIs, chondrules, and asteroids reported on the timeline below (adapted from Connelly et al. 2017; Kruijer et al. 2012). We also note the later formation of CB chondrules, presumably from a vapour–melt plume produced by a giant impact between planetary embryos after dissipation of the PPD (Bollard et al. 2015).

The main constituents in chondrites are Calcium-Aluminium rich Inclusions (CAI), chondrules and matrix (Fig. 6). CAIs represent the oldest surviving material of the PPD, constituting the first mineral assemblages to have condensed nearby the proto-Sun (Connelly et al. 2017). As they are the first solids produced in the PPD, their age effectively sets the time zero of our Solar System. Chondrules are round silicates formed ~1-3 Myr after CAIs as droplets in the gas of the PPD, before having been accreted to their parent asteroids. The origin of chondrules in the PDD remains debated, with both planetary and nebular origins proposed (Marrocchi et al. 2018). Finally, the matrix represents a heterogeneous assemblage of mineral debris, alteration phases and organic materials, forming a gangue that holds the meteorite constituents together and contains the majority of the volatile elements in chondrites. Given its fine-grained, reactive nature, the matrix of chondrites provides a sensitive indicator of secondary processes such as heating, shock, and aqueous alteration (Scott et al. 1988).

Meteorite classes are distinguished on the basis of the parent body from which they presumably originate, with the different parent bodies of meteorites having accreted at different times and locations in the PPD (Fig. 7). The parent bodies of enstatite chondrites (EC) and ordinary chondrites (L, LL, H, R; referred to as OC) likely accreted within the inner

Solar System, whilst carbonaceous chondrites (e.g., CM, CV, CI and CR; referred to as CC) accreted beyond the orbit of Jupiter (Kruijer et al. 2017). Importantly, the different types of chondrites have variable proportions of the three chondritic constituents. For instance, CAIs typically comprise 0.5 - 3 vol.% of CC and < 0.1 vol.% of EC and OC, which may at first glance seem surprising given the fact that CAIs formed close to the Sun, i.e. within the EC and OC accretion reservoir. Also, whilst EC and OC contain limited amounts of matrix, CM and CI chondrites typically contain 70 vol.% and >99 vol.% matrix, leading to the very volatile-rich character of these meteorites. Phyllosilicates are the most important hydrated phases in chondrites, reaching 95 vol.% in the most altered CM chondrites (Howard et al., 2015). Water contents in chondrites are indicators of the amount of water ice that was accreted by the parent bodies at the time of their accretion, and can therefore be used to constrain the distribution of volatile elements in the early Solar System (Marrocchi et al. 2018).

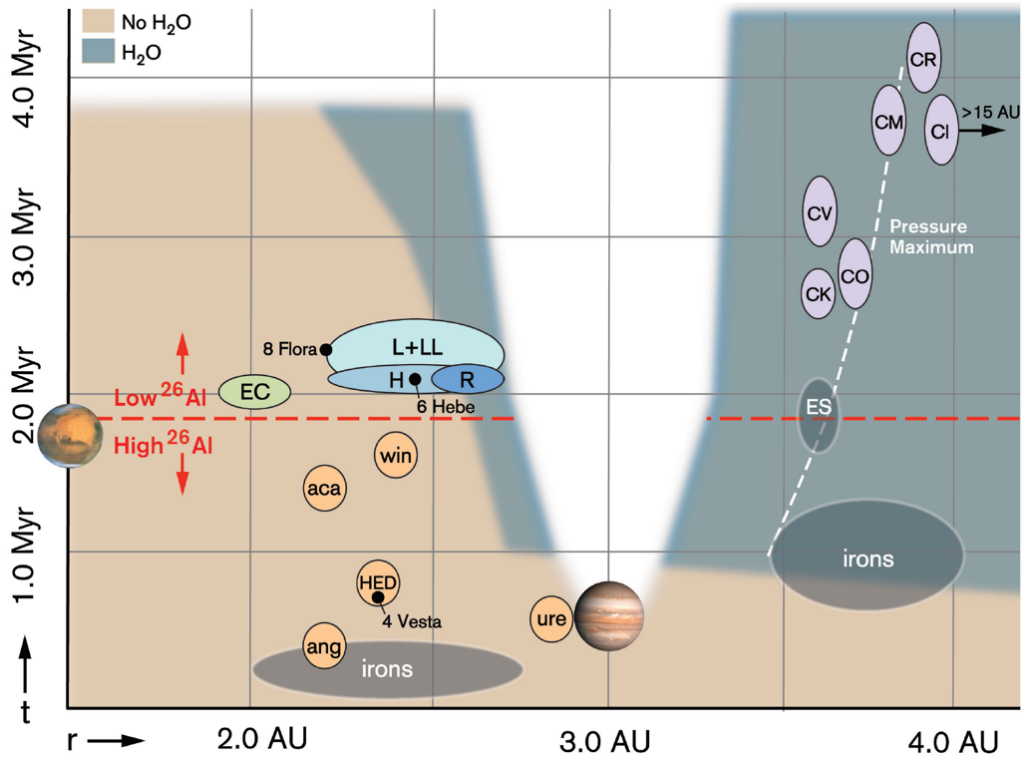

Fig. 7. Summary plot of when and where different meteorite types could have formed in the PPD (from Desch and Alexander, 2018). irons: iron meteorites. ang: angrite parent body. HED: howardite–eucrite–diogenite, thought to originate from the asteroid Vesta. L, LL, H and R are OC. CK, CO, CV, CM, CI and CR are CC.

Here below, I briefly describe key observations on CAI, chondrules and matrix, and discuss their implications regarding the dynamics and composition of the PPD.

3.1. Calcium Aluminium-rich Inclusions (CAI), the great travellers

CAIs formed at temperatures in excess of 1400 K, which can only be obtained in close proximity to the Sun. Such a close proximity to the Sun at the time of their formation is in line with their budgets of short-lived radionuclides (^{10}Be, ^{26}Al, ^{41}Ca, ^{53}Mn; with half-lives ≤ 50 Myr), which can be most easily be accounted for via spallation reactions close to the proto-Sun (Dauphas and Chaussidon, 2011). According to both U-corrected Pb-Pb dating (Connelly et al. 2017) and ^{26}Al-^{26}Mg systematics (Villeneuve et al. 2009), they represent the first solids to have condensed in the PPD. They are typically hundreds of microns in size although they can reach up to ~ 1 cm in diameter (e.g., in CV chondrites), implying their motion in the disk would not be coupled to that of the gas, so they would spiral into the Sun by radial drift and be cleared out from the PPD in ~1 Myr (Desch et al. 2018). Yet, CAIs are found to be the most abundant in carbonaceous chondrites (thought to have accreted beyond Jupiter) and relatively rare in other types of chondrites originating from the inner Solar System, where they condensed. Samples collected from Comet 81P/Wild2 by the Stardust mission (section 5) also contained grains with similar mineralogy and oxygen isotope composition to CAIs, suggesting efficient outward, PPD-wide transport after their synthesis (McKeegan et al. 2006).

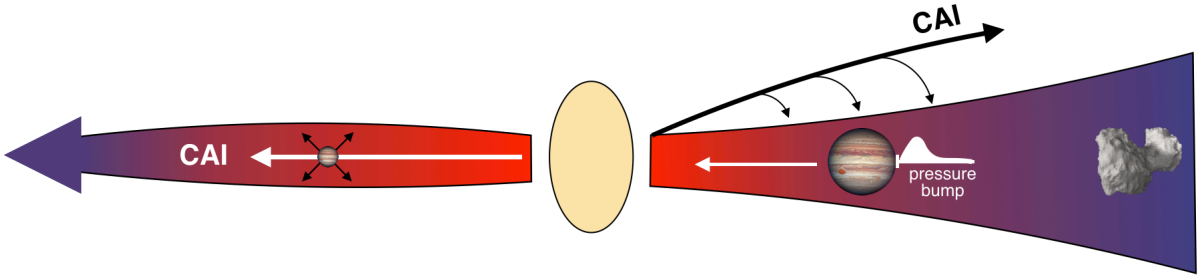

Fig. 8. Potential mechanisms accounting for the transport of CAIs to the outer Solar System. On the left, we show the process of early viscous spreading (Nanne et al. 2019), transporting CAIs to the outer Solar System before formation of Jupiter's embryo. On the right, we show the effect of disk winds (Haugbølle et al. 2019), which could transport CAIs to the formation region of CC and comets. Beyond the orbit of Jupiter, CAIs could have been accumulated in a pressure bump (Desch et al. 2018).

Two competing mechanisms, namely viscous spreading at the midplane (Yang and Ciesla, 2012) and disk winds (Haugbølle et al. 2019), are considered to have accounted for the efficient transport of refractory materials to the outer solar system (Fig. 8). The rapid expansion of early infalling material by viscous spreading would indeed readily transport early CAIs from their condensation region to the outer solar system (Nanne et al. 2019). In disk wind models, ionised gas is transported outward and upward from the disk along magnetic field lines, possibly dragging small grains whose motion would then decouple from that of the gas, therefore resulting in the grains raining back on to the disk a greater heliocentric distance (Nittler and Ciesla 2011). Both of these models could have contributed to the presence of CAIs in the outer solar system, including the accretion reservoir of CC and the comet-forming region.

CAIs transported to the outer System could have be acumulated at the outer pressure bump of early-formed Jupiter, where CV chondrites (most enriched CC in CAIs) presumably accreted.

3.2. The nebular origin of chondrules

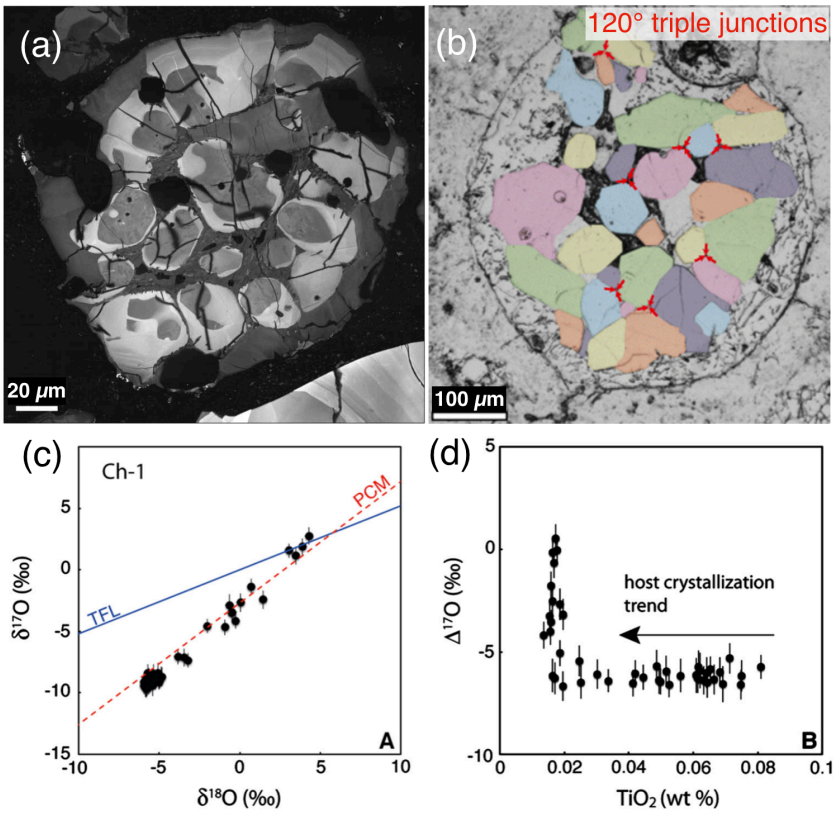

Fig. 9. Recent evidence for the nebular origin of chondrules. (a) High-resolution cathodoluminescence images of representative type I chondrules (Libourel and Portail, 2018) showing the presence of relict olivine grains within individual olivine crystals. (b) Reflected-light optical images of a chondrule where some 120 ◦ triple junctions between Mg-rich olivine crystals are indicated by red arrows (Marrocchi et al. 2018). (c) The oxygen isotopic composition of individual olivine crystals in a chondrule shows important mass-independent variations that are accounted for by gas-melt interactions. (d) Relict olivine grains, which are depleted in TiO_2, show large variation in O isotope composition (Marrocchi et al. 2018).

Whilst CAIs condensed from a ^{16}O-rich reservoir, chondrules formed from transient heating events in a ^{16}O-poor reservoir of the disk (further out in the PPD; Marrocchi et al. 2018). Chondrules represent 20-80 vol% of chondritic matter (except for CI chondrites, which have $<$ 1 vol% chondrules) but the mechanism(s) and role of "nebular" and "planetary" processes in their formation are still debated. The observation of granoblastic textures with 120° triple junctions within chondrules requires prolonged and high-temperature planetary conditions (Libourel and Krot 2007; Fig. 9). However, recently observed variations in Δ^{17}O, even in individual chondrule showing 120° triple junctions, are inconsistent with their derivation from planetary interiors (Marrocchi et al. 2018; Fig. 9). High-resolution

cathodoluminescence images of chondrules recently revealed the occurrence of relict olivine grains in chondrules (Libourel and Portail, 2018; Fig. 9). The O-isotopic variations between host olivine grains of chondrules demonstrate that chondrules formed via recycling of precursor material (probably akin to amoeboid olivine aggregates, the second oldest condensates of the Solar System after CAIs; Komatsu et al., 2018) in different environments of the PPD (Marrocchi et al. 2018). This requires complex nebular histories of protracted gas-melt interaction in the PPD, with changes in the O isotope composition of the gas phase being interpreted as reflecting the transport of chondrule precursors from the inner (^{16}O-rich) to the outer (^{16}O-poor) PPD (Marrocchi et al. 2018).

3.3. The matrix: main storage reservoir of volatile elements in chondrites

The matrix groundmass in chondrites consists of amorphous iron-rich silicate particles intimately mixed with phyllosilicates, sulfides, alteration phases (e.g., tochilinite) and organic materials. Alteration phases arose from the melting of water ice grains initially accreted within the parent body, and subsequent interaction with reactive, fine-grained minerals. The study of amorphous silicate hydration processes and formation of alteration phases in chondrites provides information on the physical and chemical environment of meteorite parent bodies (Vacher et al. 2019). A significant proportion of organic material in chondrites was likely accreted as a mixture of soluble and insoluble molecules, together with water ice grains. Part of the organic component was mobilised at the micrometre scale during parent body processes involving water circulation (Le Guillou et al. 2014; Garvie and Buseck, 2007; Zega et al., 2010; Fig. 10).

The matrix of carbonaceous chondrites encompasses a wide diversity of organic materials, mostly consisting of macromolecular and polyaromatic structures, referred to as Insoluble Organic Matter (IOM) due to being insoluble in common organic solvents (Derenne and Robert, 2010). The soluble fraction of extraterrestrial organic materials (SOM) contains carboxylic acids, ketones, aldehydes, amino acids, and a complex assortment of small molecules considered to be biologically relevant (Pizzarello, 2006). The SOM component in meteorites is commonly thought to originate from low temperature photochemical processing of icy grains in the interstellar medium and/or outer solar system (Nuevo 2012). Alternatively, this component could derive from aqueous processes on the parent body of meteorites. Although the origin of water and organic matter in chondrites remains uncertain, their close spatial association at the micron scale suggests that mutual interactions occurred during parent body aqueous alteration (Le Guillou et al. 2014; Fig. 10).

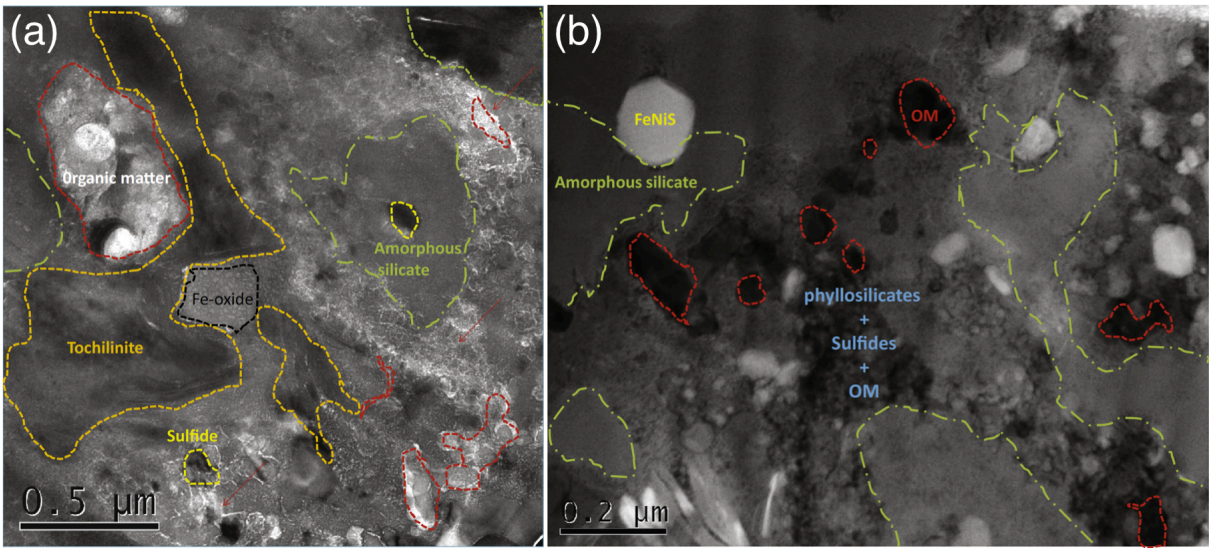

Fig. 10. (a) Bright-field TEM image of a 2 x 2 µm altered region of MET 00426 showing the close association between organic matter (red) and tochilinite (orange). (b) Dark-field STEM image of a FIB section showing patches of amorphous silicate recrystallizing into phyllosilicates. The latter are closely associated with aromatic OM. From Le Guillou et al. (2014).

Chondritic IOM is thought to represent a common component widespread in the solar system and found in any chondritic type regardless of the degree of thermal modification (Piani et al. 2012). Its widespread nature in the Solar System could originate from the fact that (i) it was inherited from the parental molecular cloud and therefore was present throughout the PSN, (ii) it originates from an ubiquitous synthesis mechanism within the PSN (Fischer-Tropsch reactions, plasma synthesis), and/or (iii) large scale mixing in the PPD was efficient enough to result in it being widely distributed in the disk, regardless of the synthesis mechanism. The macromolecular assemblage of aromatic compounds characterizing the IOM component in chondrites suggests synthesis from relatively high temperature, organic-radical-rich environments of the PSN (Derenne & Robert 2010; See chapter 5). The possible detection of chondritic IOM-like materials in comets (Fray et al. 2016) may suggest, here again, significant radial transport within the protosolar nebula.

The matrices of primitive chondrites preserve presolar components that were delivered to the PPD and incorporated into chondritic parent bodies with little modification. These are mainly carried by interstellar grains (e.g., diamonds, silicon carbides, graphite) that were produced in previous generations of stars and are presently found within the matrix of primitive chondrites (see section 4). The isotopic composition of presolar grains is extremely anomalous with respect to the bulk solar system composition, and can therefore be used to track structural and compositional heterogeneities in the early solar system, as well as investigate the relationship between the PPD and its parental molecular cloud (see section 6). Finally, one of the most puzzling questions in cosmochemistry regards the existence of a chemical complementarity between chondrites matrix and chondrules. This model proposes

that chondrules and matrices in carbonaceous chondrites are genetically linked based on their Mg/Si ratios (Hezel and Palme, 2010), and possibly molybdenum isotopes (Budde et al. 2016). In this case, the early accretion of planetesimals, as witnessed by the very old age of iron meteorites parent bodies in both the inner and outer Solar System (Kruijer et al. 2017), was inefficient such that significant amounts of unprocessed dust suspended in the PPD remained for millions of years, before accreting onto the parent bodies of primitive chondrites (Nittler and Ciesla 2011). However, as illustrated Fig. 3, the PPD is a turbulent environment where radial mixing is efficient, except in the dead zone(s), where dust rapidly accretes to form planetesimals (Chapter 5). To have preserved closed systems between chondrules and the materials making up the matrix, for significant periods of time in the PPD, appears complicated - possibly indicating that such complementarity does not exist, or is limited to certain areas in the PPD (Zanda et al. 2018, van Kooten et al. 2019).

4. Presolar and planetary noble gas components in chondrites

Stellar nucleosynthesis during supernovae, neutron-star mergers and cosmic-ray spallation reactions gradually drives the chemical evolution of galaxies and their interstellar media (McWilliam 1997). Heavier elements are assembled within stars by neutron capture processes (n,γ) known as the s-process (for slow neutron capture) and r-process (for rapid neutron capture, occurring on a timescale of a few seconds), whilst some other existing nuclei photo-disintegrate through the p-process (Meyer 1994). Each process predominantly occurs in different astrophysical environments: whereas the s-processes is dominant in AGB stars, r-process occurs in neutron mergers and supernovae. Nucleosynthetic mixtures of p-, s- and/or r-processes can be preserved into interstellar solid matter referred to as presolar grains, produced in the outflowing and cooling gas phases of previous generations of stars. As presolar grains remained mostly intact throughout their journey from star outflows to the PPD, they retain significant information about the environmental conditions of their birthplaces (e.g., Fig. 11).

The fact that interstellar matter could be preserved in primitive chondrites was discovered thanks to the detection of strange noble gas isotopic compositions. In 1964, Reynolds and Turner discovered the first nucleosynthetic isotope anomaly, corresponding to a strange Xe component (now known as Xe-HL) in the Renazzo CC. In 1969, Black and Pepin found a Ne component that was so rich in ^{22}Ne that it could not arise from any known process occurring within the Solar System. The carriers of such noble gas anomalies were progressively identified, with the finding that these were associated with HF-HCl residues, and so corresponded to refractory, non-silicate phases. Shortly after the finding of presolar noble gas components in meteorites, presolar signatures were found for other elements such as oxygen in 1973 (Clayton et al. 1973). The formal identifications of presolar diamonds as Xe-HL carriers (Lewis et al. 1987) and presolar SiC as Ne-E and s-process Xe carriers (Bernatowicz et al. 1987) was achieved in 1987, with graphite being discovered shortly after, in 1990 (Amari et al.

1990). Although they only constitute at most 0.2 ‰ of the total mass of primitive meteorites, many different types of presolar grains have been identified in meteorites (e.g., diamonds, graphite grains, silicon and titanium carbides, corundum grains, spinels, hibonites, silicon nitrides, etc.). Since oxides are rare in meteorites and parent body alteration processes easily destroy silicates, only three types of presolar grains contain significant exotic noble gas components: diamonds, graphite and silicon carbides (SiC). Presolar diamonds carry P3, P6, and HL components (mainly from combinations of r and p-processes), whilst SiC and presolar graphite grains carry the N and G (s-process) components (Ott, 2014).

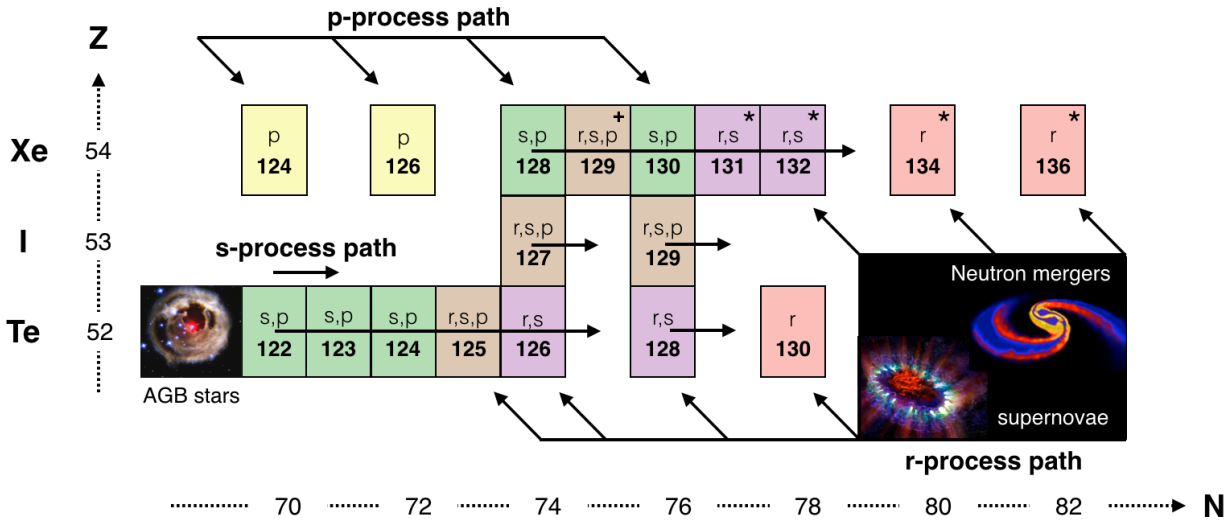

Fig. 11. Nucleosynthetic production pathways of Xe isotopes (adapted from Clayton and Ward 1978). Te: Tellurium. I: Iodine. Xe: Xenon. Z: atomic number or proton number. N: neutron number. The p-process (p, in yellow), s-process (s, in blue) and r-process (r, in red) paths are shown with the black arrows. When an isotope can be produced by several of these processes, it is color-coded by the color mixing (e.g., green is s + p, purple is r + s, brown is r + s + p).

Noble gas nucleosynthetic components in meteorites can either be separated during stepwise heating experiments (e.g., the Q component), or through extrapolation of mixing relationships with the composition of one end-member being assumed (e.g., the P3, HL, G and N components; e.g., Gilmour 2010). They can be compared with "planetary" components in meteorites, which were mainly trapped from gas of solar composition (Gilmour 2010). Relative noble gas abundances within presolar and planetary components are reported Fig. 12 (adapted from Ott 2014), showing that they all have lower He-Ne-Ar-Kr/Xe ratios than the solar composition. He and Ne are for instance much more depleted in Q than heavier noble gases, potentially pointing towards different mechanisms controlling their incorporation into meteorites (Ott, 2014). Interestingly, the subsolar component found in enstatite meteorites appears to be the least fractionated with respect to solar (with high Ar/Xe and Kr/Xe), except for Ne (the $Ne/Xe_{subsolar}$ being almost as low as that of phase Q; Fig. 12). The presence of this

component in subsolar gas-carrying ECs can significantly raise the bulk Kr/Xe of the meteorite, without significantly affecting their isotopic composition (Chapter 6). This is thought to reflect the direct implantation of solar gas into chondrule precursors, being mainly carried by enstatite and friable phases in enstatite chondrites that experienced significant solar implantation close to the Sun in the protosolar nebula (Okazaki et al. 2010).

From an isotopic point of view, the Ne and Xe isotopic compositions of presolar materials are the most diagnostic for identification of nucleosynthetic components in meteorites. Very little variation is observed for Ar isotopic ratios within presolar and Solar System components (Fig. 12), except for the anomalous G component. **For Ne,** the bulk inventory of chondrites is dominated by presolar components carried in diamonds (i.e., P3, HL, P6). As P6 and HL contributions are difficult to resolve for Ne, the adopted HL composition probably contains both components (Huss and Lewis, 1994; Fig. 12). The planetary Ne-A (Pepin, 1967) corresponds to a mixture of these three components (P3, HL, P6), plus a contribution from ^{22}Ne-rich Ne-G (Ott, 2014). **For Xe** (and heavy noble gases in general), the planetary component Q is dominant (Chapter 4).

As is the case for the ^{22}Ne-rich Ne-G and ^{38}Ar-rich Ar-G components (Fig. 12), the extremely anomalous heavy noble gas G signature carried out in SiC and presolar graphite is a reasonable match to the theoretical signature of the s-process (e.g., P3; Fig. 12). The "normal" component of SiC, labelled N, is closer to the solar composition, however with marked excesses in ^{134,136}Xe that may not be compatible with an r-process origin (Gilmour and Turner, 2007). Interestingly, the Xe-HL and Xe-P6 components in nanodiamonds show strong enrichments in r-process $^{134\text{-}136}$Xe, along with enrichments in the light isotopes, especially ^{124,126}Xe, which are produced by p-process. These excesses in heavy (H) and light (L) Xe isotopes in Xe-HL, although originating from distinct nucleosynthetic processes, appear to occur in constant relative abundances in presolar diamonds. This peculiar feature of Xe-HL is discussed in Chapter 4.

The Kr and Xe isotope compositions of air, P3, Q (and by extension AVCC) show relative depletions of the light isotopes relative to the heavy ones, when compared to solar wind. P3-gases, which are presumably trapped at the surface of nanodiamonds due to radiation-induced damages (Huss and Lewis, 1994), are thus fractionated from their presumed precursor by the same extent as Q-Xe is from solar wind, suggesting they were incorporated into their host phases through similar trapping mechanisms (Ott 2014; Chapter 4).

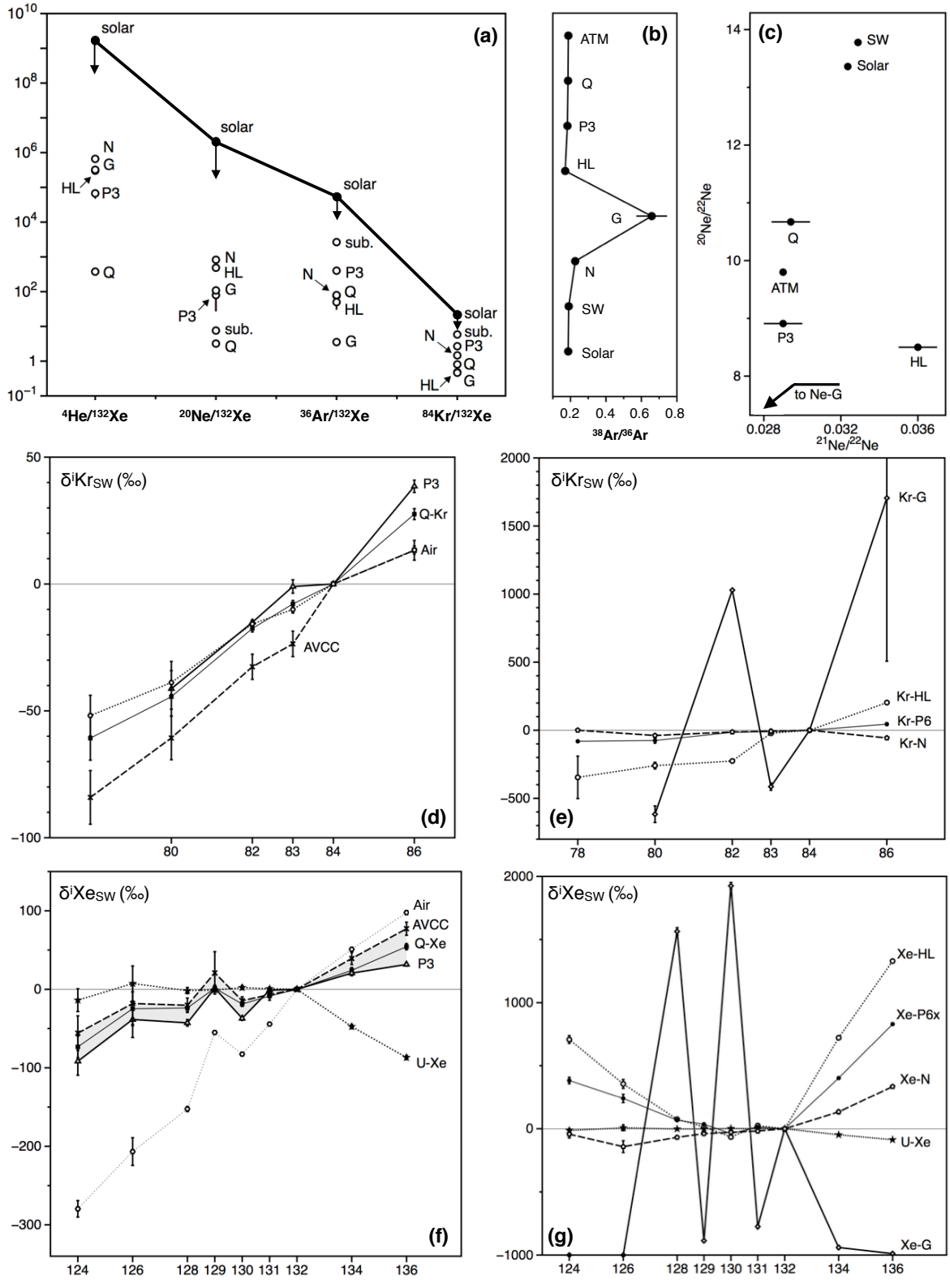

Fig. 12. Elemental (a) and isotopic (b-g) composition of planetary and presolar noble gas components trapped in meteorites. The isotopic compositions for Ar, Ne, Kr and Xe are represented in pannel b, c, d-e and f-g, respectively. For Kr and Xe, the left panels show planetary components with more "normal" signatures, whilst right panels show more extreme compositions corresponding to presolar components. Data are from Busemann et al. (2000), Ott (2014), Gilmour (2010).

5. The cometary reservoir

Comets are dusty, icy bodies (often called "dirty snowballs") orbiting around the Sun at large heliocentric distances. Most cometary nuclei travelling throughout the Solar System either originate from the putative Oort cloud (long-period comets, with orbital periods > 200 years) or the Kuiper Belt (short-period comets, with orbital periods < 20 years). Whilst Kuiper belt objects extend beyond the orbit of Neptune with an estimated mass of a few to ten percent of Earth's (Gladman et al. 2001), the yet to be directly observed Oort cloud would correspond to a spherical distribution of icy bodies in the far reaches of the Solar System. Beyond the Kuiper Belt are also scattered disk objects, which have eccentric orbits crossing those of the giant planets and extending further away from the Sun than the Kuiper belt (Fig. 13).

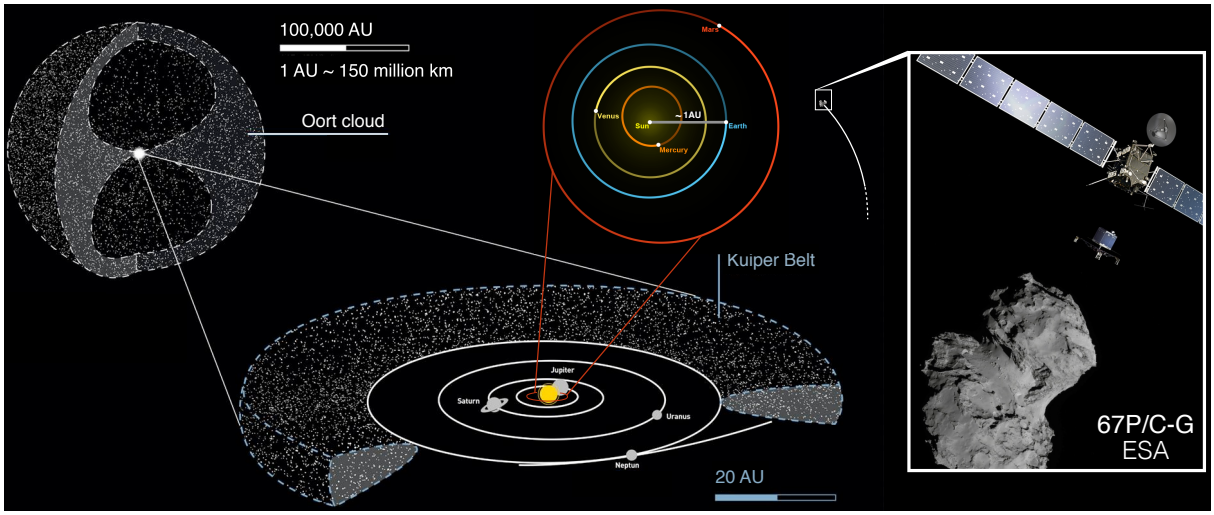

Fig. 13. Comet reservoirs in the Solar System, Oort Cloud and Kuiper Belt. Comet 67P-C/G, a Jupiter-Family comet, has recently been visited by the ESA probe Rosetta. Adapted from Donald K. Yeoman's illustration (NASA, JPL).

The Oort cloud, Kuiper belt and the scattered disk are thought to derive from the same parent population of comets known as the primordial trans-Neptunian disk, which was largely dispersed during a phase of temporary dynamical instability of the giant planets (Brasser and Morbidelli 2013). Jupiter-family comets (e.g., comet 67P/Churyumov–Gerasimenko; Fig. 13) are thought to arise from collisions between Kuiper Belt objects, which were then launched towards the Sun by the gravity of Neptune and further perturbed by the gravity of Jupiter. On the other hand, Halley-type comets are "intermediate-period comets" that would originate from much further out in the Solar System, probably the spherical Oort Cloud. Such icy bodies launched from the Oort Cloud to the inner Solar System may have been perturbed into plunging orbits by the gravitational influence of passing stars or a giant molecular cloud, or tidal forces from the disk and bulge of the Milky Way, which would have been sufficient to set them on highly elliptical paths through the inner Solar System (Gladman 2005). Halley-type

comet and long-period comet orbital inclinations can therefore be very high (as they originate in the spherical Oort cloud), compared to the relatively low orbital inclinations of Jupiter-family comets.

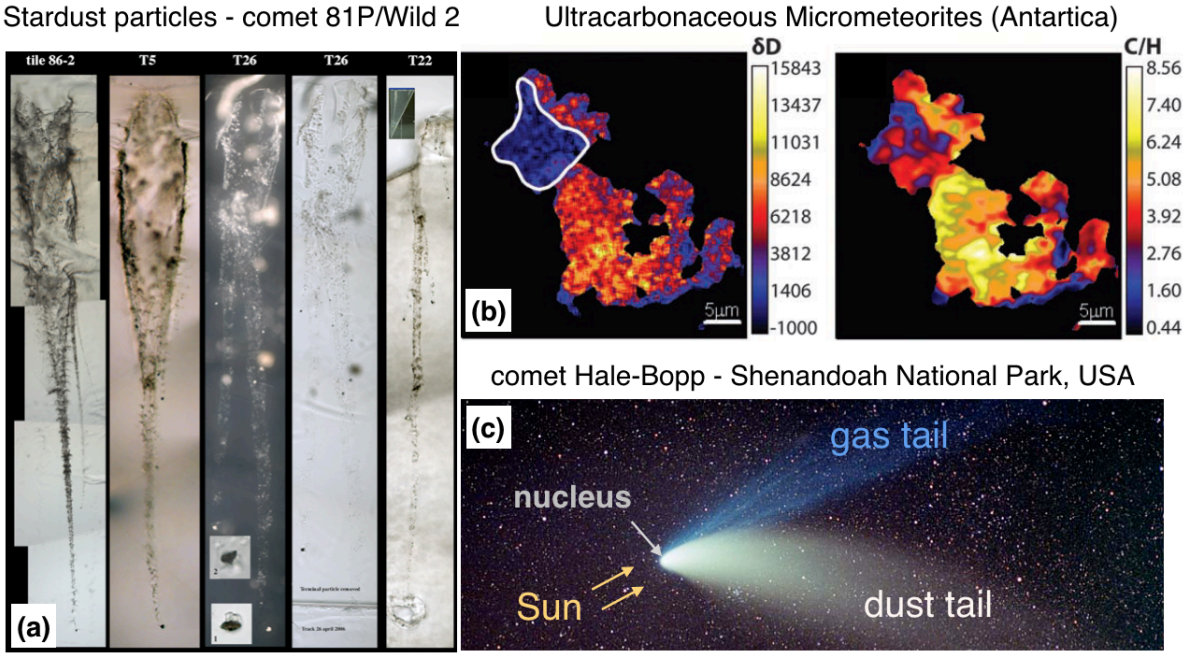

Fig. 14. Different ways of analysing cometary material. (a) Comet particle tracks in aerogel from the Stardust Mission. From National Geographic Image collection, NASA. (b) NanoSIMS (nano secondary ion mass spectrometry) isotopic and elemental maps of UCAMMs (from Duprat et al. 2010). (c) Remote spectroscopy observations of comets, with the example here of comet C/1995 O1 (Hale-Bopp). Adapted from the picture Loke Kun Tan, Red Rock state Park, California (USA).

Our knowledge of the starting composition of the Solar System, potentially preserved in its outer reaches, is limited by the lack of cometary material available on Earth for analysis. Previous analysis of cometary material has either come from micrometeorites or samples returned from comet 81P/Wild2 by the pioneer Stardust spatial mission (Fig. 14), although both these sample sets are limited and may have suffered from volatile loss during atmospheric entry and sample capture. Extraterrestrial dust collected on Earth correspond either to Interplanetary Dust Particles (IDPs) collected in the Earth stratosphere, or micrometeorites, which are collected at Earth surface, for instance in Antarctica. Some of these particles appear to be very primitive (e.g., UltraCarbonaceous Antarctic MicroMeteorites, UCAMMs; Chondritic Porous IDPs, CP-IDPs) and could have a cometary origin (Duprat et al. 2010). On the other hand, the NASA Stardust mission collected samples of comet 81P/Wild2 and returned them to Earth for laboratory analysis. These revealed important insights into the composition of cometary organic materials, which were found to be richer in oxygen and nitrogen, but poorer in aromatic compounds than organic materials in meteorites and interplanetary dust particles (Sandford et al. 2006). The presence of high D/H and ^{15}N enrichments was also identified, interpreted as evidence for some of the cometary organics to

have an interstellar/protostellar heritage (Sandford et al. 2006). Comet 81P/Wild2 was also shown to contain crystalline silicates such as olivine and pyroxene in addition to the abundant amorphous silicates commonly found in the interstellar medium, consistent with the efficient mixing of solar system and interstellar matter in the comet forming region (Fig. 8).

Spectroscopic observations of comets in the radio, infrared and UV also allow determination of the physical conditions (temperature, velocity field, density) of the cometary environments, as well as the chemical composition of these bodies. For instance, photometric and spectroscopic observations allow determining elemental ratios in the coma (e.g., CO/N_2; Ivanova et al. 2018), which can be used to infer the temperature and chemical composition of the comet. Detection of trace volatile molecules (e.g., H_2CO, CH_3OH, CH_4, C_2H_2, C_2H_6, HCN, and NH_3) provide further information regarding the composition and history of the comet (DiSanti et al. 2018). Isotopic ratios (e.g., D/H, $^{16}O/^{18}O$, $^{32}S/^{34}S$, $^{14}N/^{15}N$, $^{12}C/^{13}C$; Bockelée-Morvan et al. 2004) can also be determined remotely by high-resolution spectroscopy of molecular bands. The determination of D/H is also crucial to understand the origin of water on Earth, an ongoing debate (Altwegg et al. 2015; Chapter 6).

6. Main reservoirs of the early Solar System for planetary formation

As expressed so far in this introduction, there are multiple lines of evidence for large scale mixing in the PPD. However, from the analysis of nucleosynthetic anomalies in meteorites, there is growing evidence that multiple reservoirs developed throughout the PPD as a consequence of limited large-scale mixing. It is now widely accepted that at least two distinct reservoirs (non-carbonaceous (NC) and carbonaceous (CC); Fig; 15) emerged in the early Solar System as a result of (i) differential inheritance from the parental molecular cloud, and/or (ii) rapid formation of Jupiter, which prevented radial mixing between the two reservoirs and maintained the dichotomy over the PPD lifetime (Warren 2011; Kruijer et al. 2017; Nanne et al. 2019). This dichotomy has now been observed for many isotopic systems, including Ti, Sr, Ca, Cr, Ni, Zr, Mo, Ru, Ba, Nd, Sm, Hf, W (Burkhardt et al. 2019). Hence, bulk compositions of chondrites belonging to these two reservoirs are slightly offset as a result of small differences in their nucleosynthetic fingerprints, i.e. in the stellar sources of their presolar components (see example in $\Delta^{17}O$ vs. $\varepsilon^{54}Cr$ space, Warren 2011; Fig. 15). In general, meteorites belonging to the CC group appear to be more isotopically anomalous than those from the NC group with respect to Earth, indicative of the Earth belonging to the NC reservoir.

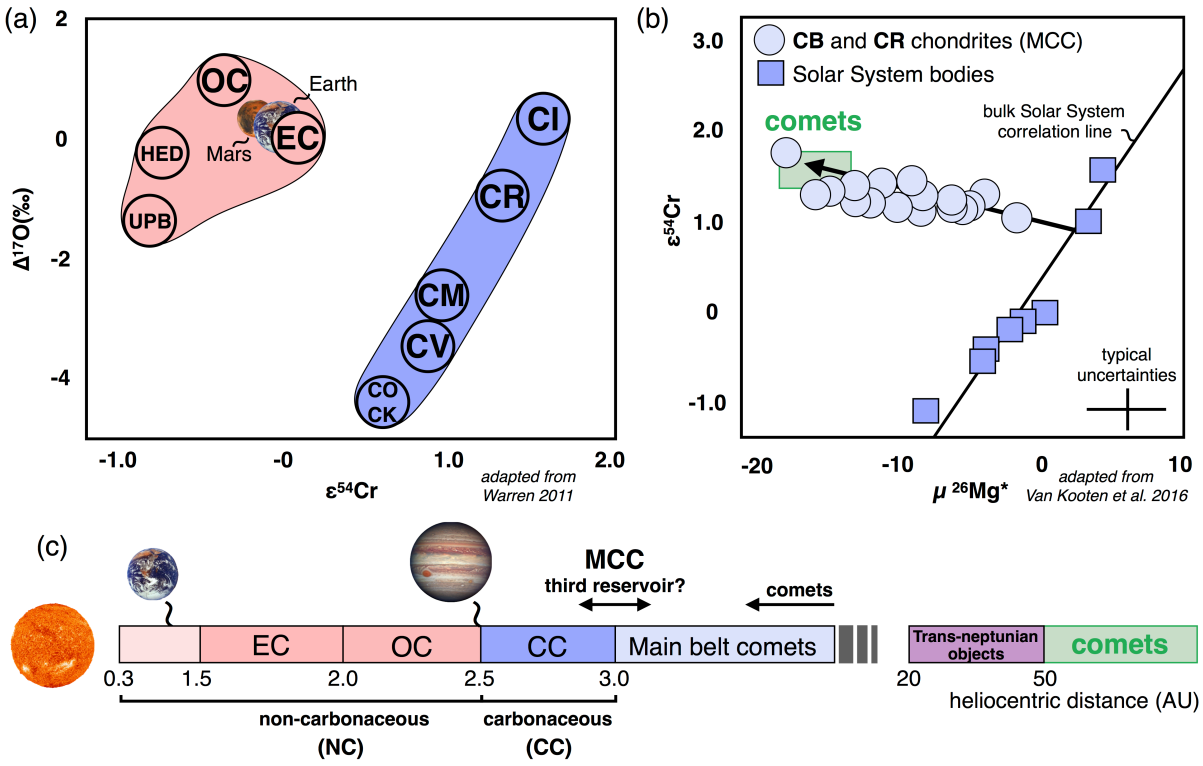

Figure 15. Nucleosynthetic signatures in different bodies of the Solar Systems and their assumed formation regions. **(a)** $\Delta^{17}O$ vs. $\varepsilon^{54}Cr$ plot of Solar System bodies showing the existence of a nucleosynthetic dichotomy between the NC (in red, from which the Earth, Mars, UPB: Ureilite Parent Body, and HED: Vesta meteorites, belong) and the CC (in blue) reservoirs (Warren 2011). CO, CK, CV, CM, CR and CI are chondritic types belonging to the CC reservoir. **(b)** $\varepsilon^{54}Cr$ vs. $\mu^{26}Mg^*$ diagram showing that CB and CR chondrites deviate from the bulk Solar System correlation line, toward the presumably ^{26}Al-poor cometary reservoir (Van Kooten et al. 2016). **(c)** Heliocentric representation of the main chondritic types (EC: enstatite chondrites, OC: ordinary chondrites, CC: carbonaceous chondrites), cometary reservoirs, as well as Earth and Jupiter forming regions. The early growth of Jupiter is thought to have prevented the large-scale homogenisation of the bulk Solar System, therefore resulting in the NC-CC dichotomy between materials from within and outwith it's orbit, respectively (Kruijer et al. 2017). A third reservoir might be considered beyond the CC reservoir, within the comet-influenced region represented by MCC.

The mechanisms allowing for the preservation of large-scale heterogeneities in the Solar System are not fully understood. Recent direct observations of PPD with the Atacama Large Millimetre/sub-millimetre Array (ALMA) telescope revealed the common occurrence of gaps and rings in the continuum (dust) emission of disks (Isella et al. 2016; Fig. 16). These could originate from gravitational instabilities, the trapping of dust in high-pressure regions, and/or the growth of dust grains, with the observed gaps in emission corresponding to deficits of dust particles inside gaps caused by dust accretion onto young planets (Gonzalez et al. 2015). In the Solar System, the current paradigm is that nucleosynthetic reservoirs were put in place by the early growth of a $\geq$ 20 Earth masses, giant planet embryo, presumably Jupiter's core. This would have blocked the inward drift of pebbles and thus starved the inner Solar System (e.g., Bitsch et al. 2019; Fig. 16), therefore hampering large-scale homogenisation of the Solar System

materials. Recent modelling and compilation work on meteoritic data require Jupiter' s core (30 Earth masses) to have potentially formed as early as 600,000 yr after CAI (Desch et al. 2018). Although the existence of a hot Jupiter around a 2 million-year old T Tauri star (Donati et al. 2016) demonstrates that giant planet formation can happen on very short timescales, the exact conditions allowing for such an early growth of giant planets in the PPD - most likely through hybrid pebble–planetesimal accretion (Alibert et al. 2018) - remain to be explored.

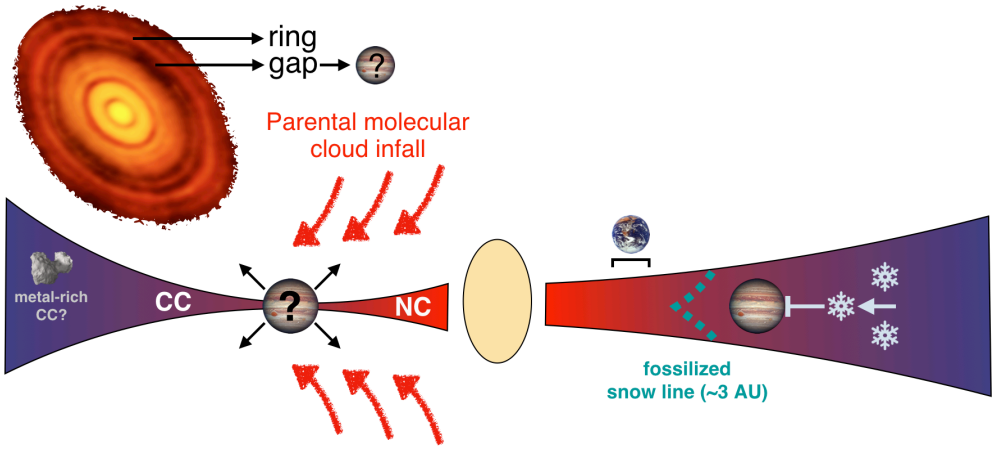

Figure 16. Inferred roles of Jupiter in the distribution of solid particles and volatile elements in the PPD. Left side: the ring and gap structure of PPDs observed with ALMA (here HD 163296; ALMA (ESO/NAOJ/NRAO), NSF) could be related to the presence of giant planets akin to Jupiter. For our Solar System, the early growth of Jupiter could have maintained a nucleosynthetic dichotomy, inherited from the parental molecular cloud, between materials accreting within the outer and inner Solar System (Nanne et al. 2019). Right side: Jupiter could have stopped the flow of icy particles drifting from the outer Solar System, therefore fossilizing the snowline at ~3 AU and accounting for the water-poor feature of the inner Solar System (Morbidelli et al. 2016).

The primordial source of the NC-CC dichotomy is debated, and could correspond to a late influx from the outer Solar System of material with a CC-like composition, which was not well-mixed with the inner Solar System due to the presence of Jupiter (Kruijer et al. 2017). Alternatively, the NC-CC dichotomy could reflect the distinct isotopic composition of later infalling material from the parental molecular cloud, with increasingly NC-like material falling onto an initially CC-like disk (Nanne et al. 2019; Fig. 16). In this view, the composition of the inner disk (i.e., the NC reservoir) would have been dominated by later infalling material, whereas the outer disk (i.e., the CC reservoir) preserved the compositional signature of the earliest disk (Pignatale et al. 2019). However, these models are relatively new and the respective roles of Jupiter and the parental molecular cloud in setting the NC-CC dichotomy may be revised in the future.

The early presence of Jupiter in the PPD is expected to have also played an important role in the distribution of volatile elements in the inner Solar System. Indeed, the location of the snowline in the PPD is a direct function of the stellar accretion rate and is expected to move inward as the accretion rate decreases with time (Bitsch et al., 2015). Based on

astronomical observations, stellar accretion rates are estimated to have decreased on average from $10^{-8}M_*$/y at 1 My to 1–5 $\times10^{-9}M_*$/y at 3 My (M_* = one solar mass ~ 2 $\times10^{30}$ kg; Hartmann et al. 1998), inducing the snowline to drift from 3 AU to 1 AU (Bitsch et al., 2015). Such a snowline drift would imply that water ice grains were ubiquitous in the inner Solar System, and formed abundant ice-rich planetesimals at the time of Earth's formation. This is at odds with the observation that meteorites originating from the inner Solar System (EC and OC) are essentially devoid of water. One possibility is that the early presence of Jupiter inhibited the inward flux of icy grains and therefore fossilised the snow line at 3 AU (Morbidelli et al. 2015; Fig. 16). Thus, although temperatures in the inner Solar System would have allowed ice to condense and icy planetesimals to form, the inner regions of the disk would have remained relatively dry due to the limited influx of volatile-rich material from beyond Jupiter (Morbidelli et al. 2015). In this context, the Earth would have grown dry, with most of its present-day inventory of volatile elements supplied either by planetary embryos colliding with the proto-Earth (e.g. Theia) or delivered through late additions of volatile-rich material from the outer regions of the Solar System. Lodders (2004) proposed the existence of a "tar line", closer to the Sun than the snow line, delimiting the front beyond which refractory organics would have been stable. Between the tar line and the snow line, dry planetesimals could have accreted significant fractions of refractory organic materials without accreting significant water. EC, for instance, could have accreted within such dry environments where the refractory organic component commonly found in chondritic material was abundant (Piani et al. 2012). Lodders (2004) even proposed that at the time of Jupiter's formation, abundant carbonaceous matter (rather than abundant water ice) was present near 5 AU, increasing the surface mass density of solids in the solar nebula accretion disk. This carbonaceous matter component, with high sticking propensity, could have helped the local accumulation of solid matter of proto-Jupiter that ultimately led to the runaway accretion of the planet (Lodders 2004).

Finally, a third reservoir represented by metal-rich carbonaceous chondrites (MCC) has been proposed to exist in the outermost parts of the Solar System, influenced by the contribution of fresh interstellar material from the cometary reservoir (Van Kooten et al. 2016; Fig. 15). In ε^{54}Cr vs. μ ^{26}Mg* space (where μ ^{26}Mg* represents the variability in the stellar-derived short-lived ^{26}Al radionuclide; ^{26}Al decays to ^{26}Mg with a half-life of 0.705 My), MCC have been shown to deviate from the bulk Solar System correlation line, toward the presumably ^{26}Al-poor cometary end-member (Fig. 15). These observations are interpreted as requiring bulk MCC to have had significant amounts (25–50%) of primordial molecular cloud matter in their precursor material (Van Kooten et al. 2016). Taken at face value and considered with the absence of evidence for significant contribution of cometary material to any other chondrite groups, these estimates may require the parent body of MCC to have accreted beyond the orbits of the gas giants, from a reservoir that was isolated from the bulk Solar System (NC and CC). Additional Al-Mg analyses in MCC may however be required to ensure

that the observed ^{26}Mg*-depleted component (van Kooten et al. 2016) does not arise from secondary artefacts, due to modern Al/Mg perturbations, as recently suggested by Luu et al. (2019). Most importantly, the very definition of the bulk Solar System correlation line in ε^{54}Cr vs. μ ^{26}Mg* space, as defined by Larsen et al. (2011) and used by Van Kooten et al. (2016), is controversial (Davis et al. 2015). But MCC also contain very fine-grained, highly pristine clasts that are extremely rich in carbon (up to > 90 wt% C; Nittler et al. 2019) and resemble anhydrous CP-IDPs considered to originate from comets. Most strikingly, micro-xenoliths found in MCC show an extreme continuum of N isotopic variation, from very light N isotopic composition ($\delta^{15}N_{AIR} = -310 \pm 20‰$), similar to that inferred for the solar nebula, to the heaviest ratios measured in any Solar System material ($\delta^{15}N_{AIR} = 4900 \pm 300‰$; Briani et al. 2016) and considered to represent the cometary/interstellar reservoir. Evidence for the contribution of cometary/interstellar material (e.g., D and ^{17,18}O-rich water ice grains) to the accretion zone of chondritic bodies is scarce (Marrocchi et al. 2018), mainly restricted to the potential preservation of interstellar water signatures in the most pristine carbonaceous (the Paris meteorite; Vacher et al. 2016) and ordinary chondrites (Deloule and Robert 1995; Piani et al. 2015). Whilst cometary/interstellar water was probably already present in the inner Solar System prior to the formation of carbonaceous chondrites (McCubbin & Barnes 2019), chondritic and cometary volatile element reservoirs would have then been efficiently isolated from one another, with their physical frontier possibly sampled by MCC only.

7. The heterogeneous nature of the terrestrial planet building blocks

Over the course of its evolution, the Solar System experienced large-scale destabilising events that resulted in its present day structural organization. Such events are thought to be triggered by the growth and/or migration of giant planets, especially Jupiter. One can consider the final effect of giant planets on the mixing rate of Solar System materials to have been ambivalent: hampering large-scale homogenisation of the nucleosynthetic inheritances in the first instance (NC-CC dichotomy), and, in the second instance, imparting a destabilising influence on nearby planetesimals resulting in their gravitational scattering in all directions (Raymond and Izidoro, 2017).

Historically, the so-called classical model of planet formation considered giant planet growth separately from terrestrial accretion (Wetherill 1992), i.e. that planet formation occurred within the inner Solar System from a given population of rocky building blocks, independently from gas giants. However, such models systematically resulted in Mercury and Mars analogues with much larger masses (typically a factor of 5 to 10) than observed today, and could neither account for the asteroid belt's orbital excitation (Raymond et al. 2018). Indeed, the mass of the asteroid belt (and likewise for the Kuiper belt) is too low (~ 5.10^{-4} the Earth mass, or ~4% of the mass of the Moon) by many orders of magnitude to account for its present-day level of dynamical excitation (broad range of eccentricities and inclinations) by

gravitational self-stirring of its constituting bodies (Morbidelli et al. 2015; Izidoro et al. 2016). In addition, the inner part of the asteroid belt is dominated by OC-like asteroids (referred to as S-types), whilst its outer part edge mainly comprises CC-like asteroids (called C-types; Gradie and Tedesco 1982; DeMeo and Carry 2013). This could indicate that the asteroid belt formed through the heterogeneous assemblage of asteroids from both within (S-types) and outwith (C-types) Jupiter's orbit. In response to these various issues with the classical model, three main scenarios of planet formation and evolution of Solar System bodies have been proposed: the Grand Tack, low-mass asteroid belt and early instability models (Fig. 17).

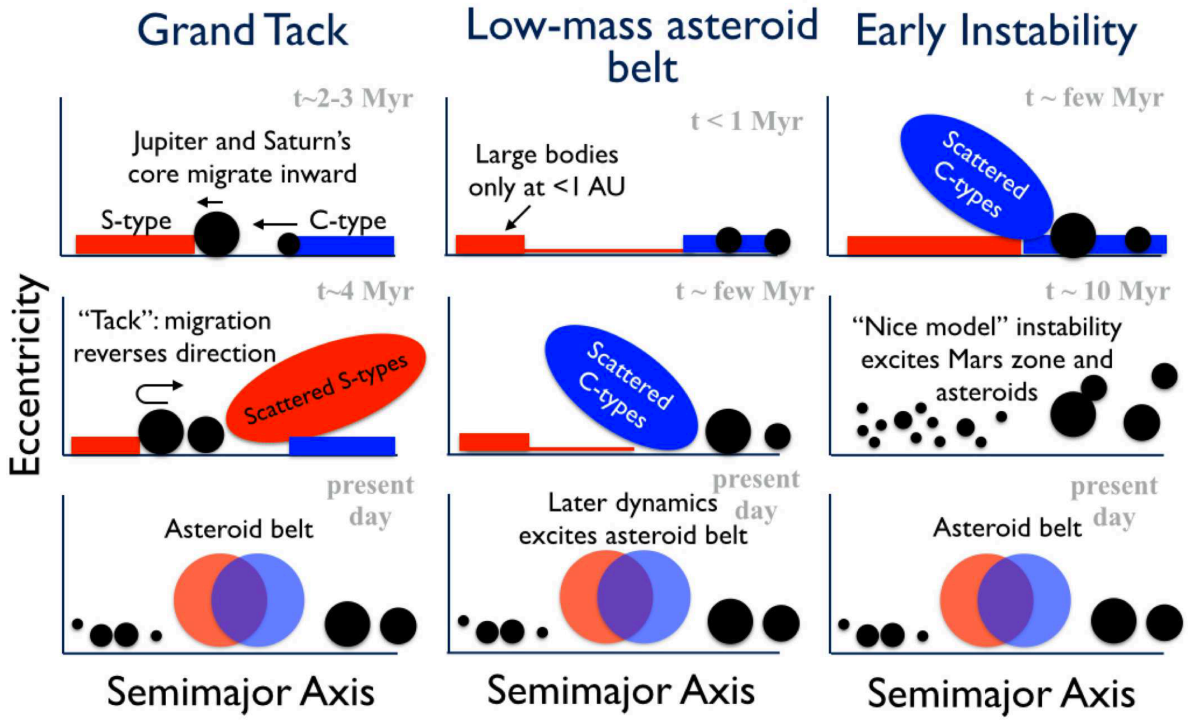

Figure 17. Illustration of three models that can each match the large-scale properties of the inner Solar System, with from left to right: the Grand Tack model (Walsh et al. 2011; Raymond and Morbidelli 2014), the low-mass asteroid belt (Hansen, 2009; Drążkowska et al. 2016), and the early instability model (Clément et al. 2018). From Raymond et al. (2018).

The Grand Tack model proposes that the early, inward-then-outward migration of Jupiter from 3-4 AU to 1.5-2 AU truncated the inner disk at ~1AU, creating a ring of planetesimals within 1 AU (similar to the initial scenario of the low-mass asteroid belt; Fig. 17). This configuration can account for the large Earth/Mars mass ratio (Walsh et al. 2011). Such migration would scatter and then replenish the asteroid belt by implantation of both inner and outer planetesimals (Walsh et al. 2011; Raymond and Morbidelli 2014). Although the exact mechanism allowing for the giant planets outward migration is not fully understood (i.e. the exact conditions allowing for Saturn to become locked in Jupiter's exterior 2:3 resonance in a shared gap in the disk; Raymond et al. 2018), this process would have induced significant inward scattering of outer Solar System objects to the terrestrial planet forming region,

potentially delivering volatile elements to Earth (Matsumura et al. 2016). The low-mass asteroid belt scenario proposes that the bulk of rocky planetesimals in the inner Solar System formed within a narrow ring that only extended from roughly 0.7 to 1 AU (Drążkowska et al. 2016; Fig. 17). In this case, the outer region of the asteroid belt would have been populated by C-type planetesimals scattered inward by the giant planets growth process (Raymond and Izodoro 2017). Finally, the early instability model assumes a giant planet instability within ~10 Myr after the dispersal of the gaseous disk (Clément et al. 2018), exciting the asteroid belt and clearing out the Mars accretion zone. The origin of C-types in the outer main belt and in the terrestrial planet forming region could be accounted for by giant planet growth scattering outer Solar System objects inward (Raymond and Izidoro 2017). In summary, all three models of Solar System evolution provide plausible astrophysical scenarios where the orbits of planetesimals belonging to the inner and outer Solar System are disrupted, and Earth's building blocks could equally originate from the inner or outer Solar System (Fig. 17).

N-body accretion simulations aimed at reproducing Earth's internal composition require accretion from a heterogeneous reservoir of material (Rubie et al. 2015). Arguments in favour of NC- or CC-like source materials for Earth's accretion can be found in the literature (Fig. 18). These are not necessarily contradictory as it can depend on the element being considered. For instance, a late ~2 (±1) % contribution of carbonaceous chondrite (CI-CM) material to a dry (EC-OC) proto-Earth (Marty 2012) would yield an Earth that mainly derives from NC materials for refractory elements, with Earth surface volatile elements mainly deriving from CC materials. However, estimates for CC contribution during Earth's main accretion and late veneer vary from almost 0 to 42%, and from 0 to 100%, respectively. Likewise, both inner and outer Solar System origins have been proposed for the Moon-forming impactor (Fig. 18). Canonical simulations of Moon-forming impacts predict that the Moon-forming impactor represented ~10% of the Earth's final mass, with the Moon being composed of ~60% impactor and ~40% proto-Earth (Canup and Asphaug, 2001). Although the CC-like origin of the Moon-forming impactor could account for the Mo isotopic composition of the mantle, it would be difficult to reconcile with the consistent isotopic similarity between the Earth and Moon (Dauphas et al. 2014). One of the main caveats encountered when trying to constrain the Earth's composition from mixing of meteoritic end-members is that the actual 'building blocks' of the Earth may not be sampled in the meteorite collection (Drake and Righter, 2002).

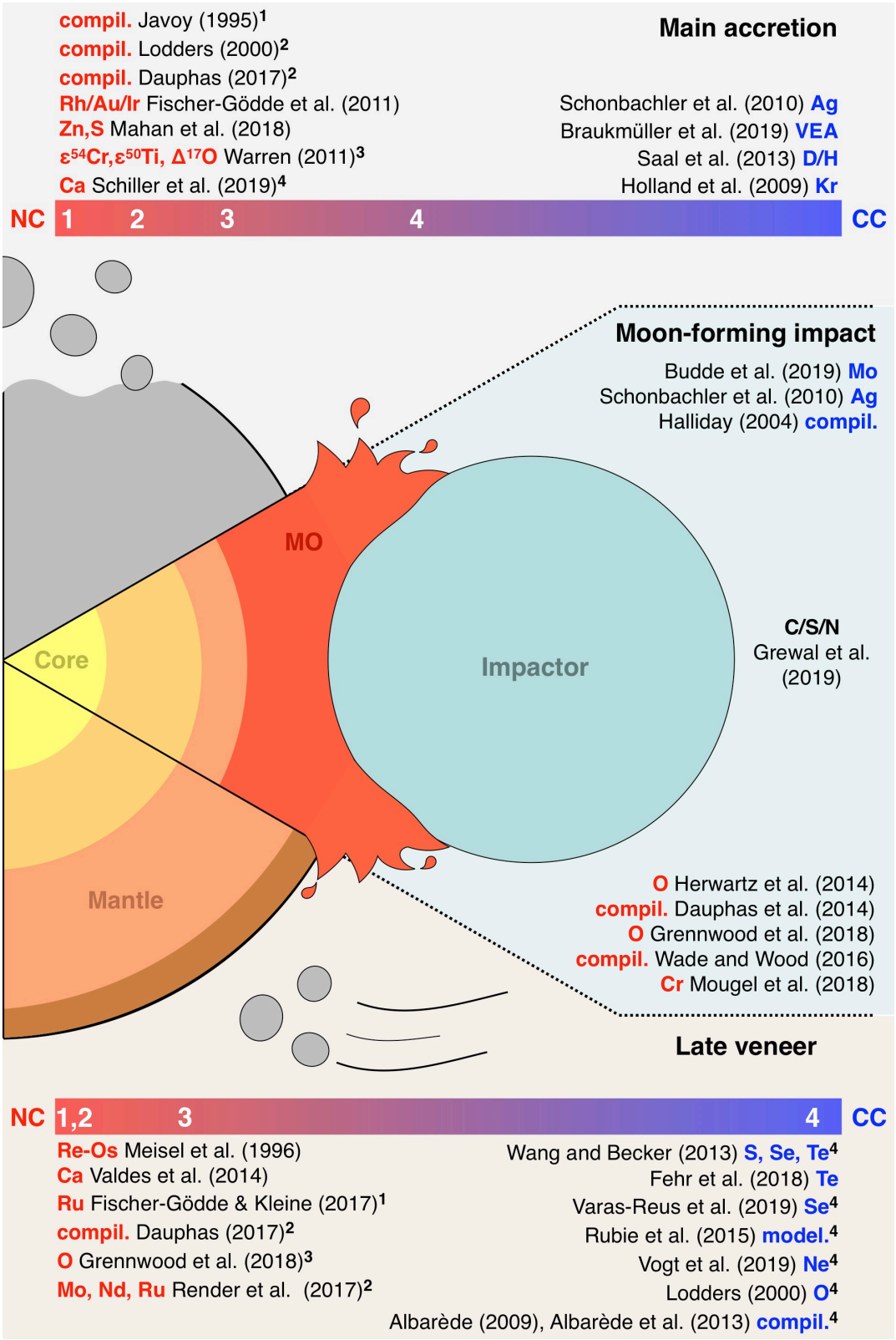

Fig. 18. Literature review of the dominant type of material (red NC or blue CC) accreted to Earth during the main stage of accretion (top), Moon-forming impact (middle), and late veneer (bottom). For each reference, the element(s) of interest are reported in bold. The two horizontal bars depict a gradient from pure NC (left) to pure CC (right), where we report numbers that refer to specific references (see the superscript numbering after corresponding references).

Importantly, Nd, Mo and Ru have distinct partitioning behaviours (being lithophile, moderately siderophile and highly siderophile, respectively), and, as such, they record different stages of Earth's accretion (Dauphas, 2017). Any change in the isotopic signature of the accreting material would therefore affect the Nd, Mo and Ru isotopic compositions of Earth's mantle differently. Yet, the Earth's nucleosynthetic signature in Mo-Nd and Mo-Ru spaces falls on the cosmic correlations defined by meteorites, with a systematic excess in s-process relative to all known types of chondrites, including EC (Dauphas et al. 2004; Render et al. 2017). This has several implications. Firstly, it indicates that the nucleosynthetic signature of Earth's building blocks (i.e., its type of material) did not change significantly during accretion, including the late veneer, and so the Earth accreted quite homogeneously (Morbidelli and Wood, 2014; Dauphas et al. 2017). Secondly, the consistent excess in s-process implies that, although the Earth's nucleosynthetic signature is best represented by EC, its building materials were fundamentally different from any known chondritic type, including EC. Taking into account O, Cr, Ni and Si isotope systematics of the BSE, it seems that a maximum of 15% EC can be present in the mixture of chondrites that would form Earth (Fitoussi and Bourdon, 2012). The refractory lithophile element to Mg ratios of the bulk Earth are within the range of CC but very different from OC and EC – both groups being depleted in refractory elements (Palme and O'Neil 2014). The latter authors argued that the Earth and CC have similar patterns of the moderately volatile elements, with similar depletions in Na and Mn. In addition, assuming that Earth's core contains about 7% Si, Palme and O'Neil (2014) determine a bulk Earth Mg/Si within the narrow range of CC, but very different from OC and EC. Based on their review, they conclude that the bulk composition of Earth is basically the same as that of CV chondrites. However, the Earth could not simply have accreted from CC material, as it would have led to an overly oxidised early Earth mantle. Recent modelling of the accretion history of Earth including core formation suggests that Earth's accretion was largely comprised of reduced materials (e.g., to accommodate the low Cr in mantle rocks; Rubie et al., 2011; Wade and Wood, 2005).

The late accretion of chondritic material to Earth after formation of the Moon and core segregation, commonly referred to as the terrestrial "late veneer" (0.3-0.7wt.% of the Earth), is required to account for the high and unfractionated chondritic abundance pattern of highly siderophile elements in the terrestrial mantle (Kimoura et al. 1974). It is unclear how much the late veneer contributed to terrestrial volatiles, although estimates range from, nearly all of Earth's volatiles being inherited during the late veneer (Albarède, 2009), to the majority of volatiles arriving during the main stage of accretion (e.g., Greenwood et al. 2018). Determining the composition of the chondritic material that made up the late veneer is therefore important for understanding the origin of Earth's volatiles. However, the timing, mass and composition of the late veneer are poorly constrained. The mantle is potentially heterogeneous in its PGE content on scales of ~100 kilometres (Pattou et al. 1996), and minor core segregation could have occurred concurrently with the late veneer addition (Chatterjee & Lassiter, 2016),

therefore hampering accurate estimate of the mass of the late veneer. It has even been speculated that mixing of differentiated outer-core material back into the mantle after core separation could potentially account for the observed noble-metal ratios and abundances in the mantle, relaxing the requirement for any late accretionary veneer of chondritic materials (Snow and Schmidt, 1998). This is however at odds with the observation of early Archaean komatiites recording a lower mantle signal of PGE depletion relative to the modern mantle (Maier et al. 2009), suggesting that siderophile elements from the late veneer were not directly added to the deep mantle, but were progressively mixed in through time, via mantle convection.

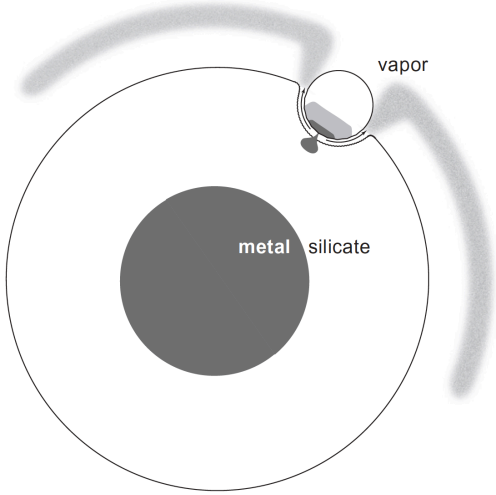

Fig. 19. Impact between an asteroid and Earth during the late veneer, inducing impactor melting (where the metal, in dark grey, separates from the silicates, in white) and vaporization. The metal fraction sinks into the core and is therefore transparent in the mass balance of the late veneer based on HSEs. The only fraction of the impactor's metal that will be seen in the terrestrial mantle and crust corresponds to the vaporised material. Figure from Albarède et al. (2013).

Uncertainties remain regarding the degree of differentiation of Earth's accretionary building blocks (Marchi et al. 2018). Some models argue for the core of the Moon-forming impactor to have constituted a possible source for the Earth's late veneer component (Sleep, 2017; Genda et al. 2017). To accrete primarily from chondritic or achondritic materials would have fundamental implications regarding the volatile inventory of Earth's building blocks. The required mass of a late veneer composed of achondritic material (which would have experienced differentiation and volatile loss before accretion to Earth) could be as high as a few wt.% of the Earth (Marchi et al. 2018). In this case, although EC-like material appear to constitute our best analogue for the composition of the late veneer (Dauphas, 2017; Fischer-Gödde & Kleine, 2017), differences in W-isotope ratio between the Moon and the Earth imply that only a small fraction of the late veneer could have consisted of differentiated enstatite chondrite-like projectiles (Morbidelli and Wood, 2015).

Each body of the Solar System has a specific oxygen isotopic composition, which potentially allows for the nature of chondritic bodies that accreted to form the Earth to be determined. Mass balance calculations based on O isotopes (Lodders 2000) predict the Earth

accreted from about 70% enstatite, 21% ordinary, 5% CV and 4% CI chondrites, that is 91% NC and 9% CC (in excellent agreement with recent estimates based on compilation of isotopic signatures of lithophile, moderately siderophile and highly siderophile elements in Earth; Dauphas 2017). However, the crucial distinction between these models regards the timing of supply of the CC material component. Dauphas (2017) concluded that the first 60 % of Earth's accretion could have comprised 9% carbonaceous chondrites, with the last 40% of terrestrial accretion (including the late veneer and Moon-forming impactor) being composed of almost pure enstatite chondrite-like material. Conversely, oxygen systematics were used to argue for a late accretion of CM-like materials (or a CI-CV mixture; Albarède et al. 2013) corresponding to the last ~10% of Earth's accretion. This means more chondritic materials in late veneer than required based on the concentration of HSE in the terrestrial mantle (0.3-0.7%; Kimoura et al. 1974). This is because the authors propose that, regardless of the impactor being differentiated or not, impacting asteroids would melt and cause most of its HSE inventory to sink into the terrestrial core and is removed from the mass balance estimate of the late veneer based on the modern mantle inventory (Fig. 18). HSE abundances in the BSE would therefore reflect the vaporised fraction (~5-10%) of impactors, which subsequently re-condensed, rained back to Earth, and became integrated into the Earth's mantle (Albarède et al. 2013; Fig. 19). Hence, the terrestrial late veneer could have constituted as much as 10 % of Earth's final accretion (i.e., almost the size of Mars!), predominantly composed of CC-like material. The authors argue that the amount of water added to Earth in this way (up to 9000 ppm of water for the BSE; Albarède et al. 2013) could have served to oxidise iron in the mantle and core (see next section), or could be in part retained in the present-day lower mantle (today containing up to 3000 ppm water; Marty 2012).

Finally, an outer Solar System late instability (referred to as the Nice model), generated by interactions between the giant planets and the primordial Kuiper belt some 500 Myr after CAI, could have destabilised outer Solar System planetesimals onto terrestrial planet-crossing orbits (Gomes et al. 2005). This late phase of impacts throughout the Solar System was proposed to correspond to the Late Heavy Bombardment (LHB) of the terrestrial planets, initially inferred from the size-age distribution of lunar craters (Tera et al., 1974; Marty et al. 2016). How much this LHB of volatile-rich bodies from the outer Solar System contributed to the volatile element inventory of the Earth is not known, and the very existence of this episode has even been cast into doubt (Chapter 2; Boehnke & Harrison, 2016).

In conclusion, although the origin, timing and nature (differentiated or not) of Earth's building blocks are not fully understood, it appears that the Earth predominantly accreted from an inner Solar System reservoir (NC), with the possibility - as illustrated by the presence of C-type bodies in the asteroid belt - to have partially grown from the accretion of volatile-rich bodies originating from the outer Solar System.

8. Planetary differentiation and mantle reservoirs

Large impacts during planetary accretion release considerable amounts of energy that is enough to generate extensive melting and magma ocean (MO) formation. There is growing evidence that the Earth was not completely solidified at the time of the last giant impact, with a global MO potentially required on the proto-Earth to account for the Moon's isotopic composition being consistently similar to Earth's (Hosono et al. 2019; Fig. 18). Deep MO formation enables liquid metal to chemically equilibrate with liquid silicates at high pressure, before being segregated to the core. The proto-Earth probably experienced multiple events of giant impact (Tucker & Mukhopadhyay 2014), resulting in a multi-stage process of core formation through planetary differentiation. The ultimate core and mantle compositions of planetary bodies rely on the extent to which siderophile (= metal-loving) elements partition into the core, which strongly depends on the pressure (P), temperature (T) and oxygen fugacity (f_{O2}) conditions of metal-silicate equilibration. Under oxidizing conditions, iron primarly remains with the silicate phase as FeO, and does not form metallic iron (Fe) that could sink to the core (Wade and Wood, 2005). Although the evolution of the f_{O2} of the growing Earth is a critical parameter for siderophile element partitioning between metal and silicate, other parameters can have significant effects, with the partition coefficients of W and Mo, for instance, being dependent on the sulphur content of the metal (Wade et al., 2012). Most of our knowledge regarding the core-mantle evolution of the Earth relies on experimental investigations in to the behaviour of elements under variable chemical conditions at high pressure (Gessmann et al., 1999; Wade and Wood, 2005; Siebert et al., 2013), and implementation of such constraints in multistage core-mantle differentiation models with N-body accretion simulations (Rubie et al. 2015). Today, the favoured scenario is that early accreting material was highly reduced, therefore allowing the early segregation of the Earth's core, followed by the accretion of more oxidised material potentially supplying the Earth surface with its budget of volatile elements (Wänke 1981; Rubie et al. 2011). Throughout the accretionary process, progressive oxidation of the mantle could also have arisen from the photodissociation of H_2O and escape of H_2 from the Earth's atmosphere (Hunten 1993), or as a natural consequence of the increasing size of the Earth allowing large scale crystallization of magnesium silicate perovskites in the lower mantle (Wade and Wood, 2005). During MO episodes, the majority of dissolved water would be expelled back to the atmosphere through bottom-up MO solidification, leaving only a small fraction of the original volatiles to be released into the atmosphere through later volcanism (Hamano et al. 2013; Elkins-Tanton 2008, 2011). Terrestrial accretion, MO evolution and atmosphere's formation are therefore closely related to one another, constituting a series of intricate events that allowed the Earth surface to progressively cool down, initiate thermally-driven mantle convection, plate tectonics, and become habitable for life. Understanding the origin and evolution of the atmosphere requires contraining its extent of interaction with the Earth's interior.

The cycling of volatiles between the Earth's surface and it's silicate interior plays a critical role in controlling the rheology and dynamics of the mantle, with the resulting surface expression seen in plate tectonics. The present-day volatile inventory of the Earth's surface is established by a balance between degassing from the Earth's interior to the surface during mantle partial melting and volcanism, and the return of volatiles to the mantle through the subduction of volatile-rich oceanic plates (Holland and Ballentine, 2006). Importantly, heterogeneities in the Earth's accretionary material and the recycling of oceanic crust and sediments into the mantle by the subduction process have produced a heterogeneous mantle. Distinct reservoirs have been identified from the analysis of radiogenic Pb, Nd and Sr isotopes in Ocean Island Basalts (OIB), incuding the HIMU component ("high μ" where $\mu = {}^{238}U/{}^{204}Pb$) representing hydrothermally altered and dehydrated oceanic crust subducted > 1.5 Ga (Weiss et al. 2016), and the enriched mantle 1 and 2 components (EM1 and EM2) including recycled oceanic crust plus, for EM1, a few per cent pelagic sediment or metasomatised sub-continental lithosphere, and for EM2, a few per cent of continent-derived sediment (Jackson & Dasgupta 2008; Fig. 20). Most data from OIBs form linear mixing arrays that converge towards the "focus zone" (FOZO; Fig. 20), characterised by elevated $^{3}He/^{4}He$ ratios testifying a deep mantle origin. The FOZO is however unlikely to correspond to the primordial, unprocessed and uncontaminated mantle, due to its moderately depleted Sr-Nd signatures and radiogenic Pb isotopes suggesting the involvement of a HIMU component (Stracke et al. 2005). Constraining the primordial origin and evolution of volatile elements on Earth, especially their extent of recycling into the solid Earth, is essential to understanding how geological processes have come to shape the Earth's surface in to the unique habitat for life we see today.

Given the protracted and extensive recycling of atmospheric gases into the solid Earth, the present-day inventory of Xe in the mantle is largely dominated (80-90%) by recycled modern atmosphere (Holland & Ballentine, 2006; Parai and Mukhopadhyay, 2015). The onset of subduction is considered to have began > 3 Ga, as evidenced by Archean-aged subducted eclogite inclusions trapped within diamonds (Shirey and Richardson, 2011) and D/H, Cl, Pb systematics of palaeoarchean komatiite melt inclusions (Sobolev et al. 2019). Although the proposal of volatile elements being subducted to the deep mantle (Marty and Dauphas, 2003) received significant criticism (e.g., Cartigny and Ader, 2003; Kerrich and Jia, 2004), the return of Archean surface volatiles to the mantle was pinpointed by the discovery of mass independently fractionated sulphur isotopes (MIF-S) in sulphides from the Cook Islands mantle plume (Cabral et al., 2003). MIF-S occurs during photochemical reactions in oxygen poor environments (Farquhar et al., 2000) and therefore only occurred in the ancient atmosphere prior to the Great Oxidation Event (GOE) some 2.45 Ga (Holland, 2006; see Chapter 7). Recently, mantle Xe isotope systematics have been used to further constrain the age of initiation of volatile regassing into the deep Earth (Parai and Mukhopadhyay, 2018). Given that (i) the isotopic composition of atmospheric Xe progressively evolved through time by mass dependent fractionation and reached the modern composition around 2 Ga ago (Avice et al.,

2018; see Chapters 6-7), and that (ii) the Xe atmospheric component in the present-day mantle is indistinguishable from modern atmosphere (Parai and Mukhopadhyay, 2015), the authors proposed that substantial full scale recycling of atmospheric xenon into the deep Earth could not have occurred before 2.5 billion years ago (Parai and Mukhopadhyay, 2018). These results are in line with recent results from the noble gas analysis of gas-rich popping rock 2πD43, indicating that effective Xe recycling could not have started earlier than about 2.8 Ga (Péron and Moreira, 2018). These results may be in line with the proposal that early subduction was fundamentally different from the present-day one, with the hot early mantle efficiently expelling volatiles back to the surface from subducting plates (Brown, 2006).

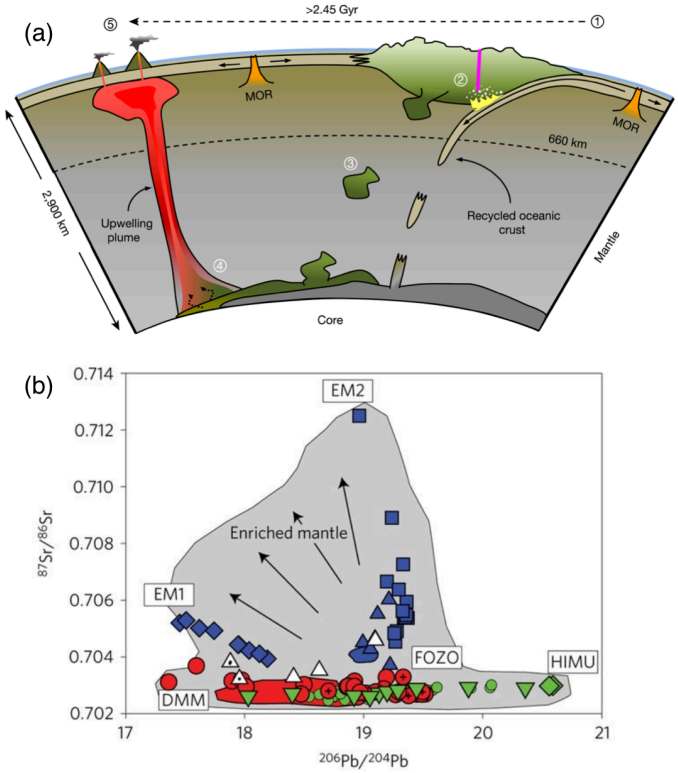

Fig. 20. Heterogeneity of the lower mantle from recycling. (a) Conceptual model for the evolution of the HIMU mantle source proposed by Weiss et al. (2016), whereby slabs of altered oceanic crust sank to the core-mantle boundary during the Archean or early Proterozoic, before being incorporated into an upwelling mantle plume. (b) Sr versus Pb isotope diagram for magmatic glasses showing some of the main mantle endmembers: the depleted MORB mantle (DMM), the enriched mantle 1 and 2 (EM1 and EM2), the HIMU mantle and the focus zone (FOZO), by Kendrick et al. (2017).

The presence of recycled components in the deep mantle could imply that whole mantle convection is an on going process, with convective mixing bringing deep mantle material to the surface and subduction taking surface material back down into the mantle. From seismic tomography studies, there is little evidence that the boundary between the lower and upper mantles (believed to be the 670 km seismic discontinuity) impedes convection and mixing (van der Hilst et al., 1997). Yet, continuous convection within the mantle should theoretically erase any remnant of primordial material and lead to a homogenously degassed mantle, which is not

the case. Even the giant impacts and MO episodes experienced by the early Earth were not sufficient to erase accretionary features within the solid Earth (e.g., Willbold et al. 2011; Mukhopadhyay 2012; Touboul et al. 2012). Signatures of Earth's volatile element accretionary sources are preserved throughout the mantle, with part of Ne in the deep mantle, and presumably helium, being directly derived from dissolution of the protosolar nebula gas into a proto-Earth MO (e.g., Yokochi and Marty 2004; Williams and Mukhopadhyay 2019). Conversely, heavy noble gases, hydrogen and nitrogen preserve the signature of their chondritic inheritances (Holland et al. 2009; Marty et al. 2012; Caracausi et al. 2016). The Ne isotopic signature of the upper mantle is furthermore purported to originate from solar wind-implanted Ne within chondritic materials (Trieloff et al. 2002; Ballentine et al., 2005), therefore corresponding to a chondritic - and not nebular - inheritance, pointing towards a heterogeneous accretion of Earth's volatiles.

9. Origin of the terrestrial atmosphere

Comparing estimates of the terrestrial water budget with the heliocentric distance at which the Earth accreted (here based on its nucleosynthetic composition from Render et al. 2017; Fig. 21), one can note that the Earth contains more water than expected (Morbidelli et al. 2012; Fig. 21). From an isotopic perspective, the D/H of Earth's ocean overlaps primitive carbonaceous chondrites and cometary materials (mostly Jupiter Family comets, JFC; Fig. 21), precluding significant contribution from the PSN to the atmosphere (Fig. 21). This is in contrast to the deep mantle, which may have preserved a nebular hydrogen, helium and neon component (Deloule et al. 1991, Hallis et al. 2015; Williams and Mukhopadhyay 2019). Therefore, to account for the volatile element composition of the bulk silicate Earth may require a late contribution from volatile-rich (CC and/or comets) material (e.g., Albarède 2009; Marty, 2012). However, the superchondritic C/N of the BSE challenges the proposition that C and N delivery solely occurred via undifferentiated CI chondrite-like material and may rather require a significant fraction of Earth's volatiles to have been accreted from differentiated C-rich planetesimals similar to the ureilite parent body (Hirschmann 2016). Alternatively, a significant fraction of terrestrial N could have been quantitatively sequestrated in the core, unlike C and H (Marty, 2012). Recent high pressure-temperature experiments investigated the fate of C-N-S alloys during core-mantle segregation and showed C is indeed much less siderophile than N under core formation conditions (Grewal et al. 2019). The authors suggest that a Moon-forming impactor with minimal CC contributions could constitute the source of major volatiles in the BSE (Grewal et al. 2019).

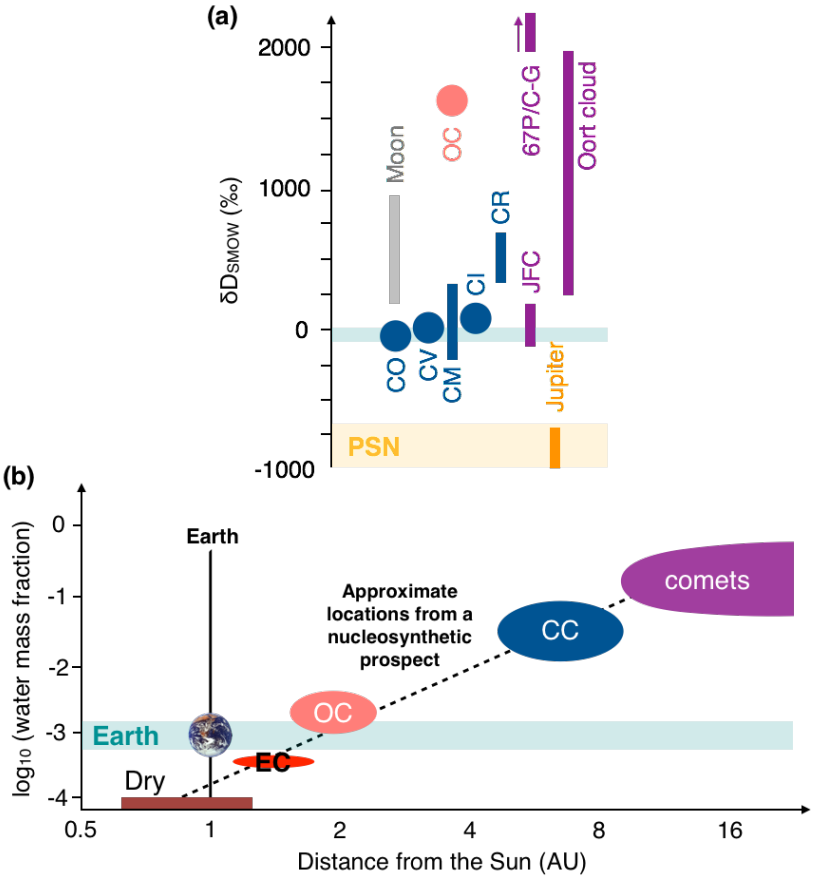

Figure 21. (a) Water isotopic composition (D/H, a) and concentration (b) in different reservoirs of the Solar System. (a) is adapted from Barnes et al. (2016). (b) is adapted from Morbidelli et al. (2012) for water contents and and Render et al. (2017) for heliocentric locations. The dashed line represents a general heliocentric trend of water content through EC, OC, CC and cometary bodies.

The isotopic and elemental composition of the Earth's atmosphere cannot be accounted for by simple degassing from the mantle (Holland et al. 2009), therefore requiring fractionation and/or mixing processes (Fig. 22). According to pure "fractionation" models (e.g., Pepin 2003), the atmosphere could be considered to have started with a solar-like composition and have experienced early fractionation (e.g., by giant impact-driven escape and/or solar EUV-driven escape; Fig. 22). In this case, the composition of the atmosphere would have been established promptly after the end of Earth's accretion (Fig. 22). However, recent findings and observations have demonstrated that such a scenario was no longer viable. Firstly, in Ne-Ar space, the Earth's atmosphere composition cannot be accounted for by kinetic fractionation processes (Marty 2012). To explain the Ne-Ar systematics of the atmosphere and mantle requires mixing between a solar-derived, and planetary component carried in primitive carbonaceous chondrites (Marty 2012; Vogt et al. 2019; Fig. 22). The potential for such a mixing scenario to also account for the heavy noble gas signature of the terrestrial atmosphere is discussed in Chapter 6. Secondly, the analysis of ancient atmospheric gases trapped in Archean rocks revealed that the isotopic composition of atmospheric Xe progressively evolved throughout geological time by mass dependent fractionation, reaching a modern-like

composition only around 2 Ga (Avice et al. 2018; Fig. 22). This isotopic evolution of atmospheric Xe over the Archean eon implies that the isotopic composition of atmospheric Xe was not established during Earth's accretion, but is rather related to xenon's selective and protracted escape from the Archean atmosphere (Avice et al. 2017; Zanhle et al. 2019; Chapters 6 and 7).

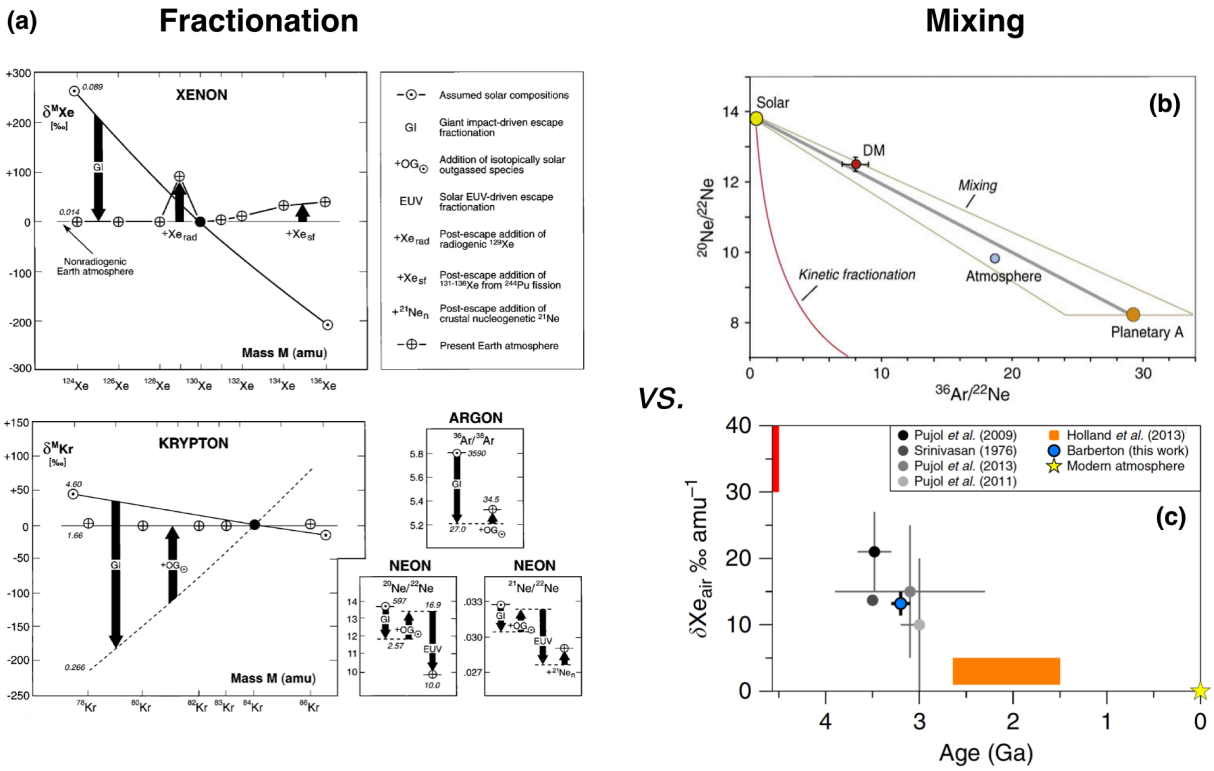

Fig. 22. First steps from "fractionation" to "mixing" models to account for the noble gas elemental and isotopic signature of atmospheric noble gases. (a) The multistage hydrodynamic escape fractionation scenario proposed by Pepin (2003) in the framework of the planetesimal blow off model. (b) Mixing diagram between a solar end-member and the Planetary-A component to account for the isotopic and elemental composition of light noble gases in the atmosphere (Marty 2012). (c) Isotopic fractionation relative to the modern atmosphere of atmospheric Xe with time (Pujol et al. 2011; Avice et al. 2017).

Among all atmospheric noble gases, Xe is the most enigmatic. First of all, it does not appear to be genetically linked to any type of chondrites, or from protosolar nebula gas. It seems to have a unique nucleosynthetic fingerprint, characterised by a relative deficit in r-process isotopes ^{134,136}Xe compared to common cosmochemical reservoirs (Fig. 23). Atmospheric Xe is depleted relative to other noble gases (Ne, Ar and Kr) when compared to solar and chondritic elemental patterns (Fig. 23). It is also strongly mass dependently fractionated in favour of the heavy isotopes, compared to any known cosmochemical components. These two features (elemental depletion and isotopic fractionation) form the "xenon paradox" (Ozima and Podosek, 2002). It is considered paradoxical as the degree of loss and isotopic fractionation is greater for Xe than for lighter noble gases, when the opposite would be expected during hydrodynamic escape (Ozima and Podosek 2002). Interestingly, noble gas elemental ratios on

Earth, Mars and possibly Venus follow the same planetary pattern as found in chondrites, except that (especially for Earth and Mars, where we have good precisions) they share this mono-elemental depletion in Xe. Earth and Mars also show similar extents of MDF with respect to a purported solar-like starting composition, reinforcing the idea that isotopic and elemental constraints are related. In Chapter 6, we discuss the possibility for the model of xenon's selective escape from the Archean atmosphere to account for its relative depletion in the atmosphere, with the pros and cons regarding the model discussed in Chapters 6 and 7.

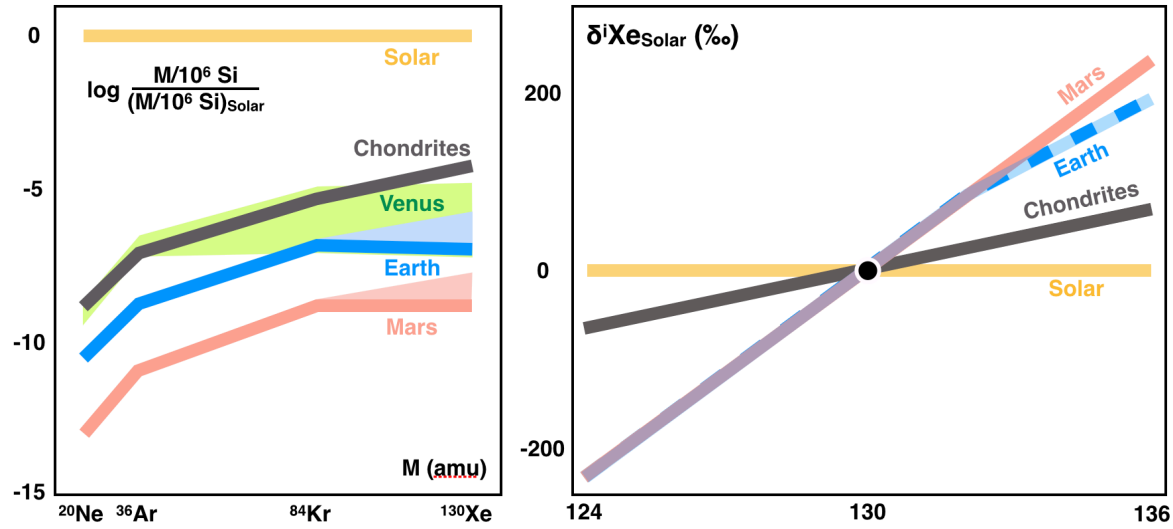

Fig. 23. Schematic illustration of the missing Xe paradox. Left panel: Abundance patterns of noble gases in the Sun ("solar"), in chondrites, and in the atmospheres of Earth, Mars and Venus. For Earth and Mars, the coloured areas represent the amount of missing Xe relative to lighter noble gases and to the chondritic pattern. Adapted from Vogt et al. (2019). Right panel: simplified comparison of the Xe isotope compositions of chondrites (Q-Xe) and the atmospheres of the Earth and Mars, expressed in deviations in parts per mil (‰) relative to the solar composition. Adapted from Marty et al. (2016).

One half of the Xe paradox (elemental depletion) could be accounted for by Xe sequestration in the solid Earth. This proposal arises from experimental and theoretical investigations showing that Xe can be accommodated into mineral lattices and magmas at depth (Chapter 6). For instance, the formation of Xe-O bonds in Xe doped hydrous silica-rich melts could account for the enhanced solubility of Xe in deep continental crust magmas (Leroy et al., 2018). However, Xe and Ar appear to have similar solubility values in silicate melts (Leroy et al., 2018), and therefore how this mechanism would account for the preferential incorporation of Xe, with respect to other noble gases including Ar, is unknown. In essence, any mechanism advocating sequestration of Xe in the Earth to account for the missing Xe paradox should be less efficient at trapping lighter noble gases. However, Kr has for instance been predicted to become sufficiently reactive at high pressure to also form Kr oxides (Zaleski-Ejgierd and Lata 2016). Furthermore, the amount of Xe that is missing from the atmosphere is enormous, corresponding to 10 to 20 times the present day inventory of atmospheric Xe (Ozima and Podosek, 2002); any natural sample would therefore be required to contain orders

of magnitude more Xe than has been previously measured to possibly indicate that such a Xe-rich reservoir exists in the silicate Earth. Alternative scenarios invoke that missing Xe could be hidden at depth in the Earth's core (e.g., Zhu et al. 2014; Stavrou et al. 2018), or was originally depleted in the accretionary building blocks of Earth and Mars (Dauphas and Pourmand, 2011).

Other hypotheses regarding the origin of the missing Xe paradox have suggested that a late addition of cometary material with a high $^{84}Kr/^{132}Xe$, as suspected from pioneering laboratory experiments showing that Kr is trapped more efficiently within amorphous ice than Xe, and solar-like isotopic composition could potentially account for the depletion of Xe on Earth (Dauphas 2003). Definite quantification of the potential role of comets in forming the atmosphere has however been hampered by the lack of reliable measurement of cometary material. Analyses of stardust grains from comet 81P/Wild 2 revealed the presence of chondritic light noble gases (Marty et al., 2008), but no information could be provided regarding the heavy noble gases. As part of this PhD thesis, novel insights into the heavy noble gas composition of cometary ices were provided by the first *in situ* measurements of the coma of a cometary body in the Solar System. This corresponds to recent results by the Rosetta space mission, which analysed the composition of the JFC 67P/Churyumov-Gerasimenko (67P/C-G). As represented Fig. 21, the D/H of 67P/C-G is 3 times the terrestrial value, therefore precluding the previously proposed hypothesis that the JFC reservoir is solely composed of Earth ocean-like water (Altwegg et al. 2015). Results associated with the analysis of comet 67P/C-G by the ROSINA mass spectrometer on board the Rosetta mission, and their implications for the origin of the atmosphere, are discussed in the chapters 2 and 6.

Uncertainties associated with the source(s) of volatile elements on Earth limit our knowledge of the composition of the primitive Earth surface reservoir, therefore making it difficult to accurately evaluate how the atmosphere evolved over geological periods of time. Although liquid water was already present on Earth's surface within a few million years following the Moon-forming impact, harsh environmental conditions as well as intense post-accretionary bombardment likely prevented the continuous habitability of early Earth's surface for several hundreds of million years (Zahnle 2006; Lunine 2006). Major environmental and atmospheric changes during the Hadean and Archean eons - ultimately leading to Earth's surface irreversible oxidation at the Archean-Proterozoic boundary (Holland, 2006) - probably accompanied/supported the development of life, whose timing is however poorly known (Van Zuilen et al. 2002). This is mainly due to the fact that (i) the conditions and processes that could possibly have driven the emergence of early life on Earth are not known (Dalai et al. 2016), and (ii) the earliest remnants of early life in the geological record are often disputed due to secondary processing (e.g., metamorphism, aqueous alteration, mixing with younger generations of organic materials; Oehler and Cady 2014; Marshall et al. 2012). Main challenges in evidencing the earliest traces of life have recently been reviewed by Javaux (2019), emphasizing the difficulties associated with the assessment of their biogenecity (i.e., life-related

character) and syngenecity (i.e., same age for organic materials and their host rocks). In Chapter 7, we present a xenon-based dating method that could potentially provide constraints regarding the syngenetic origin of ancient organic materials isolated from Archean sedimentary rocks.

Chapter 1

Noble gas analysis in geochemistry, motivations and methods

Stable noble gases (namely He, Ne, Ar, Kr and Xe) constitute a group of 23 isotopes that occupy the last column of the periodic table of elements. As such, they have a filled outer electron shell, meaning that for the most part they do not take part in chemical reactions and can therefore be considered inert. Their aversion to forming chemical bonds makes them powerful tracers of physical processes (e.g., diffusion processes, degassing, hydrodynamic escape) at micro to planetary scales. In addition, they are highly volatile and incompatible, which means that, during partial melting, they will be concentrated into the melt phase of magma and ultimately be degassed to the atmosphere. Hence, they are generally depleted in geological material, which facilitates the detection of secondary contributions from nuclear (radioactive and/or spallogenic) reactions, commonly used for dating purposes. Over the course of the last decades, noble gas geochemistry has provided a wealth of knowledge that underpins our current understanding of the Earth and Solar System. This is in part due to the fact that they exhibit unique and measurable isotopic and elemental ratios within distinct planetary (e.g., atmospheric, crustal, mantle) and cosmochemical (e.g., solar, meteoritic, cometary) reservoirs, and can therefore be used as powerful tracers for the origin of volatile elements on Earth and in the Solar System. In particular, noble gas to carbon, nitrogen, and/or water ratios can be used to bring constraints on the provenance and fluxes of these volatile elements within planetary environments, therefore allowing questions such as the origin of volatile elements within the Earth surface reservoir (biosphere, hydrosphere, atmosphere) and their relation to the emergence of life, to be tackled. This section details how noble gas isotopic and elemental compositions are determined by static mass-spectrometry, briefly touching on the different methods of extraction, separation and purification that have been used throughout this project. I will also describe the data reduction procedure and error propagation process required to produce a dataset operational for interpretations.

Noble gas isotopes can be grouped in to two major categories: primordial isotopes, which are not significantly produced by radioactive processes and therefore represent the original budget that was accreted to Earth, and secondary components, typically referring to noble gases that were/are produced by nuclear processes (radiogenic, fissiogenic, nucleogenic, cosmogenic) over geological periods of time (Table 1). Here below, we outline how primordial to secondary noble gas isotope ratios can for instance be used to set constraints on the source and degassing state of terrestrial mantle reservoirs. This relates to the work we carried out on determining the source of volcanism beneath central Europe, reported in the Appendix D of this manuscript.

1.1. Noble gases as geochemical tracers

Daughter	Half-life	Parent nuclide	Yield (atom/decay)
^{3}He	12.26 yr (β)	^{3}H	1
^{4}He	4.468 Gyr(α)	^{238}U	8
	0.7038 Gyr (α)	^{235}U	7
	14.01 Gyr (α)	^{232}Th	6
^{40}Ar	1.251 Gyr (β)	^{40}K	0.1048
^{82}Kr	(1-1.3)x10^{20} Gyr (ββ)	^{82}Se	1
^{86}Kr	4.468 Gyr (sf)	^{238}U	
	82 Myr (sf)	^{244}Pu	
^{128}Xe	*(0.7-2.9)x10^{21} Gyr (ββ)*	*^{128}Te*	1
^{129}Xe	15.7 Myr (β)	^{129}I	1
^{130}Xe	*(0.7-2.9)x10^{21} Gyr (ββ)*	*^{130}Te*	1
^{136}Xe	4.468 Gyr (sf)	^{238}U	3.5×10^{-8}
	82 Myr (sf)	^{244}Pu	7.00×10^{-5}

Table 1. Decay processes for the formation of radiogenic noble gas nuclides, including the yield (number of atoms produced per decay) for each decay reaction. sf = spontaneous fission. α, β and ββ correspond to the different types of radioactive decay (ββ corresponding to the double beta decay). Data from Ozima and Podosek (2002), Porcelli et al. (2002).

To illustrate how noble gases can be used as geochemical tracers and chronometers, I briefly present here below two examples of application: cosmogenic exposure dating and investigation of the distribution and evolution of volatile elements within distinct mantle reservoirs. The latter point is the main focus of the paper Bekaert et al. (2019c) *EPSL*, reported in Appendix D.

Samples collected from the surface of the Earth or originating from space are liable to have an addition of cosmogenic isotopes, which can then be used as a dating tool for surface processes and determination of exposure ages. Spallation reactions refer to nuclear reaction in which fast incoming particles (for instance high-energy cosmic ray particles) strike a target nucleus (in rock for instance), which results in a few protons and neutrons being sputtered off, leaving behind a lighter nucleus. As cosmic ray particles can penetrate a few meters below the surface of rocky material, cosmogenic nuclides can be used to provide information on, the duration that meteorites have travelled through space as small objects, the age of lunar craters (e.g. Eugster et al., 1977), and time that a rock has been exposed on the surface (Blard et al. 2006) all provided that production rates and target concentrations in the sample is known.

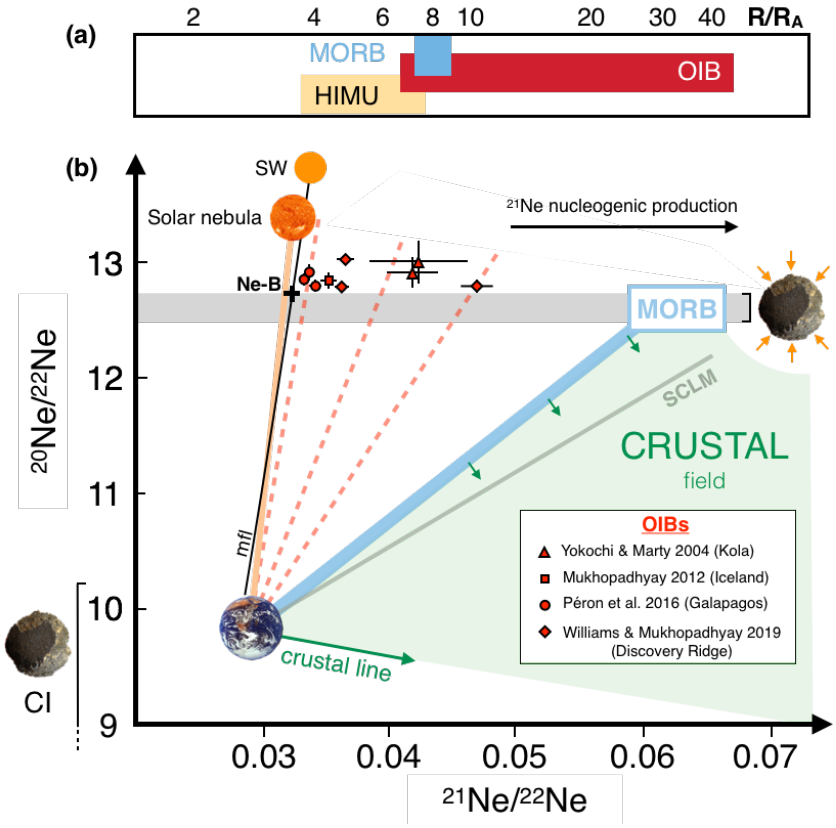

Fig. 24. (a) Summary diagram for the ranges of He isotopic composition of Mid Ocean Ridge Basalts (MORB), Ocean Island Basalts (OIB) and HIMU samples (adapted from Barfod et al. 1999). (b) Neon three-isotope plot displaying the composition of Earth's atmosphere (Earth symbol; Eberhardt et al. 1965), solar nebula gas (Sun symbol; Heber et al. 2012), solar wind (Pepin et al. 2012), the range of observed and modelled $^{20}Ne/^{22}Ne$ ratios attributed to implanted solar wind in chondritic material (grey area; Williams and Mukhopadhyay 2019), and the range of $^{20}Ne/^{22}Ne$ measured in CI chondrites (Mukhopadhyay et al. 2019). The solar nebula-air mixing line is shown as an orange line. Ne-B (Moreira and Charnoz, 2016) corresponds to our best estimate of solar-wind-irradiated material. Mass-dependent fractionation (mfl) is shown from SW as a black curve passing through Ne-B. The blue line is the MORB line (Moreira et al. 1998). The highest $^{20}Ne/^{22}Ne$ measured for OIB sources are given as red symbols (see chart legend). ^{21}Ne nucleogenic production and crustal contribution are shown as black and green thick arrows, respectively. Any data point plotting within the green field contains a crustal contribution (e.g., see the sub-continental lithospheric mantle composition; Buikin et al. 2005).

As long as a noble gas parent nuclide is extant (e.g., ^{238}U and ^{232}Th), the primordial to secondary isotope ratios (e.g., $^{3}He/^{4}He$) of a given mantle reservoir slowly decrease through time. Any episode of degassing to the atmosphere causes a decrease in the concentration of both primordial and secondary isotopes, and induces subsequent productions of secondary isotopes to more drastically affect the primordial to secondary isotope ratios of the reservoir. Degassing hence increases the rate of primordial to secondary isotope ratio decrease with time, until the point where parent nuclides eventually become extinct. From then, degassing does not affect primordial to secondary isotope ratios anymore. As a conclusion, the most degassed portions of the mantle would exhibit lower primordial to secondary isotope ratios than the less degassed portions (Parai et al. 2019). More variable $^{3}He/^{4}He$ in the OIB mantle sources

compared to the consistent $^{3}He/^{4}He \sim 8 \pm 2$ Ra for MORBs (Barford, 1999; Fig. 24) would reflect differences in the state of degassing of the respective mantle sources, with the OIB mantle source being more variably degassed than the MORB one (Fig. 24; Table 2). The OIB mantle source is thought to have experienced limited direct mixing with, and volatile transfer to, the convecting MORB mantle source (Mukhopadhyay, 2012) and to have preserved remnants of primordial volatiles that are not witnessed within the MORB mantle reservoir. Whilst the $^{20}Ne/^{22}Ne$ of the upper mantle as measured in MORBs (Moreira et al. 1998) and continental well gases (Ballentine et al., 2005) is similar to solar wind irradiated material found in chondrites ($^{20}Ne/^{22}Ne \sim 12.7$), Ne in the deep mantle exhibits $^{20}Ne/^{22}Ne > 12.7$, pointing towards a pure solar nebula origin (Fig. 24).

	OIB mantle source	MORB mantle source
represented by	Iceland (DICE)	Popping rocks (2πD43)
Degassing/processing features		
$^{3}He/^{4}He$	< 8	~ 8
$^{21}Ne/^{22}Ne$	< 0.065	~ 0.065
$^{40}Ar/^{36}Ar$	$\geq 25{,}000$	5000 - 15,000
Pu-Xe/(Pu + U)-Xe	~ 0.97	~ 0.30
Accretionary features		
I/Xe	~ 6.9	~ 7.8
$^{20}Ne/^{22}Ne$	> 12.7	12.5 - 12.7

Table 2. Compilation table of the main noble gas features of the OIB and MORB mantle sources. From Graham (2002) and Parai and Mukhopadhyay (2015). See Bekaert et al. (2019) in Appendix D.

1.2. Noble gas fractionation processes

Given their inertness, noble gases are presumably prone to fractionation effects between any two elements/isotopes with different masses (isotopes and elements) through physical processes only (e.g., diffusive loss, hydrodynamic escape, implantation). The physical laws that describe the partitioning of isotopes invariably depend on the mechanism (kinetic or equilibrium reactions for instance) driving MDF fractionation. With 9 isotopes, Xe is the most compelling tool to constrain MDF processes. It is common practice to describe MDF processes with one fractionation law represented by a single curve on a three-isotope plot. This kind of diagram, which plots one isotope ratio (isot2/isot1) against another (isot3/isot1) having the same normalizing isotope, is useful to identify two-component mixing trends, depicting straight lines in three-isotope space. The equilibrium isotope fractionation factor α_{a-b} for two components a and b is defined as the ratio of the isotope ratios for these two components at equilibrium:

$$\alpha_{a-b} = \frac{\left(\frac{isot2}{isot1}\right)_a}{\left(\frac{isot2}{isot1}\right)_b}$$

Mass fractionation laws relating three isotopes are typically expressed in the form:

$$\alpha_{isot2-isot1} = (\alpha_{isot3-isot1})^{\beta}$$

where the β exponent varies depending upon the fractionation process. In the case of an equilibrium isotope exchange (a), diffusion and kinetic fractionation (b), or gravitational isotope fractionation (c), the β exponent might equal (Young et al. 2002):

$$(a)\ \beta = \frac{\frac{1}{isot1} - \frac{1}{isot2}}{\frac{1}{isot1} - \frac{1}{isot3}};\quad (b)\ \beta = \frac{\ln\left(\frac{isot1}{isot2}\right)}{\ln\left(\frac{isot1}{isot3}\right)};\quad (c)\ \beta = \frac{isot1-isot2}{isot1-isot3}$$

The formula used to plot MDF trends in three isotope plots is given by:

$$\frac{isot2}{isot1} = \left(\frac{isot2}{isot1}\right)_{ref} * \left(\frac{\left(\frac{isot3}{isot1}\right)}{\left(\frac{isot3}{isot1}\right)_{ref}}\right)^{\beta}$$

where the reference (ref) is the anchor point of the MDF curve, corresponding for instance to the starting composition before fractionation. It is also worth noting that mass-independent fractionation (MIF) effects (any isotope effect that does not scale in proportion to mass differences in isotopes) can happen, for instance for O (Thiemens and Heindenreich III 1983; Chakraborty et al. 2008) or S (Farquhar et al. 2000), but have not been observed (as far as I am aware) for noble gases.

1.3. Noble gas isotopic and elemental analysis by static mass spectrometry

The procedure for analysing noble gases using static mass spectrometry can be broken down in to three main steps: (i) extraction, (ii) purification and, (iii) analysis. In the following section I will briefly outline how these three steps are performed at CRPG.

1.3.1. Noble gas extraction

In order to analyse noble gases firstly, the gases must be liberated from the sample. For solid samples this can be achieved either by crushing or heating the samples under vacuum. Crushing samples under vacuum is primarily utilised to extract gases held within fluid inclusions and vesicles. By crushing the sample it is possible to limit the release of radiogenic and cosmogenic nuclides that have been produced in the matrix (Bekaert et al. 2018b). In

addition, crushing allows for the different components within a given sample to be released in variable proportions; if the two main components within a given mantle-derived sample are for example air and a primordial component, crushing steps will plot along a mixing line between these two end members, therefore allowing the composition of the primordial component to be extrapolated (Moreira et al. 1998).

To release the noble gases contained within the matrix, samples are often heated using either a furnace or laser. As part of this project I utilised a quartz furnace (Bekaert et al. 2017), an induction furnace (Bekaert et al. 2017; Fig. 25), a CO_2 infrared (λ = 10.6 μm) laser (Bekaert et al. 2017, 2018b, 2019a), and a filament furnace (Bekaert et al. 2018c, 2020) (Fig. 25) each of which have advantages and disadvantages that are quickly discussed below.

For the analysis of small samples (~1mg) I employed CO_2 laser heating (Humbert et al., 2000). The volume of the laser chamber is reduced (~25 cm^3) and only the sample is heated (not the sample holder), therefore resulting in very small blanks. It acts as a very efficient extraction system, with the formation of a spherule of molten silicate during the melting temperature step indicating that more than 99% of the gas has already been extracted from the samples (Humbert et al., 2000). However, because the glue used to set the sapphire window on top of the laser chamber cannot sustain very high temperatures, samples analysed with the CO_2 laser cannot be baked at temperatures higher than 100°C prior to extraction. To counteract this drawback, samples are usually baked for longer than usual, e.g. for one week. In addition, the maximum mass that can be analysed using the CO_2 laser is typically ~ 6 mg, which limits its use to samples with high gas concentrations. Furthermore, it is not possible to measure the temperature of extraction during CO_2 laser heating, and so this method is better suited for samples where bulk gas extraction is required.

To analyse larger samples (up to several grams!) at accurate temperatures I employed the use of an induction furnace. Unlike for the laser chamber, the samples are not loaded within the extraction cell itself, but are stored under vacuum in a preparation glass line connected to the furnace. This permits the Ta crucible to be degassed at high temperature and for an infinite period of time, therefore improving the blank, prior to samples being dropped in the Ta crucible for noble gas extraction. Even if the volume of the induction furnace cell is large (2,118 cm^3), blanks can be very low (Bekaert et al. 2017). Temperatures were calibrated using an optical pyrometer, and are thus only indicative at ±100 °C. Another inconvenience with the induction furnace was that the power supply had to be increased and decreased very slowly in increments of 60°C/5 min in order to avoid damaging the glass part of the extraction system. This resulted in a complete 1800 °C extraction step, taking ~4 h.

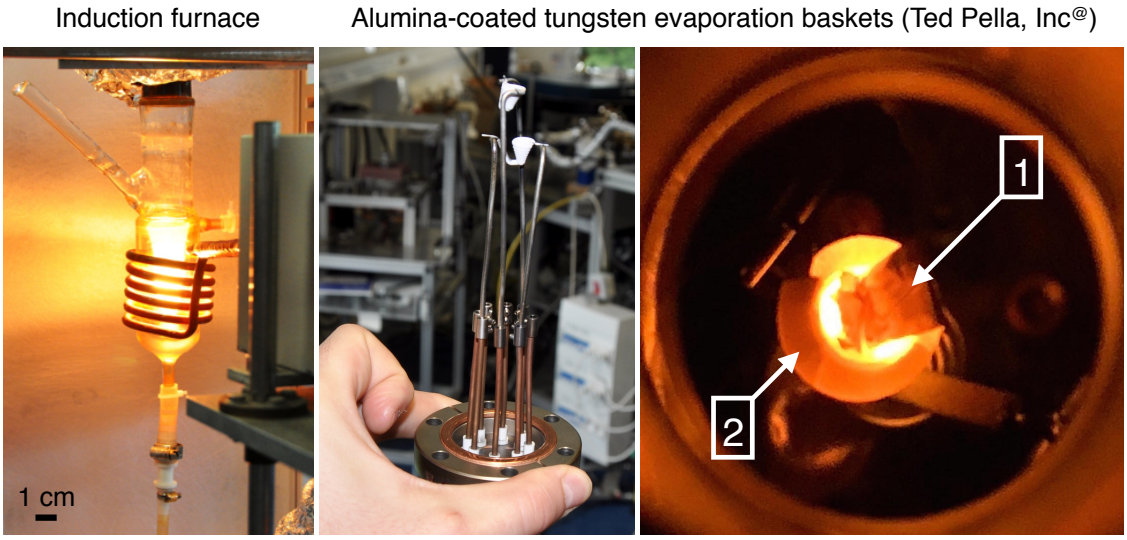

Fig. 25. Induction furnace (left) and filament furnace (middle and right) used for the analysis of lunar samples (Bekaert et al. 2017) and organic materials (Bekaert et al. 2018c, 2020), respectively. The induction furnace relies on the induction heating of a Ta crucible contained in a water-cooled Pyrex structure. For the filament furnace, samples are wrapped into tungsten foils (right panel, 1) and set in alumina-coated tungsten evaporation baskets (right panel, 2), which are welded to the feedthrough, itself supplied by a current generator (20 A). Temperature step on the right panel is ~1200°C.

Finally, the filament furnace constitutes a good compromise between the CO_2 laser extraction and the induction furnace as it allows analysing samples with masses up to ~100 mg, and also has an intermediate volume between the two (260 cm^3). The furnace consists of four alumina-coated tungsten evaporation baskets (Ted Pella Inc.) welded to a pair of nickel rods mounted on eight-pin electrical feedthrough flange. Temperatures were first estimated by using foils of pure metals with known melting points (tin, 230°C; aluminium, 660°C; copper, 1085°C; and nickel, 1455°C), and controlled during step heating by direct measurement using an optical pyrometer. Note that the temperature calibration curve of a given basket (Fig. 26) may depend on the quality of the weld between the baskets and the nickel rods, we therefore assign an accuracy of ±100 °C. Before loading the samples, each basket is degassed at ~1600°C (maximum temperature) to remove adsorbed atmospheric noble gases. Degassed evaporation baskets are systematically exposed to the atmosphere during sample loading, so blank determinations are carried out on empty baskets loaded at the same time as the sample. Samples were wrapped in tantalum foil and loaded into the baskets before baking the entire furnace at >150°C overnight under high vacuum. Depending on the material being analysed, samples may be loaded individually to avoid passive heating and degassing of other samples during analysis. The sample and the blank basket are step heated sequentially, i.e. both are analysed at a given temperature before moving on to the next temperature step (see papers reported in Appendix C and E).

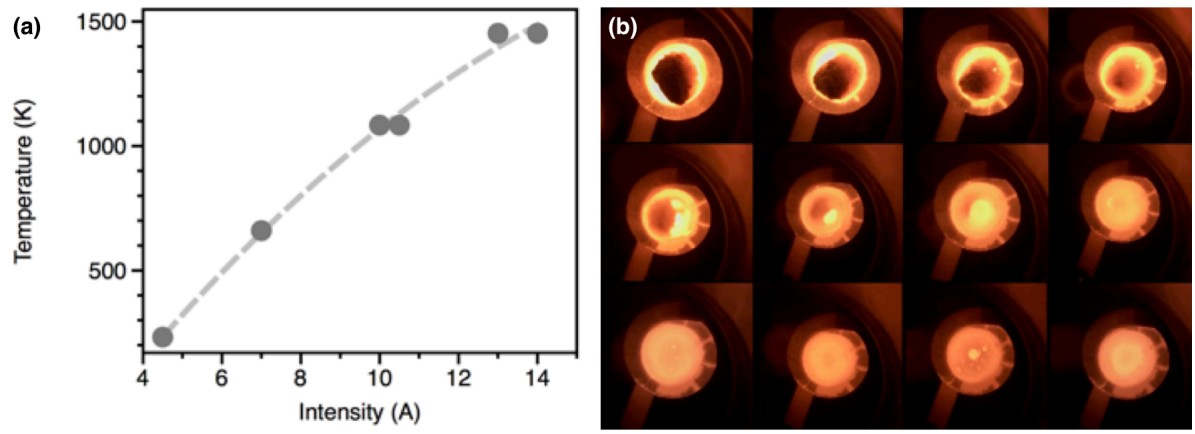

Fig. 26. (a) Calibration curve for the temperature of the filament furnace using metal foils. (b) Time evolution of the melting of a 93 mg aliquot of the Nakhlite Caleta el Cobre 022 in a filament furnace.

1.3.2. Separation and purification procedures

In general noble gases have extremely low concentrations in geological samples and so their analysis is classically operated in static mode (i.e., with the analysed gas being isolated from pumps). Static mass spectrometers are susceptible to pressure dependent effects, where mass discrimination changes dependent on the amount of gas being analysed. Furthermore, there exist molecules and atoms with the similar masses to several noble gas isotopes, which can therefore interfere with the measurement of the noble gas. For these two reasons it is crucial that each noble gas elements are admitted to the mass spectrometer at as high purity as possible.

The purification of noble gases usually takes advantage of their inert nature, by chemically removing the other reactive gases on active metal surfaces called "getters". Specifically at CRPG noble gases are purified on high purity Ti-sponge held at 500-600°C and then at room to decompose reactive molecules (e.g., water). Furthermore, an in-line Ti-sponge getter placed just after the extraction section of the line and continuously operated at 700°C allows very efficient purification of extracted gases. In total, an extracted gas sees at least 5 getters over the course of its purification process (3 being hot, and 2 being left at room temperature; Fig. 27). The purification procedure can vary from sample to sample, therefore a more detail account of the purification procedure used for different samples is given in the method sections of the corresponding papers.

At CRPG, we are able to efficiently separate all noble gases, except Kr from Xe. If we need to separate noble gases, we typically start by exposing the extracted gas to a Pyrex cold finger at liquid nitrogen temperatures for 20 minutes in order to trap Kr and Xe. Adsorption on the walls of the Pyrex tube is unlikely to induce detectable isotopic fractionation (Marrocchi and Marty, 2013). The cold finger is then closed, to isolate Kr and Xe for later analysis, and the gas is exposed to a charcoal at liquid nitrogen temperature for 10 min to trap all of the Ar., The gas is then expanded to the cryogenic head set at 34 K in order to trap Ne, but not He,

for 20 min. In this case, only He remains in the line, which can therefore be analysed first in isolation. The cryogenic head is hence heated up to 88 K in order to release Ne for analysis. The charcoal can then be put back to room temperature for Ar analysis, followed by Kr and Xe being released from the Pyrex finger at room temperature for analysis. Krypton and xenon are notable for being analysed altogether. If the sample contains a lot of Ar, there might be a significant partial pressure of Ar in the volume of the cold finger where Kr and Xe are condensed. If significant amounts of Ar were to be admitted to the mass spectrometer at the same time as Kr and Xe, the analysis can be subject to pressure effects causing the results to be meaningless. To avoid this effect, we proceed with several dilutions of the volume of the glass tube (20 cm^3) into the whole purification line (1500 cm^3), whilst keeping the glass finger at liquid nitrogen temperature to keep Kr and Xe, therefore dramatically reducing the residual partial pressure of Ar. In addition, we note that due to the total volume of the mass spectrometer being larger than that of the purification line (by a factor ~4), two minutes of equilibration of the partial pressure of gas in the mass spectrometer were required before isolating the mass spectrometer and starting the analysis.

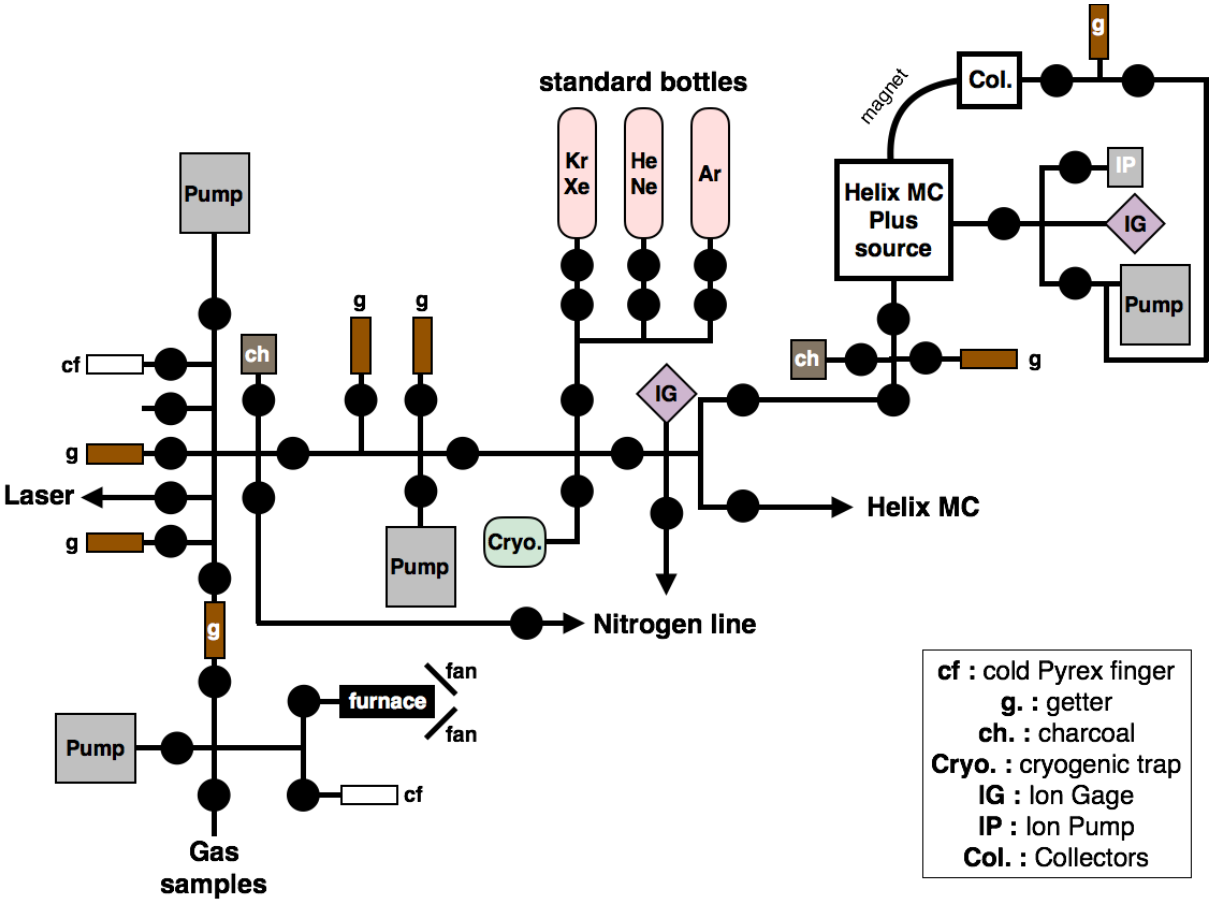

Fig. 27. Schematic representation of the Helix MC Plus extraction, purification and separation line. The furnace corresponds here to the evaporation basket furnace cooled with two fans (Bekaert et al. 2018c, 2020). The laser corresponds to the CO_2 laser (Humbert et al. 2000). Not to scale.

1.3.3. Generalities on mass spectrometers

Mass spectrometers are in essence a way of separating out different isotopes as a function of their mass in order for them to be measured accurately. All mass spectrometers including noble gas mass spectrometers work on the same principles in that they all consist of an ion source, a means to separate out the different mass (mass filter) and a method of measuring each isotope (detectors). All noble gas analyses reported in the main text of this thesis have been acquired from the Helix MC Plus (Thermofisher) mass spectrometer arrived at CRPG in 2015 (a schematic representation of the line in provided Fig. 28). This high mass resolution (> 1800) and mass resolving power (> 8000) mass spectrometer contains a newly designed modified Nier-type electron bombardment source (Nier, 1947) (Fig. 28).

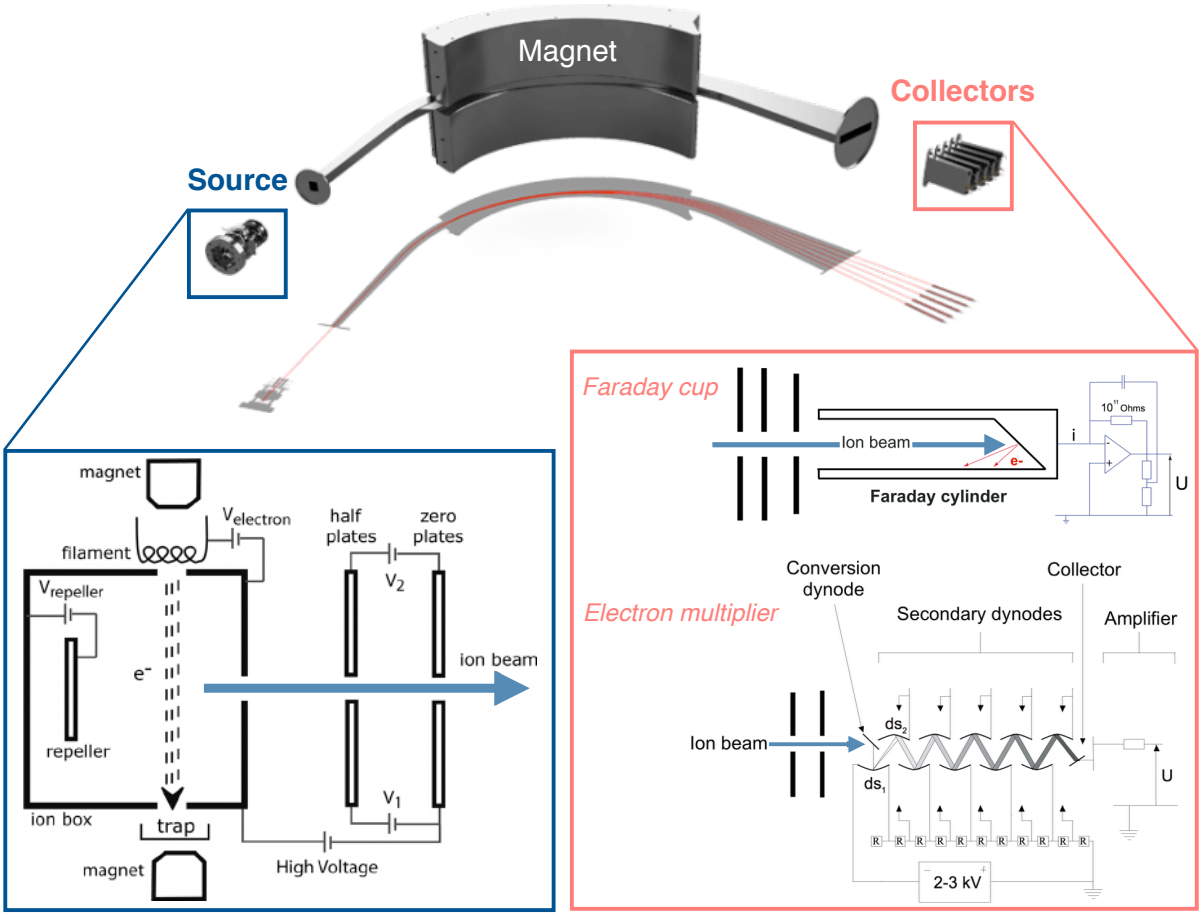

Fig. 28. Schematic representation of the Helix MC Plus noble gas mass spectrometer (Thermo Fisher company) with the source, magnet and collectors. The schematic representation of the Nier-type ion source is from Mabry et al. (2012).

Within the source, the gas is ionised by electron impact. Applying a current through a thermionic emission metal filament generates the beam of electrons, which is then directed toward the gas sample by a potential voltage difference on the trap electrode. External

magnets around the source can be used to give the path of electrons a spiral shape, therefore increasing the mean free path of the electrons within the source and increasing the rate of ionization of the sample. Generated cations (with a charge e) are then expelled from the source by a positively charged repeller plate, and are accelerated by a potential difference (called acceleration reference, V) of 9.9 kV. In the arced flight tube, the movement of each ion is controlled by its mass-dependent (mass noted m) responsiveness to the magnetic field of the magnetic sector. All ions have the same kinetic energy, which can be expressed as $E = eV = \frac{1}{2}mv^2$, where v, the velocity of a given isotope, only depends on the mass of the isotope at a fixed kinetic energy. Crucially, an ion of charge e, accelerated in an electric field with a potential voltage difference V and subject to a magnetic field B, has a m/e ratio that can be expressed as: $\frac{m}{e} = \frac{B^2.r^2}{2V}$, where r is the radius of the arced ion path. Combined with the expression of V in the kinetic energy formula yields $r = \frac{mv}{eB}$, which implies that, at fixed voltage and magnetic field, the radius of the arced path of a charged isotope only depends its velocity. This radius can finally be noted as: $r = \frac{m}{eB}.\sqrt{\frac{2eV}{m}} = \sqrt{\frac{m}{e}}.\frac{\sqrt{2V}}{B}$, indicating that at fixed acceleration reference and magnetic field, it will be proportional to the square root of the mass to charge ratio only. Hence, after their travel through the flight tube and magnet, the different elements/isotopes will be separated according to their mass to charge ratios, with the heaviest ones following the least curved trajectories, and the lightest ones being the most deviated by the magnetic field. Provided that the geometry of the mass spectrometer is fixed and the acceleration reference is kept constant, it is possible to adjust the trajectories of the different ions (i.e., the different isotopes) by varying the magnetic field. Hence, the user can select the mass/charge ratio of the ions that will be directed towards a given detector, with minimum contribution from ions with different mass/charge ratios (sent at different radii).

There are two main types of collectors used on noble gas mass spectrometers: Faraday cups and electron multipliers. The formers consist of metal cups associated with high gain resistors (~10^{12} Ohm): each charged particle of the ion beam impinging onto the cup charges its surface and generates a current, which can then be measured and used to count the total number of ions hitting the cup. Such detectors are commonly used for the most abundant noble gas isotopes (e.g., ^{4}He, ^{40}Ar). However, for low abundance elements such as ^{3}He, ^{36,38}Ar, Ne, Kr and Xe isotopes, Faraday cups are not sensitive enough and electron multipliers are used instead (with typical gains of 10^6 Ohm). A multiplier consists of a series of negatively charged dynodes (which are more and more negative towards the detector) allowing the chain production of secondary electrons. In details, when an ion impinges on the first dynode, two secondary electrons are emitted from its surface and directed towards the next dynode, where each electron will likewise generate another two secondary electrons, etc. Hence, even a limited ion beam can produce large amounts of electrons, which can be counted at the detector to derive a signal intensity.

1.3.4. Tuning the source

Prior to analysing a sample, standards are analysed to tune the source settings and optimise the sensitivity and reproducibility of the measurements. Optimizing the sensitivity means that the value of current that is measured on the detector is maximised for a given flux of ions hitting the detector. The reproducibility corresponds to the ability to measure the same intensity for multiple independent analyses of identical ion fluxes. In order to warrant a good reproducibility, the peak shape must be flat on top (so that any measure of intensity on top of the peak would give the same value), especially since hysteresis effects might cause a given peak to move slightly from one analysis to another after significant peak jumping. In other words, the peak corresponding to a given element may not always be centred at the exact same mass from one analysis to another, so ensuring the flatness and maximizing the width of the peak allows small shifts to cause no effect on the measured value of intensity (Fig. 29).

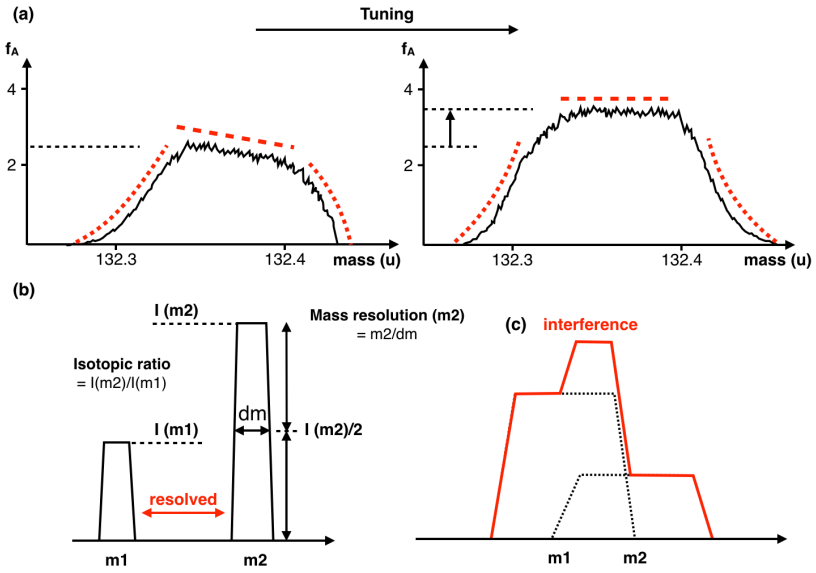

Fig. 29. The effect of source tuning and mass resolution. (a) Schematic representation of the effect of tuning the source to optimise the peak shape (symmetry of the sides, flatness and horizontalness of the top) and sensitivity. (b) Illustration of the mass resolution and computation of an isotopic ratio. (c) Expression of an overlap (interference) between two unresolved peaks.

In addition, it is important to have the sides of a given peak as sharp and as symmetric as possible. The sharpness allows resolving a given peak from its neighbours and therefore avoiding interferences. This is particularly important for Ne, which can suffer from important interferences with doubly ionised Ar and CO_2 (Fig. 30). On the Helix MC Plus spectrometer, ^{20}Ne can be partially resolved from $^{40}Ar^{++}$. However, this is not the case for ^{22}Ne and doubly charged CO_2. To correct for CO_2^{++} contribution on mass ^{22}Ne, the CO_2^{+} signal is measured and then the CO_2^{++} contribution is calculated from the preliminarily determined CO_2^{++} to CO_2^{+} ratio of the mass spectrometer at the given source settings. The derived CO_2^{++} value is then

subtracted from the measured ^{22}Ne intensity to derive the corrected abundance of ^{22}Ne in the sample (Bekaert et al. 2019c, Appendix D). The main possible isobaric interferences for noble gas analyses are reported in Table 3. Table 4 summarises the cup configuration parameters used in this study for the analysis of noble gases on the Helix MC Plus. Table 5 details the analytical procedure for each isotope.

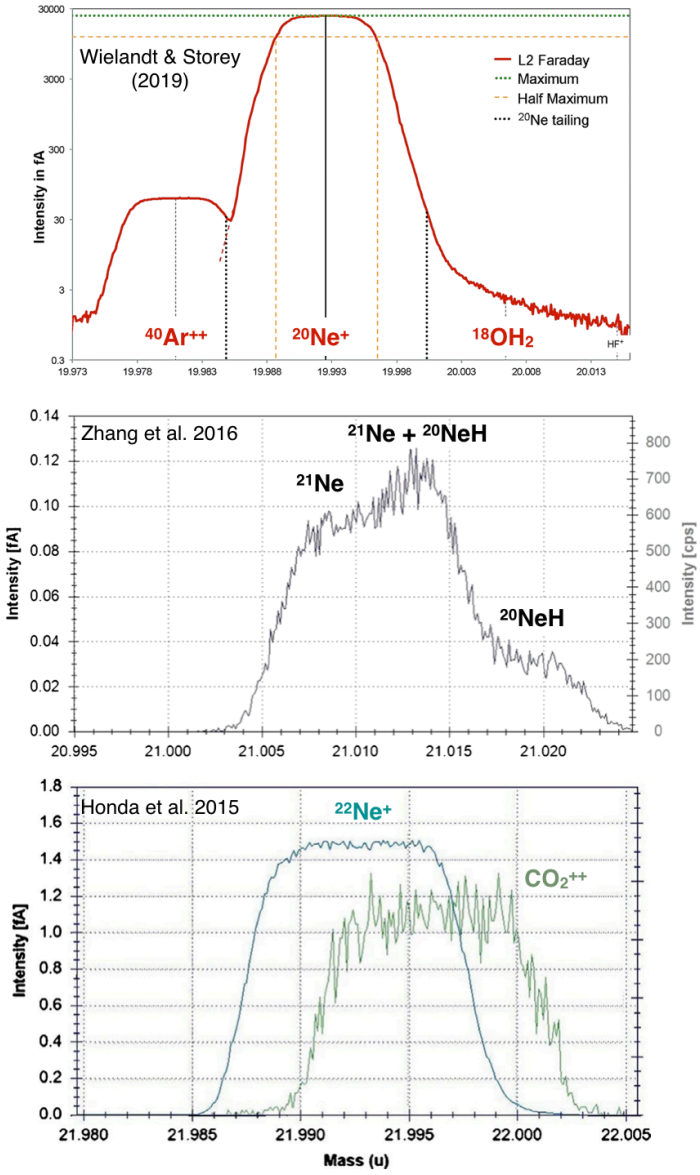

Fig. 30. Neon isotope measurement on the Helix MC Plus. From top to bottom, Ne interferences with Ar^{++} (^{20}Ne), Ne hydrides (here ^{21}Ne) and CO_2^{++} (^{22}Ne) are shown. Corresponding references are given on each figure.

Isotope	Masse (uma)	Interfering particle	Masse (amu)
^{3}He	3.0160	$^{1}H^{2}D^{+}$	3.0215
		$^{1}H_{3}^{+}$	3.0161
		$^{12}C^{4+}$	3.0000
^{4}He	4.0026	$^{12}C^{3+}$	4.0000
^{20}Ne	19.9924	$^{12}C_{3}H_{4}^{2+}$	20.0156
		$^{1}H_{2}{}^{18}O^{+}$	20.0148
		$^{1}H^{19}F^{+}$	20.0062
		$^{40}Ar^{2+}$	19.9812
^{21}Ne	20.9938	$^{20}NeH^{+}$	21.0002
		$^{12}CH_{2}{}^{12}C^{16}O^{2+}$	21.0052
		$^{63}Cu^{3+}$	20.9765
		$^{12}C_{3}{}^{1}H_{6}^{2+}$	21.0235
^{22}Ne	21.9914	$^{12}C^{16}O_{2}^{2+}$	21.9949
		$^{66}Zn^{3+}$	21.9753
		$^{12}C_{3}{}^{1}H_{8}^{2+}$	22.0312
^{36}Ar	35.9675	$^{12}C^{3+}$	36.0000
		$^{1}H^{35}Cl^{+}$	35.9766
^{38}Ar	37.9627	$^{1}H^{37}Cl^{+}$	37.9737
		$^{12}C_{3}{}^{1}H_{2}^{+}$	38.0157
^{40}Ar	39.9624	$^{12}C_{3}{}^{1}H_{4}^{+}$	40.0313
$^{78\text{-}86}Kr$	78-86	$^{12}C_{6}H_{6\text{-}12}{}^{+}$	78-86
$^{124\text{-}136}Xe$	124-136	$^{12}C_{10}H_{4\text{-}16}{}^{+}$	124-136
$^{14}N\text{-}^{14}N$	28.0062	$^{12}C^{16}O^{+}$	27.9949
		$^{12}C_{2}{}^{1}H_{4}^{+}$	28.0312
$^{14}N\text{-}^{15}N$	29.0032	$^{13}C^{16}O^{+}$	28.9982
		$^{12}C_{2}{}^{1}H_{5}^{+}$	29.0391
$^{15}N\text{-}^{15}N$	30.0002	$^{12}C_{2}{}^{1}H_{6}^{+}$	30.0468

Table 3. Main isobaric interferences for noble gas and nitrogen isotopic measurements (compiled by L. Zimmermann from Burnard et al. 2013; De Hoffmann et al. 1994; Zhang et al. 2016).

Element	He	Ne	Ar	Kr-Xe
Acceleration reference (kV)			9.9	
Electron energy (eV)	61.95	60.00	58.86	63.99
Extraction focus (%)	22.59	20.88	25.11	12.65
Extraction lens (%)	38.01	67.94	72.98	57.26
Extraction symmetry (%)	45.20	41.78	1.59	1.59
Flatapole	3.00	0.18	0	0
Horizontal symmetry (%)	30.60	38.41	-3.39	1.98
Ion repeller(V)	-4.62	-1.10	-6.42	-4.11
Rotation quad	31.40	5.00	-31.00	-31.00
Trap current (µA)	280	280	230	230
Trap voltage (V)	50.00	50.00	20.45	20.45
Vertical deflection N	106.05	90.00	85.00	85.00
Vertical deflection S	4.884	45.00	80.00	80.00

Table 4. Source tunings used for each noble gas on the Helix MC Plus.

Isotope	Mass (amu) on AX if not specified	Collector	Settling time (ms)	Integration time (s)
	He analyses - 20 cycles - manual peak centring - peak jumping mode			
baseline ^{4}He	4.5	AX	10000	2.1
^{4}He	4.494	AX	5000	8.39
baseline ^{3}He	2.7 (AX(CDD))	AX(CDD)	10000	2.1
^{3}He	2.636 (AX(CDD)	AX(CDD)	5000	16.78
	Ne analyses - 60 cycles - manual peak centring on H1 - multi-collection mode			
baseline	20	AX(CDD)	5000	4.19
^{20}Ne	19.887	AX(CDD)	5000	8.39
^{21}Ne	20.902	AX(CDD)	2000	16.78
^{22}Ne	21.923	AX(CDD)	2000	8.39
	Ar analyses - 22 cycles - manual peak centring - multi-collection mode			
baseline ^{36}Ar	10.4134 (L2(CDD))	L2(CDD)	5000	2.1
baseline ^{38}Ar	37.6040 (AX(CDD))	AX(CDD)	5000	2.1
baseline ^{40}Ar	11.5705 (H1)	H1	5000	2.1
^{36}Ar	10.4686 (L2(CDD))	L2(CDD)	5000	4.19
^{38}Ar	37.8033 (AX(CDD))	AX(CDD)	5000	4.19
^{40}Ar	11.6318 (H1)	H1	5000	4.19
	Kr analyses - 22 cycles - manual peak centring - peak jumping mode			
baseline	78.5	AX(CDD)	5000	1.05
^{78}Kr	77.96	AX(CDD)	5000	8.39
^{80}Kr	79.99	AX(CDD)	600	8.39
^{82}Kr	82.03	AX(CDD)	600	4.19
^{83}Kr	83.05	AX(CDD)	600	4.19
^{84}Kr	84.06	AX(CDD)	600	4.19
^{86}Kr	86.1	AX(CDD)	600	4.19
	Xe analyses - 22 cycles - manual peak centring - peak jumping mode			
baseline	124.1	AX(CDD)	5000	1.05
^{124}Xe	124.47	AX(CDD)	5000	16.78
^{126}Xe	126.45	AX(CDD)	600	16.78
^{128}Xe	128.37	AX(CDD)	600	8.39
^{129}Xe	129.33	AX(CDD)	600	4.19
^{130}Xe	130.33	AX(CDD)	600	4.19
^{131}Xe	131.36	AX(CDD)	600	4.19
^{132}Xe	132.39	AX(CDD)	600	4.19
^{134}Xe	134.38	AX(CDD)	600	4.19
^{136}Xe	136.34	AX(CDD)	600	4.19

Table 5. Typical settings for noble gas isotopic and elemental measurements on the Helix MC Plus at CRPG (Nancy, France).

1.3.5. Data reduction and error propagation

This section describes (i) the method used to calculate the noble gas abundances and isotope ratios, and (ii) how uncertainties on these values are propagated. It should be noted that the following calculations assume that all variables are independent, i.e. that the variance-covariance matrix of all variables is diagonal, which is probably an oversimplified view (Vermeesch, 2015). Xe abundances (^{132}Xe) and isotope ratios (^{i}Xe/^{132}Xe) are taken here as examples. The Xe concentration corrected for blank contribution ($^{132}Xe_{corr}$ in mol.g^{-1}) was determined as:

$$^{132}Xe_{corr} = \frac{^{132}Xe_{sample} - {}^{132}Xe_{blk}}{m}$$

where $^{132}Xe_{sample}$, $^{132}Xe_{blk}$, are the abundances, in moles, of ^{132}Xe analysed by the mass spectrometer for the sample and during blanks runs, and m is the sample mass (in g). The uncertainty in $^{132}Xe_{corr}$ ($\sigma_{^{132}Xe_{corr}}$) is calculated using the variance formula:

$$\sigma_{^{132}Xe_{corr}} = \left[\left(\frac{\partial ^{132}Xe_{corr}}{\partial ^{132}Xe_{sample}}\right)^2 \sigma^2_{^{132}Xe_{sample}} + \left(\frac{\partial ^{132}Xe_{corr}}{\partial ^{132}Xe_{blk}}\right)^2 \sigma^2_{^{132}Xe_{blk}} + \left(\frac{\partial ^{132}Xe_{corr}}{\partial m}\right)^2 \sigma^2_{m}\right]^{1/2}$$

The formulae for the partial derivatives of $\sigma_{^{132}Xe_{corr}}$ are given by:

$$\frac{\partial ^{132}Xe_{corr}}{\partial ^{132}Xe_{sample}} = \frac{1}{m} \qquad \frac{\partial ^{132}Xe_{corr}}{\partial ^{132}Xe_{blk}} = -\frac{1}{m} \qquad \frac{\partial ^{132}Xe_{corr}}{\partial m} = \frac{^{132}Xe_{blk} - {}^{132}Xe_{sample}}{m^2}$$

Details of the uncertainties in each term of $\sigma_{^{132}Xe_{corr}}$ are given below:

- $\sigma_{^{132}Xe_{sample}}$ is the quadratic sum of the internal error obtained by regression of the signal to time-zero and of the external error given by the standard deviation in the reproducibility over a series of measurements of standard samples.

- $\sigma_{^{132}Xe_{blk}}$ is the standard deviation of the ^{132}Xe abundances obtained during a series of blank measurements analysed under similar conditions to those of the sample.

- σ_m is the standard deviation of the weight measurements. This was obtained by performing a series of weight measurements of a given mass, using the same balance as that used for weighing samples.

Noble gas isotope ratios were computed here using the isotope ratios analysed at each cycle, rather than by computing the ratios between two signals extrapolated to time-zero after

sequential analysis. The Xe isotope ratios corrected for blank contribution and mass discrimination $\left(\left(\frac{^{i}Xe}{^{132}Xe}\right)_{corr}\right)$ are thus calculated using:

$$\left(\frac{^{i}Xe}{^{132}Xe}\right)_{corr} = \frac{\left(\frac{^{i}Xe}{^{132}Xe}\right)_{sample} \times {}^{132}Xe_{sample} - \left(\frac{^{i}Xe}{^{132}Xe}\right)_{blk} \times {}^{132}Xe_{blk}}{{}^{132}Xe_{sample} - {}^{132}Xe_{blk}} \times \frac{\left(\frac{^{i}Xe}{^{132}Xe}\right)_{atm}}{\left(\frac{^{i}Xe}{^{132}Xe}\right)_{std}}$$

where $(^{i}Xe/^{132}Xe)_{sample,blk,std,atm}$ are the isotope ratios measured for the sample, the blanks, the standards and the atmosphere (Basford et al., 1973), respectively. For clarity, we note that f= $(^{i}Xe/^{132}Xe)_{corr}$. The uncertainty in f (σ_f) is computed following:

$$\sigma_f = \left[\left(\frac{\partial f}{\partial\left(\frac{^{i}Xe}{^{132}Xe}\right)_{sample}}\right)^2 \sigma^2_{\left(\frac{^{i}Xe}{^{132}Xe}\right)_{sample}} + \left(\frac{\partial f}{\partial {}^{132}Xe_{sample}}\right)^2 \sigma^2_{^{132}Xe_{sample}} + \left(\frac{\partial f}{\partial\left(\frac{^{i}Xe}{^{132}Xe}\right)_{std}}\right)^2 \sigma^2_{\left(\frac{^{i}Xe}{^{132}Xe}\right)_{std}} + \left(\frac{\partial f}{\partial\left(\frac{^{i}Xe}{^{132}Xe}\right)_{blk}}\right)^2 \sigma^2_{\left(\frac{^{i}Xe}{^{132}Xe}\right)_{blk}} + \left(\frac{\partial f}{\partial {}^{132}Xe_{blk}}\right)^2 \sigma^2_{^{132}Xe_{blk}}\right]^{1/2}$$

The formulae for the partial derivatives of f = $(^{i}Xe/^{132}Xe)_{corr}$ are listed below:

$$\frac{\partial f}{\partial {}^{132}Xe_{sample}} = \frac{\left(\frac{^{i}Xe}{^{132}Xe}\right)_{atm} {}^{132}Xe_{blk}\left(\left(\frac{^{i}Xe}{^{132}Xe}\right)_{blk} - \left(\frac{^{i}Xe}{^{132}Xe}\right)_{sample}\right)}{\left(\frac{^{i}Xe}{^{132}Xe}\right)_{std} ({}^{132}Xe_{blk} - {}^{132}Xe_{sample})^2}$$

$$\frac{\partial f}{\partial\left(\frac{^{i}Xe}{^{132}Xe}\right)_{sample}} = \frac{{}^{132}Xe_{sample}\left(\frac{^{i}Xe}{^{132}Xe}\right)_{atm}}{\left(\frac{^{i}Xe}{^{132}Xe}\right)_{std} ({}^{132}Xe_{sample} - {}^{132}Xe_{blk})}$$

$$\frac{\partial f}{\partial\left(\frac{^{i}Xe}{^{132}Xe}\right)_{std}} = \frac{\left(\frac{^{i}Xe}{^{132}Xe}\right)_{atm}\left({}^{132}Xe_{sample}\left(\frac{^{i}Xe}{^{132}Xe}\right)_{sample} - {}^{132}Xe_{blk}\left(\frac{^{i}Xe}{^{132}Xe}\right)_{blk}\right)}{\left(\frac{^{i}Xe}{^{132}Xe}\right)^2_{std} ({}^{132}Xe_{blk} - {}^{132}Xe_{sample})}$$

$$\frac{\partial f}{\partial {}^{132}Xe_{blk}} = \frac{{}^{132}Xe_{sample}\left(\frac{^{i}Xe}{^{132}Xe}\right)_{atm}\left(\left(\frac{^{i}Xe}{^{132}Xe}\right)_{sample} - \left(\frac{^{i}Xe}{^{132}Xe}\right)_{blk}\right)}{\left(\frac{^{i}Xe}{^{132}Xe}\right)_{std} ({}^{132}Xe_{blk} - {}^{132}Xe_{sample})^2}$$

$$\frac{\partial f}{\partial \left(\frac{^{i}Xe}{^{132}Xe}\right)_{blk}} = \frac{^{132}Xe_{blk}\left(\frac{^{i}Xe}{^{132}Xe}\right)_{atm}}{\left(\frac{^{i}Xe}{^{132}Xe}\right)_{std}(^{132}Xe_{blk} - ^{132}Xe_{sample})}$$

As most laboratories currently use atmospheric Xe as a running standard, these uncertainties are cancelled out when Xe isotope ratios for different samples are compared, so we neglected the uncertainties in the isotopic ratios of atmospheric xenon. However, if in future studies sample isotopic ratios are normalised against another standard such as an artificial mixture of Xe isotopes, this may no longer be true.

Below we detail the significance of each uncertainty (σ_j):

- $\sigma_{\left(\frac{^{i}Xe}{^{132}Xe}\right)_{sample}}$ is the quadratic sum of the uncertainties in the measurement of the isotope ratio by the instrument (the internal error) and of the standard deviation over a series of standard measurements (external uncertainty). Strictly speaking, the external error in the sample measurement should be used, however, as only one measurement is usually made for a given sample run (e.g., a temperature step), it is necessary to use a proxy for this external error instead. Here, we use the external reproducibility for a series of standard runs, given by the standard deviation of the series (σ).

- $\sigma_{^{132}Xe_{sample}}$ is the uncertainty in the initial ^{132}Xe abundance (converted in moles) computed after regression of the signal over the whole analysis.

- $\sigma_{\left(\frac{^{i}Xe}{^{132}Xe}\right)_{std}}$ is the uncertainty in the "true" value of the isotope ratios measured for standards (standard error of the mean, $\sigma/(n)^{1/2}$). This corresponds to the standard deviation of the series of measurements divided by the square root of the number of measurements (between 10 and up 30 measurements made during each session of experiments).

- $\sigma_{\left(\frac{^{i}Xe}{^{132}Xe}\right)_{blk}}$ is the standard deviation of the isotope ratios measured during blank runs analyzed under similar conditions to those of the samples.

- $\sigma_{^{132}Xe_{blk}}$ is the standard deviation of the Xe blank abundances (in moles). Finally, the errors are given at 1σ (67% level confidence) or 2σ (95% level confidence).

Hence, known quantities of a standards gas with an atmospheric composition were analysed daily to ensure accurate correction for instrumental mass discrimination, calculate the sensitivity and determine the reproducibility of the mass spectrometer (for a given isotopic ratio, reproducibility (%) = standard deviation over all standards measured during the

corresponding period of analysis / mean value of this isotope ratio for all considered standard analyses). Typical Reproducibility for each isotopic ratio of Xe normalised to ^{130}Xe is given below from the typical analysis of 25 aliquots of standard (Bekaert et al. 2019c; Table 6). We also report in Fig. 31 the reproducibility of Kr and Xe standards for the analysis of 20 (Kr) and 33 (Xe) aliquots over a 3-week period of analysis (from Broadley et al. 2019, *under review*).

Isotope	^{124}Xe	^{126}Xe	^{128}Xe	^{129}Xe	^{131}Xe	^{132}Xe	^{134}Xe	^{136}Xe
Reproducibility (%)	0.71	0.72	0.45	0.34	0.20	0.30	0.30	0.36

Table 6. Typical reproducibility of the Xe standards (25 aliquots) on the Helix MC plus at CRPG (Nancy) normalised to ^{130}Xe (Bekaert et al. 2019).

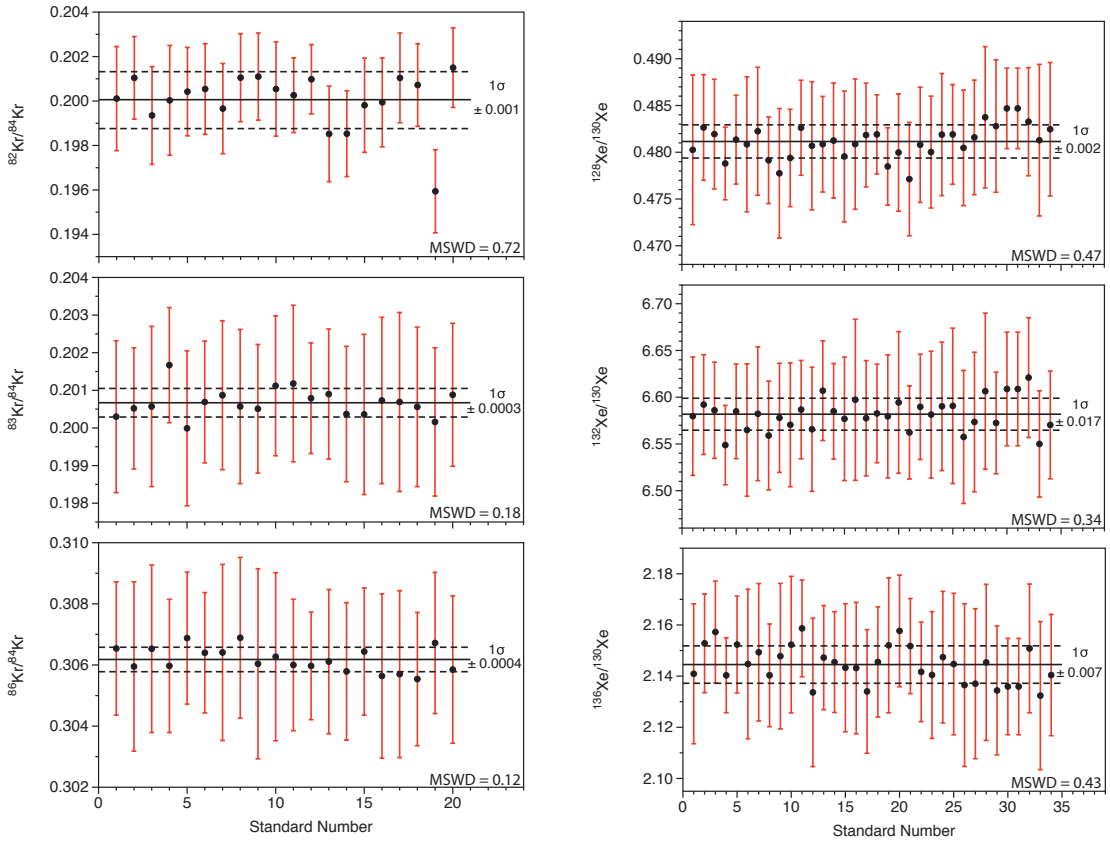

Fig. 31. Reproducibility of Kr and Xe standard. Standards shown here represent the analyses of Kr (n = 20) and Xe (n = 33) atmospheric standards over a 3-week period of analysis. Error bars on the individual standards represent the internal measurement error (1σ) and the error envelope represents the reproducibility (standard deviation) of the standard (Broadley et al. 2019, *under review*).

Chapter 2

Cometary noble gases: a missing piece of the atmospheric puzzle

Noble gases in the mantle and atmosphere have revealed that volatiles on Earth are a result of heterogeneous episodes of both solar and chondritic volatile accretion, followed by potential mass dependent fractionation during atmospheric escape. However, the primordial signature of Xe in the atmosphere is distinct from both solar and chondritic values and likely corresponds to a unique nucleosynthetic mixture with a deficit in r-process isotopes ^{134}Xe and ^{136}Xe compared to bulk Solar System reservoirs. For decades, this distinctive feature of the atmospheric Xe has been purported to reflect the contribution of an unknown reservoir originating in the outer edges of the Solar System, potentially in the comet-forming region. Pioneering laboratory experiments of noble gas trapping in ice forming at various temperatures have led to the proposal that the atmospheres of terrestrial planets (Venus, Earth and Mars) would be derived from a mixture of icy (~ comets) and asteroidal bodies (~ chondritic) (Owen et al. 1992). This is because abundance ratios of noble gases trapped in ice at ~ 50 K, corresponding to the representative temperature for the formation of comets in the Kuiper belt, fall onto a mixing line formed by noble gas elemental ratios in terrestrial planets (Owen et al. 1992).

Quantifying the contribution of cometary material to the volatile element inventory of terrestrial planets has however been precluded by the lack of elemental and isotopic measurement of cometary noble gases, which was only achieved recently during the European Space Agency's Rosetta mission to comet 67P/Churyumov–Gerasimenko (67P/C-G). The Rosetta Orbiter Spectrometer for Ion and Neutral Analysis (ROSINA) was equipped with a Double Focusing Mass Spectrometer (DFMS) that provided crucial insights into the chemical and isotopic composition of the coma of comet 67P/C-G. Interestingly, it appears that noble gas elemental ratios measured on comet 67P/C-G do not fit with expectations that had previously been formulated from laboratory experiments, therefore calling for our understanding of the behaviour of noble gases in cometary ice analogues to be re-evaluated.

2.1. The Rosetta space mission: *rendez-vous* with a comet

Launched on the 2nd of March 2004, the Rosetta space probe flew three times by Earth and Mars in three successively larger orbits, before reaching the comet on 6th of August 2014 and performing a series of manoeuvres around the comet at distances of 30 to 10 km (Fig. 32). During this time, the ROSINA mass spectrometer (Rosetta Orbiter Spectrometer for Ion and Neutral Analysis up to 300 amu; Balsiger et al. 2007), comprising of a double-focus magnetic mass spectrometer (DFMS) with a high resolution (>3000m/Δm, resolving N_2 and CO), performed analyses, some of which being reported and discussed here below. On the 12th of November, a lander module named Philae landed on the comet, but unfortunately bounced twice before settling in the shadow of a cliff where it was unable to adequately collect solar power, and therefore lost contact with Rosetta after two days, when its batteries ran out. On the 30th of September 2016, the Rosetta spacecraft ended its mission by hard landing on the comet. An overview of the Rosetta mission's main scientific goals, operations and discoveries is provided by Taylor et al. (2017).

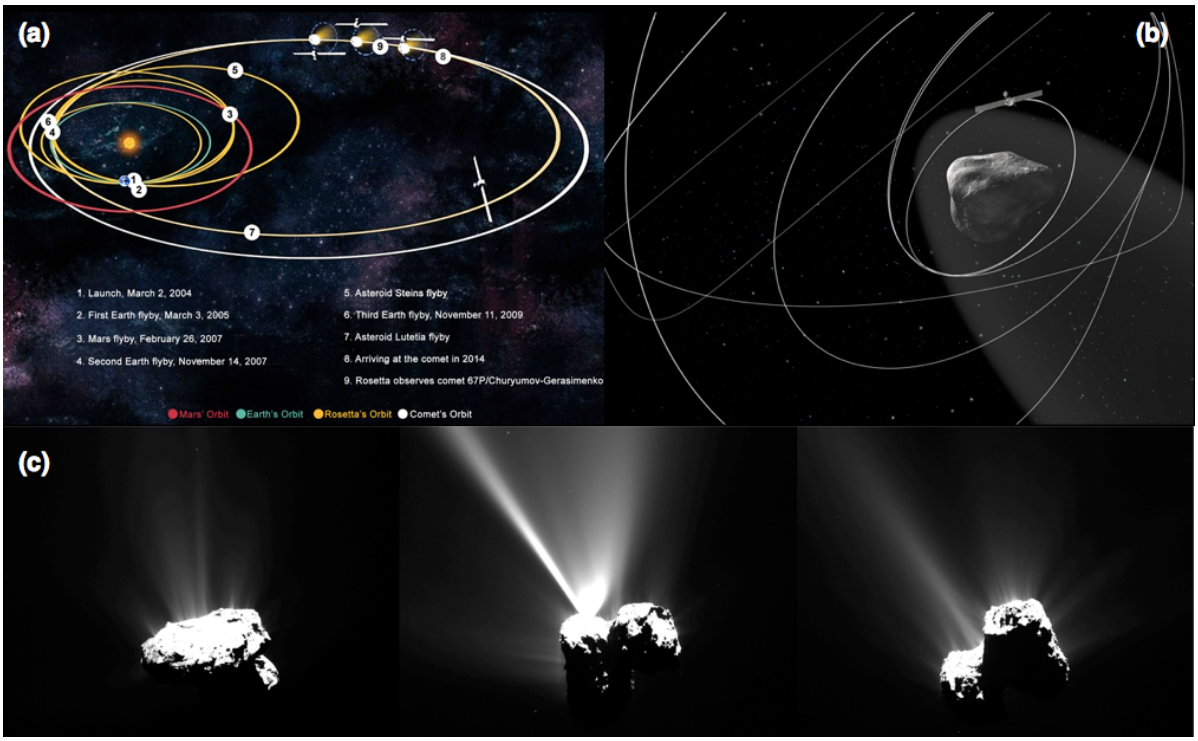

Fig. 32. Rosetta's trajectory within the Solar System (a) and orbit around comet 67P/C-G (b). Credit: ESA. (c) Images of Comet 67P/C-G taken with OSIRIS narrow-angle camera on 12 August 2015, just a few hours before the comet reached perihelion, about 330 km from the comet. Credits: ESA/Rosetta/MPS for OSIRIS Team. The effect of solar radiation heating up the nucleus can be seen, resulting in frozen ices escaping as gas into space from the comet's surface.

COSMOCHEMISTRY

Xenon isotopes in 67P/Churyumov-Gerasimenko show that comets contributed to Earth's atmosphere

B. Marty,[1]* K. Altwegg,[2,3] H. Balsiger,[2] A. Bar-Nun,[4]† D. V. Bekaert,[1] J.-J. Berthelier,[5] A. Bieler,[2,6] C. Briois,[7] U. Calmonte,[2] M. Combi,[6] J. De Keyser,[8] B. Fiethe,[9] S. A. Fuselier,[10] S. Gasc,[2] T. I. Gombosi,[6] K. C. Hansen,[6] M. Hässig,[2,10] A. Jäckel,[2] E. Kopp,[2] A. Korth,[11] L. Le Roy,[2] U. Mall,[11] O. Mousis,[12] T. Owen,[13]† H. Rème,[14] M. Rubin,[2] T. Sémon,[2] C.-Y. Tzou,[2] J. H. Waite,[10] P. Wurz[2]

The origin of cometary matter and the potential contribution of comets to inner-planet atmospheres are long-standing problems. During a series of dedicated low-altitude orbits, the Rosetta Orbiter Spectrometer for Ion and Neutral Analysis (ROSINA) on the Rosetta spacecraft analyzed the isotopes of xenon in the coma of comet 67P/Churyumov-Gerasimenko. The xenon isotopic composition shows deficits in heavy xenon isotopes and matches that of a primordial atmospheric component. The present-day Earth atmosphere contains 22 ± 5% cometary xenon, in addition to chondritic (or solar) xenon.

Comets are among the most pristine solar system materials (*1*). Their abundant volatile species, mainly in the form of ices, are intimately mixed with refractory silicate-rich phases and organics, the origins of which—either in the protosolar disk or molecular clouds and interstellar medium—are still under debate (*1*). The discovery that Comet 81P/Wild contains high-temperature minerals akin to those found in primitive meteorites with key isotopic signatures (e.g., that of oxygen) typical of solar system reservoirs (*2*) suggests that some of the cometary constituents were cycled close to the proto-Sun and were radially transported outward. However, the case of ice is less clear. Enrichments in deuterium and nitrogen-15 in comae (*3*, *4*) have been regarded as either originating from processing in the disk outskirts under irradiation or resulting from low-temperature ion-molecule reactions in molecular clouds. Another unresolved problem is the possible contribution of comets to inner-planet atmospheres. Although the D/H and $^{15}N/^{14}N$ signatures of the terrestrial atmosphere and oceans suggest an inner solar system origin for volatile elements on Earth (*5*), variations in the D/H ratio in primitive meteorites point to the contribution of interstellar water to asteroids (*6*).

Xenon, the heaviest stable noble gas, with nine isotopes of different nucleosynthetic origins (*7*, *8*), is a key element for identifying nuclear components present in presolar material. The composition of solar system Xe, represented by measurements of the solar wind (*7*), is the result of the homogenization of such components. Several radioactive decays also produce Xe isotopes, among which that of ^{129}I (half-life of 15.6 million years) decaying into ^{129}Xe provides time constraints on the early evolution of the solar system. Earth's atmosphere has a xenon composition that is unique among solar system objects and reservoirs (*9*). It is depleted relative to expectations based on the extrapolated behavior of the lighter noble gases Ne, Ar, and Kr, by a factor of ~20 relative to Kr (normalized to the abundance in chondritic meteorites). Atmospheric Xe is also isotopically (mass-dependently) fractionated, being enriched in heavy isotopes by 30 to 40 per mil per atomic mass unit (u) compared with chondritic xenon (hereafter, Q-Xe) or solar wind xenon (hereafter, SW-Xe); this is known as the xenon paradox (*10*). When corrected for mass-dependent isotopic fractionation (MDF), atmospheric Xe does not directly correspond to any known solar system component. These observations have led to the definition of a theoretical primordial component termed U-Xe (*9*) (where U stands for Ur, the German word for primordial, and not for uranium-derived fission Xe). U-Xe is close to SW-Xe for the $^{124–130}Xe$ isotopes but is depleted in the heavy Xe isotopes, particularly ^{134}Xe and ^{136}Xe. U-Xe has not been clearly identified in meteorites or planetary samples.

We report the determination of the isotopic composition of xenon in a comet. Xenon isotopes were measured with the Double Focusing Mass Spectrometer (DFMS) of the Rosetta Orbiter Spectrometer for Ion and Neutral Analysis (ROSINA) instrument suite (*11*) on the Rosetta spacecraft. DFMS is a high-mass-resolution instrument (mass divided by change in mass = 3000 at 1% peak height at a mass/charge ratio of 28 u/*e*) that measured gases emitted by comet 67P/Churyumov-Gerasimenko (67P/C-G), presumably from sublimation of ice (*3*). The Xe measurements were carried out during a series of dedicated low-altitude orbits, between 10 and 7 km from the comet's center of mass, from 14 to 31 May 2016 (*12*). Because of the high resolution of DFMS, mass/charge ratios of 129, 131, 132, 134, and 136 u/*e* were essentially free of interfering species of similar mass, as confirmed by the shapes of the peaks, whereas interference presumably due to S_4^+ was detected at mass/charge = 128 u/*e* and corrected using peak deconvolution (*12*). A slight contribution of a few percent at mass/charge = 130 u/*e*, due to S_4^+-containing ^{34}S, was also corrected. The average Xe isotope ratios were derived from this database, with uncertainties corresponding to 1 standard deviation (σ) of the mean. The ROSINA instrument was equipped with a gas calibration unit that permitted in-flight analysis of reference gases, including xenon (*12*).

Figure 1 shows the xenon composition of 67P/C-G, normalized to that of the solar wind (horizontal orange line) and to ^{132}Xe (the most abundant Xe isotope in most cases), together with other solar system compositions (terrestrial atmosphere and chondritic). The data obtained from the in-flight calibration runs are consistent with a terrestrial Xe composition, as expected, but the 67P/C-G Xe isotopic ratios deviate markedly from solar, or chondritic, values. Whereas $^{128}Xe/^{132}Xe$, $^{130}Xe/^{132}Xe$, and $^{131}Xe/^{132}Xe$ are solar-like within uncertainties, 67P/C-G Xe is strongly depleted in ^{134}Xe and ^{136}Xe, by ~40 and ~60%, respectively.

We first tested the possibility that the observed variations are due to MDF, in which case the data should align along the dotted curve of Fig. 1. The $^{129–136}Xe/^{132}Xe$ ratios could be reasonably accounted for by MDF affecting a solar-like Xe component. The required fractionation factor, however, should be extremely high, around 14% per atomic mass unit, higher than ever observed for Xe (or other noble gases) in any solar system object or reservoir. Notesco *et al.* (*13*) found no evidence for Xe isotopic fractionation upon trapping in water ice, and trapping of ionized Xe results in a MDF of no more than 1% (*14*). Alternatively, MDF could also be due to distillation enhancing isotopic fractionation during loss of Xe isotopes from a reservoir (e.g., cometary ice). To produce

[1]Centre de Recherches Pétrographiques et Géochimiques, CNRS, Université de Lorraine, 15 rue Notre Dame des Pauvres, BP 20, 54501 Vandoeuvre lès Nancy, France. [2]Physikalisches Institut, University of Bern, Sidlerstrasse 5, CH-3012 Bern, Switzerland. [3]Center for Space and Habitability, University of Bern, Sidlerstrasse 5, CH-3012 Bern, Switzerland. [4]Department of Geoscience, Tel Aviv University, Ramat Aviv, Tel Aviv, Israel. [5]Laboratoire Atmosphères, Milieux, Observations Spatiales (LATMOS), Institut Pierre Simon Laplace, CNRS, Université Pierre et Marie Curie, 4 Avenue de Neptune, 94100 Saint-Maur, France. [6]Department of Climate and Space Sciences and Engineering, University of Michigan, 2455 Hayward Street, Ann Arbor, MI 48109, USA. [7]Laboratoire de Physique et Chimie de l'Environnement et de l'Espace (LPC2E), UMR 6115 CNRS–Université d'Orléans, France. [8]Koninklijk Belgisch Instituut voor Ruimte-Aeronomie/Institut Royal d'Aéronomie Spatiale de Belgique (BIRA-IASB), Ringlaan 3, B-1180 Brussels, Belgium. [9]Institute of Computer and Network Engineering (IDA), Technische Universität Braunschweig, Hans-Sommer-Straße 66, D-38106 Braunschweig, Germany. [10]Department of Space Science, Southwest Research Institute, 6220 Culebra Road, San Antonio, TX 78228, USA. [11]Max-Planck-Institut für Sonnensystemforschung (MPS), Justus-von-Liebig-Weg 3, 37077 Göttingen, Germany. [12]Laboratoire d'Astrophysique de Marseille, CNRS, Aix Marseille Université, 13388 Marseille, France. [13]Institute for Astronomy, University of Hawaii, Honolulu, HI 96822, USA. [14]Institut de Recherche en Astrophysique et Planétologie, CNRS, Université Paul Sabatier, Observatoire Midi-Pyrénées, 9 Avenue du Colonel Roche, 31028 Toulouse Cedex 4, France.
***Corresponding author. Email: bmarty@crpg.cnrs-nancy.fr** †Deceased.

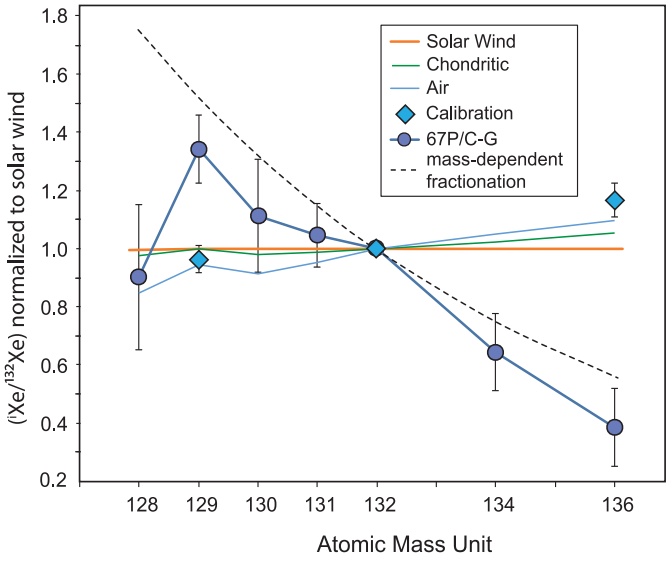

Fig. 1. Xenon isotopic composition of comet 67P/C-G's volatile fraction. Xe isotopes (^{i}Xe) were analyzed by the ROSINA DFMS on the Rosetta spacecraft. They are normalized to ^{132}Xe (ratios shown by the blue circles and line) and the solar wind composition (*7*) (horizontal orange line). Error bars, 1σ. The chondritic (*26*) (Q-Xe; green line) and atmospheric (*10*) (light blue line) compositions are also shown for comparison. The light blue diamonds show data obtained from in-flight calibration using a terrestrial Xe reference gas (*12*). The black dotted curve represents the effect of mass-dependent isotopic fractionation (MDF), for which a fractionation factor of 14% per atomic mass unit was adjusted to fit the observed $^{129-136}$Xe/^{132}Xe isotope ratios. Three MDF processes (kinetic, equilibrium, and gravity and centrifugal force) were considered and yielded curves that are indistinguishable from each other at the scale of the figure (*12*).

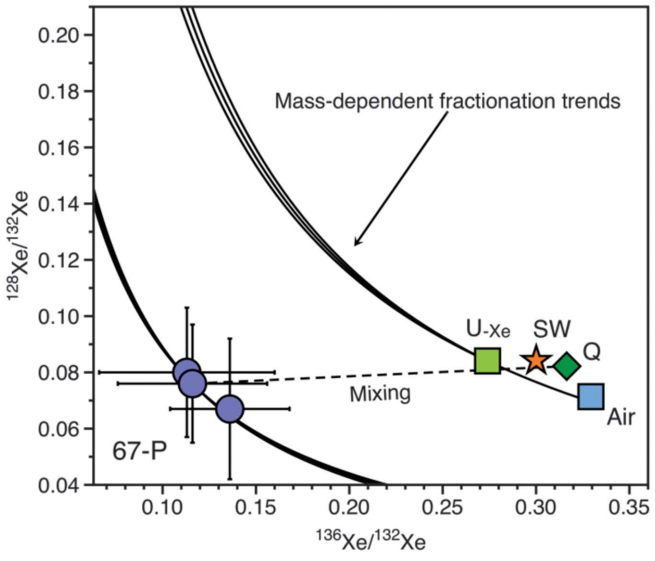

Fig. 2. Testing the origins of Xe isotope variations in comet 67P/C-G. The Xe isotopes are normalized to ^{132}Xe and the solar wind composition (*7*). Error bars, 1σ. We tested the possibility that 67P/C-G Xe is derived from MDF of primordial (U), solar wind (SW), or chondritic (Q) Xe. Three MDF processes are envisioned (*12*), yielding slightly different MDF curves (solid curves). None of these can reproduce 67P/C-G Xe from U-Xe, SW-Xe, or Q-Xe compositions. Likewise, none of the MDF curves from 67P/C-G Xe can reproduce U-Xe, SW-Xe, or Q-Xe compositions. Mixing of Q-Xe or SW-Xe with 67-P/C-G Xe is able to reproduce the composition of U-Xe (Fig. 4).

a MDF of 10% per atomic mass unit would require Xe loss on the order of 10^4 for an instantaneous fractionation factor of 1%. Such Xe depletion is not consistent with the detection of xenon in the coma of 67P/C-G, nor with the ^{132}Xe/^{36}Ar ratio of 2.5×10^{-2} estimated for the comet from our DFMS measurements [much higher than the solar ratio of 1.8×10^{-5} (*15*)]. Furthermore, degassing of a comet is essentially a one-way process in which a portion of fresh ice exposed to solar heating is sublimated, removing water vapor and volatiles trapped in ice to space. Last, xenon isotopes were analyzed over several weeks from several degassing sources without showing substantial variation (*12*), and it is unlikely that the recorded composition could correspond to a fractionated subreservoir. Thus, the Xe isotopic fractionation should have occurred before trapping in cometary ice, a possibility that cannot be discarded, given our poor knowledge of processes having taken place in the outer solar system.

The ^{128}Xe/^{132}Xe ratio does not fit into the isotopic fractionation scenario (Figs. 1 and 2). In Fig. 2, we show the results of testing whether the composition of 67P/C-G Xe can be derived from MDF of solar or meteoritic Xe. Three MDF processes are envisioned (kinetic, equilibrium, and gravity and centrifugal force) (*12*), yielding slightly different MDF trends, and none of them can reproduce 67P/C-G Xe from U-Xe, SW-Xe, or Q-Xe compositions. In contrast, mixing of Q-Xe or SW-Xe with 67P/C-G Xe reproduces the composition of U-Xe (Fig. 2).

Solar system xenon is the result of mixing of three different nucleosynthetic sources: the p-process, producing the rare ^{124}Xe and ^{126}Xe isotopes (which could not be measured here); the s-process, producing $^{128-132}$Xe isotopes; and the r-process, producing ^{134,136}Xe isotopes (*8*). Thus, the isotopic composition of cometary xenon is possibly the result of a nucleosynthetic mix that is different from that which produced solar xenon. From theoretical considerations and correlations of Xe isotopes observed in presolar grains [SiC and nanodiamonds (*8*)], the s-process Xe composition is reasonably well defined, but Xe isotope variations in presolar material require at least two different r-process compositions (*8*). Figure 3 shows mixing of 35% s-process Xe with 65% r-process Xe (*12*), the latter being defined by the two r-process compositions identified by (*8*).

This scenario accounts reasonably well for the deficits of ^{134}Xe and ^{136}Xe observed in 67P/C-G and is more consistent with the cometary ^{128}Xe/^{132}Xe ratio than the MDF model is. It implies that ^{129}Xe is enriched relative to ^{132}Xe and the solar composition by 34 ± 11% (1σ). This large monoisotopic excess could be due to a specific nucleosynthetic process preferentially producing ^{129}Xe, a possibility supported by some nanodiamond fractions with ^{129}Xe/^{132}Xe ratios up to 2.2 (*16*). Alternatively, in situ (within ice) β-decay of ^{129}I (half-life of 15.6 million years) after the start of solar system formation (SSSF) is unlikely: The ^{129}I/^{127}I ratio at the SSSF was ~1×10^{-4} (*17*), and an in situ origin after the SSSF would require an enrichment of iodine relative to xenon by three to four orders of magnitude, which is not observed in the coma of 67P/C-G (*12*). This ^{129}Xe excess could then result from in situ (within ice) or ex situ (in the ambient gas) decay of ^{129}I before the SSSF. In this case, xenon trapped in ice would be much older, by several tens of millions of years, than the SSSF. Assuming that ^{129}I and ^{127}I were produced in comparable proportions during r-process nucleosynthesis, icy grains should have trapped both I and Xe relatively shortly after their last nucleosynthetic event. This exotic Xe component would have to be older than 100 million years before the SSSF, given the half-life of ^{129}I, which is consistent with a galactic evolution origin as constrained by the initial solar system abundances of ^{129}I, ^{244}Pu, and ^{237}Cm (*18*).

Cometary noble gases are concentrated in ice (*13*, *19*, *20*), and a presolar origin for Xe would imply that cometary ice is also presolar. Such an origin is in agreement with the detection of abundant O_2 (1 to 10% relative to H_2O) released by 67P/C-G (*21*). Indeed, molecular oxygen might

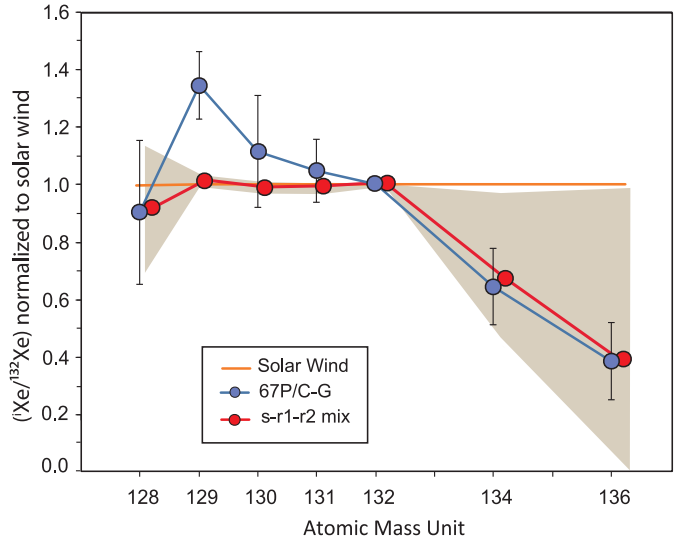

Fig. 3. Mixing of various nucleosynthetic components for the origin of 67P/C-G Xe. The Xe isotopes are normalized to ^{132}Xe and the solar wind composition (*7*) (horizontal orange line). Error bars, 1σ. The red dots represent the best fit of mixing between s-process Xe and the two r-process end-member compositions identified by (*8*) (s-r1-r2; symbols are slightly displaced to the right for better visibility) [see (*12*) for methods]. The light brown area represents the field of possibilities for random contributions of the s-process and the two r-processes.

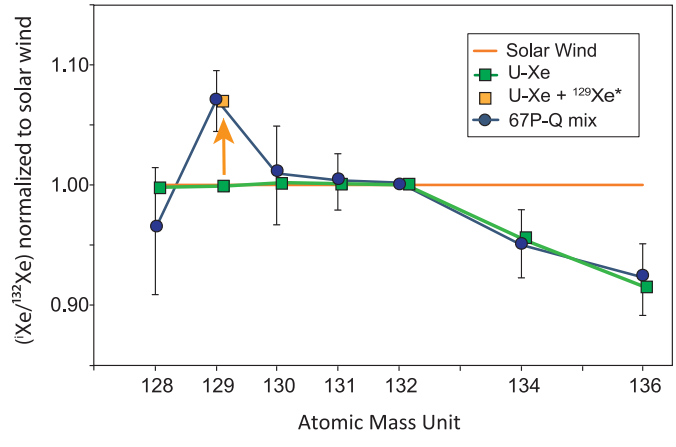

Fig. 4. A mix of chondritic and cometary Xe as the origin of a primordial atmospheric Xe component. The Xe isotopes are normalized to ^{132}Xe and the solar wind composition (*7*) (horizontal orange line). Error bars, 1σ. Symbols for U-Xe (*9*) are slightly displaced to the right for better visibility. The U-Xe composition (green squares) is well reproduced by mixing cometary (67P/C-G) Xe with Q-Xe (67P-Q; dark blue dots). The cometary contribution, 22 ± 5%, and the propagation of errors were determined using a Monte Carlo approach (*12*). The mixture is also able to reproduce the monoisotopic excess of ^{129}Xe observed in air (6.8%) (*9*), represented by the orange square.

have been produced from the radiolysis of H_2O icy grains by cosmic rays and/or hard photons before the comet was assembled (*21*), and this process would require long periods of time (10^7 to 10^9 years) in the protosolar nebula and/or low-density environments such as molecular clouds (*22*). A presolar origin is independently supported by the presence of S_2 in 67P/C-G (*23*) and HDO/H_2O and D_2O/HDO ratios closely resembling those of interstellar material (*3*).

The peculiar Xe isotopic composition of 67P/C-G provides a fingerprint of the contribution of comets to the terrestrial atmosphere. 67P/C-G Xe, which is largely depleted in ^{134}Xe and ^{136}Xe, indicates that comets may be the source of U-Xe. Mixing 22 ± 5% (1σ) cometary (67P/C-G) Xe with Q-Xe reproduces the composition of U-Xe (Fig. 4). The choice of Q-Xe for the second component—instead of, for example, solar—is consistent with observations that (i) the H, N, and Ar isotopic compositions of the atmosphere and oceans are within the range of variations observed in chondrites and different from solar values (*5*, *7*) and (ii) xenon in Earth's interior contains a chondritic component (*24*). A cometary contribution to atmospheric noble gases, suggested independently by modeling to be 19 to 27% (*25*), might have taken place during the proto-Earth growing stages (*25*) or later during the Hadean era (4.5 to 3.8 billion years ago) (*20*). Such a contribution would, however, have been minimal for the terrestrial oceans [≤1% (*12*)] and, by consequence, would not have affected the terrestrial D/H ratio.

A 22 ± 5% contribution of comets to atmospheric Xe also reproduces the 6.8 ± 0.3% (1σ) ^{129}Xe excess observed in the atmosphere (Fig. 4). This excess, classically attributed to the decay of radioactive ^{129}I trapped in the growing Earth, has previously allowed researchers to set time constraints on the accretion of Earth and the development of its atmosphere (*17*). Degassing of mantle Xe containing radiogenic ^{129}Xe through geological periods of time also contributed ^{129}Xe to the atmosphere, but probably no more than ~1% (*12*). Thus, a large fraction of the monoisotopic ^{129}Xe excess in the terrestrial atmosphere may be inherited, implying that the ^{129}I-^{129}Xe system as a geochronological tool should be reconsidered and that the Wetherill's retention time of ~100 million years after the SSSF (*17*) should be seen as a lower limit. It remains unclear whether inherited cometary ^{129}Xe is consistent with the presence in the present-day Earth atmosphere of a component derived from the fission of ^{244}Pu.

REFERENCES AND NOTES

1. M. J. Mumma, S. B. Charnley, *Annu. Rev. Astron. Astrophys.* **49**, 471–524 (2011).
2. D. Brownlee *et al.*, *Science* **314**, 1711–1716 (2006).
3. K. Altwegg *et al.*, *Science* **347**, 1261952 (2015).
4. D. Bockelée-Morvan *et al.*, *Space Sci. Rev.* **197**, 47–83 (2015).
5. B. Marty, *Earth Planet. Sci. Lett.* **313–314**, 56–66 (2012).
6. L. G. Vacher, Y. Marrocchi, M. J. Verdier-Paoletti, J. Villeneuve, M. Gounelle, *Astrophys. J.* **827**, L1 (2016).
7. A. Meshik, C. Hohenberg, O. Pravdivtseva, D. Burnett, *Geochim. Cosmochim. Acta* **127**, 326–347 (2014).
8. J. D. Gilmour, G. Turner, *Astrophys. J.* **657**, 600–608 (2007).
9. R. O. Pepin, *Space Sci. Rev.* **92**, 371–395 (2000).
10. M. Ozima, F. A. Podosek, *Noble Gas Geochemistry* (Cambridge Univ. Press, ed. 2, 2002).
11. H. Balsiger *et al.*, *Space Sci. Rev.* **128**, 745–801 (2007).
12. Materials and methods are provided as supplementary materials.
13. G. Notesco, D. Laufer, A. Bar-Nun, T. Owen, *Icarus* **142**, 298–300 (1999).
14. Y. Marrocchi, B. Marty, P. Reinhardt, F. Robert, *Geochim. Cosmochim. Acta* **75**, 6255–6266 (2011).
15. E. Anders, N. Grevesse, *Geochim. Cosmochim. Acta* **53**, 197–214 (1989).
16. G. R. Huss, R. S. Lewis, *Meteoritics* **29**, 811–829 (1994).
17. G. W. Wetherill, *Annu. Rev. Nucl. Part. Sci.* **25**, 283–328 (1975).
18. F. L. H. Tissot, N. Dauphas, L. Grossman, *Sci. Adv.* **2**, e1501400 (2016).
19. H. Balsiger *et al.*, *Sci. Adv.* **1**, e1500377 (2015).
20. B. Marty *et al.*, *Earth Planet. Sci. Lett.* **441**, 91–102 (2016).
21. A. Bieler *et al.*, *Nature* **526**, 678–681 (2015).
22. O. Mousis *et al.*, *Astrophys. J.* **41**, 1–5 (2016).
23. U. Calmonte *et al.*, *Mon. Not. R. Astron. Soc.* **462**, S253–S273 (2016).
24. A. Caracausi, G. Avice, P. G. Burnard, E. Füri, B. Marty, *Nature* **533**, 82–85 (2016).
25. N. Dauphas, *Icarus* **165**, 326–339 (2003).
26. H. Busemann, H. Baur, R. Wieler, *Meteorit. Planet. Sci.* **35**, 949–973 (2000).

ACKNOWLEDGMENTS

We thank Y. Marrocchi for comments and G. Avice for help in compiling solar system xenon data. Work was funded at the University of Bern by the State of Bern, the Swiss National Science Foundation, and the European Space Agency (ESA) PRODEX program (Programme de Développement d'Expériences Scientifiques); at MPS by the Max-Planck Society and the Federal Ministry for Economic Affairs and Energy (contract 50QP1302); at Southwest Research Institute by NASA's Jet Propulsion Laboratory (subcontract 1496541 and JPL subcontract to J.H.W. NAS703001TONMO710889); at the University of Michigan by NASA (contract JPL-1266313); through the A*MIDEX project by the French National Research Agency (grant no. ANR-11-IDEX-0001-02); by Centre National d'Études Spatiales grants at Institut de Recherche en Astrophysique et Planétologie, LATMOS, LPC2E, Laboratoire d'Astrophysique de Marseille and Centre de Recherches Pétrographiques et Géochimiques; by the European Research Council (grants no. 267255 and 69618 to B.M.); and at BIRA-IASB by the Belgian

Science Policy Office through PRODEX/ROSINA PRODEX Experiment Arrangement 90020. ROSINA would not produce results without the work of the many engineers, technicians, and scientists involved with the mission, the Rosetta spacecraft, and the ROSINA instrument team over the past 20 years, whose contributions are gratefully acknowledged. These measurements could only be performed thanks to the skillful maneuvering of the spacecraft close to the comet by the operations team in Darmstadt, Germany. Rosetta is an ESA mission with contributions from its member states and NASA. We acknowledge the work of the whole ESA Rosetta team. ROSINA data are publicly available at ESA's Planetary Science Archive at www.cosmos.esa.int/web/psa/rosetta and NASA's Planetary Data System at https://pdssbn.astro.umd.edu/data_sb/missions/rosetta/index.shtml. M.R. and K.A. performed data reduction. M.R., K.A., and B.M. analyzed the data. B.M. interpreted the data and wrote the paper. K.A., M.R., and H.B. contributed to data interpretation and the supplementary materials. All authors contributed to the ROSINA instrument and commented on and revised the manuscript.

SUPPLEMENTARY MATERIALS

www.sciencemag.org/content/356/6342/1069/suppl/DC1
Materials and Methods
Supplementary Text
Figs. S1 to S5
Table S1
References (*27*–*36*)

5 November 2016; accepted 3 May 2017
10.1126/science.aal3496

2.3. Cometary Xe: general implications

The findings that (i) comets significantly contributed heavy noble gases (at least Xe) to the atmosphere, (ii) comet 67P/C-G carries out a presolar Xe component that has not been homogenised with other Solar System materials, and (iii) the ^{129}Xe mono-isotopic excess in the atmosphere may not derive from mantle degassing but from cometary contributions (Marty et al. 2017), have broad implications regarding the origin and evolution of the atmosphere. A general summary regarding the contribution of comets to the volatile element inventory of the Earth surface reservoir is presented in Chapter 6.

Regarding the presolar origin of cometary volatiles, the Xe signature appears to be in good agreement with H, Si and S isotope data of comet 67P/C-G, which all point to the comet having preserved large amounts of unprocessed presolar matter (Hoppe et al. 2018). Prior to the Rosetta mission, various presolar signatures had been found in cometary matter, including C-rich particles with high ^{12}C/^{13}C from comet 1P/Halley (Jessberger and Kissel 1991), as well as fingerprints of "interstellar" chemistry indicated by large D and ^{15}N enrichments as well as the presence of C and O-rich presolar grains in matter from comet 81P/Wild 2 (McKeegan et al. 2006; Bockelée-Morvan et al. 2015). Presolar grain concentrations in cometary matter (600-1000 ppm; Floss et al. 2013, Leitner et al. 2012) appear to be high compared to typical abundances in chondritic matter (~ 200 ppm, Floss and Haenecour 2016), reaching up to 1.5 wt.% in one cometary particle (Busemann et al. 2009). The Si isotopic composition of the refractory component of 67P/CG was measured by ROSINA from sputtered Si neutrals, produced by the bombardment of the comets surface by solar wind protons (Wurz et al. 2015; Rubin et al. 2017). This revealed that the cometary grains were depleted in the heavy Si isotopes relative to the terrestrial and meteoritic Si isotopic composition, potentially suggesting a late contribution of Si-rich dust from a nearby star. The S isotopic composition of volatile species (H_2S, CS_2, and carbonyl sulfide) degassed from comet 67P/CG were also measured by the ROSINA mass spectrometer (Calmonte et al. 2017), revealing large depletions in ^{33}S along with smaller depletions in ^{34}S in all molecules, pointing towards a S isotopic composition that is clearly different from S present on Earth and in meteorites, but compatible with the expected composition of the ISM (Mauersberger et al. 2004).

It therefore stands to reason that the Xe trapped in ice could also be presolar in origin. This suggests that the ice is itself presolar in origin. Whether the Xe and S isotopes measured in the coma are representative of the bulk comet is not known, however if the ice in the comet is presolar in origin (i.e., not formed by condensation in the PPD) then this would have important implications regarding the origin of comet 67P/C-G. It could imply that the bulk comet is interstellar in origin. Otherwise, if the ice is a product of the protosolar nebula the mechanism by which comets are able to obtain and preserve presolar volatile components is unknown. At the same time, the outgassing pattern of volatile species observed by ROSINA from comet 67P/C-G has also been interpreted as evidence for the nucleus of the comet

containing a significant fraction of crystalline ice and clathrates (Luspay-Kuti et al. 2016). This would require the comet to have agglomerated from ices that were condensed at higher pressure and temperature, in the PPD, instead of originating from the interstellar medium where amorphous ice may dominate (Luspay-Kuti et al. 2016).

The origin of the ^{129}Xe mono-isotopic excess in the atmosphere has direct implications regarding the I–Xe age of the Earth's atmosphere (i.e., the time interval for the closure of the atmosphere). Excess ^{129}Xe from the decay of ^{129}I trapped in the growing Earth is higher in the terrestrial mantle (^{129}Xe/^{130}Xe $\geq$ 7) compared to the atmosphere (^{129}Xe/^{130}Xe ~ 6.5), suggesting that the ^{129}Xe excess in the atmosphere could originate from mantle degassing of high ^{129}Xe/^{130}Xe gas. The atmosphere's closure age, which depends on the initial abundance of iodine in the bulk silicate Earth, has been previously determined to be 100-120 Ma after the start of the Solar System (Podosek and Ozima 2000; Wetherill 1975; Porcelli and Ballentine 2002). More recent estimates of the I–Xe closure age of the Earth's atmosphere took into account Xe loss to space over the Archean eon and derived a Xe formation interval for the Earth–atmosphere system of 40^{+20}_{-10} Ma after CAI, representing a lower limit for the age of the Moon-forming impact (Avice and Marty 2014). Our recent interpretation that accounting for the U-Xe signature of the primordial atmosphere by mixing cometary and chondritic end-members can also account for the majority of the ^{129}Xe excess observed in the atmosphere would imply that degassing of ^{129}Xe produced in the mantle contributed limitedly (~1%) to the total radiogenic ^{129}Xe in the atmosphere. However, to have only ~1% of the ^{129}Xe excess observed in the atmosphere being derived from mantle degassing would imply a surprisingly low extent of mantle volatile transfer to the atmosphere. At last, note that although the mono-isotopic excess of ^{129}Xe of atmospheric Xe relative to solar and chondritic cosmochemical precursors may have been mainly acquired from comets during the Earth's formation and early evolution (Marty et al. 2017), mantle degassing also contributed ^{129}Xe to the atmosphere through geological periods of time, as witnessed by the fact that ancient atmospheric xenon trapped in Archean minerals shows a mono-isotopic excess of ^{129}Xe that is slightly less pronounced than in the present atmosphere (Avice et al. 2017, 2018; Marty et al. 2019; Chapter 7).

2.4. The Moon as a witness.

On Earth, the contrasting heavy noble gas signatures in the mantle (largely chondritic in origin; Holland et al. 2009; Caracausi et al. 2016; Péron and Moreira 2018) and atmosphere (mixture of 20% cometary plus 80% chondritic; Marty et al. 2017) may be used to argue for a late cometary contribution to the Earth, possibly related to giant planet instability about 3.9 Ga (Nice model; Brasser and Morbidelli, 2013). A relatively short spike in impact intensity within the inner solar system (some 3.95 Ga, or earlier) has indeed long been argued for based on interpretations of $^{40\text{-}39}$Ar chronology from lunar samples (e.g., Turner 1979). This "Late Heavy Bombardment" (LHB) paradigm received further support from dynamical models

involving late-stage giant planet migration (e.g., Gomes et al. 2005). These models predict contributions of icy bodies in proportions comparable to those of asteroids. The LHB model therefore predicts that the later stages of Earth's accretion and atmosphere formation would have received significant contribution from planetesimals with trans-Neptunian origins. The existence of the LHB has however been recently cast into doubt (Boehnke & Harrison 2016). Recent reviews of geo-chronological data from the inner solar system have even argued for an overall monotonic decline in the bombardment rate of early Earth - an interpretation most broadly consistent with crater counting studies (e.g., Werner & Ivanov, 2015; Fig. 33).

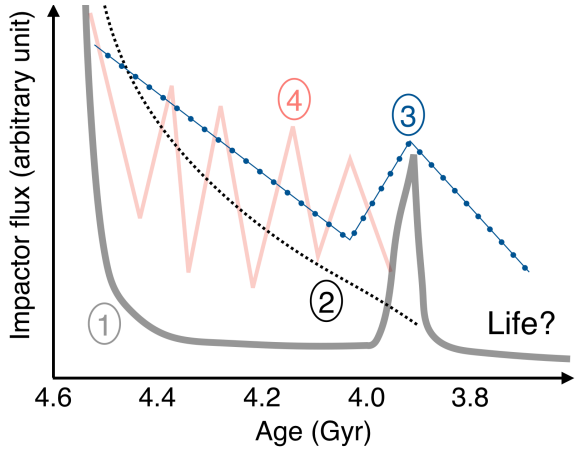

Fig. 33. Schematic representation of the different scenarios advocated for the early impact history of the Earth-Moon system, corresponding to the cataclysmic Late Heavy Bombardment (1), the smooth decline in impactor flux (2), the sawtooth-like time line (3) and the early intense bombardment (4). Adapted from Zellner (2017).

Due to the absence of resurfacing processes such as plate tectonics on the Moon, the lunar surface could represent a promising record of the chondritic and/or cometary contributions to the Earth-Moon system, after the last giant impact event. However, given that the Moon is too small to possibly retain an atmosphere, volatile elements delivered to its surface might simply be lost to space. In addition, a recent series of impact simulations aimed at quantifying the impactor-retention ratio on the Moon concluded that the average retention ratio integrated over the Moon's impact history would be about 0.20, which is significantly lower than the range of 0.5–0.6 that was previously calculated (Bottke et al. 2010; Morbidelli et al. 2012). This is in agreement with previous results by Ong et al. (2010), who derived a "velocity-dependent retention function" describing the mass fraction of the Moon impactors that is likely to be retained on the lunar surface, and concluded that the total impactor mass retained on the Moon was approximately 6.5% of the impactor mass flux, with asteroids theoretically providing six times more water to the Moon surface than comets.

The first analyses of lunar material brought to Earth by the Apollo missions led to the conclusion that the Moon was essentially devoid of indigenous water (Epstein and Taylor 1974). One scientific explanation for this was that the Moon-forming event could have been so

energetic that it basically removed most of the volatile elements from the building materials of the Moon (Canup and Asphaug 2001). However, more precise and sensitive analyses of lunar samples have progressively demonstrated that the Moon was not anhydrous, with the lunar mantle possibly containing as much water as the terrestrial one (≥ 300 ppm, as derived from the analysis of lunar volcanic glasses; Saal et al. 2008). Present day estimates of the water content (varying from Earth-like abundances to two orders of magnitude more depleted; Greenwood et al. 2018) and composition of the Moon have been documented by the analysis of primitive pyroclastic volcanic glasses (e.g., Saal et al. 2008; Hauri et al. 2011; Saal et al. 2013; Füri et al. 2014; Chen et al. 2015), mare basalt lava flows (e.g., McCubbin et al. 2010; Boyce et al. 2010; Greenwood et al. 2011; Barnes et al. 2013; Tartèse & Anand 2013; Tartèse et al. 2013, 2014; Chen et al. 2015) and plutonic rocks (e.g., McCubbin et al. 2010, Greenwood et al. 2011, Hui et al. 2013, Barnes et al. 2014). The representativeness of these mineral phases to the associated lunar reservoirs may not be straightforward, depending on for instance the fractionation processes and/or H partition coefficients (e.g., in apatite; Boyce et al. 2014).

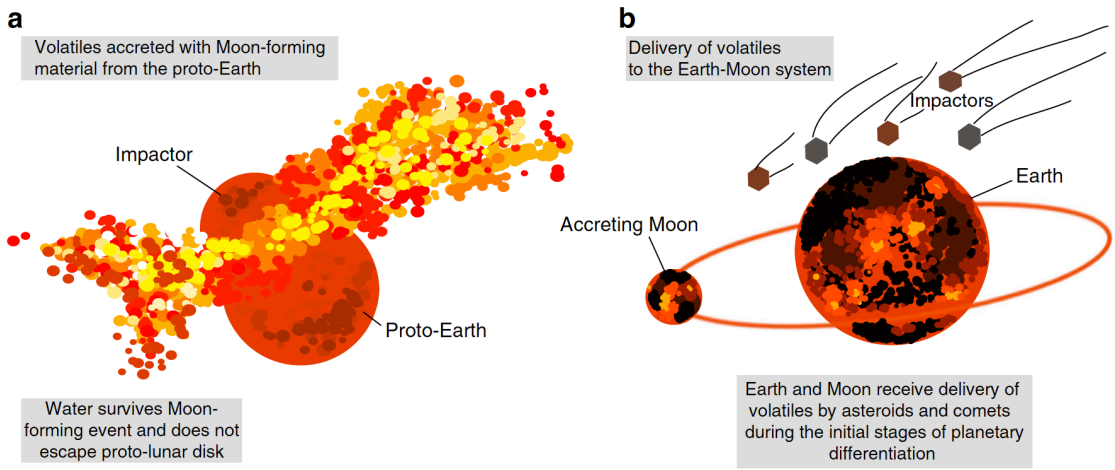

Fig. 34. Possible scenarios for the accretion of volatiles to the lunar interior, with (a) volatile accretion during Moon's formation, and/or (b) protracted delivery of volatile elements by late impactors during the 10–200 million years of crystallization of the lunar magma ocean. From Barnes et al. (2016).

In 2016, Barnes et al. proposed two main scenarios for the origin of lunar water, where the Moon could have (i) inherited significant (up to 25% of its present-day inventory) amounts of water from its precursor material, or (ii) formed anhydrous and gained the entirety of its water content from later contributions of asteroidal and/or cometary materials (Fig. 34). The early formation of a cumulate anorthositic crust, in the first few thousand years of the Moon's history (Elkins-Tanton et al. 2011), could have prevented significant water degassing and loss of volatiles, therefore allowing the Lunar Magma Ocean (LMO) to retain - at least part of - its primordial volatiles. It is therefore likely that late water delivery to the interior of the Moon could only have occurred between the Moon-forming event and the complete solidification of the lunar magma ocean (estimated between ~10 and ~200 Myr after the giant impact; Elkins-

Tanton et al. 2011). The occurrence of volatile-rich lunar soils has for instance been suggested as possible evidence for cometary impacts on the Moon (e.g. Gibson and Moore 1973; Dikov et al. 1998). More recently, Greenwood et al. (2011) reported large variations of hydrogen isotope ratios in lunar apatite (from ~ 400‰ to ~1000‰), taken as evidence for significant delivery of cometary water to the Earth-Moon system. Subsequent studies of water composition in lunar apatites found a larger variability, with δD values ranging from - 750 ‰ to + 1100‰ (Barnes et al. 2013, 2014; Tartèse et al. 2013, 2014a,b; Robinson & Taylor 2014; Robinson et al. 2016). Isotopic fractionation during H_2 degassing from crystallizing magmas (with initial δD values comparable to the terrestrial mantle; Barnes et al. 2014, Tartèse et al. 2014a,b) could for instance have resulted in high D/H ratios (Hui et al. 2017), therefore relaxing the requirement for a cometary contribution (Saal et al., 2013; Füri et al., 2014; Tartèse et al., 2014). This would imply that the Earth and Moon inherited their volatiles from a common chondritic component. The detailed analysis of the water inventory of Ti-rich lunar volcanic glasses suggests a melt source with a water composition similar to that of CCs, indicating a negligible contribution of D-rich cometary materials to the Earth-Moon system (Füri et al. 2014). Likewise, N-Ar systematics in single lunar soil grains revealed that nitrogen in the lunar surface is consistent with a binary mixture between solar wind-derived nitrogen and CCs (delivered prior to the solidification of the crust; Füri et al. 2015; Bekaert et al. 2017), with ≤ 13 % cometary contribution. This is in line with estimates from Barnes et al. (2016) who, based on H elemental and isotopic constraints on lunar water, concluded that carbonaceous chondrite-like material was the main supplier of volatiles to the Moon during its late accretion, with limited contribution (<20%) from comets. Finally, there is still the likelihood for part of the lunar volatile inventory to have been inherited from the Moon's main accretion phase, with the possibility that, below the magma ocean, the Moon preserved primitive material that was inherited from the proto-Earth (Saal et al. 2008). The final budget of volatile elements in the Moon (and Earth) would thus reflect a mixture of primordial sources (more or less altered by volatile loss processes) and later deliveries, which replenished the Earth-Moon system within the few hundred million years following the Moon-forming giant impact (Lin and Westrenen, 2018).

Interestingly, it appears that comets did not contribute significantly to the budget of terrestrial volatile elements, other than for the heavy noble gases (Marty et al. 2016; Chapter 6). The use of Xe isotopes could therefore represent the most diagnostic geochemical tool to distinguish cometary contributions to a given volatile reservoir. However, the indigenous lunar Xe isotopic composition is not yet firmly established, with trapped Xe in lunar samples presenting an isotopic composition very close to - and in most cases indistinguishable from - that of terrestrial atmospheric Xe, which was commonly attributed to ‘‘anomalous adsorption” of terrestrial Xe after sample return (Eugster 1986). In order to maximise the chance of discovering an indigenous lunar Xe signature from lunar samples, it is now recognised that Xe measurements in interior samples of anorthositic ejecta from very

recent craters should be performed (Mathew and Marti 2019). As part of this thesis, we have analysed the noble gas composition of three lunar lunar anorthosites (60025, 60215 and 65315; Bekaert et al. 2017) specifically selected for having the lowest exposure age (≤ 2 Ma) among Apollo samples, therefore containing limited cosmogenic (e.g. ^{124,126}Xe) and solar wind-derived noble gases. Our study suggested a possible contribution from cometary Xe (taken as the Xe isotopic signature measured on comet 67P/C-G; Marty et al. 2017) with noticeable depletions in ^{134,136}Xe with respect to air composition (Fig. 35). This required a high level of precision that could only be achieved by analysing large amounts of material (534.8 mg for sample 65315). Recently, depletions in the two heavy Xe isotopes have also been detected in 7 other lunar anorthosites, in both high and low temperature steps, which indicates that these signatures indeed represent a trapped component within minerals, rather than the result of surficial implantation (Pernet-Fisher and Joy, 2018). Hence, one possibility is that icy bodies including cometary material were delivered to the Moon surface prior to anorthosite crystallization, and incorporated as a lunar indigenous component. More work is however required to firmly establish whether or not this signature corresponds to cometary inputs. Alternatively, it could correspond to the implantation of ancient terrestrial atmosphere (U-Xe-like) into lunar soils, as has been proposed by Ozima et al. (2005) for the origin of lunar nitrogen and light noble gases, or, for instance, to a derivative of the solar wind (Meshik and Pravdivtseva, 2018). Indeed, it has been proposed that the pure solar-wind composition itself could be accurately modelled as a mixture of U-Xe and a heavy isotope constituent containing primarily only ^{134}Xe and ^{136}Xe (Pepin et al. 1995), implying that SW-like signatures with small deficits in these isotopes could possibly reflect temporal variations in the SW-Xe composition (Meshik and Pravdivtseva, 2018), without any requirement for a cometary contribution.

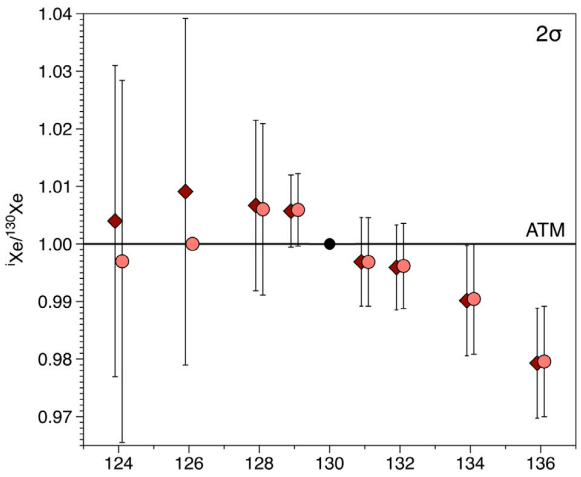

Fig. 35. Xenon isotopic spectra of the lunar anorthosite 65315 from the 400°C extraction step, non-corrected (diamonds) and corrected (circles) for cosmogenic contribution (see the average lunar bulk soil cosmogenic component, Pepin et al. 1995; Bekaert et al. 2018b). Isotope ratios are normalised to the isotopic composition of atmospheric Xenon (ATM: Basford et al. 1973). From Bekaert et al. (2017).

Conclusion and outlook

This chapter demonstrates that comets, potentially of presolar origin, are required to have significantly contributed to form the atmosphere, providing a natural explanation for the isotopic composition of U-Xe, the precursor of terrestrial atmospheric Xe. However, whether comet 67P/C-G can be considered representative of the entire cometary reservoir, and whether comets have significantly contributed other terrestrial volatile elements than Xe remains to be seen (Chapter 6). The possible occurrence of cometary Xe on the Moon, although requiring further investigation and comparison to potential SW-derived signatures, provides an interesting constraint on the late arrival of comets to the Earth-Moon system, in line with the absence of cometary signature in mantle-derived samples (Raymond et al. 2018).

Chapter 3

Cometary noble gases: an experimental investigation

The ROSINA Double Focusing Mass Spectrometer (DFMS) on-board the Rosetta spacecraft measured the elemental ratios of neutral species (noble gases, CO, N_2, H_2O) in the coma of comet 67P/C-G. The measured CO/N_2 of the comet indicates low trapping temperatures ($\leq$ 50 K; Rubin et al. 2015). However, laboratory investigations into cometary noble gas abundances suggest that the signatures measured by ROSINA require comet formation temperatures $\geq$ 70 K (Rubin et al. 2018). This inconsistency between experimental and natural conditions could be in part related to the heterogeneous nature and complex evolution history of cometary bodies in the Solar System. Firstly, comets from the Oort cloud or JFCs would have experienced varied thermal histories, as they orbit at a range of distances from the Sun, with different eccentricities. Before becoming a JFC, comet 67P/C-G underwent a series of gravitational scattering processes after which it remained at an intermediate distance from the Sun (probably between the orbits of Jupiter and Saturn) for several million years. Simulations of the thermal evolution of comet 67P/C-G during this transitional phase indicate it had already experienced very inhomogeneous temperatures, up to 90 K inside the nucleus (Guilbert-Lepoutre et al. 2016). Later on, the comet surface suffered a few meters to tens of meters erosion per perihelion passage (Keller et al. 2015), potentially corresponding to hundreds of meters of lost surface since it first entered the Solar System. The nucleus of comet 67P/C-G exhibits a strong dichotomy between its northern and southern hemispheres, with variable illumination conditions and temperatures resulting in different extents of surface processing. As multiple portions of the comet may have experienced contrasted irradiation/thermal histories, it is difficult to envision representative experimental conditions for the bulk comet. Nonetheless, processes affecting cometary surfaces can be investigated through laboratory simulations of cometary environments. In this chapter, we present a series of experiments aimed at understanding the nature, carrier phases and evolution of cometary noble gases exposed to irradiation and/or temperature variations. The potential for Xe to participate in photochemical reactions in irradiated, amorphous water ice is spectroscopically investigated. We then test the possibility for trapping/releasing processes to fractionate noble gas isotopes.

3.1. Simulating cometary environments in the laboratory

Whether cometary ices are predominantly amorphous, poly-crystalline, similar to clathrate hydrates (Kargel and Lunine, 1998), or a mixture of the three, is still debated (Luspay-Kuti et al. 2016). According to pressure and temperature conditions in the ISM and outer regions of the protosolar nebula, the building blocks of comets most likely had amorphous water ice structures, as commonly assumed in numerical models and laboratory investigations (e.g., Bar-Nun et al., 1985; Notesco et al., 2003; Yokochi et al, 2012). Laboratory experiments are however carried out at deposition rates exceeding those expected in a molecular cloud or solar nebula by many orders of magnitude, potentially inducing an experimental bias in the representativeness of the trapping mechanism. Finally, models of cometary ice formation and evolution predict that the amorphous structure of subsurface cometary ices could become crystalline during the thermal evolution of cometary nuclei, eventually leading to the formation of clathrate hydrates (Marboeuf et al. 2009, 2012). These are high pressure - *low* temperature crystalline solids in which water molecules are organised in the form of hydrogen-bonded water cages, stabilised by the inclusion of gas molecules (Luspay-Kuti et al. 2016). The formation and decomposition of different water ice structures inside cometary nuclei could have important implications regarding their volatile element retention capacity (Marboeuf et al. 2012). From their formation, in the ISM/outer PPD, to their evolution within the Solar System, cometary bodies may have been exposed to variable temperature and irradiation conditions that affected their noble gas inventory. The aim of our project is to simulate and investigate these processes in the laboratory.

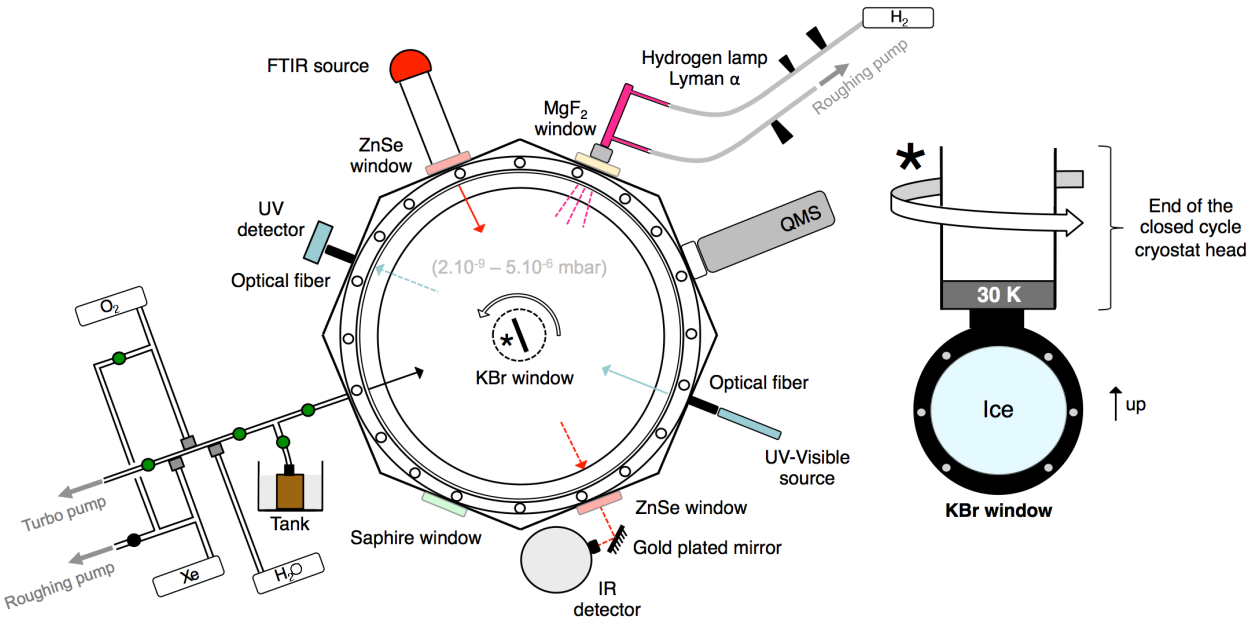

Fig. 36. Experimental setting used at the Ice Spectroscopy Laboratory (JPL-NASA) to investigate ice photochemistry by ultraviolet -visible and IR spectroscopy. The central axis of the cryogenic chamber comprises the KBr window on top of which the ice is grown by vapour deposition. The rotatable window is represented vertically on the right.

Forming cometary ice analogues requires a deposition surface whose temperature can be controlled down to ~ 20 K, and on top of which gas mixtures can be flowed and condensed at adjustable flow rates in a high-vacuum background. In diffuse environments of the ISM, photo-desorption is an extremely effective process, so the build-up of icy grains only occurs in portions of dense molecular clouds shielded from external sources of ultraviolet radiation (UV; Westley et al. 1995). Icy grains in molecular clouds are exposed to a low-intensity UV field arising from the interaction of cosmic rays with H_2, mainly consisting of a UV flux of Lyman-α photons (λ = 121.6 nm; Ligterink et al. 2015). Likewise, icy grains and cometary materials may directly be exposed to UV (predominantly Lyman-α) radiation from protostars and pre-main sequence stars (van Dishoeck et al. 2006). To simulate UV irradiation in astrochemistry ice experiments, hydrogen and deuterium UV lamps are most commonly used (Nuevo 2012). Characterization of the structure, composition and evolution of cometary ice analogues under varying temperature and irradiation conditions can be monitored by UV-visible spectroscopy and Fourier Transform Infrared Spectroscopy (FTIR). Here, we investigated the evolution of noble gas-bearing cometary ice analogues in the Ice Spectroscopy Laboratory at Jet Propulsion Laboratory (Pasadena, USA), in collaboration with Dr M.S. Gudipati. The experimental setup is schematically represented on Fig. 36.

Ice films were obtained by vapour deposition of mixtures of Xe and H_2O in adjustable proportions, onto a KBr window (transparent to UV light) at ~ 30 K (Fig. 36). The latter was set on the 360° rotatable head on top of the closed-cycle helium cryostat (Fig. 36). The thickness of the ice was adjusted by keeping the final absorbance constant, with different Xe:H_2O obtained by varying the respective gas flows using the QMS (Fig. 36). Under such experimental conditions (high deposition rates and T ≤ 30 K), efficient trapping of noble gases within amorphous water ice allows preserving the Xe to H_2O ratio of the gas phase within the ice (Bar-Nun et al., 1985; Notesco et al., 2003; Yokochi et al, 2012). After ice deposition, the cryostat was cooled down to 5 K, and the KBr window was rotated to positions allowing either irradiation or spectroscopy measurements using the FTIR or fibre optic UV-visible spectrometer (200 nm to 900 nm; Fig. 36).

UV irradiation was generated using a plasma of pure H_2, connected to the main chamber via a MgF_2 window (Fig. 36). UV spectra of this hydrogen lamplight permitted calibrating the UV-visible spectrometer using the H-alpha (Hα) spectral line of the hydrogen Balmer series, at 656.28 nm (Ligterink et al. 2015). Repeated irradiations and UV spectroscopy measurements were carried out to investigate the photochemical evolution of Xe-H_2O ices, for durations up to 36 hours. Each irradiated sample was heated step by step at 5K/min, from 5 K to 170 K, in order to follow the evolution of the synthesised ices upon thermal annealing. Each temperature step for which spectroscopic measurments were obtained was stabilised for ~10 min to ensure that thermal/chemical equilibrium had been reached. Absorbance (Abs) spectra reported in this chapter were computed as Abs = -log (Tr_{sample}/Tr_{ref}), where Tr is the transmittance of the ice, which corresponds to the quantity of transmitted UV photons at each

wavelength. This way, each positive peak at a given wavelength reveals the production of a chemical species that absorbs corresponding photons, whilst a negative peak corresponds to its consumption. The reference for normalization is always specified in the text, corresponding for instance to the transmittance spectrum of the initial ice at 5 K, before irradiation.

The UV-visible spectroscopy and FTIR monitoring of photochemically processed Xe-H_2O ices presented in this chapter did not yield conclusive results regarding the potential formation of Xe-bearing molecules in cometary ice analogues. Initially however, it was thought that the formation of Xe oxides upon irradiation had been observed. These results are presented as they were obtained, with the final finding that the signals that had been attributed to Xe oxides were in fact not related to Xe. We also investigated the behaviour of Xe in ice upon warming from T < 60 K to T > 150 K and found that part of the initially trapped Xe is retained in the water ice lattice above Xe's sublimation temperature. We investigate the potential for this partial loss to cause any isotopic fractionation of trapped Xe.

3.2. Spectroscopic investigations of Xe photochemistry in cometary ice analogues

3.2.1. UV-visible characterization of Xe-H_2O ices

Upon irradiation of Xe-H_2O ice mixtures, we noted the systematic rise of peaks corresponding to species absorbing light at about 290 and 620 nm, with an additional, broader peak around 420 nm (Fig. 37, 38). The two main peaks appear to rise synchronously upon irradiation, following decreasing production rates with irradiation dose (Fig. 37). Upon thermal annealing, peaks progressively vanish (Fig. 38). We propose that either the energy brought to the system is sufficient to break bonds formed upon photochemical processing of the ice, which would leave the possibility to reform the photoproducts when the ice is cooled back to 5 K, or the photochemical products are definitively lost and would only reform upon further irradiation. For thermal annealing experiments with $Xe/H_2O \geq 1$ (e.g., Fig. 37b), we observe irreversible decreases in the peak intensities, which are not recovered at 5 K. For $Xe/H_2O \leq 0.1$, cooling back to 5 K appears to allow the recovery of the full peak intensities, until ~90 K (e.g., Fig. 38b). In this case, irreversible decreases in the peak intensities are only observed at higher temperature (bold lines, Fig. 38b), possibly related to the increased mobility and loss of atoms. Three main peaks (290, 420 and 620 nm) are observed for Xe to H_2O ratios ranging over 4 orders of magnitude (Fig. 39). Whilst the absolute intensity of the 290 nm peak at a given irradiation dose increases with increasing Xe/H_2O, the 620 nm peak intensity is only slightly affected by varying the Xe/H_2O (Fig. 39). A double-peak shape was commonly observed at 250 and 290 nm for low Xe/H_2O (Fig. 39). Finally, we note that no significant evolution of the UV-visible spectra was observed beyond 17 h of irradiation (Fig. 38), suggesting a saturation effect of the photochemical reaction.

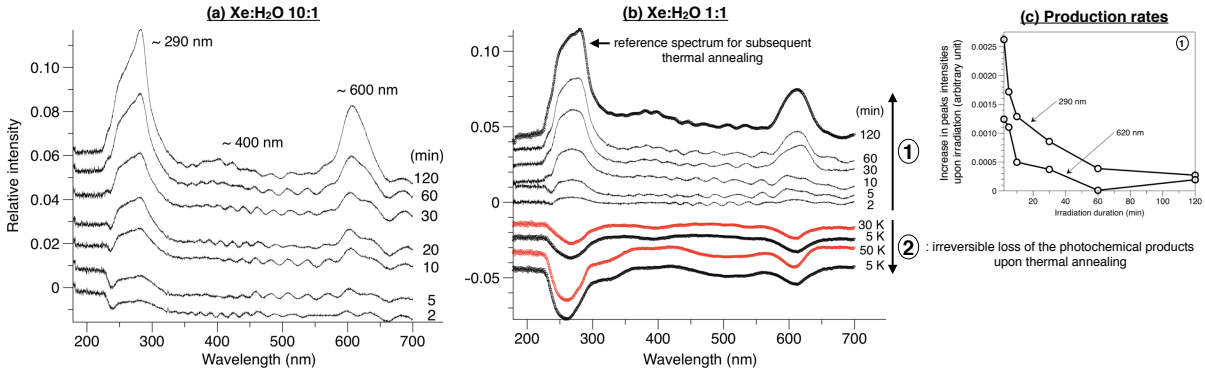

Figure 37: UV spectral evolution of 10:1 (a) and 1:1 (b) Xe:H_2O ices exposed to Ly-α irradiation at 5 K (traces vertically offset for clarity, duration of irradiation reported on the right). References for absorbance computation correspond to transmittance spectra at 5 K before irradiation. Relative increases in the 290 nm and 620 nm peaks intensities upon irradiation are shown on panel c, computed as differences in intensity between two subequent steps of irradiation. The effect of thermal annealing is shown on panel b (red spectra), materialised by the down arrow labelled 2. References for absorbance computation is this case are the transmittance spectra at 5 K after irradiation (bold line).

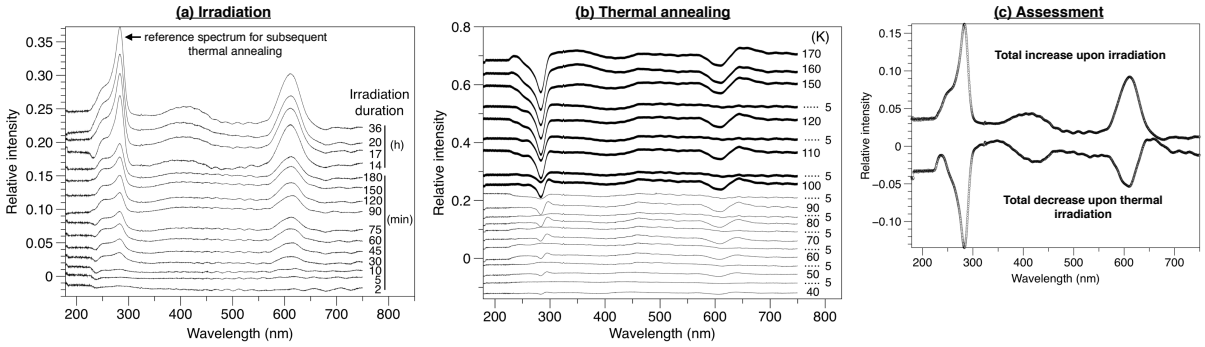

Figure 38: Detailed evolution of a 1:100 Xe:H_2O ice upon irradiaton at 5 K (a, spectra vertically shifted for clarity). The reference for absorbance computation corresponds to the transmittance spectrum at 5K before irradiation. (b) Subsequent thermal cycling from 40 K to 170 K (spectra vertically shifted for clarity). The reference for absorbance computation corresponds to the transmittance spectrum at 5K after 36 hours of irradiation (a). An assessment of the total increase in peak intensities upon irradiation (a) and decrease in peak intensities upon thermal annealing (b) is shown on panel (c).

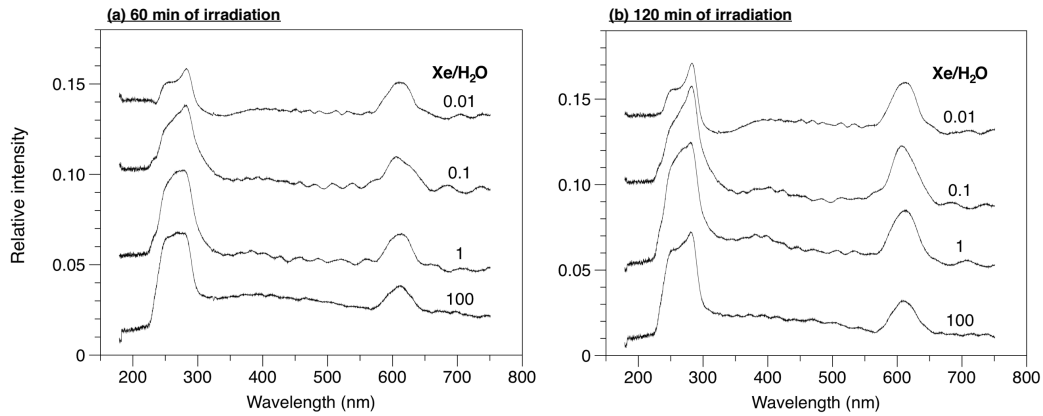

Fig. 39. UV spectra of 1:100, 1:10, 1:1 and 100:1 Xe:H_2O ices, after 60 min (a) and 120 min (b) of irradiation. Whilst the shape and intensity of the ~290 nm peak changes with the chemical composition of the ice, the 620 nm peak remains unaffected.

Based on these observations, we aimed to identify the nature of the photochemical product(s) associated with these peaks. Among potential Xe-bearing molecules, we first considered the possibility of Xe oxides (Xe-O). Photons reaching the surface of the ice induce the photo-dissociation of water molecules, therefore producing reactive radicals that can react together and/or with surrounding atoms/molecules to form photochemical products. Even at low UV photon fluxes, this process could drive the formation of complex molecules in cometary ice analogues (Ehrenfreund and Fraser 2003; Garrod and Herbst, 2006; d'Hendecourt et al., 1982). At 10 K, H and OH radicals produced by water photo-dissociation can typically move through the ice and travel up to 70 Å (Andersson et al., 2008). During such migration, water radicals could interact with water molecules and/or react with Xe atoms to form Xe-bearing molecules such as Xe-O (with covalent or, more likely, Van der Waals bonding). Xe(^{1}S)+O(^{1}D) and Xe(^{1}S)+O(^{1}S) transitions from the ground state Xe(^{1}S)+O(^{3}P) were previously determined from calculated potential energy curves subtractions by F. Schouren during his PhD (Schouren, 2001), under the supervision of Dr. M.S. Gudipati (Fig. 40). These require energies of 2 eV and 4.15 eV, respectively, corresponding to wavelengths of ~ 620 nm and 298 nm (Fig. 40). In the first instance, we concluded that the two main peaks observed upon irradiation of Xe-H_2O ice mixtures could potentially correspond to Xe-O, where Xe and O interact through Van der Waals bonding. Interestingly, Hama et al. (2009a-b, 2010) indeed observed evidence of desorbing O(^{3}P) and O(^{1}D) after vacuum ultraviolet photolysis of amorphous water ice with 157 nm light at 90 K. In this framework, the nature of the chemical species detected at ~ 400 nm is less straightforward to identify. Due to its broad shape and late appearance, it could correspond to a complex chemical species resulting from recombination chemistry. Alternatively, part of the Xe-O molecules could have been trapped in their metastable state 1^1S^+ with a binding energy close to 1.5 eV (Fig. 40). In this state, optical excitations are accessible to the charge transfer state 2^1S^+ at ~ 250 nm and to the valence state 1^1P at ~ 400 nm (broad dissociative continuum). This possibility was initially considered but there is an unsuspected fundamental problem with the hypothesis.

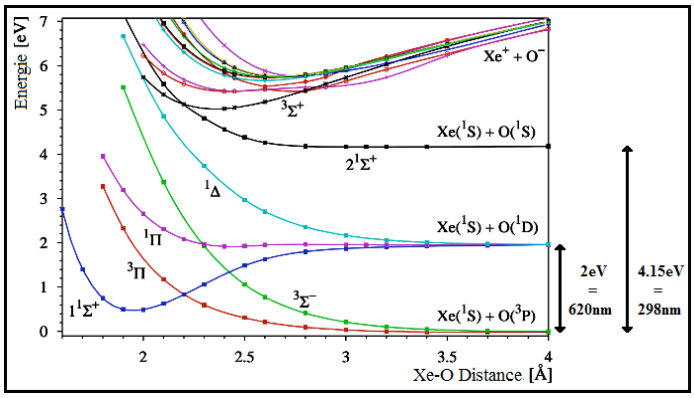

Fig. 40. Basis set superposition errors (BSSE)-corrected potential energy curves from Xe-O to CASPT2-level with calculations of transitional energies (eV) and corresponding wavelengths (nm). In fact, the *CASPT2* (i.e. an implementation of second-order multireference perturbation theory) *level* ensures a correct balance of dynamic and non-dynamic electron correlation in the wave function.

KBr windows are commonly used at the Ice Spectroscopy Laboratory for studying the behaviour of variable ice mixtures upon irradiation and thermal processing. At the start of this project, we directly investigated the evolution of Xe-H_2O ice mixtures using a new KBr window, without having done a blank experiment. A series of experiments with no deposit (no water, no Xe) onto of the KBr window was carried out later on. Upon irradiation of the KBr window only, the two peaks at 290 and 620 nm could still be observed (Fig. 41). This unusual behaviour of the KBr window could potentially be related to the hydrophilic properties of this material. One possibility is that, even at room temperature, the KBr window could preserve some water, condensing in the form of water ice at low temperature (even without the addition of any deposit). The O(^{1}D) and O(^{1}S) transitions from the ground state O(^{3}P) of monoatomic oxygen are expected to have energies that are similar to that of oxygen bound to Xe in Xe(^{1}S)-O (Schouren, 2001; personal communication with Dr. M.S. Gudipati). Although the exact origin of these peaks and nature of the "problem" with the KBr window remain unknown, they could correspond to atomic oxygen electronic transitions, without requiring Xe to be involved.

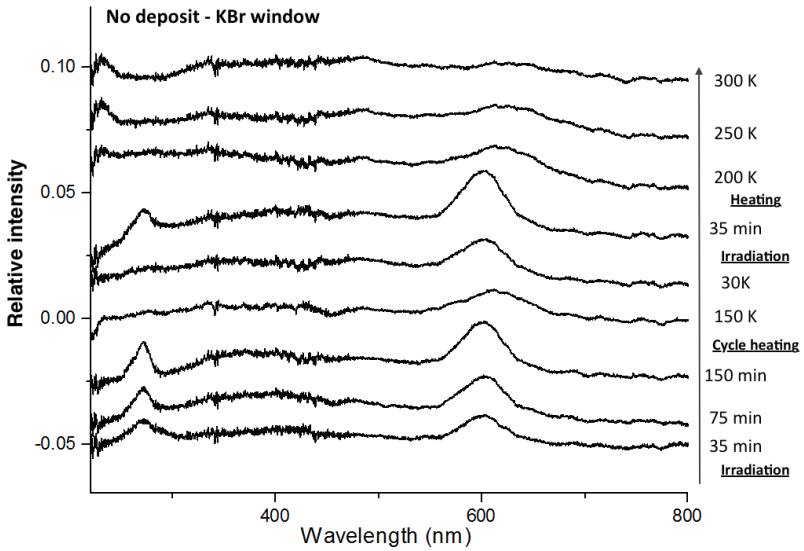

Fig. 41. UV spectra of the KBr window with no deposit on top, after 35 min, 75 min and 150 min of exposure to Ly-α irradiation at 30 K and during thermal cycling. The two previously identified peaks at ~290 and ~620 nm are still visible, although no Xe is here involved in the reaction. This could correspond to atomic oxygen from photo-dissociation of water molecules sticking to the KBr window due to its hydrophilic properties.

A new series of experiments were carried out by following the exact same experimental procedure, but using a sapphire window (not hydrophilic) instead of a KBr one. Spectra obtained using the sapphire window are reported on Fig. 42. Firstly, when no ice is condensed on top of the sapphire window, we detect no resolvable peak upon irradiation (Fig. 42). Even when water, water + O_2, and water + O_2 + Xe are added (Fig. 42), no particular peak is detected. As a conclusion, despite our preliminary interpretation of the possible occurence of Xe oxides in Xe-H_2O ices upon irradiation, no photochemical species involving Xe has unambigously been detected from our UV-visible analysis of irradiation/heating experiments.

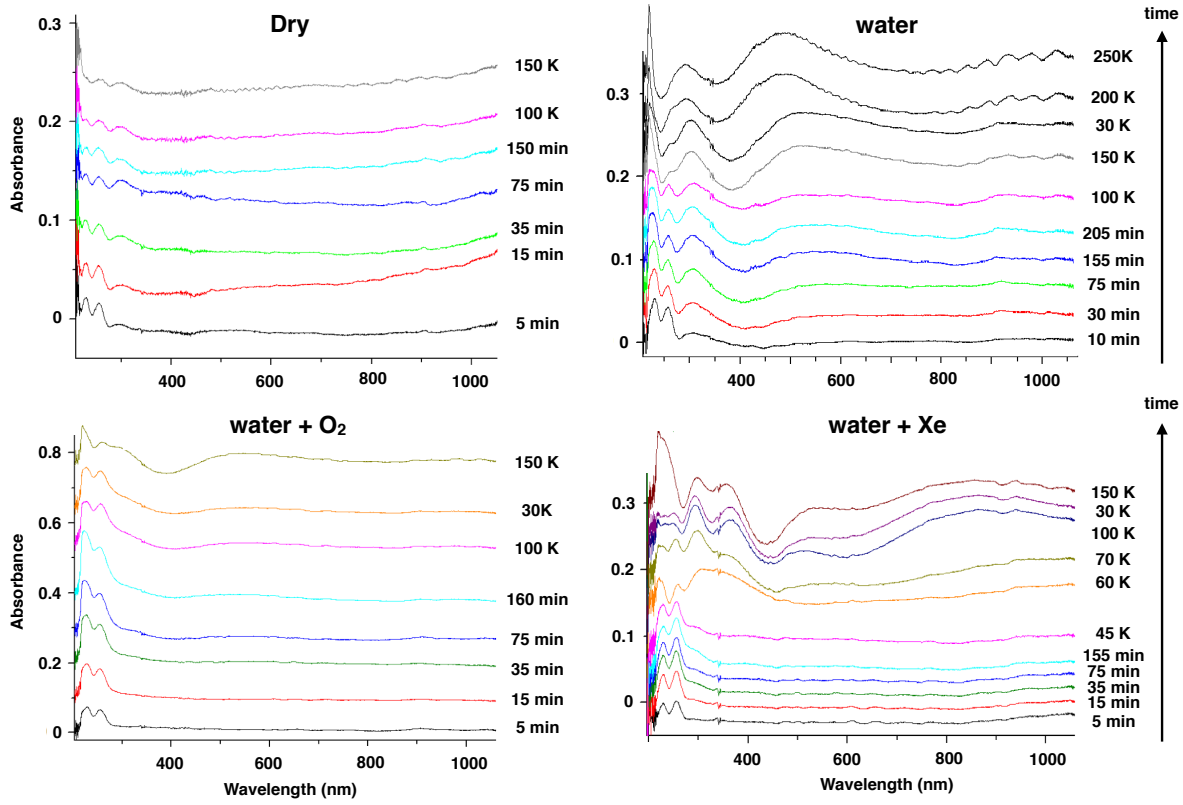

Fig. 42. UV-spectra obtained with the CaF_2 window in the case of no deposit (dry), and deposition of water, water + O_2 and water + Xe ices, for increasing doses of irradiation and upon thermal annealing. For each experiment, the time is displayed from bottom to top, with the integrated duration of irradiation and subsequent temperature steps being reported on the right of each diagram. We observe no significant difference between the spectra, with no new peaks detected when Xe is added to the mixture, indicating no evidence for the formation of any Xe-bearing photochemical component.

3.2.2 Fourier Transform Infrared Spectroscopy

FTIR measurements are particularly useful to interrogate the structure of the ice: whilst amorphous ice is characterised by a broad peak at around 3200 cm^{-1} (Fig. 43), crystalline ice shows three peaks at about 3125 cm^{-1}, 3210 cm^{-1} and 3340 cm^{-1} (depending on the temperature, pressure and thickness; Gudipati and Castillo-Rogez, 2012). These features allowed us to observe that crystalline ice can be made amorphous upon irradiation, with the progressive loss of the three characteristic peaks of crystalline ice adsorption. The transition from amorphous to crystalline ice upon warming is observed at ~ 150 K; the three peaks of crystalline ice can then be made more obvious by subsequently cooling the ice to 30 K, which causes the peaks to be sharper (Fig. 43). Unfortunately, hydrogen peroxide (H_2O_2) is the only photochemical product that we could unambiguously detect (at ~ 2850 cm^{-1}; Gudipati and Castillo-Rogez, 2012) from our series of experiments. This molecule is known to result from the photo-dissociation of water, producing OH radicals that react together to form hydrogen peroxide. Interestingly, the synthesis of this component can be enhanced in the presence of O_2 (Fig. 44). Similarly to our UV-visible investigation, no photochemical product potentially involving Xe could be detected here with FTIR.

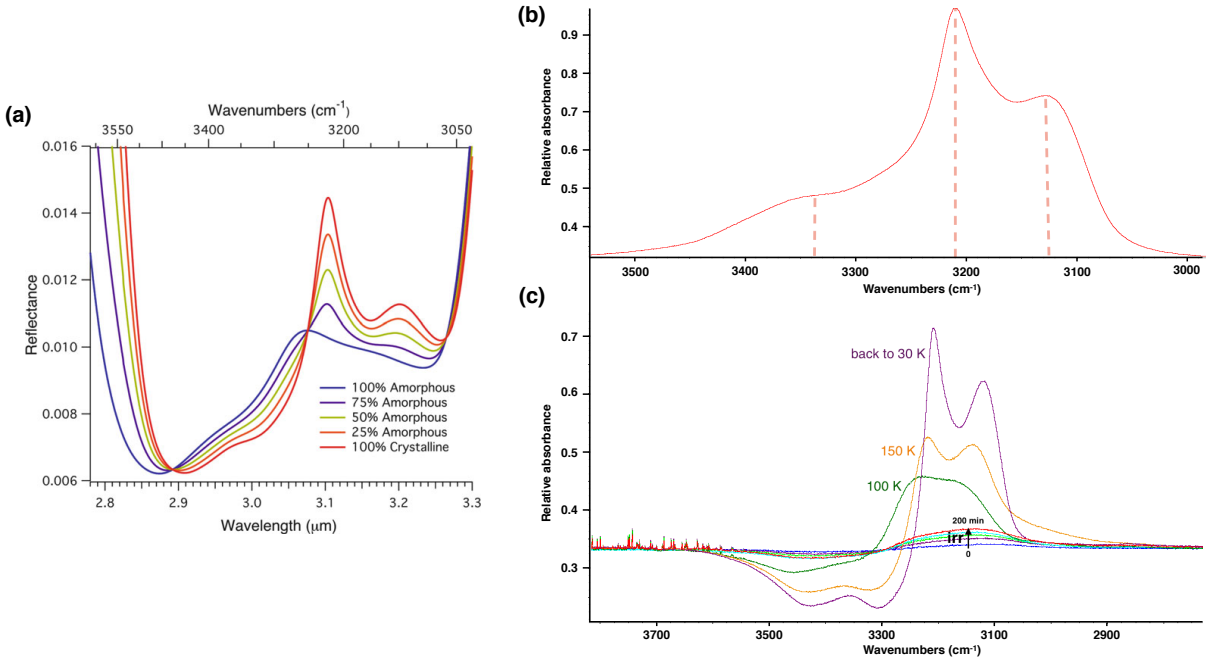

Fig. 43. (a) Model mixtures of amorphous and crystalline H2O-ice at 100 K, with grain sizes of 20 mm, from Mastrapa et al. 2009. (b) FTIR spectrum of crystalline ice obtained at the ISL. (c) Transition from amorphous to crystalline ice upon warming to 150 K. "Irr." refers to the 200 min of irradiation prior to warming. The three peaks of crystalline become more obvious when the temperature is subsequently decreased to 30 K.

3.3. Xe isotopic fractionation during its partial release from water ice

The sublimation temperature of Xe at low pressure (~10^{-9} bar) is ~ 60 K (Fig. 45). Here, we measured the composition of gases sublimating from Xe-H_2O ice mixtures upon warming from 20 K to 180 K. Although most of the Xe release does occur ~ 60 K, some of the condensed Xe is released at higher temperature (~150 K), just before crystallization of water ice, as observed by FTIR (Fig. 43). Hence, part of the initially condensed Xe remains trapped in the amorphous water ice lattice and is only released when the water ice structure experiences a structural transition from amorphous to crystalline. Likewise, the sublimation temperature of O_2 is around 38 K (Fray and Schmitt, 2009; Fig. 45). However, a considerable fraction of the O_2 is outgassed at significantly higher temperature (~ 60 K), i.e. when Xe sublimates and causes the porosity of the ice to increase (Fig. 46). In this section, we investigate the possibility of partial Xe trapping causing any significant isotopic fractionation during Xe sublimation. We measure the isotopic composition of Xe released from the ice lattice during water ice's structural transition from amorphous to crystalline, and compare it with the isotopic composition of the initially condensed Xe, and Xe fraction sublimating at ~ 60K.

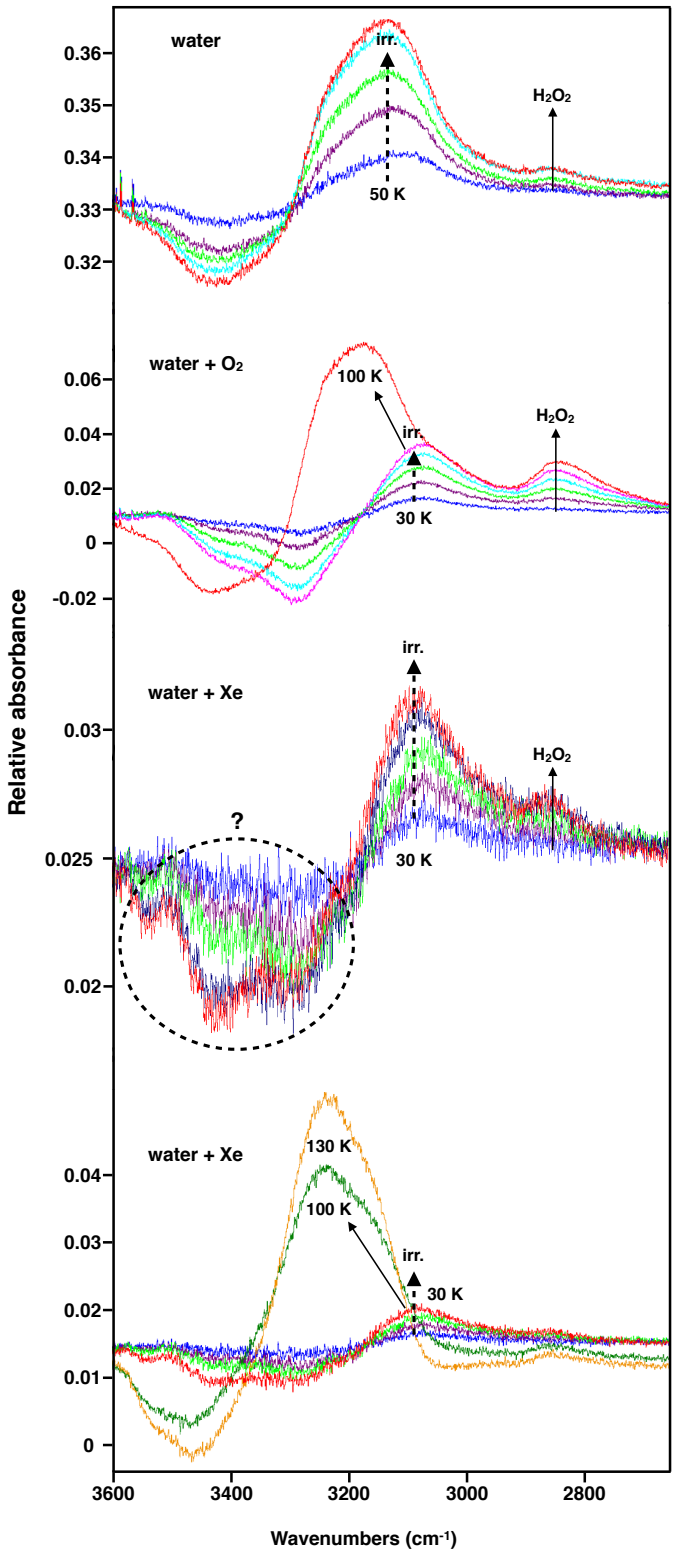

Fig. 44. FTIR spectra of a water only (top), water + O_2 (middle) and water + Xe ices deposited on top of a sapphire window. Top: only irradiation, no heating. Middle: exposure to Ly-α irradiation from the blue spectrum to the pink one and subsequent heating at 100 K (red curve). Bottom: exposure to Ly-α irradiation from the blue spectrum to the red one and subsequent heating at 100 K (green curve) and 130 K (orange curve).

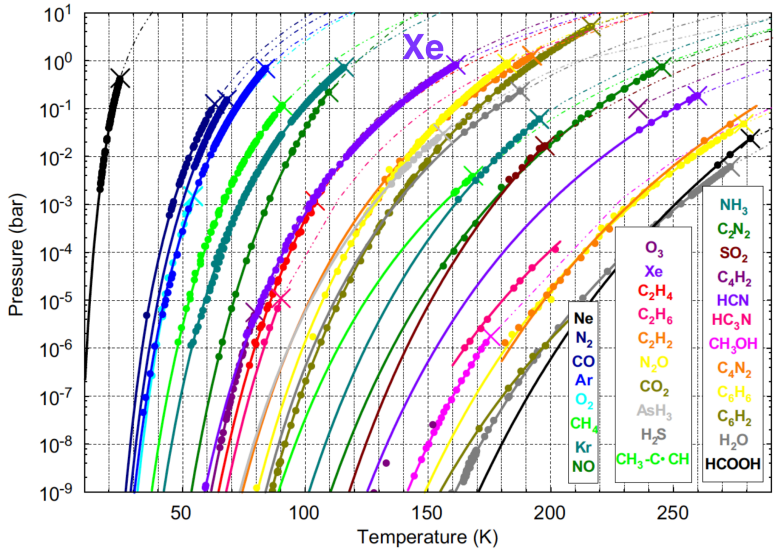

Fig. 45. Sublimation pressure as a function of temperature for a series of species (Fray and Schmitt, 2009). The curve of Xe is reported and labeled in purple.

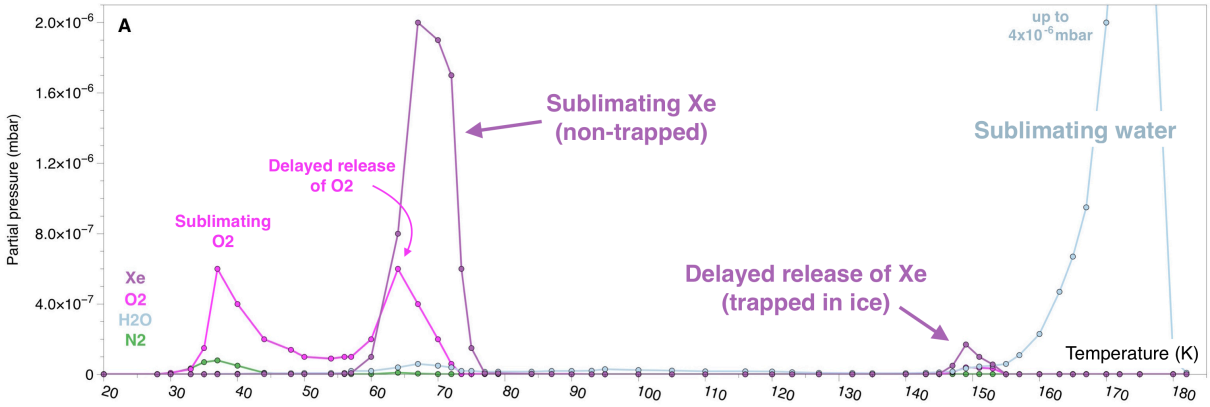

Fig. 46. Partial pressure of Xe, O_2, H_2O and N_2 (contaminant) measured on the Quadrupole Mass Analyzer as a function of temperature. The temperature is increased at a rate of 3 K/min. Rises in partial pressure indicate that the corresponding species is being released from the ice.

Noble gases have very low sublimation temperatures (≤ 60 K) indicating that a comet entering the Solar System and approaching the Sun would lose most of its noble gas budget before reaching the terrestrial planets. However, there are compelling pieces of evidence that comets significantly contributed Earth's heavy noble gas inventory (especially Xe; Marty et al. 2016, 2017). This requires a mechanism to preserve noble gases in the ice fraction of cometary bodies at higher temperature than their respective sublimation points. The retention of gaseous species in amorphous water ice above their sublimation temperature, and later release upon initiation of the amorphous to crystalline ice structural transition, has been observed for a series of volatile elements including CO and Ar (Fig. 47). A mantle of water molecules and trapped species (e.g., CO, N_2, O_2, noble gases) would form when additional molecules and/or atoms freeze-out on top of already adsorbed species, therefore burying them into the ice lattice (Fig. 48). As a result, gaseous species are locked up within the water ice lattice, and only

released upon warming, when the amorphous structure of water ice evolves, its molecules diffuse and rearrange themselves through various phase transitions. But if trapping in amorphous ice were to be the mechanism allowing Xe to be preserved in cometary ice and reach the Earth's surface, how much could this process have affected the Xe isotopic composition of comets? Would this trapping process cause any isotopic fractionation between outgassed and trapped fractions of cometary Xe? Such fractionation could occur because of differing sizes and polarizabilities of the Xe isotopes, leading to competition for the available sites in the ice.

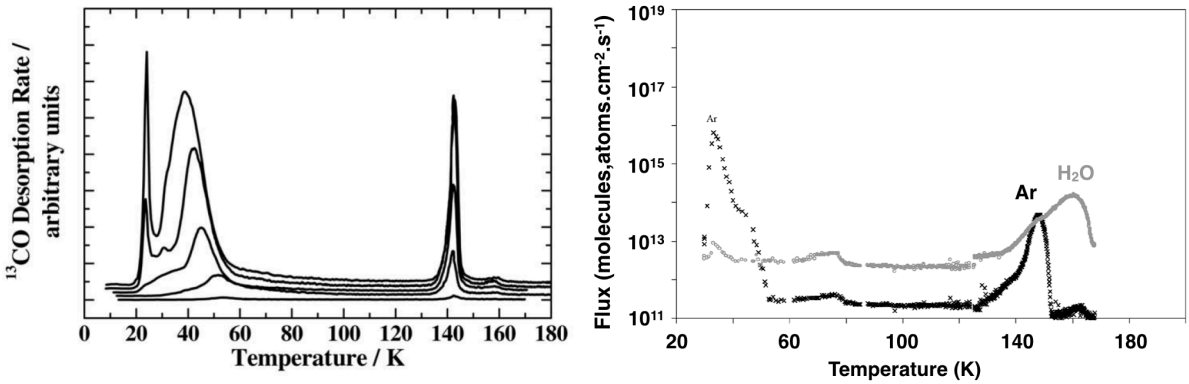

Fig. 47. (left) Desorption profiles of CO from CO-H_2O ice mixtures during experiments of temperature programmed desorption (Collings et al. 2003). (right) Fluxes of Ar and H_2O during warming up of a 0.1 µm ice layer deposited at 27 K from a H_2O:Ar = 1:1 mixture, at a rate of 10^{-3} µm.min^{-1} (Notesco and Bar-Nun 2005). Both series of experiments show that host species (here CO and Ar) can be retained within the water ice lattice above their sublimation temperatures, and are only released upon water ice crystallisation.

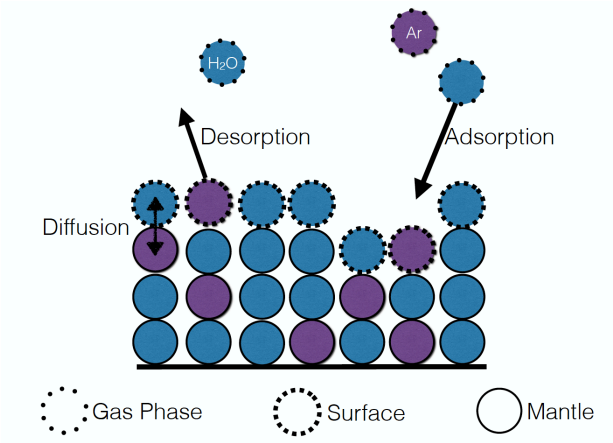

Fig. 48. Schematic diagram of the three-phase model described by Ciesla et al. (2018) in the case of the deposition and evolution of a H_2O-Ar mixture, where each species exists either in the gaseous, surface, or mantle phases. Evolution among these phases occurs through adsorption, desorption, and diffusion. Adapted from the model developed by Fayolle et al. (2011).

We analysed by static mass spectrometry at CRPG (Nancy, France) the isotopic composition of Xe released at 60 K and 150 K, with and without irradiation. To transport these samples from JPL (Pasadena, USA) to Nancy, we used four high vacuum steel tanks that had to be fully immersed in liquid nitrogen to trap sublimating/released Xe fractions (Fig. 36).

For each sample, the ice sample was kept under high vacuum (dynamic mode) until the desired temperature (60 K or 150 K) was about to be reached. The whole vacuum chamber was then set under static mode (pumps closed) and a pre-evacuated steel tank at liquid nitrogen temperature was opened for 40 min of trapping (Fig. 36). Each sample was analysed multiple times in Nancy to allow computing standard errors (see data reported in Appendix A).

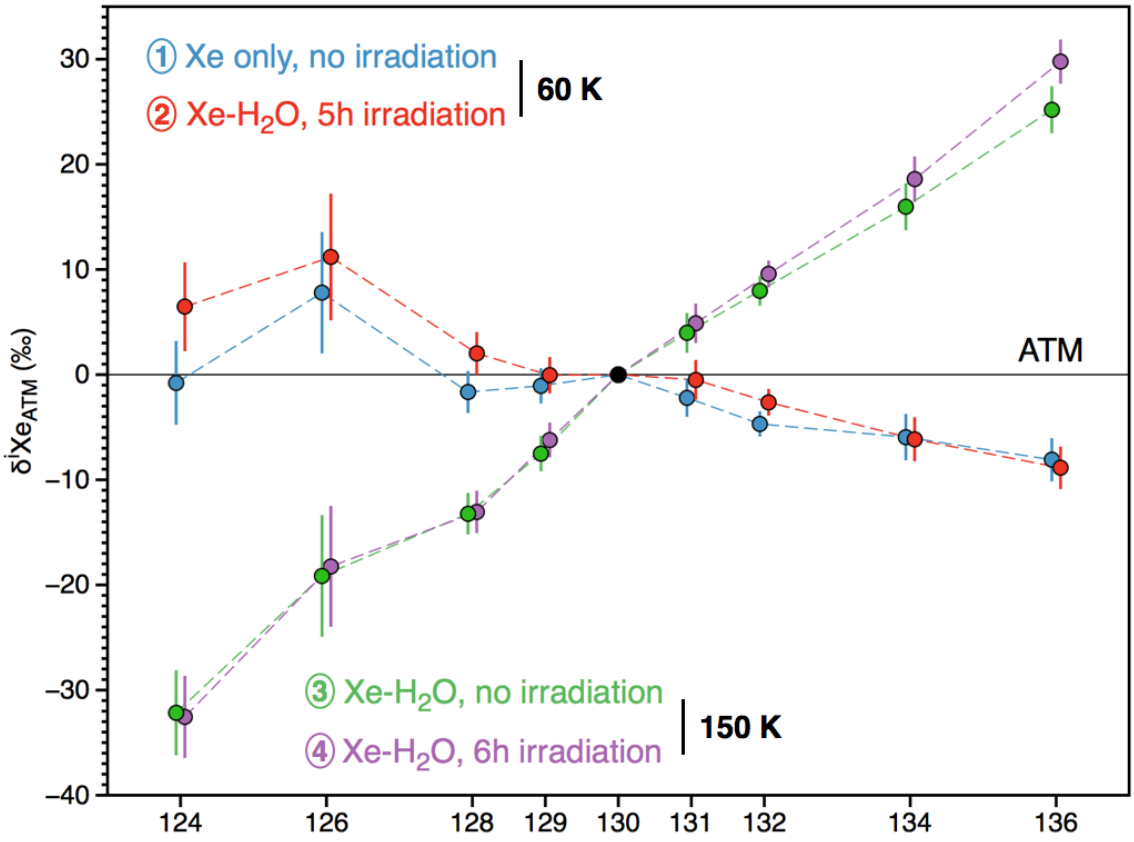

Fig. 49. Isotopic composition of Xe sublimated from ice experiments at JPL, normalised to the isotopic composition of air (ATM, Basford et al. 1973). Numbers are referred to in the main text. Sample #1 corresponds to Xe only (no water), with no irradiation, sublimated at 60K. Sample #2 corresponds to the Xe fraction sublimated at 60K from a Xe:H_2O 10%:90% that had been irradiated at 30K for 5h. Samples #3 and #4 are Xe fractions released at 150K from Xe:H_2O 10%:90% ice mixtures that had not been irradiated and irradiated for 6h at 30K, respectively. We observe that samples #3 and #4 are mass dependently fractionated in favour of the heavy isotopes with respect samples #1 and #2. Measurements were carried out on the Helix MC Plus at CRPG. Data are slightly shifted on the x-axis for clarity. Uncertainties are 1 standard error (raw data reported in Appendix A).

For the first sample, we deposited Xe only, at 30K. This pure Xe ice was heated up to 60 K with no processing. This Xe isotopic composition (blue spectrum, Fig. 49) is considered as a reference. **The second sample** corresponds to a Xe-H_2O mixture (10%-90%) irradiated at 30 K for 5 hours and heated up to 60 K (red spectrum, Fig. 49). This Xe isotopic composition is similar to that of the reference spectrum. We therefore conclude that no detectable isotopic fractionation occurs upon irradiation, and that the fraction of Xe released at

60 K from water ice (i.e., the vast majority of initially trapped Xe; Fig. 46) probably has the similar isotopic composition to the initial gas (reference spectrum). In other words, trapping and releasing Xe at its sublimation temperature would not induce measurable isotopic fractionation. **The third sample** corresponds to the fraction of Xe released at 150 K, in the case of a Xe-H_2O mixture (10%-90%) that has not been irradiated (green spectrum, Fig. 49). We find that this Xe component is mass dependently fractionated in favour of the heavy isotopes, by about 5 ‰.u^{-1}. Finally, **the fourth sample** also corresponds to Xe released at 150 K, but from an ice that had been irradiated for 6 hours. In this case, we observe the same degree of mass dependent fractionation in favor of the heavy isotopes as the third sample, hence supporting the reproducibility of this result (purple spectrum, Fig. 49). We therefore conclude for the fraction of Xe trapped in water ice and released at 150 K is enriched in the heavy isotopes by linear mass dependent fractionation with respect to the initial composition of the gas phase.

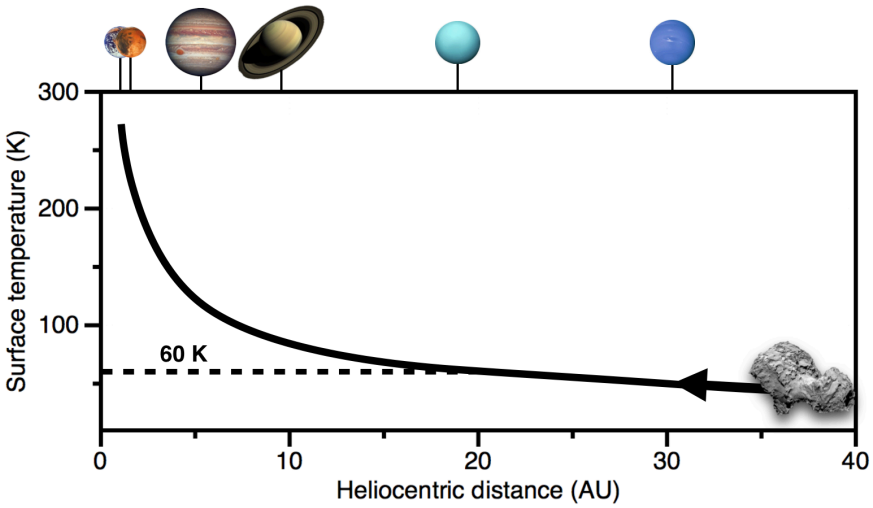

Fig. 50. Theoretical surface temperature of a cometary body (modelled as a black body with a 6% albedo) moving inward in the Solar System. This simple model shows that the surface temperature of a comet entering within 20 AU from the Sun would likely reach temperatures higher than the sublimation temperature of Xe, indicating that its Xe component brought to the terrestrial planet region would possibly be dominated by the trapped component observed at ~140 K within our experiments

Under our experimental conditions, we detect no Xe isotopic fractionation related to the irradiation of the ice. However, we observe a preferential retention of the heavy isotopes when Xe sublimates from the ice at ~ 60 K. One possibility is that lighter isotopes more easily escape the ice lattice (through diffusion for instance), resulting in enrichment of the heavy isotopes within the ice. This could have important implications regarding the noble gas inventory of cometary ices. When such cometary bodies drift inward in the Solar System or PPD, they could reach high enough temperatures for Xe to sublimate and for a mass dependently fractionated component to remain trapped in the ice lattice. Considering a cometary surface that behaves as a black body and has an albedo akin to that of comet 67P/C-

G (6%; Ciarniello et al. 2015), we can use the Stefan–Boltzmann law to compute the surface temperature of a comet (assuming no atmosphere) entering the Solar System, as a function of the heliocentric distance. The Stefan–Boltzmann law states that the total energy radiated per unit surface area of a black body across all wavelengths per unit time is directly proportional to the fourth power of the black body's thermodynamic temperature. Results of this calculation are represented on Fig. 50, supporting the idea that (at least the subsurface of) a cometary body entering the Solar System would rapidly reach temperatures greater than 60 K. Most of the noble gases carried out by comets within the Solar System may therefore be trapped in the cometary water ice lattice.

The rate of water degassing from comet 67P/C-G was relatively low at the time of noble gas measurements by the Rosetta spacecraft, whereas CO_2 was abundant. This was taken to indicate that noble gases measured from the comet were predominantly trapped in CO_2, and not H_2O, ice (Rubin et al. 2018), which would account for the poor correlation between cometary Ar and H_2O (Balsiger et al. 2015). However, our results demonstrate that noble gas release from the comet is not necessarily associated with water degassing, as most of the trapped noble gases would be released during structural transitions within the water ice lattice. In addition, trapping/releasing of volatile species from water ice is a complex process that depends on several parameters including the nature of the guest species, the guest (e.g., Xe) to host (e.g., H_2O) initial ratio, and the ice thickness (Notesco and Bar-Nun 2005). For instance, it appears that the fraction of a CO, CO_2 and Ar trapped in water ice increases with increasing ice thickness (Fayolle et al. 2011; Notesco & Bar-Nun 2005). In addition, the fraction of guest species that remains trapped within the ice above their sublimation temperature increases as the guest to host abundance ratio decreases (Notesco & Bar-Nun 2005). Given that water is expected to be much more abundant than noble gases in the solar nebula and molecular clouds ($Xe/H_2O \sim 10^{-7}$; Notesco et al. 2003), the vast majority of cometary noble gases may thus remain trapped in ice above 60 K, with no fractionation effect related to partial outgassing at the sublimation temperature. In this case, the isotopic composition of noble gases delivered to terrestrial planets might not be fractionated with respect to their initial composition in the ISM.

These results open a promising avenue of investigation into the study of Xe isotopic fractionation in cometary ice upon warming/irradiation. To further investigate these processes, I have designed a new experiment in the noble gas laboratory at CRPG, which will allow noble gas-water ice mixtures to be condensed under high vacuum at 20 K, then irradiated with an hydrogen lamp, and sequentially heated up to 180 K (Fig. 51). This set up allows precise control of the temperature of the copper substrate where condensation occurs, from 20 K to 300 K. Aliquots of sublimated/released Xe can be directly sent to the static mass spectrometer for precise analysis of their isotopic composition. This project, named "EXCITING" (Exploring Xenon in Cometary Ice by Trapping and Irradiating Noble Gases) is described in the next section.

3.4. **E**xploring **X**enon in **C**ometary **I**ce by **T**rapping and **I**rradiating **N**oble **G**ases

The EXCITING experiment was constructed as part of this thesis (Fig. 51). The vacuum system starts at pressures $\leq 5.10^{-8}$ mbar, at room temperature. First, the gas mixture can be prepared by using the QMS (loop L1), while the cryotrap is cooling down. At this stage, gases are flown with micrometre needle valves, ensuring a good control on the flux of each gas and therefore permitting to precisely adjust the respective proportions of Xe and water for instance. The cryostat is isolated from loop L1 and pumped through the mass spectrometer purification line. Once the gas mixture is adjusted and the cryotrap is at 20 K, the loop L1 is closed and loop L2 is opened (Fig. 51), therefore allowing the gas mixture to flow through the cryotrap, ion gage and QMS. This permits to simultaneously condense the ice sample, measure the pressure in the line, and analyse the composition of residual gases that have not been trapped, respectively (Fig. 51). After around 5 min of deposition, the gas supply is closed and the rest of the line, including the cryostat, is kept under high vacuum (pump 1). The ice sample can then be irradiated and/or thermally processed. In order to prepare an isotopic analysis, the cryotrap is heated up to the temperature required for Xe to be released. Just before reaching this temperature step, the system is set to static mode (pumps closed). Sublimated gases are equilibrated for a few minutes at the given temperature step, and an aliquot is sampled by taking a pipette, which is directly sent to an on-line getter connected to the mass spectrometer purification line (Fig. 51).

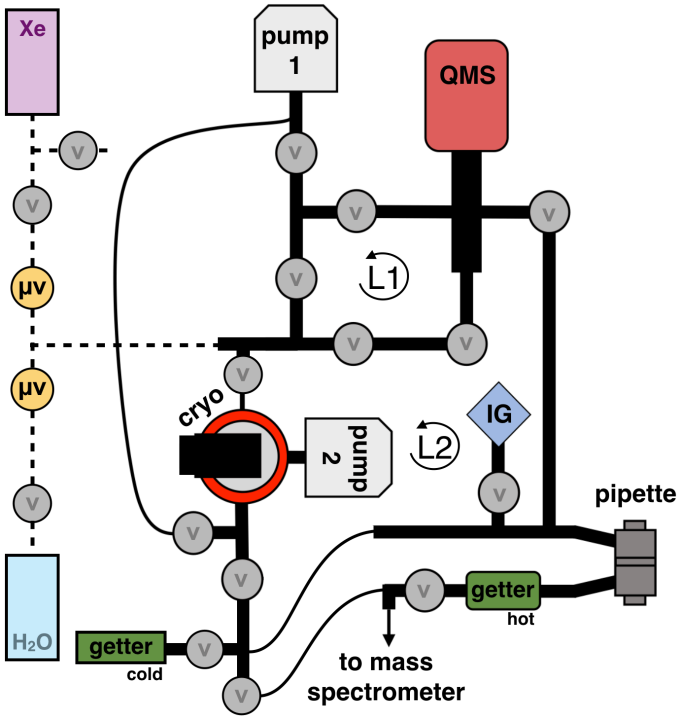

Fig. 51. Schematic representation of the EXCITING experiment. **v:** high vacuum valve. **µv:** micrometre flow control valve. **cryo:** cryogenic trap (see Fig. 52-54). **IG:** ionic gauge. L1 and L2 refer to the two loops of gas flow discussed in the main text.

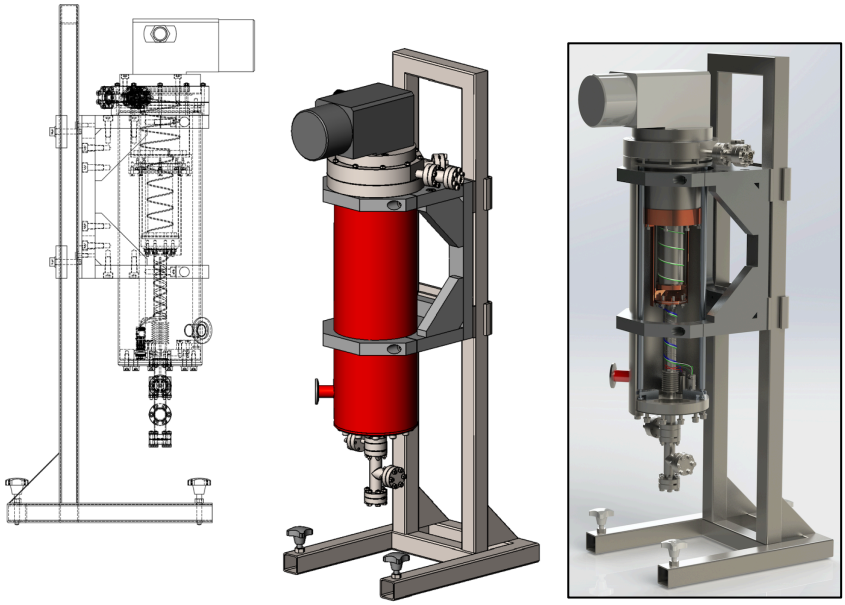

Fig. 52. Industrial scheme of the final cold head designed for the EXCITING project. Credit: Cryoscan©.

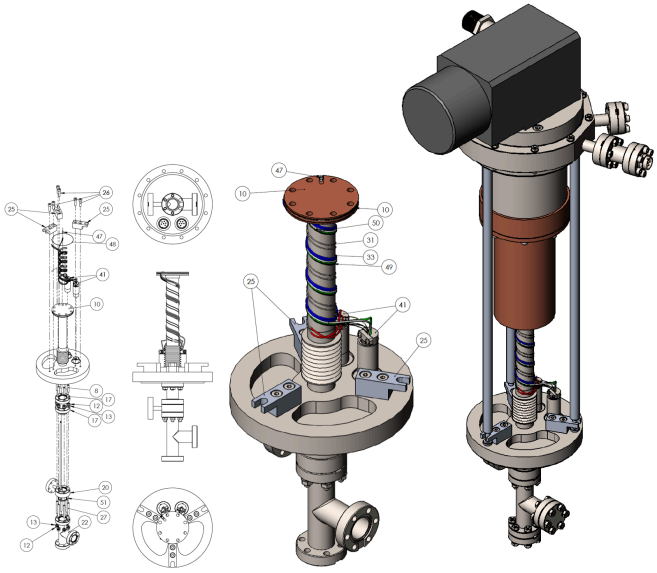

Fig. 53. Detailed industrial scheme of the cold head designed for the EXCITING project. Credit: cryoscan©.

Most of the developments related to the EXCITING experiment concern the design of the cryogenic trap. A cryogenic was modified to allow carrying experiments of ice deposition, irradiation, and temperature variation from 20 K to 180 K. The cold head is a Coolstar two-stage coldhead 6/30 delivering a cooling power of 6 W at 20 K and 30 W at 77 K. The minimum temperature specification of the cold head is 10 K. It was modified in collaboration with the Cryoscan Company (Nancy, France), expert in cryogenic systems. The final design of the cryogenic system is reported on Fig. 52-54. The gas enters the deposition chamber by a capillary facing the 15 K stage of the cold head (Fig. 54). At the bottom of the chamber, a CaF_2 window overlooks a small volume under vacuum, where the hydrogen lamp is connected.

A thermic screen was set on the first stage of the cold head to enhance its thermal insulation. A sapphire spacer was inserted between the edge of the second stage and the deposition surface to maximise temperature equilibration between these two parts. A flexible bellow was integrated as part of the ultra-high vacuum thin tube to accommodate thermic expansion effects between the surface deposition (from 20 K to room temperature) and the CF flange at the gas exit.

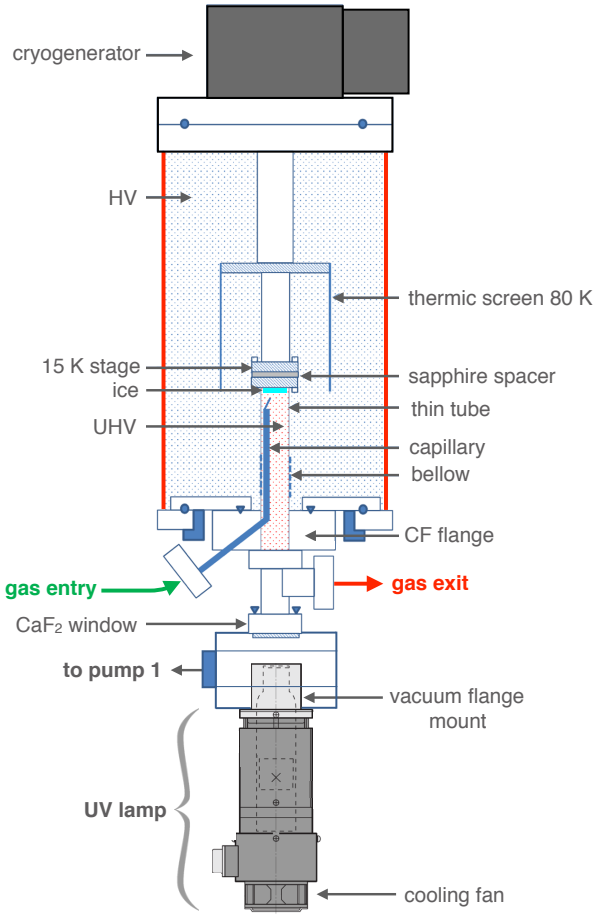

Fig. 54. Setting of the EXCITING line allowing noble gases/water mixtures to be condensed at 20 K under high vacuum and exposed to Lyman alpha light (with a H2D2 light source unit L11798 by Hamamatsu company). HV: high vacuum. UHV: ultra-high vacuum.

Today, the experiment is functional and the first analyses of Xe isotopes have started. A bottle of gas containing all noble gases as well as nitrogen has also been connected to the system. We plan on carrying out a survey of the evolution of noble gas and nitrogen elemental and isotopic compositions in water ice under various conditions of temperature, ice thickness, and irradiation dose. Matthieu Almayrac, who started his PhD in January 2019 with B. Marty, will handle this work as part of his thesis project. Preliminary experiments on EXCITING show that we reproduce the observation of trapped and sublimated Xe components upon warming of Xe-water amorphous ice mixtures (Fig. 55). Variations in the abundance ratio between Xe sublimated at 70 K and released at 140 K will be investigated for different deposition rates and gas compositions (e.g., water to Xe ratio). Likewise, the double-peak shape

of the trapped Xe component seen on Fig. 55 does not correspond to an experimental artefact, and could be related to a stepwise change in the crystalline structure of water ice (e.g., from cubic to hexagonal), leading to the sequential release of the trapped Xe component. We plan to scrutinise the release profile of Xe trapped in ice to investigate the evolution of water ice's structure, in relation with the evolution of cometary ices in the Solar System.

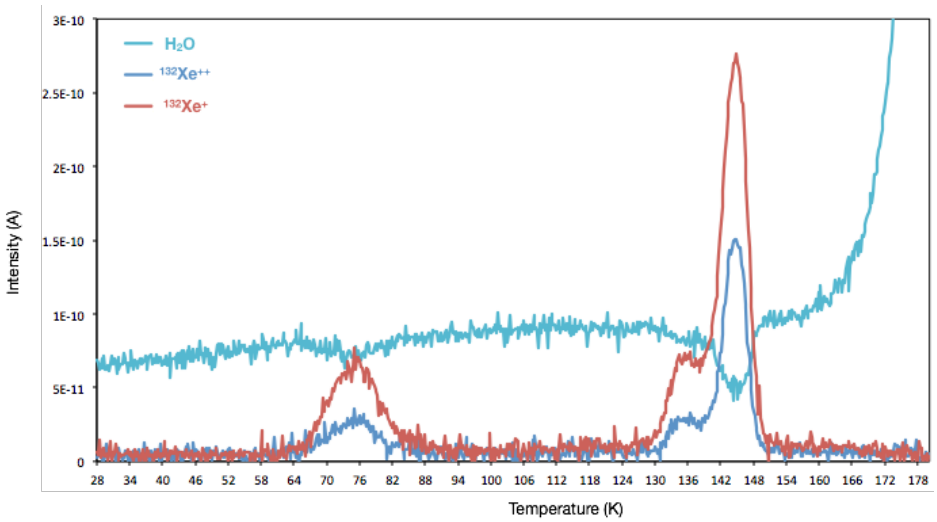

Fig. 55. Measured intensities at mass to charge ratios of 18, 66 and 132 (corresponding to H_2O, Xe^{2+} and Xe^{+}, respectively) given by the Quadrupole Mass Analyzer as a function temperature rise, at a rate of 1 K/min, on EXCITING. The peak release of sublimating and trapped Xe are observed at ~70K and ~140K, respectively. Water background is relatively high during the experiment, but sublimation is clearly observed from 160K.

Conclusion and outlook

In this Chapter, we present a series of experiments that were designed to investigate the potential for Xe-bearing chemical compounds to form in cometary ice analogues upon UV irradiation. Monitoring the chemical and structural evolution of Xe-water ice mixtures under high vacuum by FTIR and UV-visible spectroscopy did not produce conclusive results, as no Xe-bearing compound could be definitely identified. Preliminary experiments of Xe trapping in amorphous ice reveal that mass-dependent fractionation of Xe isotopes may occur upon partial release of Xe isotopes at the sublimation temperature (60 K). A fraction of the initially condensed Xe is retained in the water ice lattice above 60 K, and is only released at ~150 K when the water ice transitions from amorphous to crystalline. This trapped Xe component is mass dependently fractionated in favour of the heavy isotopes with respect to the initial composition of the gas. This finding could have important implications regarding the origin of the isotopic composition of cometary noble gases. I designed a new experimental setup called EXCITING to further investigate the behaviour of noble gases in cometary ice analogues, which is the main focus of the on-going PhD of Matthieu Almayrac, under the supervision of B. Marty and L. Piani.

Chapter 4

Noble gas components in chondrites and the origin of phase Q

Chondrites contain multiple noble gas carriers corresponding to distinct trapped (primordial) components. Pre-solar components usually have anomalous isotopic compositions with respect to the solar composition, witnessing different processes of nucleosynthesis in stars. Whereas Ne in primitive carbonaceous chondrites is dominated by a presolar component carried out in presolar diamonds, heavy noble gases are largely dominated by the so-called Q component carried out in a cryptic but ubiquitous phase (labelled phase Q) associated with organic materials. Understanding the composition and origin of distinct noble gas components in chondrites is vital for unravelling the relationships between different cosmochemical reservoirs in the Solar System. Planetary noble gases are concentrated in the meteorite matrix, with CAIs being essentially gas-free, and chondrules carrying limited amounts of trapped gases. This chapter focuses on the analysis of primitive carbonaceous chondrites (Paris meteorite) to understand the main noble gas components in meteorites, with a special regard to phase Q. The origin of phase Q is still under debate with two main scenarios being advocated: (i) direct deviation from the solar gas by implantation/trapping into organic materials, or (ii) mixing of a solar-derived precursor with presolar components. The first hypothesis received some credits from experimental investigations of the behaviour of ionised noble gases during their trapping in growing organic materials analogous to those found in chondrites (the Nebulotron experiment). The second scenario is advocated to account for small variations in the Q composition from one meteorite to the other. As part of this thesis, we investigate both scenarios by combining noble gas analyses of the IOM and bulk of the Paris meteorite (this Chapter), and developing a new generation ionisation experiment (Nebulotron) allowing further characterization of the organic materials formed in the protosolar nebula (Chapter 5). Given that planetary noble gases in chondrites are located in the matrix and therefore associated with other volatile elements (e.g., C, N, water), understanding the origin and evolution of noble gases in chondrites can also provide insights into the origin of other volatile species in chondritic material.

4.1. On the origin of phase Q

Although Ne from presolar diamonds is typically the dominant component in primitive carbonaceous chondrites (Ne-HL, contributes ~ 60% of ^{22}Ne), heavy noble gases are associated with a "planetary" component carried out in a cryptic phase called phase Q (typically containing 95% of chondritic ^{132}Xe; Ott 2014). Despite extensive efforts over the past decades, the nature and origin of phase Q is still a matter of debate. Busemann et al. (2000) measured by closed-system stepped etching the HF/HCl-resistant residues of the primitive chondrites in order to better characterise the noble gases in "phase Q". Except for the $(^{20}Ne/^{22}Ne)_Q$, the authors found that all isotopic ratios in phase Q of different meteorites are quite uniform, therefore pointing toward phase Q being a unique and widespread component in the Solar System. Q gases are elementally and isotopically fractionated relative to the solar composition in favour of heavy elements and isotopes, by about 1%.amu^{-1} for Xe isotopes. One possibility is that phase Q in different chondrites acquired their noble gases from a unique reservoir and through a unique process, e.g. including the trapping and mass-dependent fractionation of nebular noble gases, therefore resulting in a homogeneous noble gas signature.

Q gases concentrated in residues obtained after demineralization by HF/HCl show a common, surprisingly high gas-release temperature in the range 1000–1200°C for unaltered chondrites (Huss et al., 1996). With increasing metamorphic grade of the host meteorites, the abundance and temperature of Q noble gas release, decrease and increase, respectively (Huss et al. 1996). Although the exact nature of phase Q has remained elusive (Amari et al., 2013), it appears to be intimately linked with organic materials. Indeed, noble gas abundances released from acid residues by stepped combustion correlate with those of C (Ott et al., 1981), and most of the heavy noble gases (and a small amount of He and Ne) are readily released from the original HF/HCl residues by HNO_3 oxidation (Frick and Pepin 1981). Even if it does not seem to be systematic (Matsuda et al. 2010), Marrocchi et al. (2005) showed that solvation by pyridine, which causes organic materials to swell, induces significant release of Q heavy noble gases from Orgueil HF/HCl residues, again pointing to a close association of organics and noble gases. Although part of the Q gases may be associated with secondary phases such as sulphurs (Marrocchi et al. 2015), the vast majority of Q gases would reside within organic phases, possibly including a minor carbon component akin to graphene-like nano-particulates (Amari et al. 2013). The close association between organics and chondritic heavy noble gases was historically proposed to arise from the fact that noble gases were physically adsorbed on interior surfaces formed by a pore labyrinth within amorphous carbon Wacker (1989), or via impingement of low energy noble gases onto a growing surface accompanied by the formation of chemical bonds (Hohenberg et al. 2002).

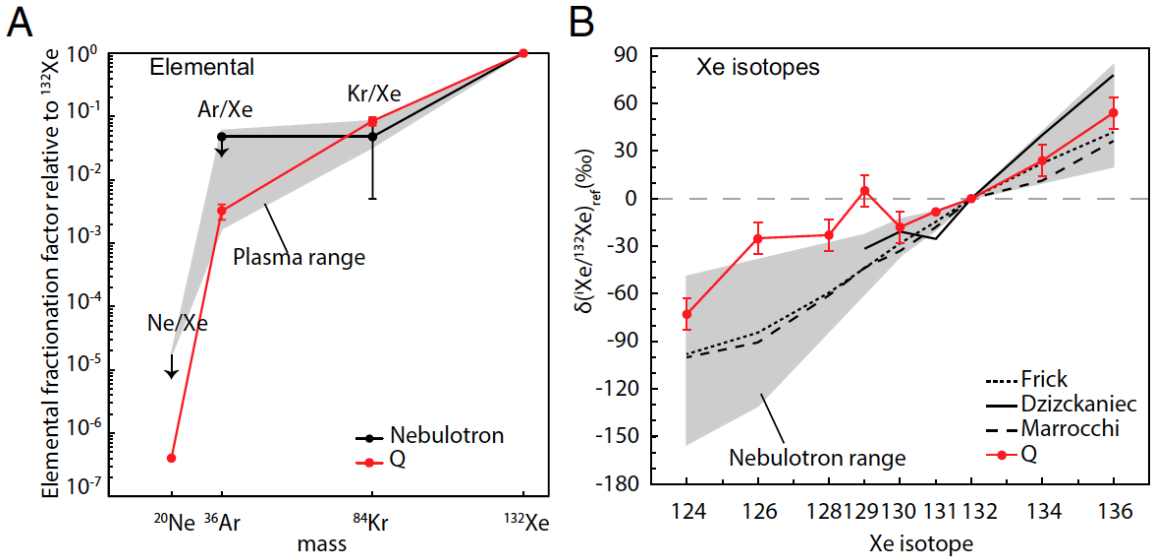

Fig. 56. Noble gas patterns in Nebulotron organics, from Kuga et al. (2015). (A) Noble gas elemental fractionation patterns in the Nebulotron solids (black dots), in synthetic solids produced in plasma experiments (gray area), and in chondritic IOM for Q gases (red dots). (B) Isotopic composition of Xe in the Nebulotron solids (gray range), in other plasma-synthesised solids (black lines) and in Q (red dots).

Importantly, most meteoritic organics are in the form of a refractory aromatic and insoluble macromolecular solid, commonly referred to as insoluble organic matter (IOM). Extensive characterization of this IOM component using a large set of analytical methods has provided a wealth of qualitative and quantitative information regarding the elemental and molecular composition of chondritic IOM (Derenne and Robert, 2010). Taken together, these results point toward a gas-phase synthesis of chondritic IOM, most likely through a process of organosynthesis in the protosolar nebula (Derenne and Robert, 2010). In this framework, noble gas fractionation from a solar, to a Q-like, composition could have occurred through noble gas incorporation into organic materials during organosynthesis. Yet, it has been demonstrated experimentally that adsorption of neutral Xe on to solid surfaces does not yield any measurable isotopic fractionation (with a maximum fractionation factor estimated to be -0.2 ± 0.1 ‰.amu^{-1}, see Marrocchi and Marty (2013) and references therein). Significant isotopic fractionation (≥ 1 %/u) can only occur when Xe is ionised (Frick et al., 1979). In this case, trapping of Xe ions onto solids consistently results in enrichments in the heavy isotopes relative to the light isotopes (Marrocchi et al., 2011 and ref. therein). Such MDF does not depend on the chemical nature of the solid surface (i.e., organic, glass, metal or mineral), or on the energetic regime of the ion-solid interaction (i.e., adsorption for E ~ 50 eV, sputtering for 50 < E < 500 eV and implantation for E > 500 eV; Marrocchi et al., 2011). Hence, plasma experiment (here after referred to as Nebulotron experiments; Chapter 5) were designed to produce refractory solid organics from mixtures of C- and N-bearing gases analogous to the composition of the protosolar nebula (i.e., CO, N_2 with addition of noble gases, at temperatures up to 1,000 K) and investigate the possibility for significant amounts of fractionated noble gases to be incorporated into organic materials. Synthesised compounds were shown to share

chemical and structural features with chondritic organics (Chapter 5), with trapped noble gases specifically reproducing the elemental and isotopic characteristics of meteoritic noble gases (Fig. 56; Kuga et al. 2015).

Organic materials produced in the microwave cavity can efficiently trap heavy noble gases (Ar, Kr and Xe), with Xe being enriched by at least one order of magnitude relative to Ar and Kr. Both Kr and Xe display a strong isotopic fractionation relative to the composition of the initial gas, with mass-dependent enrichments in heavy isotopes of ~1.3 %.amu^{-1} and ~0.9 %/u^{-1}, respectively (Kuga et al. 2015, Fig. 56). Importantly, the elemental and isotopic fractionations of noble gases in the Nebulotron us likely due to two different processes. On one side, and as previously observed from experiments of ionised noble gas trapping onto solids, the extent of elemental fractionation strongly correlates with the ionization energies of the different noble gases (Göbel et al., 1978; Ott, 2002, 2014; Rai et al., 2003; Weber et al., 1971), unlike isotopic fractionation, which correlates with mass. Hence, the observed depletion of light noble gases relative to Xe in planetary noble gas elemental patterns with respect to solar would be produced by the different ionization rates of the noble gases. On the other hand, isotopic fractionation could be the result of ambipolar diffusion processes involving differences between the kinetic energy of heavy and light isotopes (Kuga et al. 2017). Ambipolar diffusion in plasmas refers to the fact that electrons diffuse faster than ions (here noble gases), therefore creating a radial electric field that accelerates the ions toward the walls of the reaction chamber, where they are more of less efficiently implanted into already synthesised organics depending on their radial velocity. These two processes could be involved in the process of low-energy ion implantation of noble gases into carbon-rich solid compounds, therefore accounting for both the elemental and isotopic fractionation patterns of Q-gases with respect to solar.

However, one of the most outstanding features of Q gases corresponds to the extremely high abundance of heavy noble gases. Amounts of noble gases incorporated in organic solids in the Nebulotron experiment are high (with final Xe concentrations on the same order of magnitude as Q-Xe), much higher than amounts of noble gases implanted onto the surface of graphite and nanodiamonds for instance (Matsuda et al., 1992). This suggests that noble gas implantation occurring simultaneously with the growth of solid layers is a viable mechanism to enhance noble gas incorporation/burial into chondritic organics. However, even under such conditions, Xe trapping efficiencies are orders of magnitude lower than what would be required to account for the incorporation of Xe from the solar nebula gas into organic solids growing within the protosolar nebula. Thus, the most likely scenario is that formation of chondritic organics and trapping of ionised noble gases took place simultaneously, within the widespread, ionised portions of the PPD. But some uncertainties remain regarding the exact mechanisms that allowed huge quantities of noble gases found in phase Q to be trapped. Interestingly, ingrowth of ^{129}Xe from ^{129}I decay is required to account for the high and consistent ^{129}Xe/^{132}Xe ratios of Q-Xe with respect to solar (Busemann et al. 2000; Gilmour 2010). This suggests that, from a common starting reservoir, iodine was preferentially - although in constant relative

proportions - incorporated into phase Q with respect to Xe. This may be in line with our claim for Q gases to be associated with chondritic IOM, providing, due to the organophilic nature of iodine, a way to concentrate it.

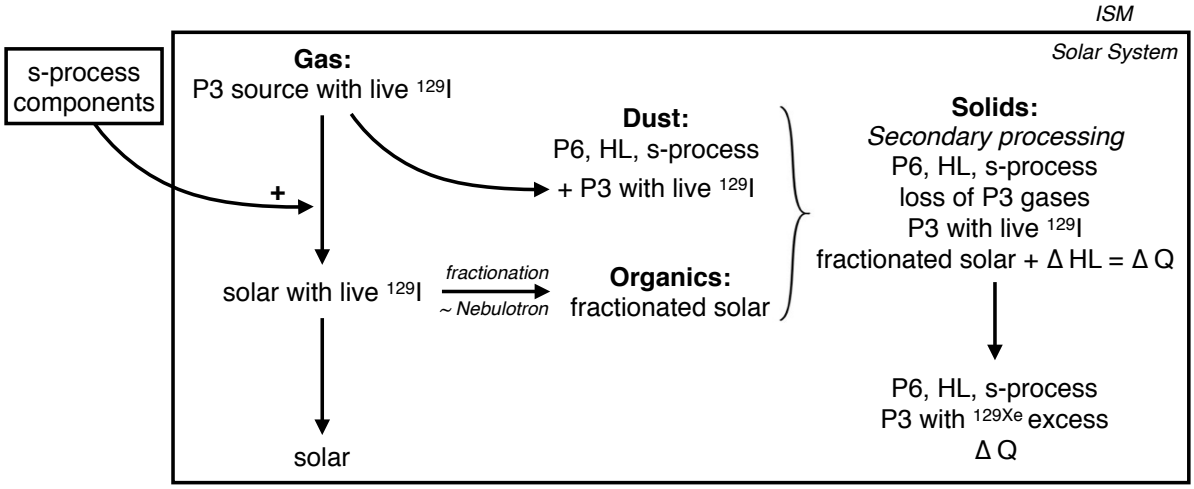

Fig. 57. Diagram illustrating a possible simple history of heavy noble gas components, adapted from the flow chart presented in Gilmour (2010).

The other scenario that has been put forward to explain the origin of phase Q arises from the fact that, when scrutinised, the Xe-Q signature appears to reflect a certain extent of isotopic variability attributed to mixing between fractionated solar gas and variable amounts of presolar components. In this case, the mean Xe-Q signature would correspond to mixing between 98.5 % of mass dependently fractionated SW-Xe, with a linear MDF of 10.2 ‰.amu^{-1} in favour of the heavy isotopes, and 1.5% Xe-HL, with an additional source of ^{129}Xe from ^{129}I decay (Gilmour 2010). The exact MDF relationship between solar Xe (from the PSN) and Solar Wind (as measured by the Genesis mission; Meshik et al. 2014) is uncertain. Although Q-Xe and SW-Xe are related to one another by MDF, the exact relation between solar Xe (precursor) and Q-Xe (product) is ultimately unknown. The non-unique isotopic signature of Q-Xe (Gilmour 2010) would indicate it does not constitute a pure end-member solely reflecting fractionation of solar gas followed by incorporation/preservation in organic material without modification. A summary figure combining Nebulotron insights with the model proposed by Gilmour (2010) is presented Fig. 57. This figure illustrates how the solar gas composition itself could have initially formed. It was indeed suggested that the widespread planetary noble gas component P3 found in chondrites (characterised by a low s-process contribution compared to solar) could represent the main precursor of the solar composition by addition of (main and weak) s-process components (Gilmour 2010). In details, SW-Xe would correspond to a mixing of 98.5% Xe-P3 with 1.5% Xe-HL (such a contribution from Xe-HL being possibly here an artefact arising from difficulties in defining the true composition of Xe-P3) that has been fractionated by 11.15 ‰.u^{-1} in favour of the light (and not heavy, as was the case for Q-Xe)

isotopes, and subsequently mixed with s-process Xe (in a 98.9 - 1.1 % proportion). The addition of s-process components could correspond to freshly synthesised materials with a noble gas composition consistent with presolar SiC. According to Gilmour (2010), the presence of live ^{129}I in P3 would indicate that P3 was isolated from a parent reservoir less than ~100 Myr before the formation of the solar system.

The paper appended here below reports the noble gas isotopic and elemental analysis of the bulk and IOM of the Paris meteorite (the least altered CC known so far), emphasizing the implications regarding the relation between Xe-HL and Q-Xe. It supports the scenario of Q-Xe originating from fractionated solar Xe plus variable additions of presolar component, especially Xe-HL (Gilmour 2010). We suggest that primitive carbonaceous chondrites preserved a more abundant fraction of presolar Xe-HL with respect to chondritic materials thought to originate from the inner Solar System, therefore pointing toward a heliocentric gradient in the amount of Xe-HL carried out in primitive chondrites.

The Meteoritical Society

4.2. The Paris carbonaceous chondrite case of study.
Meteoritics & Planetary Science 1–20 (2018)
doi: 10.1111/maps.13213

Check for updates

Primordial heavy noble gases in the pristine Paris carbonaceous chondrite

David V. BEKAERT[1*], Yves MARROCCHI[1], Alex MESHIK[2], Laurent REMUSAT[3], and Bernard MARTY[1]

[1]Centre de Recherches Pétrographiques et Géochimiques, CRPG-CNRS, Université de Lorraine, UMR 7358, 15 rue Notre Dame des Pauvres, BP 20, 54501 Vandoeuvre-lès-Nancy, France
[2]Department of Physics, Washington University, 1 Brookings Drive, Saint Louis, Missouri 63130, USA
[3]Institut de Minéralogie, de Physique des Matériaux et de Cosmochimie (IMPMC), UMR CNRS 7590 - Sorbonne, Universités - UPMC - IRD - Museum National d'Histoire Naturelle, 57 rue Cuvier, Case 52, 75231 Paris Cedex 5, France
[*]Corresponding author. E-mail: dbekaert@crpg.cnrs-nancy.fr

(Received 22 February 2018; revision accepted 08 October 2018)

Abstract–The Paris carbonaceous chondrite represents the most pristine carbonaceous chondrite, providing a unique opportunity to investigate the composition of early solar system materials prior to the onset of significant aqueous alteration. A dual origin (namely from the inner and outer solar system) has been demonstrated for water in the Paris meteorite parent body (Piani et al. 2018). Here, we aim to evaluate the contribution of outer solar system (cometary-like) water ice to the inner solar system water ice using Xe isotopes. We report Ar, Kr, and high-precision Xe isotopic measurements within bulk CM 2.9 and CM 2.7 fragments, as well as Ne, Ar, Kr, and Xe isotope compositions of the insoluble organic matter (IOM). Noble gas signatures are similar to chondritic phase Q with no evidence for a cometary-like Xe component. Small excesses in the heavy Xe isotopes relative to phase Q within bulk samples are attributed to contributions from presolar materials. CM 2.7 fragments have lower Ar/Xe relative to more pristine CM 2.9 fragments, with no systematic difference in Xe contents. We conclude that Kr and Xe were little affected by aqueous alteration, in agreement with (1) minor degrees of alteration and (2) no significant differences in the chemical signature of organic matter in CM 2.7 and CM 2.9 areas (Vinogradoff et al. 2017). Xenon contents in the IOM are larger than previously published data of Xe in chondritic IOM, in line with the Xe component in Paris being pristine and preserved from Xe loss during aqueous alteration/thermal metamorphism.

INTRODUCTION

Xenon isotopes have unique and resolvable isotopic signatures within different cosmological reservoirs of the solar system and, therefore, they constitute a powerful tool to decipher the contribution of planetary precursors (solar, chondritic, and cometary) to terrestrial planets and yield insights into the physical processes that affected planetary bodies over geological periods of time (Marty et al. 2017). While cometary materials constitute a pristine reservoir of the outer solar system building blocks, primitive meteorites (hereafter chondrites) are the only remnants of the inner solar system starting material. They consist of composite assemblages of high-temperature products from the protoplanetary disk phase (i.e., refractory inclusions, chondrules, Fe-Ni metal spherules) embedded in a volatile-rich and fine-grained matrix comprised of minerals, sulfides, and organic materials (Scott and Krot 2005). Volatile elements accreted at the time of asteroid formation may provide key information about the dynamics and physicochemical conditions of the accretionary disk where the building blocks of planetesimals formed and evolved. However, variable degrees of fluid alteration observed in the matrix of chondrites indicates that significant episodes of asteroidal alteration modified the chemistry of carbonaceous asteroids and probably affected the volatile element component inherited from this period of accretion (Palguta et al. 2010). Fluid circulations within asteroids likely arose from the melting of a

heterogeneously accreted water ice component, upon heating from the decay of extinct ^{26}Al and/or impact shocks.

The origin(s) and abundance of water accreted by carbonaceous asteroids remain(s) underconstrained (Brearley [2006] and references therein). Today, the innermost terrestrial planets contain little water relative to outer solar system planetary bodies. In the protoplanetary disk, the distribution of water ice was determined by the location of the snowline, i.e., the inner boundary of the region where the temperature is low enough for water to condense (Lecar et al. 2006). The position of the snow line is thought to have evolved through time—mostly inward, up to ~1 AU—as a function of the stellar accretion rate (Bitsch et al. 2015). The low water/rock ratios estimated from the O-isotopic characteristics of secondary minerals in carbonaceous chondrites suggest that carbonaceous asteroids formed close to the snowline, and not at greater heliocentric distances (Marrocchi et al. 2018).

Two principal sources are commonly considered regarding the origin of water ices in the region(s) of carbonaceous asteroid accretion: a locally derived water, directly condensed from the gas in the inner solar system (Alexander et al. 2012), and/or an outer disk water component inherited from the inward drift of outer solar system ices (Lunine 2006). Due to the self-shielding of ^{16}O-rich nebular CO gas by stellar UV light, the outer solar system component is ^{17,18}O-rich relative to inner solar system values (Lyons and Young 2005). It is also D-rich relative to the solar composition, possibly related to low-temperature ion-derived chemistry within the parent molecular cloud (Cleeves et al. 2014), although other scenarios such as gas-grain reactions, gas phase unimolecular photodissociation, and ultraviolet photolysis in D-enriched ice mantles have been advocated (Sandford et al. 2001). The respective proportions of local and outer solar system water ices accreted by carbonaceous asteroids are debated. Quantitative estimates of the contribution of "interstellar" ice to the inner solar system have been proposed from the analysis of hydrogen isotope ratios in the unequilibrated ordinary chondrite LL3.0 Semarkona (Piani et al. 2015) and in the pristine Paris meteorite (Vacher et al. 2016). The latter represents the least altered CM described to date (Hewins et al. 2014; Marrocchi et al. 2014; Rubin 2015). It has undergone variable degrees of alteration with moderately altered zones (CM 2.7) in direct contact with relatively fresh zones (CM 2.9) rich in Fe-Ni metal and pristine matrix (Hewins et al. 2014; Leroux et al. 2015). Such association suggests that some parts of the meteorite have been relatively preserved from the contribution of secondary fluid alteration. A schematic view of the heterogeneous accretion of the inner water ice component

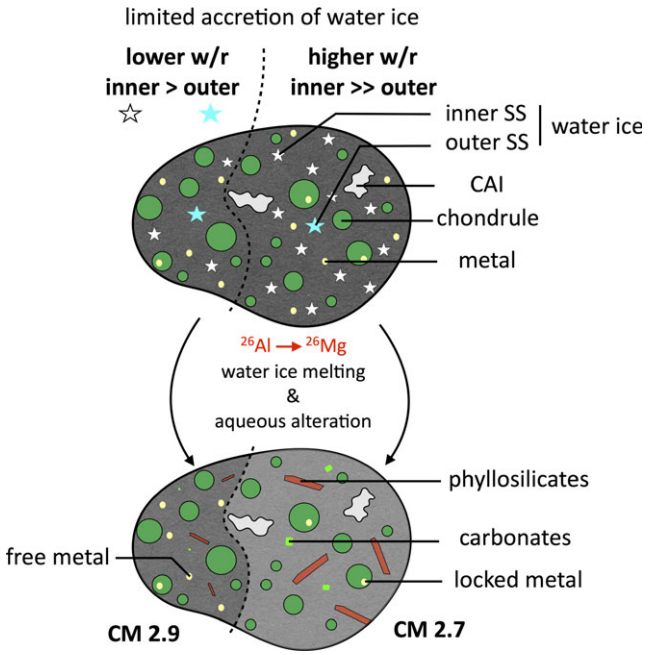

Fig. 1. A scenario for the Paris meteorite alteration history at the millimeter scale: the Paris meteorite parent body experienced a heterogeneous accretion of inner and outer solar system materials, with a limited amount of total water ice relative to other CM chondrites (Vacher et al. 2016; Piani et al. 2018). The subsequent melting of water ice induced an episode of heterogeneous aqueous alteration resulting in variable degrees of alteration with moderately altered zones (CM 2.7) in contact with relatively fresh zones (CM 2.9). The more altered (CM 2.7) zones are marked by the presence of numerous carbonates and phyllosilicates in the matrix (Fig. S1A in supporting information). These minerals are less abundant in the pristine (CM 2.9) areas, where free Fe-Ni metal is still observed (Rubin et al. 2007) (Fig. S1A). In CM 2.7 zones, Fe-Ni metal is only observed in chondrules.

—as expected to have occurred on the Paris meteorite parent body—and related degrees of subsequent alteration is provided in Fig. 1.

The Paris meteorite exhibits enrichment in its bulk δD compared to the mean value of CM chondrites (120 ± 1‰ versus −69 ± 19‰, respectively; Vacher et al. 2016, 2017). In addition, the oxygen isotope signatures in carbonates of the Paris meteorite require the mixing of 8–35% of outer disk water with the CM local fluid from which some of the ^{17,18}O-rich Ca-carbonates precipitated (Vacher et al. 2016). This is consistent with the specific in situ C/H versus D/H correlation observed for the matrix of the Paris meteorite (Piani et al. 2018), suggesting the occurrence of D-rich fluids relative to other CM chondrites and, as such, a dual origin for the icy grains accreted by the parent body. Quantitative estimates of the contribution of outer solar system ice to the inner solar system have crucial implications regarding the extent of the radial mixing in the protoplanetary disk (Vacher et al. 2016) as well as the

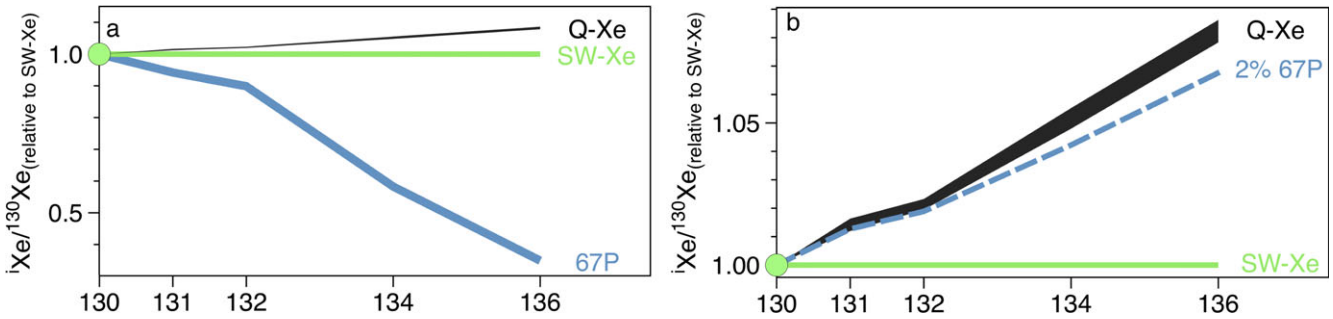

Fig. 2. a) Xenon isotopic spectra of the Q-phase (Busemann et al. 2000) and outer solar system (cometary-like; Marty et al. 2017) water ice, normalized to the solar composition (Meshik et al. 2014), showing that the Q-phase and cometary ice components have extremely different signatures for the heavy Xe isotopes. b) Magnified view of the Q-phase signature (Busemann et al. 2000) normalized to the solar composition (Meshik et al. 2014). We show that a 2% contribution of cometary ice to the total budget of Xe (with therefore 98% of Xe being of phase Q composition) would result in a measurable shift of the phase Q signature (dashed line).

origin of the water accreted by asteroids and terrestrial planets (Drake 2005). However, the dichotomy between O and H isotope composition of water in the inner and outer solar system suggests low influx of D- and ^{17,18}O-rich water ice grains from the outer part of the solar system, possibly accounted for by the presence of a Jupiter-induced gap that limited the inward drift of outer solar system material into inner parts of the protoplanetary disk (Marrocchi et al. 2018).

The occurrence of outer solar system water signatures in the Paris meteorite (Piani et al. 2018) suggests that its parent body accreted cometary-like materials, likely including cometary ice, organic materials, and silicates. Cometary ice contains abundant Kr and Xe isotopes whose nucleosynthetic signatures are distinct from any known reservoir within the inner solar system (Rubin et al. 2018). Recently, the very first measurement of the Xe isotopic composition of Comet Churyumov–Gerasimenko (here 67P/C-G) by the ROSINA mass spectrometer on-board the Rosetta spacecraft revealed a new and unique composition characterized by strong $^{134–136}$Xe deficits relative to the solar composition (Marty et al. 2017) (Fig. 2). This outer solar system signature allowed the origin of Xe isotopes in the terrestrial atmosphere to be deciphered (Marty et al. 2017) and led to the suggestion that remnants of cometary noble gases may be preserved at the present-day lunar surface (Bekaert et al. 2017). Cometary bodies appear to be extremely rich in noble gases, so limited contributions of comets to planetary bodies have the potential to drastically affect the noble gas budget of planetary atmospheres (Marty et al. 2017). Thus, isotopes of xenon may provide a means to track contributions of outer solar system (cometary-like) material to the inner solar system (chondritic-like) planetary bodies. They therefore constitute a promising tool to investigate the dual origin of the icy grains (with outer and inner solar system signatures, respectively) accreted by the parent body of the Paris meteorite. These two water ice components most likely coexisted on the parent asteroid at the time of its accretion and were not mixed together during melting and aqueous alteration (if physically isolated within the rock for example). Indeed, it is likely that ice accretion was spatially heterogeneous, as observed by the heterogeneous distribution of alteration phases in the matrix of chondrites (Le Guillou and Brearley 2014). In addition, aqueous alteration onto asteroidal parent bodies of meteorites mainly took place within geochemical microenvironments that were not connected together (Le Guillou and Brearley 2014; Pignatelli et al. 2016). This is due to the low permeability of chondrites (Bland et al. 2009), which precludes mixing between water components of different origin.

Cometary ice is extremely rich in noble gases (Rubin et al. 2018). During ice melting and subsequent aqueous alteration of the parent body, cometary noble gases may simply be lost to space, trapped within weathering products, or adsorbed onto the surface of organic materials present on the parent body, with limited isotopic fractionation (Marrocchi and Marty 2013). Alternatively, cometary noble gases might have been delivered to the meteorite parent body by isotopically distinct cometary insoluble organic matter (Fray et al. 2016), silicates, and/or presolar grains. If present in the Paris meteorite, cometary noble gases may therefore be locked in the IOM, in addition to the common chondritic IOM carrying the ubiquitous phase Q component (Busemann et al. 2000), or spread out within the bulk sample. The phase Q component is enriched in heavy elements and heavy isotopes compared to the solar wind composition (Busemann et al. 2000) (Fig. 2). Q-Xe and Q-Kr are thus enriched by ~1% u^{-1} in their heavy isotopes relative to solar Xe. Additions of nucleosynthetic components such as Xe-HL (a combination of Xe-H, which is enriched in the heavy isotopes, and Xe-L, enriched in light xenon isotopes

(Reynolds and Turner 1964; Lewis et al. 1987) are required for mass-dependently fractionated solar Xe to adequately fit Q-Xe. The association of Xe-Q with Xe-HL has been suggested by Lavielle and Marti (1992), Marti and Mathew (1998), and Busemann et al. (2000). Using solar Xe composition found in lunar regolith, Gilmour (2010) estimated the contribution of ^{132}Xe-HL to be 1.5%. Meshik et al. (2014) used solar wind Xe composition measured in Genesis return samples and calculated 1.6% ^{132}Xe-HL contribution to slightly fractionated solar wind. Crowther and Gilmour (2013) estimated the same contribution of Xe-HL using a slightly modified solar wind composition. The exact host phase of the Q-gases in chondrites is not well characterized but appears to be intimately linked with refractory organic compounds (Ott et al. 1981; Busemann et al. 2000; Marrocchi et al. 2011; Kuga et al. 2015). As depicted in Fig. 2, even a minor contribution of 2% cometary-like Xe (calculated based on ^{132}Xe and using the composition of comet 67P/C-G; Marty et al. 2017) to phase Q xenon would result in a noticeable and detectable shift of the heavy isotope ratios toward lower values. Analyzing separately the heavy noble gas isotopic composition of the IOM and bulk fragments constitutes therefore a promising way to investigate the occurrence of cometary noble gases in the Paris meteorite.

In the present study, we analyzed the Paris meteorite for its argon, krypton, and xenon isotopes by discriminating mostly pristine (2.9 CM) and mostly altered (2.7 CM) fragments of the meteorite. We also analyzed separately the insoluble organic matter (IOM) chemically isolated from a bulk sample of the Paris meteorite for Ne (low precision), Ar, Kr, and Xe isotopes. Unlike Kr and Xe, which are dominated by the Q component in primitive meteorites, neon is expected to be dominated by a presolar component in the diamonds, the Ne-HL (Ott 2014). The possibility of tracing a possible contribution of cometary organic materials together with cometary water ice opens interesting perspectives since the isotopic signature of noble gases in cometary IOM is not known. Noble gas elemental fractionation during aqueous alteration may also provide information on the extent of secondary alteration on the parent body and on the nature of the phases bearing Q-gases (Browning et al. 1996; Weimer et al. 2017).

MATERIAL AND METHODS

Preparation of the Two CM 2.7 and Two CM 2.9 Fragments

A thin section of the Paris chondrite was polished on both sides and coated under vacuum with a thin layer of pure carbon to provide conductive surfaces. Both sides of the section were examined using a scanning electron microscope (SEM) (JEOL JSM-6510) equipped with an energy dispersive X-ray (EDX) Genesis detector (CRPG, Nancy), with a 3 nA electron beam accelerated at 15 kV. After observation, the sample was polished on both sides using a 0.25 μm diamond polishing powder in ethanol to remove any residue of the pure carbon layer.

As already described in previous works for other subsamples of the Paris meteorite (Marrocchi et al. 2014; Rubin 2015; Pignatelli et al. 2016, 2017; Vacher et al. 2016), our thin section presents variable degrees of alteration on both sides characterized by significant differences in the abundance of Fe-Ni metal beads. According to the alteration scale proposed by Rubin et al. (2007), the more altered zones are characterized by the presence of numerous carbonates and phyllosilicates in the matrix and were classified as CM 2.7 (Hewins et al. 2014; Marrocchi et al. 2014; Rubin 2015). These minerals are less abundant in the more pristine areas, marked by the presence of free Fe-Ni metal and classified as CM 2.9 (Fig. S1). In CM 2.7 zones, Fe-Ni metal is mainly observed when locked in chondrules. A pristine (2.9 CM) central area is observed on both sides of the thin section, suggesting that the central part of the sample is not altered, contrary to the surrounding mostly 2.7 CM material (Fig. S1). Four pieces of the sample (~5 mg each) were selected for noble gas analysis, from the central pristine area (fragments 4 and 5, Fig. S1) and from the more altered areas (fragments 2 and 8, Fig. S1).

The four pieces were separated using a diamond wire saw (0.3 mm Ø) at very low speed, in order to prevent heating, and avoiding the use of water as a lubricant to limit contamination of the sample. Droplets of pure ethanol were periodically deposited onto the saw to facilitate the removal of dust. The four pieces were then dried at 90 °C for 1 h, before being weighted and set into the CO_2 infrared (λ = 10.6 μm) laser extraction chamber (Humbert et al. 2000) under high vacuum (10^{-9} mbar) at 110 °C for 2 days. This preheating of the sample allowed weakly bound atmospheric gases to be degassed prior to noble gas analysis.

Noble Gas Isotopic Measurements (CM 2.7 and CM 2.9 Fragments)

Argon, krypton, and xenon were extracted by heating the samples with a CO_2 infrared (λ = 10.6 μm) laser (Humbert et al. 2000). In this method, the first extraction is typically carried out by slowly increasing the laser power until the heated sample turns reddish (sample's temperature being therefore qualitatively estimated to be ~600 °C, depending on the mineralogical composition of the sample [Bekaert et al. 2017]. Here, because part of the noble gas content of the sample may be already degassed at this temperature, we only performed a single (~10 min) step of sample melting at T > 1600 °C. The formation of a

spherule of molten silicate indicated that the melting temperature of the sample had been reached, and that more than 99% of the gas had been extracted (Humbert et al. 2000). A re-extraction was carried out on fragment 4, with negligible amounts of gas being released, in line with a complete extraction of the gas upon initial melting. However, note that Huss et al. (1996) observed significant gas release at temperatures >1800 °C. The possibility to have preserved some noble gases, especially Kr and Xe, in very refractory phases of these bulk fragments cannot be excluded. If that fraction of the sample gas were to be only extracted at temperatures >1800 °C, it could not be analyzed in the present experimental setting. Series of standards were run between each sample each day for subsequent spectrometer mass discrimination corrections. Blanks accounted for <0.5% of the ^{36}Ar, ^{84}Kr, and ^{130}Xe released from the samples, making blank correction negligible. Extracted gases were purified using two Ti-sponge getters held at 650 °C for 5 min and then cooled down to room temperature over the next 5 min. Xenon and krypton were separated from Ar on the surface of a Pyrex finger held at liquid nitrogen temperature for 20 min. Argon isotopic measurements were first carried out on the remaining fraction with a Helix MC Plus (Thermofisher Scientific) mass spectrometer. The partial pressure of Ar in the volume of the glass finger was then reduced by diluting five times the volume trapped in the cold finger, still at liquid nitrogen temperature, into the whole line set under static vacuum. The Pyrex finger held at liquid nitrogen temperature was then isolated from the line during pumping. Finally, the Pyrex finger (containing the Xe and Kr) was warmed to room temperature and the gases released were exposed once again to two further hot Ti-sponge getters for final purification. The line was then divided into 3–6 sections of approximately equal volumes to carry out repeated analyses of Xe and Kr isotopes, with Xe isotopes being systematically analyzed first. Krypton and xenon isotopes were measured with a Helix MC Plus (Thermofisher Scientific) mass spectrometer by peak jumping on the central compact dynode electron multiplier AX (Compact Discrete Dynode).

Preparation of the Insoluble Organic Residue

A matrix-enriched subsample (~8 g) of the Paris meteorite (unknown lithology, CM 2.7, CM 2.9, or a mixture of the two) was crushed in an agate mortar before isolating IOM using the protocols described by Remusat et al. (2005, 2008) and Vinogradoff et al. (2017). In summary, the powdered matrix was subjected to several extractions in water (stirring under reflux for 48 h), acetone (stirring at room temperature for 2 h, twice), and dichloromethane/methanol (2:1, vol/vol, stirring at room temperature for 2 h, twice). The solid residue was then subjected three times to HF/HCl treatment by stirring successively in a mixture of HF/HCl (16 N/2 N, 2:1, vol/vol) for 24 h at room temperature under nitrogen flux. The residue was then washed several times with HCl (6 N) for 2 h at 70 °C (i.e., to remove fluoride compounds) until the final solute was colorless. The acid residue was then washed with bidistilled water until neutrality, extracted three times with acetone and a mixture of CH_2Cl_2/MeOH, 2:1 vol/vol and subsequently dried under nitrogen. A residue of about 150 mg (i.e., ~1.8 wt% of the initial sample) was recovered at the end of this procedure. Some 0.44 mg of this residue was analyzed for its noble gas content and isotopic composition by stepped pyrolysis.

Noble Gas Isotopic Measurements (IOM)

The Paris meteorite IOM (0.44 mg) was wrapped in platinum foil and then loaded into a glass sample tree. The samples were gently baked in vacuum at 150 °C for 3 days in order to remove adsorbed atmospheric gases. Noble gases were extracted by stepped pyrolysis in the temperature range 300–1768 °C using a tungsten coil. The linear current–temperature calibration curve for the coil was obtained using an optical pyrometer with a precision of ±25 °C for temperatures above 800 °C. The calibration curve was extrapolated to temperatures lower than 800 °C. Gas extraction from the IOM was thus carried out by stepwise heating at 570, 790, 980, 1225, 1539, and 1770 °C. Extraction times were adjusted as a function of temperature, i.e., (1) 15 min for the four low-temperature steps (i.e., 300–1300 °C), (2) 12 min for the 1539 °C step, and (3) 5 min for the final step (at the platinum melting point: 1770 °C). The released gases were exposed to three consecutive pellet getters containing SAES St172 getter alloy in order to remove active gases (10 min at 275 °C and 10 min at room temperature). Argon, krypton, and xenon were held on a charcoal finger at liquid nitrogen temperature for 45 min, then the residual light noble gases were analyzed for their Ne isotopes. Active charcoal immersed into liquid nitrogen was then heated to −105 °C using an external heater that surrounds the charcoal. The temperature was regulated within ±1 °C by PID controller. Calibration curves determined from air standards showed that Kr and Xe are not affected at this temperature while ~70% of the Ar is released. This procedure reduces the amount of Ar in the mass spectrometer, which has a considerable effect on the mass discrimination of krypton and xenon. Argon released from the charcoal finger was then pumped out for 5 min. The liquid nitrogen was then removed, and the charcoal finger was heated to 160 °C for 25 min to

Table 1. Neon abundances and isotopic compositions of the Paris meteorite IOM via stepwise heating. The total amount of extracted ^{20}Ne is given via the abundance-weighted mean isotopic composition.

T°C	^{20}Ne (cm^3 STP/g)	±2σ	^{21}Ne/^{22}Ne	±2σ	^{20}Ne/^{22}Ne	±2σ
572	6.14E-08	9.39E-09	0.0331	0.0047	10.5795	1.4331
790	1.95E-07	2.38E-08	0.0307	0.0016	9.4681	0.4463
980	7.71E-07	1.00E-07	0.0313	0.0006	8.7100	0.1156
1225	4.90E-07	6.42E-08	0.0338	0.0008	9.0149	0.1803
1539	1.28E-07	1.69E-08	0.0359	0.0028	10.2103	0.7385
1770	6.65E-08	9.44E-09	0.0353	0.0051	11.7341	1.6663
Total	1.71E-06	2.24E-07	0.0325	0.0012	9.1804	0.3258

Table 2. Argon abundances and isotopic compositions of the Paris meteorite IOM via stepwise heating. The total amount of extracted ^{36}Ar is given via the abundance-weighted mean ^{38}Ar/^{36}Ar.

T°C	^{36}Ar (cm^3 STP/g)	±2σ	^{38}Ar/^{36}Ar	±2σ
408	3.18E-09	1.11E-09	0.2087	0.0022
572	1.35E-07	2.09E-08	0.2613	0.0019
790	1.14E-06	1.37E-07	0.2035	0.0008
980	1.58E-06	2.02E-07	0.1932	0.0006
1225	2.92E-06	3.91E-07	0.1904	0.0002
1539	3.08E-07	4.07E-08	0.2003	0.0013
1770	6.48E-07	9.07E-08	0.1973	0.0004
Total	6.73E-06	8.84E-07	0.1958	0.0005

release Xe, Kr, and the residual fraction of Ar. Heavy noble gases were then introduced into high-sensitivity (~5×10^{-16} cm^{3}STP/Hz for Kr) mass spectrometer equipped with Baur–Signer ion source (Washington University, Saint Louis, USA) (Mabry et al. 2007; Meshik et al. 2007) for determination of Ar, Kr, and Xe abundances and ^{38}Ar/^{36}Ar, ^{86}Kr/^{84}Kr, and ^{129}Xe/^{132}Xe isotopic ratios. Blanks were measured for each extraction temperature and used to correct the data. Hot blanks (1200 °C) were also performed several times during each analytical session. The Kr and Xe concentrations within Pt foils were also measured and appeared to be negligible. The uncertainties in isotopic ratios (2σ) include hot blank, standard, and internal (statistical and internal mass fractionation) error propagation. Note that Kr extracted at 1539 °C was accidentally pumped and so no Kr data could be obtained for this temperature step.

RESULTS

All data are reported in Tables 1–7. Neon, argon, krypton, and xenon isotopic data for the IOM are reported in Tables 1, 2, 4, and 6, respectively. Noble gas isotopic data for the bulk fragments are reported in Tables 3, 5, and 7, respectively.

Argon, krypton, and xenon isotope compositions of the pristine CM 2.9 fragments, the CM 2.7 fragments, and the bulk IOM of the Paris meteorite are dominated by the Q component (Figs. 3 and 4). In agreement with Hewins et al. (2014), we consistently measured very low ^{40}Ar/^{36}Ar ratios (~3, while the atmospheric ratio is 298.56 ± 0.31; Lee et al. 2006) for the bulk CM 2.7 and CM 2.9 fragments (Table 3). Although Kr isotope compositions are similar to phase Q-Kr in CM 2.7 and CM 2.9 fragments (Fig. 3a), Xe isotopes show excesses in the heavy isotopes relative to Q-Xe (Fig. 4a). The ^{136}Xe/^{130}Xe excesses are ~2% relative to Q-Xe. Importantly, no difference could be detected between the noble gas isotope composition of the CM 2.9 and CM 2.7 fragments (Figs. 3 and 4). Likewise, no obvious difference in Kr (~1.4×10^{-8} cm^3 STP ^{84}Kr/g) and Xe (~1.7×10^{-8} cm^3 STP ^{132}Xe/g) contents between CM 2.9 and CM 2.7 fragments of the Paris meteorite is observed (Tables 5 and 7). However, argon appears to be slightly depleted in the CM 2.7 (~1.49×10^{-6} cm^3 STP ^{36}Ar/g) relative to CM 2.9 (~1.86×10^{-6} cm^3 STP ^{36}Ar/g) fragments (Table 3). A second extraction step on fragment 4 released ≤1% of the total amounts of its noble gas contents (Table 3, 5, and 7), in agreement with the fact that more than 99% of noble gases are extracted by CO_2 infrared laser heating when a spherule of molten silicate is obtained (Humbert et al. 2000).

In total, we found that 1.71×10^{-6} cm^3 STP ^{20}Ne, 6.73×10^{-6} cm^3 STP ^{36}Ar, 3.48×10^{-7} cm^3 STP ^{84}Kr, and 4.92×10^{-7} cm^3 STP ^{132}Xe were extracted from the Paris meteorite IOM over stepwise heating per gram of residue. Based on Ar and Kr release patterns, we estimate that the Kr missing step at 1539 °C would contribute <5% of the total amount of ^{84}Kr extracted from the IOM. Krypton and xenon are released altogether during the 1225 °C extraction step (>85% of ^{84}Kr and ^{132}Xe), in contrast to Ne and Ar, which are progressively released from 570 °C to 980 °C (Fig. S2 in supporting information). The peak release for neon is ~980°C. The abundance-weighted mean isotopic composition of the Paris meteorite IOM is consistent with a mixture of HL-Ne (Huss and Lewis 1994) and

Table 3. Argon abundances and isotopic compositions of the Paris meteorite CM 2.7 and CM 2.9 bulk fragments.

Sample	Mass (mg)	PT (CM)	^{36}Ar (cm^3 STP/g)	±2σ	^{38}Ar/^{36}Ar	±2σ	^{40}Ar/^{36}Ar	±2σ
Paris 2	2.42	2.7	1.48E-06	8.88E-08	0.2559	0.0018	4.3412	0.0286
Paris 8	3.50	2.7	1.50E-06	9.00E-08	0.1883	0.0008	2.6805	0.0467
Second extraction			3.34E-09	2.49E-09	0.2135	0.0090	3.3195	1.8124
Paris 4	6.54	2.9	1.87E-06	1.12E-07	0.1880	0.0005	2.9992	0.0432
Paris 5	2.98	2.9	1.85E-06	1.11E-07	0.1985	0.0009	2.5578	0.0370

PT = petrologic type.

Table 4. Krypton abundances and isotopic compositions of the Paris meteorite IOM via stepwise heating. The total amount of extracted ^{84}Kr is given via the abundance-weighted mean isotopic composition.

T°C	^{84}Kr (cm^3 STP/g)	±2σ	^{80}Kr/^{84}Kr	±2σ	^{82}Kr/^{84}Kr	±2σ	^{83}Kr/^{84}Kr	±2σ	^{86}Kr/^{84}Kr	±2σ
572	7.84E-09	1.22E-09	0.0392	0.0005	0.2023	0.0019	0.2026	0.0017	0.3079	0.0024
790	1.16E-08	1.83E-09	0.0393	0.0005	0.2020	0.0015	0.2027	0.0012	0.3104	0.0016
980	9.69E-09	1.28E-09	0.0387	0.0008	0.2003	0.0019	0.2025	0.0021	0.3077	0.0018
1225	3.02E-07	4.05E-08	0.0394	0.0006	0.2009	0.0014	0.2013	0.0014	0.3095	0.0019
1539	–	–	–	–	–	–	–	–	–	–
1770	1.67E-08	2.35E-09	0.0392	0.0004	0.2026	0.0011	0.2028	0.0013	0.3085	0.0017
Total	3.48E-07	4.72E-08	0.0394	0.0006	0.2010	0.0014	0.2015	0.0014	0.3094	0.0019

Q-Ne (Busemann et al. 2000) with possible small additions of cosmogenic Ne released during the highest temperature steps (Fig. 5). Xenon heavy isotope excesses relative to Q-Xe, similar to those reported for bulk CM 2.7 and CM 2.9 fragments, are also observed in the IOM for the 980 °C, 1225 °C, and (to a small extent) 1539 °C extraction steps (Fig. 4b). The abundance-weighted mean isotopic composition of the Paris meteorite IOM is similar to that of Q-Xe, with slight relative excesses in the heavy isotopes (Fig. 6). From a simple mass balance, we find that the Paris meteorite's IOM, which constitutes <2 wt% of the bulk sample (see the Preparation of the Insoluble Organic Residue section), contains more than 50% of the total amount of Xe present in the meteorite. The remaining Xe might reside within the soluble fraction of organic matter (removed during IOM isolation) or within mineral phases (removed during the HF/HCl treatment).

DISCUSSION

Noble Gas Signatures of the Paris Meteorite

In agreement with Hewins et al. (2014), we found the Xe signature of the Paris meteorite to be dominated by a Q-like component, as is often the case for carbonaceous chondrites (Busemann et al. 2000). Note, however, that the Xe isotopic spectrum reported by Hewins et al. (2014) for the Paris meteorite exhibits an anomalously high ^{126}Xe/^{130}Xe that we attribute to an analytical issue (Fig. 6). From the high-precision measurements conducted in this study, we confirm that the Q component dominates the Xe isotope signature of the Paris meteorite. As explained by Hewins et al. (2014), ^{38}Ar cosmogenic ages of the sample could not be determined as the argon content of Paris is dominated by the Q component, precluding a good estimate of the abundance of cosmogenic ^{38}Ar. The very low ^{40}Ar/^{36}Ar ratio (~3; Table 3) indicates limited contamination by atmospheric and radiogenic argon. Our data show no difference between CM 2.7 and CM 2.9 fragments for the Xe isotope composition, with both series of data comprising excesses in the heavy isotopes ($^{132–136}$Xe) relative to Q-Xe (Fig. 4a).

The Xe isotope composition of comets appears to be nucleosynthetically distinct from solar or Q signatures (Marty et al. 2017), which are related by mass-dependent fractionation. Cometary Xe is identical to solar Xe with the exception of the two heaviest isotopes, ^{134}Xe and ^{136}Xe. Thus, a possibility is that the solar/Q nucleosynthetic reservoir was derived from a cometary-like nucleosynthetic reservoir by addition of a nucleosynthetic component with excesses in the heavy Xe isotopes. Such a component (labeled Xe-H) has long been detected in primitive chondrites, always associated with an additional component showing overabundance of the light Xe isotopes (Xe-L) (Reynolds and Turner 1964). Xe-H and Xe-L were probably formed by different nucleosynthetic processes and the ultimate splitting of the heavy and light isotope subcomponents of Xe-HL, which have long been considered inseparable, may be achievable although no solid evidence has been found yet (Meshik et al. 2001). Gilmour and Turner (2007) demonstrated such a possibility using theoretical constraints to three-dimensional fits of xenon isotope data from presolar grains. These two components would notably be required

Table 5. Krypton abundances and isotopic compositions of the Paris meteorite CM 2.7 and CM 2.9 bulk fragments.

Sample	Mass (mg)	PT (CM)	^{84}Kr (cm^3 STP/g)	±2σ	^{80}Kr/^{84}Kr	±2σ	^{82}Kr/^{84}Kr	±2σ	^{83}Kr/^{84}Kr	±2σ	^{86}Kr/^{84}Kr	±2σ
Paris 2	2.42	2.7	1.33E-08	6.31E-10	0.0393	0.0013	0.2029	0.0044	0.2019	0.0049	0.3091	0.0067
			1.37E-08	6.84E-10	0.0397	0.0017	0.2024	0.0042	0.2025	0.0037	0.3091	0.0059
			1.44E-08	7.64E-10	0.0395	0.0014	0.2014	0.0054	0.2011	0.0067	0.3079	0.0079
		Average	1.38E-08	7.78E-10	0.0395	0.0003	0.2022	0.0010	0.2018	0.0010	0.3087	0.0010
Paris 8	3.50	2.7	1.25E-08	5.90E-10	0.0395	0.0012	0.2022	0.0038	0.2017	0.0046	0.3085	0.0057
			1.28E-08	6.12E-10	0.0396	0.0014	0.2015	0.0047	0.2030	0.0046	0.3100	0.0066
			1.27E-08	6.23E-10	0.0391	0.0015	0.2025	0.0048	0.2011	0.0049	0.3099	0.0077
		Average	1.27E-08	5.49E-10	0.0394	0.0003	0.2021	0.0007	0.2019	0.0014	0.3094	0.0012
Second extraction			7.86E-10	7.31E-11	0.0419	0.0062	0.2087	0.0279	0.2061	0.0339	0.3040	0.0303
Paris 4	6.54	2.9	1.35E-08	6.85E-10	0.0395	0.0012	0.2021	0.0050	0.2019	0.0047	0.3073	0.0071
			1.33E-08	6.47E-10	0.0393	0.0010	0.2009	0.0052	0.2025	0.0050	0.3082	0.0053
			1.30E-08	5.99E-10	0.0398	0.0014	0.2018	0.0044	0.2029	0.0040	0.3103	0.0053
			1.40E-08	7.17E-10	0.0395	0.0012	0.2028	0.0039	0.2025	0.0044	0.3093	0.0055
		Average	1.38E-08	7.65E-10	0.0396	0.0002	0.2019	0.0009	0.2024	0.0005	0.3088	0.0015
Paris 5	2.98	2.9	1.37E-08	7.10E-10	0.0395	0.0015	0.2015	0.0042	0.2019	0.0044	0.3103	0.0046
			1.43E-08	6.79E-10	0.0397	0.0016	0.2028	0.0046	0.2022	0.0042	0.3090	0.0057
			1.50E-08	8.54E-10	0.0396	0.0016	0.2013	0.0049	0.2017	0.0055	0.3091	0.0058
		Average	1.43E-08	7.58E-10	0.0396	0.0002	0.2019	0.0011	0.2019	0.0003	0.3095	0.0010

PT = petrologic type.

to be separated with extra Xe-H being added to solar, without any addition of Xe-L (Ott 2014). However, the Xe-H and Xe-L components always occur together at a constant abundance ratio (the so-called Xe-HL component), carried together in presolar nanodiamonds (Lewis et al. 1987). Gilmour et al. (2005) argued that the lack of variation in the Xe-HL component might also be a direct consequence of its definition, a different name (e.g., P3, P6) being given to any enrichment showing a different H/L ratio.

When the Xe-Q isotope composition is normalized to SW-Xe and corrected for mass-dependent fractionation, excesses in $^{134–136}$Xe are observed and are generally attributed to the contribution of a non-fissiogenic Xe component born by an unidentified carrier with the same Xe-HL isotopic composition as HL-bearing nanodiamonds (Gilmour 2010). Interestingly, Riebe et al. (2017) found that primordial Ne and Xe in the HF-solubles of the CI chondrite Ivuna also have isotopic and elemental ratios corresponding to a mixture of HL and Q. Xenon-134 and ^{136}Xe are produced only in the nucleosynthetic *r*-process (Ott 1996). While nanodiamonds are possibly unaffected by etching (Lewis et al. 1987), the exact Q-Xe composition (with the Xe-HL subcomponent, Huss and Lewis 1994) is observed by online nitric oxidation of acid residues (Busemann et al. 2000). Xe-HL host phases other than nanodiamonds have not yet been isolated (Gilmour 2010; Meshik et al. 2014) and additional Xe components (e.g., Xe-S carried by Si-C and graphite) may be required to account for the origin of the Q-Xe signature (Meshik et al. 2014). Here, we compute that a contribution of 1.8% of Xe-H to Q-Xe (calculated using the maximum $[^{131}Xe/^{136}Xe]_{Xe\text{-}H}$ given by Gilmour and Turner [2007] and the Q composition provided by Busemann et al. [2000]) can account for the $^{134–136}$Xe excesses relative to Q. This is in good agreement with previous estimates of the contribution of the Xe-HL component in carbonaceous chondrites (e.g., 1.5% Xe-HL for ^{132}Xe in Orgueil meteorite; Ott 2014). However, ^{126}Xe/^{132}Xe ratios, and their associated uncertainties, in the bulk fragments of the Paris meteorite preclude any additional contribution from Xe-L relative to the Q composition (Fig. 4a).

Excesses in the heavy isotopes ($^{132–136}$Xe) relative to Q-Xe, as observed in CM 2.7 and CM 2.9 fragments, can also be compared to the spectra of spontaneous fission of ^{238}U (dotted lines Fig. S3 in supporting information) and ^{244}Pu (dashed lines Fig. S3) (Porcelli and Ballentine 2002) that would be expected to account for the measured excesses in ^{136}Xe. However, the excesses we detected relative to Q-Xe are all relatively minor such that the $^{131–136}$Xe/^{130}Xe predicted from fission of ^{238}U and ^{244}Pu are all within error of the data points, thus preventing any accurate discrimination between a dominant contribution of ^{238}U- or ^{244}Pu-Xe (Fig. S3). The bulk U content of the Paris meteorite has been determined to be 1.01×10^{-2} μg/g (Hewins et al. 2014) (i.e., ~4.24×10^{-11} mol ^{238}U/g). By (1) using the product of the decay constant (λ_{sf}) and of the fractional yield of ^{136}Xe ($^{136}Y_{sf}$) produced by the spontaneous fission of ^{238}U ($[6.83 \pm 0.18] \times 10^{-18}$ a^{-1}; Ragettli et al. 1994) and (2) assuming a closure age of

Table 6. Xenon abundances and isotopic compositions of the Paris meteorite IOM via stepwise heating. The total amount of extracted ^{132}Xe is given via the abundance-weighted mean isotopic composition.

T°C	^{132}Xe (cm^3 STP/g)	±2σ	$^{124}Xe/^{132}Xe$	±2σ	$^{126}Xe/^{132}Xe$	±2σ	$^{128}Xe/^{132}Xe$	±2σ	$^{129}Xe/^{132}Xe$	±2σ	$^{130}Xe/^{132}Xe$	±2σ	$^{131}Xe/^{132}Xe$	±2σ	$^{134}Xe/^{132}Xe$	±2σ	$^{136}Xe/^{132}Xe$	±2σ
572	7.15E-09	1.12E-09	0.0045	0.0002	0.0040	0.0001	0.0822	0.0010	1.0467	0.0042	0.1627	0.0014	0.8231	0.0030	0.3753	0.0023	0.3153	0.0019
790	1.01E-08	1.56E-09	0.0045	0.0001	0.0040	0.0002	0.0828	0.0007	1.0343	0.0042	0.1628	0.0010	0.8198	0.0037	0.3756	0.0014	0.3153	0.0019
980	1.35E-08	1.82E-09	0.0046	0.0002	0.0041	0.0002	0.0830	0.0010	1.0365	0.0064	0.1622	0.0017	0.8193	0.0062	0.3839	0.0022	0.3244	0.0018
1225	4.26E-07	5.58E-08	0.0046	0.0001	0.0041	0.0001	0.0834	0.0006	1.0421	0.0042	0.1640	0.0011	0.8215	0.0029	0.3805	0.0010	0.3220	0.0016
1539	1.65E-08	2.38E-09	0.0045	0.0001	0.0040	0.0001	0.0828	0.0008	1.0407	0.0048	0.1624	0.0010	0.8200	0.0027	0.3784	0.0016	0.3183	0.0015
1770	1.90E-08	2.70E-09	0.0044	0.0001	0.0040	0.0001	0.0830	0.0005	1.0393	0.0044	0.1635	0.0008	0.8197	0.0026	0.3771	0.0016	0.3170	0.0012
Total	4.92E-07	6.54E-08	0.0046	0.0001	0.0041	0.0001	0.0833	0,0006	1.0417	0.0043	0.1638	0.0011	0.8213	0.0030	0.3802	0.0011	0.3215	0.0016

Table 7. Xenon abundances and isotopic compositions of the Paris meteorite CM 2.7 and CM 2.9 bulk fragments.

Sample	Mass (mg)	PT (CM)	^{132}Xe (cm^3 STP/g)	±2σ	^{124}Xe/^{132}Xe	±2σ	^{126}Xe/^{132}Xe	±2σ	^{128}Xe/^{132}Xe	±2σ	^{129}Xe/^{132}Xe	±2σ	^{130}Xe/^{132}Xe	±2σ	^{131}Xe/^{132}Xe	±2σ	^{134}Xe/^{132}Xe	±2σ	^{136}Xe/^{132}Xe	±2σ
Paris 2	2.42	2.7	1.85E-08	5.05E-10	0.00455	0.00032	0.00404	0.00037	0.08217	0.00280	1.03696	0.02681	0.16142	0.00275	0.81879	0.02407	0.38260	0.01071	0.32235	0.00869
			1.84E-08	5.46E-10	0.00461	0.00043	0.00400	0.00026	0.08160	0.00279	1.03848	0.02881	0.16231	0.00339	0.82077	0.02951	0.38349	0.01132	0.32346	0.00958
			1.96E-08	5.35E-10	0.00453	0.00022	0.00400	0.00021	0.08210	0.00299	1.04090	0.02091	0.16238	0.00278	0.81880	0.02420	0.38306	0.00812	0.32324	0.00622
	Average		1.88E-08	9.69E-10	0.00456	0.00006	0.00401	0.00004	0.08196	0.00044	1.03878	0.00281	0.16203	0.00075	0.81945	0.00161	0.38305	0.00063	0.32301	0.00083
Paris 8	3.50	2.7	1.64E-08	5.07E-10	0.00450	0.00034	0.00400	0.00028	0.08150	0.00252	1.03744	0.02818	0.16136	0.00300	0.81612	0.02628	0.38371	0.01093	0.32202	0.00965
			1.60E-08	4.82E-10	0.00460	0.00027	0.00400	0.00031	0.08171	0.00286	1.04006	0.02436	0.16196	0.00283	0.81815	0.02467	0.38301	0.00960	0.32249	0.00888
			1.61E-08	4.52E-10	0.00460	0.00036	0.00405	0.00037	0.08219	0.00270	1.03920	0.02064	0.16115	0.00219	0.81333	0.01925	0.38327	0.00960	0.32300	0.00813
	Average		1.62E-08	3.43E-10	0.00457	0.00008	0.00402	0.00004	0.08180	0.00050	1.03890	0.00189	0.16149	0.00060	0.81587	0.00342	0.38333	0.00050	0.32250	0.00069
Second extraction			1.27E-10	1.73E-11	0.00440	0.00173	0.00341	0.00156	0.07677	0.01880	1.01171	0.18563	0.15229	0.02037	0.79102	0.18915	0.38242	0.07601	0.31529	0.06146
Paris 4	6.54	2.9	1.60E-08	5.18E-10	0.00457	0.00041	0.00399	0.00042	0.08197	0.00304	1.03841	0.03003	0.16138	0.00339	0.81515	0.02970	0.38226	0.01078	0.32161	0.00994
			1.58E-08	4.48E-10	0.00458	0.00038	0.00402	0.00039	0.08182	0.00276	1.03578	0.02141	0.16158	0.00229	0.81321	0.02002	0.38068	0.00884	0.32250	0.00702
			1.53E-08	5.45E-10	0.00452	0.00043	0.00393	0.00044	0.08192	0.00366	1.03558	0.03832	0.16219	0.00420	0.81876	0.03662	0.38175	0.01594	0.32023	0.01177
			1.67E-08	4.58E-10	0.00451	0.00029	0.00400	0.00024	0.08171	0.00252	1.03334	0.01782	0.16115	0.00196	0.81588	0.01716	0.38129	0.00735	0.32143	0.00635
			1.70E-08	5.31E-10	0.00463	0.00025	0.00403	0.00036	0.08164	0.00271	1.04260	0.02896	0.16197	0.00312	0.81974	0.02726	0.38415	0.01032	0.32330	0.00962
			1.71E-08	5.33E-10	0.00462	0.00025	0.00403	0.00036	0.08184	0.00272	1.04100	0.02892	0.16205	0.00312	0.82032	0.02726	0.38309	0.01029	0.32321	0.00962
	Average		1.63E-08	6.50E-10	0.00457	0.00005	0.00400	0.00003	0.08182	0.00011	1.03779	0.00316	0.16172	0.00037	0.81718	0.00255	0.38220	0.00113	0.32205	0.00106
Paris 5	2.98	2.9	1.68E-08	5.44E-10	0.00457	0.00041	0.00399	0.00042	0.08197	0.00304	1.03843	0.03004	0.16139	0.00339	0.81516	0.02971	0.38226	0.01079	0.32160	0.00994
			1.68E-08	4.77E-10	0.00458	0.00038	0.00401	0.00039	0.08182	0.00276	1.03579	0.02142	0.16158	0.00229	0.81322	0.02003	0.38067	0.00885	0.32249	0.00702
			1.77E-08	6.32E-10	0.00452	0.00043	0.00393	0.00044	0.08193	0.00366	1.03559	0.03834	0.16219	0.00420	0.81877	0.03663	0.38174	0.01594	0.32023	0.01177
	Average		1.71E-08	7.02E-10	0.00455	0.00005	0.00398	0.00006	0.08191	0.00011	1.03660	0.00224	0.16172	0.00059	0.81571	0.00399	0.38156	0.00115	0.32144	0.00161

PT = petrologic type. Xenon abundances and isotopic compositions are computed from the average of 3–6 aliquots of gas taken from each sample. Errors are $2/\sqrt{(n-1)}$, where n is the number of duplicates.

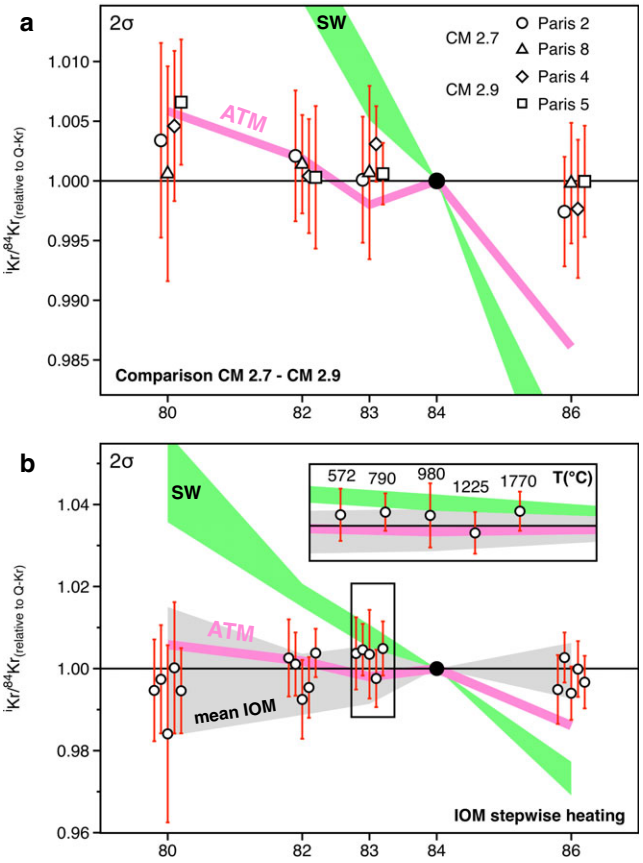

Fig. 3. Krypton isotopic spectra of the two CM 2.7 and CM 2.9 fragments (a) and of the IOM isolated from the Paris meteorite and analyzed by stepwise heating (b), normalized to the Q-phase composition (Busemann et al. 2000). Solar (Marti and Mathew 2015) and atmospheric (Basford et al. 1973) compositions are given for comparison. The gray area (b) corresponds to the abundance-weighted mean isotopic compositions of the Paris meteorite IOM. Corresponding data are given in Tables 4 and 5. Uncertainties are 2σ.

~4.5 Ga, we calculated the amount of ^{136}Xe (mol) that has been produced by the spontaneous fission of ^{238}U for each fragment of the Paris meteorite analyzed in this study. Likewise, we use the initial ^{244}Pu/^{238}U of the meteorite and the branching ratio (fission/α-emission) of ^{244}Pu (0.125%, Fields et al. 1966) to calculate the initial contents of ^{244}Pu and determine the corresponding amounts of ^{136}Xe (mol) produced by spontaneous fission of now extinct ^{244}Pu. This calculation is strongly reliant on the value of the initial ^{244}Pu/^{238}U of the parent body. A low initial ^{244}Pu/^{238}U requires significant decay of ^{244}Pu before formation of the parent body. Increasing this time interval for decay might induce the initial amount of ^{129}I to be lower than the actual value (Hudson et al. 1989). Conversely, a high initial ^{244}Pu/^{238}U might require late inputs of freshly synthesized material in the early solar system. Here, if the widely adopted chondritic ^{244}Pu/^{238}U of 0.0068 ± 0.0010 (Hudson et al. 1989) is taken (in agreement with the recently determined value of 0.0061 ± 0.0028 for angrites; Nakashima et al. 2018), we observe that the Xe isotope corrections for contributions from ^{238}U and ^{244}Pu spontaneous fission are negligible (white symbols versus gray ones, Fig. S4 in supporting information). Two explanations can then be suggested: either there is an over-addition of some HL-Xe, or the initial ^{244}Pu/^{238}U ratio is underestimated. Interestingly, estimates of the initial ^{244}Pu/^{238}U of carbonaceous chondrites have been provided for Murchison (0.120 ± 0.011), Murray (0.132 ± 0.012), and Allende (0.113 ± 0.006) (mean value of 0.122; Kuroda and Myers 1991a, 1991b). These ^{244}Pu/^{238}U ratios are two orders of magnitude higher than the chondritic ratio given by Hudson et al. (1989). Nonetheless, Xe isotope spectra of the Paris meteorite corrected for contributions from ^{238}U and ^{244}Pu spontaneous fission (using a mean value of 0.122 for the initial ^{244}Pu/^{238}U) still exhibits ^{136}Xe excess relative to phase Q (black triangles, Fig. S4). Therefore, potential ^{244}Pu-derrived Xe cannot be distinguished on top of Q-Xe. The fact that a mix of 1.8% Xe-HL and 98.2% Q-Xe matches the bulk Xe isotope composition of the Paris meteorite suggests that excesses in the heavy isotopes ($^{132–136}$Xe) relative to Q-Xe as observed in CM 2.7 and CM 2.9 fragments would mainly be caused by the addition of Xe-H from nanodiamonds uniformly mixed with the rest of the solar system materials.

The composition of Q-Kr is consistent with a component produced in the early solar system by a series of mechanisms similar to those proposed to account for Xe-Q, i.e., mass-dependent fractionation of SW-Kr and addition of presolar components dominated by Kr-HL (Gilmour 2010). The fact that Kr isotope compositions measured here for the Paris meteorite are within error of Q-Kr with no deviation potentially carried by additional presolar contributions—as reported for Xe—may be attributed to a dilution effect linked to the fact that production of Q-Kr from fractionated SW-Kr requires a greater relative contribution from Kr-HL (~4.5%) than required from Xe-HL to produce Xe-Q from fractionated SW-Xe (~1.5%) (Gilmour 2010). Contrary to the case of Xe, presolar Kr associated with nanodiamonds may not be abundant enough, relative to Q-Kr, to be detectable. Interestingly, the high contribution of Xe-HL required to reproduce the Paris meteorite IOM data, relative to previously measured IOMs from carbonaceous and ordinary chondrites (Busemann et al. 2000), may be interpreted as evidence for a high contribution of presolar material (Fig. 7). The xenon isotopes of enstatite chondrites (Patzer and Schultz 2002), ureilites (Göbel et al. 1978) and carbonaceous chondrites (average carbonaceous chondrite composition, AVCC; Pepin 2003) appear to define a trend along a mixing line between mass fractionated solar wind (Gilmour 2010) and the pure Xe-

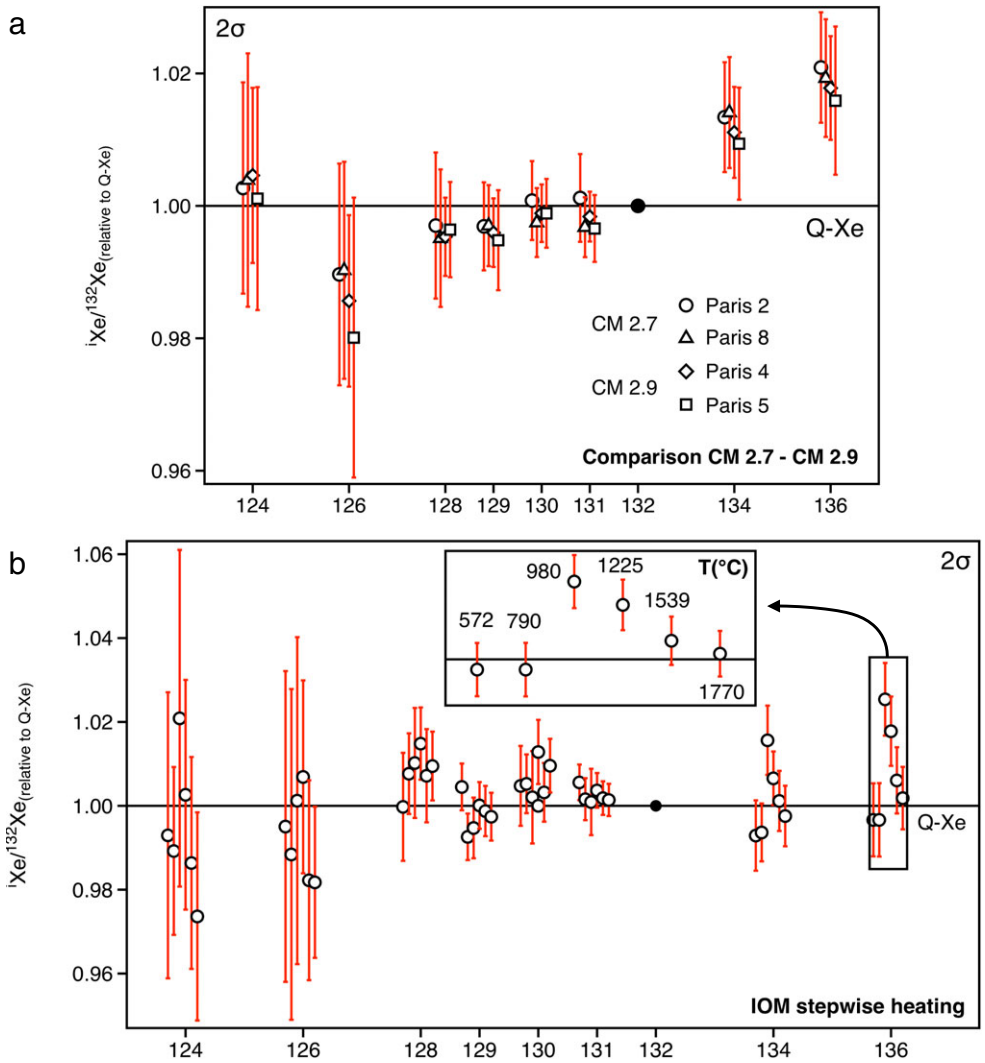

Fig. 4. Xenon isotopic spectra of the two CM 2.7 and CM 2.9 fragments (a) and of the IOM isolated from the Paris meteorite and analyzed by stepwise heating (b), normalized to the Q-phase composition (Busemann et al. 2000). For stepwise heating, isotopic ratios from increasing temperatures steps are displayed from left to right, as highlighted in the frame. The gray area (B) corresponds to the abundance-weighted mean isotopic compositions of the Paris meteorite IOM. Corresponding data are given in Tables 6 and 7. Uncertainties are 2σ.

HL endmember (Huss and Lewis 1994). While Gilmour (2010) suggested that mixing of mass fractionated solar wind with Xe-HL might occur during processing on parent bodies, we propose that these might reveal a trend for increasing amounts of presolar materials with increasing heliocentric distance. Here, the bulk fragments of the Paris meteorite appear to contain an excess of 1.8% Xe-H, relative to Xe-Q, with negligible contribution from Xe-L (Fig. 4a). The occurrence of a heterogeneous distribution of presolar carriers enriched in nuclides produced in rapid neutron capture stars (r-process) has also been observed for molybdenum isotopes in carbonaceous chondrites relative to chondritic groups formed in the inner solar system (Dauphas et al. 2002; Kruijer et al. 2017). The r-process excess in carbonaceous chondrites suggests that there was an addition of a nucelosynthetically different component to the outer solar system prior to carbonaceous chondrite formation (Kruijer et al. 2017). It is important to distinguish between the fraction of presolar material in bulk samples and the proportion of Xe-HL added to fractionated solar wind to produce the IOM signatures (Fig. 7). Bulk Xe compositions (e.g., AVCC, enstatite chondrites, ureilites, and bulk fragments of the Paris meteorite; Fig. 7) depend on the abundance of presolar material and concentration of Xe therein, the IOM abundance, and concentration/composition of Xe in "phase Q," as well as on any Xe component in other phases. This can therefore be affected by the extent of

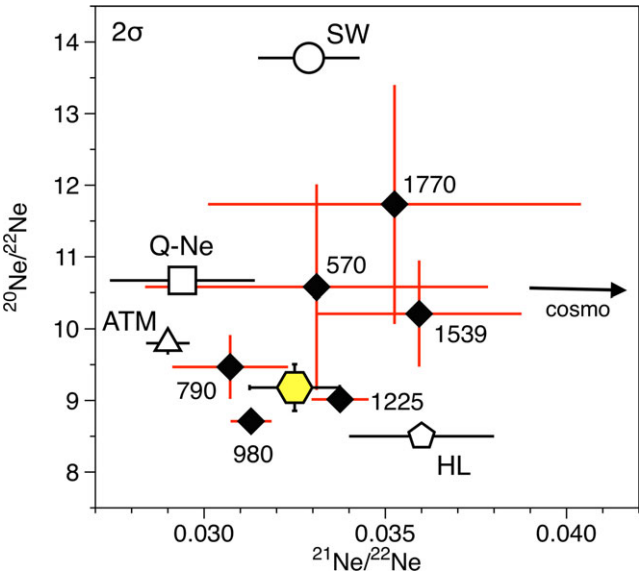

Fig. 5. Neon three-isotope diagram of the Paris meteorite's IOM upon stepwise heating. The temperature associated to each step is given next to the corresponding data point. The abundance-weighted mean isotopic composition of the Paris meteorite IOM corresponds to the yellow hexagon. Corresponding data are given in Table 1. SW = solar wind (Heber et al. 2012); ATM = terrestrial atmosphere (Ozima and Podosek 2002); Q-Ne: (Busemann et al. 2000), HL-Ne: (Huss and Lewis 1994), cosmo: typical chondritic value for the cosmogenic galactic cosmic ray endmember (Busemann et al. 2000). Uncertainties are 2σ.

thermal processing and/or physical separation of HL-bearing phases. On the other hand, the end product of Q process(es) trapping ionized Xe into organic matter with mass fractionation would depend on the composition of the ambient gas it was trapped from, and perhaps subsequent parent body incorporation of HL or mixing with some HL-bearing phases.

Origin of Chondritic Noble Gases and Their Evolution During Alteration

The exact host phase(s) of Q-gases in chondrites, although not precisely defined (Marrocchi et al. 2015), appears to be closely related to refractory organic compounds (Ott et al. 1981; Busemann et al. 2000). A presolar origin of phase Q inherited from the molecular cloud from which the Sun was later formed has been proposed to explain its association with presolar materials (Huss and Alexander 1987). An alternative view considers Q as being locally derived from an initial nebula mix now represented by the solar composition. It has been demonstrated that ~2% of Xe-H apparently present in phase Q may not be necessarily originated from stellar nucleosythesis (Meshik et al. 2016), but could result from the addition of xenon originating from chemically fractionated fission (CFF) of ^{244}Pu, which was extant during the formation of phase Q. This nucleo-chemical process typically yields ^{136}Xe to ^{134}Xe in 2:1 proportion, with little ^{132}Xe and ^{131}Xe, and no lighter isotopes, which are shielded from fission by stable isobars. This interpretation implies that phase Q is of solar, rather than of presolar origin (Meshik et al. 2016). Processes involved in the origin of Q-Xe have been investigated by plasma experiments dedicated to study the adsorption of Xe onto organics defects (Marrocchi et al. 2011) and the incorporation of fractionated noble gases during organosynthesis (Kuga et al. 2015). These two studies support a scenario in which organic materials would constitute the main carrier phase of chondritic noble gases in meteorites, with a likely common and pre-asteroidal origin (Kuga et al. 2015).

No difference was found between the Kr and Xe isotopes of the CM 2.9 and CM 2.7 fragments. This result is consistent with the lack of significant difference in the in situ molecular signature (X-ray absorption near edge structure spectra) of the organic matter contained in the least (CM 2.9) and most altered (CM 2.7) regions of the Paris meteorite matrix (Vinogradoff et al. 2017). According to Vinogradoff et al. (2017), the Paris (~2.8 CM) and Murchison (CM 2.5) IOM exhibit distinct molecular and structural signatures, as a result of hydrothermal alteration. Taken together, these results indicate that the main carrier phases of heavy noble gases were not significantly affected by the episode of hydrothermal alteration on the parent body of the Paris meteorite.

A dual origin has been proposed for the ice grains accreted by the Paris meteorite parent body, with evidence for O and H isotope signatures from both local (i.e., inner solar system) and outer solar system water ices (Vacher et al. 2016; Piani et al. 2018). Yet, we found that such a contribution of outer solar system water ice (taken with a composition similar to that of comet 67P/G; Marty et al. 2017) could only contribute <1% of the total budget of ^{132}Xe in the Paris meteorite. Shifts of the Xe heavy isotope ratios toward lower values, as expected in the case of a contribution from cometary-like Xe (Fig. 2), may be overprinted by heavy Xe isotope excesses of nucleosynthetic origin. Another possibility is that cometary-like Xe associated with the outer solar system water ice component may have been lost to space during ice melting. In this case, Xe retained in refractory organic materials would have been preserved only, without having exchanged with Xe carried by alteration fluids.

The ubiquity of the Q-phase associated with IOM implies that either (1) the IOM in carbonaceous chondrites is inherited from a unique process of organosynthesis resulting in noble gases being trapped in IOM with a Q-like signature, or (2) that several distinct

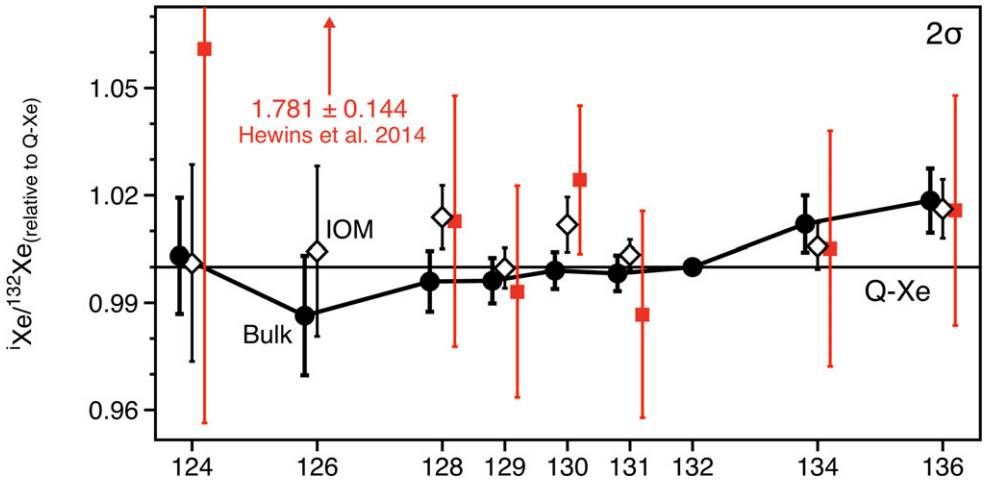

Fig. 6. Xenon isotopic spectra of the CM 2.7 and CM 2.9 fragments normalized to the Q-phase composition from Busemann et al. (2000) and compared to the bulk Xe isotope composition determined by Hewins et al. (2014). Atmospheric Xe is also given for comparison (Basford et al. 1973). Uncertainties are 2σ.

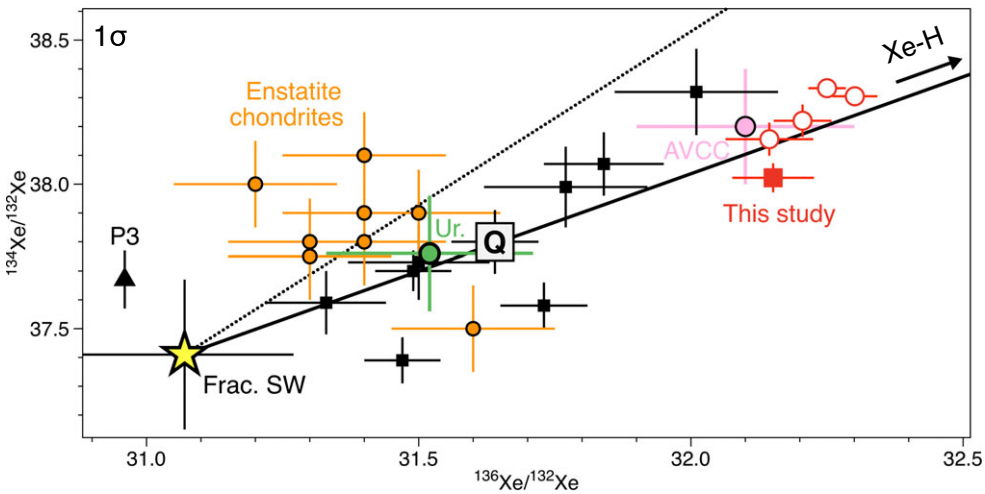

Fig. 7. Xenon three-isotope diagram ($^{134}Xe/^{132}Xe$ versus $^{136}Xe/^{132}Xe$) of the Paris meteorite's IOM and bulk fragments. The composition of Xe-Q (gray square, Busemann et al. 2000) is the average and standard error of compositions measured in IOMs from nine meteorites (black squares, Busemann et al. 2000). This accepted Xe-Q composition is accounted for by mixing of mass fractionated solar wind (Frac. SW) with Xe-HL (here Xe-H, see fig. 4 from Gilmour 2010). Bulk compositions of enstatite chondrites (circles filled with orange, Patzer and Schultz 2002), ureilites (circle filled with green, Göbel et al. 1978), carbonaceous chondrites (circle filled with pink, average carbonaceous chondrite composition, AVCC; Pepin 2003), and Paris meteorite bulk fragments (red open circles) appear to fall along this trend. The abundance-weighted mean isotopic composition of the Paris meteorite IOM (red square) also falls along this trend, with evidence for a high fraction of Xe-H relative to other IOMs from carbonaceous and ordinary chondrites (black squares, Busemann et al. 2000). P3: presolar component released at relatively low temperature in nanodiamonds (Gilmour 2010). Uncertainties are 1σ.

mechanisms of IOM synthesis (e.g., in the protosolar nebula (Remusat et al. 2006, 2009; Kuga et al. 2015), in the interstellar medium (Robert and Epstein 1982; De Marcellus et al. 2016) or on asteroids (Kebukawa et al. 2017; Vinogradoff et al. 2018) are able to yield a Q-like signature for noble gases. Interestingly, the trapping efficiency of Xe neutrals in organics is very low and does not induce measurable isotopic fractionation without ionization (Marrocchi and Marty 2013). Under ionizing conditions, the trapping efficiency of Xe ions reproduces the Xe isotope fractionation and the high xenon concentration measured in phase Q of primitive meteorites (Marrocchi et al. 2011; Kuga et al. 2015). To date and to our knowledge, organosynthesis in the ionized gas phase of the protosolar nebula (Kuga et al. 2015) is the only mechanism that accounts for the formation of an IOM carrying noble gases with Q-like elemental and isotopic fractionation patterns.

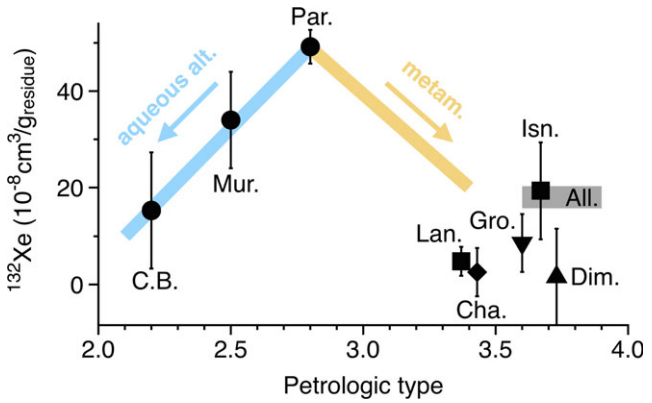

Fig. 8. ^{132}Xe contents (10^{-8} cm^3 g^{-1} $_{residue}$) of different IOM isolated from carbonaceous chondrite (Busemann et al. 2000) (from left to right, CM 2.2: Cold Bokkeveld; CM 2.5: Murchison; CM 2.8: Paris [this study]; CO 3.4: Lancé; LL 3.4: Chainpur; CV 3.6: Grosnaja; CV >3.6: Allende [petrologic type from; Bonal et al. 2006]; CO 3.7: Isna; H 3.7: Dimmit). Pathways of Xe loss upon aqueous alteration (aqueous alt.) and metamorphism (metam.), as hypothesized by Busemann et al. (2000), are displayed. Symbols refer to petrologic types (circles: CM, squares: CO, triangle pointing downward: CV, triangle pointing upward: H, diamond: LL). Uncertainties are 1σ.

Recently, Fray et al. (2016) reported the in situ detection of solid organic matter similar to the insoluble organic matter found in the carbonaceous chondrite meteorites in the dust particles emitted by comet 67P/Churyumov–Gerasimenko. We speculate that, if the IOM present in carbonaceous chondrites were contributed by at least two isotopically distinct reservoirs (e.g., a Q-like inner solar system component and an outer solar system reservoir), then a mixing between the two signatures should be observed in meteorites with different proportions of these two endmembers. This is, however, not observed in the Paris meteorite. The noble gas signature of Paris can therefore be defined as dominantly Q-like. The ubiquity of Q-like noble gases in the IOM of carbonaceous chondrites suggests that either (1) noble gases associated with cometary IOM are also Q-like (with a common origin—solar or interstellar—for the IOM in meteorites and comets) such that an addition of cometary material cannot be resolved using the noble gases or (2) cometary IOM is poor in noble gases, so that mixing with Q-like inner solar system IOM results in an unchanged Q noble gas signature. A comet sample-return mission allowing the IOM of cometary samples to be isolated and measured in the laboratory for its heavy noble gas isotopes would potentially be able to resolve these issues. Likewise, the possibility of forming a Q-like elementary and isotopic noble gas composition trapped in organic materials synthesized from the photochemical and thermal processing of interstellar ice analogues appears to be a promising avenue of investigation.

Our data indicate that Xe isotopes probably remained unaffected by the limited episode of aqueous alteration that occurred on the parent body of the Paris meteorite. To this extent, the ^{132}Xe concentrations we report for the IOM of the Paris meteorite are the highest yet measured for the IOM of carbonaceous chondrites (Fig. 8). From a simple mass balance, we find that the Paris meteorite's IOM, which constitutes <2 wt% of the bulk sample (see the Preparation of the Insoluble Organic Residue section), contains more than 50% of the total amount of Xe present in the meteorite. The mass of the residue depends on the cleanliness, abundance of gas-lacking phases, and perhaps the procedure to produce the residue. The noble gas bearing Q (and diamonds) may also contribute only <1% to the total mass of the residue. However, by considering that (1) all IOM in carbonaceous chondrites inherited a similar phase Q component, and that (2) variations of the ^{132}Xe content in carbonaceous chondrites are a function of the degree of secondary processing (thermal metamorphism and aqueous alteration; Busemann et al. 2000), we conclude that the Paris meteorite likely carries the most pristine chondritic IOM observed to date. This is in line with infrared and Raman microspectroscopy observations of the Paris meteorite organic signature, which show that the Paris meteorite has suffered minimal thermal metamorphism as well as weak aqueous alteration, leaving even the possibility to have preserved some organic matter of interstellar origin (Merouane et al. 2012). The chemistry of the Paris meteorite may thus be closely related to the early stages of the solar nebula. This is further supported by the low contents of amino acids and lack of alkylated PAHs in the Paris meteorite, the abundance and distribution of both types of molecules likely being related to episodes of aqueous alteration within carbonaceous asteroids (Martins et al. 2015). This is also in agreement with the solid-state ^{13}C nuclear magnetic resonance and electron paramagnetic resonance spectra of the Paris IOM, which show a higher proportion of aliphatic carbons and organic radicals relative to the Murchison IOM (Vinogradoff et al. 2017).

Nonetheless, we find that the ^{36}Ar/^{132}Xe ratios—which reflect the degree of secondary processing (Busemann et al. 2000)—are slightly lower in the CM 2.7 fragments relative to the CM 2.9 ones (Table 8), probably related to a preferential loss of the lightest noble gases upon aqueous alteration. Alternatively, several studies suggested that phase Q may consist of an assemblage of carrier phases and substructures that would exhibit variable resistance to alteration processes, and contain variable proportions of light and heavy noble gases (Gros and Anders 1977; Busemann et al. 2000; Marrocchi et al. 2005, 2015). A preferential loss

Table 8. Elemental composition of the Paris meteorite IOM and bulk fragments. Elemental composition of Q (Busemann et al. 2000) and bulk fragments of the Paris meteorite from Hewins et al. (2014) are given for comparison. The factor ~6 between bulk $^{36}Ar/^{132}Xe$ measured in this study and analyzed by Hewins et al. (2014) might illustrate a certain degree of inhomogeneity for noble gases concentrations in Paris at the mg scale.

		$^{20}Ne/^{36}Ar$	±2σ	$^{20}Ne/^{132}Xe$	±2σ	$^{36}Ar/^{132}Xe$	±2σ	$^{84}Kr/^{132}Xe$	±2σ
IOM	572	0.455	0.099	8.587	1.880	18.881	4.158	1.097	0.242
	790	0.171	0.029	19.307	3.801	112.871	22.089	1.149	0.254
	980	0.488	0.089	57.111	10.684	117.037	21.745	0.718	0.135
	1225	0.168	0.031	1.150	0.213	6.854	1.284	0.709	0.133
	1539	0.416	0.078	7.758	1.517	18.667	3.652	–	–
	1770	0.103	0.020	3.500	0.703	34.105	6.803	0.879	0.176
	Total	0.254	0.047	3.476	0.649	13.679	2.556	0.707	0.134
			Bulk	CM2.7	Paris 2	78.723	6.227	0.734	0.056
					Paris 8	92.593	5.891	0.784	0.038
				CM2.9	Paris 4	114.724	8.255	0.847	0.058
					Paris 5	108.187	7.865	0.836	0.056
Hewins et al. 2014 (a)		1.42	0.02	–	–	–	–	–	–
Hewins et al. 2014 (b)		0.82	0.02	408.332	46.309	583.684	13.92	–	–
Q		0.044	0.012	3.2	1	76	14	0.81	0.1

of Ar relative to Xe during aqueous alteration could thus be related to the destruction of poorly resistant phases with high Ar/Xe during early aqueous alteration. Regardless of the alteration or metamorphism degree, the isotopic ratios of phase Q from different meteorites are similar and should therefore be identical to the originally incorporated Q composition (Busemann et al. 2000).

CONCLUSION

Because the Paris meteorite parent body locally accreted only limited amounts of water ice, part of the materials constituting this meteorite have been exceptionally well preserved from secondary processing by aqueous alteration. Recently, O and H isotopic evidence for a contribution of outer solar system water ice have been found in this meteorite (Vacher et al. 2016; Piani et al. 2018). We separately analyzed pristine CM 2.9 fragments, CM 2.7 fragments, and the IOM of the Paris meteorite for their heavy noble gas isotope compositions but found no evidence for a contribution of an outer solar system noble gas component (supposed to be cometary-like; Marty et al. 2017). All our noble gas isotope data point to phase Q being the dominating carrier of noble gases, with small excesses in the heavy Xe isotopes relative to phase Q in the bulk samples being attributed to a contribution of presolar materials (r-process isotopes; Gilmour and Turner 2007). The ubiquity of the Q-phase in meteorites suggests that noble gases possibly present in cometary insoluble organic matter (Fray et al. 2016) could potentially also have Q-like signatures and be of nebular origin. The fact that no difference in the elementary and isotopic composition of Xe could be found between CM 2.9 and CM 2.7 fragments agree with the observation that the IOM (the main carrier of heavy noble gases in chondrites) shows little variation in X-ray absorption near edge structure spectroscopy between fresh and altered areas (Vinogradoff et al. 2017). The high concentration \of Xe in the Paris meteorite IOM relative to other carbonaceous chondrites' IOM also correlates with the Paris meteorite carrying the most pristine IOM and exhibiting the lowest degree of secondary processing (thermal metamorphism and aqueous alteration; Busemann et al. 2000) observed so far in meteorites (Hewins et al. 2014).

Acknowledgments—We are grateful to Brigitte Zanda who initiated a stimulating research project on the Paris meteorite, and to the Museum National d'Histoire Naturelle de Paris for allocation of this precious sample. Laurette Piani and Michael Broadley are thanked for fruitful discussions. We thank the two reviewers, Jamie Gilmour and Henner Busemann, for their constructive and insightful comments. This study was supported by the European Research Council (grant no. 695618). This is a CRPG contribution #2595.

Editorial Handling—Dr. Ingo Leya

REFERENCES

Alexander C. M. O'D., Bowden R., Fogel M. L., Howard K. T., Herd C. D. K., and Nittler L. R. 2012. The provenances of asteroids, and their contributions to the volatile inventories of the terrestrial planets. *Science* 337:721–723.

Basford J. R., Dragon J. C., Pepin R. O., Coscio M. R. Jr., and Murthy V. R. 1973. Krypton and xenon in lunar fines. Proceedings, 4th Lunar Science Conference. pp. 1915–1955.

Bekaert D. V., Avice G., Marty B., Henderson B., and Gudipati M. S. 2017. Stepwise heating of lunar anorthosites 60025, 60215, 65315 possibly reveals an indigenous noble gas component on the Moon. *Geochimica et Cosmochimica Acta* 218:114–131.

Bitsch B., Johansen A., Lambrechts M., and Morbidelli A. 2015. The structure of protoplanetary discs around evolving young stars. *Astronomy & Astrophysics* 575:A28. https://doi.org/10.1051/0004-6361/201424964.

Bland P. A., Jackson M. D., Coker R. F., Cohen B. A., Webber J. B. W., Lee M. R., Duffy C. M., Chater R. J., Ardakani M. G., McPhail D. S., and McComb D. W. 2009. Why aqueous alteration in asteroids was isochemical: High porosity ≠ high permeability. *Earth and Planetary Science Letters* 287:559–568.

Bonal L., Quirico E., Bourot-Denise M., and Montagnac G. 2006. Determination of the petrologic type of CV3 chondrites by Raman spectroscopy of included organic matter. *Geochimica et Cosmochimica Acta* 70:1849–1863.

Brearley A. J. 2006. The action of water. In *Meteorites and the early solar system II*, edited by Dante L. and McSween H.Y. Jr. Tucson, Arizona: University of Arizona Press. pp. 587–624.

Browning L. B., McSween H. Y., and Zolensky M. E. 1996. Correlated alteration effects in CM carbonaceous chondrites. *Geochimica et Cosmochimica Acta* 60:2621–2633.

Busemann H., Baur H., and Wieler R. 2000. Primordial noble gases in "phase Q" in carbonaceous and ordinary chondrites studied by closed-system stepped etching. *Meteoritics & Planetary Science* 35:949–973.

Cleeves L. I., Bergin E. A., Alexander C. M. O'D., Du F., Graninger D., Öberg K. I., and Harries T. J. 2014. The ancient heritage of water ice in the solar system. *Science* 345:1590–1593.

Crowther S. A. and Gilmour J. D. 2013. The Genesis solar xenon composition and its relationship to planetary xenon signatures. *Geochimica et Cosmochimica Acta* 123:17–34.

Dauphas N., Marty B., and Reisberg L. 2002. Molybdenum evidence for inherited planetary scale isotope heterogeneity of the protosolar nebula. *The Astrophysical Journal* 565:640.

De Marcellus P., Fresneau A., Brunetto R., Danger G., Duvernay F., Meinert C., Meierhenrich U. J., Borondics F., Chiavassa T., and Le Sergeant d' Hendecourt L. 2016. Photo and thermochemical evolution of astrophysical ice analogues as a source for soluble and insoluble organic materials in solar system minor bodies. *Monthly Notices of the Royal Astronomical Society* 464:114–120.

Drake M. J. 2005. Origin of water in the terrestrial planets. *Meteoritics & Planetary Science* 40:519–527.

Fields P. R., Friedman A. M., Milsted J., Lerner J., Stevens C. M., Metta D., and Sabine W. K. 1966. Decay properties of plutonium-244, and comments on its existence in nature. *Nature* 212:131.

Fray N., Bardyn A., Cottin H., Altwegg K., Baklouti D., Briois C., Colangeli L., Engrand C., Fischer H., Glasmachers A., Grün E., Haerendel G., Henkel H., Höfner H., Hornung K., Jessberger E. K., Koch A., Krüger H., Langevin Y., Lehto H., Lehto K., Le Roy L., Merouane S., Modica P., Orthous-Daunay F.-R., Paquette J., Raulin F., Rynö J., Schulz R., Silén J., Siljeström S., Steiger W., Stenzel O., Stephan T., Thirkell L., Thomas R., Torkar K., Varmuza K., Wanczek K.-P., Zaprudin B., Kissel J., and Hilchenbach M. 2016. High-molecular-weight organic matter in the particles of comet 67P/Churyumov–Gerasimenko. *Nature* 538:72–74.

Gilmour J. D. 2010. "Planetary" noble gas components and the nucleosynthesis history of solar system material. *Geochimica et Cosmochimica Acta* 74:380–393.

Gilmour J. D. and Turner G. 2007. Constraints on nucleosynthesis from xenon isotopes in presolar material. *The Astrophysical Journal* 657:600.

Gilmour J. D., Verchovsky A. B., Fisenko A. V., Holland G., and Turner G. 2005. Xenon isotopes in size separated nanodiamonds from Efremovka: 129Xe*, Xe-P3, and Xe-P6. *Geochimica et cosmochimica acta* 69:4133–4148.

Göbel R., Ott U., and Begemann F. 1978. On trapped noble gases in ureilites. *Journal of Geophysical Research: Solid Earth* 83:855–867.

Gros J. and Anders E. 1977. Gas-rich minerals in the Allende meteorite: Attempted chemical characterization. *Earth and Planetary Science Letters* 33:401–406.

Heber V. S., Baur H., Bochsler P., McKeegan K. D., Neugebauer M., Reisenfeld D. B., Wieler R., and Wiens R. C. 2012. Isotopic mass fractionation of solar wind: Evidencefrom fast and slow solar wind collected by the Genesis mission. *The Astrophysical Journal* 759:121.

Hewins R. H., Bourot-Denise M., Zanda B., Leroux H., Barrat J.-A., Humayun M., Göpel C., Greenwood R. C., Franchi I. A., Pont S., Lorand J.-P., Cournède C., Gattacceca J., Rochette P., Kuga M., Marrocchi Y., and Marty B. 2014. The Paris meteorite, the least altered CM chondrite so far. *Geochimica et Cosmochimica Acta* 124:190–222.

Hudson G. B., Kennedy B. M., Podosek F. A., and Hohenberg C. M. 1989. The early solar system abundance of Pu-244 as inferred from the St. Severin chondrite. Proceedings, 19th Lunar and Planetary Science Conference. pp. 547–557.

Humbert F., Libourel G., France-Lanord C., Zimmermann L., and Marty B. 2000. CO2-laser extraction-static mass spectrometry analysis of ultra- low concentrations of nitrogen in silicates. *Geostandards Newsletter* 24:255–260.

Huss G. R. and Alexander E. C. 1987. On the presolar origin of the "normal planetary" noble gas component in meteorites. *Journal of Geophysical Research: Solid Earth* 92:E710–E716.

Huss G. R. and Lewis R. S. 1994. Noble gases in presolar diamonds I: Three distinct components and their implications for diamond origins. *Meteoritics & Planetary Science* 29:791–810.

Huss G. R., Lewis R. S., and Hemkin S. 1996. The normal planetary noble gas component in primitive chondrites: Compositions, carrier, and metamorphic history. *Geochimica et Cosmochimica Acta* 60:3311–3340.

Kebukawa Y., Chan Q. H., Tachibana S., Kobayashi K., and Zolensky M. E. 2017. One-pot synthesis of amino acid precursors with insoluble organic matter in planetesimals with aqueous activity. *Science Advances* 3:e1602093.

Kruijer T. S., Burkhardt C., Budde G., and Kleine T. 2017. Age of Jupiter inferred from the distinct genetics and formation times of meteorites. *Proceedings of the National Academy of Sciences* 114:6712–6716.

Kuga M., Marty B., Marrocchi Y., and Tissandier L. 2015. Synthesis of refractory organic matter in the ionized gas phase of the solar nebula. *Proceedings of the National Academy of Sciences* 112:7129–7134.

Kuroda P. and Myers W. 1991a. Plutonium-244 dating I. Initial ratio of plutonium to uranium in the Allende meteorite. *Journal of Radioanalytical and Nuclear Chemistry* 150:35–51.

Kuroda P. and Myers W. 1991b. Plutonium-244 dating: II. Initial ratios of plutonium to uranium in the Murray and Murchison meteorites. *Journal of Radioanalytical and Nuclear Chemistry* 150:53–69.

Lavielle B. and Marti K. 1992. Trapped xenon in ordinary chondrites. *Journal of Geophysical Research* 97:20875–20881.

Le Guillou C. and Brearley A. 2014. Relationships between organics, water and early stages of aqueous alteration in the pristine CR3. 0 chondrite MET 00426. *Geochimica et Cosmochimica Acta* 131:344–367.

Lecar M., Podolak M., Sasselov D., and Chiang E. 2006. On the location of the snow line in a protoplanetary disk. *The Astrophysical Journal* 640:1115.

Lee J. Y., Marti K., Severinghaus J. P., Kawamura K., Yoo H. S., Lee J. B., and Kim J. S. 2006. A redetermination of the isotopic abundances of atmospheric Ar. *Geochimica et Cosmochimica Acta* 70:4507–4512.

Leroux H., Cuvillier P., Zanda B., and Hewins R. H. 2015. GEMS-like material in the matrix of the Paris meteorite and the early stages of alteration of CM chondrites. *Geochimica et Cosmochimica Acta* 170:247–265.

Lewis R. S., Ming T., Wacker J. F., Anders E., and Steel E. 1987. Interstellar diamonds in meteorites. *Nature* 326:160.

Lunine J. I. 2006. Origin of water ice in the solar system. In *Meteorites and the early solar system II*, edited by Lauretta D. S. and McSween H. Y. Tucson, Arizona: The University of Arizona Press. pp. 309–318.

Lyons J. R. and Young E. D. 2005. CO self-shielding as the origin of oxygen isotope anomalies in the early solar nebula. *Nature* 435:317–320.

Mabry J. C., Meshik A. P., Hohenberg C. M., Marrocchi Y., Pravdivtseva O. V., Wiens R. C., Olinger C., Reisenfeld D. B., Allton J., Bastien R., McNamara K., Stansbery E., and Burnett D. S. 2007. Refinement and implications of noble gas measurements from Genesis (abstract #1338). 38th Lunar and Planetary Science Conference. CD-ROM.

Marrocchi Y. and Marty B. 2013. Experimental determination of the xenon isotopic fractionation during adsorption. *Geophysical Research Letters* 40:4165–4170.

Marrocchi Y., Derenne S., Marty B., and Robert F. 2005. Interlayer trapping of noble gases in insoluble organic matter of primitive meteorites. *Earth and Planetary Science Letters* 236:569–578.

Marrocchi Y., Marty B., Reinhardt P., and Robert F. 2011. Adsorption of xenon ions onto defects in organic surfaces: Implications for the origin and the nature of organics in primitive meteorites. *Geochimica et Cosmochimica Acta* 75:6255–6266.

Marrocchi Y., Gounelle M., Blanchard I., Caste F., and Kearsley A. T. 2014. The Paris CM chondrite: Secondary minerals and asteroidal processing. *Meteoritics & Planetary Science* 49:1232–1249.

Marrocchi Y., Avice G., and Estrade N. 2015. Multiple carriers of Q noble gases in primitive meteorites. *Geophysical Research Letters* 42:2093–2099.

Marrocchi Y., Bekaert D. V., and Piani L. 2018. Origin and abundance of water in carbonaceous asteroids. *Earth and Planetary Science Letters* 482:23–32.

Marti K. and Mathew K. J. 1998. Noble gas components in planetary atmospheres and interiors in relation to solar wind and meteorites. *Earth and Planetary Sciences* 107:425–431.

Marti K. and Mathew K. J. 2015. Xenon in the protoplanetary disk (PPD-XE). *The Astrophysical Journal Letters* 806:L30.

Martins Z., Modica P., Zanda B., and d'Hendecourt L. L. S. 2015. The amino acid and hydrocarbon contents of the Paris meteorite: Insights into the most primitive CM chondrite. *Meteoritics & Planetary Science* 50:926–943.

Marty B., Altwegg K., Balsiger H., Bar-Nun A., Bekaert D. V., Berthelier J.-J., Bieler A., Briois C., Calmonte U., Combi M., De Keyser J., Fiethe B., Fuselier S. A., Gasc S., Gombosi T. I., Hansen K. C., Hässig M., Jäckel A., Kopp E., Korth A., Le Roy L., Mall U., Mousis O., Owen T., Rème H., Rubin M., Sémon T., Tzou C.-Y., Waite J. H., and Wurz P. 2017. Xenon isotopes in 67P/Churyumov-Gerasimenko show that comets contributed to Earth's atmosphere. *Science* 356:1069–1072.

Merouane S., Djouadi Z., d'Hendecourt L. L. S., Zanda B., and Borg J. 2012. Hydrocarbon materials of likely interstellar origin from the Paris meteorite. *The Astrophysical Journal* 756:154.

Meshik A. P., Pravdivtseva O. V., and Hohenberg C. M. 2001. Selective laser extraction of Xe-H from Xe-HL in meteoritic nanodiamonds: real effect or experimental artefact? (abstract #2158). 32nd Lunar and Planetary Science Conference. CD-ROM.

Meshik A., Mabry J., Hohenberg C., Marrocchi Y., Pravditseva O., Burnett D. S., Olinger C., Wiens R. C., Reisenfeld D., Allton J., McNamara K., Stansbery E., and Jurewicz A. J. G. 2007. Constraints on Ne and Ar fractionation in the solar wind. *Science* 318:433–435.

Meshik A., Hohenberg C., Pravdivtseva O., and Burnett D. 2014. Heavy noble gases in solar wind delivered by Genesis Mission. *Geochimica et Cosmochimica Acta* 45:1751–1788.

Meshik A. P., Pravdivtseva O. V., and Hohenberg C. M. 2016. New evidence for chemical fractionation of radioactive xenon precursors in fission chains. *Physical Review C* 93: 044614.

Nakashima D., Nagao K., and Irving A. J. 2018. Noble gases in angrites Northwest Africa 1296, 2999/4931, 4590, and 4801: Evolution history inferred from noble gas signatures. *Meteoritics & Planetary Science* 53:952–972.

Ott U. 1996. Interstellar diamond xenon and timescales of supernova ejecta. *The Astrophysical Journal* 463:344.

Ott U. 2014. Planetary and pre-solar noble gases in meteorites. *Chemie der Erde-Geochemistry* 74:519–544.

Ott U., Mack R., and Sherwood C. 1981. Noble-gas-rich separates from the Allende meteorite. *Geochimica et Cosmochimica Acta* 45:1751–1788.

Ozima M. and Podosek F. A. 2002. *Noble gas geochemistry*. Cambridge: Cambridge University Press.

Palguta J., Schubert G., and Travis B. J. 2010. Fluid flow and chemical alteration in carbonaceous chondrite parent bodies. *Earth and Planetary Science Letters* 296:235–243.

Patzer A. and Schultz L. 2002. Noble gases in enstatite chondrites II: The trapped component. *Meteoritics & Planetary Science* 37:601–612.

Pepin R. O. 2003. On noble gas processing in the solar accretion disk. *Space Science Reviews* 106:211–230.

Piani L., Robert F., and Remusat L. 2015. Micron-scale D/H heterogeneity in chondrite matrices: A signature of the pristine solar system water? *Earth and Planetary Science Letters* 415:154–164.

Piani L., Yurimoto H., and Remusat L. 2018. A dual origin for water in carbonaceous asteroids revealed by CM chondrites. *Nature Astronomy* 2:317–323.

Pignatelli I., Marrocchi Y., Vacher L., Delon R., and Gounelle M. 2016. Multiple precursors of secondary mineralogical assemblages in CM chondrites. *Meteoritics & Planetary Science* 51:785–805.

Pignatelli I., Marrocchi Y., Mugnaioli E., Bourdelle F., and Gounelle M. 2017. Mineralogical, crystallographic and redox features of the earliest stages of fluid alteration in CM chondrites. *Geochimica et Cosmochimica Acta* 209:106–122.

Porcelli D. and Ballentine C. J. 2002. An overview of noble gas geochemistry and cosmochemistry. *Reviews in Mineralogy and Geochemistry* 47:1–19.

Ragettli R. A., Hebeda E. H., Signer P., and Wieler R. 1994. Uranium-xenon chronology: Precise determination of $\lambda sf*$ 136Ys*f* for spontaneous fission of 238U. *Earth and Planetary Science Letters* 128:653–670.

Remusat L., Derenne S., Robert F., and Knicker H. 2005. New pyrolytic and spectroscopic data on Orgueil and murchison insoluble organic matter: A different origin than soluble? *Geochimica et Cosmochimica Acta* 69:3919–3932.

Remusat L., Palhol F., Robert F., Derenne S., and France-Lanord C. 2006. Enrichment of deuterium in insoluble organic matter from primitive meteorites: A solar system origin?. *Earth and Planetary Science Letters* 243:15–25.

Remusat L., Le Guillou C., Rouzaud J.-N., Binet L., Derenne S., and Robert F. 2008. Molecular study of insoluble organic matter in kainsaz CO3 carbonaceous chondrite: Comparison with CI and CM IOM. *Meteoritics & Planetary Science* 43:1099–1111.

Remusat L., Robert F., Meibom A., Mostefaoui S., Delpoux O., Binet L., Gourier D., and Derenne S. 2009. Protoplanetary disk chemistry recorded by D-rich organic radicals in carbonaceous chondrites. *The Astrophysical Journal* 698:2087.

Reynolds J. H. and Turner G. 1964. Rare gases in the chondrite Renazzo. *Journal of Geophysical Research* 69:3263–3281.

Riebe M. E., Busemann H., Wieler R., and Maden C. 2017. Closed system step etching of CI chondrite Ivuna reveals primordial noble gases in the HF-solubles. *Geochimica et Cosmochimica Acta* 205:65–83.

Robert F. and Epstein S. 1982. The concentration and isotopic composition of hydrogen, carbon and nitrogen in carbonaceous meteorites. *Geochimica et Cosmochimica Acta* 46:81–95.

Rubin A. E. 2015. An American on Paris: Extent of aqueous alteration of a CM chondrite and the petrography of its refractory and amoeboid olivine inclusions. *Meteoritics & Planetary Science* 50:1595–1612.

Rubin A. E., Trigo-Rodríguez J. M., Huber H., and Wasson J. T. 2007. Progressive aqueous alteration of CM carbonaceous chondrites. *Geochimica et Cosmochimica Acta* 71:2361–2382.

Rubin M., Altwegg K., Balsiger H., Bar-Nun A., Berthelier J.-J., Briois C., Calmonte U., Combi M., De Keyser J., Fiethe B., Fuselier S. A., Gasc S., Gombosi T. I., Hansen K. C., Kopp E., Korth A., Laufer D., Le Roy L., Mall U., Marty B., Mousis O., Owen T., Rème H., Sémon T., Tzou C.-Y., Waite J. H., and Wurz P. 2018. Krypton isotopes and noble gas abundances in the coma of comet 67P/Churyumov-Gerasimenko. *Science Advances* 4: eaar6297.

Sandford S. A., Bernstein M. P., and Dworkin J. P. 2001. Assessment of the interstellar processes leading to deuterium enrichment in meteoritic organics. *Meteoritics & Planetary Science* 36:1117–1133.

Scott E. R. and Krot A. N. 2005. Chondritic meteorites and the high-temperature nebular origins of their components. In *Chondrites and the protoplanetary disk*, vol. 341, edited by Krot A. N., Scott E. R. D., and Reipurth B. San Francisco: Astronomical Society of the Pacific. p. 15.

Vacher L. G., Marrocchi Y., Verdier-Paoletti M. J., Villeneuve J., and Gounelle M. 2016. Inward radial mixing of interstellar water ices in the solar protoplanetary disk. *The Astrophysical Journal Letters* 827:L1.

Vacher L. G., Marrocchi Y., Verdier-Paoletti M. J., Villeneuve J., and Gounelle M. 2017. Erratum: "Inward Radial Mixing of Interstellar Water Ices in the Solar Protoplanetary Disk"(2016. ApJL. 827. L1). *The Astrophysical Journal Letters* 836:L16.

Vinogradoff V., Le Guillou C., Bernard S., Binet L., Cartigny P., Brearley A. J., and Remusat L. 2017. Paris vs. Murchison: Impact of hydrothermal alteration on organic matter in CM chondrites. *Geochimica et Cosmochimica Acta* 212:234–252.

Vinogradoff V., Bernard S., Le Guillou C., and Remusat L. 2018. Evolution of interstellar organic compounds under asteroidal hydrothermal conditions. *Icarus* 305:358–370.

Weimer D., Busemann H., Alexander C. M., and Maden C. 2017. The effect of aqueous alteration on primordial noble gases in CM chondrites. *80th Annual Meeting of the Meteoritical Society*.

SUPPORTING INFORMATION

Additional supporting information may be found in the online version of this article:

Fig. S1: A) Scanning electron microscopy (SEM) images of CM 2.9 (fragment 5) and CM 2.7 (taken close to fragment 8) areas of our thin section of the Paris meteorite. The more altered zones are marked by the presence of carbonates and phyllosilicates in the matrix. These minerals are absent from the pristine areas, where free Fe-Ni metal is observed. B) Enlarged view of the two faces of our thin section of the Paris meteorite, showing the altered CM 2.7 (in blue) and the fresh CM 2.9 (in white) areas, respectively. The two yellow dotted lines show the diamond wire saw cut lines. The approximate contour lines of the four fragments (4 and 5 being CM 2.9 and 2 and 8 being CM 2.7) analyzed in this study for their heavy noble gas isotopes.

Fig. S2: ^{20}Ne, ^{36}Ar, ^{84}Kr, and ^{132}Xe pattern of release from the IOM of the Paris meteorite upon stepwise heating. Temperatures are given on the *x*-axis. The major ^{132}Xe release (>85%) occurs at 1225°C. Corresponding data are given in Tables 1, 2, 4, and 6. Uncertainties are 2σ.

Fig. S3: $^{131–136}Xe/^{130}Xe$ isotopic composition of the Paris meteorite normalized to Q-Xe (Busemann et al. 2000) (the results of the present study for the CM 2.7 and CM 2.9 bulk fragments correspond to the data points). Fission spectra for ^{238}U (left panel, dotted lines) and ^{244}Pu (right panel, dashed lines) (Porcelli and Ballentine 2002), calculated assuming that all of the excess ^{136}Xe is fissiogenic in origin, are shown for comparison. For both U and Pu, the fission spectra are within error of the data points, indicating that no distinction could be made between the major sources of fissiogenic Xe. Uncertainties are 2σ.

Fig. S4: $^{136}Xe/^{130}Xe$ measured from the four bulk fragments of the Paris meteorite (this study, in gray), normalized to the Q-phase composition (Busemann et al. 2000). For each fragment, the open ("corr. ch.") and closed ("corr. cc.") data points correspond to the $^{136}Xe/^{130}Xe$ corrected for ^{238}U- and ^{244}Pu-^{136}Xe contributions using initial $^{244}Pu/^{238}U$ of 0.0068 (chondritic value; Hudson et al. 1989) and 0.0122 (mean of carbonaceous chondrites; Kuroda and Myers 1991a, 1991b), respectively. The excess in $^{136}Xe/^{130}Xe$ relative to phase Q remains regardless of the initial $^{244}Pu/^{238}U$ taken. Uncertainties are 2σ.

4.3. Using noble gas nucleosynthetic anomalies to probe the PPD environments

Bulk nucleosynthetic anomalies in chondrites may represent primordial features of the PPD inherited from heterogeneities in the parental molecular cloud, possibly related to late injections of freshly synthesised matter during the molecular cloud infall (e.g., Clayton, 1982; Dauphas et al. 2002). Primordial heterogeneities would be preserved if for instance rapid accretion occurred before homogenization of the disk material, and/or if accretion of different meteorite classes happened sequentially with an evolving composition of the protosolar nebula. Alternatively, nucleosynthetic anomalies in chondrites could reflect fractionation processes occurring during infall (Van Kooten et al. 2016) and/or during the lifetime of the disk (e.g., Trinquier et al. 2009). Such models do not require the parental cloud to be intrinsically heterogeneous, and suggest that the PPD was possibly completely homogenised upon formation due to efficient mixing through turbulent diffusion (Trinquier et al. 2009). The heterogeneous distribution of presolar materials in chondritic and planetary bodies of the Solar System could then have arisen from subsequent fractionation processes within the PPD, possibly involving size/type sorting during transport of dust grains (Regelous et al. 2008; Dauphas et al. 2010), series of partial evaporation/condensation, and/or selective destruction of thermally labile presolar components (Trinquier et al. 2009). The Mo isotope dichotomy between NC and CC reservoirs was for instance suggested to either result from addition of *r*-process enriched material to the CC reservoir (Budde et al. 2016; Worsham et al. 2017), or preferential processing of *p*-process enriched carriers (Poole et al., 2017). Interestingly, thermal processing of dust could destroy some specific isotopically anomalous presolar phase(s) and vaporizing/releasing different phases/signatures according to their volatility. In this framework, the redox conditions of the environment would play a critical role in controlling both the efficiency of the host phase destruction, and the volatility of the element carrying the nucleosynthetic fingerprint.

Pioneering work by Huss and Lewis (1995) used presolar noble gas systematics for eighteen meteorites to derive pre-metamorphic diamond and SiC abundances in the matrix of seven chondrite classes (Fig. 58). To do so, they used Ne-A and Xe-HL contents and Ne-E and Xe-S contents to derive diamond and SiC abundances of the fine-grained matrices, respectively. Interestingly, they found that similar diamond/SiC ratios are observed across all chondrite classes, indicating that they sampled a homogenous, Solar System-wide reservoir. Furthermore, such a consistent diamond/SiC ratio despite SiC being $\geq 10^3$ times larger than diamonds suggests a limited role of grain size sorting processes in the PPD. The authors also found that, despite Orgueil (CI chondrite) having preserved the most presolar components among all samples analysed, enstatite and carbonaceous chondrites (CV and CO) may have had higher initial abundances (Fig. 58). The final abundance of presolar grains within a given matrix would mainly reflect the degree of metamorphism suffered by the host meteorite (Huss and Lewis, 1995). In this framework, the higher contribution from Xe-H suggested in Bekaert et al.

(2019a) for carbonaceous chondrites with respect to enstatite chondrties could reflect the effect of thermal processing. Indeed, EC matrices experienced higher temperatures than other chondrite classes, with no evidence for aqueous alteration. Increase of the matrix-normalized presolar grain abundances following a constant diamond to SiC ratio could have been achieved from an Orgueil matrix-like component by loss of labile phases (ice, labile organics, amorphous solids; dashed arrow, Fig. 58). The EC (noted EH on Fig. 58) metamorphic trend would then be accounted for by the preferential loss of diamonds over SiC under reducing conditions. Likewise, the CV parent matrix would have for instance initially formed by removal of volatile components from a bulk nebular starting composition represented by the matrix of Orgueil, with a higher degree of pre-accretionary thermal processing than for the EH parent. However, contrary to EC, environmental conditions would have been oxidizing for CV, therefore causing a preferential destruction of SiC compared to diamonds, and so a CV metamorphic trend going in a different trajectory than for ECs (Fig. 58; Huss and Lewis 1995). Taken together, these results suggest that, perhaps, the correlation between heliocentric distance and the amount of presolar Xe-HL from nano-diamonds could reflect the preferential loss of nano-diamonds in the inner Solar System due to enhanced thermal metamorphism under reducing conditions, and not a differential inheritance between the inner and outer Solar System as suggested by Bekaert et al. (2019a). The preponderant roles of thermal processing and environmental redox state in establishing differential presolar grain contents among chondrite classes is supported by the recent conclusions of distinct evolution of the NC and CC reservoir from Ru, Mo and W isotopes (Worsham et al. 2019). In the sequential view of the evolution of the PPD reservoirs, chondritic materials from the inner Solar System (NC) would be more thermally processed, volatile-poor and reduced than chondritic materials from beyond Jupiter (CC). Such a scenario is however not without issues, such as how to explain the fact that ordinary chondrites contain more type II chondrules characterised by low Mg# olivines (i.e., Mg# < 90) than carbonaceous chondrites, indicating their formation in more oxidizing environments (Marrocchi et al. 2018).

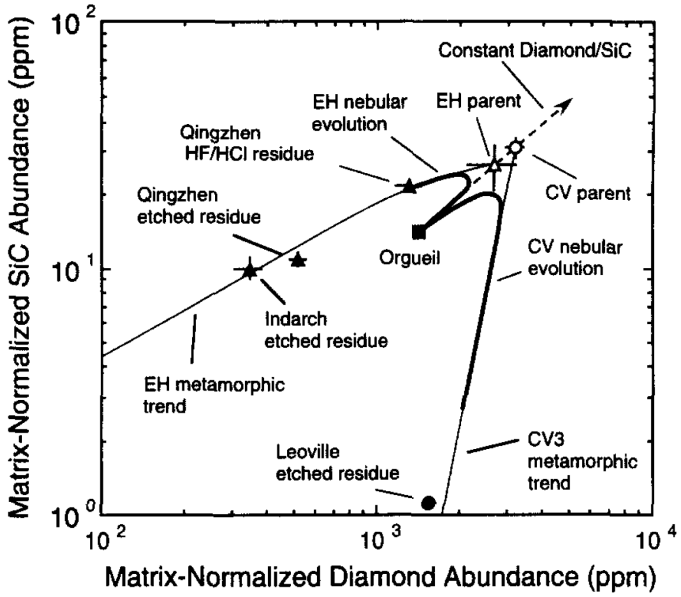

Fig. 58. Matrix-normalised abundances of SiC and diamond for the putative parent reservoirs and analysed residues from the most primitive EH and CV chondrites. Metamorphic trends are shown by light solid lines. The dashed line represents the constant diamond to Sic ratio trend passing through the Orgueil composition. Heavy solid lines represent potential trajectories of Orgueil-like materials that were thermally processed under reduced (inner Solar System) and oxidised (outer Solar System) conditions to produce the EH and CV3 chondrites, respectively. Diagram and explanations from Huss and Lewis (1995).

Finally, note that while achondrites contain limited amounts of planetary noble gases, Q-like noble gas concentrations in ureilites are unexpectedly comparable to (and in some cases even higher than) those found in the most primitive chondrites (Rai et al. 2003). Most of noble gases in ureilites are carried out by diamonds (Göbel et al., 1978; Rai et al., 2003) that, unlike nano-diamonds in carbonaceous chondrites, are of nebular (and not presolar) origin. These probably originate from shock transformation of graphite/amorphous carbon in which noble gases had been implanted as ions, as suggested by the highly fractionated elemental pattern correlating (as is the case for Q) with the respective ionization energies (Weber et al., 1971). During my thesis, we investigated the origin of noble gases in ureilites (Broadley et al. *in press*) by analysing heavy noble gases (Ar, Kr, Xe) in six unbrecciated main group ureilites, selected to cover the range of olivine Mg# seen in ureilites. Our results support the idea of the two-component mixing origin of the ureilite parent body and may highlight the heterogeneous composition of accretionary material that was present in the early inner solar system, implying that the early inner solar system was populated by both oxidised volatile-rich planetary bodies and reduced volatile-poor embryos (Broadley et al. *in press*).

Conclusion and outlook

The nature and origin of phase Q, the main carrier of heavy noble gases in chondrites, remains cryptic. Experimental investigations of noble gas trapping in growing organic materials under ionizing conditions have provided supporting evidence that the elemental and isotopic patterns of the Q signature could have been inherited from fractionation processes during the formation of insoluble organic materials in the protosolar nebula. Based on the noble gas analysis of the bulk and IOM of the Paris meteorite, the most pristine carbonaceous chondrite know to date, we provide supporting evidence that the final Q signature requires subsequent additions of a presolar component referred to as HL. Interestingly, evidence for the contribution of an interstellar-like water component has been previously found in the Paris meteorite from hydrogen and oxygen isotope systematics. We however found no evidence for cometary noble gases in the Paris meteorite. As discussed in the introduction (e.g., fig. 15), there is at present little evidence for cometary contributions within the chondritic reservoir, including the CC reservoir thought to have formed in the outer Solar System, outwith the orbit of Jupiter. The outer edges of the Solar System are populated by cometary bodies, which are characterised by extreme isotopic compositions of volatile elements (e.g., variable D/H, high $\delta^{15}N$, r-process poor Xe) that are not - or limitedly - witnessed within the chondritic reservoirs. A possibility is that these reservoirs (chondritic and cometary) were isolated from one another by a physical barrier, potentially a giant planet (Saturn? Neptune?), or a "gap" in the dynamical structure of the disk (as observed from ALMA images; *Isella et al. 2016*). This however remains, for the moment, rather speculative, but future work could further enlighten on this possibility.

Chapter 5

Extraterrestrial organic materials: an experimental investigation

Carbonaceous meteorites, the most primitive remnants of planetary body formation in the solar system, contain up to 4 wt.% carbon (Pearson et al. 2006). Organic materials in chondrites mainly occur as aromatic, macromolecular Insoluble Organic Matter (IOM, ~ 80 wt.%) and, to a smaller extent (~20 wt.%), as a complex assortment of small molecules referred to as soluble organic matter (SOM). The latter is often advocated to represent a biological interest, as primitive chondritic materials contributed to the surface of early Earth could have presumably transferred their biologically relevant molecules, therefore helping out the emergence/development of life (Pizzarello et al. 2006). Interestingly, the IOM and SOM fractions of organic materials in chondrites have extremely different compositional structures and are therefore thought to originate from very distinct environments (Rémusat et al. 2015). Whereas the IOM could originate from high temperature, radical-rich environments of the PPD (Derenne and Robert 2010), the SOM is often considered to originate from cold chemical reactions in the interstellar medium (Nuevo 2012). Note however that the composition of organic materials in the ISM/comets remains poorly constrained, and the possibility for comets and chondritic materials to share common organic source(s) is uncertain. There is a possibility that IOM and SOM fractions of chondritic organics are connected through a molecular continuum with some of the SOM originating from the processing (e.g., aqueous alteration) of part of the IOM, and some of the IOM arising from the evolution of part of the SOM through thermal processing for instance (de Marcellus et al. 2016). In addition, it is not clear if some of the IOM could have been formed in the ISM/outer Solar System, and/or some of the SOM could have been formed in the disk. The processes by which these two components were formed and evolved in space and/or within asteroids therefore remain poorly understood, and the question as to whether they are genetically related is debated.

Microwave plasma experiments designed to simulate organosynthesis potentially occurring in the irradiated surface layers of the protosolar nebula successfully reproduced some key isotopic, molecular and structural features of chondritic IOM. Here, we propose an overview of the possible source(s) of SOM and IOM in meteorites, focusing on experimental investigations aiming at simulating the processes by which it could have formed in the interstellar medium, outer solar system, PPD and/or onto the meteorite parent bodies.

5.1. SOM and IOM components in chondrites

5.1.1. Soluble Organic Matter (SOM)

Soluble organic materials in chondrites represent a complex and diverse suite of C, H, O, N and S-bearing molecules (>14,000 different compounds being found in a single meteorite; Schmitt-Kopplin et al. 2010), including carboxylic acids (the most abundant compound; Krishnamurthy et al. 1992), aromatic and aliphatic hydrocarbons, oxidised compounds (alcohols, aldehydes, ketones) and a large range of biologically relevant molecules (e.g., amino acids, sugar derivatives and nucleobases; Fig. 59). The composition and distribution of soluble molecules vary from one meteorite to another (Pizzarello et al. 2010), but it appears that abundance systematically decreases for increasing carbon number. Importantly, molecules in the extraterrestrial SOM have a complete structural diversity with all isomers being detected. This is different from molecules synthesised by biological processes, for which only one enantiomer is selected (stereo-specificity of life-related compounds), with only L-amino acids being used in the production of genetically encoded proteins. Evidence of small (<18%) enantiomeric excesses in amino acids found in carbonaceous chondrites allow the hypothesis that life's homochirality was inherited from extraterrestrial organic precursors (Engel and Macko, 1997; Pizzarello and Cronin, 2000). However, the original mechanisms allowing enantiomeric excesses in meteorites are not fully understood, and could correspond to processes occurring upon irradiation by polarised UV light with a preferential photo-dissociation of one enantiomer relative to the other (e.g., Meierhenrich et al. 2010), during aqueous alteration and/or interaction with chiral mineral surfaces (Glavin and Dworkin, 2009).

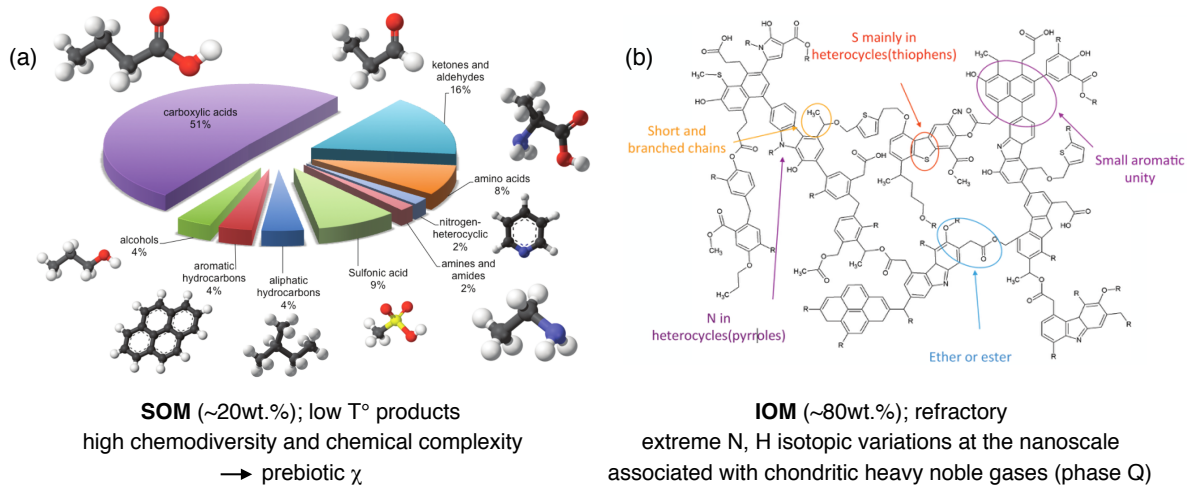

Fig. 59. Molecular composition of the SOM and IOM of the Murchison meteorite. (a) Distribution of soluble molecules in the Murchison meteorite with their model molecule represented. (b) Summary of molecular information on the chemical structure of Murchison IOM showing the main characteristics of the C skeleton and the O-, N- and S-containing groups. These two figures were adapted from Rémusat (2015), Pizzarello et al., 2006 and Derenne and Robert (2010).

There is little doubt that some of the SOM in meteorites has been in solution during parent-body hydrothermal alteration, however, it is unclear if such episodes of aqueous alteration simply mobilised the SOM initially accreted by the parent body, or produced most of the SOM *in situ*. In is generally considered that soluble compounds in meteorites originate from a complex and multi-stage series of synthesis and processing, by UV irradiation of C-bearing ices in the ISM and outer Solar System (Nuevo 2012), and/or thermal and aqueous processes of IOM degradation onto the meteorite parent bodies (accounting for the presence of aromatic compounds in the SOM; Sephton et al. 1998). Organic precursors mobilised during evolution of the parent body could have been synthesised prior to accretion, either via photochemical reactions in ice (e.g., Vinogradoff et al. 2018) or from ionization and dissociation of nebular gas in the surface layers of the PPD.

5.1.2. Insoluble Organic Matter (IOM)

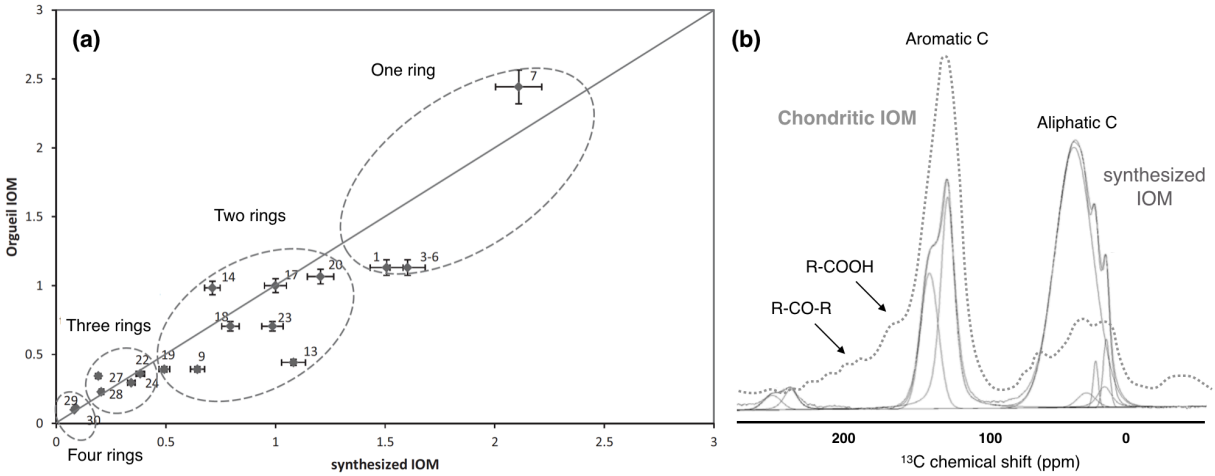

Fig. 60. Molecular composition of IOM synthesised from plasma experiments, adapted from Biron et al. (2015). (a) Relationship between relative abundances of pyrolysis products (normalised to 2-methylnaphthalene) from Orgueil IOM (Remusat et al. 2005) and synthetic IOM produced from CH_4 plasma experiments. (b) Decomposition of the solid-state ^{13}C-NMR spectrum of synthetic IOM from CH_4 plasma experiments (solid lines) compared to the typical spectrum chondritic IOM (Cody and Alexander 2005).

Based on the statistical model proposed for the molecular structure of the insoluble organic matter (IOM) isolated from the Murchison meteorite (Fig. 59b), Derenne and Robert (2010) proposed that, in the solar T-Tauri disk regions where photo-dissociation of gaseous molecules took place, aromatic structures could have resulted from the cyclisation/aromatization of short aliphatic chains in the gas. This hypothesis has been experimentally supported by plasma experiments of n-alkanes being submitted to a high frequency discharge at low pressure (Biron et al. 2015; Fig. 60). So-formed chondritic organic matter analogues exhibited similar soluble/insoluble proportions to natural samples, and successfully reproduced their hydrocarbon backbone molecular structure (Biron et al. 2015;

Fig. 60). Nebulotron experiments involving mixtures of canonical gas species reminiscent to the protosolar nebula composition (CO-N_2-H_2) have also been able to produce complex and unsaturated organic compounds with carbon structural disorder comparable to that of chondritic IOMs (Kuga et al. 2015). Whilst N-poor Nebulotron samples displayed elemental ratios and FTIR spectra comparable those of IOM from primitive chondrites, Nebulotron N-rich samples were more comparable to data obtained for ultra-carbonaceous micrometeorites (Kuga et al. 2015). Whether such Nebulotron organic materials reproduce the hydrocarbon backbone molecular structure of the IOM, as is the case for products of plasma experiments from n-alkanes, and produce some SOM relevant to that of chondrites, is not known.

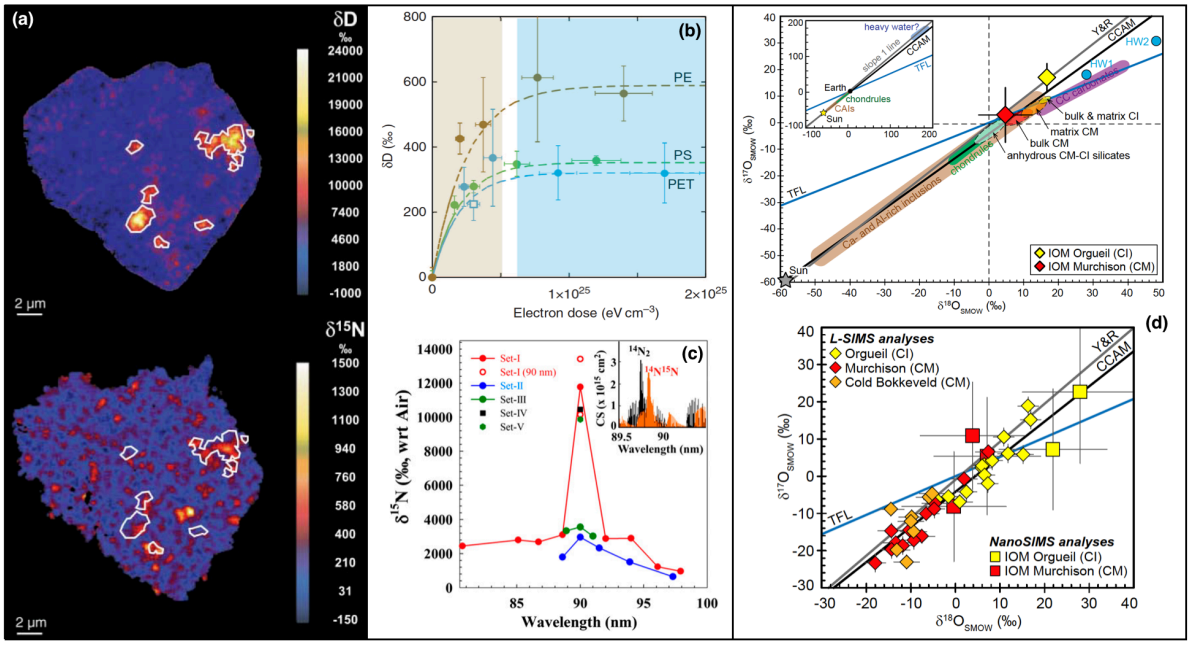

Fig. 61. Experimental and analytical insights into the origin of chondritic IOM. (a) Maps of δD and $\delta^{15}N$ of the CR2 chondrite EET 92042 IOM showing that hot spots (outlined in white) for δD do not necessarily correspond to those for N (Busemann et al. 2006). (b) δD evolution of the three polymers exposed to electron irradiation (30 keV), suggesting that ionizing radiation within the PPD could have induce quantitative deuteration of organics (Laurent et al. 2015). (c) Wavelength-dependent N-isotopic compositions with respect to air in H_2-N_2 dissociation products by VUV photons showing massive N-isotopic fractionation around 90 nm, suggesting a possible photochemical origin of ^{15}N enrichments in meteorites. Chakraborty et al. (2014). (d) $\delta^{17,18}O$ values obtained in Orgueil, Murchison, and Cold Bokkeveld IOM residues, compared to the the terrestrial fractionation line (TFL), the carbonaceous chondrite anhydrous mineral line (CCAM), Young and Russell line (Y&R), as well as the composition of multiple components of the Solar System (Sun, CI and CM chondrite components, CAIs, chondrules, carbonates and primordial water in chondrites). The O isotope composition of carbonaceous chondrite IOM falls on a slope 1 correlation line indicating it did not form on asteroidal parent bodies during low-temperature hydrothermal events, but most likely from photochemical dissociation of C-rich precursors in the gas phase (Tartèse et al. 2018).

From an isotope point of view, the chondritic IOM is characterised by the presence of (i) bulk D and ^{15}N isotope excesses relative to solar composition, with extreme cold and hot

spots at a microscopic scale (up to δD = 19,400 ± 4,600 ‰ and $\delta^{15}N$ = 3200 ±700 ‰, Busemann et al. 2006; Fig. 61), (ii) mass-independent variation in oxygen isotopes (Tartèse et al. 2018; Fig. 61), and (iii) specific elementary and isotopic patterns of noble gases associated with the so-called phase Q component (Busemann et al. 2000). Although interstellar, low-temperature ion-molecule or gas-grain reactions have long been thought to constitute the only viable mechanisms accounting for the striking enrichment in deuterium of chondritic IOM relative to the solar hydrogen reservoir, ionizing radiation within the protosolar nebula could quantitatively explain the deuteration of extraterrestrial organics (Laurent et al. 2015; Fig. 61). From an experimental point of view, chondritic IOM analogues synthesised by plasma experiments exhibit H isotopic variations (Robert et al. 2017) and noble gas signatures similar to those found in chondrititic organic matter (Kuga et al. 2015). This is however not the case for nitrogen, whose drastic isotopic variations in chondritic IOM have, so far, never been reproduced in the laboratory.

Hence, compositional and isotopic characteristics of the IOM bear a unique record of the processes and environmental conditions of IOM synthesis. Nebulotron products from plasma experiments are systematically depleted in ^{15}N by 15–25 per mil relative to the initial N_2 gas (Kuga et al. 2014), but isotope fractionation of N in the protosolar nebula could have resulted from specific isotope exchange in pre-dissiociative states (Muskatel et al. 2011). This scenario has been substantiated by photodissociation experiments with UV light from a synchrotron radiation source illuminating a N_2-H_2 mixture (Chakraborty et al. 2014; Fig. 61). The produced NH_3 shows dramatic ^{15}N excesses up to 12,000 ‰, demonstrating the possibility of extreme ^{15}N enrichments with FUV photons (Fig. 61). Another potential scenario is self-shielding within the PSN illuminated by solar photons (Thiemens and Heindenreich III 1983; Clayton 2002): far UV light (FUV) dissociates H_2, CO and N_2 and leads to the formation of reactive radicals that then evolve to form organic materials. Molecules hosting abundant isotope pairs like $^{14}N^{14}N$ or $C^{16}O$ have more efficient adsorption bands than those involving rare isotopes (D, ^{15}N, $^{17,18}O$). Dissociation of the latters will occur at greater depths in the illuminated gas cloud, resulting in progressive isotope enrichments in the recombined molecules with optical depth. Further isotope exchange with dust and convection in the disk would homogenise and disseminate isotope excesses, but how these isotope anomalies in the gas phase could have been transferred into organic solids is not known. At last, mass independent fractionation of oxygen has been observed in experiments involving ionization of gaseous oxygen-bearing molecules by either electric discharge in O_2 to produce ozone (Thiemens and Heindenreich III 1983) or FUV photodissociation of CO (Chakraborty et al. 2008). The processes responsible for such MIF are however still debated (e.g., Chakraborty et al. 2008; Lyons and Young 2005; Lyons et al., 2009).

5.1.3. A one-pot synthesis model for the SOM and IOM in chondrites?

According to pyrolytic and spectroscopic data on Orgueil and Murchison, amino acids in meteorites would neither be derived from the hydrolysis of IOM, nor originate from a common precursor (Remusat et al. 2005). Yet, a common origin for the SOM and IOM has been suggested from experimental investigations of aqueous activity in planetesimals (Kebukawa et al. 2017), photo- and thermo-chemical evolution of astrophysical ice analogues (de Marcellus et al. 2016). Whether the SOM and IOM share a common origin and are related by a molecular continuum, or originate from separate sources in the PPD/ISM, remains to be understood. On one hand, convincing evidence has been brought from plasma experiments, statistical models and isotopic analyses of natural samples that most of the chondritic IOM originates from organosynthesis in the irradiated, ionised regions of the PPD. Here, we further characterise the isotopic and molecular composition of Nebulotron organics and compare them to natural samples to derive the pros and cons of the nebular organosynthesis model. We also investigate the potential for this mechanism to also produce at least part of the SOM found in meteorites.

In this chapter, we investigate the molecular structure of Nebulotron organic products by Gas Chromatography mass spectrometry (GC-MS) and Curie point pyrolysis GC-MS (Py GC-MS), and test the model of the origin of organic materials in chondrites from the irradiated surface layers of the disk by using a numerical model of dust transport in a turbulent disk (Lagrangian Implicit Dust Transport in 3D, LIDT3D). The molecular composition of the Nebulotron SOM is then investigated for variable partial pressure of H_2 (from $< 1\%$ to $> 60\%$). At high partial pressure of H_2, organic matter production rates were very small and so measurements were carried out by Orbitrap mass spectrometry. In a second part, we explore the hydrocarbon backbone of the Nebulotron IOM by ^{13}C Nuclear Magnetic Resonance spectroscopy (^{13}C-NMR), and compare it with results obtained on chondritic IOM and products from n-alkane plasma (Biron et al. 2015). We also investigate the H and N isotopic composition of Nebulotron organic materials by NanoSIMS. Taken together, these results are used to argue the case for an intricate origin of chondritic organic materials.

5.2. Simulating nebular organosynthesis...

5.2.1. ...in the laboratory.

The main sources of ionization in the upper layers of the PPD mainly consist in stellar and interstellar UV and X-ray photons, as well as cosmic rays from the interstellar medium. Importantly, photons that ionise noble gases and dissociate N_2 and CO molecules have wavelengths below 100 nm (wavelength under which any type of window has a transmittance

of zero), which is extremely challenging to simulate in the laboratory, as it requires the use of window-less setup involving differential pumping. As part of this thesis, I worked on three distinct settings mimicking processes of irradiation of CO-H_2-N_2 gaseous mixtures in the upper layers of the protosolar nebula:

- the high-purity **Nebulotron** experiment, which I developed during this thesis.

- the **APSIS** setting (**A**tmospheric **P**hotochemistry **SI**mulated by **S**ynchrotron, at LATMOS, Guyancourt, France), commonly used to simulate photochemical processes occurring in the atmosphere of Titan (Tigrine et al. 2016).

- the **DESIRS** line (**D**ichroïsme **Et** **S**pectroscopie par **I**nteraction avec le **R**ayonnement **S**ynchrotron) at synchrotron SOLEIL (Nahon et al. 2012; Gif-sur-Yvette, France).

The latter two were specifically set up to allow for irradiation experiments involving photons with wavelengths < 100 nm. Conversely, the Nebulotron plasma experiment uses electrons as a source of ionization. Broadly speaking, a plasma environment corresponds to an electrically neutral medium of positively and negatively charged particles, with a high electrical conductivity. In ~ 1 mbar gas discharges akin to the Nebulotron, electronic densities (and ionic, as imposed by the quasi-neutrality of plasmas) are in the range 10^8 – 10^{14} particles.cm^{-3}. These densities are generally low compared to the neutral density, which is ~ 10^{16} particles.cm^{-3}. Under these conditions, the ionization degree α, defined as:

$$\alpha = \frac{electron\ density}{electron\ density + neutral\ density}$$

is in the range of 10^{-8} – 10^{-2}. The Nebulotron consists in a "cold plasma" environment, indicating it is out of thermodynamic equilibrium with the temperature of electrons being orders of magnitude higher (on the order of 10^4 K) than those of ions and neutral species (~800 K). In the Nebulotron, electrons and heavy particles initiate dissociation and ionization of molecular and atomic species, therefore initiating a series of chemical reactions producing hydrocarbon monomers that can subsequently polymerise and form solid particles. For this reason, the Nebulotron is characterised as a dusty plasma environment, with small solid particles being formed inside the plasma torch. The mechanisms and kinetics of dust formation in plasma are not fully understood, but it consists in a first phase of nucleation (i.e., formation of a solid nucleus in the gas), followed by a sequence of aggregation, accumulation and polymerization (i.e. agglomeration of several nuclei and assemblages of nuclei). Solid particles in the gas may keep growing in size through these processes, until they reach a surface and create a deposition phase akin to thin-films (Cavarroc, 2007). In the Nebulotron, all these steps occur in a very short time scale as deposition occurs around the torch, in a concentric fashion, indicating that the whole chain of reactions from ionization to deposition takes place vertically from the centre of the discharge to the surface. Importantly, organic solids thus synthesised in the plasma discharge remain very close to the torch, and could therefore experience secondary (thermal and/or irradiation) processing.

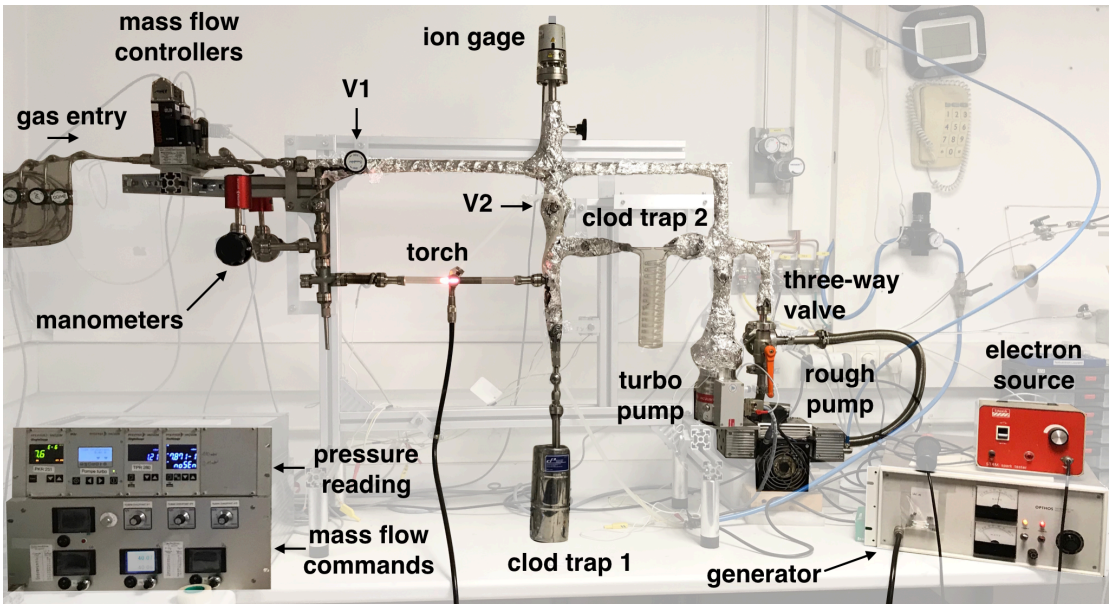

Fig. 62. Picture of the high vacuum, high purity Nebulotron setup built for the purpose of this project. The background of the image was artificially made white to emphasise the main components of the Nebulotron line, which are labelled in bold.

As part of this thesis, we did not further investigate noble gas trapping processes (Kuga et al. 2014, 2015, 2017), but aimed at investigating the molecular structure of organic materials synthesised in the Nebulotron (IOM, but also SOM if any is being produced), and compare it with chondritic organics. This project required improving the representativeness of the Nebulotron experiment for the conditions of the protosolar nebula. In previous versions of the Nebulotron, the main gases introduced in the reaction chamber where CO and N_2, with a small fraction ($\leq$ 1%) of H_2 coming in part from contamination. The line was only pumped under primary vacuum, therefore precluding efficient degassing of the walls of the line and elimination of residual water. Here, we designed a brand new version of Nebulotron, with a high-vacuum, high purity reactor and an all-metal set up allowing the system to be baked over 120°C and pumped down to pressures of 10^{-7} mbar (Bekaert et al. 2018a; Fig. 62). At the end of a given experiment, solids were recovered by disconnecting the quartz reactor from the line and gently scratching its interior surface to recover organic materials (Fig. 63). Organic materials were then stored under primary vacuum in a glass bottle at CRPG, and eventually transported to the Metis laboratory of organic chemistry (UPMC, Paris) for extraction and analysis of the SOM and IOM (Fig. 63), in collaboration with Dr. S. Derenne. All experiments reported in this chapter were carried out with a power input of the microwave discharge of 50 W and total gas pressures ~1 mbar. Hence, the main parameter we changed from one experiment to the other is the chemical composition of the gas. All Nebulotron products analysed by ^{13}C-NMR were also analysed by GC-MS and Py GC-MS. The gas mixture used in Bekaert et al. (2018a) is taken as reference, i.e. that materials synthesised for secondary processing experiments and NanoSIMS analyses were produced under the same experimental conditions as reported in Bekaert et al. (2018a), although they correspond to distinct syntheses.

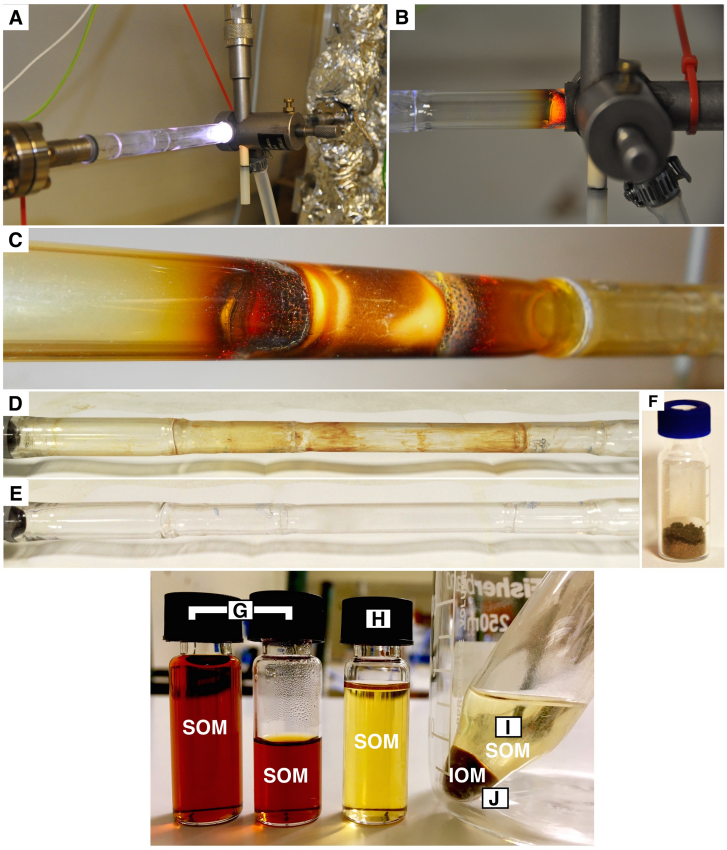

Fig. 63. Typical proceedings of a Nebulotron experiment, with the start of the plasma (a), the formation of organic materials that grow onto the surface of the reactor (b), the end of the experiment were organics can be observed (c) and recovered by scratching the interior of the quartz tube (d), which is then clean for the next experiment (e). Produced materials are stored under primary vacuum in a glass bottles (f) until they are taken to the Metis laboratory of organic chemistry (UPMC, Paris) for SOM-IOM separation (SOM: G-H-I, IOM: J) and analysis.

5.2.2. ...using numerical simulations

Our ability to produce realistic models of dust transport and mixing in PPD environments is limited by our knowledge of the exact conditions of the disk (e.g., dynamical structure, origin of turbulence, temperature and chemistry of the gas), as well as the fact that simulations are often time and computing power consuming and one wants to simplify the underlying physics to work with parameterised codes. By tracking the dynamical evolution of ice grains in the PPD and recording the environments they were exposed to, Ciesla & Sandford (2012) found that icy grains originating in the outer disk could experience sufficient UV irradiation and thermal warming in the disk to produce complex organic materials. Turbulent diffusion is hence a central mechanism accounting for the disk-wide transport of small particles in the PPD. Its formalism in numerical simulations is naturally expressed in Eulerian form, which does not allow the trajectories of individual particles to be studied, as made possible in the Lagrangian formalism. In 2011, Charnoz et al. proposed a new method (the Lagrangian Implicit Dust Transport in 3D code, LIDT3D) to combine these two formalisms through a

simple stochastic and physically justified procedure for modeling turbulent diffusion of super-particles corresponding to clouds of single sized dust grains, in a Lagrangian form. The Lagrangian description permits to investigate the evolution of each super-particle individually (Charnoz et al. 2011). At each step of the simulation (from t to t+dt), a "remapping" is processed by shifting the system to an Eulerian frame, adapted to mimic the dynamical evolution of the size distribution through processes such of gas drag and turbulence (Charnoz et al. 2015). After calculating each tracer's displacement from t to t+dt, the system is mapped back to a Lagrangian description in order to compile the new spatial distribution of sized grains.

As part of my thesis, I collaborated with Prof. S. Charnoz (IPGP, Paris) to implement in LIFT3D the production and transport of organic materials from the upper, irradiated layers of PPDs (referred to as the photosphere of the disk). I investigated the efficiency of disk-wide transport of organic materials by carrying out numerical simulations of dust transport in turbulent disks, with arbitrary organic matter production rates in the photosphere of the PPD (Bekaert et al. 2018a). As LIDT3D is written in Fortran 90, I had to work on the software *Aquamacs* to modify it, using *X11* to compile the f.90 file into an executable file and run the code (from few hours to few weeks, depending on the characteristics of the modelled PPD), and finally using *IDL - Interactive Data Language* to visualise the data. Output files were sometimes extremely heavy, reaching ~100 Go each. A very complex formalism is used in the astrophysical community to express the different physical and chemical parameters allowing describing the physics of PPDs. The most important of these are reported here below in Table 7. One of the main drawbacks of the LIDT3D code is that it simulates a static and isothermal gaseous disk structure, which means that the temperature of the gas at any radius will be uniform in the vertical direction, and constant with time. A way of implementing a time-dependent model of a gas disk in LIDT3D is proposed in the general perspectives of this thesis manuscript. Here below, I give some of the basic equations used to model the physics of the PPDs in LIDT3D. More details about the LIDT3D code can be found in the corresponding literature (Charnoz et al. 2011, 2012, 2015).

$\mathbf{M}$ = mass accretion rate	$\boldsymbol{\mu}$ = mean molecular mass of the gas
$\boldsymbol{\phi}$ = grazing angle	$\boldsymbol{L_*}$ = star luminosity
$\boldsymbol{\tau}$ = optical depth	$\boldsymbol{\kappa}$ = average opacity at wavelengths of dust thermal emission
$\boldsymbol{\Omega_V}$ = keplerian angular frequency	$\boldsymbol{\gamma}$ = adiabatic index of the gas
$\mathbf{c_s}$ = isothermal sound speed	$\mathbf{G}$ = gravitational constant
$\boldsymbol{M_*}$ = star mass	$\boldsymbol{\alpha}$ = turbulence parameter (0.01)
$\mathbf{k_B}$ = Boltzmann constant	$\boldsymbol{\sigma_B}$ = Stefan-Boltzmann constant
$\mathbf{T}$ = gas temperature	$\mathbf{r}$ = heliocentric distance (radius)
$\mathbf{H}$ = pressure scale height	$\mathbf{z}$ = vertical distance from the midplane

Table 7. Formalism used to parameterise the physical structure of the PPD.

The locally isothermal gas disk hypothesis provides simple gas density, temperature and velocity fields for the whole simulation (Charnoz et al. 2011). The temperature is defined as:

$$T(r,z) = \frac{c_s(r,z)^2 * \mu}{k_B}$$

Transport of particles through time, resulting from the competition between their settling to the midplane and vertical diffusion under turbulent gas drag, directly depends on the temperature field of the gas disk. Indeed, the turbulent diffusion coefficient of the gas (Dg) and of dust particles (Dd) are respectively given by:

$$Dg = \alpha * c_s * H = \alpha * \frac{{c_s}^2}{\Omega_v} = \alpha * k_B * \frac{T}{\mu * \Omega_v} = \alpha * k_B * \frac{T}{\mu * \sqrt{G * \frac{M_*}{r^3}}}$$

where α is usually set to 0.01, $H = c_s/\Omega_v$ and $\Omega_v = \sqrt{G * \frac{M_*}{r^3}}$

Hence, Dd is given by:

$$Dd = \frac{Dg}{Sc}$$

where Sc is the Schmitt number, tending to unity for very small particles (perfect gas-particles coupling) and increasing to infinity in the case of very big particles (completely decoupled from the gas motion). The dust scale height is slightly different from the disk pressure scale height H as it results from equilibrium between particles settling under vertical gravity and their vertical mixing because of turbulent gas drag (Brauer et al. 2008). In our case, we use the 3D gas density function proposed by Takeuchi and Lin (2002):

$$\rho_g(r,z) = \rho_0 * r^p * \exp\left(\frac{-z^2}{2 * H_0^2 * r^{q+3}}\right)$$

where ρ_0 and H_0 are the density and pressure scale height at 1AU, respectively, p and q being two constants. In the case of a central star mass of 0.5 M_*, these conditions for example yield a simulated disk with a temperature of 204 K at a unit radius, with a gas surface density of 200 $kg.m^{-2}$ (consistent with Brauer et al. 2008). The parameterization of the modelled disks is hence very simple, if not simplistic with respect to natural conditions. The thermal structure is only described by the relation $T(r)=500*\left(\frac{r}{1\,au}\right)^{\frac{-1}{2}}$ K, where r is the distance from the central star. This type of disk is therefore isothermal, i.e. the temperature is vertically uniform at a given radius. This is obviously unrealistic as, especially in the upper layers of the disk we are interested in, significant heating comes from irradiation by the central star. In the perspectives of this thesis manuscript I propose a way of improving the temperature profile of the gas disk simulated in the LIDT3D code.

The Astrophysical Journal Letter

Bekaert et al. (2018a)

The Astrophysical Journal, 859:142 (12pp), 2018 June 1

High-temperature Ionization-induced Synthesis of Biologically Relevant Molecules in the Protosolar Nebula

David V. Bekaert[1], Sylvie Derenne[2], Laurent Tissandier[1], Yves Marrocchi[1], Sebastien Charnoz[3], Christelle Anquetil[2], and Bernard Marty[1]
[1] Centre de Recherches Pétrographiques et Géochimiques, UMR 7358 CNRS—Université de Lorraine, 15 rue Notre Dame des Pauvres, BP 20, F-54501 Vandoeuvre-lès-Nancy, France; dbekaert@crpg.cnrs-nancy.fr
[2] METIS, UMR CNRS 7619, EPHE-Sorbonne Université, 4 Place Jussieu, F-75252 Paris Cedex 05, France
[3] Institut de Physique du Globe/Universite Paris Diderot/CEA/CNRS, F-75005 Paris, France
Received 2018 January 29; revised 2018 March 30; accepted 2018 April 13; published 2018 June 1

Abstract

Biologically relevant molecules (hereafter biomolecules) have been commonly observed in extraterrestrial samples, but the mechanisms accounting for their synthesis in space are not well understood. While electron-driven production of organic solids from gas mixtures reminiscent of the photosphere of the protosolar nebula (PSN; i.e., dominated by CO–N_2–H_2) successfully reproduced key specific features of the chondritic insoluble organic matter (e.g., elementary and isotopic signatures of chondritic noble gases), the molecular diversity of organic materials has never been investigated. Here, we report that a large range of biomolecules detected in meteorites and comets can be synthesized under conditions typical of the irradiated gas phase of the PSN at temperatures = 800 K. Our results suggest that organic materials—including biomolecules—produced within the photosphere would have been widely dispersed in the protoplanetary disk through turbulent diffusion, providing a mechanism for the distribution of organic meteoritic precursors prior to any thermal/photoprocessing and subsequent modification by secondary parent body processes. Using a numerical model of dust transport in a turbulent disk, we propose that organic materials produced in the photosphere of the disk would likely be associated with small dust particles, which are coupled to the motion of gas within the disk and therefore preferentially lofted into the upper layers of the disk where organosynthesis occurs.

Key words: meteorites, meteors, meteoroids – minor planets, asteroids: general – protoplanetary disks

1. Introduction

Comets and asteroids (and by extension meteorites) are the leftover solids of the formation and evolution of the solar system. Both are composed of an important proportion of organic materials ranging from simple molecules to macromolecular assemblies. For instance, comets contain a large proportion of complex organic materials (Capaccioni et al. 2015), with (i) glycine, the simplest proteinaceous amino acid, having been detected in both the cometary samples returned from the stardust mission (Elsila et al. 2009) and the coma of comet 67P/Churyumov–Gerasimenko (Altwegg et al. 2016), and (ii) high-molecular-weight organic matter (Fomenkova et al. 1994). Likewise, an extreme molecular complexity has been reported in carbonaceous chondrites (Schmitt-Kopplin et al. 2010), including a large range of biologically relevant molecules (Botta & Bada 2002). The origin of biomolecules in extraterrestrial bodies is not yet understood while it is of prime interest since external deliveries to the early Earth may have constituted an essential source of prebiotic molecules that contributed to the emergence of life (Chyba & Sagan 1992). Such exogenous supplies of organic materials could have occurred during episodes of large bombardment (e.g., during either a late veneer episode or the Terrestrial Late Heavy Bombardment around 4.0–3.8 Gyr ago) or through the continuous infall of interplanetary dust particles (IDPs; Whittet 1997).

From the interstellar medium (ISM) to the Earth's surface, the processes by which organic molecules were formed and made successively more complex vary over environmental conditions, depending on the availability of carbon and energy. Laboratory studies aiming at reproducing natural pathways of OM synthesis have proposed a series of mechanisms accounting for the presence of OM in many reservoirs of the solar system. Laboratory experiments simulating the photochemical and thermal processing of interstellar icy grains predict a wide variety of interstellar biomolecules including amino acids and nucleobases, which have never been unambiguously detected in the ISM (Nuevo 2011)—the detection of interstellar glycine being still under debate (Snyder et al. 2005). Biomolecules synthesized in the laboratory under conditions relevant to the ISM include aldehydes, simple sugars (some of which have been detected in the ISM; Hollis et al. 2000), urea, glycerol (and a number of its derivatives), hydantoin, uracil, and amino acids, especially glycine, as well as amphiphilic molecules (see Nuevo 2011 for a review). If present in the ISM, these molecules could have been delivered to the protoplanetary disk (PPD) and incorporated into the meteorite parent bodies, or (partly) destroyed en route into the disk via thermal and stellar UV processing.

As an alternative, the molecular diversity observed in meteorites could have been established during aqueous alteration processes on their parent body (e.g., aqueous alteration of polycyclic aromatic hydrocarbons, Shock & Schulte 1990; or interstellar hexamethylenetetramine, Vinogradoff et al. 2017), where warm and slightly alkaline conditions could have been favorable for the formose reaction to occur (Kopetzki & Antonietti 2011). Recently, a one-pot hydrothermal synthesis

of amino acid precursors along with macromolecular chondritic insoluble organic matter (IOM) has been proposed to occur during planetesimal aqueous activity (Kebukawa et al. 2017).

A third possibility to account for the wide diversity of biomolecules within meteorites is formation by organosynthesis within the protosolar nebula (PSN). The Fischer–Tropsch-type (FTT) catalytic reduction of CO by hydrogen in the presence of NH_3 is a possible source of organic materials and amino acids (Hayatsu et al. 1971; Nuth et al. 2008). The action of electric discharge on a mixture of CH_4, N_2, and H_2O with traces of NH_3 also produces nonprotein amino acids including those found in the Murchison meteorite (Wolman et al. 1972). Interestingly, weakly to fully ionized regions (i.e., plasma environments) are common in PPDs (Fromang et al. 2002; Walsh et al. 2012) and laboratory simulations of organosynthesis from an ionized gas-phase reminiscent of radical-rich plasma environments in the PSN (the Nebulotron experiments) have succeeded in reproducing key specific features of the chondritic IOM, including the soluble/insoluble proportions and the hydrocarbon backbone molecular structure (Biron et al. 2015), the elementary and isotopic patterns observed for chondritic noble gases (Kuga et al. 2015), as well as the occurrence of D/H hot and cold spots (Robert et al. 2017).

Here, we investigate the possible occurrence of biomolecules in organic materials synthesized from an ionized gas phase reminiscent of the PSN photosphere, where nitrogen and oxygen are initially supplied as N_2 (20%) and CO (60%), in addition to H_2(20%). The PSN photosphere corresponds here to the irradiated upper layers of the disk, exposed to stellar UV photons and X-rays and interstellar UV photons and cosmic rays. Under the canonical PSN composition, CO and N_2 molecules represent the main carrier of carbon and nitrogen atoms ($CO/CH_4 = 5$–20), $N_2/NH_3 = 10$–100) even if H_2 is largely dominant ($CO/H_2 \sim 6.10^{-4}$, $N_2/H_2 \sim 1.10^{-4}$; Iro et al. 2003). The photodissociation of CO molecules was likely effective throughout the PSN (Visser et al. 2009). The highest degrees of ionization, fractional abundances of electrons, and organic radical densities are reached in the upper layers of the disk, directly exposed to strong UV fields from the early Sun and from the ISM (Walsh et al. 2012), where most of the PSN organosynthesis is thus expected to occur (see Kuga et al. 2015 for further details). Interestingly, the remarkable variations observed for the stable isotopes of hydrogen, nitrogen, and oxygen among solar system objects and reservoirs may be accounted for by isotope fractionation during photodissociation by far-UV (FUV) light and subsequent photochemistry of diatomic molecules (e.g., CO, N_2, H_2; Chakraborty et al. 2008, 2014; Muskatel et al. 2011).

Through the use of a high-vacuum Nebulotron experiment we show that organic material can be synthesized within the irradiated upper layers of the PSN. Analysis of the molecular composition of the soluble organic matter (SOM; Neb-SOM) and IOM (Neb-IOM) fractions was carried out by gas chromatography–mass spectrometry (GC–MS) after trimethylsilyl derivatization and by Curie point pyrolysis GC–MS in the presence of tetramethylammonium hydroxide (TMAH)—these derivatizations allow the detection of polar molecules. We discuss the biological interest of several molecules detected in the SOM and IOM recovered from the Nebulotron experiment and address the astrophysical relevance and implications of organosynthesis in the hot and irradiated photosphere of the PSN, before subsequent distribution throughout the PPD. The spreading of organic materials synthesized in the photosphere of the disk is tested using a simple approach based on a numerical model of dust transport in a turbulent PPD (Charnoz et al. 2011; Charnoz & Taillifet 2012). This approach involves several uncertainties, about which we are explicit, but allows the general outlines of organic materials transport from the photosphere of the PSN to be evaluated.

2. Materials and Method

2.1. The Nebulotron Synthesis

The Nebulotron consists of a high-vacuum glass line in which adjustable gas mixtures can be flowed through a microwave (2.45 GHz) plasma discharge. For the purpose of this study, an all-metal set was used to build a high-vacuum reactor where the reaction chamber only is made from Pyrex glass, thus precluding the use of any organic joint. Before experiments, the whole system was pumped by a turbomolecular pump and baked for at least two days at ~180°C. Typical pressure before starting an experiment was $\sim 1.10^{-6}$ mbar at room temperature. A high purity gas-mixture of CO (60%), N_2 (20%), and H_2 (20%) was then flowed continuously through the plasma discharge using high-vacuum digital mass flow controllers. The total pressure in the reactor was ~1 mbar, as is commonly used for plasma experiments (see, e.g., Biron et al. 2015; Kuga et al. 2015, 2017; Robert et al. 2017) because at lower pressure the mean free path of electrons becomes too high relative to the size of our reactor. In such a case, almost no collision would occur between electrons and diatomic molecules with all electrons being neutralized onto the walls of the quartz tube. The power input of the microwave discharge was set to 50 W and the plasma was activated for 16 hr. Under these conditions, electrons and heavy particles at 800–1000 K induce the dissociation and ionization of molecular and atomic species (Kuga et al. 2015), leading to the condensation of ions and/or radicals and to the growth of solid particles onto the quartz tube surface. At the end of the experiment, solids were recovered by gently scratching the surface of the quartz reactor. Averaged solid production rates, computed as the total mass of organic materials recovered at the end of the experiment divided by the duration of the synthesis, are only indicative as they do not take into account the fractions of organic materials that are either carried away by the gas, destroyed in the reaction chamber, or lost during final collection. The organic condensates were then stored inside a desiccator at room temperature until they were recovered for separation by organic solvent extraction.

2.2. Scanning Electron Microscopy

Secondary electron imaging of organic materials produced in the high-vacuum Nebulotron and deposited in situ on a silicon wafer placed at the bottom of the quartz tube reactor was made at Centre de Recherches Pétrographiques et Géochimiques (CRPG), Nancy, France, using a scanning electron microscope (SEM) JEOL JSM-6510 equipped with an Energy Dispersive X-ray Genesis detector. A 3 nA electron beam accelerated at 15 kV was used for the observations.

2.3. Soluble Organic Matter (SOM)–Insoluble Organic Matter (IOM) Separation

The soluble fraction of the plasma-produced organic materials was extracted by stirring at room temperature in a 2:1 v/v mixture of dichloromethane and methanol. The extract was separated from the insoluble residue through centrifugation at 3500 rotations per minute and 4°C for 30 minutes. The supernatant was further concentrated using rotary evaporation and conserved in pyridine, a polar aprotic solvent for GC–MS analysis. The insoluble pellet (IOM) was dried under nitrogen. The mass balance was achieved by weighting the IOM and SOM after their separation and by comparing their sum to the initial mass of organic materials recovered from the Nebulotron synthesis.

2.4. Gas Chromatography–Mass Spectrometry (GC–MS) and Curie Point Pyrolysis GC–MS (Py GC–MS)

Analysis of the SOM and IOM of the Nebulotron were carried out by GC–MS of trimethylsilyl (TMS) derivatives and by Py GC–MS in the presence of tetramethylammonium hydroxide (TMAH), respectively (Remusat et al. 2005; Gallois et al. 2007). For the TMS derivatization, 50 μL of pyridine solution of the Neb-SOM are dried at 40°C under a N_2 flux and further added to 50 μL of BSTFA/TMCS: 99/1. After heating at 70°C for 30 minutes and drying at 40°C under a N_2 flux, the residue was dissolved in 50 μL of pyridine. 1 μL of the resulting solution was injected in GC–MS. The GC–MS device was an Agilent Technologies 6890N gas chromatograph coupled with an Agilent Technologies 5973 Network mass spectrometer. A fused silica capillary column coated with chemically bound Restek RXi-5SilMS (30 m × 0.25 mm i.d., 0.5 μm film) was used in a GC oven programmed from 80°C (30 s) to 100°C at 10°C minutes^{-1} and from 100°C to 320°C at 4°C minutes^{-1} with He as carrier gas at 1 mL mn^{-1}. The injector temperature was 280°C in split mode. The mass spectrometer was operated with an electron energy of 70 eV, an ion source temperature of 220°C, and by scanning masses from 29 to 700 amu at 2.2 scan s^{-1}.

Pyrolysis was performed using tubular ferromagnetic wires with a Curie temperature of 650°C. The wires were inductively heated using a high-frequency generator (Pilodist Curie point pyrolyzer) up to Curie temperature and maintained at this temperature for 9.9 s. For the TMAH derivatization, a few milligrams of IOM were placed in the pyrolysis wire prior to addition of a few microliters of TMAH at 25% in methanol. The pyrolysis unit was coupled to a Trace GC Ultra-DSQ MS device (ThermoFischer Technologies). The GC oven program included a first isothermal step at 50°C for 10 minutes prior to heating to 320°C at 2°C minutes^{-1} and the MS scan ranged from 29 to 800 amu at 2 scan s^{-1}.

Identification of the different compounds in both SOM and IOM pyrolysate was based on mass spectra, GC retention times, and comparison with literature data.

2.5. Numerical Simulations

Numerical simulations were carried out using the Lagrangian Implicit Dust Transport in 3D (LIDT3D) code developed by Charnoz et al. (2011, 2015), Charnoz & Taillifet (2012), Taillifet et al. (2014), and Charnoz et al. (2015). This numerical model simulates the diffusive transport of dust particles in a turbulent PPD using Lagrangian numerical simulations in combination with the Eulerian turbulent diffusion formalism, where representative particles (called "super-particles") are followed individually in the disk, taking into account gas drag and turbulent diffusion modelized as a stochastic process (Charnoz et al. 2011, 2015; Charnoz & Taillifet 2012; Taillifet et al. 2014). Here, we implemented the synthesis of organic materials from the photosphere of the PPD. Importantly, we stress that defining absolute production rates for organic materials synthesized in the photosphere of the PSN is extremely challenging since the effect(s) of different variables (e.g., degree of ionization of the gas, local pressure, gas composition) on the production rate are not yet constrained. In particular, H_2 is largely dominant in a PSN, while CO dominates the composition of the gas phase in the Nebulotron experiment. In the present study, we thus propose an a priori approach based on arbitrary production rates allowing the general sketch of the transport of organic materials synthesized in the photosphere of the disk to be evaluated. These production rates, which are orders of magnitude lower than the actual production rates derived from the Nebulotron experiments, are given in the respective figure captions. In this simple approach, we also consider that all grains have an initial budget of organic matter that is proportional to the volume of the particle. This component is a proxy of the potential inheritance from alternative processes of organosynthesis (e.g., from the ISM, by FTT reaction and/or aqueous alteration processes).

We computed the 3D transport of 30,000 super-particles subject to gravitational settling, radial drift, and turbulent diffusion, starting from a homogeneous disk (Charnoz et al. 2011). Thermal structure was set as $T(r) = 500\left(\frac{r}{1\text{ au}}\right)^{-1/2}$ K, where r is the distance from the central star. Particle granulometric cumulative distribution was computed as $x^{-2.5}$ between 1 μm and 1 cm in radius, in agreement with telescopic observations (Sicilia-Aguilar et al. 2011). The turbulence parameter α was set to 10^{-2} in order to adequately model the highly turbulent motion of particles in the upper layers of the disk, where organosynthesis occurs. We considered the presence of a dead zone from 1 to 6 au, in which the turbulence parameter α was set to 10^{-4}. In this laminar and non-accreting region of the disk, the first planetesimals are expected to form because of low fragmentation rates and low radial drift (Birnstiel et al. 2010; Charnoz & Taillifet 2012).

For each dust particle of the simulation, we considered an organic matter (SOM + IOM) content that increases when the particle is located in the photosphere of the disk. Because of their sticking efficiency (Kouchi et al. 2002), we assume that organic materials synthesized in the photosphere likely stick to the dust particles present in the local environment. The final amount of organic materials thus trapped onto the surface of a grain will depend on: (i) the surface of the grain, and (ii) the time the particle spent within the photosphere of the disk. The photosphere of the disk is taken as $2 \times H$ (that is mostly relevant in the irradiation-dominated regions of the disk, beyond 10 au—see, e.g., Figure 9 of Baillie & Charnoz 2014), where H is the local pressure height scale (see, e.g., Fromang & Papaloizou 2006). At time zero (t_0), all particles are randomly distributed throughout the system (from 0.3 to 50 au). After 500 years, when good mixing conditions have been reached, the OM synthesis starts in the photosphere and its subsequent transport within the disk is computed. Note that grain size evolution through fragmentation or coagulation (Ciesla 2006) was not considered in this study, as it would have drastically

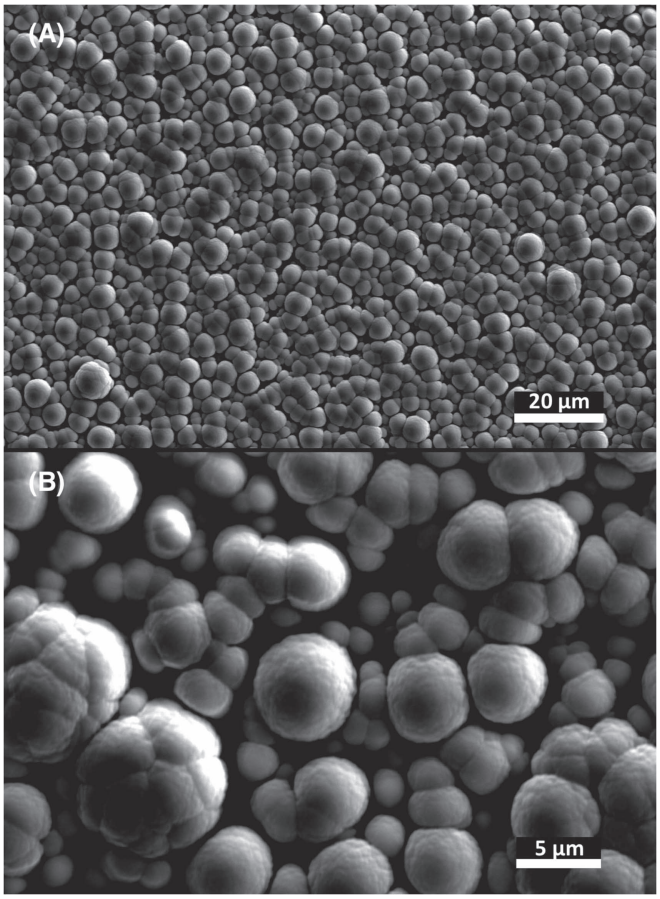

Figure 1. Secondary electron imaging (15 kV) of organic materials produced in the high-vacuum Nebulotron and deposited in situ on a silicon wafer placed at the bottom of the quartz tube reactor (magnification A: ×900, B: ×3300). We observe free μm-sized globules as well as larger globule aggregates of several microns in radius.

complicated the tracking of organic materials from one particle to another one. This limitation is discussed in Section 5.2.

3. Scanning Electron Imaging of the Nebulotron Condensates

Analogs of organic globules, which have been found in carbonaceous chondrite meteorites and IDPs (De Gregorio et al. 2010), are observed when a silicon wafer is set in the reaction chamber of the Nebulotron for in situ deposition of organic materials (see the Scanning Electron Microscopy image: Figure 1). Similar structures have already been observed from plasma experiments using benzene and anthracene (Saito & Kimura 2009). We observe that single globules of the Neb-OM have diameters of about 1 μm, although most globules are aggregated to form several μm-sized spherical structures (Figure 1).

4. Chemical Diversity and Biological Interest of the Nebulotron SOM and IOM

After 16 hr of organosynthesis, 54 mg of organic materials were produced in the plasma discharge, thus corresponding to a minimum production rate of $\sim$0.3 mg hr^{-1}, of which 80% are IOM and 20% SOM. The GC–MS trace of the SOM and the Py GC–MS trace of the IOM are given in Figure 2. The list of molecules identified in GC/MS and Py GC/MS are given in Tables 1 and 2, respectively.

While only SOMs are formed through laboratory simulations of the photochemical and thermal processing of interstellar ices (De Marcellus et al. 2016), Nebulotron experiments classically produce both soluble and insoluble materials (Biron et al. 2015). The SOM/IOM ratio of the Nebulotron condensate is 0.25, in agreement with the ratios reported for meteoritic OM, from 0.01 in the Tagish Lake chondrite to 0.3 in the Murchison and Murray CM chondrites (Pizzarello et al. 2006). A large molecular diversity is observed for the SOM and IOM of the Nebulotron condensates, with oxygen and nitrogen atoms being efficiently incorporated into highly functionalized, linear, and cyclic compounds.

The Neb-SOM contains several molecules of biological interest that have been detected in the SOM of primitive carbonaceous meteorites (e.g., hydroxy and carboxylic acids, urea, hydantoin, uracil, glycerol, and glycine derivatives; Sephton 2002; Pizzarello et al. 2006; Figure 2(A); Table 1).

Hydroxy acids detected in the Neb-SOM include lactic acid, 2-hydroxyisobutyric acid, and glycolic acid (Figure 2(A); Table 1). The conversion of glycolic acid, the smallest α-hydroxy carboxylic acid, leads to the formation of glycine (Simakov et al. 2013), the simplest but crucial proteinaceous amino acid. Some of the lactic acid derivatives are intermediate species in autocatalytic pathways of reductive carbon assimilation from carbon oxides in complex organic structures of primordial metabolism (Morowitz et al. 2000). Note here that 2-methyl-propenoic acid identified in the Neb-IOM pyrolysate (Figure 2(B); Table 2) is the product of dehydration of the 2-hydroxyisobutyric acid, pointing to the presence of common structures in soluble and insoluble OM fractions.

Carbodiimide, the major compound of the Neb-SOM (Figure 2(A)), is a reactive condensing agent capable of assembling amino acids into peptides in liquid water (Hartmann et al. 1984). Moreover, carbodiimide is the stable isomer of cyanamide, an interstellar molecule and accepted prebiotic condensing agent that hydrolyzes into urea in liquid vapor (Duvernay et al. 2004) and that is the most abundant product of the pyrolysate of Neb-IOM (Figure 2(B)). The Neb-SOM also comprises urea (Figure 2(A); Table 1), a nitrogen-bearing basic component of living systems that is required for the phosphorylation of nucleosides under prebiotic conditions. In addition, because of its high polarity and dehydrating ability, molten urea allows the thermal polymerization of amino acids under prebiotic conditions to be made (Mita et al. 2005). Formyl urea is also released upon Neb-IOM pyrolysate (Figure 2(B); Table 2). Glycerol, which is detected in NEB-SOM (Figure 2(A); Table 1), was likely involved in the prebiotic formation of triacylglycerols, which possibly formed the first cell membranes within which the first biochemical reactions took place (Nuevo et al. 2010).

Uracil—the only pyrimidine-based nucleobase detected so far in carbonaceous meteorites (Pizzarello et al. 2006)—is detected in both Neb-SOM and Neb-IOM pyrolysate (Figure 2; Tables 1, 2). In Neb-SOM, it occurs along with dihydrouracil, 2,4-dihydroxypyrimidine (the enol form of uracil) and 2-hydroxy-4-amino-pyrimidine (the enol form of the nucleobase cytosine; Figure 2(A); Table 1). Dihydropyrimidinone, a related compound, is detected in NEB-IOM pyrolysate. Uracil and cytosine are ubiquitous as nucleobases in ribonucleic acids (RNA), and thus probably played a key role during the

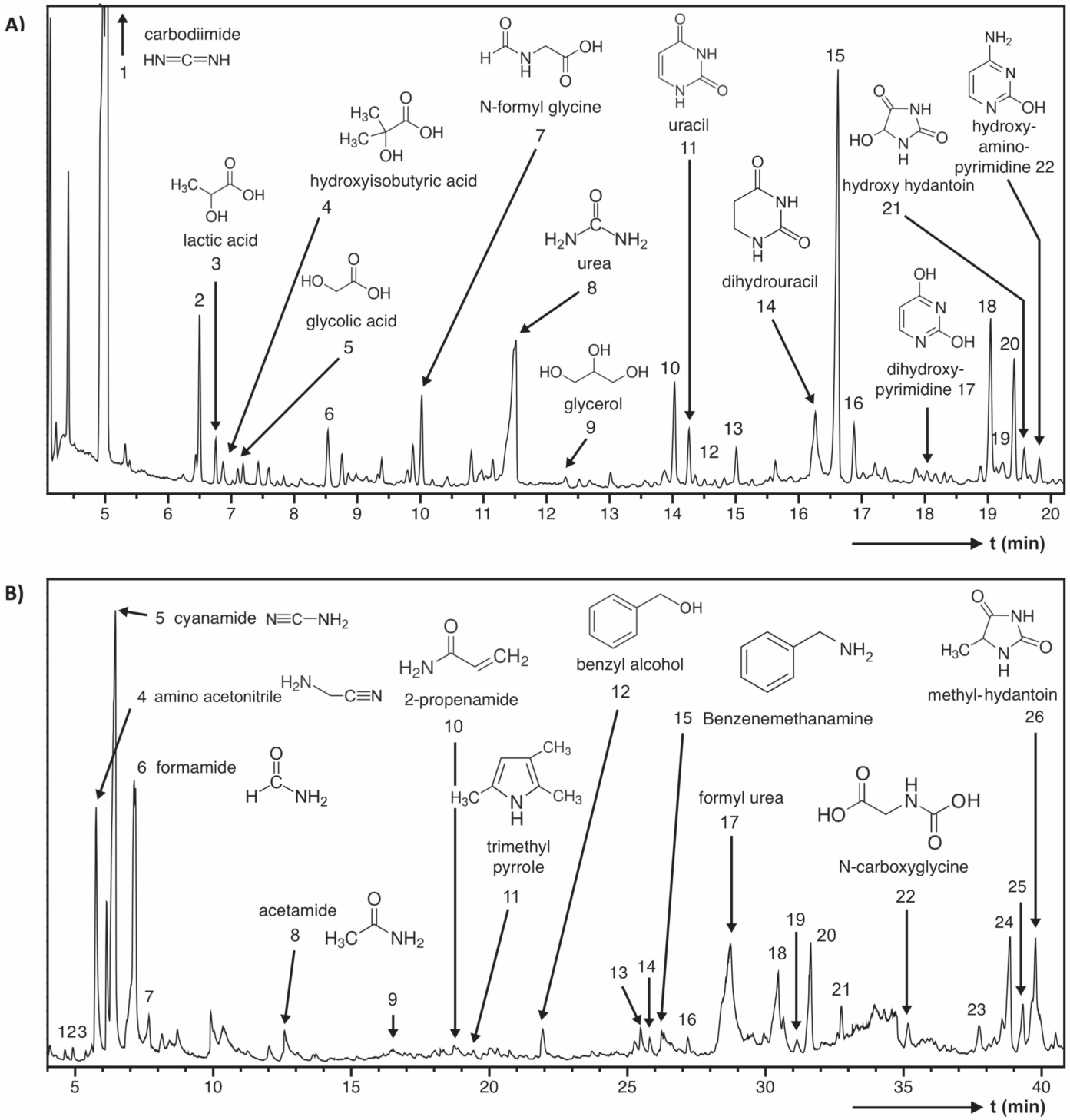

Figure 2. (A) GC–MS trace of the SOM extracted from the Nebulotron organic condensate and derivatized using BSTFA. Numbers refer to Table 1. (B) GC–MS trace of pyrolysate of the IOM isolated from the Nebulotron organic condensate in the presence of TMAH. Numbers refer to Table 2.

hypothesized "RNA world," currently regarded as a primitive stage in the early evolution of life (Gilbert 1986).

5-hydroxy-2,4-imidazolidinedione and 1-methyl-2,4-imidazolidinedione, two derivatives of hydantoin, are also identified in the Neb-SOM and Neb-IOM pyrolysate, respectively (Figure 2, Tables 1, 2). Hydantoin, commonly formed by condensation of urea and glycolic acid, is of prime interest for prebiotic chemistry since it reacts upon hydrolysis to form carbamoyl amino acids, the precursors of N-carboxyanhydride amino acids that can polymerize into poly- and oligopeptides (i.e., primitive proteins; Danger et al. 2006). Moreover, imidazolidinediones are typical pyrolysis products of protein amino acids in the presence of TMAH (Gallois et al. 2007). Finally, we report in the Neb-SOM the presence of N-formylglycine, which is known to yield glycine through hydrolysis (Bernstein et al. 2002). It must be noted that the oxidation product of this compound, N-carboxyglycine, is present in the pyrolysate of Neb-IOM, supporting again the

Table 1
List of the Identified Compounds through GC–MS in the SOM Extracted from the Nebulotron Organic Condensate after Derivatization Using BSTFA

#	Mass	Ions	Molecule Detected
1	186	171, 73, 45, 78, 186	carbodiimide
2	188	115, 131, 73, 173, 43	4-hydroxy-4-methyl-2-pentanone
3	234	147, 73, 117, 191, 45, 133	lactic acid
4	248	147, 73, 131	2-hydroxyisobutyric acid
5	220	147, 73, 173, 205, 45	glycolic acid
6	?	156, 75, 73, 55, 43, 47	UC
7	247	73, 147, 188, 104, 204	N-formylglycine
8	204	147, 189, 73, 130, 171, 45, 52, 59, 87, 157	urea
9	308	73, 147, 205, 218, 133, 117, 103, 45	glycerol
10	?	73, 102, 117, 147, 131, 45	UC
11	256	241,147, 99, 73, 255, 45, 113, 126, 59	uracil
12	255	240, 255, 147, 73, 45, 180	Pyrrole-2-carboxylic acid
13	?	73, 213, 129, 117, 45, 228	UC
14	258	243, 100, 73, 147, 59, 45, 258	dihydrouracil
15	?	229, 147, 73, 86, 100, 59, 45, 244	UC
16	?	100, 271, 73, 141, 256, 45	UC
17	256	73, 147, 256, 241, 100, 45	2, 4-dihydroxypyrimidine
18	255	73, 99, 100, 171, 241, 255	UC
19	246	75, 116, 131, 147, 231, 73, 45, 61	malonamide
20	270	73, 99, 100, 171, 255, 270	UC
21	332	147, 73, 317, 189, 202, 45, 174, 100, 117, 131	5-hydroxy-2,4-imidazolidinedione
22	255	240, 254, 73, 98, 170, 112, 45	2-hydroxy-4-amino-pyrimidine

Note. Note that the compounds occur as their silylated counterparts due to BSTFA derivatization. Numbers refer to the trace reported in Figure 1(A). UC: unidentified compound.

relationship between the two pools of synthesized OM. The early fermentation reaction of glycine could have provided a decisive energy source for primitive organisms (Clarke & Elsden 1980).

In addition to the products described above, the Neb-IOM pyrolysate also contains amides (formamide, acetamide, propanamide, and propenamide), heterocyclic nitrogenous compounds containing a pyrrole moiety (pyrrole, trimethylpyrrole), and aminoacetonitrile, which all present a biological interest (Figure 2(B); Table 2). Formamide, the simplest amide, is considered as the main building block in the origin of nucleic acids and could thus have been the starting point for prebiotic synthesis (Šponer et al. 2011). Acetamide is one among simple model molecules for the peptide linkage in polypeptides and proteins (Duvernay et al. 2004). This typical pyrolysis product from amino sugars has been detected on comet 67P/Churyumov–Gerasimenko (Goesmann et al. 2015). Moreover, malonamide, the amide of malonic acid was identified in the NEB-SOM (Figure 2(A); Table 1). Malonic acid, along with other small dicarboxylic acids, is a key compound in metabolic pathways. Pyrrole is notably formed upon pyrolysis of serine (Gallois et al. 2007). Moreover, it can further react with aldehydes to yield porphyrins (Chadha & Choughuley 1984), one of the best-known families of porphyrin metal complexes being heme, a cofactor of the protein hemoglobin. Note that the 1H-pyrrole-2-carboxylic acid identified in the Neb-SOM (Table 1) is closely linked to the amino acid (hydroxy)proline, the 2,5-dihydro-1H-pyrrole-2-carboxylic acid also being termed 3,4-Dehydro-DL-proline. Finally, aminoacetonitrile is a central molecule in the Strecker synthesis of glycine and is considered as one of the predominant ways to form amino acids in prebiotic environment and more especially in the Urey-Miller-type experiments (Miller 1996). Two compounds comprising a benzene ring and a functionalized substituent, namely, benzyl alcohol and benzenemethanamine, also contribute to the Neb-IOM pyrolyzate (Figure 2(B); Table 2).

5. Astrophysical Relevance

5.1. High-temperature Organosynthesis in the Photosphere of the PSN

These results demonstrate that electron-driven chemical reactions within radical-rich plasma environments in the PPD could supply biologically relevant molecules to the building blocks of asteroids and thus contribute to the molecular diversity of the SOM in carbonaceous chondrites (Botta & Bada 2002; Schmitt-Kopplin et al. 2010). However, pyrolysis of carbonaceous chondrite IOM yields a poorly functionalized assemblage of aromatic compounds (Remusat et al. 2005) that differs from the molecular composition reported in this study for the Neb-IOM. This indicates that either the IOM synthesized in the gas phase of the disk was subject to secondary processing accounting for its evolution toward a chondritic-like composition, or that an alternative synthesis route is at the origin of the IOM of primitive meteorites (Figure 3). For instance, the thermal alteration of organic matter is known to be associated with a step of carbonization (in the 100–500°C temperature range), which is characterized by chemical changes starting with the loss of labile chemical groups containing heteroelements (O, N) followed by that of aliphatic units, resulting in the relative enrichment in aromatic structures (aromatization; Alexander et al. 2007). Likewise, part of the biomolecules detected here in the Neb-IOM may be made soluble only during parent body aqueous alteration and secondary processing (Herd et al. 2011). While the SOM component of primitive meteorites would correspond to a pristine and undisturbed component, their IOM may partly originate from the photo- and thermo-processing of organic precursors (De Marcellus et al. 2016). Once formed in the

Table 2
List of the Identified Compounds through Pyrolysis GC–MS in the Presence of TMAH in the IOM Extracted from the Nebulotron Organic Condensate

#	Mass	Ions	Molecule Detected
1	100	41, 69, 39, 100, 85,	2-methyl-propenoic acid
2	102	43, 74, 71, 55, 59, 87	butanoic acid
3	81	81, 80, 39, 53, 42, 78, 82	1H-Pyrrole
4	84	83, 84, 58, 42, 40, 43, 57	aminoacetonitrile
5	70	69, 70, 42, 53, 71, 67	cyanamide
6	73	73, 44, 42, 43, 45, 41, 56, 58, 72, 74	formamide
7	?	58, 74, 89	UC
8	87	44, 87, 72, 43, 45, 42	Acetamide
9	87	58, 87, 57, 86, 88, 59, 42	propanamide
10	99	98, 55, 44, 58, 72, 99	2-propenamide
11	109	108, 109, 94, 67, 42	2,3,5-trimethyl-1H-pyrrole
12	122	91, 122, 121, 77, 65, 51, 39	Benzyl alcohol
13	?	125, 40, 68, 39, 96, 58	UC
14	146	115, 55, 59, 87, 45, 114	UC
15	135	58, 91, 134, 135, 42, 44, 65, 77	benzenemethanamine
16	111	111, 82, 55, 42, 56, 68	2,3-dihydro-4(1H)-pyrimidinone
17	130	44, 72, 102, 58, 42, 45	formyl urea
18	?	113, 56, 58, 85	UC
19	?	56, 140, 42, 112, 83, 69	UC
20	?	42, 127, 58, 70	UC
21	?	139, 54, 39, 82, 58, 110, 124	UC
22	161	102, 58, 42, 59, 130, 161	N-carboxyglycine
23	?	42, 127, 98, 70, 55, 138, 153	UC
24	?	128, 42,43, 100, 70, 56, 136	UC
25	140	140, 55, 83, 54, 70, 40, 111, 82,	uracil
26	142	42, 127, 142, 56, 57, 58, 70, 99	1-methyl-2,4-imidazolidinedione

Note. Note that the compounds occur as their methylated counterparts due to TMAH. Numbers refer to the trace reported in Figure 1(B). UC: unidentified compound.

photosphere of the disk, organic material interaction with soft X-rays and/or ionized molecules (H_2D^+; Robert et al. 2011) could lead to the deuterium enrichments observed in extra-terrestrial organic matter. These results indicate that part of the biomolecules detected in the SOM of primitive meteorites could have been synthesized in the photosphere of the PSN, but that a unique environment/mechanism of organosynthesis may not account for both the SOM and IOM observed in meteorites. A similar conclusion was reached from pyrolytic and spectroscopic studies of the IOM and SOM from Orgueil and Murchison carbonaceous chondrites (Remusat et al. 2005).

Importantly, chondritic noble gases are intimately associated with the IOM in meteorites, likely pointing to a common and pre-asteroidal accretion origin. It is demonstrated that ionizing conditions were required for the chondritic noble gas isotopes to be efficiently incorporated in organic materials and fractionated as systematically observed in chondrites (Marrocchi et al. 2011; Kuga et al. 2015). This suggests that the IOM of meteorites is mainly formed within organic-radical-rich environments of the PSN, as attested by the macromolecular structure of the IOM isolated from Murchison meteorite (Derenne & Robert 2010). Based on previous Nebulotron experiments (Kuga et al. 2015), we conclude that radical-rich environments in the PSN probably supplied most of the chondritic IOM, and could also have supplied part of the biomolecules observed in comets and meteorites. However, it is not yet possible to discriminate the exact conditions (e.g., redox) that led to the synthesis of organic molecules in the photosphere of the disk. The respective contributions of radicals, ions, and neutral species, as well as the possible role of catalysts (e.g., grain surfaces) in the chemical reaction leading to the formation of organic molecules in the gas phase of the PSN are not unraveled. The photosphere of the disk contains the highest concentrations in both ionized species and radicals within the disk, and therefore, regardless of the exact nature of the dominating reagents (ions, radicals, and/or neutral species), constitutes the more likely environment for organosynthesis to occur.

Ionization sources in PPDs are multiple (UV photons from parent T-Tauri stars, X-rays, and excess UV photons from accretion shocks and lightning, interstellar UV photons and cosmic rays, radioactive decays of ^{26}Al and ^{40}K isotopes, thermal excitation in the hot zones), making the synthesis of organic molecules potentially ubiquitous in the PSN (Figure 3). The synthesis of organic compounds, including biomolecules, in the PSN would be the most effective in the disk's photosphere, where the degrees of ionization, fractional abundances of electrons, and organic radical densities are the most elevated (Walsh et al. 2012; Robert et al. 2017). This does not, however, preclude other pathways of biomolecule synthesis in the ISM (Nuevo 2011) or during asteroidal aqueous alteration (Kebukawa et al. 2017; Figure 3), but indicates that meteoritic and cometary biomolecules were possibly supplied from radical-rich plasma environments in the PSN. The different synthesis routes of organic materials in the PSN are summarized in Figure 3. By analogy with the outward transport of crystalline silicates to the region of long-period comet formation (Bockelée-Morvan et al. 2002), organic materials synthesized in the solar nebula—e.g., formamide, glycine—could have been efficiently transported outward by turbulent motion or by bipolar outflows to the regions where they are now detected in comets. Infrared observations of classical T-Tauri stars demonstrate that simple molecules (e.g., CO_2, HCN, C_2H_2) are common in protostellar nebulae and that the gas temperatures (200–800 K) and emitting areas are consistent with the emission originating in a warm disk atmosphere (Carr & Najita 2011). Reaction rates of the various chemical processes at stake in the Nebulotron experiment would likely be smaller in the effective photosphere of the PSN where H_2 and He largely dominate the gas composition (Iro et al. 2003) and the gas pressure is <1 mbar (Walsh et al. 2010). The photon-dominated region (PDR; with gas temperatures of a few thousand K) is almost fully ionized (Glassgold et al. 2004; Woitke 2015). The underlying warm molecular layer (WML; with gas temperatures $\leqslant 1000$ K) is also largely ionized but with a mean lifetime of organic molecules being much longer than in the PDR. The WML has a very active chemistry and is mainly responsible for the observable line emissions in the near-IR and mid-IR (Woitke 2015). These two layers of the disk constitute here the so-called photosphere of the PSN (Figure 3). The high temperature of neutral gas in the Nebulotron plasma (800–1000 K) is mostly relevant to thermal conditions expected for the WML of the disk where organosynthesis takes place (Glassgold et al. 2004; Figure 3).

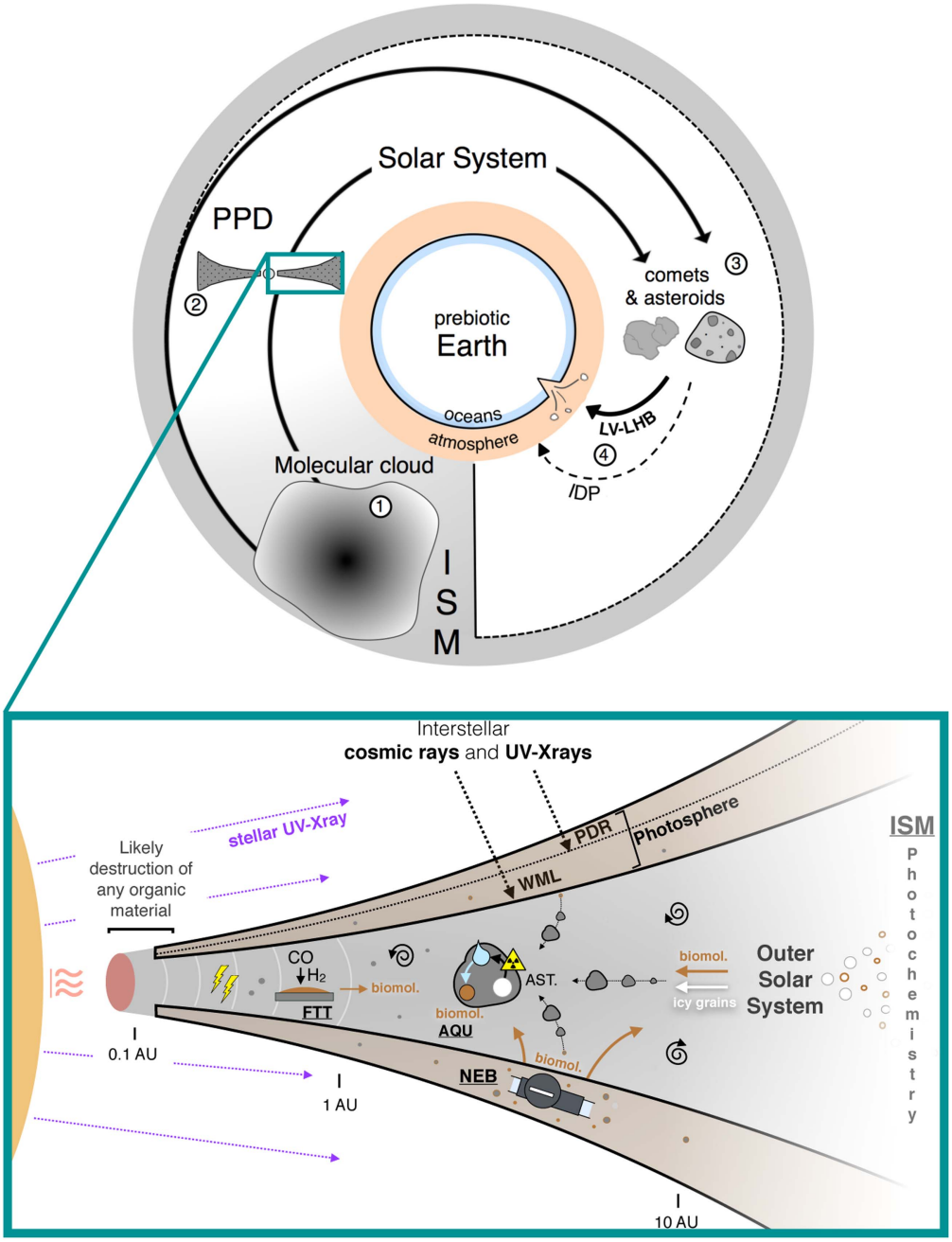

Figure 3. Possible exogenous sources of organic molecules on prebiotic Earth. Interstellar materials are either unprocessed by the PPD phase and directly incorporated into cometary bodies, or processed by the PPD phase and incorporated into comets and asteroids. Both comets and asteroids were supplied to the early Earth during the final building stages of the Earth (Late Veneer episode, LV, or, more probably, Late Heavy Bombardment, LHB; Marty et al. 2016). Subsequent and continuous addition through the continuous infall of interplanetary dust particles (IDPs) is also considered (Whittet 1997). The zoomed-in section highlights the principal routes of extraterrestrial biomolecule synthesis/processing in the PSN. FTT: Fischer–Tropsch-type (FTT) catalytic reduction of CO by hydrogen (Hayatsu et al. 1971; Nuth et al. 2008). Thunderbolts refer to processes of organosynthesis induced by spark discharges (Wolman et al. 1972; Desch & Cuzzi 2000). The melting of accreted ice upon radioactive heating may induce processes of organosynthesis during aqueous alteration (AQU) of asteroids (AST; Kopetzki & Antonietti 2011; Kebukawa et al. 2017). NEB refers to the Nebulotron experiments, with a high-temperature organosynthesis upon irradiation in the photosphere (i.e., photon-dominated region, PDR, and Warm Molecular Layer, WML; Kuga et al. 2015) of the PSN (this study). Nebular organic materials and biomolecules (including supplies from the ISM) would be widely distributed in PPDs through turbulent diffusion (depicted as whirls), thus pointing to a complex origin of the extraterrestrial organics that were delivered to prebiotic Earth.

In this region, the gas temperature is thought to be higher than that of the grains (Walsh et al. 2010; Woitke 2015). The temperature of the surface of the quartz tube reactor in the Nebulotron experiment, also lower (~500 K) than that of the gas, might therefore be considered as analogous to the surface of solid particles lofted to the WML by turbulent diffusion (see Section 5.2).

The irradiation of an achiral ice mixture with circularly polarized light in the UV range has successfully produced amino acids with enantiomeric excesses proportional to the number of polarized photons and of opposite signs with respect to light polarization (De Marcellus et al. 2011). This latter point brings a possible explanation to the longstanding issue of the origin of biomolecules laevo-rotatory (L) amino acids

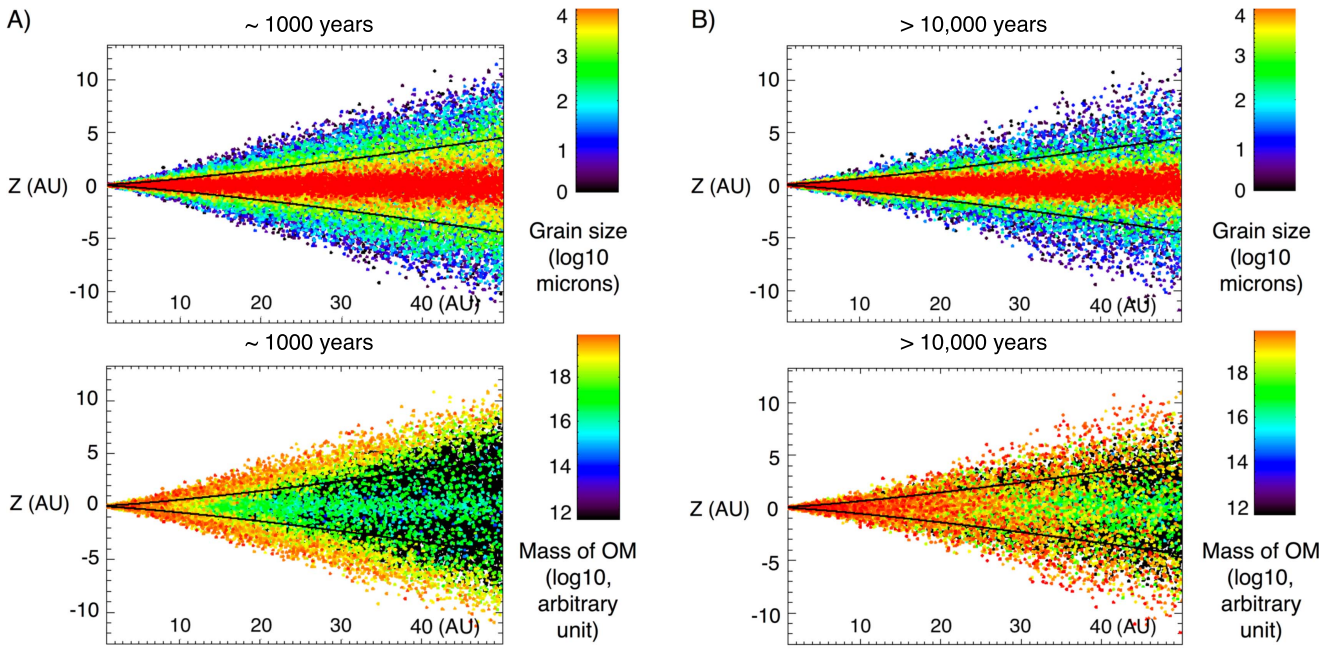

Figure 4. Grain size and mass distribution of organic materials in the disk, after ∼1000 years (A) and >10,000 years (B) of numerical simulation. The solid horizontal lines show the location of the pressure scale height (H; Charnoz et al. 2011). The grain size distribution clearly shows the sedimentation process, with small particles being widely spread vertically, whereas big particles sediment rapidly and gather close to the midplane ($z = 0$). Small particles are coupled with the turbulent motion of the gas and are therefore continuously lofted to the photosphere of the disk (taken over $2{*}H$) where organosynthesis occurs. Initial content of organic matter: 10^{-14} kg m^{-3}. Production rate in the photosphere: 10^{-18} kg m^{-2} s^{-1}.

homochirality in living systems. In this scenario, exogenous organics displaying slight L excess (Pizzarello et al. 2006) would have been delivered to early Earth, thus transferring their asymmetry to the prebiotic building blocks of life (Figure 3). While chiral excesses would be hard to generate in the context of liquid-water reactions on meteorite parent bodies or FTT reactions, biomolecule synthesis within the irradiated environments of the disk provides an alternative pathway for the formation of molecules relevant to life in space and opens a promising avenue of investigation for achiral chemistry upon irradiation in the PSN photosphere. Analyzing organic materials synthesized in the high-vacuum Nebulotron plasma setting for their nitrogen and hydrogen isotopes might also provide a test to extrapolate experimental results to some natural environments. The fact that nitrogen trapped in organics produced during plasma organosynthesis does not reproduce the ^{15}N enrichments observed in meteorites IOM (Kuga et al. 2014), whereas some H isotope anomalies are reproduced (Robert et al. 2017) is consistent with D/H versus ^{15}N/^{14}N variations in meteoritic organics (Aléon 2010), potentially pointing to different isotope fractionation mechanisms for H and N in the PSN.

5.2. LIDT3D Code and Turbulent Diffusion of Organic Materials in the Disk

The turbulent diffusion of dust grains subject to gravitational settling, radial drift, and turbulent diffusion in a PPD has been investigated by a stochastic and physically justified procedure developed by Charnoz et al. (2011) and Charnoz & Taillifet (2012). Our simple approach, based on this numerical model of dust transport, predicts the general outlines of the transport of organic materials—including biomolecules—synthesized in the photosphere of the disk and investigates their relationship with dust grains (see Section 2.5).

Figures 4(A)–(B) display both the grain size distribution and the repartition of organic materials in the disk, after ∼1000 years and >10,000 years evolution, respectively. At ∼1000 years, we observe a sedimentation process, with the largest particles already settling to the midplane (in red; $z = 0$), while smaller particles are distributed over the height of the disk because of their diffusion due to the turbulent motion of the gas (Charnoz et al. 2011). The fraction of organic matter present at the midplane (in green; Figure 4(A)), associated with the larger particles of the disk, would experience little exposure to irradiation in the photosphere and, thus, would remain preserved as pristine material. These materials would rapidly be incorporated into the first planetary bodies forming at the midplane after inward drift. In contrast, the fraction of organic matter present in the upper layers of the disk (in red; Figure 4(A)) is associated with the particles of smaller sizes. The motion of small dust particles is tightly coupled to that of the gas (Charnoz et al. 2011). Hence, small grains are preferentially lofted by turbulent diffusion to the photosphere of the disk where organosynthesis occurs. In addition, they have high surface/volume ratios, thus maximizing the amount of organic materials possibly trapped at the surface of dust particles. Organic materials covering the surface of silicate grains would likely enhance their sticking efficiency (Kouchi et al. 2002). This would result in increased grain coagulation rates, thus favoring conditions that trigger streaming instabilities (Bai & Stone 2010; Drążkowska & Dullemond 2014) and an enhanced growth of macroscopic bodies such as planetesimals or future asteroids (Kouchi et al. 2002; Figure 3). Such a transport of newly formed organic materials (including biomolecules) from the irradiated and hot regions of the disk, where they are synthesized, to shielded parts of the midplane would ensure their efficient preservation in meteorite parent bodies, and would account for the intimate association of

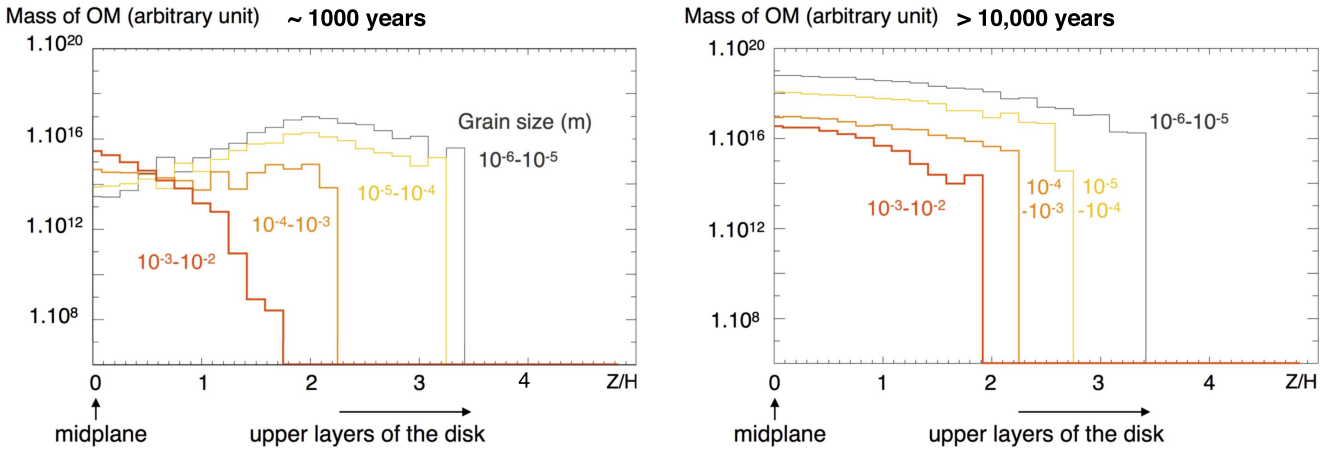

Figure 5. Vertical distribution of the OM as a function of the size category and vertical position of the particles integrated from 7 to 50 au (i.e., over the radius of the disk except the dead zone). The vertical position is given as the actual height (Z) normalized to the pressure height scale at the corresponding radius (Z/H ratio). The picture is displayed at ~1000 years and more than 10,000 years of numerical simulation. Initial content of organic matter: 10^{-14} kg m^{-3}. Production rate in the photosphere: 10^{-18} kg m^{-2} s^{-1}.

meteoritic organic matter and silicates as observed in meteorites (Zega et al. 2010).

In Figure 4(B) (>10,000 years), we observe that the fraction of organic matter associated with the smaller particles (in red) is progressively distributed in the PPD by turbulent diffusion and gas drag. Organic materials synthesized in the photosphere of the disk could thus potentially represent precursors of meteoritic and cometary organics, before their thermal/photoprocessing and subsequent modification by secondary parent body processing. The coupled effect of gas drag and turbulent diffusion induces an inward transport of dust in the disk's midplane where the disk is sub-Keplerian toward the region of planetesimal formation, while favoring outward transport (toward the comet formation region) in the disk's upper layers (Charnoz et al. 2011) where the disk is super-Keplerian.

The same conclusions can be drawn from the analysis of Figure 5, which displays the distribution of the OM as a function of the size and vertical position of the particles integrated from 7 to 50 au (i.e., over the radius of the disk except the dead zone). The vertical position is given as the actual height (Z) normalized to the pressure height scale at the corresponding radius (Z/H ratio). We observe that, whereas large particles dominate the budget of organic matter close to the midplane at ~1000 years, small particles dominate this budget after 10,000 years of simulation. This is due to the fact that small particles are continuously lofted to the photosphere of the disk where organosynthesis occurs. They accumulate more and more organic materials and keep being transported throughout the disk—including to the midplane—by turbulent diffusion (Figure 3). Note that alternative pathways of organic matter synthesis (Figure 3) may be effective in the deeper layers of the disk (e.g., FTT reactions, asteroidal aqueous alteration that may occur at later times), but are not modeled here, the main point of this discussion being to track the transport of organic materials synthesized in the photosphere of the PSN.

As depicted in Section 2.5, defining absolute production rates for organic materials synthesized in the photosphere of the PSN is extremely difficult. Here, our a priori approach based on arbitrary production rates allows the general sketch of the transport of organic materials synthesized in the photosphere of the disk to be evaluated. Interestingly, the possibility that the disk is mostly laminar in its midplane (Inutsuka & Sano 2005; Okuzumi & Hirose 2011) and very turbulent in its upper layers (see, e.g., Schnepf et al. 2015) is heavily debated. An almost laminar midplane ($\alpha \sim 10^{-4}$) would promote coagulation as a result of lower encounter velocities between particles. In the case of a PPD containing a dead zone, it has been shown that coagulation processes rapidly produce big particles, up to 10 cm in size, close to the disk's midplane (Charnoz & Taillifet 2012). Here, grain size evolution through fragmentation or coagulation could not be taken into account since it would have drastically complicated the tracking of individual super-particles content of organic matter. We note that the effect of a dead zone mainly affects the largest grains (>0.1 mm in size; Charnoz & Taillifet 2012), which are not the main carriers of organic materials in our simulations (Figures 4–5). We find that organic materials synthesized in the photosphere of the PSN would likely be associated with small dust particles, which are coupled to the motion of the gas and therefore preferentially lofted to the upper layers of the disk where organosynthesis occurs. Larger particles would likely settle at the midplane before experiencing inward radial drift and being trapped in the dead zone where enhanced particle growth occurs (Charnoz & Taillifet 2012). According to our model, in the case of low production rates in the photosphere of the disk, most of the organic matter present in the disk would correspond to materials inherited from alternative processes of organosynthesis, distributed in volume within the particles (Figure 3). In this case, the dead zone, which concentrates the largest particles, would be enriched in organic materials relative to the rest of the disk (Figure 6(A)). In the case of high organic matter production rates in the photosphere relative to the content of organic materials distributed in volume within particles and inherited from alternative processes of organosynthesis (Figure 6(B)), organic materials are mostly associated with the smallest grains, which are spread out within the disk by turbulent diffusion and little affected by the presence of the dead zone. Over the lifetime of the disk, the gas phase is expected to progressively dissipate (which is not simulated here using the LIDT3D code because of mass conservation), thus allowing the smaller particles to definitively settle at the midplane and be incorporated in the planetary bodies. If freely

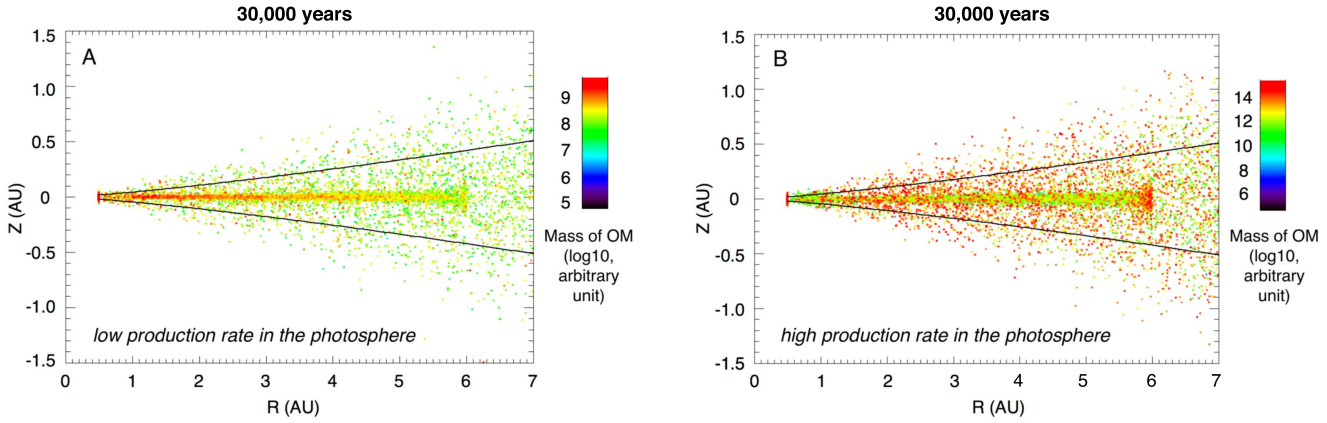

Figure 6. Mass distribution of organic materials in the inner part of the disk, where a dead zone is present (from 1 to 6 au), after 30,000 years of numerical simulation, in case of low (A) and high (B) organic matter production rates in the photosphere. The initial budget of organic matter of each grain (proportional to the volume of the particle and taken as a proxy of the potential inheritance from alternative processes of organosynthesis; Figure 3) is the same for both simulations. The solid horizontal lines show the location of the pressure scale height (H; Charnoz et al. 2011). Initial content of organic matter: 10^{-14} kg m^{-3} for (A)–(B). Production rate in the photosphere: 10^{-26} kg m^{-2} s^{-1} (A) and 10^{-20} kg m^{-2} s^{-1} (B).

transported in the gas phase and not trapped at the surface of silicate grains, organic globules as synthesized in the reaction chamber of the Nebulotron ($\sim$1 μm in size; Figure 2) would experience a wide transport within the PPD, by analogy with the random and extensive trajectories of μm-sized particles subject to turbulent diffusion in the PSN (Charnoz et al. 2011; Figure 3). Organic globules synthesized in the photosphere of the PSN could thus represent precursors of the globules observed in carbonaceous chondrite meteorites and IDPs (De Gregorio et al. 2010).

It should be noted that the gas disk considered in this paper is a simple, turbulently active, and non-evolving parameterized gaseous disk (Takeuchi & Lin 2002; Charnoz et al. 2011) that has been chosen for the sake of simplicity. Very short timescales (on the order of tens of thousand years) were sufficient to derive the general sketch of such a transport. The total amount of organic materials present in the disk increased linearly with time after only a few thousand years, following the same trend of organic matter spatial distribution as described in this paper. Note that the diffusion time of particles from the photosphere of the disk (at $z = 2{*}H$) to the midplane (at $z = 0$) is given by $(2{*}H)^2/D_{\rm d}$, with $D_{\rm d}$ the dust diffusion coefficient given calculated as $D_{\rm d} \sim \alpha{*}{\rm Cs}{*}{\rm H}/{\rm Sc}$, where Cs is the local sound velocity and Sc is the Schmidt coefficient tending to 1 in the limit of very small particles and increasing to infinity for large particles (Youdin & Lithwick 2007). According to our model, the diffusion time of small particles ($\propto 1/\alpha$) would thus increase by two orders of magnitude for a disk with an α parameter set at 10^{-4} instead of 10^{-2}. Grain size evolution through coagulation, which has not been taken into account here, should play an important role in the transport of newly formed organic materials (including biomolecules) from the irradiated and hot regions of the disk, where they are synthesized, to shielded parts of the midplane were they would be preserved in meteorite parent bodies.

6. Conclusion

A high-vacuum plasma setting was designed to produce organic condensates from a high purity gas phase reminiscent of the irradiated environments in the PSN. Recovered materials exhibit a large range of biomolecules, including amino acid and nucleobase derivatives, which have been detected in meteorites and are expected to have played a key role in the emergence of life on prebiotic Earth. This finding does not preclude other pathways of biomolecules synthesis in the ISM and/or during asteroidal aqueous alteration but indicates that processes of biomolecule synthesis could have been also effective in the hot and ionized photosphere of the PSN. The apparent extensive radial mixing that occurred in the early solar system and the multiple potential sources of organics and biomolecules in the inner solar system (e.g., inward contribution of interstellar/cometary organics, high-temperature synthesis in the photosphere or FTT reactions in the PSN, aqueous alteration of organic materials onto meteorite parent bodies) point to a complex origin of the extraterrestrial organic matter and biomolecules that were delivered to prebiotic Earth.

Laurette Piani and Michael Broadley are thanked for participating in fruitful discussions. We thank Delphine Lequin for technical assistance. We gratefully acknowledge the two anonymous reviewers and the Editor for their constructive comments. This study was supported by the European Research Council (PHOTONIS project, grant agreement No. 695618 to B.M.). This is CRPG-CNRS contribution 2587. Author contributions: D.B., Y.M., L.T., and B.M. participated in designing and building the high-vacuum Nebulotron. D.B. did the organic synthesis and recovery from the discharge tube. D.B., S.D., and C.A. performed the soluble organic matter (SOM)—insoluble organic matter (IOM) separation and analyses by GC–MS and Curie point pyrolysis GC–MS (Py GC–MS). D.B. and S.C. did the numerical simulations. All the authors discussed the results and their interpretations. D.B., Y.M., B.M., S.D., and S.C. wrote the manuscript. The authors declare no competing financial interests.

ORCID iDs

David V. Bekaert https://orcid.org/0000-0002-1062-6221
Yves Marrocchi https://orcid.org/0000-0001-7075-3698
Sebastien Charnoz https://orcid.org/0000-0002-7442-491X
Bernard Marty https://orcid.org/0000-0001-7936-1519

References

Aléon, J. 2010, ApJ, 722, 1342
Alexander, C. O. D., Fogel, M., Yabuta, H., & Cody, G. D. 2007, GeCoA, 71, 4380
Altwegg, K., Balsiger, H., Bar-Nun, A., et al. 2016, SciA, 2, e1600285
Bai, X. N., & Stone, J. M. 2010, ApJ, 722, 1437
Baillie, K., & Charnoz, S. 2014, A&A, 786, 35
Bernstein, M. P., Dworkin, J. P., Sandford, S. A., Cooper, G. W., & Allamandola, L. J. 2002, Natur, 416, 401
Birnstiel, T., Dullemond, C. P., & Brauer, F. 2010, A&A, 513, A79
Biron, K., Derenne, S., Robert, F., & Rouzaud, J. N. 2015, M&PS, 50, 1408
Bockelée-Morvan, D., Gautier, D., Hersant, F., Huré, J. M., & Robert, F. 2002, A&A, 384, 1107
Botta, O., & Bada, J. L. 2002, SGeo, 23, 411
Capaccioni, F., Coradini, A., Filacchione, G., et al. 2015, Sci, 347, aaa0628
Carr, J. S., & Najita, J. R. 2011, ApJ, 733, 102
Chadha, M. S., & Choughuley, A. S. U. 1984, OrLi, 14, 469
Chakraborty, S., Ahmed, M., Jackson, T. L., & Thiemens, M. H. 2008, Sci, 321, 1328
Chakraborty, S., Muskatel, B. H., Jackson, T. L., et al. 2014, PNAS, 111, 14704
Charnoz, S., Aléon, J., Chaumard, N., Baillié, K., & Taillifet, E. 2015, Icar, 252, 440
Charnoz, S., Fouchet, L., Aleon, J., & Moreira, M. 2011, ApJ, 737, 33
Charnoz, S., & Taillifet, E. 2012, ApJ, 753, 119
Chyba, C., & Sagan, C. 1992, Natur, 355, 125
Ciesla, F. J. 2006, ApJL, 654, L159
Clarke, P. H., & Elsden, S. R. 1980, JMolE, 15, 333
Danger, G., Boiteau, L., Cottet, H., & Pascal, R. 2006, JAChS, 128, 7412
De Gregorio, B. T., Stroud, R. M., Nittler, L. R., et al. 2010, GeCoA, 74, 4454
De Marcellus, P., Fresneau, A., Brunetto, R., et al. 2016, MNRAS, 464, 114
De Marcellus, P., Meinert, C., Nuevo, M., et al. 2011, ApJL, 727, L27
Derenne, S., & Robert, F. 2010, M&PS, 45, 1461
Desch, S. J., & Cuzzi, J. N. 2000, Icar, 143, 87
Drążkowska, J., & Dullemond, C. P. 2014, A&A, 572, A78
Duvernay, F., Chiavassa, T., Borget, F., & Aycard, J. P. 2004, JAChS, 126, 7772
Elsila, J. E., Glavin, D. P., & Dworkin, J. P. 2009, M&PS, 44, 1323
Fomenkova, M. N., Chang, S., & Mukhin, L. M. 1994, GeCoA, 58, 4503
Fromang, S., & Papaloizou, J. 2006, A&A, 452, 751
Fromang, S., Terquem, C., & Balbus, S. A. 2002, MNRAS, 329, 18
Gallois, N., Templier, J., & Derenne, S. 2007, J. Anal. Appl. Phys., 80, 216
Gilbert, W. 1986, Natur, 319, 618
Glassgold, A. E., Najita, J., & Igea, J. 2004, ApJ, 615, 972
Goesmann, F., Rosenbauer, H., Bredehöft, J. H., et al. 2015, Sci, 349, aab0689
Hartmann, J., Nawroth, T., & Dose, K. 1984, OLEB, 14, 213
Hayatsu, R., Studier, M. H., & Anders, E. 1971, GeCoA, 35, 939
Herd, C. D., Blinova, A., Simkus, D. N., et al. 2011, Sci, 332, 1304
Hollis, J. M., Lovas, F. J., & Jewell, P. R. 2000, ApJL, 540, L107
Inutsuka, S. I., & Sano, T. 2005, ApJL, 628, L155
Iro, N., Gautier, D., Hersant, F., Bockelée-Morvan, D., & Lunine, J. I. 2003, Icar, 161, 511
Kebukawa, Y., Chan, Q. H., Tachibana, S., Kobayashi, K., & Zolensky, M. E. 2017, SciA, 3, e1602093
Kopetzki, D., & Antonietti, M. 2011, New J. Chem., 35, 1787
Kouchi, A., Kudo, T., Nakano, H., et al. 2002, ApJL, 566, L121
Kuga, M., Carrasco, N., Marty, B., et al. 2014, E&PSL, 393, 2
Kuga, M., Cernogora, G., Marrocchi, Y., Tissandier, L., & Marty, B. 2017, GeCoA, 217, 219
Kuga, M., Marty, B., Marrocchi, Y., & Tissandier, L. 2015, PNAS, 112, 7129
Marrocchi, Y., Marty, B., Reinhardt, P., & Robert, F. 2011, GeCoA, 75, 6255
Marty, B., Avice, G., Sano, Y., et al. 2016, E&PSL, 441, 91
Miller, S. L. 1996, OLEB, 26, 201
Mita, H., Nomoto, S., Terasaki, M., Shimoyama, A., & Yamamoto, Y. 2005, IJAsB, 4, 145
Morowitz, H. J., Kostelnik, J. D., Yang, J., & Cody, G. D. 2000, PNAS, 97, 7704
Muskatel, B. H., Remacle, F., Thiemens, M. H., & Levine, R. D. 2011, PNAS, 108, 6020
Nuevo, M. 2011, in Proc. Frank N. Bash Symp., New Horizons in Astronomy, ed. S. Salviander, J. Green, & A. Pawlik (Trieste: SISSA), 004, https://pos.sissa.it/149/004/
Nuevo, M., Bredehöft, J. H., Meierhenrich, U. J., d'Hendecourt, L., & Thiemann, W. H. P. 2010, AsBio, 10, 245
Nuth, J. A., III, Johnson, N. M., & Manning, S. 2008, ApJL, 673, L225
Okuzumi, S., & Hirose, S. 2011, ApJ, 742, 65
Pizzarello, S., Cooper, G. W., & Flynn, G. J. 2006, in Meteorites and the Early Solar System II, Vol. 1, ed. D. S. Lauretta & H. Y. McSween, Jr. (Tucson, AZ: Univ. Arizona Press), 625
Remusat, L., Derenne, S., Robert, F., & Knicker, H. 2005, GeCoA, 69, 3919
Robert, F., Derenne, S., Lombardi, G., et al. 2017, PNAS, 114, 870
Robert, F., Derenne, S., Thomen, A., Anquetil, C., & Hassouni, K. 2011, GeCoA, 75, 7522
Saito, M., & Kimura, Y. 2009, ApJL, 703, L147
Schmitt-Kopplin, P., Gabelica, Z., Gougeon, R. D., et al. 2010, PNAS, 107, 2763
Schnepf, N. R., Lovelace, R. V., Romanova, M. M., & Airapetian, V. S. 2015, MNRAS, 448, 1628
Sephton, M. A. 2002, Nat. Prod. Rep., 19, 292
Shock, E. L., & Schulte, M. D. 1990, Natur, 343, 728
Sicilia-Aguilar, A., Henning, T., Dullemond, C. P., et al. 2011, ApJ, 742, 39
Simakov, A., Miller, G. B., Bunkan, A. J., Hoffmann, M. R., & Uggerud, E. 2013, PCCP, 15, 16615
Snyder, L. E., Lovas, F. J., Hollis, J. M., et al. 2005, ApJ, 619, 914
Šponer, J. E., Mládek, A., Šponer, J., & Fuentes-Cabrera, M. 2011, JPCA, 116, 720
Taillifet, E., Baillié, K., Charnoz, S., & Aléon, J. 2014, in LPSC, 45, 2086
Takeuchi, T., & Lin, D. N. C. 2002, ApJ, 581, 1344
Vinogradoff, V., Bernard, S., Le Guillou, C., & Remusat, L. 2017, Icar, 305, 358
Visser, R., Van Dishoeck, E. F., & Black, J. H. 2009, A&A, 503, 323
Walsh, C., Millar, T. J., & Nomura, H. 2010, ApJ, 722, 1607
Walsh, C., Nomura, H., Millar, T. J., & Aikawa, Y. 2012, ApJ, 747, 114
Whittet, D. C. B. 1997, in Planetary and Interstellar Processes Relevant to the Origins of Life (Netherlands: Springer), 249
Woitke, P. 2015, EPJWC, 102, 00011
Wolman, Y., Haverland, W. J., & Miller, S. L. 1972, PNAS, 69, 809
Youdin, A. N., & Lithwick, Y. 2007, Icar, 192, 588
Zega, T. J., Alexander, C. M. D., Busemann, H., et al. 2010, GeCoA, 74, 5966

5.4. From laboratory to canonical conditions

5.4.1. On the distribution of CO in the PPD

It is apparent that the gas mixtures used in the Nebulotron are not canonical (CO fractional abundance of 10^{-4}). Starting molecules in the Nebulotron (CO, N_2, H_2) are those dominating within the PPD, but the proportion of H_2 is very much reduced to allow enough material to be synthesised for subsequent analysis. However, there are several lines of evidence that the distribution of CO in the disk is not uniform. First of all, high spatial resolution observations of gas lines in disks provide direct information on the abundance and distribution of volatile species such as NH_3, N_2H^+, and H_2O (Salinas et al. 2016). Among all gaseous tracers of the PPD mass distribution, CO is the most widely used as it is highly abundant, relatively chemically stable, and readily detectable (Molyarova et al. 2017). The distribution of CO gas is controlled by two main mechanisms acting radially and vertically in PPD: the snowline and the warm molecular layer, respectively (Fig. 64).

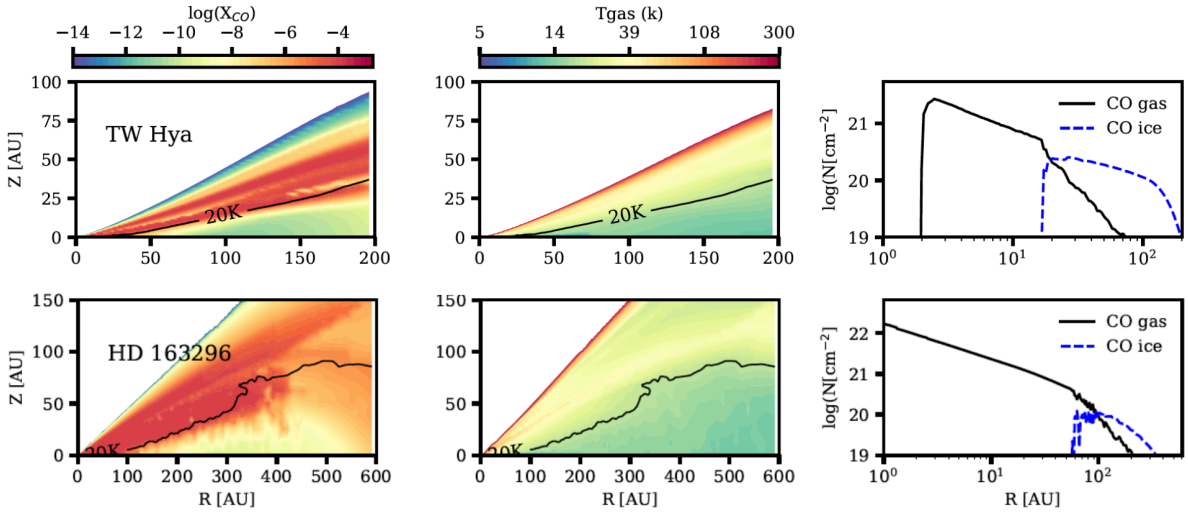

Fig. 64. Modelled chemical structures of two PPDs (TW Hya and HD 163296), showing the CO gas abundance (first column), gas temperature (second column), as well as the column density profiles of CO gas and CO ice. CO abundance structures are derived from spatially resolved CO isotopologue line observations of PPDs with high angular resolution $C^{18}O$ line observations from ALMA archive, in combination with detailed thermo-chemical models. Adapted from Zhang et al. (2019).

On the heliocentric distance scale, CO freezes out as ice beyond the snowline and exists as gas inside its snowline. As the icy grains coagulate and form pebbles, they drift inward (Birnstiel et al. 2010), deplete the outer disk of CO ice, and as CO-ice-covered pebbles drift across the CO snowline, CO sublimates, resulting in enhanced partial pressures of CO vapour just within the CO snowline (see the CO distribution around the snow line of HD163296; Fig. 64). Given that water is still frozen onto grain surfaces at such distance from the Sun, this process results in result in super-solar C/ O and C/ H ratios in the gas between water and CO

snowlines (Öberg and Bergin, 2016). A disk where almost all dust exterior to 40 au forms pebbles, drifts inward and deposits its CO content around 30 au would result in more than a tenfold increase of the local C/ H ratio between the CO_2 and CO snowlines.

In the vertical direction, the CO gas is dominant in a middle layer referred to as the warm molecular layer, with a lower boundary corresponding to where CO freezes out, and an upper boundary corresponding to where CO is photo-dissociated by stellar or external radiation (the Photon Dominated Region). This layered structure has been commonly observed in channel maps of CO line observations of PPDs (Rosenfeld et al. 2013; Pinte et al. 2018). Destruction of CO in the warm molecular layer involves dissociation or ionization radiation, either from UV, X-ray, or cosmic ray. For instance, models suggest that a cosmic ray ionization rate $\geq 10^{-17}.s^{-1}$ induces an order of magnitude depletion of CO gas over a few Myr timescale (Schwarz et al. 2018; Bosman et al. 2018). Photochemical processes converting CO into more complex, less volatile organic molecules akin to the Nebulotron experiment could possibly account for the observed CO depletion above the warm molecular layer (Fig. 64). Deeper in the disk, CO could be trapped as ice in large grains that settle to the midplane and efficiently sequestrate CO as a solid phase through sequential processes of vertical mixing and dust settling (Krijt et al. 2016). Importantly, the chemical processing rates of CO gas depend on the thermal and ionization structures of disks, which in turn depends on many physical properties, including the stellar luminosity, UV luminosity, disk flaring structure, and dust size distribution (Zhang et al. 2019).

Although local enhancements of the relative abundance of CO gas may allow getting closer to the chemical composition used within our Nebulotron experiments, CO/H_2 in the PPD would still be orders of magnitude lower that in the laboratory. But still, supporting evidence that organic chemistry is active within the gas phase of PPDs has been recently provided with the first detection of formic acid in a PPD using the ALMA telescope (Favre et al. 2018). In the next section, we aim at getting closer to canonical conditions of the protosolar nebula by increasing the partial pressure of H_2 within the Nebulotron discharge, and investigate the effect on the nature/composition of the produced organics.

5.4.2. Increasing the partial pressure of H_2: on the way to canonical conditions

One of the major issues we faced when increasing the partial pressure of H_2 within Nebulotron experiments was the decrease of organic matter production rates. When the H/C within the discharge is increased by a factor of four, the production rate can decrease by one order of magnitude (Fig. 65). Note however that production rates provided in Fig. 65 are indicative, as they have no associated uncertainties. But at very low deposition rate, it was complicated to recover any organic material, as these were not forming dust but films covering the internal surface of the reactor. Likewise, we could not estimate the efficiency of mass loss processes (e.g., sputtering, gas drag) within the discharge during these experiments. However,

even if production rates are given as indicative (Fig. 65), they clearly show a decrease (potentially exponential) with increasing H/C. Syntheses carried out at high H/C did not produce sufficient material for it to be analysed by GC-MS or ^{13}C-NMR. We therefore decided to characterise them by Orbitrap mass spectrometry coupled with an electrospray ionization source (Orthous-Daunay et al. 2019), which is extremely sensitive for the analysis of small amounts of organic materials. This method does not allow analysing the IOM, so we focused on the characterization of the fraction of Nebulotron condensates that is soluble in a methanol and toluene (1:2) mixture (Orthous-Daunay et al. 2019), in collaboration with François Régis Orthous-Daunay (FROD) from IPAG in Grenoble (France). For each synthesis, a ~7cm-long piece of quartz tube exactly fitting into the Nebulotron reactor was placed inside the discharge. Despite very low organic matter production rates, organic films could be grown onto the internal surface of the quartz tube, which was then recovered and sent to FROD for SOM extraction and analysis following the procedure reported in Orthous-Daunay et al. (2019).

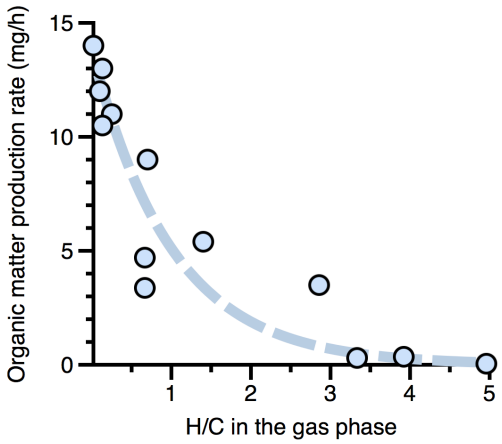

Fig. 65. Organic matter production rates (mg/h) observed for a series of Nebulotron syntheses with variable H/C ratios in the initial gas mixture (H being from H_2 and C being from CO) in the gas mixture. The exponential fit (dashed blue line) is given for indication, to materialise the decrease in production rate for higher H fractional abundances.

Fully determined kinetic models for large molecules are not yet available, but molecular growth patterns during processes such as polymerization have been empirically described (Wesslau 1956; see Orthous-Daunay et al. 2019 for more details regarding polymerization models). The extent and growth rate of a polymerization reaction is linked to the mass distribution of the molecules formed during the process. FROD carried out a mass spectrometry study of these distributions among chondrites and synthetic mixtures formed under experimental conditions reminiscent of astrophysical environments. Those laboratory experiment residues were produced from ice photo-irradiation experiments, UV processing of liquid phases and/or ionised gas. These experiments all aim at simulating extraterrestrial environments where organic molecules could be synthesised (ISM-outer SS, inner solar system and PPD gas phase, respectively). The Orbitrap mass spectrometry provides the mass

distribution of mixtures with resolution and precision high enough to un-doubtfully identify molecular formula. In every sample, CH_2 patterns (corresponding to molecules with R-$(CH_2)_n$ formula) are detected. From each CH_2 pattern, the free parameters of the Wesslau model for polymerization can be adjusted to match the observed distribution (see Danger et al. 2013 and Orthous-Daunay et al. 2019 for more details). Note that "polymerization", perhaps misleading here as considered molecules are much smaller than polymers, is used as a general term for molecular growth. Each sample has from 3 to 15 CH_2 families, with up to 30 members. In synthetic samples, the calculated extent of polymerization reactions systematically increases with time and/or temperature, whereas the growth factor of the polymerization reaction does not appear to depend on time or temperature (FROD, personal communication). The SOMs from meteorites define a polymerization scheme (Figure 66) that significantly differs from that defined by synthetic samples, including Nebulotron condensates from CO-N_2 mixtures with less than 1% H_2 (Kuga et al., 2015).

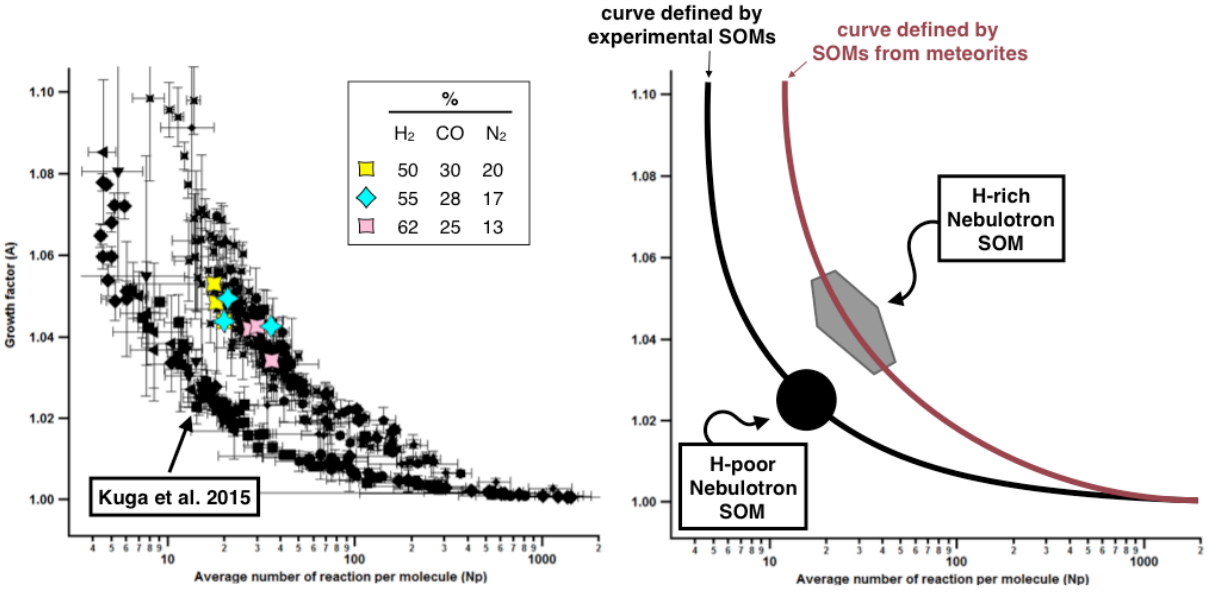

Fig. 66. Molecular growth pattern of the Nebulotron SOM as derived from Orbitrap analyses, compared with that of extraterrestrial SOM and with other laboratory experiments aiming at reproducing the extraterrestrial SOM. Axes A (growth factor) and Np (Average number of reaction per molecules) correspond to the free parameters of the Wesslau model matching the polymerisation pattern of the corresponding organic materials. The whole dataset shown on the left panel is sketched on the right panel, with the black curve corresponding to synthetic organic materials from laboratory experiments, and the red curve corresponding to natural samples. The Nebulotron SOM is the only experiment falling on the trend depicted by natural SOMs. In collaboration with François-Régis Orthous Daunay (IPAG, Grenoble).

As part of this thesis, I synthesised new Nebulotron condensates at high hydrogen partial pressures, up to 62% H_2 (Fig. 66). Unlike previous laboratory-derived SOMs, data points derived from the orbitrap analysis of H-rich nebulotron SOM were observed to fall on the trend defined by SOMs from meteorites, instead of that defined by synthetic samples. This implies that the condensation scheme of organic molecules produced within the Nebulotron at

high H_2 partial pressure well mimics that undergone by organic molecules found in extraterrestrial samples. In other words, this finding suggests that gas phase chemistry within plasma environments of the PPD at high partial pressures of hydrogen is able to reproduce the mass distribution of meteoritic SOM. This supports our previous conclusion that organic materials produced within the photosphere could have been widely dispersed in the PPD through turbulent diffusion, providing a mechanism for the distribution of organic meteoritic precursors prior to any thermal/photo-processing and subsequent modification by secondary parent body processes. These promising results are still being processed, and their implications still under discussion.

5.5. Hydrocarbon backbone of the Nebulotron IOM

Six Nebulotron IOMs synthesised from variable gas mixtures have been analysed by ^{13}C-Nuclear Magnetic Resonance spectroscopy, Gas Chromatography mass spectrometry (GC-MS) and Curie point pyrolysis GC-MS. The different compositions of the starting gas mixtures are reported on Fig. 67, with the corresponding H/C ratios.

5.5.1. ^{13}C-Nuclear Magnetic Resonance spectroscopy

Solid-state ^{13}C-nuclear magnetic resonance has become the preeminent technique for determining the structure of insoluble organic compounds. Based on nuclear spin excitation in a magnetic field, this method allows identifying C-bearing chemical functions within organic materials based on their so-called chemical shift (δ). In details, a microwave field leading to resonance conditions induces transitions between nuclear spin states. The nuclei of certain atoms have a nuclear magnetic moment (a non-zero spin, e.g. ^{13}C), implying they behave like dipoles characterised by a magnetic quantum size. A NMR signal is observed when the field is disturbed by a secondary field perpendicular to a characteristic frequency (frequency Larmor). Then the spins resonate, and their response is registered as a ^{13}C-NMR signal. The position of each signal in the NMR spectrum is determined by δ. It is characteristic for the chemical functions in which the nucleus is engaged. In order to enhance the sensitivity of ^{13}C-NMR spectroscopy measurements, a so-called cross-polarization (CP) sequence is commonly used. It involves the magnetization transfer from ^{1}H to the low abundance nuclei. The solid-state ^{13}C-NMR spectra recorded in the present work were obtained at 125 MHz (Bruker AV500 spectrometer) using a 4 mm resonance Bruker MAS (Magic Angle Spinning) probe at 14kHz. Free induction decays were analysed with the Bruker TopSpin program and spectra were decomposed using the Dmfit program (Massiot et al. 2002). The chemical shifts were standardised to the TMS scale (0 ppm) and were adjusted using ^{13}C-labeled adamantane. The assignment of the signals was performed according to Gardinier et al. (2000).

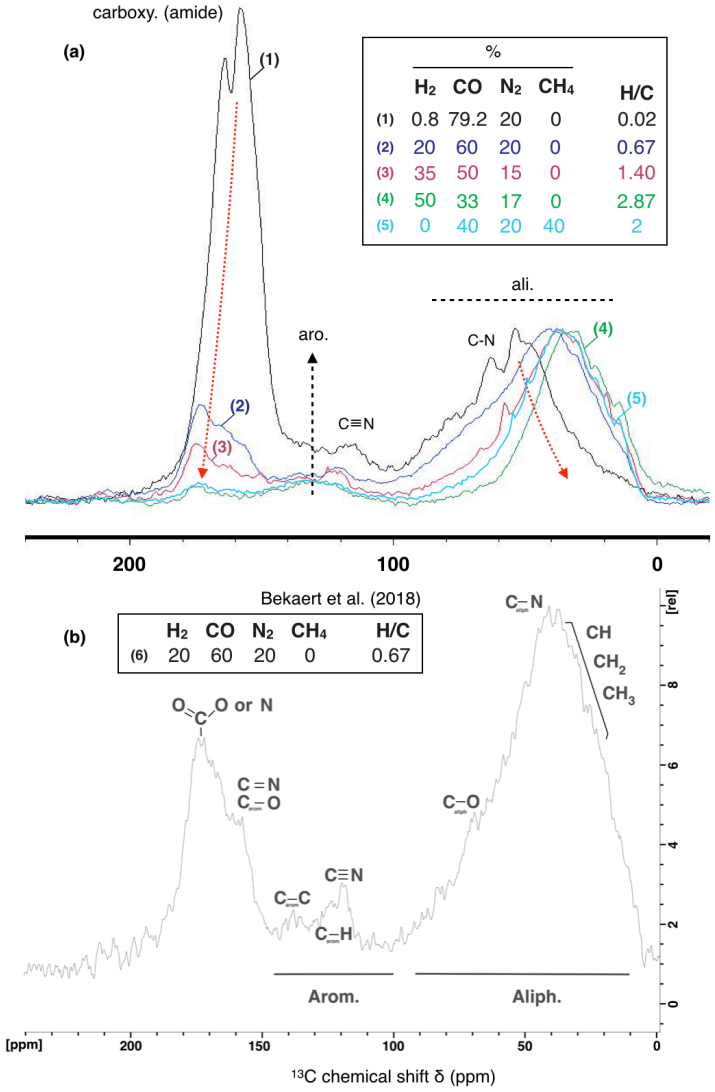

Fig. 67. Solid-state ^{13}C-NMR spectra of Nebulotron IOMs. (a) Evolution of the ^{13}C-NMR spectra of Nebulotron IOM for increasing H/C in the discharge, materialised by the dashed red arrows. The compositions of starting gas mixtures are color-coded according to the key provided in the box. A few functional groups are reported on the spectra, but more are provided in (b), which corresponds to the detailed solid-state ^{13}C-NMR spectrum of the organic material analysed in Bekaert et al. (2018a). "carboxy. (amide)", "aro." and "ali." refer to the carboxylic acid/amides, aromatic C and aliphatic C peaks, respectively.

All Nebulotron IOMs synthesised for the purpose of this study have ^{13}C-NMR spectra (Fig. 67) showing clear differences compared to organics found in meteorites (Fig. 61), with basically a limited contribution from aromatic rings relative to extraterrestrial IOM and, conversely, a higher proportion of amides and carboxylic acids (Fig. 67). For the synthesis with almost no H_2, no aromatic ring is detected, but the amide/carboxylic acid peak is extremely high (H/C = 0.02, Fig. 67). Interestingly, the aromatic signal seems to grow slowly when the partial pressure of hydrogen is increased in the discharge, suggesting that a significantly more aromatic material could be formed from a canonical gas with orders of magnitude more H with

respect to C (samples 4 and 5, Fig. 67). However, production rates in this case would be expected to be very small, although the timescales of the PPD (millions of years) do not preclude that this pathway of organosynthesis significantly contributed to the budget of extraterrestrial organic materials. Importantly, Nebulotron IOM previously synthesised from n-alkane plasmas also contained more aliphatic compounds than found in chondritic IOM, but with a much higher fraction of aromatic compounds than obtained here from CO-N_2-H_2 syntheses (Biron et al. 2015; Fig. 60). The aromaticity of organic materials as found in chondrites could also have been acquired during secondary processing of primitive materials akin to those produced in the Nebulotron, which is experimentally investigated in section 5.5.3. of this manuscript.

5.5.2. GC-MS of SOM and Py GC-MS of IOM

The SOM of Nebulotron organics synthesised with ~80% CO and <1% H_2 contains chemical compounds extremely rich in heteroelements (e.g., cyanuric acid; Fig. 68), with an associated IOM that does not resemble that of meteorites (as previously observed by Bekaert et al. 2018a). It is poorly aromatic, and its pyrolysate contains complex molecules rich in N and O (e.g., triazine derivatives; Fig. 68). However, when the H/C is increased, we observe that extremely N- and O-rich molecules are no longer present. The SOM of Nebulotron products from a gas mixture with H/C ~ 2.9 still contains the main biologically relevant molecules observed by Bekaert et al. (2018a), but the associated IOM is significantly evolved towards more chondritic-like composition, with the presence of aromatic compounds (toluene, pyrrole, benzene) typically found in chondritic IOM (Biron et al. 2015). Interestingly, nitrogen in chondritic IOM occurs mainly as pyrroles (Remusat et al. 2005). These observations are in line with the rise in the aromatic peak and decrease in functionalised C seen in ^{13}C-NMR spectroscopy for the H/C ~ 2.9 sample (Fig. 67). The fact that biologically relevant molecules have been observed for the SOM of all Nebulotron experiments carrying CO in the initial gas mixture (from H/C ranging from 0.02 to 2.87) strengthens our conclusion that (at least part of) organic materials - including biomolecules - found in meteorites and comets could have been synthesised from the ionised surface layers of the disk (Bekaert et al. 2018a). In addition, the IOM structure is observed to evolve towards that of chondritic IOM when the H/C of the gas mixture is increased and the experiment is hence made more representative of natural conditions. Still, the H/C in the gas phase of the Nebulotron experiment remains orders of magnitude lower than the canonical ratio of the protosolar nebula, as required to produce enough material for analysis (Fig. 65). Further increasing the H/C of the gas phase (and waiting for significant periods of time) would presumably allow getting closer and closer to the final organic product found in meteorites. Alternatively, secondary processing during thermal/aqueous processing could potentially account for the differences still observed between high H/C Nebulotron products and natural samples.

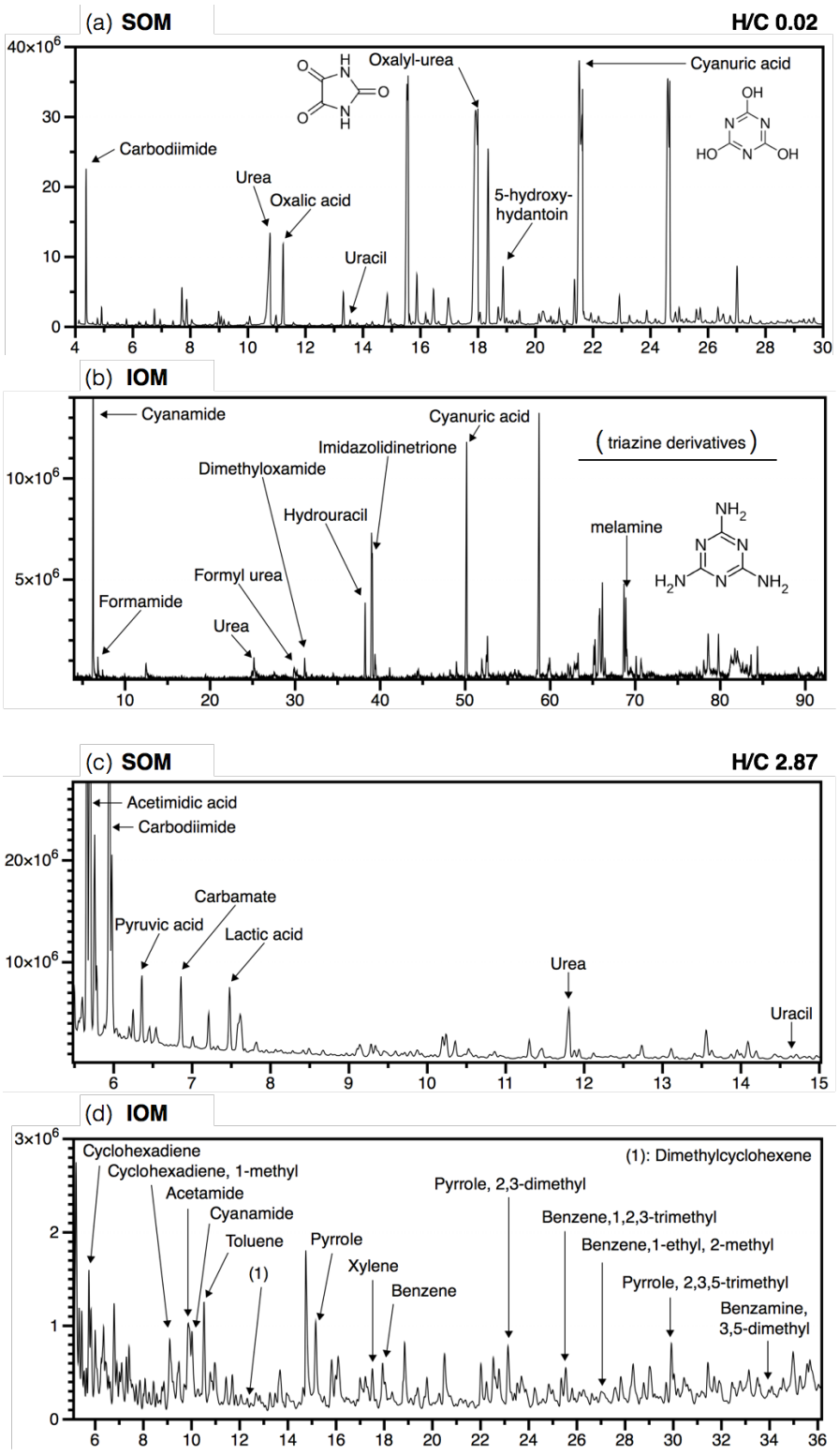

Fig. 68. GC–MS (a,c) and Py GC–MS (b,d) traces of the SOM and IOM of Nebulotron organic condensates derivatised using N,O-Bis(trimethylsilyl)trifluoroacetamide (BSTFA) and Tetramethylammonium hydroxide TMAH, respectively. Panels a-b and c-d correspond to the low and high H/C syntheses reported in Fig. 67 (H_2 0.8%, CO 79.2% N_2 20% and H_2 50%, CO 33% N_2 17%, Fig. 67, respectively). At low H/C, synthesised molecules can be extremely rich in heteroelements (N and O) for both the SOM and IOM. At high H/C, biomolecules are still observed in the SOM, and aromatic compounds are present in the IOM.

5.5.3. Parent body processing: thermal metamorphism and aqueous alteration

Aqueous and especially thermal alteration of organic materials onto the parent bodies of meteorite could have largely affected the structure and composition of chondritic organics (Rémusat 2015), inducing a major loss of free monocarboxylic acids and depletion of straight relative to branched chain compounds (Aponte et al. 2011). In little hydrated carbonaceous chondrites (e.g., Renazzo, CR carbonaceous chondrite), organic matter occurs mainly as isolated particles (Le Guillou et al., 2014). More heavily altered chondrites, like Orgueil (CI), have an additional diffuse organic component that is finely intergrown with phyllosilicates and hydrous minerals (Garvie and Buseck, 2007; Zega et al., 2010; Le Guillou et al., 2014). Such an association leads to the conclusion that mineral surfaces may have played a role in the synthesis and/or remobilization of some of the organic matter. This points towards a complex, multi-stage origin of chondritic organics, with one component being accreted as discrete organic particles, and the other having migrated throughout the matrix and been trapped in phyllosilicates (Garvie and Buseck, 2007; Le Guillou et al., 2014; Fig. 10). As part of this thesis, we carried out two complementary and preliminary experiments investigating the thermal metamorphism due to heating by the decay of short-lived radionucleides, and aqueous alteration effects onto organo-mineral mixtures, representative of the ones observed in chondrite matrix, to try and shed light on the possible effects of such interactions on the structure and composition of organic materials.

The design of the first experiment is represented Fig. 69. It corresponds to a simulation of aqueous alteration where some N- and O-free Nebulotron IOM from CH_4 plasma experiments (Biron et al. 2015) was agitated in water at 60°C for 6 month under a nitrogen atmosphere (Fig. 69). The aim was to investigate how oxygen atoms from water molecules could possibly be incorporated into this IOM component. The Pyrochromatogram of the IOM prior to the aqueous alteration experiment is reported and analysed by Biron et al. (2015), and that of the altered IOM is presented Fig. 69. Overall, we find similar compounds to those previously identified by Biron et al. (2015), with for instance a series of cyclopentadiene, cyclohexadiene, toluene, indane, benzene, naphtalene, fluorene and phenantrene derivatives (Fig. 69). In addition, we detect O-bearing molecules such as small carboxylic acids (e.g., carbonic acid, propanoic acid, butanoic acid, pentanoic acid, butanedioic acid), as well as larger carboxylic acids deriving from aromatic compounds (benzoic acid, phthalic acid, 1,3-benzenedicarboxylic acid, 2-naphtoic acid, 1,2,4-benzenetricarboxylic acid; Fig. 69), which suggests that, under the conditions of our aqueous alteration simulation, oxygen was successfully incorporated into the IOM structure, therefore resulting in its chemical diversification. These preliminary results are promising, indicating that the IOM accreted by the meteorite parent bodies was perhaps not chemically inert, and implying that - at least part of - the chemodiversity observed in chondritic organic materials could originate from the aqueous processing of the IOM. These results are in line with results from solid-state NMR, S K-edge XANES and IR spectrometry

(Cody and Alexander 2005; Yabuta et al. 2005; Orthous-Daunay et al. 2010, 2013) suggesting that hydrothermal alteration can oxidise the IOM.

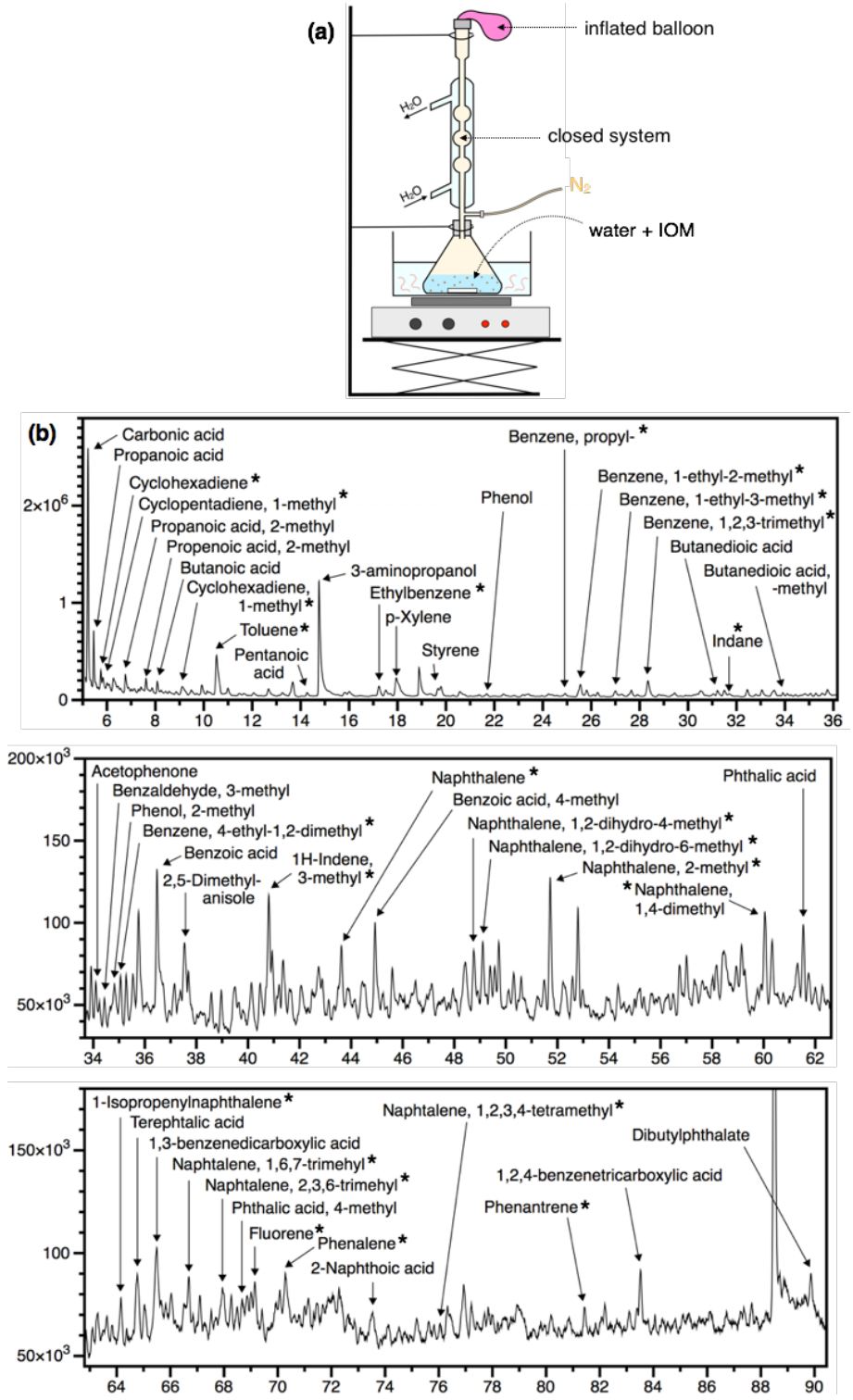

Fig. 69. Aqueous alteration experiment from pure CH_4 plasma IOM (Biron et al. 2015). (a) Schematic drawing of the experiment. (b) Py GC–MS trace of the altered IOM derivatised using TMAH. We observe the same aromatic compounds as reported by Biron et al. (2015) (identified with asterisks), plus some O-bearing aliphatic and aromatic compounds, presumably formed during aqueous alteration of the IOM.

The second experiments presented here corresponded to organic materials from CO-N_2-H_2 Nebulotron synthesis (same conditions as Bekaert et al. 2018a) exposed to different temperatures (25°C, 50°C, 100°C) for 15 days, to investigate the effect of thermal metamorphism (Fig. 70). These materials were encapsulated into sealed glass tubes for thermal processing experiments and Fourier Transform Raman Spectroscopy (FT-Raman) analyses. The latter reveal a progressive cyclisation (1, Fig. 70) and loss of aliphatic chains (2, Fig. 70) upon heating, in agreement with the initiation of the carbonization process (Alexander et al. 2007). These preliminary results comfort our proposal that thermal processing of primitive organic compounds in the disk and/or onto their parent body could account for the modification of primitive, Nebulotron-like organic compounds towards chondritic-like materials.

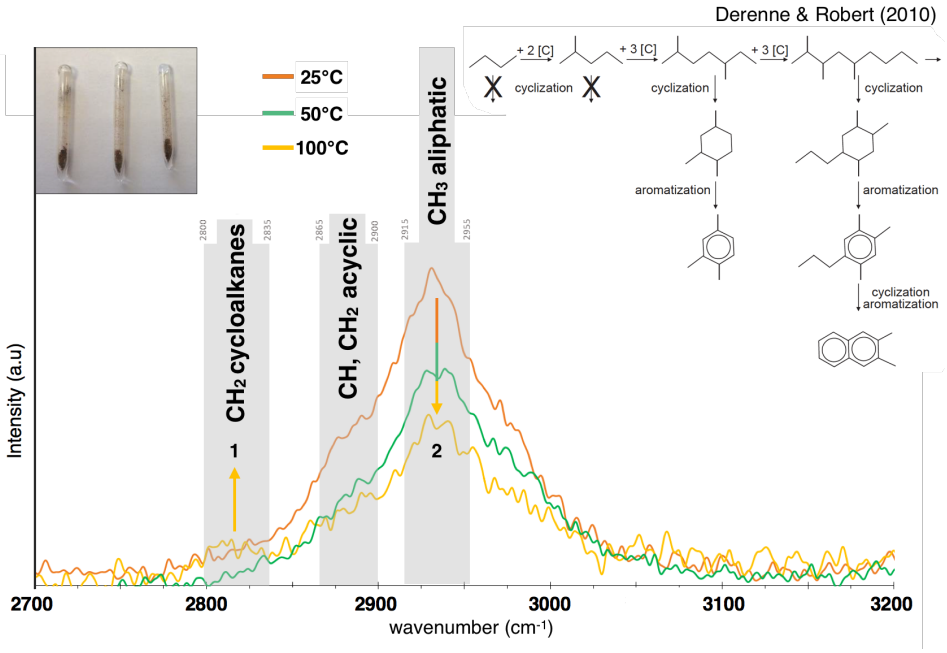

Fig. 70. FT-Raman of Nebulotron organic matter (same conditions as Bekaert et al. 2018a) heated to 25°C, 50°C and 100°C for 15 days. Indexation of the molecules based on (Socrates 2001). Collaboration with R. Mosser-Ruck and J. Touche (georessources, Nancy). Also reported is the illustration of a possible formation pathway of aromatic moieties in the gas phase of the protosolar nebula (heteroelements not taken into account; Derenne and Robert 2010). Our FTRS results suggest that part of the cyclisation/aromatization in the formation process of chondritic IOM could also have a thermal origin.

Preliminary results presented as part of this thesis support the idea that secondary processing could both account for the chemical diversification (via incorporation of heteroelements in IOM derivatives) and aromatization of extraterrestrial organics. The Raman spectroscopy analysis of Polyaromatic Carbonaceous Matter (PCM) from 42 chondrites supports the idea that organic macromolecules accreted by each chondrite group were broadly similar (Quirico et al. 2009), reflecting the composition of macromolecules available in the protosolar nebula during the formation of the first planetesimals and asteroids (Remusat 2015). In the model proposed by Derenne and Robert (2010), successive addition of single-carbon units, initially as free organic radicals in the gas phase, would naturally result in the elongation

(chain length ≥ 7C), spontaneous cyclization and subsequent aromatization of organic compounds, as commonly observed upon thermal treatment of aliphatic polymers (Madorsky 1964). One possibility is that this cyclization/aromatization process (schematically represented Fig. 70), which appears to occur for pure CH_4 plasma (Fig. 61; Biron et al. 2015), is limited in the case of CO-N_2-H_2 Nebulotron products due to the efficient incorporation of heteroelements hindering the cyclization step. This may however not be the case under natural conditions of the protosolar nebula, where the abundance of H_2 would be orders of magnitude higher than that of heteroelements. Increasing the chemical maturity of Nebulotron products as synthesised in this thesis, towards more chondritic-like (i.e. aromatic) compounds, may nonetheless require their thermal annealing in the disk and/or onto their parent body.

5.6. Isotope effects (N and H) - a requirement for photochemistry involvement?

5.6.1. NanoSIMS investigations

Nanoscale Secondary Ion Mass Spectrometry is based on the analysis of secondary ions produced when a sample is bombarded by a primary ion beam (either Cs^+ or O^-). Among other particles, ions are sputtered from the upper few nanometers of the sample surface. Afterwards the secondary ions from the sample are transferred with high transmission to a high mass-resolution, multi-collection mass-spectrometer, where they are counted by electron multiplier detectors. The yield of secondary ions produced from a sample surface critically depends on a number of parameters like its chemical composition, crystal structure, as well as the parameters of the primary beam. A controlled raster of highly focused primary beam allows secondary ion images to be produced with high spatial resolution. The NanoSIMS N50 we used at the Museum of National History of Paris is equipped with a multi-collector system that allows simultaneous collection of up to 5 different isotopes, which means that five different images can be recorded from the same sputtered volume. In our project, we carried out H, D, ^{13}C, $^{12}C_2$, $^{12}C^{14}N$, $^{12}C^{15}N$, ^{28}Si maps for Nebulotron organics synthesised *in-situ*, on top of silicon wafers placed inside the Nebulotron torch. This allowed us generating isotopic maps for H and N, as well as investigating the distribution of C.

Samples were introduced in the airlock one week before the analytical session to let them outgas, so the total vacuum pressure in the analysis chamber during the measurements remained below 1.10^{-9} mbar. Same image parameters were used through all sessions. A 16 keV primary Cs^+ beam was rastered over a surface of 20 x 20 μm^2 to acquire 256 x 256 pixel images at a raster speed of 2 ms/pixel. Each image is the result of stacks of 20 frames, corresponding to an analysis lasting about 20 min. Prior to each analysis, a 500 pA primary current was used for 5 min to pre-sputter the sample surface before analysis (30 x 30 μm^2), in order to remove gold coating, surface contamination and reach steady state sputtering conditions (Thomen et al., 2014). Secondary ions were collected by electron multipliers with a dead time of 44 ns. We

used Hamamatsu discrete dynode electron multipliers with a dead time of 44 ns in multi-collection mode. For H isotopes, the primary current was 10 pA and the mass spectrometer was set to a mass resolving power of 4000. For N, the primary current was 2 pA and the mass resolving power set at 8000 to resolve isobaric interferences, such as $^{12}C^{14}N^-$ from $^{12}C_2H_2^-$. All NanoSIMS data were processed with the LIMAGE software developed by Larry Nittler, Carnegie Institution in Washington DC (USA). Regions of interest (ROI) for isotopic ratio computations on LIMAGE where defined by (i) eliminating regions with the lowest 20% of ^{12}C intensity, and (ii) selecting a centred squared ROI covering ~80% of the surface area of analysis to remove the borders of the images where contamination from the surrounding material could occur (Fig. 72). Instrumental fractionation was corrected for by measuring a terrestrial kerogen. The error bars reported in this study are 1σ errors and combine counting statistics and external reproducibility.

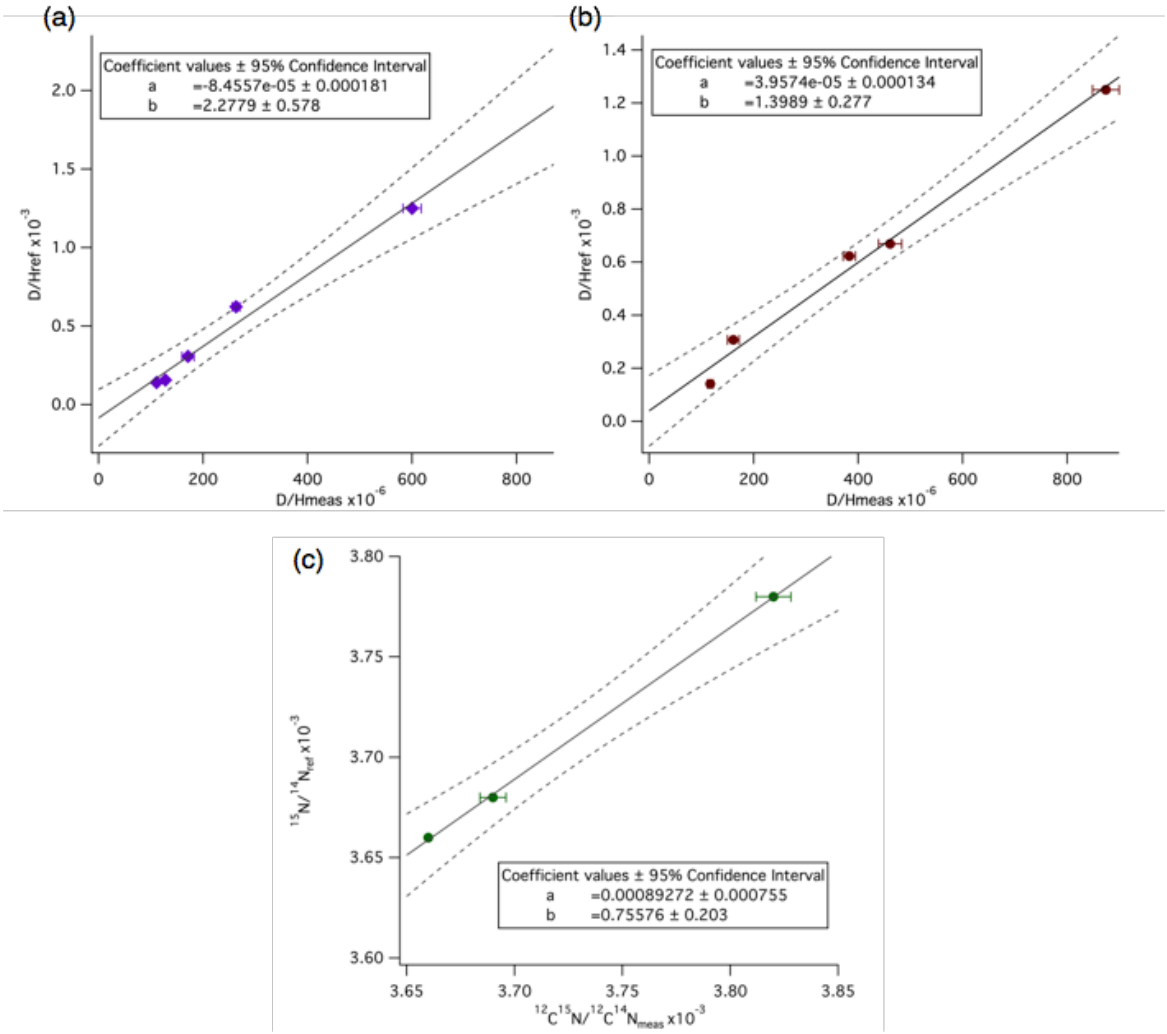

Fig. 71. Comparisons between reference and measured values of the standards for the two sessions of H (a-b) and the session of N (c) isotopic measurements. These correlations were used to correct our measurements of the isotopic composition of Nebulotron products for instrumental fractionation.

Results presented as part of this thesis were acquired during three different sessions of analysis at the Museum of National History of Paris: October 2017 (^{13}C, $^{12}C_2$, $^{12}C^{14}N$, $^{12}C^{15}N$, ^{28}Si), June 2017 (H, D, ^{12}C) and May 2018 (H, D, ^{12}C). Hence, the first session was dedicated to N isotope measurements, whereas the next two were used for H isotope measurements. All these analyses were carried out with Laurette Piani and Adriana Gonzalez. Three (a type-3 kerogen, IOM Gro95502, IOM Orgueil) and five (a type-3 kerogen, IOM Gro95502, IOM Orgueil, HDPS MDPS, and a type-3 kerogen, IOM Gro95502, NDPS, MDPS, HDPS) standards were used for N and H isotopic measurements, respectively (Fig. 71). NDPS, MDPS and HDPS correspond to D-labeled Polystyrenes with 1xSMOW, 4xSMOW, and 8xSMOW hydrogen isotopic ratios, where SMOW refers to the Standard Mean Ocean Water value (Bardin et al. 2015). IOM Gro95502 and IOM Orgueil refer to the insoluble organic matter isolated from the corresponding L3 and CI meteorites.

One of the requirements for the purpose of this study was to carry out *in-situ* measurements on the Nebulotron deposits, instead of collecting a bulk sample that is pressed in indium with no knowledge about the spatial structure of the deposit. To do so, we carried out experiments where silicon wafers (~1cm long) were placed at the bottom of the quartz tube reactor before synthesis in the high-vacuum Nebulotron. We often faced problems where the silicon wafers were observed to move inside the reactor, being either dragged by the gas flow or pushed away from the torch during synthesis. Up to three wafers could be used at once for organic deposition in the reactor. Organic materials deposited on a given silicon wafer could however be analysed *in-situ* by sticking the wafer onto the NanoSIMS sample holder using a copper double-face adhesive tape. Transects along the samples were carried out to investigate the D/H and $^{15}N/^{14}N$ spatial distributions. Note that we also carried out irradiation experiments where a given sample deposited on top of a wafer was irradiated, either using a VUV-beam (N isotope measurements) or by simulating interaction between organics and the ionised gas phase of the protosolar nebula (H isotope measurements). These two experiments of secondary processing are detailed here below.

° Hydrogen isotope analyses

Typical H, D, ^{12}C maps of Nebulotron organic materials deposited on top of a silicon wafer are provided Fig. 72. Overall, we always observed the Nebulotron maps to be homogeneous for its H isotopic composition, i.e. we never observed any hot or coldspot. However, synthesis-a and synthesis-b on Fig. 73 correspond to transects carried out throughout two Nebulotron deposits corresponding to the same gas composition as reported in Bekaert et al. (2018a). Although these were produced from the same gas mixture and under similar conditions (power 50W, P~1 mbar), they show distinct, but spatially consistent, δD values of ~1500 and 440 ‰, respectively (Fig. 73).

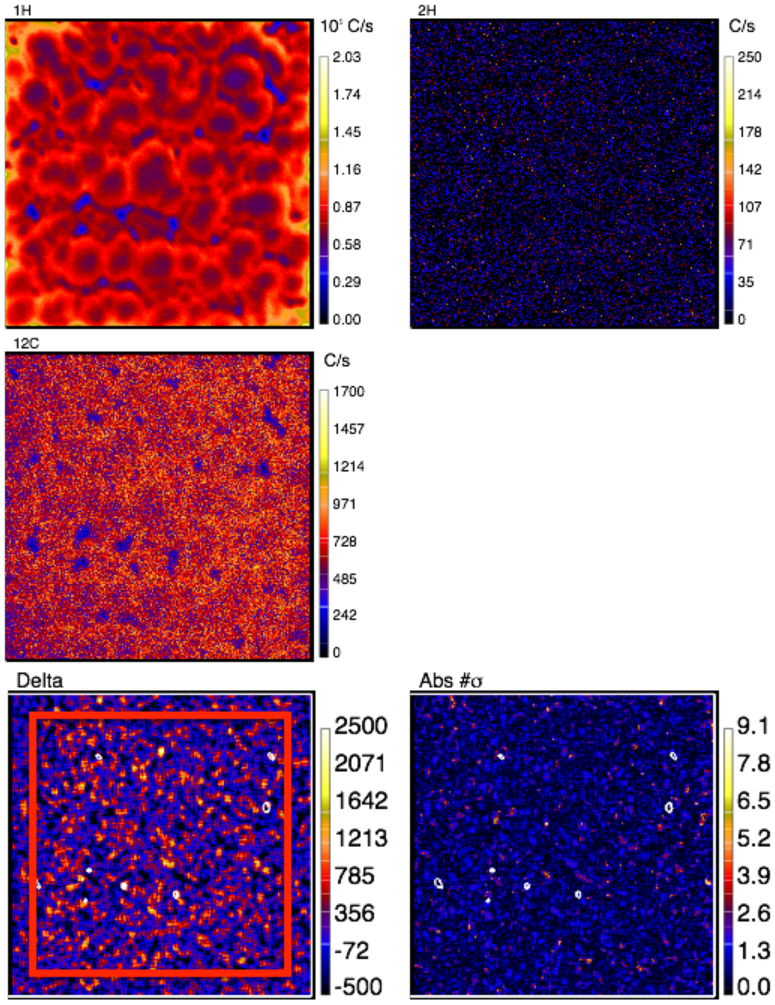

Fig. 72. Typical H, D, ^{12}C maps of Nebulotron organic materials deposited on top of a silicon wafer. Free µm-sized globules as well as larger globule aggregates of several microns in radius are observed on the H map, similar to observations from secondary electron imaging (Bekaert et al. 2018a). The delta map refers to δD values with their associated uncertainties reported on the Abs map. The red square represents the surface area finally considered (ROI) for computation of bulk isotopic composition.

Exp. 22h-a and Exp. 8h-a, Exp. 22h-b (Fig. 73) correspond to organic deposits on top of silicon wafers that were placed inside the Nebulotron reactor during the same experiments as Synthesis-a and Synthesis-b. In other words, all wafers labelled "a" and "b" come from the same respective syntheses. Exp. 8h and Exp. 22h refer to wafers that have been further exposed to a pure H_2 plasma for 8h and 22h, respectively. An illustration of these experiments is provided Fig. 73, where a pure H_2 plasma is shown, with the wafer being processed designated by the white arrow. The latter is hence placed at the exit of the plasma, where the ionised gas interacts with the surface of the wafer, therefore mimicking the interaction between organics and the ionised gas phase of the protosolar nebula. Note that if the wafer were placed closer to the torch, the plasma would most likely destroy organic materials.

We observe that, each experiment of exposure to ionised H_2 induces a lowering (materialised by the black arrows) in the δD ratios of the organic materials, from ~1500 to

~940 (22h, a), and from 440±18 to 175±12 (8h, b) and 129±40 ‰ (22h, b). Interestingly, we carried out one organosynthesis experiment with a different composition of the gas mixture: CO-H_2 instead of CO-N_2-H_2. The measured δD value was determined to be indistinguishable from the composition of the starting gas, at -150 ‰. Hence, the two take-home messages from these series of experiments are that (i) organic materials synthesised within the Nebulotron show variable, but always positive, δD values, from ~0 to ~1670 ‰ with respect to the starting gas composition, and that (ii) exposing these Nebulotron products to the tail of a pure H_2 plasma induces a lowering of the bulk δD value towards the composition of the gas. The origin of a variability of bulk δD values of organic materials synthesised with the Nebulotron is as of yet not understood.

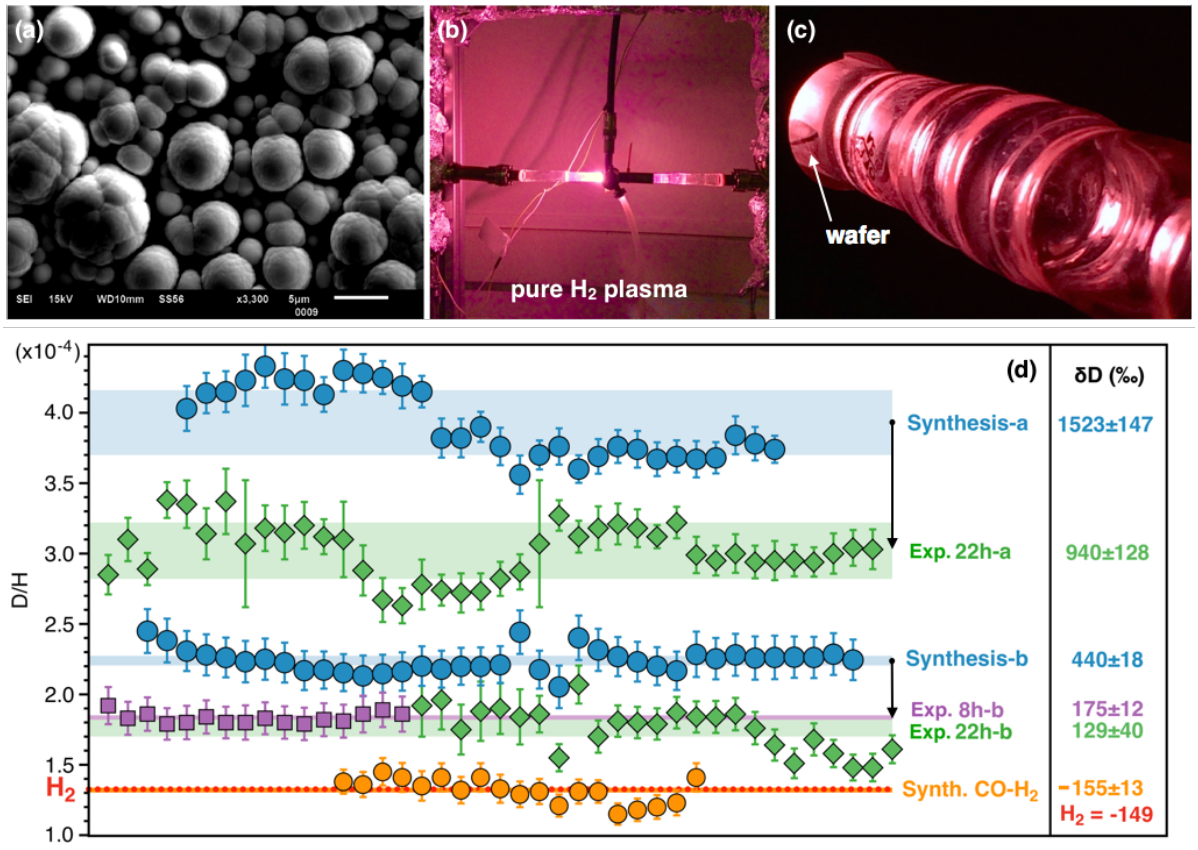

Fig. 73. Simulating the interaction between free-floating organic materials in the PPD and the ionised gas phase of the protosolar nebula. (a) Secondary electron imaging of Nebulotron condensates deposited on top of a silicon wafer (Bekaert et al. 2018a). (b) Pure H_2 Nebulotron experiment where an organic-bearing wafer (c) is placed within the tail of the plasma. (d) H isotopic measurements of Nebulotron organic materials. In blue are two independent syntheses corresponding to the experimental conditions reported in Bekaert et al. (2018a). In purple (8h) and green (22h) are organic materials processed in pure H_2 plasma. Orange data points correspond to a CO-H_2 synthesis (no N_2). The isotopic composition of the H_2 bottle is given in red. Shaded areas represent standard deviation on the mean of each experiment.

Interestingly, we have been computing indicative C/H ratios for all wafers analysed here, apart for Exp. 8h-b. As depicted Fig. 74, there seem to be a general trend towards higher C/H for higher δD values. This could indicate that most of the δD variations observed here are caused by H dilution. In particular, the decreasing δD values observed when organic materials are exposed to the pure H_2 plasma tail would correspond to the incorporation of H, inducing an isotopic equilibration with the gas phase. If this process were to have been effective in the PPD, it could indicate that organic materials transported within the ionised gas phase of the disk experienced H isotopic equilibration with the gas phase of the PPD.

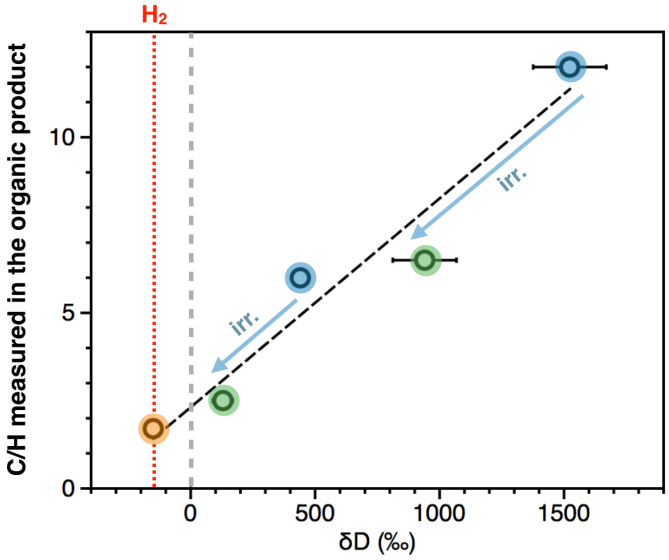

Fig. 74. C/H vs. δD composition of Nebulotron organic materials deposited onto silicon wafers and analysed by NanoSims. The δD composition of the gas (H_2) is given for reference.

° Nitrogen isotope analyses

Typical ^{13}C, $^{12}C_2$, $^{12}C^{14}N$, $^{12}C^{15}N$ and ^{28}Si maps of Nebulotron organic materials deposited on top of a silicon wafer as well as a summary of our N isotopic measurements are provided Fig. 75 and 76, respectively. As for H, we always observed the Nebulotron maps to be homogeneous is N isotopic composition, with no hot or coldspot as observed in meteorites. The N isotope composition of a Nebulotron organic materials condensed under similar conditions to those presented in Bekaert et al. (2018a) appears to be slightly depleted in ^{15}N (Fig. 75) with respect to the starting N_2 composition (0 ‰; Fig. 76). This is in agreement with previous findings by Kuga et al. (2014) that aerosols are depleted in ^{15}N by 15–25‰ relative to the initial N_2 gas, whatever the experimental setup is. Such isotopic fractionation has been attributed to mass-dependent kinetic effect(s) (Kuga et al. 2014).

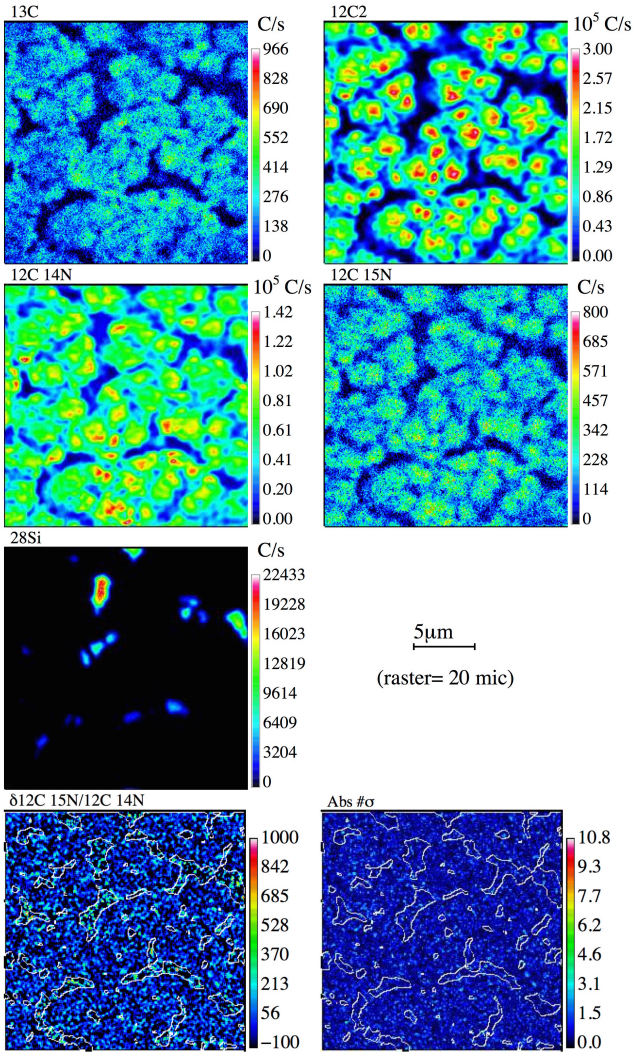

Fig. 75. Typical ^{13}C, $^{12}C_2$, $^{12}C^{14}N$, $^{12}C^{15}N$, ^{28}Si maps of Nebulotron organic materials deposited on top of a silicon wafer. ^{28}Si spots represent holes in the organic deposit. The $\delta^{15}N$ map (bottom left) does not reveal the occurrence of any hotspot.

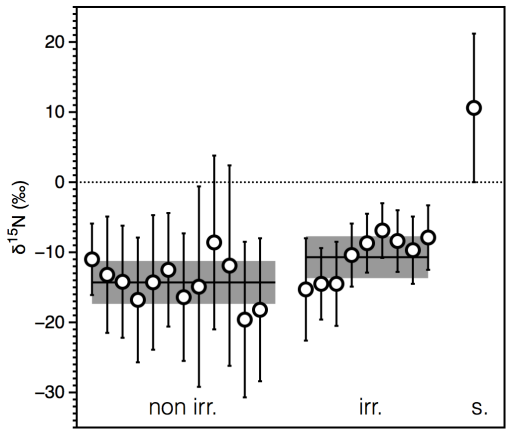

Fig. 76. N isotopic composition of Nebulotron (non-irr. and irr.) and synchrotron (S.) organic samples. Irradiation corresponds here to exposure to a narrow bandwidth extreme ultraviolet laser source, in collaboration with Dr. B. Gans (Laboratoire de Photophysique Moléculaire of Orsay, France). Shaded areas represent standard deviation on the mean of each experiment.

A Nebulotron organic deposit originating from the same synthesis as the sample labelled "non irr." (similar to that used by Bekaert et al. 2018a) was also irradiated for 12h using a narrow bandwidth extreme ultraviolet laser source (set at 70.67 nm, 2.10^{10} photons/cm^2.s^{-1}) developed by Dr. Bérenger Gans at the Laboratoire de Photophysique Moléculaire of Orsay (France). This wafer was set onto a KF flange using a copper double-face adhesive tape, before being connected to the laser chamber using the setting shown in Fig. 77. Unfortunately, the N isotope composition of the irradiated sample (irr.) is similar within error to the initial, non-irradiated sample (non-irr., Fig. 76), indicating this irradiation experiment did not yield any ^{15}N enrichment. Either our irradiation experiment simply cannot cause N isotopic fractionation, or the photon flux was not sufficient enough to cause detectable isotopic effect for a 12h-long irradiation. In the next section, we further investigate the possibility to cause significant N isotope fractionation using photochemical sources with orders of magnitude higher photon fluxes.

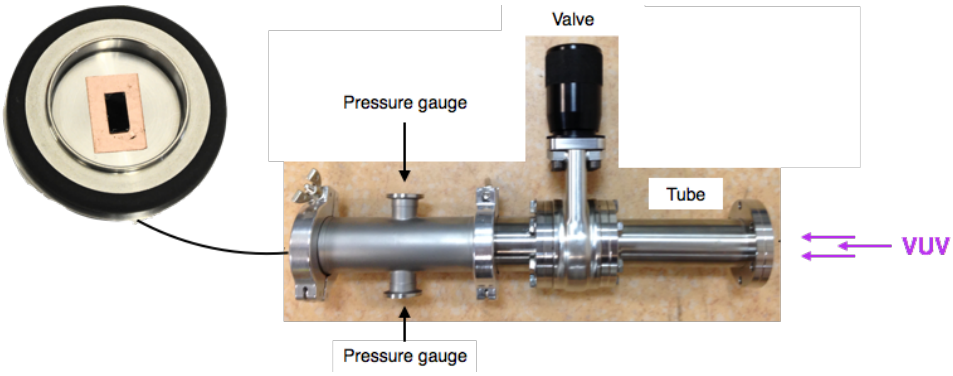

Fig. 77. Experimental setup used at the Laboratoire de Photophysique Moléculaire of Orsay (France) to irradiate Nebulotron organics deposited on top of a silicon wafer with an extreme ultraviolet laser source developed by Dr. Bérenger Gans.

The last point on Fig. 76 corresponds to the measurement of organic materials presumably synthesised during synchrotron experiments of VUV-photodissociation of simple gases relevant to the atmosphere of Titan (N_2-CH_4) at 15 eV (83 nm), in collaboration with the LATMOS group led by N. Carrasco. Part of this study is discussed in the next section.

5.6.2. Photon-driven organosynthesis

So far, plasma experiments have been unable to account for the large N isotope variations observed among Solar System objects and reservoirs (Kuga et al. 2014), therefore calling for alternative processes probably implying UV and X-ray irradiation in the disk either by self-shielding (Thiemens and Heindenreich III 1983; Clayton 2002) or by pre-dissociation effects (Muskatel et al. 2011; Chakraborty et al. 2014). As part of this thesis, I have been involved in studies investigating the production efficiency of N-bearing organic molecules using photons as source of molecule ionization/dissociation on the APSIS experiment (at LATMOS, Guyancourt, France) and DESIRS line of the synchrotron SOLEIL (Saclay, France).

On APSIS, we have designed an experiment to provide experimental insights into pathways of photochemistry-driven molecular growth within outer circumstellar envelopes, to draw a more complete picture of the chemical processes occurring within these molecule-rich environments. A simplified circumstellar envelope environment was therefore reproduced in the laboratory through gas-phase experiments exposing relevant gas mixtures of CO-N_2-H_2 to an Extreme Ultra Violet (EUV) photon source set at 73.6 nm (2.10^{13} - 4.10^{14} ph.s^{-1}.cm^{-2}; Tigrine et al. 2016). The detection and identification of complex, neutral and ionic species in the photochemical reactor was achieved through in-situ mass spectrometry analysis of neutral and cationic molecules. We for instance detected the production of N_2H^+, as well as oxygenated ion molecules (e.g., HCO^+ and H_3O^+) in circumstellar envelope environments, all of which were detected in circumstellar environments and PPDs. We observed neutral N-rich organic species including triazole and aromatic molecules, implying that photoionization and photo-dissociation processes occurring in the photon-dominated region of PPDs could play an important role in the synthesis route of nebular organic molecules. At last, note that we designed a system to trap condensable species in the gas flux, transport the trapped gas and analyse it for its N and H isotopic composition in Nancy at the stable isotope laboratory but, unfortunately, the amount of trapped gas was always too low to allow good quality measurements.

From the 17 to the 22 of July 2018, we spent one week **on the DESIRS** line at synchrotron SOLEIL to investigate the synthesis of gaseous and solid organics by photon irradiation of CO-CH_4-N_2 gas mixtures (91.2 nm, $\geq 10^{15}$ ph.s^{-1}.cm^{-2}) to see if we could produce ^{15}N-rich anomalies in organic gases and solids. Interestingly, our collaborators from LATMOS had tentatively succeeded in producing organic solid particles by VUV-photodissociation of simple gases relevant to the atmosphere of Titan (N_2-CH_4) at 15 eV (83 nm) using the VUV photochemical cell APSIS coupled with DESIRS. The organic sample mass was however recovered from the tube of the primary pump (Fig. 78) and so its origin and extent of processing on its way to the pump's tube was uncertain. It had a very pristine morphology compared to common Nebulotron products (Fig. 78). The δ^{15}N of this sample as measured by NanoSIMS (Fig. 76, sample "S") appears barely positive. Given the dubious place where these organic materials were collected, we considered that we needed to carry out similar experiments allowing organic materials to be trapped and collected within the reaction chamber.

One of the central ideas of the new project I was involved in was therefore to use a closed system allowing the accumulation of organic molecules potentially produced by interaction of the synchrotron light and gaseous species. Such a closed system is real challenge as it requires (i) a good airtightness (here KF connections, which turned out not to be sufficient to maintain a good vacuum during irradiation and prevent a rise in the blank contribution), as well as (ii) a window-less system allowing the synchrotron light (10^{15} photons/s in a 7% bandwidth) to reach the gas with no differential pumping. The later was achieved by using thin membranes that resist to the pressure difference between the chamber (10^{-4} to 10^{-2} mbar) and the DESIRS line (10^{-8} mbar) whilst letting a part of the

synchrotron light (≤ a few %) entering the reaction chamber. The synchrotron light was tuned at 13.8 eV (90 nm), which falls in the photodissociation continuum of both N_2 and CO and was responsible for the highest ^{15}N-enrichments in experiments reported by Chakraborty et al. (2014). At the same time, a quadrupole mass spectrometer (QMS Hiden) connected to the main chamber was used to measure the composition of gaseous molecules within the reaction chamber and search for newly produced organic compounds.

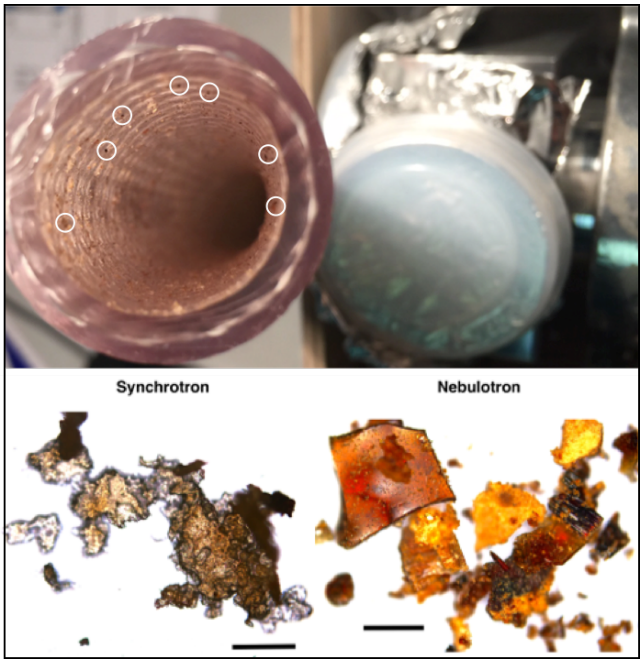

Fig. 78. Observation of organic deposits onto the inner walls of a primary pump exit after VUV-photodissociation of N_2-CH_4 mixtures on DESIRS (synchrotron SOLEIL, Saclay, France). Picture from N. Carrasco. Below are shown observation with Optical Microscope of these materials (synchrotron) compared to Nebulotron products. Thick black lines represent 400 µm.

No organic solid was ever recovered from these experiments, regardless if it involved CO-N_2-H_2 or CH_4-N_2 mixtures. One of the main issues we met (after that of contamination and blank rising under static mode) was the ageing of the membrane upon irradiation, with a systematic decrease in transmission (measured with a photodiode) through time. Unfortunately, such decrease in transmission was not due to organic deposition, but photo-deterioration of the membrane itself. During our run, we modified the device set up to move the focal point of the beam light away from the membrane and increase the size of interaction surface whilst reducing the photon density at the membrane surface. Interestingly, condensable organic gases were concentrated with a cold trap during experiments involving CO-N_2-H_2, before being released in the pre-evacuated reaction chamber to measure their composition on the QMS (Fig. 79). Here, we can clearly see the production and trapping of C_2 and C_3 hydrocarbons, as well as potential HCN at mass 27. These results however remain preliminary, and will be refuted/confirmed/improved during a potential next run at SOLEIL

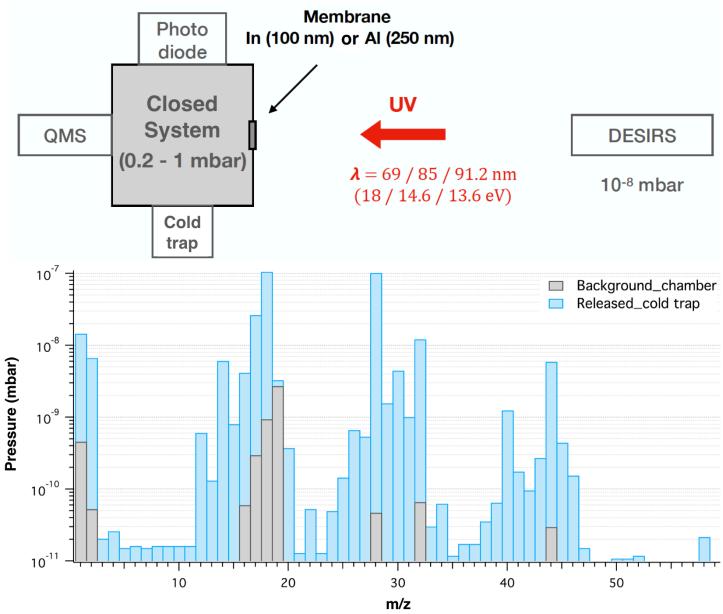

Fig. 79. Schematic representation of the experimental setup we used on the DESIRS line, with two mass spectra being reported for a CO:N_2:H_2 experiment at 1 mbar (13.6 eV). The grey spectrum corresponds to the background signal of the chamber set under static. The blue spectrum corresponds to the release of condensable species accumulated in the clod finger during 4h30 of irradiation.

Conclusion and outlook

The chemical, structural and isotopic diversity of organic materials found in primitive chondrites points towards an intricate origin, potentially involving multiple sources and various steps/extents of secondary (aqueous and/or thermal) processing. In this chapter, I argued the case for most part of the IOM found in chondrites to represent a nebular by-product of organosynthesis occurring within the ionised environments of the protosolar nebula. Experimental investigations of this production pathway may use electrons and/or photons as source of irradiation. The latter are more difficult to use as they require windowless experimental setup, and yield very small production rates. Nonetheless, photodissociation and photoionisation of atoms and molecules could have played a critical role in the chemical evolution of PPDs (Heays et al. 2017). Plasma experiments allow synthesizing large amounts of material that can be more easily characterised and compared to natural samples for assessing the relevance of this organosynthesis pathway. Taken together, these characterizations indicate that some (e.g., noble gas elemental and isotopic patterns, hydrocarbon backbone, D/H variations, production of biologically relevant molecules) but not all (e.g., extreme ^{15}N and D enrichments, aromaticity of the IOM for plasma experiments involving CO, chemodiversity of the SOM) of the features of chondritic organics can be reproduced in the laboratory. One potential bias may arise from our limitation to reproduce physico-chemical conditions that are relevant to the canonical conditions of the disk. To this extent, we investigated the effect of increasing the partial pressure of H_2 in the plasma discharge. This yielded a rise in the aromatic signal, indicating that higher H/C ratios in the disk ($\sim 10^4$) compared to the experiments (0.02-2.7) may be the key to allow for chondritic-like materials to be produced. From numerical simulations of dust particle transport in a turbulent PPD, we conclude that organic materials synthesised in the photosphere of the disk could thus potentially represent precursors of meteoritic and cometary organics, before their thermal/photoprocessing and subsequent modification by secondary parent body processing. Preliminary experiments of secondary processing of Nebulotron products indicate that these may significantly modify the structure and isotopic composition of nebular organics, potentially representing another missing link between Nebulotron products and chondritic organics.

Chapter 6

A recipe for the terrestrial atmosphere

As illustrated in the introduction, the nature of the Earth's main accretion building blocks is debated, but any model suggests it was dominated by inner Solar System-like material (NC) akin to enstatite chondrites. However, the nature of the Moon-forming impactor and late veneer are completely open to debate, from one pure end-member (EC-like) to the other (CI-like). Over the last twenty years, there seems to have been a change of paradigm regarding the origin of the isotopic and elemental composition of noble gases in the terrestrial atmosphere. The previously held idea that these could all be accounted for by hydrodynamic escape fractionation in the planetesimal blow off model (Pepin 2003) has progressively been replaced by the proposal that these could all be accounted for by mixing between different types of chondritic and cometary materials. This proposal, initially suggested from Ne-Ar correlations (Marty 2012), is now commonly accepted (Vogt et al. 2019; Williams and Mukhopadhyay, 2019). In the Chapter 2 of this thesis, we showed that the isotopic composition of the progenitor of atmopsheric Xe (U-Xe) could be well accounted for by mixing between cometary (~20%) and chondritic/solar (~80%) sources. Whether such mixing can also account for the Kr isotopic signature of the atmosphere is now discussed in this Chapter, demonstrating that the cosmochemical component to be mixed with cometary Xe to form U-Xe was most likely chondritic (and not solar) Xe. The scenario where xenon's escape from the terrestrial atmosphere over the Archean eon significantly contributed to the missing Xe paradox is tested through mixing calculations between cometary and chondritic end-members, allowing the primitive composition of the Earth surface reservoir to be modelled. We finally infer the most likely noble gas to water composition of the precursor material to the Earth surface reservoir, and compare it with known ratios from the meteorite collection. This chapter consists in a paper that is currently under review at *Scientific Reports*.

The origin and fate of volatile elements on Earth revisited in light of recent noble gas data obtained from comet 67P/Churyumov-Gerasimenko

- under review at Scientific Reports -

David V. Bekaert[1]*; Michael W. Broadley[1]*; Bernard Marty[1]

[1]*Centre de Recherches Pétrographiques et Géochimiques, UMR 7358 CNRS - Université de Lorraine, 15 rue Notre Dame des Pauvres, BP 20, 54501 Vandoeuvre-lès-Nancy, France.*

*Corresponding authors: dbekaert@crpg.cnrs-nancy.fr;

Abstract

The origin of terrestrial volatiles remains one of the most puzzling questions in planetary sciences. The timing and composition of chondritic and cometary delivery to Earth has remained enigmatic due to the paucity of reliable measurements of cometary material. This work uses recently measured volatile elemental ratios and noble gas isotope data from comet 67P Churyumov Gerasimenko (67/P-C), in combination with chondritic data from the literature, to reconstruct the composition Earth's ancient atmosphere. Comets are found to have contributed ~20% of atmospheric heavy noble gases (i.e., Kr and Xe) but limited amounts of other volatile elements (water, halogens and likely organic materials) to Earth. These cometary noble gases were likely mixed with chondritic - and not solar - sources to form the atmosphere. We show that an ancient atmosphere composed of chondritic and cometary volatiles is more enriched in Xe relative to the modern atmosphere, requiring that 8-12 times the present-day inventory of xenon was lost to space. This potentially resolves the long-standing mystery of Earth's "missing xenon", with regards to both Xe elemental depletion and isotopic fractionation in the atmosphere. The inferred Kr/H_2O and Xe/H_2O of the initial atmosphere suggest that the Earth's surface volatiles might not have been fully delivered by the late accretion of volatile-rich carbonaceous chondrites. Instead, "dry" materials akin to enstatite chondrites potentially constituted a significant source of chondritic volatiles now residing on the Earth's surface. We outline the working hypotheses, implications and limitations of this model in the last section of this contribution.

Introduction

Earth's early atmosphere experienced a complex history of impact erosion, mantle outgassing and late additions during periods of heavy asteroid and cometary bombardments[1]. The purported Moon forming impact is speculated to have removed a significant fraction of the proto-Earth's atmosphere[2] and resulted in a deep magma ocean estimated to have lasted for several million years[3]. Although the presence of a Late Heavy Bombardment (LHB), inferred from the lunar cratering record, has recently been cast into doubt[4], the net flux of extraterrestrial materials crossing Earth's orbit was arguably higher during the infancy of the solar system[5]. Given its inner solar system origin, the Earth is expected to have grown dry. Volatile-rich bodies (carbonaceous chondrites - hereafter CC - and/or comets) striking the Earth after core formation have been suggested as the suppliers of volatiles that formed the terrestrial oceans and atmosphere, as well as delivering primitive organic materials[6]. The late

accretion of chondritic material to Earth after formation of the Moon and core segregation, commonly referred to as the terrestrial "late veneer" (~0.5wt.% of the Earth), is required to account for the high and unfractionated abundances of highly siderophile elements in the terrestrial mantle[7]. However, the final stages of Earth's accretion have been argued to be predominantly derived from the inner solar system and to resemble enstatite chondrites (EC), which are considered to be our best analogues for the main building blocks of the Earth[8,9]. The atmosphere (ATM) might therefore be considered as a complex mix between inherited solar and chondritic volatiles, plus later introduction of chondrites and/or comets[10]. To date, deciphering whether the majority of the Earth's volatiles were derived from cometary or chondritic sources has been hampered by the lack of reliable measurements of cometary material.

The isotopic composition of atmospheric xenon is unique within the solar system. It is isotopically fractionated relative to any known cosmochemical end-member, by about 3.5%.u^{-1} in favour of the heavy isotopes[6], presumably as a result of the energetic hydrodynamic escape of a hydrogen-rich primordial atmosphere[11]. Such isotope fractionation can be corrected for by assuming mass-dependency, therefore yielding a primordial isotope composition consistent with either a solar or chondritic composition for most isotopes. After correcting for mass fractionation however, the heaviest isotopes ^{134}Xe and ^{136}Xe of the atmosphere, which were contributed by nucleosynthetic r-process only, are under abundant relative to solar/chondritic compositions. In other words, when chondritic or solar Xe signatures are fractionated by hydrodynamic escape to the extent needed to match the light-isotope ratios of the atmosphere, they contribute more ^{136}Xe relative to ^{130}Xe than the atmosphere actually contains[11] (Fig. 1). Subtraction of a putative fission component from air-Xe worsens these discrepancies, implying that pure chondritic or solar Xe sources are firmly ruled out as the only progenitors of terrestrial volatiles. The non-radiogenic terrestrial Xe spectrum (labelled U-Xe) was initially computed from corrections for mass-dependent fractionation and fissiongenic/radiogenic contributions, and multi-dimensional fits to carbonaceous chondrite stepwise heating data[11]. By definition, U-Xe is marked by deficits in ^{134}Xe and ^{136}Xe relative to common nucleosynthetic reservoirs (solar and chondritic) and, when fractionated by MDF to match air, it falls below the current atmospheric isotope composition at ^{129}Xe and $^{131\text{-}136}$Xe, corresponding to later additions of radiogenic (^{129}Xe derived from ^{129}I) and fissiogenic ($^{131\text{-}136}$Xe derived from ^{244}Pu) components (Fig. 1). Recently, large depletions in ^{134}Xe and ^{136}Xe were identified in comet 67P/Churyumov-Gerasimenko (67P/C-G)[12], with the addition of ~22±5% cometary xenon to a chondritic/solar atmosphere being found to match the U-Xe composition[12] (Fig. 1). This discovery provides a natural mechanism for the origin of U-Xe on Earth, implying the U-Xe signature was not a widespread component in the early solar system, but rather the result of a unique mixing of cometary and chondritic/solar sources on the primitive Earth.

Novel insights into the timing of isotopic fractionation of atmospheric Xe were recently provided by the analysis of ancient atmosphere trapped within fluid inclusion in Archean

quartz samples, showing Xe isotope signatures intermediate between U-Xe and the modern atmosphere and pointing towards a global and protracted evolution of atmospheric Xe isotopes[13]. Conversely, Kr isotope signatures in ancient atmosphere samples were consistently found to be indistinguishable from modern composition[13]. To find a higher degree of mass dependent fractionation (MDF, from U-Xe to modern atmosphere) for Xe, despite Kr being a lighter element, is unexpected, suggesting that a Xe-specific process is required to account for atmospheric Xe MDF throughout the Archean[13-16]. Due to the fact that Xe has a low ionization potential relative to the other noble gases, atmospheric Xe could have been readily ionized by enhanced ultraviolet (EUV) radiation[14]. Ionised Xe could then have then been being dragged along open magnetic field lines and lost to space via ionic coupling with escaping H^{+}[13,15-16] or becoming trapped in organic hazes formed within the CH_4-rich early atmosphere[14].

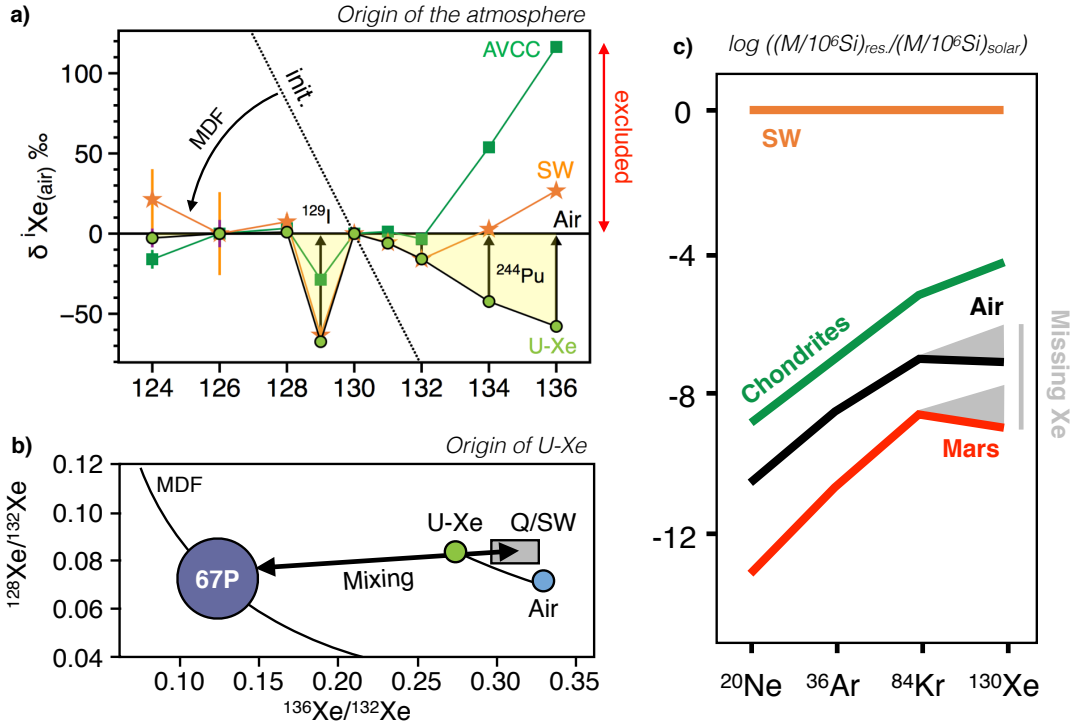

Figure 1. Origin of atmospheric Xe's precursor (U-Xe). (a) AVerage Carbonaceous Chondrite Xe (AVCC-Xe)[11], solar wind xenon (SW[32]) and U-Xe[11] signatures mass-dependently fractionated to the extent where their $^{126}Xe/^{130}Xe$ matches the Air-Xe value. Initial U-Xe composition is shown by dotted line. It appears that post-MDF AVCC-Xe and SW-Xe compositions contribute more ^{136}Xe relative to ^{130}Xe than the atmosphere actually contains, therefore excluding chondritic and solar components as the only sources of atmospheric volatiles[11]. The mass-dependently fractionated signature of U-Xe exhibits deficits in ^{129}Xe and $^{131-134}Xe$ that correspond to latter additions of radiogenic and fissiogenic contributions from ^{129}I and ^{244}Pu, respectively[11]. (b) Mixing diagram between cometary and Q[33]/SW-Xe[32] components to account for the origin of U-Xe in the terrestrial atmosphere (modified from 12), as modelled by the thick arrow. Subsequent evolution from U-Xe to Air by MDF is represented by the solid curve. (c) Comparison of the abundance patterns of noble gases in the Sun, in volatile-rich primitive chondrites and in the atmospheres of Earth and Mars (modified after 17-18). Earth and Mars are depleted in xenon relative to krypton and meteorites, with Kr/Xe close to the solar abundance.

Many of the atmosphere's major constituents, including H, N and Ar are isotopically similar to chondrites. However, Xe in the atmosphere exhibits a high degree of mass-dependent isotopic fractionation in favour of the heavy isotopes, as well as an underabundance of 10-20 times the value expected given the chondritic abundance pattern of Ne, Ar and Kr on Earth[17-19] (Fig. 1; Table 1). Both features are referred to as the missing Xe paradox[19]. Untangling the missing Xe problem requires that the $^{84}Kr/^{132}Xe$ of the atmosphere and potentially the mass dependent fractionation of atmospheric Xe both be accounted for. The extent of Xe loss to space over the Hadean and Archean eons has not yet been quantified[13,19]. To explain the missing Xe in the atmosphere, it has been proposed that the delivery of solar-like Kr to the atmosphere, with negligible associated Xe addition, following the main stage of atmospheric loss, could potentially resolve the missing Xe (in fact, "extra Kr")[10], as well as why Kr isotopes are not fractionated. Pioneering laboratory-based experiments indeed revealed that Kr is trapped more efficiently within amorphous ice than Xe[20], so a late addition of cometary material with a suspected high $^{84}Kr/^{132}Xe$ and solar-like isotopic composition could potentially account for the depletion of Xe on Earth. This could also explain the similar $^{84}Kr/^{132}Xe$ abundances on Earth and Mars, which are difficult to reconcile by evoking fractionation processes alone given the substantial differences (e.g., heliocentric distance, mass, timing of formation) between the two planets[21]. Identifying and resolving potential cometary contributions on Earth is vital to understanding how Earth acquired its atmosphere and became hospitable to life.

Xenon sequestration in a variety of terrestrial reservoirs (including shales[22], ice[23], clathrates[24], continental crust[25], as well as Earth's mantle[26] and/or core[27]) and preferential retention in the solid Earth relative to other noble gases during degassing have also been proposed to contribute to Xe elemental depletion in the atmosphere. Due to the limited storage capacity of the associated surface reservoirs, the shale, clathrate and ice hypotheses can be ruled out. However, whilst Xe is relatively inert under ambient and neutral conditions, the potential for its enhanced reactivity at high-temperature and high-pressure[28], and possible incorporation in to mineral phases at depth, is commonly used to argue for Xe to be stored in the Earth's interior. Here again, although theoretical and experimental investigations suggest possible Xe incorporation into silicate phases found in the Earth's crust, even the highest measured crustal concentrations of Xe are still three orders of magnitude below that required to account for the missing Xe[29], therefore excluding the upper continental crust as the main ‘‘missing’’ reservoir. Likewise, Xe abundance in volcanic rocks and xenoliths indicate that the upper mantle reservoir contains 10-100 times less Xe than the present-day atmospheric Xe inventory[28] (hereafter $ATM_{Xe;}$), making it an unlikely resting place for Xe and leaving the deeper mantle and/or core as the only possible sinks. Finally, and perhaps most crucially, explaining the under abundance of atmospheric Xe (relative to Kr and chondritic) by trapping it in silicate reservoirs could only account for abundance ratios and not for Xe isotopic fractionation.

Establishing whether or not the Earth atmosphere is truly deficient in Xe relative to its starting composition requires the composition of the primordial atmosphere to be known. Recently obtained volatile elemental compositions and noble gas isotopic data from Comet 67P/C-G by the Rosetta spacecraft[12,31] now offer the potential for cometary and chondritic contributions to the early Earth to be quantified. In this contribution, we present a thought experiment using recently measured volatile elemental ratios and noble gas isotope data from comet 67P Churyumov Gerasimenko (67/P-C) to reconstruct the composition and noble gas signature of the Earth's ancient atmosphere from simple mixing calculations. First, we use Kr isotopic systematics to elucidate on the nature of the main component (solar vs. chondritic) that was mixed together with comets to form the terrestrial atmosphere precursor. We then determine the cometary contribution required to produce the volatile element compositions (noble gas, water, carbon, nitrogen, halogens) observed in Earth's modern surface reservoir (ESR: atmosphere, hydrosphere, continental and oceanic crusts). This allows us to simulate the initial atmosphere composition as formed by the mix of comets and chondrites, and compare it with the present-day atmospheric composition in order to test the scenario of Xe loss to space over the Archean eon having partially, or fully, contributed to missing Xe. Finally, correcting the present-day atmosphere for its missing Xe offers the potential for the nature of the chondritic component responsible for most of the volatile element delivery to the ESR to be determined, based on its inferred noble gas to water ratio. The main working hypotheses used here to build up this thought experiment and their corresponding implications are presented and discussed in the last section of this manuscript, entitled "Working hypotheses: pros and cons".

1) Identifying the sources of heavy noble gases in the atmosphere.

Measurements of Xe isotopes within comet 67P/C-G indicate that the early atmosphere (U-Xe) is the result of mixing between cometary (22%) and chondritic/solar (78%) sources[12]. To address whether cometary noble gases were mixed with solar or chondritic gases to form the atmosphere, we utilise recently determined Kr isotopes from comet 67P/C-G[31]. Krypton measurements from the Rosetta Orbiter Spectrometer for Ion and Neutral Analysis (ROSINA) aboard the Rosetta spacecraft show that the Kr isotopes from the coma of comet 67P/C-G are broadly similar to solar, but with depletions in ^{83}Kr and ^{86}Kr isotopes[31]. Comparing the Kr isotopic composition of comet 67P/C-G with the two potential atmospheric progenitors, solar[32] and chondritic (taken to be phase Q[33]), we show that mixing between cometary and Q-Kr can best replicate the composition of the modern atmosphere. Importantly, the atmospheric Kr composition cannot be reproduced by addition of comets to a solar-like signature (Fig. 2), irrespective of the Kr isotopes being considered (Fig. S1). Using Monte Carlo simulations (Supplementary Information), we calculate the amount of cometary Kr addition required to best replicate the modern atmosphere from a chondritic atmosphere as being 21±5%. This suggests that (i) comets may have also contributed significant quantities of Kr to the

atmosphere and (ii) cometary noble gases were predominantly mixed with chondritic - and not solar - sources to form the atmosphere[12]. However, as discussed in the "working hypotheses: Pros and Cons" section entitled ", the addition of cometary Kr to a chondritic atmosphere does not succeed in exactly reproducing the $^{83}Kr/^{86}Kr$ signature of the atmosphere (Fig. S1), which could be accounted for by the extreme isotopic variability of the comet nucleosynthetic precursors (Fig. S2).

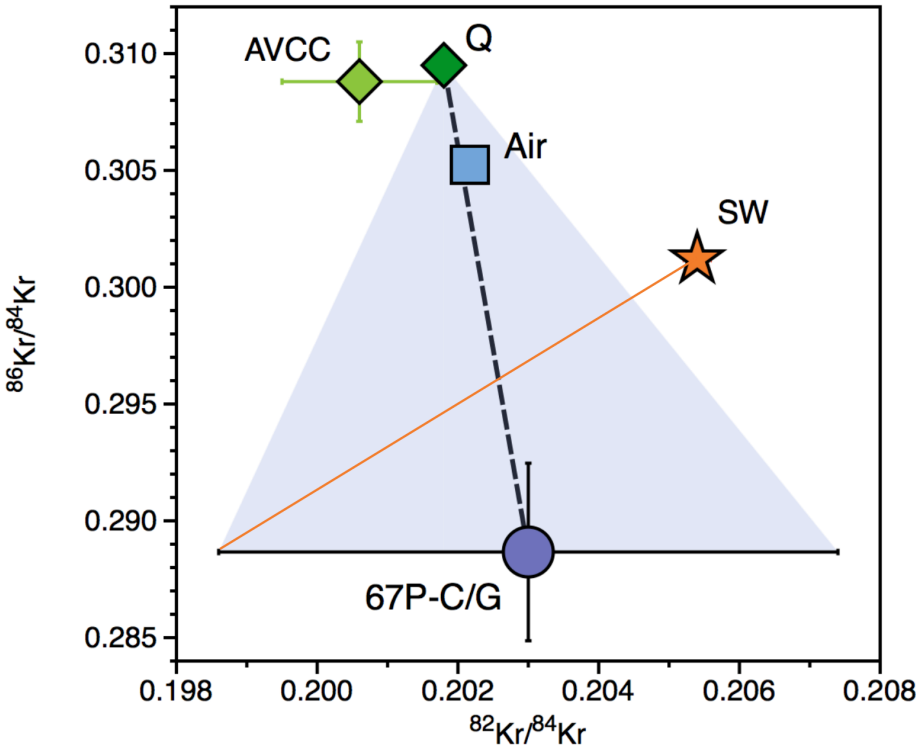

Figure 2. Cometary Kr within the Earth's atmosphere. The Kr isotopic composition of the atmosphere is shown to lie intermediate between the chondritic Q component[33] and the composition of comet 67P/C-G[31]. The unique Kr isotopic composition of the atmosphere could therefore be the result of mixing between chondritic and cometary endmembers (black dashed line). The addition of cometary Kr to an original solar atmosphere[32] (orange line) fails to reproduce the modern atmosphere. AVCC-Kr[11] is also displayed. Error bars are 1σ.

Using the estimate of cometary Kr in the atmosphere we find that the mass of cometary material that accreted to Earth was ~$9.8.10^{18}$ kg (Supplementary Information). This is more than one order of magnitude lower than the mass of comets inferred to have struck the Earth during the purported Late Heavy Bombardment (LHB)[34], suggesting previous predictions of late cometary accretion may be overestimated. Our estimate however represents a minimum value for the total mass of comets potentially supplied to Earth during main accretion since it does not consider atmospheric loss through impact erosion after the arrival of comets.

2) The role of comets in supplying volatiles to Earth.

The amount of other cometary volatiles on Earth may now be calculated from the

water, carbon, nitrogen, and halogen to Xe (or Kr) ratios of cometary and chondritic end-members (see methods). Assuming that comet 67P/C-G is representative of cometary bodies that were scattered throughout the inner solar system (see the "Working hypotheses: Pros and Cons" section), the cometary contribution to terrestrial water, for instance, is computed by combining the cometary Xe/H_2O[31] with the requirement to have ~22±5% cometary Xe and Kr contribution to the atmospheric inventory[12]. In this case, the absolute maximum cometary contribution to the ESR budget of water is 5% (Fig. 3). This value relies on the $^{132}Xe/H_2O$ of the chondritic end-member (Table 2) and is obtained by maximizing the chondritic $^{132}Xe/H_2O$, i.e. by using the upper limit given by the dry EC-like component for the chondritic end-member. Increasing the water content of the chondritic-endmember decreases the cometary contribution to terrestrial water (Fig. 3), therefore resulting in cometary contributions to terrestrial water being <0.07% for a CC end-member. Mean cometary contributions to terrestrial water for CC, OC and EC endmembers are 0.016%, 0.15% and 0.2%, respectively. Importantly, these values are in good agreement with the amount of cometary water that would be expected to accrete to Earth ($\leq 2.1.10^{18}$ kg H_2O, that is ≤ 0.15 wt.% of the oceans) from the addition of ~ $9.8.10^{18}$ kg of cometary material that is required to account for the cometary Kr contribution in the atmosphere.

The same calculation can be performed for nitrogen and carbon, combining the cometary and chondritic $^{132}Xe/N$ and $^{132}Xe/C$ (Table 2) with the 22±5% cometary contribution to terrestrial Xe[12]. The nitrogen depletion in OC relative to EC and CC (Table 2) implies that, if OC were to be the main source of terrestrial volatiles, the cometary contribution to terrestrial nitrogen would be very high, on the order of 15%, and up to 80% (Fig. 3). The common high $\delta^{15}N$ values (840 ± 71)[35] in cometary matter exclude significant cometary contribution to the terrestrial N inventory ($\delta^{15}N$ = 0‰). High cometary contributions to the terrestrial budget of N in case of a binary mixture between OC and comets therefore potentially precludes OC as the main source for chondritic volatiles on Earth's surface. Conversely, CC- and EC-like end-members require the cometary contribution to terrestrial nitrogen to be ≤2% (Fig. 3). Although the quantities of major volatile species delivered to Earth from comets are minor compared to chondrites, they may still have had a substantial impact on the geochemical signature of the Earth's volatiles, given extreme difference in isotopic signatures between the two accretionary reservoirs. For instance, the addition of a few percent cometary N, enriched in heavy ^{15}N[35] could substantially raise the $\delta^{15}N$ of the atmosphere from primitive negative values found in the mantle ($\delta^{15}N$= -25‰)[36] towards the current atmospheric value (Fig. S3).

Mixing comets with a CC-like endmember requires the cometary carbon contribution to the ESR to be low (mean contribution of 0.6%; Fig. 3). Mixing with OC or EC endmembers on the other hand leaves the possibility for comets to have contributed up to 15% of terrestrial carbon. Our estimates of the maximum amount of cometary organic materials supplied to Earth after the Moon forming impact ($<4\times10^{21}$g, see methods) indicate that comets potentially

provided up to 2000 times the present day mass of the biosphere (~2×10^{18}g). Interestingly, CC materials constituting up to 20wt.% of the late veneer[37] could have contributed up to 1x10^{23}g of organic matter, in agreement with the fact that comets could only contribute a few wt.% at maximum to the budget of Earth surface's carbon in the case of significant contribution from CC-like bodies (Fig. 3). In the case of a limited contribution from CC-like material in the ESR, there is a possibility for comets to have contributed significantly (several tens of wt.%) to the carbon budget in the ESR (Fig. 3). In addition, comets may be enriched in prebiotic molecules relative to chondrites, with potentially up to ~500μg/g glycine in comets[38] compared to ~2.5μg/g in CM chondrites[39]. Based on these estimates, we calculate that up to 5x10^{18}g of cometary glycine could therefore have been supplied to early Earth, which is significantly higher than the maximum estimated contribution from CC as part of the late veneer (3.6x10^{17}g of glycine). However, the preservation rate of extraterrestrial, biologically relevant molecules upon delivery to early Earth depends on the physical properties of the impactor (size, density, porosity, speed, trajectory) and the atmosphere (density, height, composition; Fig. S4)[40]. The low density and high porosity of comet 67P/C-G[41] could offer the potential for efficient aerobraking of small cometary impactors and early fragmentation upon atmospheric entry, therefore limiting pyrolysis (and thus favouring potential preservation) of organic molecules (Fig. S4). Yet, a genetic link between extraterrestrial organic materials (cometary or chondritic) and the emergence of life on Earth remains poorly understood.

Finally, using the halogen concentrations in the coma of Comet 67P/C-G[42], we calculate that comets contributed very limited amounts (< 0.5%) to the budget of terrestrial halogens (Fig. 3), in line with the elemental and isotopic ratios of heavy halogens being chondritic on Earth[41]. The terrestrial Br/Cl ($(3.0\pm0.2)\times10^{-3}$) is indeed indistinguishable from the chondritic ratio ((2.6 ± 0.8)x10^{-3})[43], but significantly lower than the cometary value (in the range 0.02-0.2, with a mean value of 0.08)[42]. However, part of halogens present in the comet may reside in the non-volatile fraction of the comet, including organic phases, which was not measured by the Rosina instrument on-board the Rosetta spacecraft. For instance, the iodine content of comet 67P/C-G ice is too low to account for the ^{129}Xe excess observed in the ice of comet 67P/C-G[12]. Using this ^{129}Xe excess to derive a minimal amount of additional cometary iodine, assuming a ^{129}I/^{127}I ratio at the moment of the solar system formation of ~1×10^{-4} (44), requires the comets to have an unrealistic bulk ^{127}I concentration around 230 ppm, suggesting the large ^{129}Xe monoisotopic excess observed in the comet originate from (i) a specific nucleosynthetic process preferentially producing ^{129}Xe or (ii) decay of ^{129}I in the ambient gas or dust before solar system formation[12].

Our model predicts comets to have contributed negligibly to all the aforementioned volatile species, except for the heavy noble gases, whose concentrations are high in cometary ice[31] (Fig. 4). Importantly, the timing of chondritic and cometary deliveries with respect to the Moon-forming giant impact (occurring ≥40 Myr after solar system formation)[45] is crucial to address their potential for having supplied organic materials that contributed to the emergence

of life. Due to the fact that comets are extremely rich in organic materials and have high eccentricities and hyperbolic trajectories, they are compelling candidates for having seeded early Earth with biologically relevant molecules. The contrasted heavy noble gas signatures in the Earth's mantle (chondritic[46,47]) and atmosphere (mixture of 20% cometary plus 80% chondritic[12]) may be used to argue for a late cometary bombardment of the Earth, possibly related to the giant planet instability about 3.9 Gy ago (referred to as the Nice model)[18,48]. The latter would notably have triggered the dispersal of the trans-Neptunian disk and of the asteroid belt, leading to a heavy bombardment of all terrestrial planets. One promising avenue of investigation to further constrain the timing of cometary supplies to the Earth-Moon system is to determine whether or not cometary volatiles are preserved on the present day Moon surface[49-51].

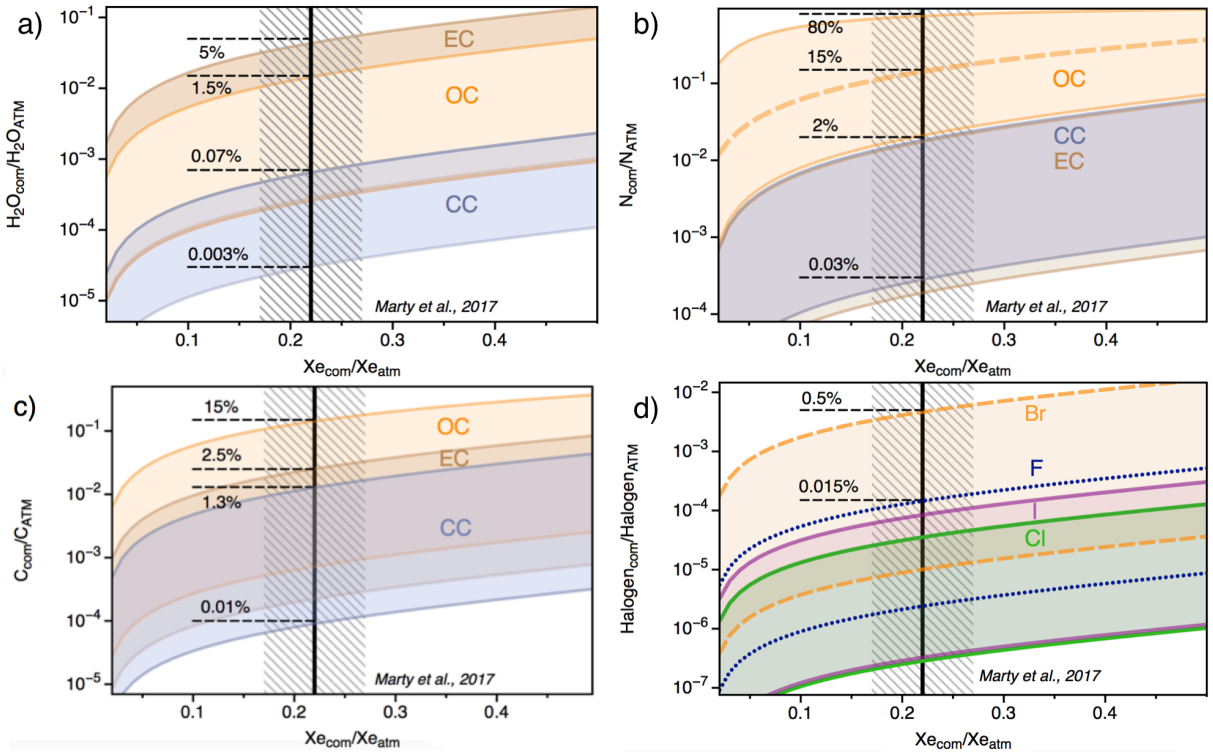

Figure 3. Cometary contribution to terrestrial water (a), nitrogen (b), carbon (c) and halogens (d). This is constrained by the 22 ± 5% cometary contribution to terrestrial ^{132}Xe[12], using the $^{132}Xe/H_2O$, $^{132}Xe/N$, $^{132}Xe/C$, $^{132}Xe/F$, $^{132}Xe/Cl$, $^{132}Xe/Br$ and $^{132}Xe/I$ of cometary and chondritic sources (Table 2). While cometary noble gases appear to be extremely enriched in ice, part of halogens present in the comet may reside in the non-volatile fraction of the comet, which possibly escaped measurement from the Rosetta spacecraft. This suggests that estimates for the cometary contribution to terrestrial halogens should be considered as minima. See methods for details on computation.

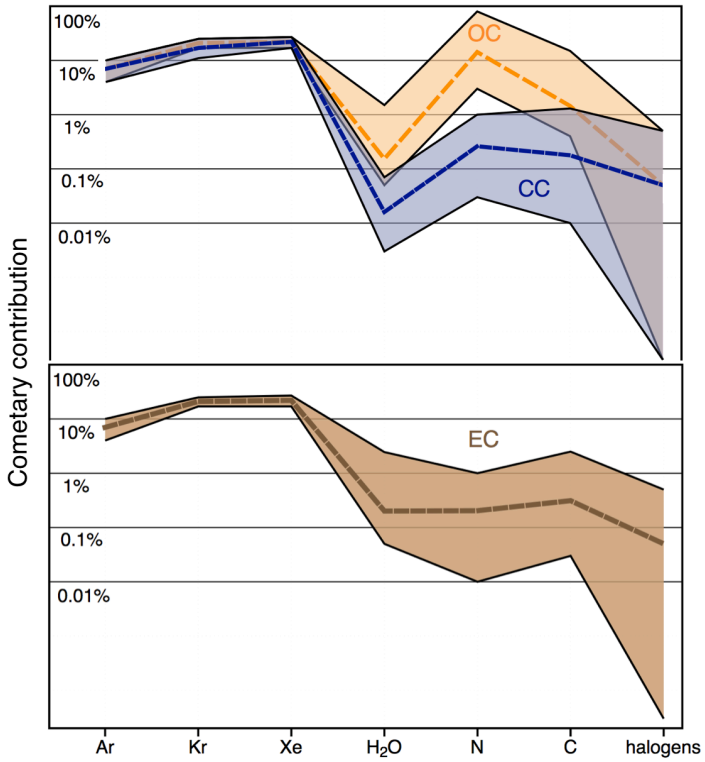

Figure 4. Cometary contribution to the ESR inventory of noble gases, water, nitrogen, carbon and halogens. Medians of distribution are displayed as dashed lines. Comets likely contributed negligibly to all the aforementioned volatile species, except for the heavy noble gases (~20%). High cometary contribution to terrestrial nitrogen, as required in the case of a binary mixture between OC and comets, preclude OC-like materials as the main source of chondritic volatiles in the atmosphere.

3) Constraining the extent of " Xe loss".

The depletion of Xe (missing Xe) in the atmosphere from the expected chondritic abundance pattern (Figure 1) remains an outstanding problem regarding the origin of the atmosphere. Mixing Kr and Xe between cometary and chondritic sources by taking into account the elemental ratios of each endmember is able to directly reproduce the isotopic composition of U-Xe, the modern isotopic composition of terrestrial atmosphere Kr and the $^{84}Kr/^{36}Ar$ ratio of modern atmosphere (Fig. 5). However, accounting for the present day Xe isotope composition and $^{132}Xe/^{36}Ar$ of the atmosphere requires atmospheric Xe to have been both fractionated in favour of the heavy isotopes, and to have lost 6-16 times the present-day atmospheric inventory of Xe (Fig. 5). Here, we combine two different approaches to set constraints on the extent of Xe specific loss to space after completion of the primitive atmosphere. The first method (A) computes the difference between the $^{84}Kr/^{132}Xe$ of the initial atmosphere, as formed by the mix of comets and chondrites, and the present-day atmospheric $^{84}Kr/^{132}Xe$, therefore requiring the $^{84}Kr/^{132}Xe$ of the chondritic component in the atmosphere to be defined. The second method (B) relies only on the apparent level of missing cometary Xe, without the need to define a chondritic endmember. Details regarding these two methods are provided in the Methods section.

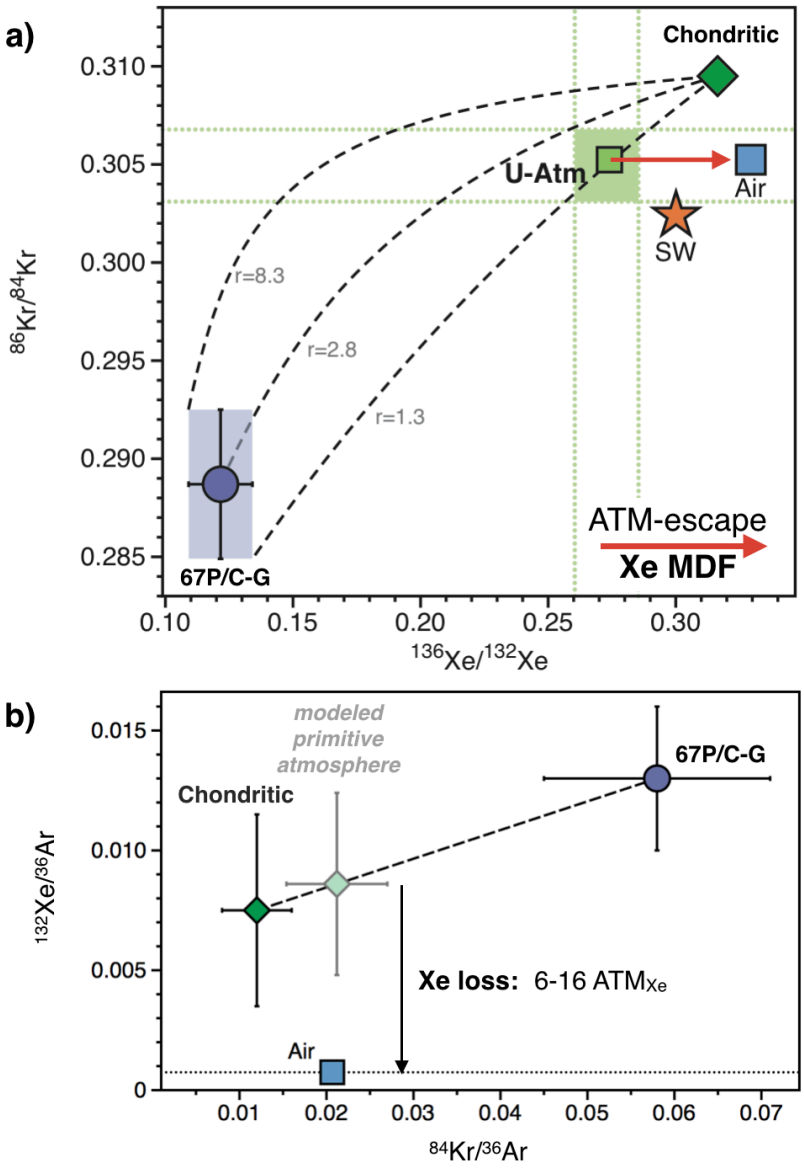

Figure 5. Origin and evolution of heavy noble gases in the terrestrial atmosphere from isotopic (a) and elemental (b) constraints. (a) Dashed curves represent mixing lines between comet 67/P-C and the chondritic Q component with ratios (r) equalling 8.3, 2.8 and 1.3, defined by the maximum, mean and minimum values for the $^{84}Kr/^{132}Xe_{comet}$ / $^{84}Kr/^{132}Xe_{chondrie}$, respectively. Whereas the isotopic composition of the chondritic end-member is taken as Q[33], the considered range of elemental compositions corresponds to that of EC, which spans all chondritic ratios reported in Table 1. Horizontal and vertical doted lines show ranges of values corresponding to the 21±5% cometary Kr and 22±5% cometary Xe[12] required to form the primitive atmosphere. Reconciling elemental and isotopic constraints requires the Kr and Xe isotope compositions of the primitive atmosphere to be indistinguishable from modern atmospheric Kr and U-Xe, respectively (U-Atm). Subsequent fractionation of Xe isotopes toward higher $^{136}Xe/^{132}Xe$ would account for the present day composition of air, with limited contribution from fission-derived Xe. The Xe-specific process driving atmospheric Xe MDF in favour of the heavy isotopes over the Archean[13,16] could - at least partially - account for the Earth's missing Xe, with negligible loss (if any) of atmospheric Kr through time. (b) Modelling the primitive atmosphere by mixing 80% chondritic and 20% cometary noble gases[31] requires the subsequent loss of 6 to 16 times the present day inventory of atmospheric Xe to account for the present modern composition of the terrestrial atmosphere.

(A) The terrestrial atmosphere, taken as a mix of comets (~20%) and chondrites (~80%) for ^{84}Kr and ^{132}Xe would result in ^{84}Kr/^{132}Xe ~3, which is significantly lower than the present-day atmospheric value (27.8, respectively; Table 1). Increasing the early atmospheric ^{84}Kr/^{132}Xe from ~3 to 27.8 requires a mechanism to account for the specific loss of atmospheric Xe. We show that, to form the modern atmosphere from the original mix of chondrites and cometary noble gases, between 7.5-23 ATM_{Xe} must be lost (Fig. 6a), in agreement with previous estimates for the extent of Earth's missing Xe (10-20 masses of ATM_{Xe})[19]. This computation relies on the ^{84}Kr/^{132}Xe of the chondritic end-member (Table 2), which has long been recognized to be ~1.3 ± 0.3 for bulk CC and OC[52] (see value of 1.2 ± 0.4 from our compilation, Table S1) and to be more variable for EC (see Table S1).

(B) The observation that the isotopic composition of atmospheric Kr has remained constant since the early Archean[13] suggests that the total inventory of Kr in the ESR might have been little affected since the last major episode of impact erosion on the atmosphere, considered to be the Moon forming event. From the amount of cometary Kr residing in the ESR (21±5%), we utilise the cometary ^{84}Kr/^{132}Xe ratio[29] to determine theoretical amounts of cometary Xe that should be expected in the ESR. Comparing these theoretical values with the previous estimates of cometary Xe in the ESR, i.e. 22±5% of the total inventory, yields that 3-12 ATM_{Xe} are missing from the ESR (Fig. 6b).

	^{84}Kr/^{132}Xe
Comet 67P/C-G	4.7±1.1
Q	0.81±0.05
CC	1.20±0.36
EC	1.84±1.14
sub-solar	5.86±0.84
Solar	20-29 (24.4)
Mars atmosphere	20.5±2.5
Mars interior	1.2
Earth atmosphere	27.8

Table 1. ^{84}Kr/^{132}Xe in different cosmochemical reservoirs of the solar system: comets[31], chondrites (Q[33], CC, EC; see Table S1), the subsolar component in EC[53], solar (range given by 54, estimated value by 32), Martian reservoirs (surface[55] and interior[56]), as well as the present-day terrestrial atmosphere[19].

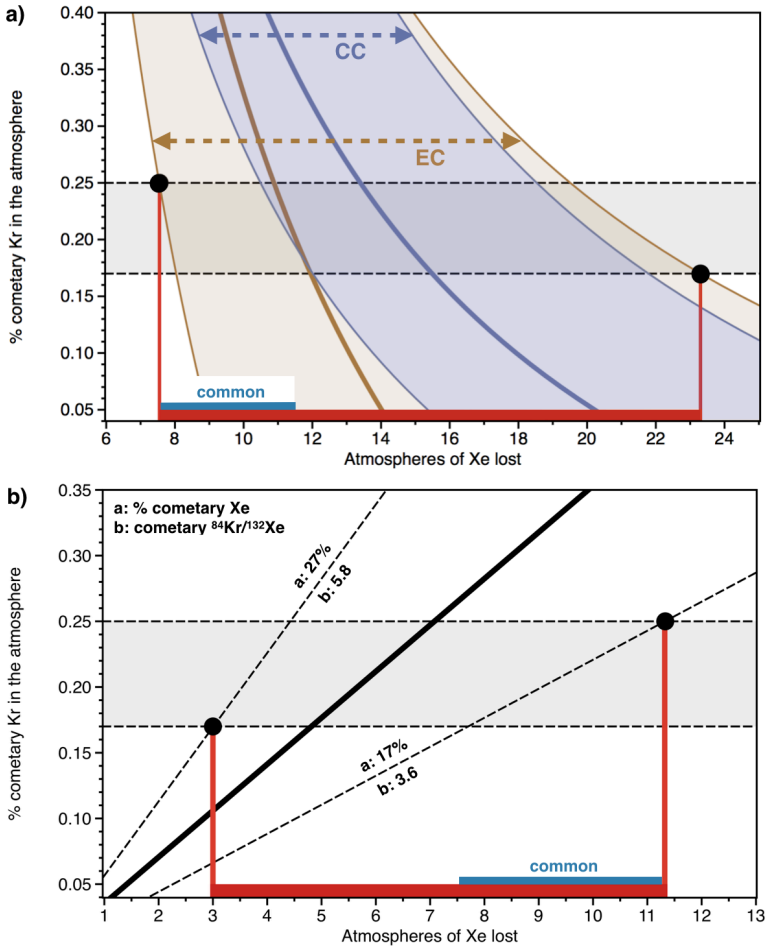

Figure 6. Constraining the extent of the Earth atmosphere missing Xe (a) Discrepancy between the $^{84}Kr/^{132}Xe$ of the initial atmosphere, as formed by the mix of comets and chondrites (Table 1), and its present-day $^{84}Kr/^{132}Xe$ permits the amount of atmospheric Xe lost as a function of the $^{84}Kr/^{132}Xe$ of the chondritic end-member to be derived (8-23 Xe atmospheric masses lost). The solid and dashed curved lines represent the medians of distribution for mixing with EC and CC, respectively. **(b)** Discrepancy between the $^{84}Kr/^{132}Xe$ of comet 67P/C-G (4.7 ± 1.1)[29] and the calculated cometary Kr and Xe contributions (~20%) enables the extent of atmospheric Xe loss to be estimated (3-11.5 Xe atmospheric masses lost). The "common" range: the only possibility for the extent of Xe loss from the atmosphere is at the intersection between 7.5-23 ATM_{Xe} and 3-11.5 ATM_{Xe}, i.e. ~8 to 12 ATM_{Xe} being missing from the present-day inventory. See methods for details on computation.

The $^{84}Kr/^{132}Xe$ ratio in comets (=4.7±1.1) as measured in the coma of Comet 67P/C-G[31] indicates that comets may have a chondritic-like noble gas elemental ratios, and not that of solar (Table 1). In order to have the same cometary contribution for both Kr and Xe (around 20%), mass balance considerations indeed require that cometary and chondritic end members that formed the Earth had similar $^{84}Kr/^{132}Xe$ ratios. Taking into consideration the range of $^{84}Kr/^{132}Xe$ values measured in Comet 67P/C-G and the uncertainties associated with the isotopic mixing constraints (21±5% and 22±5% cometary Kr and Xe, respectively) necessitates the chondritic $^{84}Kr/^{132}Xe$ component to be ≥2. Enstatite chondrites have abundant sub-solar noble gas component ($^{84}Kr/^{132}Xe$ = 5.86 ± 0.84)[53], causing their bulk $^{84}Kr/^{132}Xe$ to be higher

and more variable than other chondrite types (Table 1). Whilst accounting for the isotopic ratios of Kr released from ECs does not necessarily require a solar Kr contribution[53], Xe data for some subsolar gas-carrying ECs suggest the presence of SW-Xe. Okazaki et al. (2010) acknowledged that the Xe composition of subsolar gas may also be identical to that of Q gas. Hence, although the subsolar component in ECs may not constitute an isotopic component, it has a significant effect on bulk noble gas elemental ratios, specifically in raising the $^{84}Kr/^{132}Xe$ to higher values. Taken together, these data suggest that a source of solar-wind irradiated materials akin to that which accreted to form the EC parent body (or angrites, as seen from the analysis of D'Orbigny glass samples[57]) might be required to form the noble gas composition of the primitive atmosphere. Independent estimates of Xe loss assuming an EC-like chondritic endmember result in a common range of possible values, at the intersection between 3-11.5 ATM_{Xe} and 7.5-23 ATM_{Xe}, i.e. ~8 to 12 atmosphere masses of Xe being lost from the present-day inventory (see "common" range, Fig. 6).

The non-solar $^{84}Kr/^{132}Xe$ ratio for the comet 67P/C-G[31] refutes the idea that the two-step atmospheric formation model of fractionated solar plus late cometary addition[10] was responsible for the origin and evolution of the atmospheric noble gas composition. The present finding that up to 12 atmospheres of Xe could have been lost from the atmosphere since the Hadean eon potentially resolves the long-standing mystery of Earth's "missing xenon", which turns out to be predominantly "lost Xe". Assuming a Rayleigh-type distillation during the loss of 8-12 ATM_{Xe} to space requires the instantaneous isotopic fractionation α to be high, in the range 15-18‰u^{-1} (13). To date, significant isotopic fractionation (10 ± 4‰u^{-1}) has only been achieved under ionizing conditions[58,59], as suggested to occur in models of Xe loss to space and trapping in organic hazes[14]. The preferential incorporation of heavier Xe isotopes into archean organic hazes would have indeed left the atmosphere enriched in light Xe. Any subsequent atmospheric loss could have fractioned and ultimately resulted in the heavy Xe-enriched atmosphere we see today[14]. High α values up to 18‰u^{-1} might therefore result from the combination of isotopic effects from both escaping to space, and trapping in to organic hazes.

Martian meteorites suggest that escape of atmospheric Xe terminated much earlier (4.2–4.3 Gyr ago) on Mars relative to Earth[60]. The early formation of Mars (≤2.7 Myr after CAI formation)[61] may imply that the EUV flux responsible for Xe ionization and escape on Earth was much stronger in the early Martian atmosphere. In combination with the lower escape velocities expected on Mars, one can predict early and extensive Xe escape from the Martian atmosphere. Interestingly, the presence of Martian methane[62] indicates that trapping and fractionating ionized Xe in organic hazes might also have been a viable process for driving atmospheric Xe evolution on Mars. Given the differences between terrestrial planets, the atmospheres of Venus, Earth and Mars probably experienced contrasted evolutions. Analysing the Venusian atmosphere for its Kr and Xe composition therefore has the potential to discriminate between models of Xe fractionation on common planetary precursors[61], versus on planets themselves, as suggested by this study.

The possibility for some Xe to have partially remained sequestrated in the solid Earth under the form of stable chemical compounds, and for this mechanism to have contributed to the missing Xe paradox, cannot be discarded. However, we note that the potential to have sequestrated Xe in a given reservoir does not solve the missing Xe problem if there is a chance for Ar and Kr to be likewise sequestered - as seems to be the case[63]. To this extent, the mechanism accounting for missing Xe is required, not only to apply to Xe, but to be Xe specific. Because of their high density, solid Xe particles could preferentially segregate in the Earth's deeper regions[64]. However, the potential for large enough solid Xe inclusions to form and be transported into the core through gravitational segregation is highly questionable given the extremely low Xe abundance of the mantle. At present, less than 10% of the total inventory of heavy noble gases in the bulk silicate Earth resides in the mantle (Table 2). For the missing Xe to reside in the core would require the latter to store 10 to 20 ATM_{Xe}, i.e. more than 100 to 200 times more Xe than the total inventory of the mantle. Although Xe oxides are stable in the Xe–O system at pressures and temperatures of the Earth's lower mantle, neither Xe silicates, which would naturally decompose, nor oxides, which would be reduced by metallic iron, can exist in its strongly reducing environment[65]. Theory and experiment have also demonstrated that Xe and Fe do not react at pressures up to 155 GPa[66,67], therefore arguing against the likelihood of Xe partitioning into core-forming metal. Recently, Zhu et al. (2014)[68] showed that stable $XeNi_3$ and $XeFe_3$ would emerge at 200 GPa and 250 GPa, respectively. However, difficulties arise in finding a mechanism that can trap Xe at low pressure and deliver it to a depth where such stable Xe-bearing phases would emerge. In other terms, stable Xe–Fe and/or Xe-Ni compounds would be unstable until they reach core pressures, and so the process by which iron and/or nickel could have dragged Xe into the core are not well understood. Importantly, the high pressure required for potentially trapping some Xe in the deep mantle phases on Earth could not be achieved on Mars, where the maximum pressure in the core only reaches 50 GPa[69], further suggesting that this mechanism is unlikely to have resulted in the missing Xe observed for Mars and Earth. Interestingly, the much higher solubility of Ar in $MgSiO_3$ perovskite relative to Xe led Shcheka and Keppler (2012)[70] to suggest that, instead of having been preferentially retained in the solid Earth, Xe might have been depleted very early in the Earth's lower mantle relative to lighter noble gases during crystallization of perovskite from a magma ocean. The purported Xe-rich primordial atmosphere could then have been lost to space, before degassing of the lower mantle replenished Ar and Kr, but not Xe, into the atmosphere. Importantly, as it is the case for all of the aforementioned models, this scenario cannot account for the observed isotopic evolution of atmospheric Xe over the Archean eon[13]. Xenon ions escape in a photo-ionized hydrogen wind, possible in the absence of a geomagnetic field or along polar magnetic field lines that open into interplanetary space [16], is so far the only viable mechanism accounting for both the isotopic composition and elemental depletion of Xe isotopes in the terrestrial atmosphere.

4) On the nature of the chondritic component in the atmosphere.

Variations in the noble gas to water ratio over chondritic types are extremely large (several orders of magnitude difference between EC and CC). Although elemental ratios in meteorites may change with time and during processes involving thermal metamorphism and/or aqueous alteration[33], differences in the noble gas to water ratio between CC and EC/OC are primarily controlled by the amount of water within the respective chondritic types, reflecting the heliocentric distance at which the parent bodies accreted[71] (see section 5). Low $^{84}Kr/H_2O$ ratios (~$6.2x10^{-11}$) are therefore characteristic of CC, whilst $^{84}Kr/H_2O$ ratios over ~$5.3x10^{-10}$ are representative of drier materials akin to EC and OC (Table 2). Although the present-day $^{84}Kr/H_2O$ ratio of the ESR appears to plot in the range of OC and EC, the $^{132}Xe/H_2O$ of the ESR is close to (but still higher than) that of CC (Fig. 7; Table 2). This is likely due to the fact that the present-day $^{132}Xe/H_2O$ of the ESR needs to be corrected for its lost Xe to represent the $^{132}Xe/H_2O$ of the primitive ESR. By correcting the present-day inventory of the ESR for Xe loss, we find that the original $^{132}Xe/H_2O$ of the primitive Earth also matches the composition of chondritic materials with $^{132}Xe/H_2O$ similar to OC and EC (Table 2; Fig. 7). In order to compare the noble gas to water ratio of the primitive Earth as formed by mixtures of comets and chondrites with that of the present day ESR, we need to now estimate how planetary processes would have affected the noble gas to water ratio of the ESR over geological periods of time.

The atmospheric mass and composition of the early Earth likely resulted from an interplay of impact erosion, volatile element dissolution in the magma ocean, outgassing from the solid Earth, and late deliveries[1]. Although preferential dissolution of water into the magma ocean would have raised the noble gas to water ratio of the Earth's surface, the vast majority of water dissolved within the magma ocean is expected to have been expelled back to the atmosphere during rapid bottom-up magma ocean solidification[3,72,73], leaving only a small fraction of the original volatiles to be released into the atmosphere through later volcanism. The final amount of water in the atmosphere should therefore be close to the initial budget of the atmosphere and magma ocean[3]. After magma solidification and cooling, an ocean is expected to rapidly form on the surface of the proto-Earth[73]. The presence of an ocean at the surface of a protoplanet during subsequent impacts has been shown to extensively enhance atmospheric loss to space[2]. Whilst impact-driven loss may not elementally or isotopically fractionate the noble gases as it involves bulk ejection of the atmosphere, it can efficiently contribute to their overall depletion with respect to water[1]. Interestingly, the proto-Earth probably experienced multiple events of giant impact leading to sequential episodes of magma ocean outgassing and rapid formation of proto-oceans[74], so impact erosion of the atmosphere likely played a key role in altering the Earth's atmospheric mass and composition[2], including the noble gas to water ratio of the ESR.

Partial loss of water from the ESR by hydrodynamic escape and/or subduction of seawater to the mantle could also have modified the noble gas to water ratio of the ESR over

geological periods of time. The loss of 1/3 of a global ocean unit by hydrodynamic escape of H_2 has been suggested to account for the shift in $f(O_2)$ state of the upper mantle from the very low oxidation state equivalent to primitive differentiated bodies, to its present oxidized state[75]. Models of Xe ions escape in photo-ionized hydrogen winds also predict that the extent of hydrogen loss required to account for atmospheric Xe evolution could be one order of magnitude less than the mass of the present day oceans[16]. Parai & Mukhopadhyay (2018)[76] recently used the isotopic composition of Xe in the geological record (ancient atmosphere and mantle) to constrain the timing of onset and extent of volatile elements recycling into the solid Earth. They show that downwellings before 2.5 Ga were arguably dry, with the median H_2O concentration in downwellings at 3 Ga being ~0.61 p.p.m. H_2O, compared to modern-day slabs subducting beyond depths of magma generation (~400–1,000 p.p.m. H_2O[77]). According to continental freeboard studies, sea level changes since the Archean were limited to less than 500m[78]. The total mass of water within the ESR is therefore thought to have been established early and to have remained roughly constant over geological periods of time, potentially since the conclusion of the Earth's last main accretionary stage, with the net flux of water to the surface being balanced by the return through subduction[79]. The initial mass of the early oceans, as determined by mass balance calculations, would have been 20wt.% greater than at present[80], suggesting that variations in the budget of water in the ESR would have been limited since formation of the primitive ocean after magma ocean solidification. The noble gas to water ratio of the ESR could therefore have been established early during Earth's history, with impact-driven loss of the early atmosphere constituting the main process in driving noble gas to water fractionation of the ESR with respect to its precursor material composition. In this case, the noble gas to water ratio of the ESR should be taken to reflect a minimal value for the noble gas to water ratio of the building blocks it accreted from.

The possibility to have had even drier precursors (i.e., with higher noble gas to water ratios) and a preferential loss of Kr and Xe relative to H_2O during impact events leaves the potential for Earth to have predominantly acquired its volatile elements from EC-like asteroids (Fig. 7-8). Taking the maximum extent of previously determined missing Xe to reach $20*ATM_{Xe}$[19] would further increase the inferred $^{132}Xe/H_2O$ of the primitive Earth (Fig. 7), and strengthen our interpretation. Finally, estimates of water contents in the bulk mantle range from 1 MTO[81] up to 12 MTO[6], with a mean value of around 2 to 3 MTO potentially residing in the solid Earth[82]. When considering an extreme scenario where all the water now potentially residing in the Earth's mantle originated from the surface would lower the $^{84}Kr/H_2O$ of the primitive Earth down to $3.2.10^{-10}$ and $1.4.10^{-10}$ for 5 MTO and 12 MTO, respectively, yet still remaining above the maximum $^{84}Kr/H_2O$ of CC ($9.5.10^{-11}$).

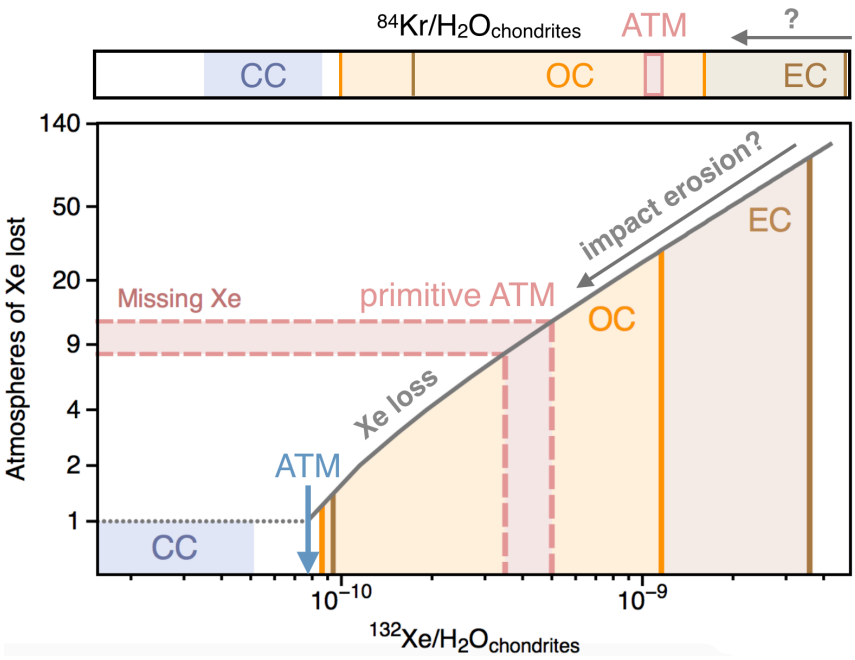

Figure 7. Origin and evolution of heavy noble gases in the terrestrial atmosphere as constrained by the extent of missing Xe. The present-day atmosphere is corrected for 8-12 atmospheric masses of Xe loss, therefore allowing its primitive $^{132}Xe/H_2O$ to be estimated. While impact erosion of the atmosphere could have driven preferential loss of noble gases relative to water during accretion (i.e. decreasing $^{132}Xe/H_2O$)[1], a preferential loss of water relative to noble gases during accretion (i.e. increasing $^{132}Xe/H_2O$) is unlikely. The finding that the $^{132}Xe/H_2O$ of the proto-Earth may have been toward the end-member of EC, which were progressively supplied throughout the Earth's accretion history, suggests that the majority of the Earth' surface volatiles may have been delivered during the main phases of terrestrial accretion. This is in line with the $^{84}Kr/H_2O$ of the ESR being similar to EC, but distinct from CC.

Whilst it is commonly thought that planets in the inner solar system first grew dry, with water and atmophile elements being subsequently contributed by volatile-rich materials originating from large heliocentric distances[6,83,84], our results suggest that CC may not have been the primary source of volatiles in the ESR. This is in line with the predominantly inner solar system origin of the latest stages of Earth's accretion[8,9]. Bulk water concentrations for EC range from <0.05%[85] to ~0.5%[86], indicating that the 100% EC phase of the final 40% of terrestrial accretion[9] can provide between 0.8 and 8 global ocean units (1.38×10^{24}g of H_2O), with the late veneer potentially supplying another 0.7 global ocean unit[37]. This suggests that the bulk of Earth's water could have accreted with its main building blocks, before the giant impact[37], and that Earth's volatiles potentially originated from drier precursors than previously thought. However, estimates of water contents in EC are highly variable[86], with the ever-present issue of air contamination correction. Firmly establishing whether or not the latest stages of Earth's main accretion could have contributed sufficient water to the ESR will require additional, more precise measurements of water in EC. The main conclusions of this contribution regarding the origin and evolution of volatile elements - especially heavy noble gases - in the ESR are reported in Fig. 8.

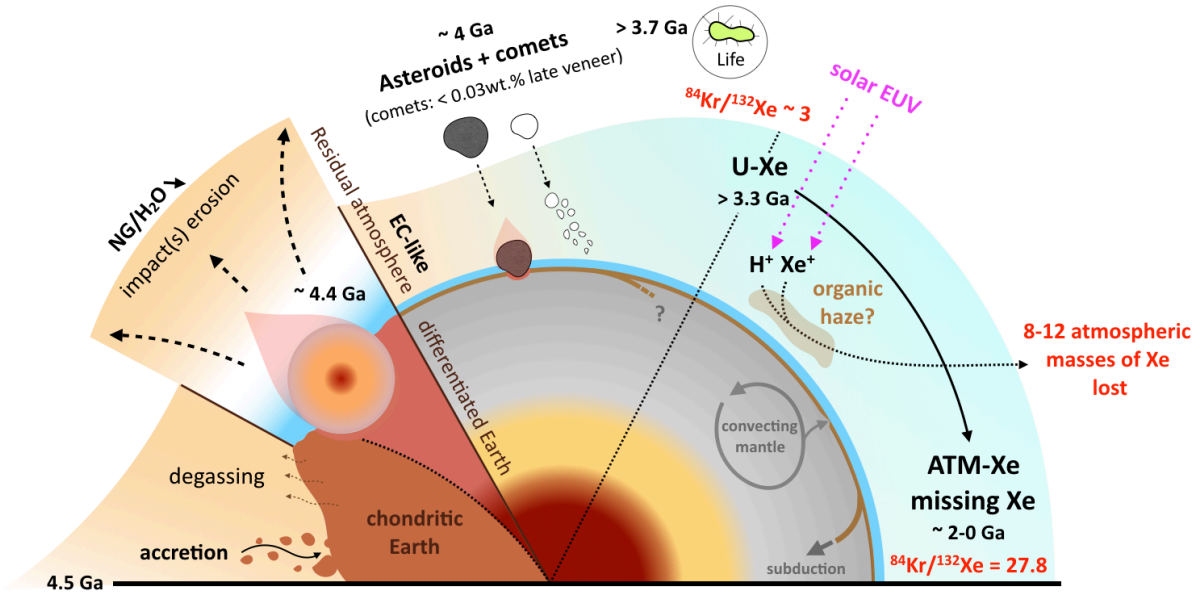

Figure 8. Schematic view of the origin and evolution of heavy noble gases in the atmosphere. Heavy noble gases are chondritic in the solid Earth[46-47], in line with the Earth being dominantly composed of chondritic accreting blocks. The Earth's early atmosphere has a complex history of impact erosion, outgassing from the solid Earth and late supplies by asteroidal and cometary bombardments. The addition of ~ 22% cometary heavy noble gases to a Q-like[33] atmosphere is able to resolve the origin of U-Xe[12] and atmospheric Kr. Subsequent and protracted fractionation of atmospheric Xe is thought to have been driven by Xe escape to space with 8-12 atmospheric masses of Xe being lost over the Archean eon[13].

5) Working hypotheses: pros and cons.

The present paper uses previously published data on the noble gas isotopic composition and volatile element content of cometary and chondritic materials to infer on the origin and composition of the primitive ESR. In line with results from previous studies[18,84], we predict comets to have contributed negligibly to the terrestrial volatile budget, except for the heavy noble gases. This work includes some assumptions that we outline in detail below, regarding (a) the relationship between the isotopic signature of comet 67P/C-G and other components in the solar system, and its representativeness for the bulk cometary reservoir, (b) the composition of cometary and chondritic end-members for mixing calculations, and (c) the effect of planetary processes on the global noble gas to water ratio of the ESR.

(a) The European Space Agency Rosetta mission to comet 67P/C-G represents the first detailed *in situ* measurements including trace elements such as noble gas isotopes of a cometary body in the solar system. Nucleosynthetic differences between distinct solar system reservoirs, such as observed for Ti, Sr, Ca, Cr, Ni, Zr, Mo, Ru, Ba, Nd, Sm, Hf, W, and Os isotopes between CC (from the outer solar system) and EC/OC (from the inner solar system)[87], indicate that nucleosynthetic heterogeneities may develop over large spatially distinct reservoirs in the solar system. The discovery of molecular O[88] and S_2[89] in the coma of comet 67P/C-G, as well as small deviations of $^{12}C/^{13}C$ in CO and CO_2 relative to solar composition[90], suggests it formed at least in part from icy grains originating from the interstellar medium. A possibility is that the

noble gas signature of comet 67P/C-G represents the composition of the outer solar system/interstellar reservoir from which comets originally formed[12] and therefore, other the noble gas signature of comets having accreted from the same region as comet 67P/C-G should reflect a similar nucleosynthetic mixture. In this framework, it is however surprising that no evidence for a cometary noble gas contribution to the CC reservoir (especially Xe) could be found so far[91].

The Kr and Xe signature measured in comet 67P-C/G define a nucleosynthetic component that is unique within our solar system, with notable depletions in ^{83}Kr, ^{86}Kr, ^{134}Xe and ^{136}Xe relative to the "normal" (N) composition[12,31]. The Kr isotopic signature of comet 67P/C-G would be best accounted for by a mix of presolar N-Kr plus 2-5% G-Kr[31] (Fig. S6), with additions of G-Kr being invoked to account for the deficit in ^{83}Kr/^{84}Kr relative to N-Kr[92]. However, the G-Kr nucleosynthetic component shows such a huge isotopic variation relative to N-Kr[92,93] that the final Kr isotopic composition of any cometary material formed by mixing G and N components would be highly sensitive to the extent of G-Kr contribution (Fig. S2). Although we consider the presolar Kr signature of comet 67P/C-G to be representative of Jupiter family comets (JFC) in general, cometary materials with small variations in the amount of G-Kr could have brought Kr to Earth with a slightly different isotopic signature than that measured in comet 67P/C-G (Fig. S2). This may in part explain why the addition of comet 67P/C-G to a chondritic atmosphere does not succeed in exactly reproducing the ^{83}Kr/^{86}Kr signature of the atmosphere (Fig. S1).

The Xe isotope composition of comet 67P-C/G is marked by a deficit in isotopes that are only produced by r-process (i.e., ^{134}Xe and ^{136}Xe) relative to common nucleosynthetic reservoirs (solar and chondritic; Fig. 9). Conversely, the Xe-HL and Xe-N components carried by presolar nanodiamonds and SiC, respectively[93], are characterized by higher ^{134}Xe/^{132}Xe and ^{136}Xe/^{132}Xe relative to the solar composition (Fig. 9). Importantly, all Xe isotope cosmochemical reservoirs within the solar system are related by MDF and mixing relationships (Fig. 9). The isotopic composition of Xe in chondrites and solar wind could potentially have derived originally from cometary Xe through the addition of r-process rich material[11] (e.g. ~3.2% of Xe-H, with the Xe-H composition ref. 94). Comets may therefore constitute a best estimate for the composition of the primitive solar system. This scenario requires that p-process derived (Xe-L) and r-process derived (Xe-H) fractions of Xe-HL be separated from one another, which, although expected from an astrophysical point of view, is at odds with their constant abundance ratio in presolar nanodiamonds found in meteorites[11,91,93]. If Xe-L and Xe-H are considered to be inseparable from one another, then this would require cometary Xe to also have had a deficit in p-process derived isotopes relative to the solar composition, which could only be compensated for by an addition of pure p-process Xe[95] - in itself inconsistent with the initial hypothesis of Xe-L and Xe-H being inseparable. Interestingly, the relative r-process deficit in cometary material could be a widespread feature of the bulk cometary reservoir. For instance, metal-rich carbonaceous chondrites thought to have accreted in the outermost regions

of the PSN, beyond the orbit of Neptune, are thought to have accreted significant amounts of primordial molecular cloud material[96,97]. Their analysis reveals the occurrence of a $^{26}Mg^*$-depleted component, interpreted to reflect the contribution from an r-process poor, cometary component[97].

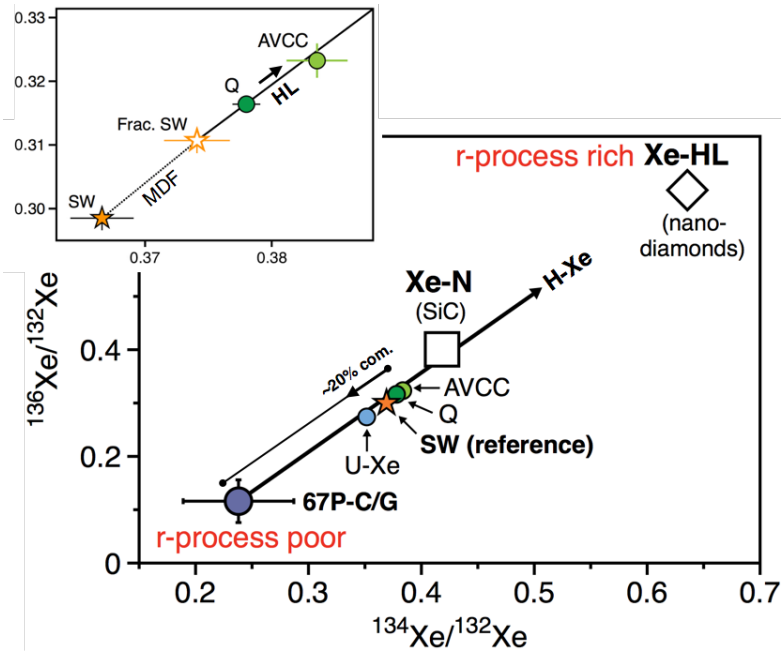

Figure 9. Three-isotope diagram of Xe isotopes showing the relationships between planetary and cosmochemical reservoirs. The solar composition (SW)[32] is intermediate between, on one side, the r-process depleted cometary signature[12], and, on the other side, the HL-Xe and N-Xe components carried out by presolar nanodiamonds and SiC, respectively[92,93]. The relationship between SW, Q and AVCC is shown in the upper left panel. The AVCC signature represents a slightly higher contribution of HL-Xe from fractionated SW-Xe, relative to Q-Xe[91], which was itself produced by 98.5% SW-Xe that experienced linear mass dependent fractionation of 10.2 u^{-1} favouring the heavy isotopes, and mixing with 1.5% Xe-HL[93]. At last, we show the U-Xe composition[11], accounted for by mixing ~20% cometary Xe with ~80% chondritic Xe[12]. In this plot, we note that the MDF line (dotted line) is interestingly very close to general mixing trends.

From a dynamical point of view, it is unlikely that only one type of comet impacted the early Earth[84], but the isotopic composition of noble gases within long-period comets akin to those now belonging to the Oort cloud (OCC) is unknown. Hence, whilst it cannot be stated with certainty that all comets (Kuiper belt objects and long period comets) have the same noble gas isotopic signature as comet 67P/C-G, it cannot be dismissed either, and the nucleosynthetically distinct nature of noble gases in comet 67P/C-G remains our best analogue to the signature of the bulk cometary reservoir. We note that most comets present comparable enrichments in D relative to H, as well as consistent enrichments in ^{15}N relative to ^{14}N[35], suggesting that comets from the OCC and JFC both have sampled a common reservoir. Addressing the potential variability of noble gases within cometary material, and how this would affect our estimates of the cometary contribution to the terrestrial atmosphere, will require the analysis of new cometary materials belonging to different dynamical families, which would only be achievable though future spatial missions.

(b) We consider the elemental ratios of noble gases within sublimating cometary ice and measured within the coma of comet 67P-C/G to be representative of the bulk comet composition. Yet, phases other than ice (namely organic materials and silicates) may contribute the bulk composition of cometary noble gases. The highest content of ^{132}Xe measured so far for the insoluble organic matter of a carbonaceous chondrite is $2.2.10^{-11}$ mol ^{132}Xe/g (Paris meteorite[85]), which is 2-3 orders of magnitude lower than the concentration of ^{132}Xe in cometary ice (~$7.4.10^{-9}$ mol ^{132}Xe/g)[29]. Heavy noble gas concentrations in silicate phases, as measured in meteorites, are orders of magnitude lower than those found in chondritic IOM. Hence, although some uncertainties remain regarding the dust to ice ratio of cometary materials, mass balance considerations clearly indicate that the noble gas composition of ice controls that of the bulk comet. Importantly, fractionation of cometary noble gases could potentially have occurred during their release from the cometary surface; discrepancies in the outgassing velocities between Ar, Kr and Xe were taken into account to derive the cometary ice elemental composition used in this study[31].

Regarding chondrites, bulk elemental ratios used in the present study could have been modified from their initial values by several processes, including thermal metamorphism, aqueous alteration and cosmogenic isotope production. However, parent body processes resulting in larger depletions of Ar and Kr relative to Xe in chondrites only cause elemental ratios to vary within a maximum factor of ~3[33,52,90]. Interestingly, EC, which represent the most metamorphosed chondritic group, show the highest ^{84}Kr/^{132}Xe, indicating that the effect of thermal metamorphism has not been sufficient enough to overprint the higher ^{84}Kr/^{132}Xe of the trapped subsolar component[53]. Finally, the isotopes we use to compute elemental ratios (^{36}Ar, ^{84}Kr and ^{132}Xe) are abundant and limitedly produced by spallation reactions (unlike e.g., ^{38}Ar, ^{83}Kr or $^{124\text{-}128}$Xe)[54] so that the production of cosmogenic isotopes would not affect so much the considered elemental ratios. Unlike noble gas abundances and elemental ratios, noble gas to water ratios vary over several orders of magnitude difference between EC/OC and CC (Table 2). These variations are fundamentally controlled by the amount of water accreted within the respective parent bodies, reflecting a gradient in the heliocentric distance at which parent bodies of the different meteoritic groups accreted[71]. Although the Kr/Xe/water ratios measured in chondrites might not exactly represent the composition of materials supplied to Earth during planetary accretion, we consider their subsequent modification to have been sufficiently limited to permit their use in this study.

At last, we note that some uncertainties remain regarding the degree of differentiation of the Earth's accretionary building blocks[98], so the use of bulk chondrite compositions in our mixing calculations may induce a bias in the resulting estimates of the mass of chondritic material being required to supply chondritic volatiles to the atmosphere. Likewise, heavy noble gases in the mantle, as determined from the analysis of popping rocks[46] and CO_2 well gases[47], are chondritic in origin, so degassing of mantle-derived volatiles over geological periods of time could have significantly contributed the chondritic component in the atmosphere. It is not clear

how much the late additions of chondritic material (e.g., as part of the late veneer) and the degassing of chondritic noble gases from the mantle, contributed to form the atmosphere, respectively. From mass balance considerations, a ~0.5 wt.% of the Earth late veneer contribution of chondritic material would not be sufficient in supplying chondritic noble gases to the atmosphere[6], therefore requiring significant contribution from mantle degassing. However, the required mass of a late veneer being mainly composed of achondritic material that had experienced differentiation and volatile loss before accretion to Earth could be as high as a few wt.% of the Earth[92]. Although this is an interesting point that would merit further investigation, how the accretion of achondritic material to the Earth would affect the estimates presented in this contribution is ultimately unknown.

(c) Processes involved in enriching or depleting the various isotopes of Xe over geological timescales are not completely understood. The scenario we favour here (Xe escape to space) is so far the only viable mechanism accounting for both the isotopic composition and elemental depletion of Xe isotopes in the terrestrial atmosphere. It notably relies on the fact that, due to the enhancement of the EUV emission of the young Sun at 3.5 Ga, atmospheric Xe photoionization rate was increased by about 4000% (against ~1000% for lighter noble gases)[14]. However, the exact conditions allowing for such an isotopic evolution and loss of atmospheric Xe through escape may vary depending on the possible time evolution of, e.g., the terrestrial magnetic field, the stellar UV flux, and/or the H_2 partial pressure in the atmosphere. One possibility is that Xe isotopic evolution was not as continuous and protracted as previously thought; for instance, it could have been restricted to polar windows opening within the geomagnetic field, outbursts of high solar activity, or limited to transient episodes of abundant hydrogen, or a combination of all three[16].

Likewise, we conclude in section 4 for the noble gas to water ratio of the ESR to have been established early during Earth's history, with impact-driven loss of the early atmosphere constituting the main process driving noble gas to water fractionation of the ESR with respect to its precursor material composition. However, it should be noted that our knowledge of how planetary processes affected the budget of volatile elements within the ESR over geological periods of time suffers from several caveats that hamper definitive conclusions to be drawn from the considerations presented in this contribution. The extent of C[99], N[100] and noble gas[101] recycling into the mantle is subject to debate and could have significantly altered the initial composition of the ESR. Better constraining the conditions and effects of the Moon-forming giant impact on the terrestrial budget of volatile elements, the extent of volatile transfers between the Earth's interior and its surface during the subsequent magma ocean episode, the timing of the onset of subduction and volatile recycling in to the solid Earth, as well as the composition and evolution of the primitive atmosphere, will ultimately allow the main type of chondritic material that supplied the Earth surface with most of its volatile elements to be further elucidated.

		Chondrites			Comet	ESR	BM
		CC	**OC**	**EC**	**67P/C-G**	**2.90E^{25}g**	**4.01E^{27}g**
Noble gases	^{36}Ar	$(2.59^{0.74}_{1.17})\times10^{-11}$	$(3.75^{2.41}_{7.36})\times10^{-12}$	$(8.32^{5.56}_{13.1})\times10^{-12}$	$(4.31\pm1.70)\times10^{-08}$	1.97×10^{-10}	$(7.78\pm4.29)\times10^{-14}$
	^{84}Kr	$(3.66^{1.27}_{1.03})\times10^{-13}$	$(7.56^{2.21}_{4.58})\times10^{-14}$	$(5.93^{2.86}_{5.94})\times10^{-14}$	$(2.52\pm1,16)\times10^{-09}$	4.08×10^{-12}	$(1.90\pm1.10)\times10^{-15}$
	^{132}Xe	$(3.35^{1.23}_{1.12})\times10^{-13}$	$(6.25^{1.56}_{2.77})\times10^{-14}$	$(3.64^{2.29}_{3.50})\times10^{-14}$	$(5.34\pm2.54)\times10^{-10}$	1.47×10^{-13}	$(1.71\pm0.45)\times10^{-16}$
	H_2O	$(5.71^{0.56}_{0.57})\times10^{-03}$	$(2.39^{1.61}_{3.05})\times10^{-04}$	$(0.28:2.78)\times10^{-04}$	$(1.11\pm0.22)\times10^{-02}$	3.05×10^{-03}	$(2.00\pm0.96)\times10^{-04}$
	δD(‰)	-32 to 92	-120	-130	0 to 2000	0	-
	^{14}N	$(5.21^{1.29}_{1.04})\times10^{-05}$	$(3.57^{2.73}_{3.75})\times10^{-07}$	$(2.30^{0.80}_{1.43})\times10^{-05}$	$(1.80\pm1.00)\times10^{-03}$	1.23×10^{-05}	$(8.98\pm4.59)\times10^{-08}$
	δ^{15}N(‰)	~ +40	~ 0	-30 ± 10	840 ± 71	0	-
	^{12}C	$(1.67^{0.41}_{0.46})\times10^{-03}$	$(8.33^{5,00}_{11.4})\times10^{-05}$	$(3.08^{0.70}_{0.50})\times10^{-04}$	$(3.70\pm2.80)\times10^{-02}$	2.66×10^{-04}	$(6.36\pm2.49)\times10^{-05}$
Halogens	^{35}Cl	$(2.89^{0.96}_{2.24})\times10^{-06}$	$(1.61^{1.16}_{3.07})\times10^{-06}$	$(1.68^{0.92}_{2.15})\times10^{-06}$	$(1.55\pm0.31)\times10^{-07}$	9.59×10^{-02}	2.68×10^{-04}
	^{19}F	$\sim2\times10^{-06}$	$\sim5\times10^{-07}$	$(1.05:2.63)\times10^{-06}$	$(7.83\pm0.62)\times10^{-07}$	-	-
	^{79}Br	$(2.48^{1.20}_{2.03})\times10^{-09}$	$(7.70^{6.00}_{26.0})\times10^{-10}$	$(3.98^{3.19}_{2.94})\times10^{-09}$	$(8.60\pm0.70)\times10^{-09}$	3.91×10^{-04}	4.04×10^{-06}
	^{127}I	$(3.15^{1.28}_{1.14})\times10^{-10}$	$(1.81^{0.08}_{1.73})\times10^{-10}$	$(4.41^{2.80}_{0.55})\times10^{-10}$	$(4.06\pm2.23)\times10^{-11}$	1.23×10^{-04}	1.01×10^{-07}

Table 2 I Noble gas, volatile element and halogen composition of chondritic material (CC, OC and EC), comet 67P/C-G and terrestrial reservoirs (ESR, bulk mantle "BM") in mol/g. Literature data used to construct this table are provided in Supplementary information. Here, we report values for the median, first (Q1) and third (Q3) quartiles of each data set ($\text{Median}^{Median-Q1}_{Q3-Median}$, see methods). Concentrations for the ESR and BM are normalised to the mass of the corresponding reservoir, reported in bold beneath the column headers[43]. Given the large uncertainties and limited amount of measurements, the water content in EC is provided as a range of extreme values reported in the literature[84-85]. Note that noble gas elemental ratios may not be derived from this table; we recommend computing average values of compiled ratios (as done here for EC, see supplementary information), rather than ratios of median values.

Acknowledgments

Laurette Piani, Guillaume Avice and Peter Barry are acknowledged for participating in fruitful discussions. Exchanges with Kathrin Altwegg, Martin Rubin, and the ROSINA instrument team were also much appreciated. We gratefully thank the six anonymous reviewers of this paper, and the Editor for his careful handling of our manuscript. This study was supported by the European Research Council (grant PHOTONIS 695618).

Additional Information

Competing Interests: The authors declare that they have no competing interests.

Author Contributions

D.V.B. and M.W.B. performed all calculations and modelling and prepared the first draft of the manuscript. D.V. B., M.W.B. and B.M. initiated the project. All authors were involved in the discussion of ideas and preparation of the manuscript.

Methods

Determining the composition of chondritic end-members. In order to derive a representative concentration for a given element within a given type of chondrite (CC, OC and EC), we applied interquartile range calculations on data compiled from the literature (see Supplementary Information). Due to the fact that concentrations of volatiles within chondrites can vary across several orders of magnitude and are not necessarily normally distributed, the use of mean values and standard deviations to derive the average composition of each end-member may not be justified. In addition, extreme outliers might artificially influence the value of the mean, while keeping the median of the dataset unaffected. For this reason, we computed the median concentration of Ar, Kr, Xe, N, C and H_2O within the three chondritic end-members (CC, EC and OC) and determined statistical dispersion of the data by calculating the interquartile range (IQR). The IQR calculates the difference between the 25th (Q_1) and the 75th (Q_3) percentiles, i.e. IQR = Q_3 - Q_1. The IQR provides a method for excluding extreme outliers and providing a range within which 50% of the data lie. In Table 2, we report values for the median, first (Q1) and third (Q3) quartiles of each data set ($\mathsf{Median}^{Q1}_{Q3}$). The ranges of values we use for mixing calculations are taken as [Median-Q1;Median+Q3]. Interquartile ranges are robust measures of variability, in a similar manner that medians are robust measures of central tendency. Just like medians, interquartile ranges are excellent for avoiding large effects on potentially skewed distributions, which is not the case for means and standard deviations.

Computing the extent of Xe loss. The first approach aims at determining the initial $^{84}Kr/^{132}Xe$ of the atmosphere by mixing cometary and chondritic end-members with known $^{84}Kr/^{132}Xe$ ratios. Using the $^{84}Kr/^{132}Xe$ of comets and chondrites (Table 1), we derive theoretical

$^{84}Kr/^{132}Xe$ ratios for the initial atmosphere. These ratios are systematically lower than the present day atmospheric $^{84}Kr/^{132}Xe$ (Table 1), therefore requiring that part of the atmospheric ^{132}Xe was lost. For each theoretical $^{84}Kr/^{132}Xe$, we compute how many times the present-day budget of atmospheric ^{132}Xe should be lost to fit the actual $^{84}Kr/^{132}Xe$ of the present-day atmosphere.

The second approach is based on the fact that ~22% of the atmospheric Kr and Xe are cometary in origin. We calculate the amount of Kr corresponding to 21±5% of the present-day inventory of the ESR (Table 2). Using the $^{84}Kr/^{132}Xe$ ratio in cometary ice, we derive a theoretical budget of Xe that would have been brought to Earth by comets. This budget of Xe is compared to the actual amount of atmospheric Xe being cometary in origin in the ESR, i.e. 22±5% (ref 12; Table 2). We find that this theoretical budget of cometary Xe in the atmosphere is higher than the actual budget of the present-day ESR. This is likely accounted for by the fact that part of atmospheric Xe has been lost to space, therefore yielding a present day amount of Xe in the ESR being significantly lower than what had been initially accreted by early Earth. We therefore compute how many times the present-day budget of Xe in the ESR would be required to be added (i.e., corrected for its loss) to fit the cometary Xe budget of the primitive ESR.

Computing the cometary contribution to terrestrial volatiles. Cometary contribution to the budget of Kr and Xe in the ESR is ~22%, with the remaining ~78% being derived from chondritic material (ref 12). Cometary contribution to the ESR budget of water (taken as an example here) can be computed if the noble gas to water elemental ratio is known for both cometary (referred to as "com.") and chondritic (referred to as "ch.") end-members:

$$\frac{H_2O_{com.}}{H_2O_{ch.}} = \frac{H_2O_{com.}}{^{132}Xe_{com.}} * \frac{^{132}Xe_{com.}}{^{132}Xe_{ch.}} * \frac{^{132}Xe_{ch.}}{H_2O_{ch.}} \quad (1)$$

noted as: $\beta = \alpha * \gamma$

with $\alpha = \frac{^{132}Xe_{com.}}{^{132}Xe_{ch.}}$, $\beta = \frac{H_2O_{com.}}{H_2O_{ch.}}$ and $\gamma = \frac{\frac{H_2O_{com.}}{^{132}Xe_{com.}}}{\frac{H_2O_{ch.}}{^{132}Xe_{ch.}}}$.

The cometary $^{132}Xe/H_2O$ is taken as that of comet 67P/C-G, therefore causing the γ parameter to be function of the chondritic $^{132}Xe/H_2O$ only. We note:

$$x = \frac{^{132}Xe_{com.}}{^{132}Xe_{ATM}},\ y = \frac{H_2O_{com.}}{H_2O_{ATM}} \text{ and } \alpha = \frac{x}{1-x},\ \beta = \frac{y}{1-y}.$$

For each value of x, which is the fraction of cometary Xe in the atmosphere (taken from 0 % to 100 %), we calculate the corresponding value of α and derive β for given values of chondritic $^{132}Xe/H_2O$ (i.e., different values of γ). This allows the corresponding contributions of

comets to the budget of terrestrial surface water (parameter y) to be calculated. The same calculations have been carried out using the noble gas to carbon, nitrogen and halogen elemental ratio for both cometary and chondritic end-members (Table 2).

Computing the $^{132}Xe/H_2O$ of the chondritic component in the atmosphere. We establish here the equation giving the $^{132}Xe/H_2O$ of the initial atmosphere as a function of the cometary or chondritic $^{132}Xe/H_2O$. We have:

$$\left(\frac{^{132}Xe}{H_2O}\right)_{ESR,model} = \frac{^{132}Xe_{ESR}}{H_2O_{ESR}} = \frac{^{132}Xe_{com.} + {}^{132}Xe_{ch.}}{H_2O_{com.} + H_2O_{ch.}} \quad (2)$$

which equals to:

$$\left(\frac{^{132}Xe}{H_2O}\right)_{ESR,model} = \frac{^{132}Xe_{com.}}{H_2O_{com.}} * \frac{\left(1 + \frac{^{132}Xe_{ch.}}{^{132}Xe_{com.}}\right)}{\left(1 + \frac{H_2O_{ch.}}{H_2O_{com.}}\right)} = \frac{^{132}Xe_{com.}}{H_2O_{com.}} * \frac{\left(1 + 1/\alpha\right)}{\left(1 + 1/\beta\right)} \quad (3)$$

$$\left(\frac{^{132}Xe}{H_2O}\right)_{ESR,model} = \frac{^{132}Xe_{ch.}}{H_2O_{ch.}} * \frac{\left(\frac{^{132}Xe_{com.}}{^{132}Xe_{ch.}} + 1\right)}{\left(\frac{H_2O_{com.}}{H_2O_{ch.}} + 1\right)} = \frac{^{132}Xe_{ch.}}{H_2O_{ch.}} * \frac{(\alpha+1)}{(\beta+1)} \quad (4)$$

By considering a constant mass of water within the ESR since the last major episode of impact erosion of the atmosphere, which is presumably the Moon forming event, the ESR can be corrected for its loss of Xe through atmospheric escape in order to derive theoretical $^{132}Xe/H_2O$ for the primitive atmosphere. In equation (4), we note that the initial $^{132}Xe/H_2O$ of the ESR only depends on the $^{132}Xe/H_2O$ of the chondritic end-member. A theoretical value for the $^{132}Xe/H_2O$ of the chondritic component in the atmosphere can therefore be calculated for any given extent of Xe loss, with:

$$ATM_{Xe}lost = \frac{\left(\frac{^{132}Xe}{H_2O}\right)_{ESR,model}}{\left(\frac{^{132}Xe}{H_2O}\right)_{ESR,observed}} = \frac{\frac{^{132}Xe_{ch.}}{H_2O_{ch.}} * \frac{(\alpha+1)}{(\beta+1)}}{\left(\frac{^{132}Xe}{H_2O}\right)_{ESR,observed}} \quad (5)$$

Computing the maximum mass of comets striking the Earth after the Moon-forming impact. Due to the fact that part of the volatile elements accreted during the later stages of accretion may have been lost through impact erosion of the Earth surface, the total mass of comets that struck the Earth over its accretionary history cannot be determined. However, because the loss of Kr from the Earth surface reservoir is thought to have been limited since the Moon-forming giant impact, the maximum mass of cometary materials that were accreted on Earth after this episode can be calculated from the amount of cometary Kr now residing in the ESR. We use the 22% cometary ^{84}Kr in the ESR to derive the corresponding amount of water ice that would have been brought by comets based on the $^{84}Kr/H_2O$ ratio of comet 67P/C-G (Table 2). We find that the maximum amount of water that

would have been brought by comets along with cometary Kr after the Moon-forming impact is ~1.08 x 10^{20} mol H_2O (~1.95 x 10^{21} g H_2O). According to Pätzold et al. (2016), the most likely composition mix of comet 67P/C-G has approximately four times more dust than ice by mass, with a ratio of 1:1 for organic carbonaceous particles and silicates. The cometary ice composition is at least ~80 wt.% H_2O, with the remaining 20 wt.% being mainly composed with CO, CO_2, CH_3OH, CH_4, H_2S and N-compounds including CN, HCN, NH_3 and N^{30}. In a first approximation, we assume that cometary ice is 100 wt.% H_2O and use the total mass of cometary water being brought to Earth (~1.95 x 10^{21} g H_2O) to derive the total mass of comets accreted by Earth (~9.76 x 10^{21} g). This equals ~0.03 wt.% of the late veneer, taken as 0.5 wt.% of the Earth, and would correspond to a sphere with a diameter of ~340 km with d: 0.5 g/cm^3. Along with water, comets could therefore have brought up to 4×10^{21}g of organic materials.

References

1 Schlichting, H. E., & Mukhopadhyay, S. Atmosphere impact losses. *Space Science Reviews*, *214*(1), 34 (2018).

2 Genda, H., & Abe, Y. Enhanced atmospheric loss on protoplanets at the giant impact phase in the presence of oceans. *Nature*, *433*(7028), 842 (2005).

3 Hamano, K., Abe, Y., & Genda, H. Emergence of two types of terrestrial planet on solidification of magma ocean. *Nature*, *497*(7451), 607 (2013)

4 Boehnke, P., & Harrison, T. M. Illusory late heavy bombardments. *Proceedings of the National Academy of Sciences*, *113*(39), 10802-10806 (2016).

5 Morbidelli, A., Lunine, J. I., O'Brien, D. P., Raymond, S. N., & Walsh, K. J. Building terrestrial planets. *Annual Review of Earth and Planetary Sciences*, *40* (2012).

6 Marty, B. The origins and concentrations of water, carbon, nitrogen and noble gases on Earth. *Earth and Planetary Science Letters*, *313*, 56-66 (2012).

7 Kimura, K., Lewis, R.S., Anders, E., Distribution of gold and rhenium between nickel–iron and silicate melts: implications for the abundance of siderophile elements on the Earth and Moon. *Geochim. Cosmochim. Acta* 38, 683–701. (1974).

8 Fischer-Gödde, M., & Kleine, T. Ruthenium isotopic evidence for an inner Solar System origin of the late veneer. *Nature*, *541*(7638), 525 (2017).

9 Dauphas, N. The isotopic nature of the Earth's accreting material through time. *Nature*, *541*(7638), 521 (2017).

10 Dauphas, N. The dual origin of the terrestrial atmosphere. *Icarus*, *165*(2), 326-339 (2003).

11 Pepin, R. O. On the isotopic composition of primordial xenon in terrestrial planet atmospheres. In *From dust to terrestrial planets* (pp. 371-395). Springer, Dordrecht (2000).

12 Marty, B. et al. Xenon isotopes in 67P/Churyumov-Gerasimenko show that comets contributed to Earth's atmosphere. *Science*, *356*(6342), 1069-1072 (2017).

13 Avice, et al., Evolution of atmospheric xenon and other noble gases inferred from Archean to Paleoproterozoic rocks. *Geochimica et Cosmochimica Acta*, *232*, 82-100 (2018).

14 Hébrard, E., & Marty, B. Coupled noble gas–hydrocarbon evolution of the early Earth atmosphere upon solar UV irradiation. *Earth and Planetary Science Letters*, *385*, 40-48 (2014).

15 Bekaert, D. V., Broadley, M. W., Delarue, F., Avice, G., Robert, F., & Marty, B. Archean kerogen as a new tracer of atmospheric evolution: Implications for dating the widespread nature of early life. *Science Advances*, *4*(2), eaar2091 (2018).

16 Zahnle, K. J., Gacesa, M., & Catling, D. C. Strange messenger: A new history of hydrogen on Earth, as told by Xenon. *Geochimica et Cosmochimica Acta*, *244*, 56-85 (2019).

17 Porcelli, D., Ballentine, C. J., & Wieler, R. (2002). An overview of noble gas geochemistry and cosmochemistry. *Reviews in mineralogy and geochemistry*, *47*(1), 1-19.

18 Marty et al., Origins of volatile elements (H, C, N, noble gases) on Earth and Mars in light of recent results from the ROSETTA cometary mission. *Earth and Planetary Science Letters*, *441*, 91-102 (2016).

19 Ozima M. and Podosek F. A. Noble gas geochemistry. Cambridge, UK: Cambridge University Press (2002).

20 Bar-Nun, A., & Owen, T. Trapping of gases in water ice and consequences to comets and the atmospheres of the inner planets. In *Solar System Ices* (pp. 353-366). Springer, Dordrecht (1998).

21 Owen, T., & Bar-Nun, A. Comets, impacts, and atmospheres. *Icarus*, *116*(2), 215-226 (1995).

22 Bernatowicz, T. J., Podosek, F. A., Honda, M., & Kramer, F. E. The atmospheric inventory of xenon and noble gases in shales: the plastic bag experiment. *Journal of Geophysical Research: Solid Earth*, *89*(B6), 4597-4611 (1984).

23 Wacker, J. F., & Anders, E. Trapping of xenon in ice: implications for the origin of the Earth's noble gases. *Geochimica et Cosmochimica Acta*, *48*(11), 2373-2380 (1984).

24 Sanloup, C., Mao, H. K., & Hemley, R. J. High-pressure transformations in xenon hydrates. *Proceedings of the National Academy of Sciences*, *99*(1), 25-28 (2002).

25 Sanloup, et al., Retention of xenon in quartz and Earth's missing xenon. *Science*, *310*(5751), 1174-1177 (2005).

26 Ozima, M. Noble gases under pressure in the mantle. *Nature*, *393*(6683), 303 (1998)

27 Zhu, L., Liu, H., Pickard, C. J., Zou, G., & Ma, Y. Reactions of xenon with iron and nickel are predicted in the Earth's inner core. *Nature Chemistry*, *6*(7), 644 (2014).

28 Grochala, W. Atypical compounds of gases, which have been called 'noble'. *Chemical Society Reviews*, *36*(10), 1632-1655 (2007).

29 Drescher, J., Kirsten, T., & Schäfer, K. The rare gas inventory of the continental crust, recovered by the KTB Continental Deep Drilling Project. *Earth and Planetary Science Letters*, *154*(1-4), 247-263 (1998).

30 Moreira, M., Kunz, J., & Allegre, C. Rare gas systematics in popping rock: isotopic and elemental compositions in the upper mantle. *Science*, *279*(5354), 1178-1181 (1998).

31 Rubin et al., Krypton isotopes and noble gas abundances in the coma of comet 67P/Churyumov-Gerasimenko. *Science Advances*, *4*(7), eaar6297 (2018).

32 Meshik, A., Hohenberg, C., Pravdivtseva, O., Burnett, D. Heavy noble gases in solar wind delivered by Genesis mission. *Geochimica et cosmochimica acta*, *127*, 326-347 (2014).

33 Busemann, H., Baur, H., & Wieler, R. Primordial noble gases in "phase Q" in carbonaceous and ordinary chondrites studied by closed-system stepped etching. *Meteoritics & Planetary Science*, *35*(5), 949-973 (2000).

34 Gomes, R., Levison, H.F., Tsiganis, K., Morbidelli, A. Origin of the Cataclysmic Late Heavy Bombardment Period of the Terrestrial Planets. Nature 435, 466–469 (2005).

35 Jehin, E., Manfroid, J., Hutsemekers, D., Arpigny, C., & Zucconi, J. M. (2009). Isotopic ratios in comets: status and perspectives. *Earth, Moon, and Planets*, *105*(2-4), 167-180.

36 Cartigny, P., Boyd, S., Harris, J., & Javoy, M. Nitrogen isotopes in peridotitic diamonds from Fuxian, China: the mantle signature. *Terra Nova*, *9*(4), 175-179 (1997).

37 Greenwood et al., Oxygen isotopic evidence for accretion of Earth's water before a high-energy Moon-forming giant impact. *Science Advances*, *4*(3), eaao5928 (2018).

38 Crovisier et al., The composition of ices in comet C/1995 O1 (Hale-Bopp) from radio spectroscopy-Further results and upper limits on undetected species. *Astronomy & Astrophysics*, *418*(3), 1141-1157 (2004).

39 Sephton, M. A. Organic compounds in carbonaceous meteorites. *Natural Product Reports*, *19*(3), 292-311 (2002).

40 Chyba, C. F., Thomas, P. J., Brookshaw, L., & Sagan, C. Cometary delivery of organic molecules to the early Earth. *Science*, *249*(4967), 366-373 (1990).

41 Pätzold, et al., A homogeneous nucleus for comet 67P/Churyumov–Gerasimenko from its gravity field. *Nature*, *530*(7588), 63 (2016).

42 Dhooghe et al., Halogens as tracers of protosolar nebula material in comet 67P/Churyumov–Gerasimenko. *Monthly Notices of the Royal Astronomical Society*, *472*(2), 1336-1345 (2017).

43 Clay et al., Halogens in chondritic meteorites and terrestrial accretion. *Nature*, *551*(7682), 614 (2017).

44 Wetherill, G. W. Radiometric chronology of the early solar system. *Annual Review of Nuclear Science*, *25*(1), 283-328 (1975).

45 Halliday, A. N. A young Moon-forming giant impact at 70–110 million years accompanied by late-stage mixing, core formation and degassing of the Earth. *Philosophical Transactions of the Royal Society of London A: Mathematical, Physical and Engineering Sciences*, *366*(1883), 4163-4181 (2008).

46 Péron, S., & Moreira, M. Onset of volatile recycling into the mantle determined by xenon anomalies. *Geochemical Perspective Letters*, *9*, 21 (2018).

47 Holland, G., Cassidy, M., & Ballentine, C. J. Meteorite Kr in Earth's mantle suggests a late accretionary source for the atmosphere. *Science*, *326*(5959), 1522-1525 (2009).

48 Brasser, R., & Morbidelli, A. (2013). Oort cloud and Scattered Disc formation during a late dynamical instability in the Solar System. *Icarus*, *225*(1), 40-49.

49 Gibson, E. K., & Moore, G. W. Volatile-rich lunar soil: evidence of possible cometary impact. *Science*, *179*(4068), 69-71 (1973).

50 Greenwood, J. P., Itoh, S., Sakamoto, N., Warren, P., Taylor, L., & Yurimoto, H. Hydrogen isotope ratios in lunar rocks indicate delivery of cometary water to the Moon. *Nature Geoscience*, *4*(2), 79 (2011).

51 Bekaert, D. V., Avice, G., Marty, B., Henderson, B., & Gudipati, M. S. Stepwise heating of lunar anorthosites 60025, 60215, 65315 possibly reveals an indigenous noble gas component on the Moon. *Geochimica et Cosmochimica Acta*, *218*, 114-131 (2017).

52 Mazor, E., Heymann, D., & Anders, E. Noble gases in carbonaceous chondrites. *Geochimica et Cosmochimica Acta*, *34*(7), 781-824 (1970).

53 Okazaki, R., Takaoka, N., Nagao, K., & Nakamura, T. Noble gases in enstatite chondrites released by stepped crushing and heating. *Meteoritics & Planetary Science*, *45*(3), 339-360 (2010).

54 Wieler R. Noble gases in the solar system. Rev Mineral Geochem 47:21-70 (2002).

55 Garrison, D. H., & Bogard, D. D. (1998). Isotopic composition of trapped and cosmogenic noble gases in several Martian meteorites. *Meteoritics & Planetary Science*, *33*(4), 721-736 (2002).

56 Ott U. Noble gases in SNC meteorites: Shergotty, Nakhla, Chassigny. *Geochimica et Cosmochimica Acta* 52:1937-1948 (1988).

57 Busemann, H., Lorenzetti, S., & Eugster, O. (2006). Noble gases in D'Orbigny, Sahara 99555 and D'Orbigny glass—Evidence for early planetary processing on the angrite parent body. *Geochimica et cosmochimica acta*, *70*(21), 5403-5425.

58 Marrocchi, Y., Marty, B., Reinhardt, P., & Robert, F. Adsorption of xenon ions onto defects in organic surfaces: Implications for the origin and the nature of organics in primitive meteorites. *Geochimica et Cosmochimica Acta*, *75*(20), 6255-6266 (2011).

59 Kuga, M., Marty, B., Marrocchi, Y., & Tissandier, L. Synthesis of refractory organic matter in the ionized gas phase of the solar nebula. *Proceedings of the National Academy of Sciences*, 201502796 (2015).

60 Cassata. W. S. Meteorite constraints on Martian atmospheric loss and paleoclimate. *Earth and Planetary Science Letters*, 479, 322-329 (2017).

61 Dauphas, N., & Pourmand, A. Hf–W–Th evidence for rapid growth of Mars and its status as a planetary embryo. *Nature*, *473*(7348), 489 (2011).

62 Formisano, V., Atreya, S., Encrenaz, T., Ignatiev, N., & Giuranna, M. Detection of methane in the atmosphere of Mars. *Science*, *306*(5702), 1758-1761 (2004).

63 Rosa, A. D., Bouhifd, M. A., Morard, G., Briggs, R., Garbarino, G., Irifune, T., ... & Pascarelli, S. (2020). Krypton storage capacity of the Earth's lower mantle. *Earth and Planetary Science Letters*, *532*, 116032.

64 Jephcoat, A. P. Rare-gas solids in the Earth's deep interior. *Nature*, *393*(6683), 355 (1998).

65 Zhu, Q., Jung, D. Y., Oganov, A. R., Glass, C. W., Gatti, C., & Lyakhov, A. O. Stability of xenon oxides at high pressures. *Nature chemistry*, *5*(1), 61 (2013).

66 Caldwell, W. A., Nguyen, J. H., Pfrommer, B. G., Mauri, F., Louie, S. G., & Jeanloz, R. Structure, bonding, and geochemistry of xenon at high pressures. *Science*, *277*(5328), 930-933 (1997).

67 Nishio-Hamane, D., Yagi, T., Sata, N., Fujita, T., & Okada, T. No reactions observed in Xe-Fe system even at Earth core pressures. *Geophysical Research Letters*, *37*(4) (2010).

68 Zhu, L., Liu, H., Pickard, C. J., Zou, G., & Ma, Y. Reactions of xenon with iron and nickel are predicted in the Earth's inner core. *Nature chemistry*, *6*(7), 644 (2014).

69 Marinova, M. M., Aharonson, O., & Asphaug, E. Mega-impact formation of the Mars hemispheric dichotomy. *Nature*, *453*(7199), 1216 (2008).

70 Shcheka, S. S., & Keppler, H. The origin of the terrestrial noble-gas signature. *Nature*, *490*(7421), 531 (2012).

71 Morbidelli, A., Lunine, J. I., O'Brien, D. P., Raymond, S. N., & Walsh, K. J. Building terrestrial planets. *Annual Review of Earth and Planetary Sciences*, *40* (2012).

72 Elkins-Tanton, L. T. Linked magma ocean solidification and atmospheric growth for Earth and Mars. *Earth and Planetary Science Letters*, *271*(1-4), 181-191 (2008).

73 Elkins-Tanton, L. T. Formation of early water oceans on rocky planets. *Astrophysics and Space Science*, *332*(2), 359-364 (2011).

74 Tucker, J. M., & Mukhopadhyay, S. Evidence for multiple magma ocean outgassing and atmospheric loss episodes from mantle noble gases. *Earth and Planetary Science Letters*, *393*, 254-265 (2014).

75 Sharp, Z. D., McCubbin, F. M., & Shearer, C. K. A hydrogen-based oxidation mechanism relevant to planetary formation. *Earth and Planetary Science Letters*, *380*, 88-97 (2013).

76 Parai, R., & Mukhopadhyay, S. Xenon isotopic constraints on the history of volatile recycling into the mantle. *Nature*, *560*(7717), 223 (2018).

77 Korenaga, J., Planavsky, N. J., & Evans, D. A. Global water cycle and the coevolution of the Earth's interior and surface environment. *Phil. Trans. R. Soc. A*, *375*(2094), 20150393 (2017).

78 Galer, S. J. G. Interrelationships between continental freeboard, tectonics and mantle temperature. *Earth and Planetary Science Letters*, *105*(1-3), 214-228 (1991).

79 Parai, R., & Mukhopadhyay, S. How large is the subducted water flux? New constraints on mantle regassing rates. *Earth and Planetary Science Letters*, *317*, 396-406 (2012).

80 Lecuyer, C., Gillet, P., & Robert, F. The hydrogen isotope composition of seawater and the global water cycle. *Chemical Geology*, *145*(3-4), 249-261 (1998).

81 Halliday, A. N. The origins of volatiles in the terrestrial planets. *Geochimica et Cosmochimica Acta*, *105*, 146-171 (2013).

82 Dauphas N, Morbidelli A. Geochemical and planetary dynamical views on the origin of Earth's atmosphere and oceans. In *Treatise on geochemistry*, 2nd edn, vol. 6 (eds HD Holland, KK Turekian), 1–35, Oxford, UK: Elsevier (2014).

83 Albarede, F. Volatile accretion history of the terrestrial planets and dynamic implications. *Nature*, *461*(7268), 1227 (2009).

84 Barnes, J. J., Kring, D. A., Tartese, R., Franchi, I. A., Anand, M., & Russell, S. S. (2016). An asteroidal origin for water in the Moon. *Nature communications*, *7*, 11684.

85 Javoy, M. The birth of the Earth's atmosphere: the behaviour and fate of its major elements. *Chemical Geology*, *147*(1-2), 11-25 (1998).

86 Jarosewich, E. (1990). Chemical analyses of meteorites: A compilation of stony and iron meteorite analyses. *Meteoritics*, *25*(4), 323-337.

87 Burkhardt, C., Dauphas, N., Hans, U., Bourdon, B., & Kleine, T. (2019). Elemental and isotopic variability in solar system materials by mixing and processing of primordial disk reservoirs. *Geochimica et Cosmochimica Acta*, *261*, 145-170.

88 Bieler, A., et al. Abundant molecular oxygen in the coma of comet 67P/Churyumov–Gerasimenko. *Nature*, *526*(7575), 678 (2015).

89 Calmonte, U., et al. Sulphur-bearing species in the coma of comet 67P/Churyumov–Gerasimenko. *Monthly Notices of the Royal Astronomical Society*, *462*(Suppl_1), S253-S273 (2016).

90 Hässig, M. et al. Isotopic composition of CO_2 in the coma of 67P/Churyumov-Gerasimenko measured with ROSINA/DFMS. *Astronomy & Astrophysics*, *605*, A50 (2017).

91 Bekaert, D. V., Marrocchi, Y., Meshik, A., Remusat, L., & Marty, B. Primordial heavy noble gases in the pristine Paris carbonaceous chondrite. *Meteoritics & planetary science*, *54*(2), 395-414 (2019).

92 Huss, G.R., Lewis, R.S. and Hemkin, S., The "normal planetary" noble gas component in primitive chondrites: Compositions, carrier, and metamorphic history. *Geochimica et Cosmochimica Acta*, 60(17), pp.3311-3340 (1996).

93 Gilmour, J. D. "Planetary" noble gas components and the nucleosynthesis history of solar system material. *Geochimica et Cosmochimica Acta* 74:380–393 (2010).

94 Ott, U. (1996). Interstellar diamond xenon and timescales of supernova ejecta. *The Astrophysical Journal*, *463*, 344.

95 Avice, G., Moreira, M, and Gimour, J.D. (2020) Xenon isotopes identify large scale nucleosynthetic heterogeneities across the solar system. *The Astrophysical Journal. in press.*

96 Nittler, L. R. et al. A cometary building block in a primitive asteroidal meteorite. *Nature Astronomy*, 1 (2019).

97 Van Kooten, E. M. et al. Isotopic evidence for primordial molecular cloud material in metal-rich carbonaceous chondrites. *Proceedings of the National Academy of Sciences*, *113*(8), 2011-2016 (2016).

98 Marchi, S., Canup, R. M., & Walker, R. J. Heterogeneous delivery of silicate and metal to the Earth by large planetesimals. *Nature Geoscience*, *11*(1), 77 (2018).

99 Barry, P. H., de Moor, J. M., Giovannelli, D., Schrenk, M., Hummer, D. R., Lopez, T., ... & Bini, G. (2019). Forearc carbon sink reduces long-term volatile recycling into the mantle. *Nature*, *568*(7753), 487.

100 Förster, M. W., Foley, S. F., Alard, O., & Buhre, S. (2019). Partitioning of nitrogen during melting and recycling in subduction zones and the evolution of atmospheric nitrogen. *Chemical Geology*, *525*, 334-342.

101 Holland, G., & Ballentine, C. J. (2006). Seawater subduction controls the heavy noble gas composition of the mantle. *Nature*, *441*(7090), 186.

Supplementary materials related to this Chapter are reported in Appendix B.

Conclusion and outlook

As part of this Chapter, we show that (i) mixing between cometary and chondritic end-members can account for the Kr and Xe isotopic signature of the atmosphere, (ii) Xe loss to space over the Archean possibly contributed to most of the missing Xe - therefore accounting for its paradox-, and (iii) the materials that supplied the Earth surface reservoir with its volatile inventory were possibly drier than previously thought. Since comets are essentially devoid of Ne, they would have negligibly contributed the ESR inventory of Ne. However, to have terrestrial atmophile elements deriving from relatively dry precursors is in apparent contradiction with the Ne isotopic composition of the atmosphere requiring a late (post-giant impact) arrival of ~ 4 wt.% of the Earth in the form of CI-like material (Marty 2012; Vogt et al. 2019; Fig. 80). In details, the Ne isotopic signature of the terrestrial atmosphere ($^{20}Ne/^{22}Ne$ = 9.8) would be accounted for by mixing a solar, mantle-derived signature ($^{20}Ne/^{22}Ne \geq 12.5$; Ne-B, Black 1972), with late contributions from CI-like chondrites ($^{20}Ne/^{22}Ne \sim 8.5$). Such a late arrival of volatile-rich material would be able to provide the Earth surface reservoir with more volatile elements than present today in the atmosphere (Marty 2012). How Ne and Kr-Xe systematics could be reconciled is not straightforward, unless the supplier materials for volatile elements within the ESR corresponded to an unsampled type of chondritic material, which was poor in water (i.e., with a high heavy noble gas to water ratio) but contained a similar Ne isotopic composition to CI chondrites (i.e., with limited solar wind implantation, as inferred for dust remained at large heliocentric distances in the PPD, where solar wind was shielded by dust opacity; Moreira and Charnoz 2016).

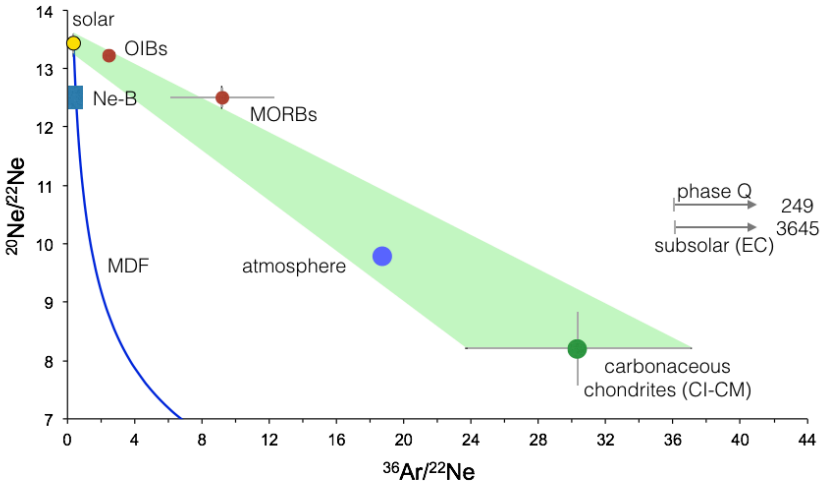

Fig. 80. $^{36}Ar/^{22}Ne$ vs. $^{20}Ne/^{22}Ne$ systematics of the MORBs, OIBs, solar gas, solar wind implanted materials (Ne-B), carbonaceous chondrites (CI-CM), phase Q, subsolar (EC) and terrestrial atmosphere, showing that latter requires significant contribution from CI-like material (adapted from Marty 2012). Most importantly, this diagram shows that the isotopic and elemental composition of the terrestrial atmosphere cannot be accounted for by fractionation of a solar-derived composition, as historically argued for by Pepin (2003). Instead, mixing between a solar and a CI-CM-like component, with little contribution from Ne-B, may account for the signature of MORBs, OIBs and the atmosphere. Whether the solar-derived component corresponds to solar, Ne-B, or a mixture of both, is so far uncertain.

Chapter 7

Early Earth evolution and the emergence of life

The conditions and processes that drove the emergence and development of early life on Earth are poorly understood. The observation that life can thrive within the most hostile terrestrial environments (from -20°C to 120°C, pH ≤ 1 and ≥ 11, at high pressure, high salinity, or within desiccated media, etc.) suggests that life could have developed under extreme conditions. It is therefore difficult to conceive that life emerged in isolation on Earth, and is not present anywhere else in the universe. By understanding how life developed on Earth, we can envisage looking outwards for conditions that could lead to the development of extraterrestrial life.

Austere environmental conditions on early Earth would have prevented living forms to emerge for several hundreds of millions of years after the Moon-forming impact. The physical and chemical conditions allowing for the synthesis of the building blocks of biomolecules and functional bio-structures are then far from being unravelled. Abiotic, biologically relevant molecules could have been synthesised endogenously on the primitive Earth (e.g., in the vicinity of hydrothermal vents in the oceans, or through photochemical reactions in the atmosphere), or supplied by exogenous sources (Chapter 6). Stromatolites, microfossils, and carbon isotope data, which constitute the main available sources of information regarding the timing of life's emergence, indicate that life was already extant and flourishing on Earth ~3.5 Ga (Schopf 2006). How the molecular building blocks of life were initially assembled as the very first cells is not known.

The chemical evolution of the atmosphere was marked by a rapid shift from anoxic to oxic surface conditions at the transition between the Archean and Proterozoic eons (~2.4 Ga; Holland 2006). Whilst the existence of anoxygenic photosynthetic organisms could date back to 3.4 Gyr ago (Westall et al. 2006), oxygenic photosynthetic organisms would only have emerged ~2.7 Gyr ago (Canfield 2006; Kasting and Howard 2006). The exact role of oxygenic photosynthesis and cyanobacteria in raising oxygen levels in the atmosphere around 2.4 Ga is uncertain, with a magmatic (Gaillard et al. 2011) and hydrogen loss (Zahnle et al. 2013) origins of the Great Oxidation Event being also proposed. The isotopic evolution of atmospheric Xe over the Archean eon (Avice et al. 2018) could provide unique insights into the chemical evolution of the atmosphere. Based on the hypothesis of a global, protracted and continuous evolution of atmospheric Xe isotopes (which may not be straightforward to achieve in the model of Xe escape as an ion; Zahnle et al. 2019), we suggest that the noble gas analysis of ancient organic materials isolated from Archean sedimentary rocks could be used to test their syngenetic origin.

7.1. Environmental conditions on the primitive Earth

Although the Moon-forming event probably did not cause the whole Earth to melt (as witnessed by the preservation of primordial, solar Ne in the lower mantle - which would have been lost to the surface otherwise; Fig. 24), it did leave the Earth with a global magma ocean and a hot, CO_2-rich steam atmosphere that progressively cooled down toward gentler environmental conditions, with water progressively condensing from steam after ~2 Myr (Zahnle 2006; Fig. 81). The magma ocean cooling rate would have been controlled by the presence of a primitive atmosphere resulting in thermal blanketing, with a runaway greenhouse state being sustained by both incoming solar radiation and escaping geothermal heat (Zahnle 2006). Harsh volcanism, high temperatures and radiation doses, as well as intense post-accretionary bombardment (Koeberl 2006), possibly postponed the establishment of a habitable world (Fig. 81). Indeed, for the first hundreds of million years of Earth's evolution, massive bombardment of the planet probably took place (Nisbet & Sleep 2001), with the largest impacts possibly frustrating the evolution of primitive living forms (Maher and Stevenson, 1988; Sleep et al., 1989). Whereas high-velocity impact fireballs are expected to be so energetic that the preservation of any molecular species from the impactor itself is unlikely, large impacts could have provided substantial local enrichments of exogeneous prebiotic reagents, eventually supporting life's emergence (Bada et al., 1994; Pasek and Lauretta, 2007; Furukawa et al., 2009).

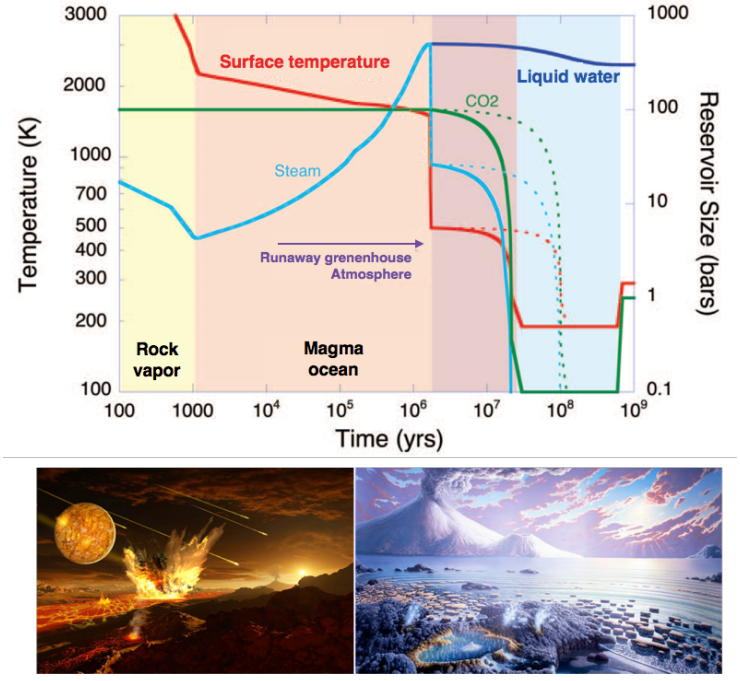

Fig. 81. A history of temperature, water, and CO_2 during the Hadean showing that the surface conditions of the early Earth were doubtlessly uninhabitable for the first million years after the Moon-forming impact (Zahnle 2006). Below, are reported two artistic views of how the Earth surface could have evolved from an inhospitable environment (left), to a habitable world (right). From Addison Wesley Longman Inc.

The analysis of Jack Hills zircons suggests that continental crust and water were already present on Earth 4.4 Ga (Blichert-Toft and Albarède 2008; Mojzsis et al. 2001). Stellar evolution models indicate that the Sun was 20–30% less luminous under primitive conditions (Newman and Rood, 1977), implying that, if the composition of the primitive atmosphere was identical to that of the present-day, the whole Earth surface should have been frozen into a snowball Earth. Hence, the presence of liquid water, already acting as a weathering agent 4.4 Ga (Wilde et al., 2001) requires a particularly efficient greenhouse effect for the early Earth to be have been kept unfrozen (so-called "faint young Sun paradox"; Feulner, 2012). To solve this paradox, it is notably suggested that contributions from CH_4 and hydrocarbon gases, especially ethane (C_2H_6; Haqq-Misra et al., 2008), were significant within the CO_2-dominated primitive atmosphere.

Several lines of evidence suggest that atmospheric oxygen levels were extremely low ($< 10^{-5}$ times the Present Atmospheric Level; PAL) for the first ~ 2.3 Gyrs of Earth's history (Holland, 2006; Ohmoto et al. 2014). The transition between the Archean and Proterozoic eons was marked by a rapid shift from anoxic to oxic surface conditions, referred to as the Great Oxidation Event and likely related to the onset of oxygenic photosynthesis (GOE; Fig. 82). The driving-mechanism behind this transition from a past reducing atmosphere to a modern-like, O-rich environment is still ambiguous as direct measurement of the partial pressure of O_2 (PO_2) in ancient rocks is impossible due to the high reactivity of oxygen. Proxies for the evolution of the PO_2 in Earth's early atmosphere consist for instance in MIF-S, the presence of banded iron formations (BIFs) related to the abundance of Fe^{II} in deep oceans (Kappler et al. 2005), or transition metal isotopic compositions in shales (Anbar et al., 2007; Ostrander et al. 2019). Indeed, signals of mass-independent fractionation of sulfur isotopes (MIF-S) recorded in Archean sediments would have originated from the photolysis of SO_2 and SO, producing polymerised elemental S on one side, and sulphates from the oxidation of elemental S by CO_2 and H_2O on the other side, with opposite $\Delta^{33}S$ signatures (Farquhar et al., 2000). This pathway of MIF-S production requires (i) significant amounts of atmospheric methane to have acted as a reducing agent in the formation of elemental S polymers, as well as (ii) very low levels of O_2 to prevent absorption of shortwave photons by tropospheric ozone (O_3) and ensure the formation of sulphates and elemental sulphur (Farquhar and Wing, 2003). Hydrogen escape was much more vigorous in the past, particularly due to the enhanced EUV flux from the young Sun (Claire et al. 2012), resulting in the photolysis of water molecules producing O_2 and (escaping) H_2 (Zahnle et al. 2013). This process could have played a key role in driving the progressive oxidation of the Earth's surface, which could not have uniquely been produced by the onset of oxygenic photosynthesis, as photosynthesis-derived O_2 would not have been stable in a reduced atmosphere (Zahnle et al. 2013). However, peaks of sub-aerial volcanism around 2.45 Ga could have released large amounts of sulphate to the oceans, whose subsequent reduction released significant amounts of oxygen ending up in the atmosphere and potentially contributing to the GEO (Gaillard et al. 2011; Ciborowski and Kerr 2016).

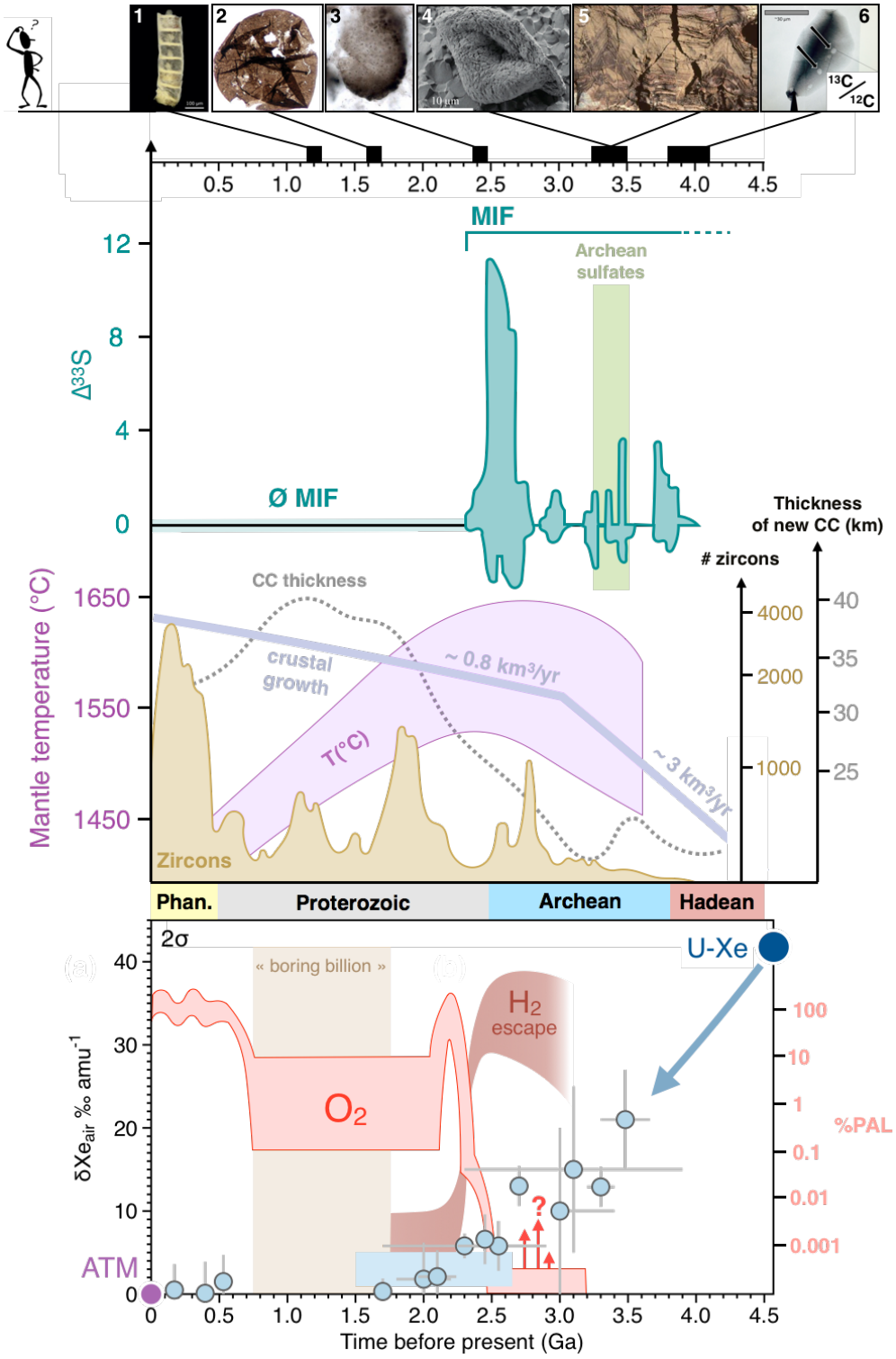

Figure 82. Main geological, geochemical and biological changes observed over Earth's geological history. From top to bottom: the timeline of early life development is adapted from Van Zuilen et al. (2002), Adam et al. (2017) and Javaux (2019). The $\Delta^{33}S$ versus geological age plot highlighting the existence of a prominent mass independent signal prior to 2.5 Ga is from Johnston (2011). The time evolution of the number of zircons, continental crust thickness and crustal growth rate are from Hawkesworth et al. (2019). Mantle temperature is from Herzberg et al. (2010). Evolution of the hydrogen escape and amount of O_2 (%PAL: percentage of oxygen relative to present atmospheric level) in the atmosphere are from Zahnle et al. (2013) and Lyons et al. (2014), respectively. Xenon isotopic data are from compilation by Avice et al. (2018).

Several crucial changes in the environmental conditions of the Earth's surface seem to have taken place in the late Archean eon, with the end of extensive hydrogen escape and Xe isotopic evolution, the rise of atmospheric O_2 and cessation of the mechanism inducing MIF-S (Fig. 82). This period also marks the start of mantle's irreversible cooling from a peak mantle temperature ~1600°C around 2.5-3.0 Ga (Korenaga 2008; Fig. 82). Given that (at least some of) these processes were likely interconnected, the detailed description of atmospheric xenon isotopic evolution could yield important insights into the conditions/mechanisms underlying the evolution of the Archean atmosphere. This requires (i) understanding the timing and nature of the process that caused this isotopic evolution (and possibly also the elemental depletion of atmospheric Xe with respect to lighter noble gases; Chapter 6), and (i) checking that lighter noble gases (especially Kr) did not also undergo some extent of fractionation over geological periods of time.

7.2. Timing of life's emergence

On early Earth, several environments/mechanisms could have played a role in the emergence of life. For instance, hydrocarbon molecules could have been synthesised at ultramafic sea floors through Fischer-Tropsch type reactions, implying the reduction of aqueous CO_2 under conditions of excess H_2, itself produced by the hydration of olivine and orthopyroxene minerals (the so-called serpentinization process; Berndt et al., 1996; Guzmán-Marmolejo et al., 2013). The suitability of this process under natural conditions has however been called into question (McCollom and Seewald, 2001). Alternatively, HCN chemistry could have yielded a wide range of crucial biomolecules, including nucleobases (Oro-Orgel synthesis; Oro and Guidry 1960), amino acids (Strecker synthesis from aldehydes and amino nitriles; Miller and Trump 1980) and phospholipids (Sutherland, 2016). However, such synthesis routes also require unrealistic geochemical conditions (McCollum, 2013) and unlikely concentrations of intermediate compounds, including formamide ($HC(O)NH_2$; Dalai et al. 2016). Importantly, steep thermal, redox and chemical gradients in the vicinity of hydrothermal vents could have supported thermodynamically favourable metabolic reactions at the initiation of the earliest living systems. Methane, di-hydrogen and metal sulfides would have been abundant close to black smoker vents ($pH < 3$, $T > 250$°C), whilst white smoker ones ($pH > 9$, $T < 90$°C) could have provided suitable conditions for the formose reaction (self-condensation of formaldehydes into sugars) to occur (Deamer et al. 2019). Here again, while hydrothermal conditions simulating experiments succeeded in producing (Marshall, 1994) and polymerizing (Kawamura et al., 2005) amino acids, or RNA-like Molecules (Da Silva et al., 2015), the required concentrations of reactants are invariably too high to be geologically plausible (Dalai et al. 2016). Interestingly, Patel et al. (2015) proposed a one-pot reaction approach in which precursors of ribonucleotides, amino acids and lipids could be derived from ultraviolet light-driven chemistry of hydrogen cyanide and hydrogen sulfide in protometabolic systems. But

whatever the considered pathways, it is bound to happen that suitable natural conditions, if achieved at some point, would be reached in very local and transient environments.

Before being assembled as the very first cells, the molecular building blocks of life must have been polymerised into complex and functional macromolecules. Today, enzymes catalyse the production of membrane forming phospholipids, as well as the polymerization of DNA-RNA oligomers from nucleotide monomers and peptides from amino acids. On prebiotic Earth, geological and chemical processes must have been effective to stabilise, concentrate, protect, and catalyse the abiotic oligomerization of biomolecules. Two majors scenarios are considered for the concentration of bio-monomers in terrestrial and oceanic aqueous environments: wetting/drying cycles in Earth surface environments (lagoons, evaporitic stretches, volcanic crater lakes) resulting in concentrated solutions of organic compounds historically called the "primordial soup" (Lahav et al. 1978), and adsorption of dissolved organic molecules into the interlayer spaces of settling clay minerals (Feuillie et al., 2013). The chain of events that led to self-replicating cells is however far from being unravelled, and several theories about the nature of the first living systems are still under consideration (e.g., the "metabolism-first" theory, Kaddour and Sahai 2014; the "iron-sulfur world", Wächtershäuser, 1990; or the "RNA world", Gilbert 1986). In fact, the very fact of defining "life" is challenging in itself (Cleland & Chyba 2002). In a systematic way, experimental investigations of endogenous synthesis get product yields that decrease with increasing carbon chain length (Dalai et al. 2016), with the hypothetical proto-cell from which all current living organisms may descend (the so-called Last Universal Common Ancestor, LUCA; Koonin 2003) being orders of magnitude more complex than any biomolecule assembled in laboratory simulations. In other words, the process of life emergence is far from being resolved.

The major atmospheric changes outlined in the previous section (Fig. 82) probably accompanied/supported life's emergence. Whilst 3.8 Gyr-old banded iron formations in Isua (Greenland) may be related to the microbial oxidation of ferrous iron (Konhauser et al., 2002), stromatolites (laminated rocks produced by microbial precipitation and/or trapping of minerals) from the Strelley Pool Formation (3.426–3.35-Ga; Australia) constitute one of the strongest cases that has so far been documented for early traces of life on Earth (Wacey, 2010). Likewise, secure identifications of microfossils do not extend to more than ~3.5 Gyr (Schopf et al. 2007; Alleon et al. 2018; Fig. 82). Older potential remnants of life (Mojzsis et al., 1996; McKeegan et al., 2007) are still debated (van Zuilen et al., 2002; Lepland et al., 2005), although fractionated carbon isotopes compositions in sedimentary rocks suggests that life may have already been present on Earth around 4 Ga (Rosing, 1999; Fig. 82). Main challenges in evidencing the earliest traces of life have recently been reviewed by Javaux (2019), emphasizing the difficulties associated with the assessment of their biogenecity (i.e., life-related character) and syngenecity (i.e., same age for organic materials and their host rocks).

7.3. What noble gases can tell us about Archean environments?

Noble gases have provided a wealth of information regarding the environmental conditions during the Archean eon. The atmospheric $^{40}Ar/^{36}Ar$ was lower in the Archean (143 ± 24; Pujol et al. 2013) than the present-day value of 298.6 (Lee et al., 2006). Whilst ^{36}Ar is primordial in origin, ^{40}Ar has been produced by the radioactive decay of the potassium isotope ^{40}K, with a half-life of 1.25 Gyr. A lower $^{40}Ar/^{36}Ar$ in the Archean atmosphere is consistent with the formation of a crustal volume equivalent to 80±10% of the present-day one between 3.8 Ga and 2.5 Ga, implying that a large reservoir of felsic crust had already been extracted during the Archean. Yet, there is a considerable disagreement in the literature on the nature of the continents through time, with some advocating for a predominantly mafic crust until ~3-2.5 Ga or later (Tang et al. 2016; Smit and Mezger, 2017) and others arguing for felsic continents since at least 3.5 Ga (Greber et al. 2017).

The analysis of N-Ar isotope and halogens to Ar elemental variations in inclusion fluids trapped in Archean quartz, for instance, have allowed demonstrating that the partial pressure of N_2 and $\delta^{15}N$ in the atmosphere (Marty et al. 2013), as well as the salinity of the oceans (Marty et al. 2018), has not significantly changed since the Archean (Fig. 83). Nitrogen constraints imply that N_2 played a limited role in the thermal budget of the Earth, and that the partial pressure of CO_2 was most likely <0.7 bar in the Archean (Marty et al. 2013). A near-constant salinity of the oceans through time has important implications for the stabilisation of the continental crust, the amount of O_2 being dissolved within the oceans at the time of life emergence, as well as for the global habitability of the ancient Earth and the evolution of metazoan life (Marty et al. 2018).

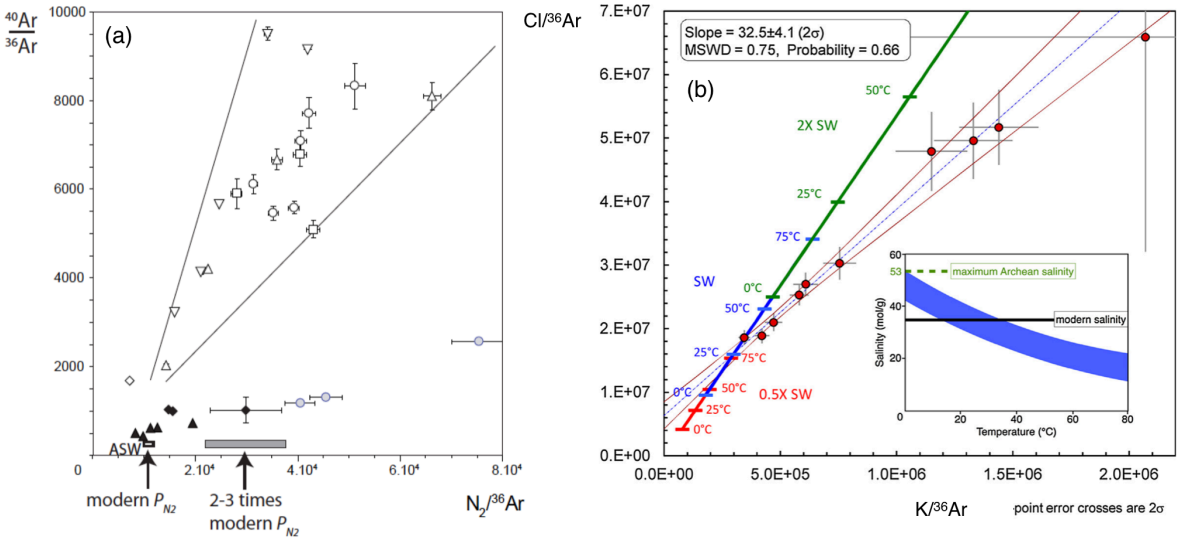

Fig. 83. Determination of the partial pressure of N_2 in the atmosphere (Marty et al. 2013) and salinity of the oceans (Marty et al. 2018) during the Archean eon as derived from the analysis of N-Ar isotope and halogens to Ar elemental variations, respectively, in inclusion fluids trapped in Archean quartz.

As part of this thesis, we set out to provide new insights into the isotopic evolution of atmospheric noble gases and timing of early life's development by investigating the noble gas composition of ancient organic materials. Indeed, the timeline of early life development presented in Fig. 82 is notably based on the analysis of morphological and/or geochemical traces of ancient life in the rock record (Javaux 2019). These are however often disputed as abiotic processes may mimic or alter them (e.g., Lollar et al. 2002; Garcia-Ruiz et al. 2003; Cosmidis & Templeton, 2016), and subsequent contamination by more recent generations of organic materials (Oehler and Cady 2014; Marshall et al. 2012) may hamper reliable determination of the age of organic materials of interest. Importantly, the search for microfossils in Archean rocks is either carried out through the observation and analysis of thin rock sections, or via the isolation and study of kerogens (e.g., Delarue et al. 2016). The latters correspond to the insoluble organic matter residues of the HF-HCl digestion of Archean sedimentary rocks that underwent no, or low, metamorphism (Durand and Nicaise 1980). This method allows concentrating organic materials, therefore increasing the chances to find evidence for life-related structures. However, the relation of these organic materials to the surrounding minerals is lost during digestion of the host rock, precluding information to be derived from the spatial relationship between mineral and organic phases. Some uncertainties therefore remain regarding the syngenecity of apparent biogenic structures, with the potential for secondary deposition of carbonaceous matter limiting our ability to accurately date the emergence and evolution of life on Earth. In analogy with heavy noble gases in meteorites being intimately associated with organic materials (Chapter 4), terrestrial carbonaceous lithologies may likewise be able to trap and preserve considerable amounts of heavy noble gases. On Earth, carbon-rich lithologies and shales indeed constitute a significant reservoir for atmospheric Xe, to the point where they have been proposed as potential carriers of the missing Xe (Podosek et al. 1982; Bernatowicz et al. 1984). Here, we investigated by stepwise heating in a filament furnace (Chapter 1) the possible occurrence of trapped ancient atmospheric Ar, Kr, and Xe in kerogens isolated from Archean sedimentary rocks (Bekaert et al. 2018c, 2020).

In the first instance, we analysed kerogen MGTKS3, isolated from the 3.0 Gyr old Farrel Quartzite (Pilbara Craton, Western Australia; Delarue et al. 2016), which we used to test the possibility for ancient atmospheric gases to be retained in Archean carbonaceous materials. We found that large quantities of noble gases were released upon thermal cracking of the kerogen (at ~500°C), with a Xe isotope signature that was enriched in the light isotopes with respect to the modern atmospheric composition, by 9.8 ± 2.1 ‰.amu^{-1}, whilst lighter noble gases were not fractionated (Bekaert et al. 2018c). When reported on a model evolution curve of atmospheric Xe isotopes through time, this extent of MDF provided a model age of 3.0 ± 0.2 Gyr, in excellent agreement with the actual age of the host rock (Fig. 84), therefore pointing towards a syngenetic origin for kerogen MGTKS3 (Bekaert et al. 2018c; Appendix C). The Xe isotope signature of this sample also displayed a mono-isotopic deficit in ^{129}Xe with

respect to its MDF trend when normalised to modern atmosphere, a feature that is characteristic of Archean atmospheric Xe (Avice et al. 2017) due to the fact that the modern atmosphere contains more ^{129}Xe from degassing of mantle-derived gas with high ^{129}Xe/^{130}Xe, than the Archean atmosphere did contain (Bekaert et al. 2018c).

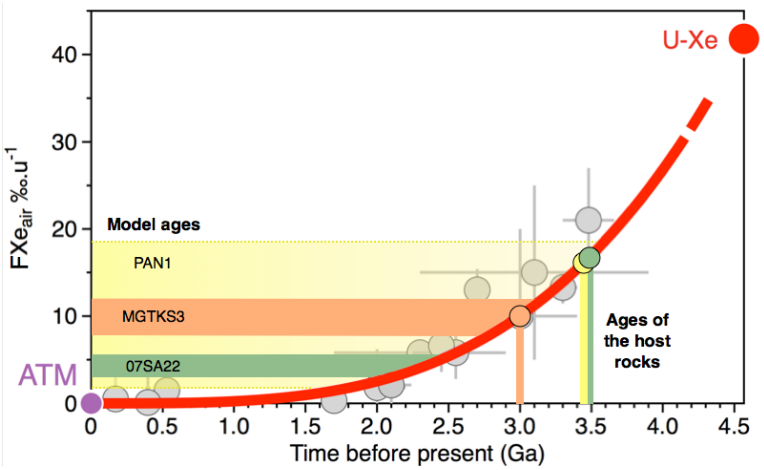

Fig. 84. Time evolution (red curve) of the degree of MDF of atmospheric Xe relative to modern atmosphere (FXe), as modelled from the dataset compiled by Avice et al. (2018), starting from a U-Xe composition (Pepin 1994; Marty et al. 2017). Reporting the degrees of MDF (y-axis, 2σ) of trapped Xe components in Archean kerogens (MGTKS3: Bekaert et al. 2018c; PAN1 and 07SA22: Bekaert et al. 2020) onto this evolution curve allows deriving model ages that can be compared with those of the host rocks (vertical bars). Whilst a good fit between the model and host rock ages is observed for kerogen MGTKS3, the model age for 07SA22 is lower than that of the related host rock, and the large uncertainty associated with the model age of PAN1 does not allow firm conclusion to be drawn.

We received more Archean kerogens (isolated from 3.4 to 1.8 Gy-old cherts; Delarue et al. 2016) to analyse for heavy noble gases, in order to apply this new Xe-based dating method and also test their syngenetic origin. Although these analyses further confirmed that Xe isotopes from the Archean atmosphere can be retained within kerogens, new Xe-derived model ages were this time lower than expected from the ages of host rocks (Fig. 84; Bekaert et al. 2020). In detail, all samples but two (PAN1 and 07SA22) gave similar Xe isotopic compositions to modern air (Bekaert et al. 2020). Due to little amounts of gas being present in kerogen PAN1, uncertainties related to its Xe isotopic composition were significant (Fig. 84). Conversely, large amounts of gas were extracted from kerogen 07SA22, with a trapped Xe component displaying a degree of MDF of -4.2 ± 0.65 ‰.amu^{-1}. This corresponds to the expected composition of atmospheric Xe isotopes some 2.3 ± 0.2 Ga (2σ), which is younger than the age of the host rock (3.47 Gyr, Armstrong et al. 1990; Fig. 84, Bekaert et al. 2020). These results suggest the presence of an Archean atmosphere component, with an initially trapped Xe that was at least partially lost and/or mixed together with some Xe carried out by younger generations of organic materials (Bekaert et al. 2020). We therefore conclude that the Xe-based dating tool to represent a promising, but not fool proof, tool to constrain the timing of early life's blossoming (Appendix E). These works calls for further analytical development;

one promising idea would be to for instance couple *in situ* laser ablation techniques, which may require the use of ultrasensitive, resonance ionization mass spectrometry, to measure Xe isotopic compositions for individual organic microstructures. Importantly, from all the analyses of Archean kerogens reported as part of this thesis, little to no variation in the isotopic composition of trapped Kr components were detected, in line with the modern-like isotopic composition of Kr in the Archean atmosphere (Avice et al. 2017, 2018). The next section further describes the conditions required for Xe's specific escape as an ion from the Archean atmosphere.

7.4. Atmospheric Xe's isotopic evolution over the Archean eon

As exposed in the bibliographical review and Chapter 6, present-day atmospheric Xe is elementally depleted by a factor of 10-20 relative to lighter noble gases and mass dependently fractionated in factor of heavy isotopes by ~35 ‰.amu^{-1} compared to its primitive composition (Ozima and Podosek 2002). Atmospheric xenon's isotopic evolution occurred throughout the Archean (Avice et al. 2018), suggesting Xe was progressively lost from the atmosphere over geological periods of time. Hydrodynamic escape of neutral Xe can be ruled out as a possible origin of Xe's protracted isotopic evolution over the Archean eon as this mechanism would have affected all lighter noble gases, and most importantly, it would only be possible during first 100 Myr of Earth's history, when EUV flux from the young Sun was > 300 times the modern one (Zahnle 2015). Interestingly, Xe is the only noble gas that is more easily ionised than H or H_2 (Fig. 85). Recently, 1-D numerical simulations of hydrodynamic diffusion-limited hydrogen escape from highly-irradiated CO_2-H_2-H atmospheres demonstrated that Xe is the only noble gas capable of escaping as an ion in a photo-ionised hydrogen wind (Zahnle et al. 2019). This model of Xe's escape as an ion from the upper atmosphere was formalised by a series of numerical simulations carried out by K. Zahnle (NASA Ames; Zahnle 2015; Zahnle et al. 2019). It relies on a fractionation mechanism that is specific to Xe, and that can last for ~ 2.5 Gyr, even at modest increase of solar EUV activity.

Xenon in the atmosphere can be ionised either directly by incident photons (λ < 102.3 nm, especially those > 91.17 nm which are not absorbed by H) or via charge exchange reactions with H^+, H_2^+, and CO_2^+ (Fig. 85). Whilst species with higher ionization thresholds than hydrogen would mainly remain as neutrals in the upper atmosphere (i.e., all noble gases but Xe), Xe would be predominantly found as an ion. In addition, Kr ions (Kr^+) possibly formed in the atmosphere would be readily neutralised by hydrogen, implying that the lifetime of Kr^+ in an H-dominated atmosphere is very short (Zahnle et al. 2019). Conversely, Xe^+ would be very slow to recombine in hydrogen, and therefore largely persist as an ion (Zahnle et al. 2019). We cannot exclude that part of atmospheric Kr escaped to space following a mechanism similar to Xe, but if so, the extent of loss must have been limited such that no significant isotopic fractionation was induced over geological periods of time. As described by

Zahnle et al. (2019), ions interact strongly with each other through the Coulomb force, especially at low temperatures. If the escaping hydrogen is significantly ionised, the strong Coulomb interactions between ions would permit Xe^+ to escape at hydrogen escape fluxes, well below what would be required for neutral Kr or Ne to escape. Under these circumstances, the fractionating process of hydrodynamic escape could apply uniquely to Xe, over a wide range of hydrogen escape fluxes, despite its greater mass relative to lighter noble gases (Zahnle et al. 2019).

(a)

Element	Ionization threshold
He	24.59 (50.42 nm)
Ne	21.56 (57.51 nm)
Ar	15.76 (78.67 nm)
N_2	15.58 (79.59 nm)
H_2	15.43 (80.36 nm)
Kr	14.00 (88.57 nm)
CO_2	13.78 (89.98 nm)
O	13.62 (91.04 nm)
H	13.60 (91.17 nm)
H_2O	12.62 (98.26 nm)
CH_4	12.61 (98.32 nm)
Xe	12.13 (102.3 nm)

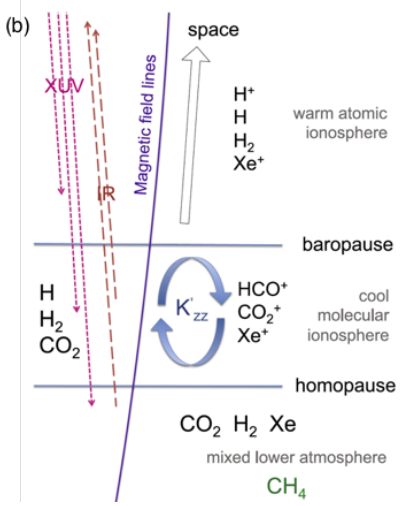

Fig. 85. (a) Ionization thresholds of interested atmospheric species (from compilation by Lide 1995 and Zahnle et al. 2019). (b) Structure of a CO_2-H_2 upper atmosphere pertinent to the Xe escape model showing the efficiency of Xe escape as an ion to depend on the geomagnetic field, the vigour of the hydrogen escape, and the ability for Xe ions to be transported through the molecular ionosphere to the baropause by vertical movements of molecular ions themselves. From Zahnle et al. (2019).

In summary, the Xe ion escape model requires several conditions to be met. Firstly, during the Archean, solar EUV irradiation must have exceeded 10 times that of the modern Sun. This is not a problem for the Hadean Earth, as statistical and observational analyses of the Sun's past activity predict that the EUV flux were higher in the past than today by several orders of magnitude (Ribas et al. 2005; Claire et al. 2012). Whilst the EUV flux 4.4 Ga was possibly 10 to 63 times higher than today, it would have been only 2.5 to 5 times higher than at present 3.2 Ga (Claire et al. 2012). Whether or not the solar EUV irradiation was sufficient during the Archean eon to sustain Xe ionization in the upper atmosphere is therefore unclear. Secondly, the total mixing ratio of hydrogen in the atmosphere must have exceeded 1% (equiv. to 0:5% CH_4), and transport amongst the ions in the lower ionosphere must have allowed Xe ions to reach to the base of the outflowing hydrogen corona (Fig. 85; Zahnle et al. 2019). The latter point is not easy to achieve due to Coulomb interactions between ionised Xe and molecular ions that are not escaping, coupled with the effect of gravity, which constantly tends to pull Xe ions back to Earth's surface. For this reason, the hydrogen-mixing ratio is required to be kept substantially high throughout the Archean (Zahnle et al. 2019).

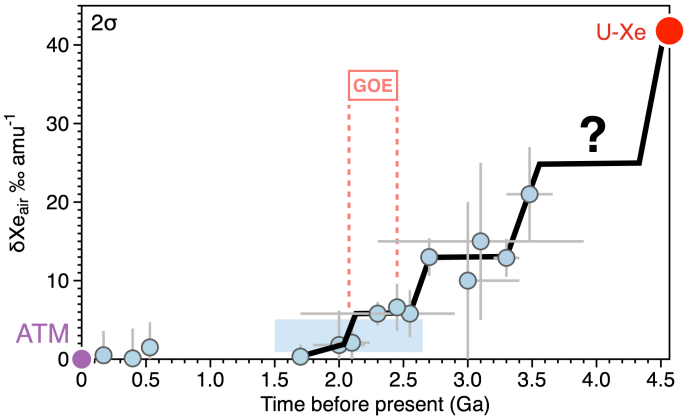

Fig. 86. Isotopic evolution of Xe isotopes in the terrestrial atmosphere (blue points from compilation by Avice et al. 2018) from the U-Xe progenitor to modern atmosphere (ATM). This diagram illustrates the possibility for such evolution to have been discontinuous (black think line scenario), therefore precluding the use of the Xe isotopic composition as a timestamp for providing model ages (Bekaert et al. 2018c, 2019). Of particular interest is the time range around the GOE, coinciding to a first order approximation with the end of Xe isotopic evolution. Obtaining more information about the timing between Xe isotopes reaching a modern-like composition and the GOE may provide interesting insights into the environmental changes that affected the surface of the Earth at this period of time.

Although, at first glance, isotopic data of ancient atmospheric Xe seem to fit a power law evolution curve (Bekaert et al. 2018c, 2020), the process of Xe escape as an ion from the upper atmosphere might have been discontinuous (limited to small apertures or short episodes; Fig. 86), e.g. if restricted to polar windows by a geomagnetic field, dominated by outbursts of high solar activity, and/or limited to transient episodes of abundant hydrogen (Zahnle et al. 2019). Interestingly, although Xe ions do not react with H, H_2, or CO_2, they can be neutralised by nearly resonant charge exchange with O_2 (Anicich, 1993). Hence, the rise of stable O_2 in the atmosphere during the GOE could also have contributed to stop the process of Xe escape, with charge exchanges between Xe^+ and O_2 rendering Xe neutral. The evolution of atmospheric Xe isotopic composition would therefore reflect an extended history of hydrogen escape, ending with the oxidation of the Earth's atmosphere. In particular, Archean atmospheric Xe isotope systematics have recently been used to suggest a potential ~300 Myr long burst of mantle activity and degassing to the atmosphere at the end of the Archean eon (Marty et al. 2019). This proposal relies on the observation of a stepwise change in the $^{129}Xe/^{130}Xe$ of the atmosphere around 2.5 Ga (Marty et al. 2019; Fig. 87), interpreted as evidence for huge fluxes of high $^{129}Xe/^{130}Xe$ mantle-derived gas that could not have occurred within a classical plate tectonics regime (Marty et al. 2019). This intense mantle degassing episode could have drastically affected the thermal evolution of the Earth, as well as the chemical composition of its atmosphere, shortly before the GOE (Fig. 87). In a general way, one way of further scrutinizing the possible relationship between the oxidation of the atmosphere and atmospheric Xe's isotopic evolution (Fig. 86) would be to search for additional ~2.5 Gyr-old atmospheric samples (in kerogens, quartz and/or barytines) to analyse for high precision Xe isotopes.

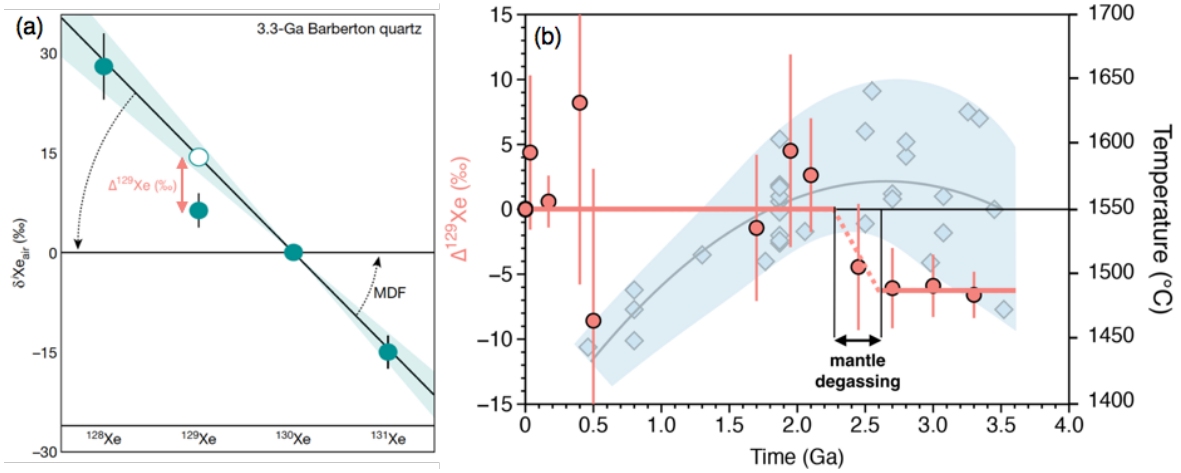

Fig. 87. (a) Xe isotope composition of Archean air (here from fluid inclusions in 3.3-Ga hydrothermal quartz Barberton, South Africa) normalised to the composition of modern air (horizontal black line), showing a depletion in $^{129}Xe/^{130}Xe$, denoted $\Delta^{129}Xe$, compared to the apparent degree of MDF with respect to modern atmosphere. (b) Time evolution of $\Delta^{129}Xe$ in ancient atmospheric gases (Marty et al. 2019) compared to petrological estimates of mantle potential temperature (TP) for non-arc lavas (Herzberg et al. 2010). The light grey curve represents the fit through the TP data, and the light blue shaded area exemplifies the evolution of TP through time. The stepwise change in the $\Delta^{129}Xe$ values between 2.5 and 2.2 Ga could be accounted for by an episode of intense degassing to the atmosphere. Adapted from Marty et al. (2019).

As part of this thesis, we have been providing new noble gas data about the composition of the ancient atmosphere through the analysis of Archean kerogens. Obviously, to have an isotopic evolution of atmospheric Xe that was not continuous but stepwise (e.g., Fig. 86) would render the use of Xe isotopes as a dating tool more complex. If so, it will be extremely interesting to understand the underlying mechanisms behind each step of Xe isotopic evolution, potentially recording the evolution of the solar activity, atmospheric composition, magnetic field, or a conjunction of these. For now, still assuming a continuous and protracted evolution (Fig. 84), we can use the degrees of MDF with respect to modern atmosphere and apparent $\Delta^{129}Xe$ measured in kerogens to test the proposal of a stepwise evolution of the $\Delta^{129}Xe$ in the atmosphere (Marty et al. 2019). Although the large uncertainties associated with kerogen PAN1 do not allow providing any meaningful constraint, except that they appear to be in line with the presence of a non-null $\Delta^{129}Xe$ some $\geq$ 2.55 Ga, kerogen 07SA22 would appear in good agreement with a $\Delta^{129}Xe \sim 0$ around 2.3 Ga (Fig. 88).

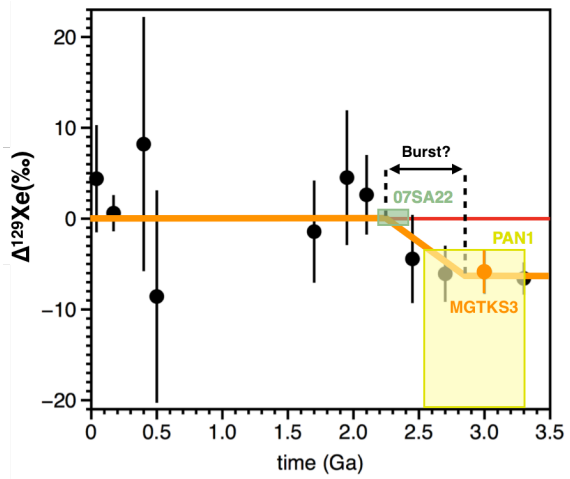

Fig. 88. Time evolution of the deficit of ^{129}Xe (Δ^{129}Xe) in ancient atmospheric gases, with the stepwise evolution model proposed by Marty et al. (2019). Δ^{129}Xe values determined for the three Archean kerogens analysed as part of this thesis and found to have preserved Xe isotopic signatures from the Archean atmosphere are reported for comparison (MGTKS3, Bekaert et al. 2018c, Marty et al. 2019; PAN1 and 07SA22, Bekaert et al. 2020).

Conclusion

Since the first proposal of "chondritic-like" Xe trapped in Archean hydrothermal quartz by Pujol et al. (2011), there have been more Xe isotopic data acquired from ancient atmospheric samples, ultimately providing us with a relatively robust overview of the isotopic evolution of atmospheric Xe during the Archean eon (Avice et al. 2018). In 2018, three papers from independent groups (Parai and Mukhopadhyay 2018 from Saint-Louis/UC Davis, USA; Bekaert et al. 2018c from CRPG; Péron and Moreira 2018 from IPGP Paris) have proposed to use the isotopic evolution of atmospheric Xe as a dating tool, or at least as a time indicator. Parai and Mukhopadhyay (2018) and Péron and Moreira (2018) used Archean Xe isotope systematics to provide constraints on the timing of the onset of subduction on Earth. On our side, we proposed to use atmospheric Xe's isotopic evolution curve to provide model ages for Archean organic materials. The analysis of kerogen MGTKS3 (Pilbara craton, Western Australia) constituted a proof of concept for the method (Bekaert et al. 2018c), but additional analyses turned out to demonstrate that ideal cases such as kerogen MGTKS3 were perhaps not common in nature (Bekaert et al. 2020). Although lower Xe-derived model ages for the kerogens than the ages of the host rocks may ultimately be interpreted in terms of secondary processing (e.g., gas loss during metamorphism, multicomponent mixing) or non-syngenecity, the Xe-based dating tool for ancient organic materials appears to require further analytical development than presented as part of this thesis manuscript. Better understanding/modelling the physical mechanism that drove the isotopic evolution of atmospheric Xe over geological periods of time (Zahnle et al. 2019) will also allow establishing whether or not it was a global, continuous and protracted process, as assumed so far to draw the power law evolution of atmospheric Xe isotopes (Fig. 84; Bekaert et al. 2018c, 2020).

General Conclusion

The main objective of this thesis was to better understand the origin and distribution of volatile elements in the Solar System and on early Earth. I have been able to show that the dynamical and chemical evolution of the protoplanetary disk naturally produced a heterogeneous assembly of chondritic materials characterised by variable volatile contents and nucleosynthetic signatures. In the first instance, turbulent mixing of dust particles in the protosolar nebula would have acted in favour of the large-scale homogenisation of the disk's matter. For instance, organic materials synthesised within the photosphere of the disk could have been widely dispersed in the protoplanetary disk through turbulent diffusion. These would have been preferentially associated with small-sized dust particles, which are preferentially coupled to the turbulent motion of gas and therefore preferentially lofted to the upper layers of the disk where organosynthesis occurs (Bekaert et al. 2018a). During this process of organosynthesis, heavy noble gases from the protosolar nebula would have been incorporated into organic materials, before being mixed in with variable amounts of presolar components (e.g., Xe-HL) on meteorite parent bodies to produce the ubiquitous phase Q component (Chap. 3).

The presence of a dichotomy between the nucleosynthetic signatures of so-called non-carbonaceous (NC) and carbonaceous chondrites (CC) requires a physical mechanism to impede full-scale mixing of the PDD matter, possibly corresponding to the early formation of giant planets acting as barriers to inward transport of dust particles (Kruijer et al. 2017). Planetary bodies accreted inside (NC) and outside (CC) the orbit of Jupiter would hence have received distinct nucleosynthetic inheritances from the molecular cloud parental to the Solar System (Nanne et al. 2019). In addition, physico-chemical environments on both sides of Jupiter would have been different, with the inner Solar System being more reduced and hotter than the outer Solar System, where more oxidizing conditions prevailed (Huss and Lewis, 1995; Worsham et al. 2019). However, the presence of significant amounts of organic materials (Piani et al. 2012), sulphides (Rubin and Choi, 2009) and halogens (Clay et al. 2017) in enstatite chondrites (NC reservoir) indicates that the inner Solar System was not devoid of volatile elements, although deficient in water (Morbidelli et al. 2012).

All astrophysical scenarios accounting for the low-mass yet dynamically excited state of the asteroid belt and larger Earth/Mars mass ratio than expected from classical simulations require significant disruption of the orbits of inner and outer Solar System planetesimals, potentially related to the large-scale migration of giant planets (Raymond et al. 2018). One of the most compelling pieces of evidence for the presence of both inner and outer Solar System planetesimals in the early inner Solar System is the asteroid belt, which is populated by both S-type (analogous to NC materials) and C-type (analogous to CC materials) asteroids at its inner and outer edges, respectively. Likewise, noble gas analyses within ureilites support the

idea of a two-component mixing origin of the ureilite parent body, implying that the early inner Solar System - feeding zone of the proto-Earth - was populated by both oxidised volatile-rich planetary bodies and reduced volatile-poor embryos (Broadley et al. in press). Later on, when the gas of the protosolar nebula dissipated, the orbits of planetary bodies in the debris disk would again have been disrupted. Some models even suggest the potential for giant planet instabilities to occur within ~10 Myr (Clément et al. 2018), and up to ~500 Myr (Gomes et al. 2005) after the dispersal of the gaseous disk. The astrophysical context of the Solar System's early evolution and planetary formation processes therefore offers the possibility for Earth's building blocks to have originated from pretty much anywhere in the Solar System, from both the NC and CC reservoirs.

A cross section of volatile element reservoirs throughout the Earth, from the core to the atmosphere, roughly allows reconstructing the time evolution of the terrestrial accretion. The deepest parts of the Earth record its interaction with the gas phase of the protosolar nebula, which was ingassed to the growing proto-Earth during the first million years of the Solar System evolution. This is the most obvious from the Ne isotopic analysis of deep mantle-derived/influenced samples (e.g., Yokochi and Marty 2004; Williams and Mukhopadhyay 2019), but could also be the case for hydrogen (Hallis et al. 2015). Dissolution of a prospective nebular atmosphere into the mantle during periods of global magma ocean would have preferentially overprinted the signature of these light elements, whilst leaving the chondritic signature of Earth's building blocks to dominate the inventory of heavier volatile elements (e.g. Kr and Xe; Mizuno et al. 1980; Broadley et al. 2019). After dissipation of the protosolar nebula, terrestrial planets continued to grow through collisional accretion of planetary bodies within a debris disk. Most of the terrestrial upper mantle preserves the signature of a chondritic inheritance, with Ne, Kr and Xe all pointing towards the unique composition found in meteorites (Holland et al. 2009; Péron and Moreira 2018). Although there are some uncertainties regarding the extent of degassing of the upper mantle as derived from I-Pu-Xe systematics (Bekaert et al. 2019c), mantle degassing could have significantly contributed to form the atmosphere. The Ne isotope signature of the atmosphere could for instance be accounted for by a ~ 1:1 mixing between ^{20}Ne from mantle degassing and ^{20}Ne from a late contribution of CI-like materials (Marty 2012; Vogt et al. 2019).

The cessation of Earth's main accretion was marked by a series of giant impacts (Tucker & Mukhopadhyay 2014), the last of which corresponded to the Moon-forming event (Canup and Asphaug 2001). Although these episodes were extremely energetic and likely resulted in the loss of (at least part of) primitive terrestrial atmospheres, Earth's mantle was never fully homogenised, as witnessed by the preservation of geochemical heterogeneities dating back from its early accretion (e.g., Willbold et al. 2011; Mukhopadhyay 2012; Touboul et al. 2012). The establishment of Earth's atmosphere was not a simple process. Instead, it is the result of the complex interplay between impact erosion, volatile element dissolution in magma oceans, outgassing from the solid Earth, and late deliveries (Schlichting & Mukhopadhyay 2018). A

late veneer to the Earth-Moon system is notably required to account for the elevated concentration of highly siderophile elements within their respective mantle and surface reservoirs (Kimoura et al. 1974; Day et al. 2007). In addition, the peculiar Xe isotopic composition of the terrestrial atmosphere reflects a unique fingerprint of cometary material inheritance (Marty et al. 2017). About 20% of atmospheric Xe would hence have been supplied by comets, originating from the outermost edges of the Solar System, with the other ~80% representing the chondritic inheritance (represented by the Q signature), from degassing of the Earth's main accretion materials and late veneer (Bekaert et al. *under rev.*). This cometary fingerprint in the Earth's atmosphere is not witnessed in the primordial signature of mantle-derived samples, but could be present at the lunar surface (Bekaert et al. 2017), therefore pointing towards a late contribution of comets to the Earth-Moon System. These would however have had a limited influence on the water, nitrogen, carbon and halogen inventory of the Earth surface reservoir, a relatively small mass of comets (~ 1.10^{19} kg) being required to account for the noble gas composition of the atmosphere (Chapter 6; Marty et al. 2016; Barnes et al. 2016).

The Earth represents ~51% of all the mass of the present-day inner Solar System (i.e., within the orbit of Jupiter), but still none of the meteorites from our present-day collection constitute a good analogue for the building material of our planet. From an isotopic point of view, the Earth's composition is best represented by enstatite chondrite-like materials (Dauphas et al. 2017; Render et al. 2017), suggesting the main source of Earth's accretionary bodies had an inner Solar System origin. However, the nature and origin of the Moon-forming impactor and late veneer are open for debate, with geochemical arguments pointing towards both a pure NC or a pure CC origin (Fig. 18). The Earth's volatile element inventory could thus have been established from the heterogeneous accretion of planetary bodies originating from various heliocentric distances within the Solar System. By proposing a heavy noble gas isotope-based mixing model between cometary and chondritic end-members, we show in Chapter 6 that the initial noble gas to water ratio of the primitive Earth would most likely require a dry origin (i.e., akin to enstatite chondrites and not carbonaceous chondrites) of chondritic volatile elements on Earth. This would suggest that most of the terrestrial water was potentially acquired during Earth's main accretionary phase, from chondritic precursors containing little amounts of water. This would be in line with scenarios advocating that the bulk of Earth's water was accreted before the Moon-forming giant impact (e.g., Greenweood et al. 2018). However, further testing the reliability of using atmospheric noble gas to water ratios to infer the nature of Earth's building blocks will likely require better constraints to be provided on how planetary and geological processes (impacts, subduction, atmospheric escape) affect these ratios over time.

Major changes in the composition of the atmosphere and geodynamical regime of the Earth happened between 3 Ga and 2 Ga. This period of time marked the transition from a reducing atmosphere to a modern-like, O-rich environment, as well as the start of efficient

volatile element recycling within the solid Earth (Parai and Mukhopadhyay, 2018). It is characterised by the end of the protracted evolution of atmospheric xenon's isotopic composition (Avice et al. 2018), potentially related to the cessation of extensive hydrogen escape (Zahnle et al. 2013). It is now well established that life was already present on Earth some 3 Ga, but the exact timing of its emergence and diversification is still poorly documented. Being able to assess the syngenecity of ancient organic materials in the Archean sedimentary record constitutes one of the main challenges to improve our knowledge of early life's evolutionary history. Here, I show that ancient insoluble organic materials (kerogens) can trap and preserve heavy noble gases from their depositional environment. This process "fossilises" the isotopic composition of atmospheric Xe at the time of their formation, which can then be used to provide model ages for the kerogens (independently from their host rocks) based on the evolution curve of atmospheric Xe isotopes (Bekaert et al. 2018c). We speculate that comparing Xe-derived model ages with the actual ages of the host rocks could hence provide a means to test the syngenetic origin of ancient organic materials (Bekaert et al. 2018c). In practice, the outcomes of this method become challenging to interpret in the case where lower Xe-derived model ages than expected from the ages of host rocks are obtained. This could indicate that initially trapped Xe components were at least partially lost and/or mixed together with some Xe carried out by younger generations of organic materials (Bekaert et al. 2020), but no clear conclusion can yet be drawn regarding the presence of a syngenetic organic compound. Nonetheless, ancient organic materials in the Archean sedimentary rock record constitutes a promising archive of atmospheric noble gases, which, combined with the analysis of fluid inclusions in quartz and barites, should ultimately allow new light to be shed on the timing and conditions of the terrestrial atmosphere's evolution.

General Perspectives

Heavy noble gases in cometary and chondritic matter

There is no doubt that analysing the noble gas isotopic composition (especially Xe) of another cometary body in the Solar System (either *in-situ* or thanks to a cometary sample return mission) will allow the representativeness comet 67PC-G to be better assessed (Marty et al. 2017). Likewise, it could be of equal importance to investigate the noble gas isotopic composition of the icy moons of Jupiter and Saturn, which have recently been proposed to originate from CI chondrites and comets (Néri et al. 2019). In hindsight, the experimental work presented in Chapter 3 has essentially returned inconclusive results, with no detection of Xe-bearing molecules in irradiated cometary ice analogues. However, the potential reactivity of Xe atoms in cometary ice analogues should definitely be further investigated by varying the chemical composition of the ice, temperature, pressure, as well as the dose and type of irradiation. For instance, we investigated the ionization dynamics of Xe atoms interacting with water ice using the recently developed Resonant Two-Step Laser Ablation Mass Spectrometry at the Ice Spectroscopy Laboratory (NASA, JPL) and found that coulomb explosions of multiply ionised xenon could be triggered in water ice (Bekaert et al. 2019b). Although the exact mechanism accounting for the generation of Coulomb explosions in these experiments is not clear, it could be due to electron impact processes resembling cometary electron and ion bombardment (Bekaert et al. 2019b). Whether or not electron and ion bombardment could induce significant chemical modifications to, and potentially outgassing from, cometary ices should be further examined, e.g. using an electron gun to bombard Xe-H_2O ice mixtures with increasing doses/energies of electrons. Regarding the EXCITING experiment, I would say that everything is yet to be discovered. If confirmed, the fact that the fraction of Xe trapped in amorphous ice above Xe's sublimation temperature is mass dependently fractionated in favour of the heavy isotopes with respect to the starting gas composition could have important implications regarding the noble gas inventory of comets reaching the terrestrial planet forming region. The potential isotopic effects of varying the Xe to H_2O ratio, the deposition rate and the dose of UV irradiation should all in turn be investigated. The same experiments will also be carried out for lighter noble gases in order to test if this mechanism could also affect the Ar and Kr isotopic composition of cometary ice. Finally, it seems that working with mixtures of noble gas and pure water ice could yield different noble gas trapping and release patterns than "dirty" (more realistic) ices containing e.g., CO_2, CH_4, CO (Kouchi and Yamamoto, 1995). Hence, different chemical compositions of the carrier phase of noble gas in cometary analogues might be tested to investigate the effect of changing the ice composition on noble gas trapping/fractionation processes.

Concerning noble gas components in chondrites and the origin of phase Q (Chapter 3), it remains unknown how chondritic organics were able to incorporate such large amounts of

heavy noble gases from the protosolar nebula. One possible avenue of investigation would be to carry out additional experiments of noble gas trapping into growing organics (M. Kuga's thesis) using the new generation, high-purity Nebulotron. Importantly, it would also be crucial to know whether or not cometary organics carry the same Q signature as chondritic materials, as has been sugggested to be the case for Ne in cometary silicates (Marty et al., 2008). This could definitely help answering the question of whether or not cometary and chondritic IOM share a common (protosolar nebula-derived) origin. If this is the case, it will be interesting to see how much Xe-HL would be required (Gilmour 2010) to account for the cometary Q-Xe signature, therefore testing if the model of Xe-HL contribution increase with heliocentric distance, suggested for the chondritic reservoir (Bekaert et al. 2019a), also applies to comets. On the other hand, it would be interesting to see if the Xe isotopic composition determined on comet 67P/C-G (Marty et al. 2017) could represent a precursor to the solar Xe composition (in other words, would it be possible to incorporate the cometary Xe isotopic composition within the flowchart presented in Fig. 57).

Origin of organic materials in extraterrestrial samples

Investigations into the structural and chemical composition of Nebulotron products (Chapter 5) constitute an on-going project that is far from being concluded. First of all, the origin of (non-reproducible) D-enrichments in Nebulotron organics (Fig. 73) is not known. Likewise, where and when chondritic IOM acquired its ^{15}N-enrichments remains to be unravelled. Laboratory investigations of photon-driven organosynthesis (on the APSIS experiment at LATMOS or DESIRS line at the Synchrotron SOLEIL) appear extremely promising, but more development is required. One interesting pathway to explore relates to the secondary processing of Nebulotron organics by thermal metamorphism and/or aqueous alteration. Preliminary results and literature data discussed in Chapter 5 suggest that thermal processing would result in the cyclization, likely loss of heteroelements and ultimate aromatization of the IOM. Aqueous alteration could instead cause a chemical diversification of the IOM, materialised by the incorporation of heteroelements (here O) into its molecular structure. Additional laboratory experiments are required to confirm these results, varying the temperature/duration of the simulations and multiplying the analytical techniques (e.g., FTIR, Raman spectroscopy, orbitrap mass spectrometry) employed to characterise the reaction products. In a general sense, it would be interesting to systematically determine the bulk elemental composition (H, C, O and N) of Nebulotron products for various starting gas mixtures, with and without secondary processing. It is however important to keep in mind that the perfect laboratory analogue of chondritic organic materials might never be produced, in line with their alleged intricate and multiple stage origin in meteorites.

Numerical models of dust transport in PPDs

As part of this thesis, we used the LIDT3D code (Charnoz et al. 2012) to mimic the 3D transport of super-particles subject to gravitational settling, radial drift, and turbulent diffusion, starting from a homogeneous disk characterised by an isothermal gas structure. Obviously, many processes that presumably took place in the PPD could not be modelled in these simulations, e.g. disk winds, magneto-rotational instabilities, streaming instabilities, early formation of planetesimals, etc. The first steps towards establishing a more realistic model would be to allow (i) grain size evolution through fragmentation or coagulation processes, and (ii) evolution of the physical parameters of the disk with time. In the simulations reported in Bekaert et al. (2018a), the surface density, temperature and pressure of the gas are fully parameterised (an example is given on Fig. 89a-d). Simulated disks therefore naturally reach a "steady state" after a certain period of time (depending for instance on the turbulence parameter value, presence or not of a dead zone, and grain size distribution), where large particles have settled to the midplane (Fig. 89e) and small ones are still being lifted to the upper layers of the disk by turbulent diffusion. Once this steady state has been reached, the total amount of organic materials within the PPDs monotonically increases (Fig. 89f).

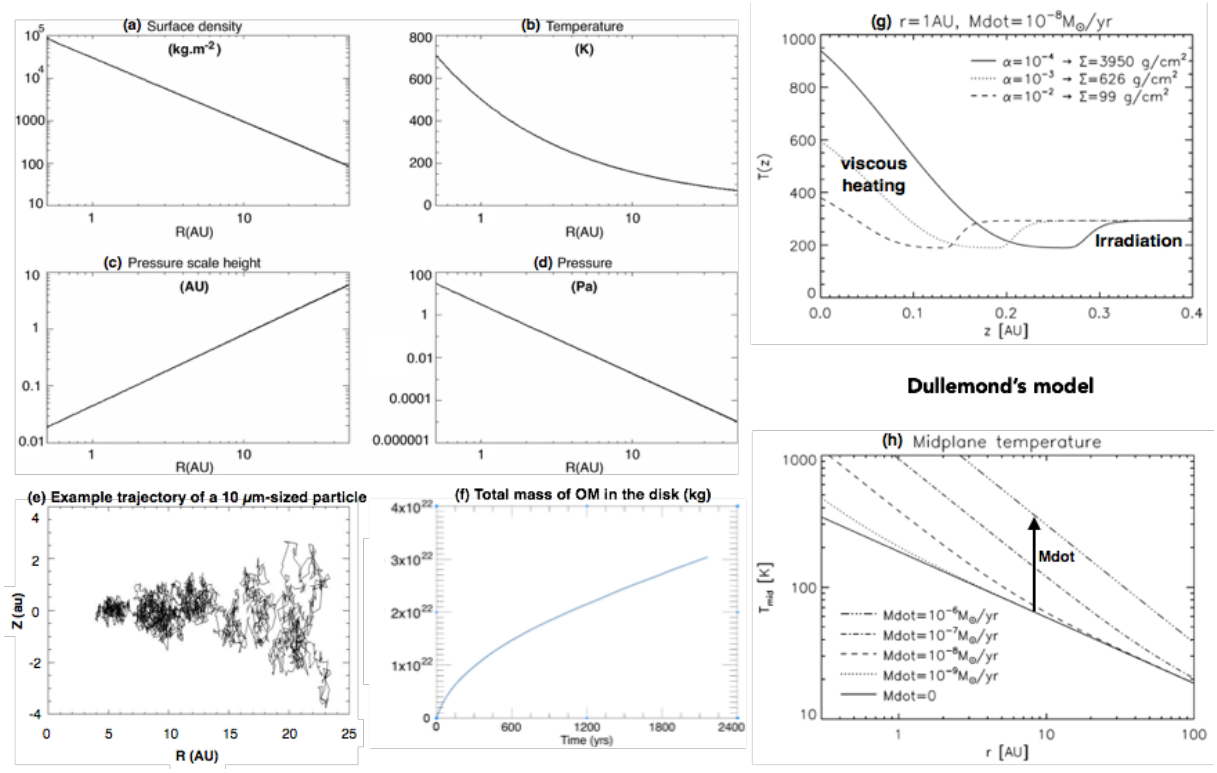

Fig. 89. Improving the parameterization of the gas phase's structure of the disk in LIDT3D. (a-d) Radial profiles of the surface density (a), temperature (b), pressure scale height (c), and local pressure (d) of the gas in LIDT3D for a central star of 1 solar mass. An example of path of a 10 µm-sized particle in the R/Z plane of the disk (Charnoz et al. 2011) is given in (e). (f) Time evolution of the total mass of organic matter (OM) in a non-evolving disk (arbitrary production rate in the upper layers of the disk; Bekaert et al. 2018a). (g-h) Thermal structure of a disk where viscous heating and radiative cooling at the midplane, as well as stellar irradiation within the upper layers are considered (Dullemond 2013). The effect of increasing the mass accretion rate (Mdot) on the midplane temperature is shown in (h).

Implementing the transfer/destruction of organic materials during dust growth/fragmentation in the LIDT3D is not trivial. But theoretically, a conservative transfer of organic materials during grain coagulation/fragmentation could be assumed. Hence, the mass of organic materials in a particle formed by the merging of sub-particles would equal the sum of organic materials initially carried out by the sub-particles. Likewise, particles formed by fragmentation would inherit a fraction of the initial organic content that is proportional to their mass fraction with respect to the initial particle.

The temperature structure of this 3D analytical model could be improved by considering the thermal effects of viscous heating and radiative cooling at the midplane, as well as stellar irradiation within the upper layers of the flaring disk (Fig. 89g; Dullemond 2013). In this case, the temperature at the midplane and upper layers are controlled by the stellar mass accretion rate (Mdot, Fig. 89h) and luminosity of the central star, respectively, which can both the described by time-dependent functions to produce a fully evolving disk structure. The effect of viscous heating due to the accretion process at a given radius (dominant at the midplane) can be expressed as a function of the mass accretion rate (T_{visc} = f(Mdot); Oka et al. 2011). The vertical structure of the disk at a given radius is then given by $T(z) = \left(T_{visc}^4 + T_{irr}^4\right)^{1/4}$, where T_{irr} corresponds to the thermal effect of irradiation by the central star (Dullemond 2013). Once computed, the local temperature is used to derive the local sound speed (Cs) and surface density, assuming a given dust opacity (either parameterised, or taken as the Rosseland mean opacity of the disk medium ~ 0.3; Oka et al. 2011). This is on-going work that we have initiated in the framework of L. Gourmand's internship at IPGP. Whilst our work presented in Bekaert et al. (2018a) only deals with the very first thousands to tens of thousands of years of the disk's evolution, implementing organosynthesis processes within an evolving disk where dust growth is allowed will bring important insights into the incorporation of organic materials in early forming planetesimals.

Noble gases: are they always inert?

Due to their particularly stable electronic configuration, noble gases are considered to be non-reactive (i.e., they stay as monoatomic gas), and therefore constitute reliable physical tracers. Such absolute inertness would not stand anymore when considering ionised environments such as planetary atmospheres (Zahnle et al. 2019) or the protosolar nebula (Kuga et al. 2015). In addition, heavier noble gases (Ar, Kr, Xe) have valence electrons that can be screened by core electrons, hence making them less strongly bound to the atomic nucleus and potentially prone to chemical interactions. To date, many stable Ar, Kr and Xe compounds have been synthesised in the laboratory (especially for Xe; e.g., Haner & Schrobilgen 2015). The potential for xenon's enhanced reactivity at high-temperature and high-pressure, and possible incorporation in to mineral phases at depth, has been used to argue for the missing Xe to possibly be stored in the Earth's interior (Chapter 6). It is now critical to evaluate, for each of these chemical reactions involving Xe's incorporation into solid

compounds, whether or not lighter noble gases would be likewise incorporated (if yes, to what extent compared to Xe) and whether or not these processes could induce significant enough isotopic fractionation of Xe isotopes to account for the full missing Xe paradox. By analogy, large fractionation effects of N isotopes have recently been experimentally observed during metal-silicate partitioning (analogous to planetary core formation) over a large range of oxygen fugacities (Dalou et al. 2019). This could in part account for the present-day N isotopic dichotomy between Earth's surficial (^{15}N-enriched) and deep reservoirs (^{15}N-depleted; Dalou et al. 2019).

Regarding Xe's enhanced reactivity, terrestrial-like Xe released at medium to high temperatures (>1000 °C) from lunar anorthosites (Lightner and Marti, 1974; Leich and Niemeyer, 1975; Bekaert et al. 2017; Mathew and Marti 2019), a behaviour attributed to ‘‘irreversible" adsorption. Likewise, it has recently been shown that neutral atmospheric helium can be adsorbed in large quantities onto the surface of mineral grains and that very high temperatures are required (> 900 °C) to release this adsorbed component (Protin et al., 2016). These observations may underline the potential limits of considering noble gases as being absolutely inert under neutral conditions within extreme geological environments, therefore calling for further investigation of their reactivity with mineral surfaces.

Interpreting Xe isotopic signatures in ancient kerogens

As detailed in Chapter 7, deconvoluting Xe signals from multiple organic matter components in the case of mixing between a syngenetic end-member and younger generation(s) of organic material appears extremely challenging (Bekaert et al. 2020). Measuring the Xe isotopic composition of individual organic microstructures would definitely require new analytical developments, potentially coupling *in situ* laser ablation techniques with ultrasensitive, resonance ionization mass spectrometry (Gilmour et al. 1994). One way of potentially circumventing issues related to the occurrence of multiple generations of OM within a given sample may also be to accurately separate them based on their thermal sensitivities, as illustrated by Rock Eval studies (Delarue et al. 2018). In this case, it would be required to first (i) carry out Rock Eval investigations to distinguish the different pools of organic matter and determine whether or not a thermo-recalcitrant component (possibly syngenetic) can be identified and isolated by sequential thermal cracking, and then (ii) accordingly adapt the stepwise heating procedure for noble gas analysis.

Appendices

Please note that the work published as part of this thesis is available on line (open access)

* Supplementary materials related to Marty et al. (2017) *Science* (Chapter 2) can be dowloaded at: www.sciencemag.org/content/356/6342/1069/suppl/DC1

* The manuscript and supplementary materials for Bekaert et al. (2017) *GCA* (Chapter 2) can be found at: https://www.sciencedirect.com/science/article/pii/S0016703717305446#m0005

* Supplementary materials related to Bekaert et al. (2018c) *Science Advances* (Chapter 7, Appendix C) can be found at: https://advances.sciencemag.org/content/4/2/eaar2091/tab-figures-data

* Supplementary materials related to Bekaert et al. (2019a) *MAPS* (Chapter 4) can be dowloaded at: https://onlinelibrary.wiley.com/doi/full/10.1111/maps.13213

* The manuscript and supplementary materials for Bekaert et al. (2019b) *Geochemical Journal* (General Perspectives) can be found at:
https://www.jstage.jst.go.jp/article/geochemj/53/1/53_2.0548/_article/-char/ja/

* Supplementary materials related to Bekaert et al. (2019c) *EPSL* (Appendix D) can be dowloaded at: https://www.sciencedirect.com/science/article/pii/S0012821X19304583#se0150

* Supplementary materials related to Bekaert et al. (2020) *Precambrian Research* (Chapter 7, Appendix E) can be found at:
https://www.sciencedirect.com/science/article/pii/S0301926819303535

Appendix A: Xe isotopic data from ice experiments at JPL (NASA, CA, USA).

Appendix B: Supplementary materials associated with the paper reported in Chapter 6, under revision at *Scientific Reports*.

Appendix C: Bekaert et al. (2018c) *Science Advances,* discussed in Chapter 7

Appendix D: Bekaert et al. (2019c) *EPSL.*

Appendix E: Bekaert et al. (2020) *Precambrian Research,* discussed in Chapter 7

Appendix A

Chapter 3

		^{124}Xe	^{126}Xe	^{128}Xe	^{129}Xe	^{131}Xe	^{132}Xe	^{134}Xe	^{136}Xe
					^{130}Xe				
	(n)								
	1	0,02480	0,02291	0,47494	6,49248	5,15357	6,51378	2,50297	2,10388
	2	0,02519	0,02319	0,47773	6,53022	5,16933	6,52394	2,50504	2,11660
	3	0,02502	0,02295	0,47411	6,49302	5,14889	6,52057	2,49891	2,10858
	4	0,02529	0,02299	0,47650	6,51453	5,18367	6,54559	2,50399	2,11983
	5	0,02536	0,02290	0,47615	6,52805	5,15619	6,51980	2,50519	2,12967
	6	0,02533	0,02307	0,47903	6,53473	5,17355	6,52295	2,51213	2,12247
	7	0,02517	0,02305	0,47890	6,53619	5,17883	6,52734	2,51030	2,11591
	8	0,02526	0,02279	0,47517	6,50738	5,16227	6,53048	2,51488	2,12383
	9	0,02520	0,02289	0,47549	6,51054	5,17118	6,52918	2,52062	2,12899
	10	0,02504	0,02317	0,47504	6,53852	5,19364	6,53943	2,52774	2,13294
	11	0,02502	0,02308	0,47414	6,53906	5,17783	6,54395	2,51663	2,12458
	12	0,02540	0,02293	0,47740	6,51203	5,18259	6,52755	2,52356	2,12865
	13	0,02507	0,02292	0,47829	6,53143	5,17827	6,53611	2,51656	2,11747
	14	0,02527	0,02301	0,47980	6,53476	5,18346	6,54497	2,51820	2,12935
	15	0,02477	0,02280	0,47358	6,50860	5,15481	6,51600	2,51049	2,12460
	16	0,02514	0,02297	0,47650	6,50049	5,18219	6,55788	2,53391	2,13397
	17	0,02520	0,02305	0,47372	6,51915	5,17167	6,53118	2,52320	2,13842
	18	0,02506	0,02313	0,47569	6,52907	5,17987	6,55333	2,52634	2,13006
	19	0,02495	0,02312	0,47470	6,49195	5,15448	6,53907	2,51201	2,12880
	20	0,02541	0,02284	0,47609	6,50014	5,16637	6,52927	2,52819	2,13755
	21	0,02515	0,02280	0,47438	6,50934	5,16285	6,50945	2,51555	2,13162
	22	0,02503	0,02292	0,47592	6,49392	5,16027	6,50989	2,52306	2,12865
	23	0,02539	0,02299	0,47656	6,54365	5,19482	6,56531	2,54669	2,14042
#1	Average	**0,02515**	**0,02298**	**0,47608**	**6,51736**	**5,17133**	**6,53204**	**2,51722**	**2,12595**
	1σ/√n	**0,00004**	**0,00002**	**0,00038**	**0,00366**	**0,00278**	**0,00319**	**0,00238**	**0,00194**
	1	0,02525	0,02320	0,47751	6,50363	5,17554	6,54774	2,51564	2,12183
	2	0,02547	0,02315	0,47925	6,54838	5,19543	6,57025	2,52568	2,13400
	3	0,02505	0,02295	0,47732	6,50686	5,18430	6,54571	2,51144	2,12080
	4	0,02543	0,02306	0,47671	6,49218	5,16180	6,52601	2,50780	2,11402
	5	0,02590	0,02321	0,47906	6,54099	5,19077	6,56634	2,52663	2,12261
	6	0,02509	0,02277	0,47585	6,52948	5,18261	6,55136	2,51445	2,12397
	7	0,02539	0,02354	0,47999	6,51391	5,16457	6,54528	2,51141	2,11617
	8	0,02529	0,02303	0,47516	6,52547	5,15590	6,52827	2,51143	2,11731
	9	0,02517	0,02295	0,47745	6,50866	5,16770	6,52280	2,52116	2,12005
	10	0,02516	0,02287	0,47722	6,51106	5,16549	6,51972	2,51097	2,12071
	11	0,02532	0,02296	0,47785	6,52300	5,18102	6,53401	2,51208	2,13283
	12	0,02535	0,02304	0,47930	6,55873	5,19728	6,56737	2,51620	2,13854
	13	0,02531	0,02298	0,47768	6,53129	5,16834	6,54120	2,51573	2,12155
	14	0,02548	0,02304	0,47844	6,53295	5,18983	6,55379	2,52291	2,12846
	15	0,02538	0,02306	0,47595	6,53545	5,20561	6,55214	2,51910	2,12865
	16	0,02532	0,02306	0,48058	6,52062	5,19675	6,55707	2,52493	2,12721
#2	Average	**0,02533**	**0,02305**	**0,47783**	**6,52392**	**5,18018**	**6,54557**	**2,51672**	**2,12430**
	1σ/√n	**0,00005**	**0,00004**	**0,00039**	**0,00453**	**0,00388**	**0,00412**	**0,00154**	**0,00176**

	(n)								
	1	0,02430	0,02243	0,47107	6,47991	5,22257	6,62795	2,57451	2,19804
	2	0,02450	0,02215	0,46890	6,46201	5,18347	6,57068	2,56332	2,19006
	3	0,02456	0,02237	0,47093	6,47755	5,19585	6,61613	2,56347	2,18861
	4	0,02470	0,02225	0,46936	6,46071	5,19827	6,61604	2,57287	2,19376
	5	0,02409	0,02218	0,46838	6,45304	5,18833	6,60329	2,55397	2,18428
	6	0,02434	0,02227	0,46946	6,45620	5,20053	6,59985	2,56649	2,18386
	7	0,02421	0,02242	0,47021	6,49304	5,21375	6,61352	2,57559	2,20103
	8	0,02420	0,02244	0,47002	6,45811	5,18888	6,59267	2,57120	2,18668
	9	0,02420	0,02244	0,47060	6,47292	5,20084	6,61355	2,57901	2,20336
	10	0,02450	0,02250	0,47367	6,49813	5,21906	6,64657	2,57934	2,21202
	11	0,02433	0,02238	0,46993	6,46942	5,17694	6,58019	2,56653	2,18613
	12	0,02454	0,02257	0,47219	6,49184	5,22203	6,63853	2,58286	2,20273
	13	0,02438	0,02203	0,46954	6,47649	5,20282	6,62329	2,57034	2,20327
	14	0,02400	0,02230	0,47037	6,47766	5,19563	6,61136	2,56970	2,20082
	15	0,02455	0,02264	0,47294	6,51061	5,22967	6,65748	2,59197	2,21574
	16	0,02442	0,02245	0,47142	6,46750	5,21432	6,63162	2,58208	2,20624
#3	Average	**0,02436**	**0,02236**	**0,47056**	**6,47532**	**5,20331**	**6,61517**	**2,57270**	**2,19729**
	1σ/√n	**0,00005**	**0,00004**	**0,00036**	**0,00410**	**0,00386**	**0,00575**	**0,00231**	**0,00249**
	1	0,02444	0,02245	0,47030	6,45851	5,19468	6,60271	2,57182	2,20648
	2	0,02417	0,02247	0,47000	6,47465	5,20929	6,62494	2,58511	2,20439
	3	0,02428	0,02260	0,47014	6,48964	5,19205	6,61983	2,58288	2,21856
	4	0,02413	0,02208	0,46826	6,47672	5,19703	6,59825	2,57043	2,19895
	5	0,02464	0,02222	0,46896	6,47198	5,20066	6,62977	2,56696	2,19648
	6	0,02450	0,02239	0,47362	6,51635	5,23058	6,64530	2,59293	2,20869
	7	0,02437	0,02240	0,47194	6,48969	5,23870	6,65847	2,58066	2,21334
	8	0,02444	0,02230	0,47116	6,47442	5,21679	6,63016	2,58619	2,21344
	9	0,02452	0,02238	0,47341	6,49008	5,22291	6,64589	2,58354	2,21248
	10	0,02433	0,02260	0,46946	6,47243	5,20602	6,62953	2,58509	2,21433
	11	0,02449	0,02243	0,47034	6,47696	5,20706	6,62141	2,57474	2,20573
	12	0,02438	0,02257	0,46942	6,48140	5,19066	6,61339	2,56863	2,19795
	13	0,02413	0,02221	0,47298	6,50123	5,19407	6,62071	2,58197	2,19391
	14	0,02445	0,02228	0,47039	6,49360	5,22087	6,62296	2,57392	2,21656
	15	0,02413	0,02249	0,46880	6,48443	5,20028	6,60770	2,58023	2,20523
	16	0,02418	0,02225	0,47128	6,49450	5,20930	6,64120	2,58504	2,20956
	17	0,02441	0,02241	0,47046	6,47706	5,20595	6,62324	2,57870	2,20471
#4	Average	**0,02435**	**0,02238**	**0,47064**	**6,48374**	**5,20805**	**6,62562**	**2,57934**	**2,20711**
	1σ/√n	**0,00004**	**0,00004**	**0,00040**	**0,00337**	**0,00347**	**0,00396**	**0,00180**	**0,00182**
Standard	Average	**0,02517**	**0,02280**	**0,47687**	**6,52429**	**5,18274**	**6,56282**	**2,53228**	**2,14330**
	1σ/√n	**0,00005**	**0,00005**	**0,00052**	**0,00407**	**0,00347**	**0,00510**	**0,00252**	**0,00250**

Xe isotopic data obtained for the four ice samples from our experiments at JPL. The numbers of the experiments refer to the numbers used in the main text and Fig. 49, where #1 - #2 are the two samples sublimated at 60K, and #3 - #4 are the two samples released at 150K. The isotopic composition of the standard (n=19) measured during the corresponding period of analysis is given for comparison.

Appendix B
Chapter 6

The origin and fate of volatile elements on Earth revisited in light of recent noble gas data obtained from comet 67P/Churyumov-Gerasimenko

David V. Bekaert[1]*; Michael W. Broadley[1]*; Bernard Marty[1]

Supplementary Information

S1° Determining the composition of chondritic endmembers (excel compilation)

S2° Literature data used to construct Table 2.

S3° Computing the contribution of cometary krypton in the atmosphere.

Fig. S1° Kr three isotope plots refute a significant contribution from solar Kr to the atmosphere.

Fig. S2° Kr three isotope plots: Kr-N and Kr-G mixtures to reproduce the cometary signature.

Fig. S3° Percentage of cometary nitrogen accreted to Earth and the resulting effect on the composition of the Earth's surface.

Fig. S4° Efficient aerobracking of low-density cometary material upon entry in the atmosphere.

S2° Literature data used to construct Table 2.

Calculations for volatile element concentrations in CC, OC and EC are reported in the excel file provided as a Supplementary material ("compilation-SR-Bekaert.xls"). References used to calculate the IQR for each volatiles species is reported here below.

	CC	OC	EC
^{36}Ar	Mazor et al. (1970)[1] Nakamura (2006)[2]	Schelhaas et al. (1990)[7] Heymann and Mazor (1968)[8] Hashizume and Sugiura (1995)[9]	
^{84}Kr	Bekaert et al. (2019)[3] Haack et al. (2012)[4] Okazaki and Nagao (2017)[5] Srinivasan et al. (1978)[6]	Schelhaas et al. (1990)[7] Heymann and Mazor (1968)[8] Alaerts et al. (1979)[10]	Patzer and Schultz (2002)[11] Okazaki et al. (2010)[12] Crabb and Anders (1982)[13]
^{132}Xe		Schelhaas et al. (1990)[7] Heymann and Mazor (1968)[8] Alaerts et al. (1979)[10]	
H_2O	Jarosewich (1990)[14] Piani et al. (2018)[15]	Jarosewich (1990)[14]	Javoy (1995)[16] Jarosewich (1990)[14]
^{12}C	Alexander et al. (1990)[17] Kerridge (1985)[18] Jarosewich (1990)[14] Piani et al. (2018)[15]	Grady et al. (1986)[18] Jarosewich (1990)[14]	Jarosewich (1990)[14]
^{14}N	Kerridge (1985)[19] Kung and Clayton (1978)[20]	Kung and Clayton (1978)[19] Hashizume and Sugiura (1995)[9]	Grady et al. (1986)[18] Kung and Clayton (1978)[19]

Given that the $^{84}Kr/^{132}Xe$ of enstatite chondrites defines a unique component (Q + subsolar), we take the standard deviation to compute the average value and range of $^{84}Kr/^{132}Xe$ in this mixture. The mean $^{84}Kr/^{132}Xe$ of enstatite chondrites (=1.84 ± 1.14; Table 1) is calculated by taking the mean and standard deviation of all $^{84}Kr/^{132}Xe$ (n=73) reported by [11,12,13]. The choice of IQR to define the range of $^{84}Kr/^{132}Xe$ in enstatites is not necessarily justified given that all data points lie on a mixing line between these two components. Nevertheless the choice of IQR to calculate the $^{84}Kr/^{132}Xe$ of enstatite components would not critically change our conclusions (1.84±1.14 for SD vs. $1.6^{0.7}_{1.0}$ for IQR).

Halogen (^{35}Cl, ^{79}Br, ^{127}I) concentrations in chondritic endmembers and in terrestrial reservoirs (ESR and BM), as well as the mass of the respective terrestrial reservoirs, are from [21]. ^{19}F concentrations in chondrites are from [22]. Halogens concentrations in cometary ice are from [23] for ^{35}Cl, ^{19}F and ^{79}Br, and from [24] for ^{127}I.

Noble gas, water, nitrogen and carbon concentration in the ESR and bulk mantle are from compilation by [25]. $\delta^{15}N$(‰) values for chondritic endmembers and bulk comets are from [26] and [27], respectively. Noble gas concentrations in cometary ice are from [28-29]. Water content and dust to ice ratio of cometary material (used to compute the concentrations of volatile elements in cometary matter) is from [30]. δD(‰) values for each chondritic endmember are from compilation by [31], with the range of cometary δD(‰) values given by [27].

S3° Computing the contribution of cometary krypton in the atmosphere

Mixtures were calculated for each Kr isotopes by taking 10^5 isotopic compositions ($^{i}Kr/^{84}Kr$) from the normal error distribution of comet 67P/C-G[29], chondritic (Q)[32], and atmospheric Kr[33] (Table S1).

Component	$^{80}Kr/^{84}K$ r	±	$^{82}Kr/^{84}K$ r	±	$^{83}Kr/^{84}K$ r	±	$^{84}Kr/^{84}K$ r	$^{86}Kr/^{84}$ Kr	±
Atmosphere	3.96	0.02	20.217	0.021	20.136	0.021	=100	30.524	0.025
Q-Kr	3.937	0.07	20.18	0.02	20.18	0.02	=100	30.95	0.05
67P/C-G	3.87	0.38	20.30	0.44	18.73	0.15	=100	28.87	0.38

Table S3. Compilation of Kr isotopic ratios for each reservoir used to calculate cometary Kr contributions to the atmosphere. The Kr isotopic data for comet 67P/C-G is the average of three measurements[29], with the associated standard deviation. All ratios are normalised to ^{84}Kr and uncertainties are given to 1σ.

The contribution of cometary Kr to the atmosphere is given by:

$$\%\left(\frac{^{i}Kr}{^{84}Kr}\right)_{com-Kr} = \frac{\left(\frac{^{i}Kr}{^{84}Kr}\right)_{chond-Kr} - \left(\frac{^{i}Kr}{^{84}Kr}\right)_{atm-Kr}}{\left(\frac{^{i}Kr}{^{84}Kr}\right)_{chond-Kr} - \left(\frac{^{i}Xe}{^{84}Kr}\right)_{com-Kr}}$$

where $(^{i}Kr/^{84}Kr)_{chond}$, $(^{i}Kr/^{84}Kr)_{atm}$ and $(^{i}Kr/^{84}Kr)_{com}$ are the $^{i}Kr/^{84}Kr$ ratio (i = $^{80\text{-}84}Kr$) of chondritic-Kr, atmospheric-Kr and cometary-Kr respectively. The error weighted mean cometary contribution to the atmosphere is the calculated by:

$$\%(com-Kr) = \frac{\Sigma i\left(\frac{\%\left(\frac{^{i}Kr}{^{84}Kr}\right)_{com-Kr}}{\sigma^2\left(\%\left(\frac{^{i}Kr}{^{84}Kr}\right)_{com-Kr}\right)}\right)}{\Sigma i\left(\frac{1}{\sigma^2\left(\%\left(\frac{^{i}Kr}{^{84}Kr}\right)_{com-Kr}\right)}\right)}$$

with σ^2 given by:

$$\sigma^2{}_{\%(com-Kr)} = \frac{1}{\Sigma i\left(\frac{1}{\sigma^2{}_{\%\left(\frac{^{i}Kr}{^{84}Kr}\right)_{com-Kr}}}\right)}$$

where $\%(^{i}Kr/^{84}Kr)_{com\text{-}Kr}$ and $\sigma^2{}_{\%}(^{i}Kr/^{84}Kr)_{com\text{-}Kr}$ are the mean cometary contribution to the modern atmosphere and the associated error for each Kr isotopic ratio, respectively. The calculated cometary contribution to a Q atmosphere is 21 ± 5%.

Fig. S1° Kr three isotope plots refute a significant contribution from solar Kr to the atmosphere.

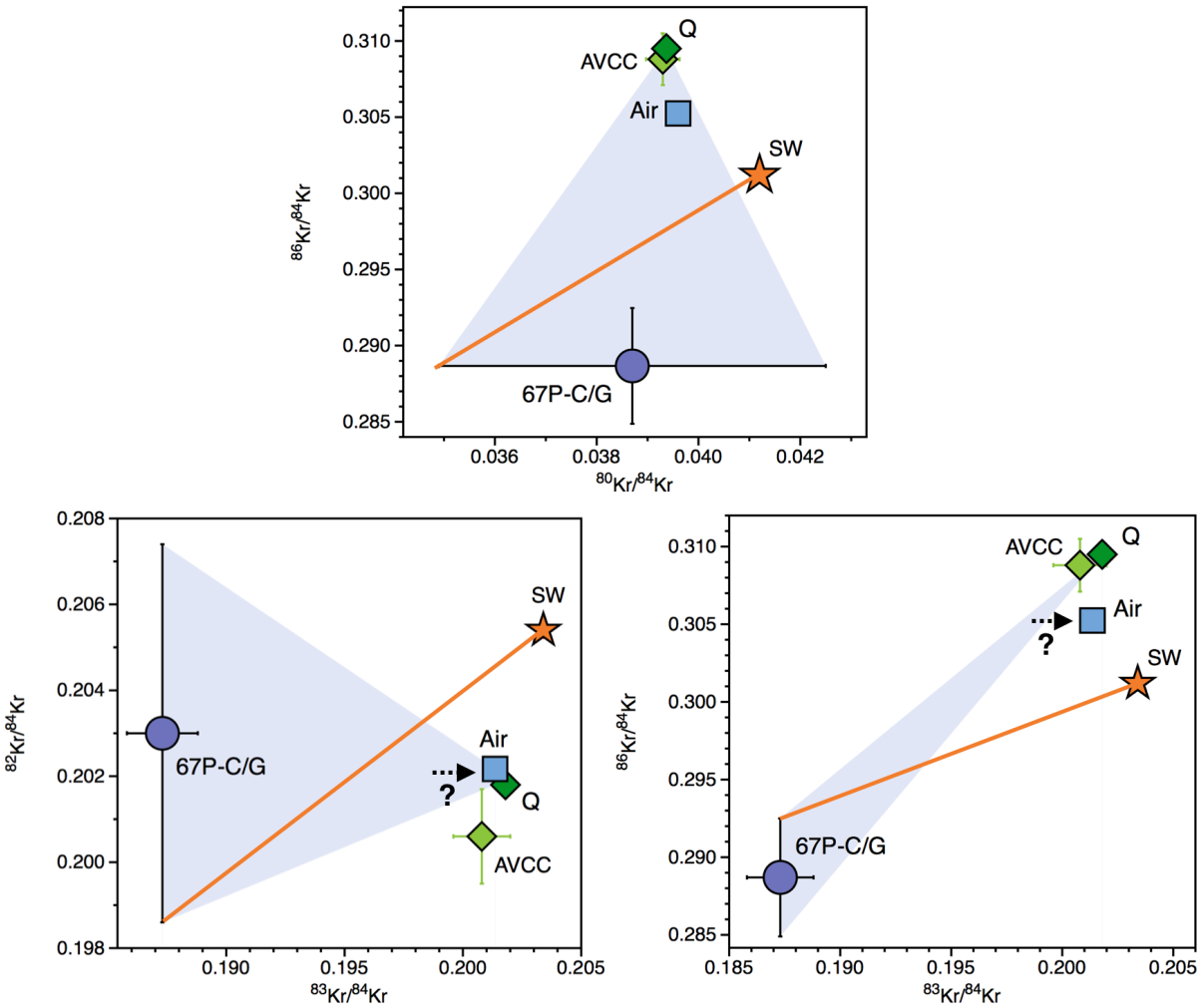

Fig. S2° Kr three isotope plots: Kr-N and Kr-G mixtures to reproduce the cometary signature. Percentages correspond to the fractions of G-Kr.

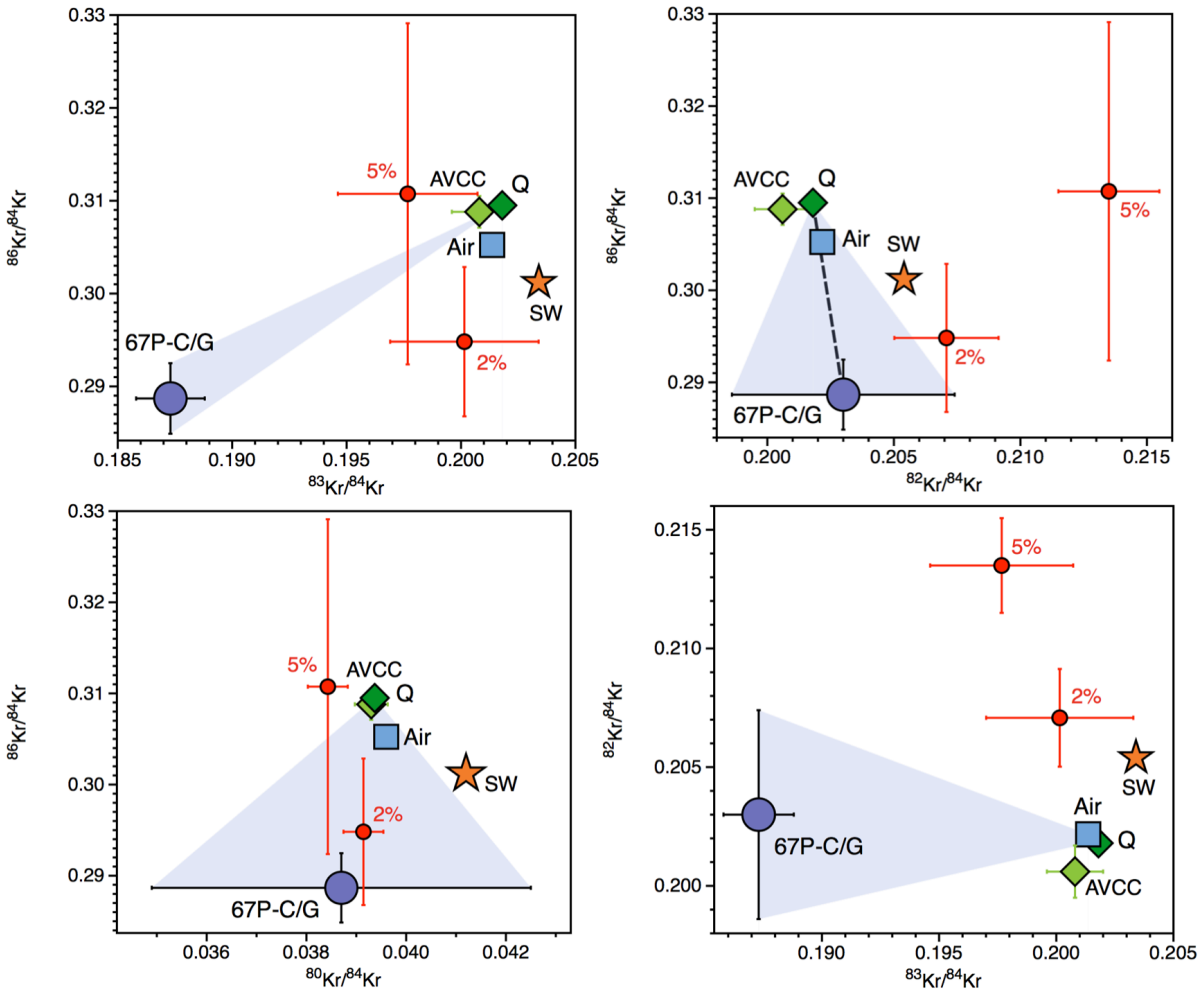

Fig. S3. Percentage of cometary nitrogen accreted to Earth and the resulting effect on the composition of the Earth's surface

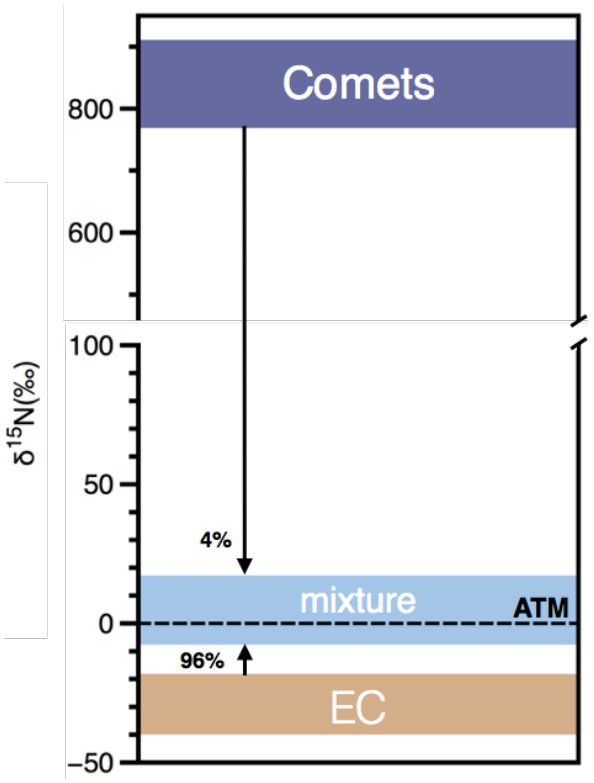

The mass of comets inferred to have been supplied to Earth would only have brought ~5% of the N in the atmosphere. Yet, the large ^{15}N enrichment of comets[27] may still have significantly raised the EC-like $\delta^{15}N$ found in the mantle[34] towards modern day atmospheric values.

Fig. S4° Efficient aerobraking of low-density cometary material upon entry in the atmosphere.

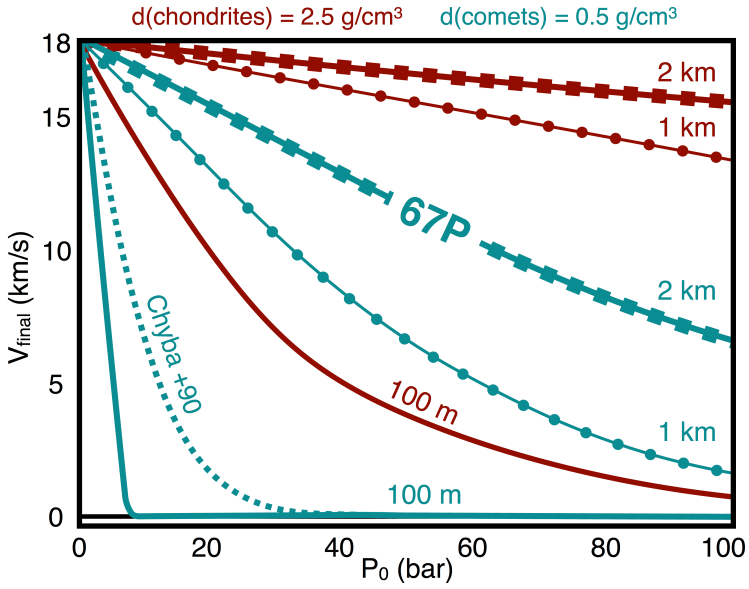

This figure corresponds to Fig. 1 from Chyba et al. (1990), modified using new cometary data from comet 67P/C-G[30]. Impact velocities are displayed as a function of surface atmospheric pressure for cometary (in green) and chondritic (in brown) impactors Incidence angle is taken as 0°, with radii defined as 100, 1000 and 2000m. The density of comet 67P/C-G has been determined to be low[30] (0.5g/cm^3 instead of e.g. 1g/cm^3, as used by Chyba et al. (1990)). This allows cometary impactors with radii of 100 m to be efficiently aerobraked (see the "Chyba +90" dashed green curve relative to the solid green curve adapted to comet 67P/C-G) and effectively reach the surface of the primitive Earth with low impact velocities. Note however that this requires high atmospheric pressures ($\geq$ 5 bar), which might not have been the case in the Archean[36].

Appendix B references

1. Mazor, E., Heymann, D., & Anders, E. Noble gases in carbonaceous chondrites. *Geochimica et Cosmochimica Acta*, *34*(7), 781-824 (1970).
2. Nakamura, T. (2006). Yamato 793321 CM chondrite: Dehydrated regolith material of a hydrous asteroid. *Earth and Planetary Science Letters*, *242*(1-2), 26-38.
3. Bekaert, D. V., Marrocchi, Y., Meshik, A., Remusat, L., & Marty, B. (2019). Primordial heavy n
4. Haack, H., Grau, T., Bischoff, A., Horstmann, M., Wasson, J., Sørensen, A., ... & Greenwood, R. C. (2012). Maribo—A new CM fall from Denmark. *Meteoritics & Planetary Science*, *47*(1), 30-50.
5. Okazaki, R., & Nagao, K. (2017). Primordial and cosmogenic noble gases in the Sutter's Mill CM chondrite. *Meteoritics & Planetary Science*, *52*(4), 669-689.
6. Srinivasan, B., Lewis, R. S., & Anders, E. (1978). Noble gases in the Allende and Abee meteorites and a gas-rich mineral fraction: investigation by stepwise heating. Geochimica et Cosmochimica Acta, 42(2), 183-198.
7. Schelhaas, N., Ott, U., & Begemann, F. Trapped noble gases in unequilibrated ordinary chondrites. *Geochimica et Cosmochimica Acta*, *54*(10), 2869-2882 (1990).
8. Heymann, D., & Mazor, E. Noble gases in unequilibrated ordinary chondrites. *Geochimica et Cosmochimica Acta*, *32*(1), 1-19. (1968).
9. Hashizume, K., & Sugiura, N. Nitrogen isotopes in bulk ordinary chondrites. *Geochimica et cosmochimica acta*, *59*(19), 4057-4069 (1995).
10. Alaerts, L., Lewis, R. S., & Anders, E. Isotopic anomalies of noble gases in meteorites and their origins—III. LL-chondrites. *Geochimica et Cosmochimica Acta*, *43*(9), 1399-1415 (1979).
11. Patzer, A., & Schultz, L. Noble gases in enstatite chondrites II: The trapped component. *Meteoritics & Planetary Science*, *37*(4), 601-612 (2002).
12. Okazaki, R., Takaoka, N., Nagao, K., & Nakamura, T. Noble gases in enstatite chondrites released by stepped crushing and heating. *Meteoritics & Planetary Science*, *45*(3), 339-360 (2010).
13. Crabb, J., & Anders, E. (1982). On the siting of noble gases in E-chondrites. *Geochimica et Cosmochimica Acta*, *46*(11), 2351-2361.
14. Jarosewich, E. Chemical analyses of meteorites: A compilation of stony and iron meteorite analyses. *Meteoritics*, *25*(4), 323-337 (1990).
15. Piani, L., Yurimoto, H., & Remusat, L. A dual origin for water in carbonaceous asteroids revealed by CM chondrites. *Nature Astronomy*, 1 (2018).

16. Javoy, M. The integral enstatite chondrite model of the Earth. *Geophysical Research Letters*, *22*(16), 2219-2222 (1995).
17. Alexander C. M. O'D., Arden J. W., Ash R. D., and Pillinger C. T. Presolar components in the ordinary chondrites. Earth. Planet. Sci. Lett. 99, 220-229 (1990).
18. Grady, M. M., Wright, I. P., Carr, L. P., & Pillinger, C. T. Compositional differences in enstatite chondrites based on carbon and nitrogen stable isotope measurements. *Geochimica et Cosmochimica Acta*, *50*(12), 2799-2813 (1986).
19. Kerridge, J. F. Carbon, hydrogen and nitrogen in carbonaceous chondrites: Abundances and isotopic compositions in bulk samples. *Geochimica et Cosmochimica Acta*, *49*(8), 1707-1714 (1985).
20. Kung, C. C., & Clayton, R. N. Nitrogen abundances and isotopic compositions in stony meteorites. *Earth and Planetary Science Letters*, *38*(2), 421-435 (1978).
21. Clay, P. L., Burgess, R., Busemann, H., Ruzié-Hamilton, L., Joachim, B., Day, J. M., & Ballentine, C. J. Halogens in chondritic meteorites and terrestrial accretion. *Nature*, *551*(7682), 614 (2017).
22. Brearley, A. J., & Jones, R. H. Halogens in chondritic meteorites. In *The Role of Halogens in Terrestrial and Extraterrestrial Geochemical Processes* (pp. 871-958). Springer, Cham. (2018).
23. Dhooghe, F., De Keyser, J., Altwegg, K., Briois, C., Balsiger, H., Berthelier, J. J., ... & Fiethe, B. Halogens as tracers of protosolar nebula material in comet 67P/Churyumov–Gerasimenko. *Monthly Notices of the Royal Astronomical Society*, *472*(2), 1336-1345 (2017).
24. Marty, B. et al. Xenon isotopes in 67P/Churyumov-Gerasimenko show that comets contributed to Earth's atmosphere. *Science*, *356*(6342), 1069-1072 (2017).
25. Marty, B. The origins and concentrations of water, carbon, nitrogen and noble gases on Earth. *Earth and Planetary Science Letters*, *313*, 56-66 (2012).
26. Füri, E., & Marty, B. Nitrogen isotope variations in the Solar System. *Nature Geoscience*, *8*(7), 515 (2015).
27. Jehin, E., Manfroid, J., Hutsemekers, D., Arpigny, C., & Zucconi, J. M. (2009). Isotopic ratios in comets: status and perspectives. *Earth, Moon, and Planets*, *105*(2-4), 167-180.
28. Marty, B., Avice, G., Sano, Y., Altwegg, K., Balsiger, H., Hässig, M., ... & Rubin, M. Origins of volatile elements (H, C, N, noble gases) on Earth and Mars in light of recent results from the ROSETTA cometary mission. *Earth and Planetary Science Letters*, *441*, 91-102 (2016).

29. Rubin, M., Altwegg, K., Balsiger, H., Bar-Nun, A., Berthelier, J. J., Briois, C., ... & Fuselier, S. A. Krypton isotopes and noble gas abundances in the coma of comet 67P/Churyumov-Gerasimenko. *Science advances*, *4*(7), eaar6297 (2018).
30. Pätzold, M., Andert, T., Hahn, M., Asmar, S. W., Barriot, J. P., Bird, M. K., ... & Weissman, P. R. A homogeneous nucleus for comet 67P/Churyumov–Gerasimenko from its gravity field. *Nature*, *530*(7588), 63 (2016).
31. Barnes, J. J., Kring, D. A., Tartèse, R., Franchi, I. A., Anand, M., & Russell, S. S. An asteroidal origin for water in the Moon. *Nature communications*, *7*, 11684 (2016).
32. Busemann, H., Baur, H., & Wieler, R. Primordial noble gases in "phase Q" in carbonaceous and ordinary chondrites studied by closed-system stepped etching. *Meteoritics & Planetary Science*, *35*(5), 949-973 (2000).
33. Ozima M. and Podosek F. A. Noble gas geochemistry. Cambridge, UK: Cambridge University Press (2002).
34. Cartigny, P., Boyd, S., Harris, J., & Javoy, M. Nitrogen isotopes in peridotitic diamonds from Fuxian, China: the mantle signature. *Terra Nova*, *9*(4), 175-179 (1997).
35. Chyba, C. F., Thomas, P. J., Brookshaw, L., & Sagan, C. Cometary delivery of organic molecules to the early Earth. *Science*, *249*(4967), 366-373 (1990).
36. Marty, B., Zimmermann, L., Pujol, M., Burgess, R., & Philippot, P. Nitrogen isotopic composition and density of the Archean atmosphere. *Science*, *342*(6154), 101-104 (2013).

ATMOSPHERIC SCIENCE

Archean kerogen as a new tracer of atmospheric evolution: Implications for dating the widespread nature of early life

David V. Bekaert,[1]* Michael W. Broadley,[1] Frédéric Delarue,[2] Guillaume Avice,[3] Francois Robert,[2] Bernard Marty[1]

Understanding the composition of the Archean atmosphere is vital for unraveling the origin of volatiles and the environmental conditions that led to the development of life. The isotopic composition of xenon in the Archean atmosphere has evolved through time by mass-dependent fractionation from a precursor comprising cometary and solar/chondritic contributions (referred to as U-Xe). Evaluating the composition of the Archean atmosphere is challenging because limited amounts of atmospheric gas are trapped within minerals during their formation. We show that organic matter, known to be efficient at preserving large quantities of noble gases, can be used as a new archive of atmospheric noble gases. Xe isotopes in a kerogen isolated from the 3.0–billion year–old Farrel Quartzite (Pilbara Craton, Western Australia) are mass fractionated by 9.8 ± 2.1 per mil (‰) (2σ) per atomic mass unit, in line with a progressive evolution toward modern atmospheric values. Archean atmospheric Xe signatures in kerogens open a new avenue for following the evolution of atmospheric composition through time. The degree of mass fractionation of Xe isotopes relative to the modern atmosphere can provide a time stamp for dating Archean kerogens and therefore narrowing the time window for the diversification of early life during the Archean eon.

INTRODUCTION

Because the noble gases are chemically inert, they can yield important insights into the physical processes that affected Earth's atmosphere over geological periods of time. The Xe isotope composition of the Archean atmosphere has been shown to have evolved through geological periods of time toward the modern atmosphere (*1*, *2*). Xe trapped in barite and in fluid inclusions in hydrothermal quartz of Archean ages present Xe isotopic ratios intermediate between modern atmospheric Xe and planetary precursors, showing that atmospheric evolution as a result of mass-dependent fractionation (MDF) was a protracted process still ongoing during the Archean eon [see the study of Avice *et al.* (*2*) and references therein]. However, the limited amounts of ancient atmosphere trapped and preserved in minerals during formation make resolving ancient atmospheric signatures difficult. Carbon-rich lithologies are enriched in heavy noble gases compared to air and seem to be particularly retentive for Xe even at high temperatures (>600°C) (*3*, *4*). Isotopic analyses of large quantities of atmospheric gas possibly contained in organic materials recovered from Archean aged host rocks could potentially allow better constraints on the isotopic composition of atmospheric Xe during the Archean, providing that the organic matter can be shown to be syngenetic [see the study of Avice *et al.* (*2*) and references therein]. Comparing the measured degree of Xe MDF with the value predicted by atmospheric Xe isotope evolution at the time of host rock formation could provide a method to test the syngenetic origin of ancient organic materials.

Earth's atmosphere likely underwent massive escape as the result of giant asteroid impacts (*5*). Primary atmospheric volatiles may therefore have been erased so that Earth's volatile element inventory was largely supplied by late chondritic/cometary deliveries (*6*). From the analysis of fluid inclusions in Archean quartz [Barberton, South Africa, 3.3 billion years (Gy)], the precursor of the modern terrestrial atmosphere has been confirmed as being similar to the U-Xe signature (*2*). U-Xe was initially defined as a theoretical primordial component (*1*), which was required to explain the deficit in heavy Xe isotopes when modern atmospheric Xe is corrected for MDF and compared to solar or chondritic signatures. U-Xe is similar to the solar composition for $^{124–132}$Xe isotopes but exhibits significant depletions of the heavy ^{134,136}Xe isotopes (*1*). Although chondritic and solar compositions are linked by MDF, the U-Xe component appears to be related to a reservoir that is nucleosynthetically different from solar/chondritic compositions. The occurrence of the U-Xe signature in the primitive terrestrial atmosphere (*1*, *6*) is at odds with the chondritic signatures identified for Xe (*7*) and Kr (*8*) in Earth's mantle, which would have been inherited during Earth's main stages of formation. However, the origin of the U-Xe signature in the primitive atmosphere has been recently unraveled in light of the first measurement of the isotopic composition of Xe in a comet by Rosetta spacecraft (*6*). The isotopic composition of cometary Xe shows a deficit in the heavy ^{134,136}Xe isotopes relative to solar Xe and allows the primordial atmospheric component to be computed as a mixture between pure cometary Xe (~20%) and a chondritic (or solar) component (~80%) (*6*).

Remnants of cometary contributions to Earth's inventory during the last phases of terrestrial accretion (referred to as the late accretion episodes) may also be preserved at the present-day lunar surface (*9*). Note that alternative models have been proposed regarding the origin of U-Xe. The primary terrestrial atmosphere has been proposed to have been enriched in ^{134}Xe and ^{136}Xe due to ejection of these isotopes from plutonium/uranium-rich lithologies during fission of the now-extinct ^{244}Pu [chemical fractionation fission process (*10*)]. A giant impact event, such as the one proposed to have formed the Moon, could then have induced major loss of this primary atmosphere, leaving a remaining Xe component that was complimentarily depleted in ^{134}Xe and ^{136}Xe isotopes. However, the time elapsed between Earth's accretion

[1]Centre de Recherches Pétrographiques et Géochimiques, CNRS, Université de Lorraine, UMR 7358, 15 rue Notre Dame des Pauvres, BP 20, 54501 Vandoeuvre-lès-Nancy, France. [2]Institut de Minéralogie, de Physique des Matériaux et de Cosmochimie, Sorbonne Universités—Muséum National d'Histoire Naturelle, Université Pierre et Marie Curie, Université Paris 06, UMR CNRS 7590, IRD UMR 206, Paris, France. [3]Division of Geological and Planetary Sciences, California Institute of Technology, 1200 East California Boulevard, Pasadena, CA 91125, USA.
*Corresponding author. Email: dbekaert@crpg.cnrs-nancy.fr

and the hypothesized giant impact [that is, 30 to 100 million years after the formation of the solar system (*5*)] would be insufficient to allow the accumulation of ^{134}Xe and ^{136}Xe in a primary atmosphere required to account for the subsequent ^{134,136}Xe depletion observed in U-Xe relative to solar/chondritic compositions.

The MDF of U-Xe toward modern atmospheric values is likely to have resulted from Xe escape to space, a process that can also account for the depletion of Xe in air relative to other noble gases [the so-called missing Xe problem (*2*, *11*)]. Thus, the atmosphere became progressively depleted in Xe, relative to the abundance pattern defined by lighter noble gases, and mass dependently fractionated [both properties of atmospheric Xe being referred to as the Xe paradox (*2*)]. In contrast, other atmospheric noble gases were not affected (Ne and Ar) or little affected (Kr), indicating that this escape was Xe-specific. Because Xe is more easily ionized than other noble gases (and other atmospheric species such as CO_2 and N_2), it has been proposed that only processes involving ionization, such as the interaction of the atmosphere with solar ultraviolet light, could have played a role (*2*, *11*, *12*). Ionized Xe would have been dragged away via ionic coupling with escaping H^+ (*12*), thus resulting in the observed long-term evolution of atmospheric Xe (*2*, *11*).

Because they constitute a significant reservoir for atmospheric Xe, carbon-rich lithologies and shales were also proposed as potential carriers of the missing atmospheric Xe (*13*). Bernatowicz *et al.* (*14*) experimentally demonstrated that Xe trapping in sedimentary rocks could account qualitatively, but not quantitatively, for the missing atmospheric Xe. Organic materials trapped within Archean aged rocks therefore potentially record Archean atmospheric signatures retained since formation. However, the processes by which organic materials were produced in Archean environments have not achieved consensus. Several mechanisms including life-related synthesis (*15*), photochemistry and prebiotic synthesis in the atmosphere (*11*, *16*), and geological activity and hydrothermalism (*17*) could have formed organic materials on primitive Earth. Kerogens, that is, chemically isolated insoluble organic matter (IOM), are generally considered to correspond to the sedimentary biological organic matter entrapped in silicified sediments. Investigations about the elemental (H/C and N/C ratios used as a proxy of organic matter preservation) and isotopic composition (δ^{13}C used to track autotrophic metabolism such as photosynthesis) of Archean kerogens provide information on the effect of thermal alteration and/or on the evolution of early life (*18*–*21*). Therefore, the pristine nature of kerogens may represent a mixture of other organic materials originating from secondary hydrothermalism (*17*), from endolithic bacteria (*22*), and/or from modern contamination occurring during sampling (*23*). Because of this multiplicity of potential organic sources, the syngenecity of Archean isolated kerogen and their host rock may not be warranted, thus resulting in ages of the kerogens being potentially decoupled from the geological age of the host rock. Novel criterion is then required to guarantee accurate dating of organic material retrieved from Archean rocks.

Here, we investigate the possible occurrence of trapped ancient atmospheric Ar, Kr, and Xe in a kerogen isolated from black chert originating from the 3.0-Gy-old Farrel Quartzite (Farrel formation, Pilbara Craton, Western Australia). The analysis of multiple new and novel Archean organic kerogens has the potential to trace the temporal evolution of Xe isotopic signatures in the early atmosphere. In this case, the evolution curve of atmospheric Xe isotopes could provide a new tool for confirming an Archean origin for organic samples, thus providing independent age constraints on the development and widespread nature of early life.

RESULTS

Raman spectroscopy

The MGTKS3 kerogen was isolated from a black chert layer originating from the 3.0-Gy-old Farrel Quartzite (Pilbara Craton, Western Australia) and analyzed by Raman spectroscopy in the spectral window from 1000 to 1900 cm^{-1} (see Materials and Methods for details concerning kerogen isolation and Raman spectroscopy). Raman spectra determined on in situ organic matter from the siliceous main matrix and on related kerogen exhibit the same line profile (Fig. 1). These Raman spectra are characterized by the occurrence of the defect (D; ca. 1350 cm^{-1}) and graphite (G; ca. 1600 cm^{-1}) bands, representative of thermally altered kerogens (*24*). Raman line shapes suggest that the MGTKS3 IOM underwent a maximum temperature peak metamorphism of ~350°C (±50°C), in line with the greenschist facies metamorphism that has affected the Farrel Quartzite (*15*). Note that microscopic observations show that organic clots are missing within secondary micro-hydrothermal veins. In accordance, Raman spectroscopy performed on secondary micro-hydrothermal veins does not reveal the existence of carbonaceous matter (Fig. 1), thus precluding any postdeposition contamination and suggesting that studied kerogen consists of syngenetic organic material from the siliceous matrix.

Noble gas analysis

The two aliquots of sample MGTKS3 measured in this study (~6 mg each) yielded identical results. Significant amounts of Ar (1.8×10^{-12} mol ^{36}Ar.g^{-1}), Kr (~4.5×10^{-13} mol ^{84}Kr.g^{-1}), and Xe (5.0×10^{-14} mol ^{130}Xe.g^{-1}) were extracted from the kerogen isolated from the MGTKS3 black chert sample (tables S1 to S3). This corresponds to a ^{130}Xe enrichment

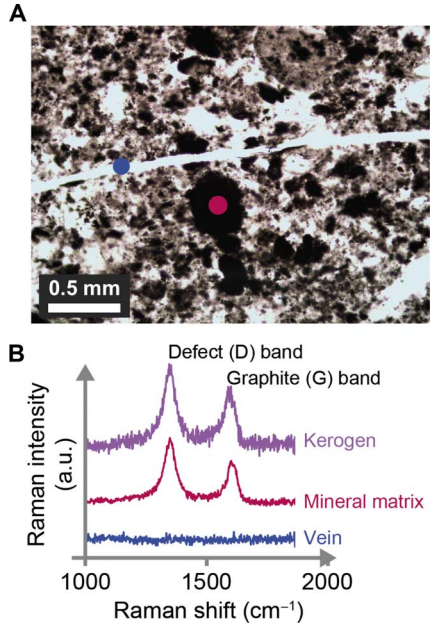

Fig. 1. Raman spectra determined on the kerogen isolated from the black chert sample, on the mineral matrix, and on the secondary hydrothermal veins. (**A**) Transmitted light photography showing that organic matter particles are present in the main mineral matrix but virtually absent in secondary hydrothermal veins. (**B**) Raman spectra determined on the mineral matrix and on the kerogen suggest that the kerogen mostly comprises organic matter from the main mineral matrix. No organic feature is detected in secondary hydrothermal veins. a.u., arbitrary unit.

factor (f) of 250 relative to $^{130}Xe/^{36}Ar$ of air [$f = (([^{130}Xe]/[^{36}Ar])_{sample}/([^{130}Xe]/[^{36}Ar])_{ATM}$], in agreement with the Xe enrichment factors observed in sedimentary rocks (*4*). Argon isotopes reveal an excess contribution of radiogenic ^{40}Ar, with a $^{40}Ar/^{36}Ar$ ratio reaching 2300 [$^{40}Ar/^{36}Ar_{ATM}$: 298.6 (*25*); table S3]. The Kr isotopes are similar to modern atmosphere (Fig. 2 and table S2). All the isotopic spectra of Xe trapped in the kerogen isolated from MGTKS3 consistently exhibit excesses of the light isotopes ($^{124–129}Xe$) together with depletions of heavy isotopes ($^{131–136}Xe$) relative to the modern atmosphere (Fig. 2). We selected the Xe isotope spectrum with the highest deviations from modern atmosphere [9.8 ± 2.1 per mil (‰) per atomic mass unit (amu) at 2σ, 500°C extraction step] as the most representative signature of the trapped component, that is, the one with the least contribution from the modern atmospheric component (Fig. 3). Isotopic fractionation of Xe was computed by error-weighted correlations following the same procedure as that of Avice *et al.* (*2*), that is, by using the stable, nonfissiogenic, non-radiogenic $^{126,128,130}Xe$ isotopes, in addition to ^{131}Xe [only negligibly contributed by the fission of ^{238}U (*26*)]. The red dashed line on Fig. 2 corresponds to the isotopic fractionation of U-Xe relative to modern air [−41.8‰ amu^{-1}; (*1*)]. To derive the isotopic composition of Xe from Barberton Quartz (Fig. 2) (*2*), multiple crushing experiments on several grams of quartz samples were required. The average Xe concentration of each sample was 8.6×10^{-17} mol $^{130}Xe.g^{-1}$. About 580 times more Xe was trapped in the kerogen MGTKS3. This allowed a precision of ≤8‰ (2σ) on average over all the Xe stable isotopes (Fig. 2) to be reached by stepwise heating of a few milligrams of Archean kerogen.

Deviations from the MDF line are in agreement with observed isotopic spectra of Xe retained in Archean fluid inclusions of Barberton quartz (*2*). Monoisotopic depletions of ^{129}Xe and large excesses of the heaviest isotopes relative to the mass fractionation trends are detected in both spectra (Fig. 2). Once corrected for mass fractionation relative to U-Xe, the $^{131–136}Xe$ excesses are fully compatible with the presence of products of the spontaneous fission of ^{238}U (fig. S1). Xe isotopes extracted from the comparatively recent organic materials yielded Xe isotopic compositions indistinguishable from the modern atmospheric composition (Fig. 2 and table S1).

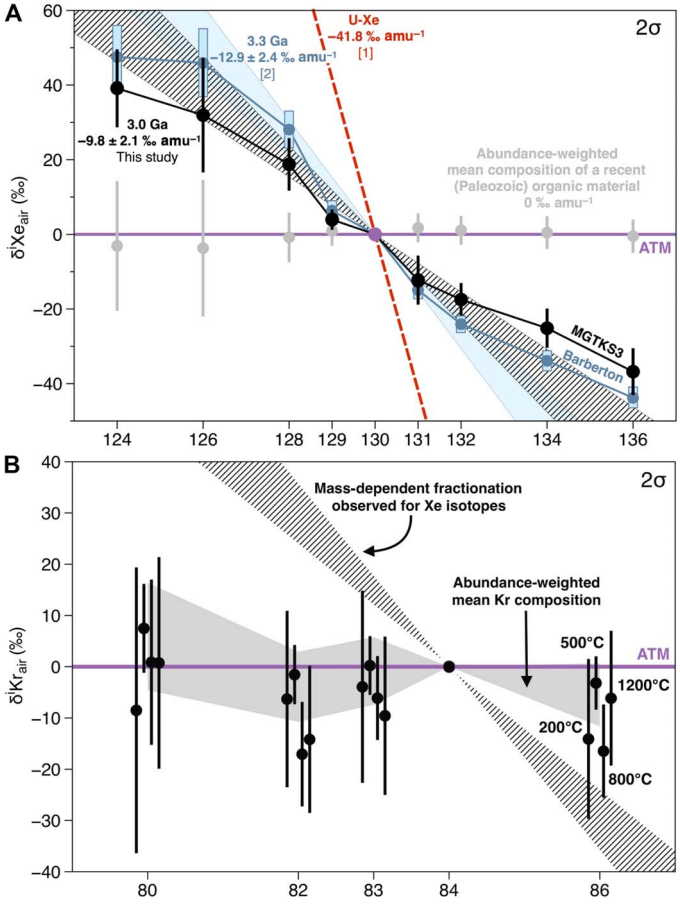

Fig. 2. Isotopic composition of Xe and Kr in the kerogen of the MGTKS3 black chert. The sample is shown relative to the isotopic composition of the modern atmosphere (*25*) and expressed using the δ notation $\delta^{i}Xe_{air} = ((^{i}Xe/^{130}Xe)_{ker}/(^{i}Xe/^{130}Xe)_{air} - 1)*1000$. (**A**) The isotope spectrum of Xe in Barberton quartz samples (3.3 Gy) from Avice *et al.* (*2*), the mass fractionation line of U-Xe (*1*), and the isotopic composition of Xe in a comparatively recent organic material (here the anthracite sample; table S1) are given for comparison. The error envelopes of the MGTKS3 kerogen and Barberton quartz mass fractionation lines are given at 2σ. No mass-dependent isotopic fractionation of Xe isotopes is observed for a recent organic material (table S1). (**B**) The MDF line derived from Xe data is reported for comparison. The abundance-weighted mean composition of Kr in the kerogen of the MGTKS3 black chert sample is essentially atmospheric. Errors are 2σ.

DISCUSSION

Ancient atmospheric Xe in kerogens

This study provides new evidence that the suspected evolution of Xe isotopes in the terrestrial atmosphere has been a global, continuous, and protracted process. Xe trapped in the MGTKS3 kerogen is mass dependently fractionated by −9.8 ± 2.1‰ amu^{-1} (2σ) relative to modern atmospheric Xe (Figs. 2A and 3). Because Xe isotopes extracted from the younger kerogens yielded Xe isotopic compositions similar to those of the modern atmosphere, it is unlikely that Xe MDF occurred during the sample's heating and gas extraction. Because the trapping of Xe atoms in organics does not yield measurable isotopic fractionation without ionization (*27*), Xe isotope fractionation likely did not occur during precipitation of the black chert. In addition, trapping onto solids would favor the heavy isotopes (*27*) and not the light ones as observed here.

The isotopic composition of trapped Kr is similar to that of the modern atmosphere. If Xe isotopes were to have been fractionated during thermal alteration going up to greenschist facies metamorphism, Kr isotopes should also be fractionated to the same extent (or more for a mass-dependent process), which is not observed (Fig. 2). In addition, Raman spectra of the MGTKS3 kerogen suggest that the sample underwent a maximum temperature peak metamorphism of ~350°C, whereas the temperature of main release of the Archean trapped component is around 500°C (Fig. 3). This suggests that the thermal metamorphism experienced by the sample did not significantly affect the trapped Xe component, although the effect of prolonged heating within the geological environment on Xe retention is ultimately unknown. The relative enrichment in light $^{124–129}Xe$ isotopes, together with depletions of heavy $^{131–136}Xe$ isotopes relative to the modern atmosphere, is typically attributed to an Archean atmospheric signature (*2*). These observations indicate that an ancient atmospheric component is likely to have been efficiently trapped and preserved in the MGTKS3 Archean kerogen over geological periods of time. This opens a new avenue for analyzing the past atmosphere by using kerogens as an archive of atmospheric noble gases.

Trapping and preservation of Xe atoms in kerogens

The preservation of atmospheric Xe records in organic materials requires efficient trapping mechanisms. Differences in adsorption coefficients of

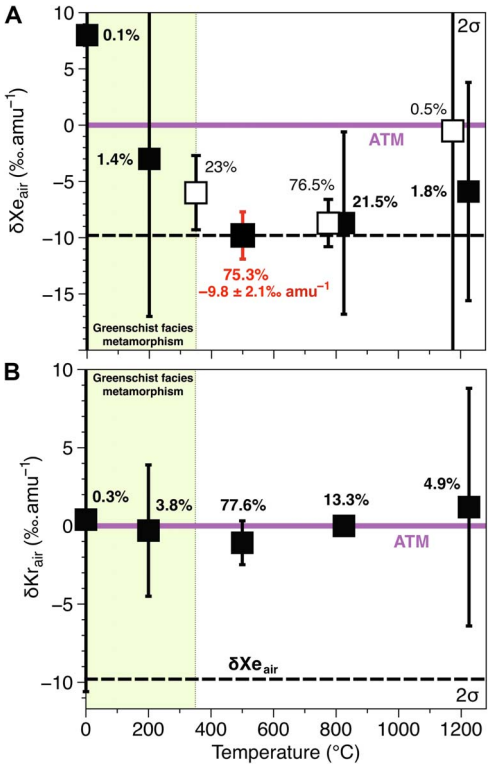

Fig. 3. Degree of mass fractionation (‰ amu^{-1}) of Xe and Kr isotopes isolated from the MGTKS3 black chert kerogen. Degrees of MDF are given for each temperature step relative to the isotopic composition of the modern atmosphere (*25*). The fractions of ^{130}Xe (**A**) and ^{84}Kr (**B**) released for each extraction step relative to the total amount of ^{130}Xe and ^{84}Kr extracted from each aliquot, respectively, are given in percentage. Both series of Xe analysis are shown, with the first and second series represented by open and closed symbols, respectively. Percentage of total gas released during each heating step is displayed beside the symbols. The Xe isotope spectrum with the highest deviations from modern atmosphere (9.8 ± 2.1‰ amu^{-1}, 500°C) is taken as being the most representative signature of the trapped component. This trapped component dominates the budget of Xe isotopes in the sample because more than 75% of the total amount of ^{130}Xe is extracted at this temperature. Errors are 2σ.

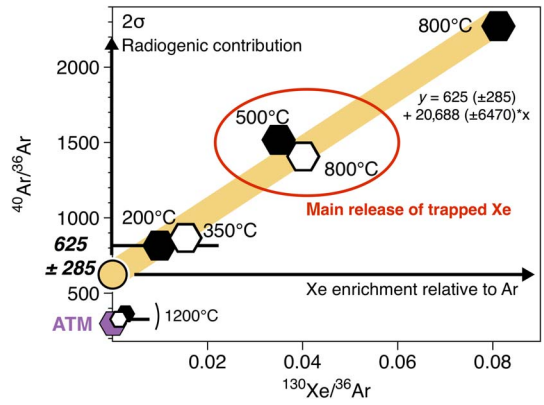

Fig. 4. Mixing diagram of the ^{40}Ar/^{36}Ar ratios as a function of the ^{130}Xe/^{36}Ar ratios. The two series of experiments are represented in open and solid symbols, respectively. The linear trend depicted over stepwise heating of the kerogen isolated from the MGTKS3 black chert sample indicates that the initial ^{40}Ar/^{36}Ar of the fluid [625 ± 285 (2σ)] was higher than the Archean atmospheric ^{40}Ar/^{36}Ar ratio of 143.6 ± 48 (2σ) (*36*), thus confirming that the initial fluid had an excess of radiogenic ^{40}Ar*, possibly related to interaction with crustal and/or hydrothermal reservoirs.

noble gases on activated charcoals [$\alpha_{Xe} \sim 30^{*}\alpha_{Ar}$ at room temperature (*28*)] are unlikely to account for the Xe enrichments relative to Ar observed in sedimentary rocks (*4*). Specific trapping mechanisms are thus required to explain ^{130}Xe enrichment factors relative to ^{36}Ar and to air as observed in our sample ($f = 250$). Several models have been proposed for the strong retention of Xe atoms within organics. Adsorption onto surface-associated defects could account for unusually high retention of heavy noble gases (*29*). This has been experimentally demonstrated to occur for several natural samples, including minerals (*9*, *30*, *31*). The heavy noble gases that are thus "irreversibly adsorbed" onto carbonaceous matter can only be removed by heating the samples at medium to high temperatures (up to 700°C) (*31*), making the process of anomalous adsorption different from common physisorption due to van der Waals forces. In addition, strong retention of Xe in organic materials may be caused by the presence of labyrinth-with-constrictions (*31*) or single-walled nanotube structures (*32*), causing an enhanced adsorption of Xe by electron shell interactions with carbon atoms. Both processes involve an active discrimination of Xe with respect to small atoms due to restricted pathway radii, on the order of the atomic radius. Additional mechanisms may be related to the presence of dangling functional groups (for example, –COOH) inside Xe diffusion paths (*33*), which would delay/prevent Xe mobility within the organic matrix. During the sample's carbonization [first grade of thermal alteration (*24*)], the structural changes of the carbonaceous matter result in structural units of nanometer-sized polyaromatic layers that, coupled to the effect of polyaromatic layer stacking, would drastically reduce the porosity of the sample. In addition to the effect of thermal alteration on organic matter features, the achievement of a closed system during silicification and the very low diffusion coefficients for Xe resulting from its large radius probably contribute together to the preservation of the trapped Xe component in Archean kerogen over geological periods of time.

The syngenecity of organic material cracking before 350°C is highly disputable because it can originate from several postdeposition contaminations (*34*) and/or from residual bitumen (soluble fraction of organic matter) for which syngenecity is still an open issue (*23*). In turn, the Xe-trapped component related to these thermolabile organic materials could not be considered as syngenetic. Thermal cracking of syngenetic Archean stricto sensu kerogens occurs at higher temperature. For instance, Spangenberg and Frimmel (*35*) demonstrated that late Archean organic matter cracked at about 450°C. Thus, the release of Archean Xe in the range of 400° to 600°C should be closely related to the cracking of syngenetic and thermorecalcitrant organic material.

Depositional environment

The occurrence of radiogenic ^{40}Ar* (^{40}Ar/^{36}Ar up to 2300) (Fig. 4 and table S3) and fissiogenic $^{131-136}$Xe (fig. S1) produced by the decay of ^{40}K and spontaneous fission of ^{238}U, respectively, suggests that there is a contribution from crustal fluids within the sample. The ^{40}Ar/^{36}Ar ratio can be expressed as a function of ^{130}Xe/^{36}Ar

$$\frac{^{40}\mathrm{Ar}}{^{36}\mathrm{Ar}} = \frac{^{40}\mathrm{Ar}_{\mathrm{init}} + {}^{40}\mathrm{Ar}^{*}}{^{36}\mathrm{Ar}} = \left(\frac{^{40}\mathrm{Ar}}{^{36}\mathrm{Ar}}\right)_{\mathrm{init}} + \left(\frac{^{40}\mathrm{Ar}^{*}}{^{130}\mathrm{Xe}}\right) \mathrm{x} \left(\frac{^{130}\mathrm{Xe}}{^{36}\mathrm{Ar}}\right) \quad (1)$$

where ^{40}Ar$_{init}$ is ^{40}Ar inherited from the fluid that interacted with the kerogen (either at the time of the chert formation or during thermal alteration going up to greenschist facies metamorphism) and ^{40}Ar* is

radiogenic ^{40}Ar produced in situ by the decay of ^{40}K. The linear trend depicted over stepwise heating in a three-isotope diagram of the $^{40}Ar/^{36}Ar$ ratio versus the $^{130}Xe/^{36}Ar$ ratio indicates that the initial $^{40}Ar/^{36}Ar$ ratio of the fluid, given by the *y* intercept of the regression line, was at least 625 ± 285 (2σ) (Fig. 4). This is higher than the Archean atmospheric $^{40}Ar/^{36}Ar$ ratio of 143.6 ± 48 (2σ) (*36*), in line with the occurrence of a fluid presenting radiogenic ^{40}Ar in excess of the atmospheric composition, probably related to interaction with crustal and/or hydrothermal reservoirs. At any temperature step, the $^{130}Xe/^{36}Ar$ ratios up to 8×10^{-2} are higher than the atmospheric ratio [$^{130}Xe/^{36}Ar_{ATM} = 1.13 \times 10^{-4}$ (*25*); Fig. 4], thus revealing a contribution from the Xe-enriched trapped component. Contribution from the modern atmosphere (^{36}Ar) component decreases with increasing temperature steps. The main release of the trapped Xe component occurs at ~500°C (Fig. 3). At higher temperature, the residual gas is dominated by the strongly retained Xe component and by in situ produced radiogenic $^{40}Ar^*$.

The trapped Xe component could have been incorporated in organic materials at the same time as the black chert formation or, alternatively, supplied later by secondary hydrothermal fluids circulating in the continental crust and interacting with the sample during its burial. In both cases, the fluids carrying dissolved Xe are expected to be at isotopic equilibrium with the Archean atmosphere composition, regardless of the possible fissiogenic contributions from their interaction with rocks. In the case of the studied Archean sample, the lack of any postdepositional organic material, as revealed by microscopic observations and Raman spectroscopy, and the high-temperature release of the Xe component suggest that the degree of mass fractionation detected for Xe isotopes corresponds to a pristine Archean signature. Note that the deficit of $^{129}Xe^*$ from the decay of the now-extinct ^{129}I ($T_{1/2}$: 16 Ma) relative to the atmospheric composition (Fig. 2) argues against a contribution from mantle-derived fluids (*2*). The depletion in ^{129}Xe relative to the Xe mass fractionation line likely reflects a lower $^{129}Xe^*$ excess in the Archean atmosphere relative to the present (*2*).

Heavy noble gas escape to space and MDF of a U-Xe–like precursor

As observed in this study, Kr isotopes are not significantly mass fractionated in Archean records compared to modern air [see the study of Avice *et al.* (*2*) and references therein]. This implies that the physical process that drove continuous Xe loss from the atmosphere did not significantly affect lighter noble gases. Because of its low ionization potential relative to Kr, atmospheric Xe would have been readily ionized by ultraviolet radiation from the early Sun before being dragged along open magnetic field lines and lost to space via ionic coupling with escaping H (*12*). Such a process can account for the continuous MDF of Xe isotopes in the atmosphere, whereas Kr isotopes, with a higher ionization potential, would not have been affected. Nonetheless, even if ionized (and lost to space) to a minor extent, MDF of atmospheric Kr isotopes through time is a possibility. To date, no Archean record permitted the atmospheric precursors of Kr to be deciphered [see the study of Avice *et al.* (*2*) and references therein]. The initial Kr isotopic composition of the atmosphere could be chondritic- [Q-Kr; (*37*)] or solar-like (*38*) or could have resulted from a mixture of both components. Kr isotopes extracted at 500°C (>75% release; Fig. 3) show a potential MDF of −1.08 ± 1.40‰ amu^{-1} (2σ), in favor of the light isotopes (Fig. 5). Whereas Q-Kr is depleted in the light isotopes relative to modern air, solar Kr is mass dependently fractionated in favor of the light isotopes, and thus appears to be a better candidate for the precursor atmospheric Kr (Fig. 5), in agreement with the conclusion reached by Holland *et al.* (*8*). Additional analyses of Archean Kr signatures are required to confirm this possibility.

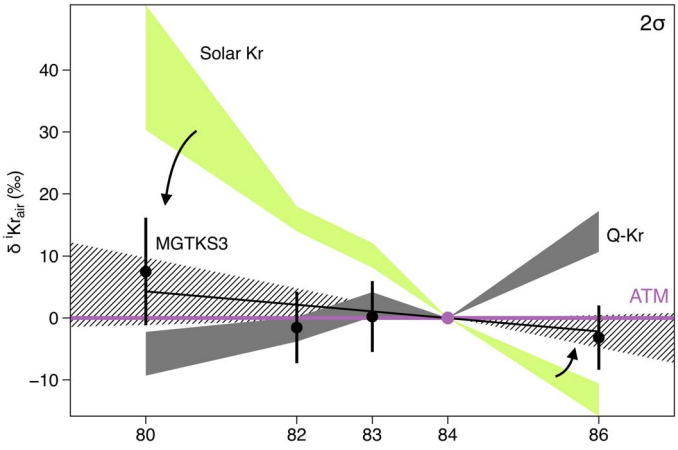

Fig. 5. Isotopic composition of Kr in the kerogen of the MGTKS3 black chert. The sample is shown relative to the isotopic composition of the modern atmosphere (*25*) and expressed using the δ notation $\delta^{i}Kr_{air} = (({}^{i}Kr/{}^{84}Kr)_{ker}/({}^{i}Kr/{}^{84}Kr)_{air} - 1)*1000$. The chondritic krypton [Q-Kr; (*37*)] and solar Kr (*38*) compositions are given for comparison. Whereas Q-Kr is depleted in the light isotopes relative to modern air, solar Kr is mass dependently fractionated in favor of the light isotopes, relative to modern air, and thus appears to be a better candidate for the precursor atmospheric Kr, although additional and repeated analyses of Archean Kr signatures are required to confirm this interpretation.

Dating the blossoming and widespread nature of early life

The earliest evidence of life remains subject to debate (*39*). Because ages of kerogens may potentially be decoupled from the geological age of the host rock, accurately dating organic material retrieved from Archean rocks requires the organic materials to be dated independently. Using Ar-Ar dating is complicated by the potential for the kerogens to be overprinted by the radiogenic contribution from the host rock, inheriting an unknown radiogenic component during formation and/or having K contents affected during the sample's isolation. The light Xe isotope signature in kerogens only relies on the composition of the atmosphere at the time of Xe trapping and does not rely on understanding the chemistry of the sample and host rock. The degree of mass fractionation of Xe trapped in Archean organic materials relative to modern atmosphere therefore provides a potentially new and unique tool for dating microfossil-bearing metasediments.

The MDF of atmospheric Xe with time relative to modern atmosphere can be modeled as a power law ($y = 0.238*x^{3.41}$) fitting the literature data of Xe isotope mass fractionation in ancient samples as well as the initial (U-Xe) and final (modern atmosphere) compositions (Fig. 6 and fig. S2). When reported on the evolution curve of atmospheric Xe, the degree of mass fractionation detected for Xe isotopes (9.8 ± 2.1‰ amu^{-1}, 2σ) provides a model age of 3.0 ± 0.2 Gy (2σ) for the silica-embedded kerogen (Fig. 6). This age for the kerogen MGTKS3 is in excellent agreement with the geological age of the chert [2.95 Gy (*15*)]. From a physical basis, the use of a power law to model Xe isotope evolution in the atmosphere has been classically chosen in the framework of Rayleigh fractionation [for example, in the case of hydrodynamic escape of neutral species (*40*)]. Dauphas (*41*) used a phenomenological model, such as the generalized power law, as a proxy of atmospheric Xe isotope fractionation law. Fundamentally, Xe escape is a function of both solar radiation [extreme ultraviolet (XUV)] from the early Sun (required to

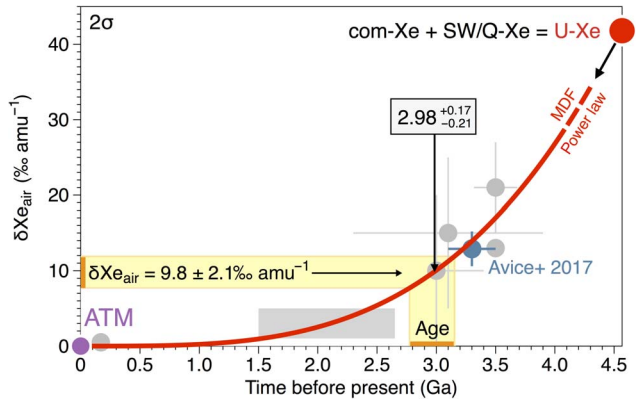

Fig. 6. MDF of atmospheric Xe with time relative to modern atmosphere. The red curve was established from a power law ($y = 0.238*x^{3.41}$) fitting the literature data of Xe isotope mass fractionation in ancient samples [see the study of Avice *et al.* (*2*) and references therein] as well as the initial [U-Xe, the precursor of Earth's atmosphere (*1*)]) and final [modern atmosphere (*25*)] compositions of the atmosphere. Isotopic composition is expressed in per mil per atomic mass unit relative to the modern atmosphere (purple dot) (*25*). The degree of MDF obtained in this study for the kerogen isolated from the MGTKS3 black chert sample (9.8 ± 2.1‰ amu^{-1}, 2σ) can be used to estimate the age of the sample from the evolution curve of the isotopic fractionation of atmospheric Xe. This method would provide a model age of 3.0 ± 0.2 Gy (2σ) for the kerogen embedded in silica, in excellent agreement with the geological age of the chert [2.95 Gy (*15*)].

ionize Xe) and H^+ escaping rate (required to drag Xe) (*12*). Although the evolution of H escape over time is not well constrained, Ribas *et al.* (*42*) found that stellar fluxes can be very well approximated by power-law relationships. Because a linear relation is expected between the hydrogen escape rate and the solar radiation level (*43*), we speculate that the power law that we determine in this study may be related to an effective XUV power law. Our model assumes a continuous and nondisrupted evolution of Xe isotopes in the past atmosphere. This hypothesis remains to be verified at the high-resolution level by multiple analyses of atmospheric Xe isotopes trapped in ancient samples.

This method should also be applied on a case-by-case basis, taking into account the geological history of each sample. Multiple sources of postdepositional carbonaceous materials (*17*), mass fractionation effects during the sample's maturation and/or partial filling/emptying of the sample's porosity by secondary fluid circulations (*4*), as well as metamorphism and reset processes (*44*) could all possibly alter the trapped Xe component over geological time scales. In the absence—or limit—of this potential bias, any apparent age given by this method should be seen as a minimal age because the trapped composition is expected to reflect the last chemical equilibration between the kerogen and the atmosphere (possibly air or air-saturated fluids).

The Great Oxygenation Event that occurred about 2.3 Ga (*45*) thoroughly changed the course of biological evolution. Before the rise of O_2 in the atmosphere, CH_4 was probably an important trace atmospheric constituent that contributed to the greenhouse effect, balancing the lower luminosity of the early Sun (*46*). Extensive H loss during the Archean constitutes an alternative to organic burial for removing photosynthetic reductants from the atmosphere and permitting O_2 accumulation. Tracking the evolution of Xe isotopes in the past atmosphere offers a crucial observational basis to constrain hydrogen loss to space and provide information about the timing of Earth surface's irreversible oxidization at the time of life emergence (*45*). Estimates of the gradual changes in the H rate of escape could conceivably yield estimates of H_2 concentrations in early Earth's atmosphere. This information is highly relevant to the origin of life because redox conditions in the atmosphere control the efficiency of prebiotic organic compound production through abiotic Miller-Urey–type synthesis (*16*). Last, note that constraining the extent and timing of atmospheric Xe MDF may provide information about terrestrial planets' paleoclimates. The limited Xe MDF that occurred in the Martian early atmosphere (before 4.2 Ga) suggests that Martian hydrogen escape was not sufficient enough to support long-term MDF of Xe isotopes in the Martian atmosphere and, thus, that limited amounts of liquid water—yielding H_2 by photodissociation—were present on Mars at this period of time (*47*).

CONCLUSION

The large amounts of noble gases preserved in organic matter, when compared to fluids trapped in minerals, unlock a previously untapped reservoir and allow the evolution of atmospheric Xe to be determined with unprecedented resolution. Archean atmospheric Xe signatures in undisturbed kerogens open up new horizons for analyzing the past atmosphere. This study presents new evidence that atmospheric Xe was progressively enriched in heavy isotopes and depleted in light isotopes during the Archean eon. Precise heating steps permit modern versus ancient atmosphere to be distinguished and should help to constrain the mechanisms of noble gases trapping in organic materials. Noble gases can be used as powerful tools to provide information about the depositional environment of organic materials at the time of life diversification. The degree of mass fractionation relative to modern atmosphere can provide a model age for dating the last chemical equilibration between the organic matter and the atmosphere.

MATERIALS AND METHODS

Samples

The MGTKS3 black chert sample was collected from the ca. 3.0-Gy-old Farrel Quartzite at the Mount Grant locality in the Goldsworthy greenstone belt, Pilbara Craton, Western Australia. The Farrel Quartzite is composed of a clastic formation up to 80 m thick containing fine- to very coarse–grained sandstone, including quartzite with minor conglomerate, mafic to ultramafic volcanoclastic layers, evaporite beds, and black chert layers (*15*). This unit underwent greenschist facies metamorphism and was pervasively silicified (*15*, *24*). The ca. 30-cm-thick microfossil-bearing black chert occurs in the uppermost part of the Farrel Quartzite and is closely associated with evaporite beds.

Two Paleozoic—so comparatively younger—natural organic materials were also analyzed for their Xe isotope composition following the same analytical protocol: a type III kerogen from Champclauson (Gard, France; Stephanian, Upper Carboniferous) and an anthracite sample from La Motte-d'Aveillans (Isère, France; Upper Carboniferous). These two samples were selected to test whether geologically younger organic materials would yield modern atmospheric Xe isotope compositions.

IOM isolation from the MGTKS3 black chert sample

The MGTKS3 kerogen was isolated through successive demineralization of ca. 200 g of black chert using HF-HCl treatments at room temperature (*24*). Soluble organic compounds were first removed by stirring powdered cherts in dichloromethane/methanol (2/1, v/v). Carbonates were then dissolved using hydrochloric acid (HCl; 37%). Samples were then centrifuged and washed with distilled water until reaching neutrality. The concentration of the kerogen was achieved by acid maceration

at room temperature in a mixture of HF (40%) and HCl (37%) acids (2:1, v/v). Samples were again centrifuged and washed with distilled water. Neoformed fluorides were degraded using HCl (37%) at 60°C (24 hours). Finally, the kerogen was centrifuged/washed with distilled water before being dried through successive steps of acetone rinsing and evaporation.

Raman spectroscopy

Raman spectra were obtained using a Renishaw inVia microspectrometer, equipped with a 532-nm argon laser. The laser was focused on the sample using a DMLM Leica microscope with a 50× lens. The spectrometer was first calibrated with a silicon standard before the analytical session (*24*). For each target, we determined the Raman shift intensity in the spectral window from 1000 to 1900 cm^{-1} including the first-order disorder carbon (D) and graphite (G) bands. Spectra acquisition was achieved after two successive iterations using a time exposure of 40 s. A laser power below 1 mW was used to prevent any thermal alteration during the spectra acquisition.

Noble gas analysis

Ar, Kr, and Xe were extracted from the kerogen by step heating using a filament furnace (*48*). The furnace consists of four alumina-coated tungsten evaporation baskets (Ted Pella Inc.) welded to a pair of nickel rods mounted on eight-pin electrical feedthrough flange. Temperatures were estimated by using foils of pure metals with known melting points (tin, 230°C; aluminum, 660°C; copper, 1085°C; and nickel, 1455°C) and were controlled during heating steps by direct measurement using an optical pyrometer. Before loading the samples, each basket was degassed at ~1600°C to remove any adsorbed atmospheric noble gases. The samples were wrapped in tantalum foil and loaded into the baskets before baking the entire furnace at >150°C overnight under high vacuum. Samples were loaded individually to avoid indirect heating and degassing of other samples during analysis. Kerogen MGTKS3 (12 mg in total) was split into two aliquots (~6 mg each). The first aliquot was heated over three temperature steps (~350°, ~800°, and ~1200°C), and only Ar and Xe isotopes were measured. The second aliquot was heated over four temperature steps (~200°, ~500°, ~800°, and ~1200°C), with Kr isotopes being measured in addition to Ar and Xe.

Gases released during step heating were first purified on an in-line Ti-sponge getter heated to 600°C to remove any active species. Kr and Xe were then condensed onto a quartz tube at liquid nitrogen temperatures for 20 min. The remaining Ar in the preparation line was then expanded to a further series of Ti-sponge getters, three at 550°C and one at room temperature for a further 20 min to remove any final reactive species. The Ar fraction was expanded into the spectrometer (Helix MC Plus, Thermo Fisher Scientific) and analyzed using peak jumping mode on faraday (^{40}Ar) and compact dynode multiplier ($^{36,38}Ar$) collectors. After Ar analysis, any remaining gas was pumped. To remove the remaining Ar trapped within the quartz tube, three dilutions from the glass tube (20 cm^3) to the whole line (1500 cm^3) in static mode were made to reduce the partial pressure of Ar. Kr and Xe gas fractions were then released from the tube at room temperature and purified on getters following the same protocol as Ar. Both Kr and Xe were simultaneously expanded into the spectrometer and analyzed using the compact dynode multiplier, with Xe isotopes being measured first, followed by the measurement of Kr isotopes. Blanks were measured at the same temperature as the samples using a basket loaded with empty tantalum foil packets. Blanks at 500°C, the temperature at which most of the gas from the samples was released, were 2.4×10^{-13} mol ^{40}Ar, 8.6×10^{-17} mol ^{84}Kr, and 1.2×10^{-18} mol ^{130}Xe. These amounts correspond to <3% of the ^{40}Ar and ^{84}Kr and <1% of the ^{130}Xe released from the sample, making blank corrections minimal. Note that our calibration standard for the Kr is not well calibrated, so Kr abundances are only indicative, although the Kr isotope compositions are accurate. Error propagation for Ar, Kr, and Xe isotopic analyses is detailed in Appendix B of Bekaert *et al.* (*9*).

SUPPLEMENTARY MATERIALS

Supplementary material for this article is available at http://advances.sciencemag.org/cgi/content/full/4/2/eaar2091/DC1

table S1. Xe isotopic composition of the kerogen isolated from the MGTKS3 black chert sample and from two Paleozoic—so comparatively younger—kerogens (an anthracite and a type III kerogen called Champclauson) by stepwise heating.

table S2. Kr isotopic composition of the kerogen isolated from the MGTKS3 black chert sample by stepwise heating.

table S3. Ar isotopic composition of the kerogen isolated from the MGTKS3 black chert sample by stepwise heating.

fig. S1. Fission spectrum of MGTKS3 kerogen Xe corrected for mass fractionation relative to U-Xe.

fig. S2. Comparison of power law/exponential law fit of the literature data [see the study of Avice *et al.* (*2*) and references therein] on the evolution of atmosphere Xe isotope fractionation over geological periods of time.

REFERENCES AND NOTES

1. R. O. Pepin, On the origin and early evolution of terrestrial planet atmospheres and meteoritic volatiles. *Icarus* **92**, 2–79 (1991).
2. G. Avice, B. Marty, R. Burgess, The origin and degassing history of the Earth's atmosphere revealed by Archean xenon. *Nat. Commun.* **8**, 15455 (2017).
3. U. Frick, S. Chang, Ancient carbon and noble gas fractionation. *Proc. Lunar Sci. Conf.* **8**, 263–272 (1977).
4. T. Torgersen, B. M. Kennedy, M. C. van Soest, Diffusive separation of noble gases and noble gas abundance patterns in sedimentary rocks. *Earth Planet. Sci. Lett.* **226**, 477–489 (2004).
5. K. Zahnle, L. Schaefer, B. Fegley, Earth's earliest atmospheres. *Cold Spring Harb. Perspect. Biol.* **2**, a004895 (2010).
6. B. Marty, K. Altwegg, H. Balsiger, A. Bar-Nun, D. V. Bekaert, J.-J. Berthelier, A. Bieler, C. Briois, U. Calmonte, M. Combi, J. De Keyser, B. Fiethe, S. A. Fuselier, S. Gasc, T. I. Gombosi, K. C. Hansen, M. Hässig, A. Jäckel, E. Kopp, A. Korth, L. Le Roy, U. Mall, O. Mousis, T. Owen, H. Rème, M. Rubin, T. Sémon, C.-Y. Tzou, J. H. Waite, P. Wurz, Xenon isotopes in 67P/Churyumov-Gerasimenko show that comets contributed to Earth's atmosphere. *Science* **356**, 1069–1072 (2017).
7. A. Caracausi, G. Avice, P. G. Burnard, E. Füri, B. Marty, Chondritic xenon in the Earth's mantle. *Nature* **533**, 82–85 (2016).
8. G. Holland, M. Cassidy, C. J. Ballentine, Meteorite Kr in Earth's mantle suggests a late accretionary source for the atmosphere. *Science* **326**, 1522–1525 (2009).
9. D. V. Bekaert, G. Avice, B. Marty, B. Henderson, M. S. Gudipati, Stepwise heating of lunar anorthosites 60025, 60215, 65315 possibly reveals an indigenous noble gas component on the Moon. *Geochim. Cosmochim. Acta* **218**, 114–131 (2017).
10. A. P. Meshik, O. V. Pravdivtseva, C. M. Hohenberg, New evidence for chemical fractionation of radioactive xenon precursors in fission chains. *Phys. Rev. C* **93**, 044614 (2016).
11. E. Hébrard, B. Marty, Coupled noble gas–hydrocarbon evolution of the early Earth atmosphere upon solar UV irradiation. *Earth Planet. Sci. Lett.* **385**, 40–48 (2014).
12. K. J. Zahnle, Xenon fractionation and Archean hydrogen escape, *46th Lunar and Planetary Science Conference*, The Woodlands, TX, 16 to 20 March, 2015.
13. F. A. Podosek, M. Honda, M. Ozima, Sedimentary noble gases. *Geochimica et Cosmochimica Acta*, **44**, 1875–1884 (1980).
14. T. J. Bernatowicz, F. A. Podosek, M. Honda, F. E. Kramer, The atmospheric inventory of xenon and noble gases in shales: The plastic bag experiment. *J. Geophys. Res. Solid Earth* **89**, 4597–4611 (1984).
15. K. Sugitani, K. Grey, A. Allwood, T. Nagaoka, K. Mimura, M. Minami, C. P. Marshall, M. J. Van Kranendonk, M. R. Walter, Diverse microstructures from Archaean chert from the Mount Goldsworthy–Mount Grant area, Pilbara Craton, Western Australia: Microfossils, dubiofossils, or pseudofossils? *Precambrian Res.* **158**, 228–262 (2007).
16. S. L. Miller, G. Schlesinger, Carbon and energy yields in prebiotic syntheses using atmospheres containing CH_4, CO and CO_2. *Orig. Life* **14**, 83–90 (1984).
17. A. O. Marshall, J. R. Emry, C. P. Marshall, Multiple generations of carbon in the Apex chert and implications for preservation of microfossils. *Astrobiology* **12**, 160–166 (2012).

18. Y. Watanabe, H. Naraoka, D. J. Wronkiewicz, K. C. Condie, H. Ohmoto, Carbon, nitrogen, and sulfur geochemistry of Archean and Proterozoic shales from the Kaapvaal Craton, South Africa. *Geochim. Cosmochim. Acta* **61**, 3441–3459 (1997).
19. J. L. Eigenbrode, K. H. Freeman, Late Archean rise of aerobic microbial ecosystems. *Proc. Natl. Acad. Sci. U.S.A.* **103**, 15759–15764 (2006).
20. C. P. Marshall, G. D. Love, C. E. Snape, A. C. Hill, A. C. Allwood, M. R. Walter, M. J. Van Kranendonk, S. A. Bowden, S. P. Sylva, R. E. Summons, Structural characterization of kerogen in 3.4 Ga Archaean cherts from the Pilbara Craton, Western Australia. *Precambrian Res.* **155**, 1–23 (2007).
21. D. Frédéric, R. François, S. Kenichiro, T. Romain, D. Rémi, D. Sylvie, Investigation of the geochemical preservation of *ca*. 3.0 Ga permineralized and encapsulated microfossils by nanoscale secondary ion mass spectrometry. *Astrobiology* **17**, 1192–1202 (2017).
22. T. R. R. Bontognali, A. L. Sessions, A. C. Allwood, W. W. Fischer, J. P. Grotzinger, R. E. Summons, J. M. Eiler, Sulfur isotopes of organic matter preserved in 3.45-billion-year-old stromatolites reveal microbial metabolism. *Proc. Natl. Acad. Sci. U.S.A.* **109**, 15146–15151 (2012).
23. K. L. French, C. Hallmann, J. M. Hope, P. L. Schoon, J. A. Zumberge, Y. Hoshino, C. A. Peters, S. C. George, G. D. Love, J. J. Brocks, R. Buick, R. E. Summons, Reappraisal of hydrocarbon biomarkers in Archean rocks. *Proc. Natl. Acad. Sci. U.S.A.* **112**, 5915–5920 (2015).
24. F. Delarue, J. N. Rouzaud, S. Derenne, M. Bourbin, F. Westall, B. Kremer, K. Sugitani, D. Deldicque, F. Robert, The Raman-derived carbonization continuum: A tool to select the best preserved molecular structures in Archean kerogens. *Astrobiology* **16**, 407–417 (2016).
25. D. Porcelli, C. J. Ballentine, R. Wieler, An overview of noble gas geochemistry and cosmochemistry. *Rev. Mineral. Geochem.* **47**, 1–19 (2002).
26. R. A. Ragettli, E. H. Hebeda, P. Signer, R. Wieler, Uranium-xenon chronology: Precise determination of λ_{sf*} $^{136}Y_{sf}$ for spontaneous fission of ^{238}U. *Earth Planet. Sci. Lett.* **128**, 653–670 (1994).
27. Y. Marrocchi, B. Marty, Experimental determination of the xenon isotopic fractionation during adsorption. *Geophys. Res. Lett.* **40**, 4165–4170 (2013).
28. S. Dushman, *Scientific Foundations of Vacuum Technique* (John Wiley & Sons, 1957), 806 pp.
29. Y. Marrocchi, B. Marty, P. Reinhardt, F. Robert, Adsorption of xenon ions onto defects in organic surfaces: Implications for the origin and the nature of organics in primitive meteorites. *Geochim. Cosmochim. Acta* **75**, 6255–6266 (2011).
30. J. Yang, R. S. Lewis, E. Anders, Sorption of noble gases by solids, with reference to meteorites. I: Magnetite and carbon. *Geochim. Cosmochim. Acta* **46**, 841–860 (1982).
31. J. F. Wacker, M. G. Zadnik, E. Anders, Laboratory simulation of meteoritic noble gases. I. Sorption of xenon on carbon: Trapping experiments. *Geochim. Cosmochim. Acta* **49**, 1035–1048 (1985).
32. V. Simonyan, J. K. Johnson, A. Kuznetsova, J. T. Yates Jr., Molecular simulation of xenon adsorption on single walled carbon nanotubes. *J. Chem. Phys.* **114**, 4180–4185 (2001).
33. A. Kuznetsova, J. T. Yates Jr., J. Liu, R. E. Smalley, Physical observation of xenon in open single walled carbon nanotubes: Observation of a quasi-one-dimensional confined Xe phase. *J. Chem. Phys.* **112**, 9590–9598 (2000).
34. S. Derenne, F. Robert, A. Skrzypczak-Bonduelle, D. Gourier, L. Binet, J.-N. Rouzaud, Molecular evidence for life in the 3.5 billion year old Warrawoona chert. *Earth Planet. Sci. Lett.* **272**, 476–480 (2008).
35. J. E. Spangenberg, H. E. Frimmel, Basin-internal derivation of hydrocarbons in the Witwatersrand Basin, South Africa: Evidence from bulk and molecular δ^{13} C data. *Chem. Geol.* **173**, 339–355 (2001).
36. M. Pujol, B. Marty, R. Burgess, G. Turner, P. Philippot, Argon isotopic composition of Archaean atmosphere probes early Earth geodynamics. *Nature* **498**, 87–90 (2013).
37. H. Busemann, H. Baur, R. Wieler, Primordial noble gases in "phase Q" in carbonaceous and ordinary chondrites studied by closed-system stepped etching. *Meteorit. Planet. Sci.* **35**, 949–973 (2000).
38. A. Meshik, C. Hohenberg, O. Pravdivtseva, D. Burnett, Heavy noble gases in solar wind delivered by Genesis mission. *Geochim. Cosmochim. Acta* **127**, 326–347 (2014).
39. M. A. van Zuilen, A. Lepland, G. Arrhenius, Reassessing the evidence for the earliest traces of life. *Nature* **418**, 627–630 (2002).
40. D. M. Hunten, R. O. Pepin, J. C. G. Walker, Mass fractionation in hydrodynamic escape. *Icarus* **69**, 532–549 (1987).
41. N. Dauphas, The dual origin of the terrestrial atmosphere. *Icarus* **165**, 326–339 (2003).
42. I. Ribas, E. F. Guinan, M. Güdel, M. Audard, Evolution of the solar activity over time and effects on planetary atmospheres. I. High-energy irradiances (1–1700 Å). *Astrophys. J.* **622**, 680 (2005).
43. F. Tian, O. B. Toon, A. A. Pavlov, H. De Sterck, A hydrogen-rich early Earth atmosphere. *Science* **308**, 1014–1017 (2005).
44. F. L. Staplin, Sedimentary organic matter, organic metamorphism, and oil and gas occurrence. *Bull. Can. Petrol. Geol.* **17**, 47–66 (1969).
45. D. C. Catling, K. J. Zahnle, C. P. McKay, Biogenic methane, hydrogen escape, and the irreversible oxidation of early Earth. *Science* **293**, 839–843 (2001).
46. A. A. Pavlov, J. F. Kasting, L. L. Brown, K. A. Rages, R. Freedman, Greenhouse warming by CH_4 in the atmosphere of early Earth. *J. Geophys. Res.* **105**, 11981–11990 (2000).
47. W. S. Cassata, Meteorite constraints on Martian atmospheric loss and paleoclimate. *Earth Planet. Sci. Lett.* **479**, 322–329 (2017).
48. R. Burgess, P. Cartigny, D. Harrison, E. Hobson, J. Harris, Volatile composition of microinclusions in diamonds from the Panda kimberlite, Canada: Implications for chemical and isotopic heterogeneity in the mantle. *Geochim. Cosmochim. Acta* **73**, 1779–1794 (2009).

Acknowledgments: We thank L. Zimmermann, Y. Marrocchi, and K. Zahnle for fruitful discussions. We also thank V. Rouchon and O. Belhadj (Center for Research on the Preservation of Collections, USR 3224) for Raman microspectroscopy. **Funding:** This study was supported by the European Research Council (grants PaleoNanoLife 2011-ADG_20110209 to F.R. and PHOTONIS 695618 to B.M.). This is Centre de Recherches Pétrographiques et Géochimiques–CNRS contribution #2549. **Author contributions:** D.V.B. did the noble gas analyses, discussed the results and their interpretations, and wrote the manuscript. M.W.B. participated in the noble gas analyses, discussed the results and their interpretations, and participated in writing the manuscript. F.D. did the IOM isolation from the MGTKS3 black chert sample, performed Raman analyses, discussed the interpretations, and participated in writing the manuscript. G.A., F.R., and B.M. discussed the results and their interpretations and participated in writing the manuscript. **Competing interests:** The authors declare that they have no competing interests. **Data and materials availability:** All data needed to evaluate the conclusions in the paper are present in the paper and/or the Supplementary Materials. Additional data related to this paper may be requested from the authors.

Submitted 16 October 2017
Accepted 30 January 2018
Published 28 February 2018
10.1126/sciadv.aar2091

Citation: D. V. Bekaert, M. W. Broadley, F. Delarue, G. Avice, F. Robert, B. Marty, Archean kerogen as a new tracer of atmospheric evolution: Implications for dating the widespread nature of early life. *Sci. Adv.* **4**, eaar2091 (2018).

Earth and Planetary Science Letters 525 (2019) 115766

Appendix D

Contents lists available at ScienceDirect

Earth and Planetary Science Letters

www.elsevier.com/locate/epsl

Novel insights into the degassing history of Earth's mantle from high precision noble gas analysis of magmatic gas

David V. Bekaert [a,*], Michael W. Broadley [a], Antonio Caracausi [b], Bernard Marty [a]

[a] Centre de Recherches Pétrographiques et Géochimiques, UMR 7358 CNRS – Université de Lorraine, 15 rue Notre Dame des Pauvres, BP 20, 54501 Vandoeuvre-lès-Nancy, France
[b] Instituto Nazionale di Geofisica e Vulcanologia, Sezione di Palermo, 90146 Palermo, Italy

ARTICLE INFO

Article history:
Received 14 March 2019
Received in revised form 2 August 2019
Accepted 8 August 2019
Available online xxxx
Editor: F. Moynier

Keywords:
noble gas
MORB
Eifel
mantle
xenon
volatiles

ABSTRACT

The noble gas isotope composition of the mantle can provide unique insights into the origin and evolution of volatile elements on Earth. Xenon isotopes combine primordial signatures with contributions from extinct and extant radionuclides, therefore offering the potential to set constraints on both the nature of Earth's planetary precursor(s) and the timing of their contributions. However, measuring the Xe isotope composition of mantle-derived samples to sufficiently high-precision has proven difficult due to (i) large occurrence of a modern-like atmospheric component in the mantle, and (ii) contribution from shallow and post-eruptive atmospheric contamination. Mantle-derived samples therefore exhibit only small deviations from the modern atmospheric composition, making the identification and deconvolution of mantle-derived Xe signals challenging. Here, we use the Giggenbach sampling method to concentrate magmatic noble gases from the Eifel volcanic area (Germany) into glass bottles in order to conduct high-precision analyses of Ne, Ar and Xe isotopes. The three samples collected from Victoriaquelle and Schwefelquelle wells (South East Eifel) show variable contributions from atmospheric contamination, with the least contaminated sample reaching $^{40}Ar/^{36}Ar$ ~8,300. Our data indicate that the mantle beneath the Eifel volcanic area, and by extension the Central European Volcanic Province, resembles the convective upper mantle reservoir with limited evidence for an OIB-like deep plume source contribution. It has a geochemical signature that is similar (e.g. in Ne isotopic composition, $^{40}Ar/^{36}Ar$, $^{129}Xe/^{130}Xe$ and $^{129}Xe/^{136}Xe$) to the mantle source of the so-called popping rocks (thought to best represent the upper mantle), with an additional source of ^{238}U-derived Xe and low $^{3}He/^{4}He$ that we attribute to the influence of an ancient subducted component (HIMU). A dichotomy exists between the main sources of fissiogenic xenon isotopes measured in popping rocks and Eifel gas, which appear to be mainly derived from ^{244}Pu and ^{238}U, respectively. According to their respective ratios of ^{244}Pu- to ^{238}U-derived Xe, the mantle sources for Eifel volcanism and popping rocks would have experienced extensive and limited degassing, respectively. In this regard, high Pu–Xe/(Pu+U)–Xe may no longer be considered as being indicative of a mantle deep origin, therefore calling for the geochemical differences between plume and MORB sources to be redefined, with the possibility that volatile signatures within the solid Earth may be more heterogeneously distributed than previously thought.

1. Introduction

The cycling of volatile elements (i.e., H, C, N, halogens and noble gases) between Earth's surface and its silicate interior plays a crucial role in controlling the evolution of the atmosphere and oceans, as well as the rheology and dynamics of the mantle. The discovery that primordial krypton (Holland et al., 2009, Bravo Dome gas field in New Mexico, United States) and xenon (Caracausi et al., 2016, Eifel volcanic area, Germany; Péron and Moreira, 2018, popping rocks) components in the mantle are of chondritic origin allowed major advances in our understanding of Earth's accretion history to be made. Although no Kr or Xe data from mantle-derived sources points toward a solar contribution in the mantle, neon, and presumably helium, in the deep mantle have solar-like isotopic signatures, suggesting that these gases were trapped early during terrestrial accretion, before dissipation of the solar nebula (Yokochi and Marty, 2004; Williams and Mukhopadhyay, 2019). However, the Ne isotopic signature of the upper mantle has been purported to originate from solar wind-implanted Ne within chon-

* Corresponding author.
E-mail address: dbekaert@crpg.cnrs-nancy.fr (D.V. Bekaert).

https://doi.org/10.1016/j.epsl.2019.115766

dritic materials (Ballentine et al., 2005), indicating the Earth may have accreted volatiles from multiple reservoirs. Heterogeneous accretion may also be evident for H isotopes, with both a solar (Hallis et al., 2015) and/or chondritic (Loewen et al., 2019) origin being argued for. The presence of light – and not heavy – solar noble gases in the mantle may be related to the higher solubility of He and Ne in silicate melts and/or to their elemental depletion in chondrites relative to heavy noble gases (Tucker et al., 2012). Krypton, xenon and likely argon in the mantle were presumably delivered together with major volatiles such as nitrogen by asteroidal material before mantle 'closure' (i.e., within <100 Myr after the start of Solar System formation – Caracausi et al., 2016). Subsequent evolution of the mantle heavy noble gas inventory was dominated by atmosphere recycling via subduction (Holland and Ballentine, 2006) as well as degassing to the atmosphere and radiogenic productions within the mantle (Allègre et al., 1983; Marty, 1989; Ozima and Podosek, 2002; Mukhopadhyay and Parai, 2019).

Given the protracted and extensive recycling of atmospheric gases into the solid Earth, the present-day inventory of Xe in the mantle is largely dominated (80–90%) by recycled modern atmosphere (Holland and Ballentine, 2006; Parai and Mukhopadhyay, 2018). Differences in chemical signatures between mid-ocean ridge basalts (MORB) originating from the convecting upper mantle and intraplate volcanic samples, including ocean island basalts (OIB) which tap in to the deep mantle, has been used to argue that the mantle is geochemically heterogeneous, with the MORB and OIB mantle sources experiencing different degassing histories (Kellogg and Wasserburg, 1990). In particular, the MORB mantle is characterised by elevated $^{3}He/^{4}He$ (8 ± 2 Ra, where Ra $= 1.39 \times 10^{-6}$, the $^{3}He/^{4}He$ ratio of air), $^{20}Ne/^{22}Ne$ ($\sim$12.5) and $^{21}Ne/^{22}Ne$ ($\geq$0.065), as well as high $^{40}Ar/^{36}Ar$ (up to 40,000) ratios, relative to air (Sarda et al., 1985; Burnard et al., 1997; Graham, 2002; Moreira et al., 1998; Péron and Moreira, 2018). The OIB mantle source is thought to have experienced limited direct mixing with, and volatile transfer to, the convecting MORB mantle source (Mukhopadhyay, 2012). As a consequence, the OIB mantle source has preserved remnants of primordial volatiles (e.g., gases trapped from the solar nebula) isolated since Earth's accretion (Craig and Lupton, 1976; Allègre et al., 1983; Honda et al., 1993; Mukhopadhyay, 2012; Williams and Mukhopadhyay, 2019), which are not witnessed, or are less prevalent, within the MORB mantle reservoir. Although OIBs can be classified into different categories depending on their chemical composition – HIMU type sources ("high-μ"; $\mu = {}^{238}U/{}^{204}Pb$, Pettke et al., 2018), two varieties of enriched mantle (EM 1 and EM 2; Zindler and Hart, 1986) and FOZO (Focal Zone, first defined by Hart et al., 1992) –, we simply refer to OIB as the largely undegassed deep mantle reservoir typified by the Iceland plume, which is characterised by high $^{3}He/^{4}He$ (up to 50 Ra, where Ra is the atmospheric $^{3}He/^{4}He$: 1.39×10^{-6}, Stuart et al., 2003) and $^{20}Ne/^{22}Ne$ (>12.5; Yokochi and Marty, 2004; Péron et al., 2016; Mukhopadhyay, 2012; Williams and Mukhopadhyay, 2019).

Xenon has nine isotopes, which constitute a powerful tool for discriminating between MORB and OIB mantle sources. Radiogenic ^{129}Xe and $^{131-136}Xe$ were produced early in Earth's history by β-decay of extinct ^{129}I ($T_{1/2} = 15.7$ Ma) and spontaneous fission of extinct ^{244}Pu ($T_{1/2} = 80.0$ Myr), respectively (Porcelli and Ballentine, 2002). These extinct radioactive nuclides provide a timestamp for the formation and subsequent evolution of different mantle reservoirs (Mukhopadhyay, 2012). In addition, spontaneous fission of extant ^{238}U ($T_{1/2} = 4.468$ Gyr) continuously produces $^{131-136}Xe$. The fissiogenic Xe isotopes are produced in different proportions by ^{244}Pu and ^{238}U, allowing the Pu- and U-derived Xe to be deconvolved. A reservoir that has remained closed to volatile loss over Earth's history should have 97% of the fission Xe isotopes being produced from ^{244}Pu (Azbel and Tolstikhin, 1993). As episodes of degassing after the extinction of ^{244}Pu will lead to progressively lower (Pu/U)-derived Xe, this ratio can be used to constrain the degassing history of different mantle sources, (e.g., Allègre et al., 1983; Kunz et al., 1998; Moreira et al., 1998; Caffee et al., 1999; Mukhopadhyay, 2012; Tucker et al., 2012; Petö et al., 2013; Parai and Mukhopadhyay, 2015).

Steady-state mantle models have long required ^{129}Xe and primordial noble gases such as ^{3}He, ^{22}Ne and ^{36}Ar in the volatile-depleted upper mantle to be derived from a primitive volatile-rich lower mantle via plume input (Porcelli and Wasserburg, 1995). However, differences in I/Xe (as seen in the $^{129}Xe^{*}/^{130}Xe$, where $^{129*}Xe$ is the decay product of extinct ^{129}I) between the MORB and OIB mantle sources indicate that the differentiation of these two reservoirs occurred during the existence of ^{129}I (80 Myr) and has resisted homogenisation ever since despite the Moon forming impact and 3 Gyr of subduction (Mukhopadhyay, 2012; Parai and Mukhopadhyay, 2015). This implies that plumes could not have supplied Xe, and all of the primordial volatiles, to the MORB source. Combined with the production of $^{131-136}Xe$ from the fission of extinct ^{244}Pu (half-life = 80 Myr), I–Pu–Xe closure ages for the different mantle reservoirs have been calculated through $^{129*}Xe/^{136*}Xe$ ratios, where $^{136*}Xe$ is the decay products of extinct ^{244}Pu (Allègre et al., 1983; Marty, 1989; Mukhopadhyay, 2012; Caracausi et al., 2016). Given that ^{129}I has a shorter half-life than ^{244}Pu, mantle domains with a higher $^{129*}Xe/^{136*}Xe$ should have become closed to volatile loss earlier, assuming that both reservoirs started with the same I/Pu ratio. In this case, the lower $^{129*}Xe/^{136*}Xe$ in OIB samples (Mukhopadhyay, 2012) compared to MORB (Parai and Mukhopadhyay, 2015) would suggest that the upper mantle became closed to volatile loss earlier than the deep OIB mantle source, which is unlikely. It has therefore been suggested that the lower mantle had a lower I/Pu ratio than the upper mantle. Indeed, for the upper mantle to have a younger closure age than the lower mantle would require the upper MORB source mantle to have had an initial I/Pu ratio 3.5 times higher than that of the lower mantle (e.g., Caracausi et al., 2016). Such differences in I/Pu between the MORB and OIB mantle sources could have resulted from several processes, including (i) later addition of volatile-rich, high I/Pu chondritic material to the upper mantle (Caracausi et al., 2016; Mukhopadhyay, 2012), (ii) sequestration of I from the lower mantle into the core (Jackson et al., 2018), and/or (iii) rapid degassing of mantle volatiles to the surface (Clay et al., 2017).

Given that Xe in mantle-derived samples is dominated by modern atmospheric Xe, identifying and deconvoluting the mantle-derived Xe signatures can be challenging. Submarine basaltic glasses (Moreira et al., 1998) and well gases (Holland et al., 2009) constitute compelling samples to provide insights into the composition of mantle-derived volatiles. However, well gases may also have a significant contribution from lithospheric components, and basaltic glasses have low noble gas abundances, hampering high precision noble gas isotopic measurements of the least abundant isotopes. In order to circumvent this difficulty, volcanic CO_2-rich free gases (i.e., gases that have been released from their host magma at depth before travelling to the surface) are analysed, as they also carry mantle-derived noble gases (Moreira et al., 2018; Caracausi et al., 2016). Free gases in the Eifel region (Germany) and Massif Central (France) show significant mantle contributions in light and heavy noble gases, therefore providing an opportunity to investigate the mantle's volatile history (Caracausi et al., 2016; Moreira et al., 2018).

The origin of the Central European Volcanic Province (CEVP), which includes the Massif Central and the Eifel regions, is debated with both upwelling mantle plumes and melting of upper mantle material being advocated as possible drivers of volcan-

ism under Europe (e.g., Buikin et al., 2005; Bräuer et al., 2013; Caracausi et al., 2016; Moreira et al., 2018). The volcanism in Eifel is presently dormant, but not extinct (youngest eruption ~11 ka, Schmincke, 2007). Volatiles escaping from East Eifel degassing centre are characterised by high CO_2 fluxes (>99 vol.%), with high $^3He/^4He$ ratios (up to 5.6 Ra) and $\delta^{13}C$ values within the MORB range (average -4.6 ± 0.6‰), pointing to a mantle-derived origin of Eifel volcanic gases (Bräuer et al., 2013). According to the relative abundances of magmatic N_2, He and Ar, the Victoriaquelle and Schwefelquelle wells (South East Eifel) show the highest contribution of mantle-derived gas in the Eifel region (Bräuer et al., 2013). Their $\delta^{15}N$ values are close to the MORB range, with Ne isotope compositions also being consistent with an upper mantle signature (Bräuer et al., 2013). Likewise, the chemical signature of the Lignat gas (Massif Central, France) resembles the MORB source mantle, requiring little to no plume contribution (Moreira et al., 2018). Yet, tomographic images show evidence for a low-velocity structure at depth down to 2,000 km, representing deep mantle upwelling under central Europe, which may feed smaller upper-mantle plumes expressed in the Eifel region (Goes et al., 1999; Ritter, 2007; Weber et al., 2007). Recently, high precision Xe isotope measurements from the Victoriaquelle Well were shown to be consistent with a deep undegassed mantle plume origin (Caracausi et al., 2016). The source of volcanism in the CEVP therefore remains enigmatic.

In this contribution, we focus on determining the origin of the volcanism in the CEVP by carrying out high-precision analyses of Ne, Ar and Xe isotopes for three free gas samples collected with Giggenbach bottles from the Victoriaquelle and Schwefelquelle wells. By comparing the geochemical signature of the mantle beneath the CEVP with those of the MORB and OIB reservoirs, we provide novel insights regarding the origin of the CEVP, and relationship between the upper and lower mantle in terms of degassing histories and present-day heterogeneities.

2. Samples and methods

2.1. Sampling and gas preparation

Noble gas isotopic compositions were determined in samples of volcanic free gas collected from the Victoriaquelle and Schwefelquelle wells in the Eifel volcanic district (Germany). These two locations are close to the village of Heckenmünster, south of the inferred plume centre, near the city of Gerolstein (Bräuer et al., 2013). The springs are at a distance of approximately 100 m from each other and are both characterised by high gas/water ratios. In order to optimize magmatic noble gas concentration into sampling volumes, we used 200 cm^3 pre-evacuated (10^{-3} Pa) glass flasks equipped with double Teflon stopcocks and filled with 50–80 cm^3 of 7N NaOH solution (Giggenbach and Goguel, 1989). The solution absorbs reactive gases (water vapour, CO_2, SO_2, H_2S, HCl, HF), allowing the build up of a large partial pressure of non-reactive gases (N_2, H_2, O_2, CO, hydrocarbons and noble gases) in the headspace volume. Once in the laboratory, collected volcanic gases were rapidly transferred by volume equilibration into 500 cm^3 steel tanks for storage. This procedure of gas sampling vastly increases the amount of gas available for analysis, whilst also increasing the efficiency of purification of the samples in the laboratory since H_2O and CO_2 have been largely removed from the pristine gas.

The samples analysed in this study were collected during two sampling sessions at Victoriaquelle and Schwefelquelle wells. In May 2018, Giggenbach bottles labelled E2 and E3 were collected from Schwefelquelle and Victoriaquelle wells, respectively. In September 2018, only the Victoriaquelle well could be sampled following the Giggenbach method (sample E4 in the present study) as the water level at Schwefelquelle well was too low to form a seal for noble gas sampling. Two steel tanks (Schw-t and Vict-t) from a previous sampling trip in 2015 were also analysed for their Ne and Ar isotope composition. In this case, purification was carried out using the same purification line as Caracausi et al. (2016) and gases were then analysed using the same procedure as detailed here below. All samples were analysed for their Ne, Ar and Xe isotope compositions using the Helix MC *Plus* (Thermofisher Scientific) noble gas mass spectrometer at the Centre de Recherches Pétrographiques et Géochimiques (CRPG) noble gas analytical facility, following the analytical procedures described in Supplementary Information. Neon, argon and xenon blank contributions were measured before running the samples and found to be insignificant (<1%). Therefore, blank corrections were not applied to the abundances or isotope ratios reported here. Standard runs were analysed before and during each analytical session. The three samples collected in Giggenbach bottles and analysed in this study are referred to as E2, E3 and E4. These were analysed using a different purification line than used by Caracausi et al. (2016). Finally, we report He isotope measurements for samples collected in 2015 from Schwefelquelle and Victoriaquelle wells, and analysed at the Instituto Nazionale di Geofisica e Vulcanologia in Palermo.

2.2. Extrapolating mantle signatures

The Monte Carlo linear least square code adapted from Parai and Mukhopadhyay (2015) was used to compute best fit mixings of ^{132}Xe from initial mantle, modern atmosphere (recycled into the mantle and acting as a contaminant during sampling), ^{238}U-fission Xe and ^{244}Pu–Xe, with $^{128-136}Xe$ isotopes being taken into account (Supplementary Information). Also, air contamination of the pristine mantle component generates hyperbolic trends in $^{20}Ne/^{22}Ne$–$^{40}Ar/^{36}Ar$ and $^{40}Ar/^{36}Ar$–$^{129}Xe/^{130}Xe$ spaces (e.g., Mukhopadhyay, 2012; Fig. S1). Best-fit hyperbola reflecting two-component mixing between air and mantle are determined using total least-squares hyperbolic fits, therefore allowing the mantle source $^{40}Ar/^{36}Ar$ and $^{129}Xe/^{130}Xe$ ratios to be extrapolated. First, the $^{40}Ar/^{36}Ar$ of the mantle source is calculated by extrapolation to a mantle $^{20}Ne/^{22}Ne$ value (12.5, 13.22 or 13.8, depending on the Ne isotope composition of the source; Fig. S1, Table S1). The curvature of the two-component mixing hyperbolic array is parameterized as $k = (^{36}Ar/^{22}Ne)_{mantle}/(^{36}Ar/^{22}Ne)_{atm}$. We use a grid search to find the combination of k and mantle $^{40}Ar/^{36}Ar$ that minimizes the χ^2 cost function:

$$\chi^2 = \sum_{i=1}^{N} \frac{1}{N^2} * \left[\left(\frac{\text{x\_meas} - \text{x\_fit}}{\sigma_{\text{x\_meas}}} \right)^2 + \left(\frac{\text{y\_meas} - \text{y\_fit}}{\sigma_{\text{y\_meas}}} \right)^2 \right]$$

where (x_meas $\pm$ σ_{x_meas}, y_meas $\pm$ σ_{y_meas}) are the N observed data points for a given sample and (x_fit, y_fit) are the closest points to the data along a candidate hyperbola. The error associated with the extrapolated $^{40}Ar/^{36}Ar$ of the mantle is calculated using the method described by Parai and Mukhopadhyay (2015), with the 1 sigma confidence interval (68.3%) being defined where the fit degrades by a fixed amount $\chi^2 \leq \chi^2$ min + 2.30 (for a 2 parameter fit; e.g., Press et al., 1992). In the $^{129}Xe/^{130}Xe$–$^{40}Ar/^{36}Ar$ space ($k = (^{130}Xe/^{36}Ar)_{mantle}/(^{130}Xe/^{36}Ar)_{atm}$), the mantle source $^{129}Xe/^{130}Xe$ is then computed by extrapolation to the mantle $^{40}Ar/^{36}Ar$. The final error associated with the mantle source $^{129}Xe/^{130}Xe$ takes into account propagation of the mantle $^{40}Ar/^{36}Ar$ uncertainty. Note that $^{36}Ar/^{22}Ne$ and $^{130}Xe/^{36}Ar$ values for the mantle source (which define the k parameters) were freely varied between 4–12 and 2.0–4.3 $\times$ 10^{-4}, respectively, in order to span the full range of possibilities from MORB- to OIB-like elemental compositions (Graham, 2002).

The code was tested on published data for different types of mantle sources. Results are reported in Fig. S1 and Table S1.

3. Results

3.1. Helium, neon and argon

Helium isotopic ratios measured in the present study (4.1–4.2 Ra; Table S2) for the Schwefelquelle and Victoriaquelle wells are in excellent agreement with those reported by Bräuer et al., 2013 (4.2–4.5 Ra). The $^{20}Ne/^{22}Ne$ of samples E2, E3 and E4 range from 10.3 to 11.2 (Table S3), which is higher than the maximum previously found $^{20}Ne/^{22}Ne$ for Eifel free gas (10.6; Bräuer et al., 2013), but still lower than the maximum value from stepwise crushing of mantle xenoliths (11.88; Buikin et al., 2005). Samples E2-E4 plot on the mixing line between air and the MORB end-member (Fig. 1). The two samples collected using steel tanks and analysed for their Ne isotope composition (Schw-t and Vict-t) plot along the same mantle-atmosphere mixing line as samples from Giggenbach bottles (Fig. 1). Argon isotope compositions of samples E2, E3 and E4 show increasing contributions of air contamination ($^{40}Ar/^{36}Ar$ of 8,287 ± 140, 4,040 ± 69 and 1,974 ± 45, respectively), with $^{38}Ar/^{36}Ar$ being consistently within error of the atmospheric ratio (Table S4). These $^{40}Ar/^{36}Ar$ ratios are higher than reported by Caracausi et al., 2016 for E1 ($^{40}Ar/^{36}Ar$ = 1,780; Fig. 2), indicating higher mantle contributions. The maximum $^{40}Ar/^{36}Ar$ reported here (~8,300) is the highest value yet measured for Eifel free gas.

3.2. Xenon

The Xe isotopic spectra of samples E2-E4 show excesses in radiogenic $^{129}Xe^*$ and fissiogenic $^{131-136}Xe$ relative to modern atmosphere (Fig. 2; Table S5-S6) supporting the presence of a mantle-derived component in Eifel free gases. These excesses are correlated (Fig. 3), indicating they have a common origin, and are higher than those reported for sample E1 (Caracausi et al., 2016, Fig. 2), in agreement with the lower contributions of air contamination seen for Ar isotopes. The $^{129}Xe/^{136}Xe$ of the Eifel magmatic gas appears similar to that of the source of popping rocks (Péron and Moreira, 2018; Fig. 3a). Fission spectra for Xe isotopes in E2-E4 indicate a dominant contribution from ^{238}U-derived Xe, with limited contribution from ^{244}Pu-derived Xe (Fig. 3b). In contrast, the source of popping rocks is dominated by ^{244}Pu-derived Xe (Péron and Moreira, 2018; Fig. 3).

3.3. Composition of the mantle beneath Eifel

A least-square hyperbolic fit through Eifel data (see section 2.2) yields a $^{40}Ar/^{36}Ar$ of $39,400^{+2900}_{-15200}$ (Fig. S1) and a $^{129}Xe/^{130}Xe$ of $7.84^{+0.09}_{-0.45}$ for a mantle source $^{20}Ne/^{22}Ne$ of 12.5 (Fig. 4). Extrapolating the $^{20}Ne/^{22}Ne$ to 13.8 would yield a mantle source $^{40}Ar/^{36}Ar$ of $64,800^{+4900}_{-30,700}$ (Fig. S2), which would not significantly change our conclusions. Results of linear least squares determinations of initial, recycled atmospheric, Pu- and U-fissiogenic Xe components for Eifel (Caracausi et al., 2016; This study), popping rocks (Péron and Moreira, 2018) and Lignat (Moreira et al., 2018) samples are reported in Table 1. These indicate that E2 (which is the Eifel gas least contaminated by air, $^{40}Ar/^{36}Ar$ ~8,300) is best accounted for by mixing $93.3^{+1.2}_{-1.2}$% modern air with $5.2^{+1.1}_{-1.1}$% AVCC, $1.1^{+0.1}_{-0.2}$% U-derived Xe and $0.4^{+0.3}_{-0.2}$% Pu-derived Xe. The I–^{129}Xe/Pu–^{136}Xe and Pu–^{136}Xe/(Pu+U)–^{136}Xe for the source of Eifel gas are $13.8^{+25.4}_{-5.3}$ and $0.21^{+0.13}_{-0.14}$, respectively). Importantly, linear least squares determinations of initial, recycled atmospheric, Pu- and U-fissiogenic Xe components in the Eifel gas (sample E2, this study) give consistent outcomes if ^{128}Xe is taken or not into account (Table 1).

4. Discussion

4.1. Origin of the Central European Volcanic Province

In neon three-isotope space (Fig. 1), Eifel samples reflect a two component mixing between air and the MORB source, requiring negligible if any contribution from an OIB-like source. This is consistent with Ne data reported by Bräuer et al. (2013) for the Schwefelquelle and Victoriaquelle wells, interpreted to reflect a mixture of atmospheric and MORB-like Ne, that had been additionally affected by mass dependent fractionation (MDF, Fig. 1). These results are at odds with Ne isotope data on ultramafic xenoliths from the Eifel region by Buikin et al. (2005), which were interpreted to suggest the presence of hot spot-type, OIB-like noble gases in the Eifel region. However, the authors acknowledge that contributions from variably fractionated atmosphere-derived contaminants and variably fractionated mantle-derived noble gases are involved in individual Eifel xenoliths, and consider only one sample (DW1) to define a reliable hyperbola fit in the $^{40}Ar/^{36}Ar$ versus $^{20}Ne/^{22}Ne$ space. Our data, which do not show evidence for significant MDF, as also seen in the consistently atmospheric $^{38}Ar/^{36}Ar$ ratios (Table S4), confirm that Ne isotopes in the Eifel gas exclude a significant deep mantle plume contribution of the Iceland, Reunion, or Kerguelen type for Ne (Fig. 1). Extrapolating the $^{21}Ne/^{22}Ne$ of the Eifel gas source to a $^{20}Ne/^{22}Ne$ of 12.5 by error weighted least squares linear regression through the Eifel data points yields a range of values that is distinct from popping rocks and "HIMU-like MORBs" (Tucker et al., 2012), but which overlaps with the range of depleted MORBs (DMM, Fig. 5). Although analysing more Eifel samples with varying $^{20}Ne/^{22}Ne$ will ultimately help better constraining the $^{21}Ne/^{22}Ne$ of the Eifel source, this suggests potential contribution from a degassed MORB-like mantle source.

The $^{40}Ar/^{36}Ar$ of the source constrained by Ne isotopes ($39,400^{+2900}_{-15200}$, Fig. 4) is similar to that estimated for the more radiogenic MORB ($^{40}Ar/^{36}Ar$ up to 40,000; Graham, 2002), and not OIB ($^{40}Ar/^{36}Ar$ ~5,000 to ~10,000; Colin et al., 2015; Mukhopadhyay, 2012), reservoir. Likewise, the $^{129}Xe/^{130}Xe$ of the Eifel source ($7.84^{+0.09}_{-0.45}$) is characteristic for the MORB reservoir (7.44–7.83; Moreira et al., 1998; Tucker et al., 2012), but distinct from OIB (6.98 ± 0.07; Mukhopadhyay, 2012). The highest $^{129}Xe/^{130}Xe$ measured in the Eifel samples (6.94 for sample E2) is similar to the value of the OIB source as defined by the Iceland plume composition (6.98 ± 0.07; Mukhopadhyay, 2012). For the Xe isotope composition of Eifel magmatic gas to have a plume origin would require that sample E2 is 100% mantle-derived gas, which is not possible. This suggests that an OIB-like mantle plume origin for volcanism the Eifel area, and by extension volcanism in the Central European Volcanic Province (CEVP), is unlikely. Taken together, Ne, Ar and Xe systematics indicate that the source of magmatic gas in Eifel is similar to the MORB source mantle. The potential increase in mantle-derived gas contribution in Eifel over the last years, as seen in the increasing $^{40}Ar/^{36}Ar$ from 2005 (Bräuer et al., 2013; Caracausi et al., 2016) to 2018 (this study), could be related to a rise in the flux of magmatic volatiles beneath the Eifel region. However, the different sampling methods used in both studies (steel tanks versus Giggenbach bottles, respectively) may preclude firm comparison of the two results.

4.2. Degassing history of mantle reservoirs

Based on Xe isotope measurements in the Victoriaquelle well gas, Caracausi et al. (2016) concluded for the origin of Eifel magmatism to be related to a deep mantle plume. This result was primarily based on a significant ^{244}Pu-derived Xe contribution, and computed Pu–Xe/(Pu+U)–Xe and $^{129}Xe_I/^{136}Xe_{Pu}$ ratios that

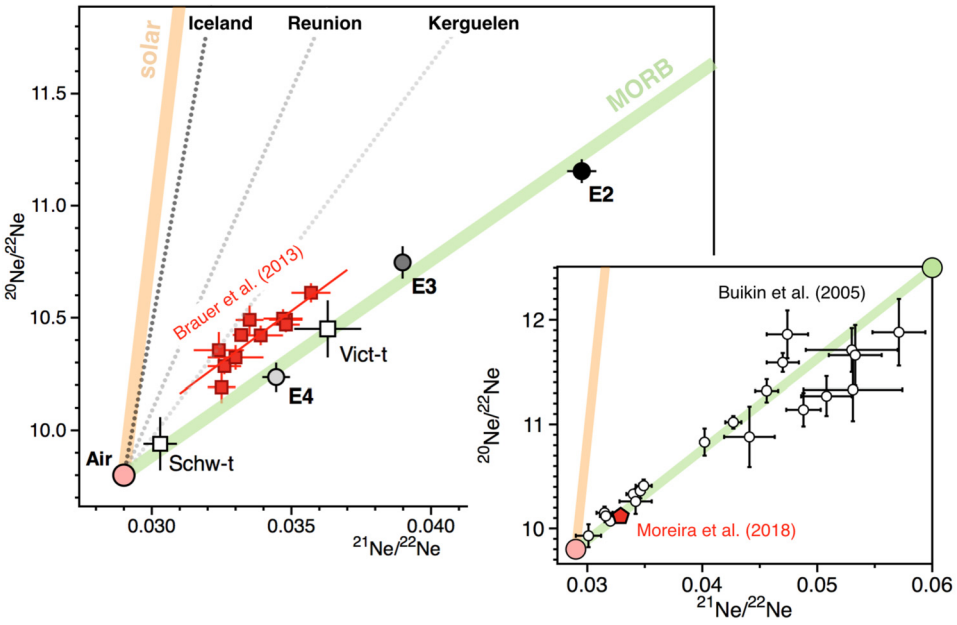

Fig. 1. Neon three-isotope plot displaying the three Eifel samples (E2, E3 and E4), air, solar and MORB, together with different OIB endmembers. Two samples of Eifel gas from steel tanks were also analysed for their Ne isotope compositions (white squares Schw-t and Vict-t). Eifel samples define a mixing line between Air and MORB compositions, requiring no contribution from a plume-like source. Data reported by Bräuer et al. (2013) for Victoriaquelle and Schwefelquelle wells, Moreira et al. (2018) for the Lignat thermal spring (Massif Central, France) and Buikin et al. (2005) for ultramafic xenoliths from the Eifel Quaternary volcanic field "Dreiser Weiher", are shown for comparison. Error bars indicate $\pm 1\sigma$. Air composition is from Ozima and Podosek (2002).

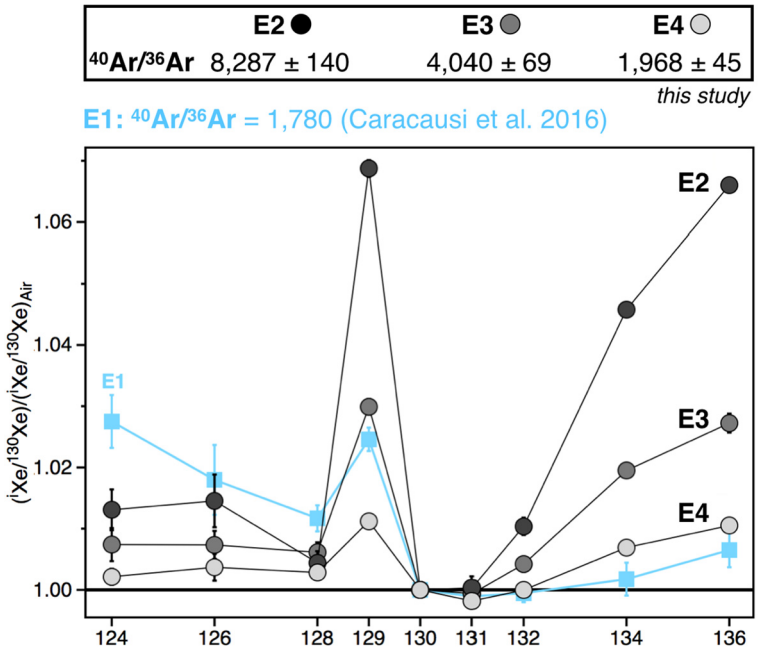

Fig. 2. Argon and xenon isotope composition of the three Eifel samples (E2, E3 and E4) analysed in this study. Xenon isotopic composition of E2, E3 and E4 are normalised to air and to ^{130}Xe, and compared to the xenon isotope composition reported by Caracausi et al. (2016) for the Eifel source (E1). Although E1 shows a greater enrichment in the light isotopes, E2-E4 show greater excesses in radiogenic ^{129}Xe and fissiongenic $^{131-136}Xe$, indicating greater contributions from mantle-derived components. This suggests that E1 might have been partially fractionated in favour of the light isotopes during purification and/or analysis. Error bars indicate $\pm 1\sigma$. Air composition is from Ozima and Podosek (2002).

overlap those from the Icelandic and Rochembeau rift plumes (Parai and Mukhopadhyay, 2015). From linear least squares fitting calculations, our data indicate a predominant contribution from ^{238}U-derived Xe, as well as "MORB-like" Pu–Xe/(Pu+U)–Xe and $^{129}Xe_I/^{136}Xe_{Pu}$ ratios (Table 1), regardless if ^{128}Xe is taken in to account or not. However, these outcomes are associated with much larger uncertainties when ^{128}Xe is not taken into account (Table 1). Henceforth, we only consider the results using ^{128}Xe for sample E2. Importantly, determining the initial, recycled atmospheric, Pu- and U-fissiogenic Xe components in the Eifel gas as measured by Caracausi et al. (2016) gives more contrasted outcomes depending on whether ^{128}Xe is taken into account (Table 1). If ^{128}Xe is taken into account, the data are best accounted for by mixing $91.4^{+0.8}_{-0.8}$% air, $8.2^{+0.8}_{-0.7}$% AVCC and $0.3^{+0.1}_{-0}$% ^{244}Pu-derived Xe with negligible contribution from ^{238}U-derived Xe. In this case, $^{129}Xe_I/^{136}Xe_{Pu}$ and Pu–Xe/(Pu+U)–Xe ($5.8^{+1}_{-0.8}$ and $0.96^{+0}_{-0.01}$, re-

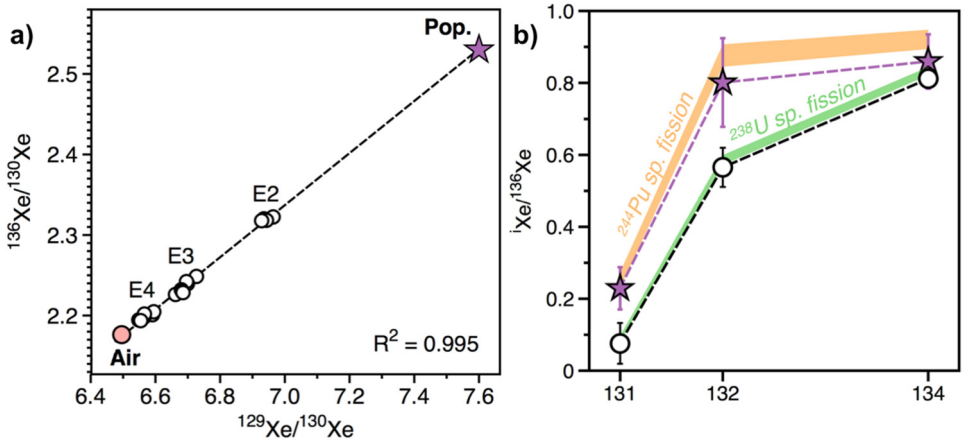

Fig. 3. a) $^{129}Xe/^{130}Xe$ vs. $^{136}Xe/^{130}Xe$ diagram showing air (in pink), Eifel samples (white circles) and popping rock 2πD43 (purple star, Péron and Moreira, 2018). b) Fission spectra of E2 (white circles) and popping rock 2πD43 (purple star, Péron and Moreira, 2018) compared with the fission spectra for fission of ^{238}U (green area) and ^{244}Pu (orange area). Irrespective of their degassing histories, the mantle sources of Eifel gas and popping rocks have therefore preserved similar $^{129}Xe/^{136}Xe$, although the main fissiongenic sources of ^{136}Xe excess are different (^{244}Pu for popping rocks and ^{238}U for the Eifel gas). Air composition is from Ozima and Podosek (2002). (For interpretation of the colours in the figure(s), the reader is referred to the web version of this article.)

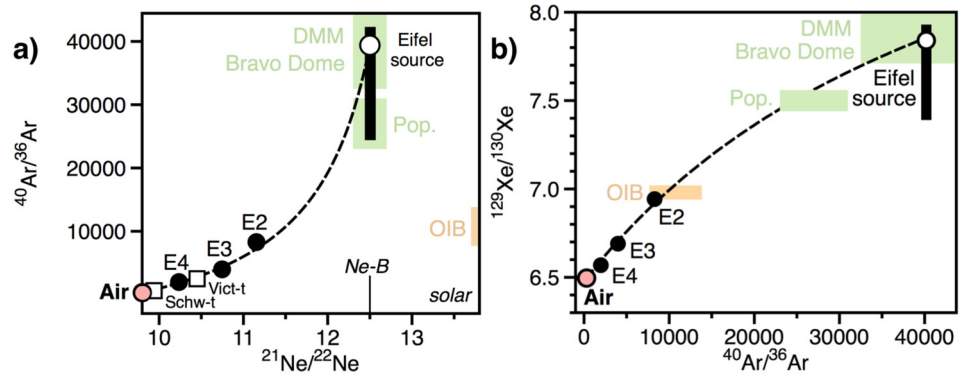

Fig. 4. Ne–Ar (a) and Ar–Xe (b) correlations for the Eifel gas. The data reflect mixing between a mantle component and post-eruptive atmospheric contamination. A least-squares hyperbolic fit through the data yields a $^{40}Ar/^{36}Ar$ ratio of $39,400^{+2900}_{-15200}$ (Fig. S1) and a $^{129}Xe/^{130}Xe$ of $7.84^{+0.09}_{-0.45}$, for a MORB-like $^{20}Ne/^{22}Ne$ ratio of 12.5. DMM, Bravo Dome, popping rocks and OIB compositions are from Tucker et al. (2012). Air compositions are from Ozima and Podosek (2002).

Table 1
Outcomes of Monte Carlo linear least square simulations adapted from Parai and Mukhopadhyay (2015). We tested the code on SWIR-E and SWIR-W samples reported by Parai and Mukhopadhyay (2015; in italics) to ensure similar results were obtained. The code was then run for popping rocks (Péron and Moreira, 2018), Lignat (Moreira et al., 2018), Eifel E1 (with and without ^{128}Xe being taken into account; Caracausi et al., 2016) and Eifel E2 (this study). The ranges of values for OIB and MORB as compiled by Caracausi et al. (2016) are also given for comparison.

Sample	I–$^{129}Xe/Pu–^{136}Xe$	Pu/(Pu+U)–^{136}Xe	%Mantle contribution	%Pu	%U
SWIR-E	$8.8^{+20.3}_{-3.6}$	$0.31^{+0.20}_{-0.21}$	$7.8^{+4.2}_{-4.1}$	$1.0^{+0.7}_{-0.7}$	$1.4^{+0.4}_{-0.3}$
Parai+15	$8.3^{+14.6}_{-3.2}$	$0.32^{+0.19}_{-0.20}$	$8.3^{+4.1}_{-3.9}$	$1.1^{+0.6}_{-0.7}$	$1.4^{+0.4}_{-0.4}$
SWIR-W	$10.3^{+27.3}_{-4.4}$	$0.28^{+0.20}_{-0.20}$	$11^{+6.7}_{-6.4}$	$1.5^{+1.1}_{-1.1}$	$2.5^{+0.6}_{-0.6}$
Parai+15	$10.8^{+40.3}_{-4.8}$	$0.27^{+0.20}_{-0.21}$	$11^{+6.9}_{-6.3}$	$1.4^{+1.2}_{-1.1}$	$2.5^{+0.7}_{-0.6}$
Popping rock	$3.6^{+8.5}_{-1.2}$	$0.99^{+0.01}_{-0.78}$	$0^{+23.7}_{-0}$	$3.3^{+1.7}_{-2.3}$	$0^{+2.5}_{-0}$
Lignat	$2.8^{+0.2}_{-0.3}$	$0.94^{+0}_{-0.01}$	$0^{+0.9}_{-0}$	$0.2^{+0.1}_{-0}$	0^{+0}_{-0}
Eifel E1 (+128)	$5.8^{+1}_{-0.8}$	$0.96^{+0}_{-0.01}$	$8.2^{+0.8}_{-0.7}$	$0.3^{+0.1}_{-0}$	0^{+0}_{-0}
Eifel E1 (−128)	$213.5^{+7.1}_{-7.2}$	$0.05^{+0.01}_{-0.01}$	$2.8^{+1.1}_{-1.1}$	0^{+0}_{-0}	$0.1^{+0.1}_{-0}$
Eifel E2 (+128)	$13.8^{+25.4}_{-5.3}$	$0.21^{+0.13}_{-0.14}$	$5.2^{+1.1}_{-1.1}$	$0.4^{+0.3}_{-0.2}$	$1.1^{+0.1}_{-0.2}$
Eifel E2 (−128)	$600.1^{+8.2}_{-583.5}$	$0.01^{+0.18}_{-0.01}$	$2.7^{+1.7}_{-1.1}$	$0^{+0.4}_{-0}$	$1.3^{+0}_{-0.2}$
OIB range	2.3–4	0.72–1			
MORB range	5–50	0.05–0.5			

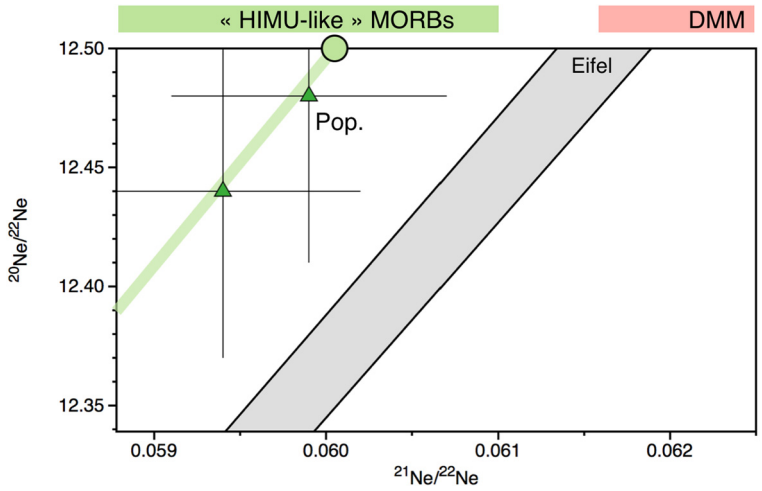

Fig. 5. Neon three-isotope plot displaying the extrapolated $^{21}Ne/^{22}Ne$ for a range of MORB and DMM samples (values extrapolated to $^{21}Ne/^{22}Ne = 12.5$; Tucker et al., 2012). Note that, according to Xe isotopes (Fig. 7), HIMU-type MORBs are referred to as MORBs. Also shown as green triangles are the two upper points for popping rocks (Pop., Moreira et al., 1998). Error weighted least squares linear regression through the Eifel data points gives an error envelope that is represented as a grey area. The extrapolated $^{21}Ne/^{22}Ne$ for the Eifel source appears to be distinct from the MORB range as sampled by popping rocks but overlaps with the field of the DMM.

spectively; Table 1) are consistent with the classical view of OIB-like signatures. However, if ^{128}Xe is excluded, the data are best accounted for by mixing $97^{+1.2}_{-1.1}$% air, $2.8^{+1.1}_{-1.1}$% AVCC and $0.1^{+0.1}_{-0}$% ^{238}U-derived Xe with negligible contribution from ^{244}Pu-derived Xe. In this case, $^{129}Xe_I/^{136}Xe_{Pu}$ and Pu–Xe/(Pu+U)–Xe ($213.5^{+7.1}_{-7.2}$ and $0.05^{+0.01}_{-0.01}$, respectively; Table 1) are in better agreement with the classical view of MORB-like signatures.

Importantly, Xe isotope spectra of samples E2-E4 show greater contributions of mantle-derived gas compared to sample E1 (Fig. 2; Caracausi et al., 2016). Yet, the light isotope excess reported by Caracausi et al. (2016) is greater than observed in the present study, indicating that data reported for sample E1 have been fractionated in favour of the light isotopes, as recently suggested by Moreira et al. (2018). Data points corresponding to repeated measurements of a single sample from Caracausi et al. (2016) appear to plot along MDF lines (Fig. 8 and Fig. S3), suggesting that isotope fractionation occurred during gas analysis rather than during sampling. Analytical issues might have occurred during sample preparation, especially during purification. In the present paper, gases were collected using Giggenbach bottles, therefore removing reactive gases and allowing the build up of a large partial pressure of noble gases. This procedure of gas sampling vastly improved the efficiency of purification of the samples for analysis. In addition, samples were purified using a different purification line than Caracausi et al. (2016). Taking together these considerations, we conclude that the dataset reported in the present study is more appropriate to constrain the source of volcanism in the Eifel region.

Taken together, our result show the mantle reservoir sampled by the Eifel volcanism to have a geochemical signature ($^{40}Ar/^{36}Ar$, $^{129}Xe/^{136}Xe$, Ne isotope composition; Fig. 1 and 4) that is similar to the convective upper mantle, with low Pu–Xe/(Pu+U)–Xe. Despite large error bars at the 1-sigma level, heavy Xe excesses measured in popping rocks, thought to best represent the upper mantle, appear to be dominated by ^{244}Pu-derived Xe (Péron and Moreira, 2018). We calculate the I-Xe/Pu-Xe and Pu–Xe/(Pu+U)–Xe of the popping rock source to be $3.6^{+8.5}_{-1.2}$ and $0.99^{+0.01}_{-0.78}$, respectively (Table 1). According to the Pu–Xe/(Pu+U)–Xe, the MORB sources for Eifel volcanism and popping rocks would therefore have experienced extensive and limited degassing, respectively, whilst both sampling the convective mantle. Likewise, the source of the Lignat thermal spring (Massif Central, France) analysed by Moreira et al. (2018) is best accounted for by an I–Xe/Pu–Xe of $2.8^{+0.2}_{-0.3}$ and a Pu–Xe/(Pu+U)–Xe of $0.94^{+0}_{-0.01}$ (Table 1). These values for popping rock and Lignat fall within the range of OIB (2.3–4 and 0.72–1, respectively) but are distinct from what has been commonly considered as the MORB range (5–50 and 0.05–0.5, respectively; Caracausi et al., 2016). The atmospheric contribution required to explain the Lignat data is extremely high ($99.7^{+0.01}_{-0.9}$% air, Table 1). Nonetheless, the fissiogenic isotope ratios for the Lignat gas require a $0.2^{+0.1}_{-0}$% contribution of Pu-derived Xe with no contribution of U-derived Xe. If truly representative of the mantle source then this would suggest that variable Pu–Xe/(Pu+U)–Xe might co-exist within the CEVP source(s), with fissiogenic Xe isotope being derived from both ^{244}Pu (Lignat gas, Moreira et al., 2018) and ^{238}U (Eifel gas, this study). However, drawing definite conclusion from Lignat gas is difficult given the large amount of atmospheric contamination, with only two of the four fissiogenic isotopes (^{134}Xe and ^{136}Xe) being in excess of air. Also note that the mean mantle contribution computed for popping rocks and Lignat gas (Table 1) are 0%, despite respective $^{129}Xe/^{130}Xe$ being in excess of air, which requires positive mantle contributions. A statistical bias during deconvolution of atmosphere- and mantle-derived signatures for these samples might be introduced during translation of ^{130}Xe-normalised ratios, as provided in the corresponding studies, into ^{132}Xe-normalised ratios, causing significant correlated errors in the ^{132}Xe-normalised ratios used for the calculations (Supplementary Information). As shown in Fig. 8b, Lignat gas data points might also show some extent of mass dependent fractionation, therefore causing a potential bias in the determination of its Pu–Xe/(Pu+U)–Xe.

The $^{3}He/^{4}He$ ratios, the slopes of mantle-air mixing lines in the Ne three isotope plot (Fig. 1) and the Pu–Xe/(Pu+U)–Xe are interpreted as reflecting the extent of degassing experienced by a given mantle reservoir. As depicted on Fig. 6, the OIB-like mantle sources akin to Iceland (Mukhopadhyay, 2012) and Rochambeau (Petö et al., 2013) exhibit high $^{3}He/^{4}He$ and $^{20}Ne/^{21}Ne_E$ ratios (where $^{20}Ne/^{21}Ne_E$ reflects the slope of mantle-air mixing lines in the Ne three isotope plot) that are not seen in samples deriving from the convective mantle. Although OIB-like mantle sources show consistently high Pu–Xe/(Pu+U)–Xe, it appears that samples from the convective upper mantle span the whole range of Pu–Xe/(Pu+U)–Xe values (Fig. 6) implying that fissiogenic Xe excesses in mantle-derived samples may not relate solely to different states of degassing and cannot therefore yield any strong indication regarding the source of volcanism (MORB or OIB). In other

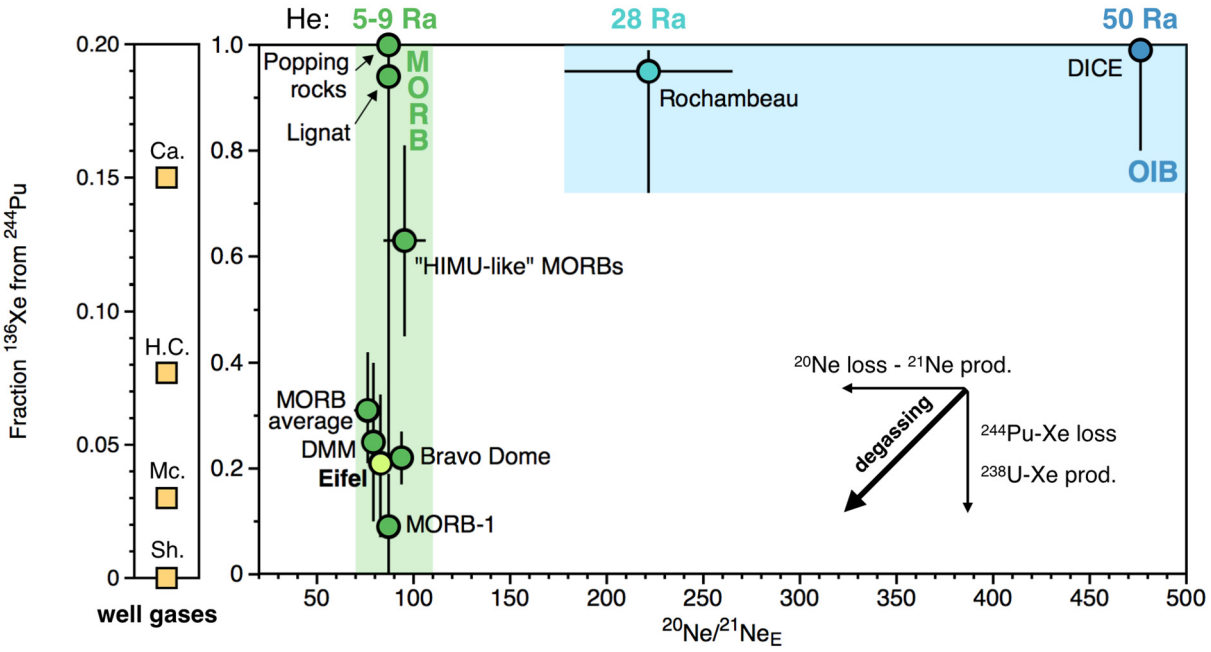

Fig. 6. Fractions of ^{136}Xe derived from ^{244}Pu vs. slopes of air-mantle mixing lines in Ne three-isotope space (^{20}Ne/^{21}Ne$_E$). Two OIB-like samples, Rochambeau (Petö et al., 2013) and DICE (Mukhopadhyay, 2012), are represented. Popping rocks are computed from data by (Péron and Moreira, 2018). MORB-1 is computed by Mukhopadhyay (2012) from popping rock data by Kunz et al. (1998). "Himu-like" MORBs and DMM are from Tucker et al. (2012). The error-weighted MORB average composition computed by Parai and Mukhopadhyay (2015) is also shown. Also represented are well gases data. The Bravo Dome mantle composition is from Holland and Ballentine (2006) and computation by Parai and Mukhopadhyay (2015). Other well gas data (Ca.: Caroline, Australia; H.C.: Harding County; Mc.: McElmo Dome; Sh.: Sheep Mountain; orange squares) are from Caffee et al. (1999), for which the Ne isotope composition of the mantle source is not known. Eifel (this study) is shown in light green. Differences in ^{130}Xe/^{22}Ne between highly degassed (MORB) and less degassed (e.g., Iceland or Rochambeau) mantle components (Williams and Mukhopadhyay, 2019) appear to be too small to account for hyperbolic mixing trends allowing to span a large range of Pu/(Pu+U)–Xe for a single 20/21$_E$.

words, high Pu–Xe/(Pu+U)–Xe may no longer be considered as being indicative of a deep undegassed origin for the sampled mantle sources. Likewise, whilst the ^{129}Xe$_I$/^{136}Xe$_{Pu}$ of Eifel gas ($13.8^{+25.4}_{-5.3}$) overlaps with the range MORB range (5-50), the ^{129}Xe$_I$/^{136}Xe$_{Pu}$ of popping rocks and Lignat ($3.6^{+8.5}_{-1.2}$ and $2.8^{+0.2}_{-0.3}$, respectively) are in better agreement with the OIB range (2.3-4; Table 1, Fig. S4). This indicates that, although MORB and OIB reservoirs can be discriminated from their differences in I/Xe (Fig. 4), they may no longer be distinguished on the basis of their ^{129}Xe$_I$/^{136}Xe$_{Pu}$ relationship.

The isotopic composition of atmospheric Xe evolved throughout the Archean via mass-dependent fractionation up until 2.5 Gyr ago, starting from a precursor (titled U-Xe) exhibiting deficits in ^{134}Xe and ^{136}Xe (Avice et al., 2018). Early recycling of atmospheric xenon with an isotopic composition intermediate between U-Xe and modern atmospheric Xe would render precise deconvolution of the chondritic, atmospheric, fissiogenic and radiogenic contributions to the mantle Xe array difficult (Péron and Moreira, 2018). It would also complicate the identification of primordial sources (solar, chondritic) of Xe in the mantle. Heavy noble gases (Kr, Xe) in the upper mantle carry signatures that are distinct from solar (as defined by Meshik et al., 2014), but similar to chondrites (Holland et al., 2009; Caracausi et al., 2016; Péron and Moreira, 2018). However, no unambiguous, high precision heavy noble gas data allowing chondritic and solar sources to be discriminated have been reported so far for the deep, undegassed mantle sampled by OIB-like plumes.

4.3. Noble gas reservoirs in the mantle

In a ^{129}Xe/^{130}Xe vs. ^{136}Xe/^{130}Xe diagram, OIB- and MORB-air mixing lines have distinct slopes, with the OIB line being slightly steeper due to lower ^{129}Xe/^{136}Xe for the MORB source (Fig. 7; Tucker et al., 2012). From the ^{129}Xe/^{130}Xe of the Iceland plume source (6.98±0.07; Mukhopadhyay, 2012), we calculate the corresponding ^{136}Xe/^{130}Xe (Fig. 7) and plot the composition of the Iceland source in Fig. 8. According to this diagram, higher ^{129}Xe/^{136}Xe in OIB relative to MORB cannot be related solely to recycling of atmospheric Xe or by adding fissiogenic ^{136}Xe to MORB Xe (Mukhopadhyay, 2012). Interestingly, the source of popping rocks (Péron and Moreira, 2018) and Eifel samples (this study) plot along a single line passing through the MORB mantle as previously defined by the popping rock 2πD43 mean composition (see compilation by Moreira et al., 2018). Irrespective of their degassing histories, the mantle sources of Eifel gas and popping rocks have preserved similar ^{129}Xe/^{136}Xe, although their main sources of fissiogenic Xe appear to be different (^{244}Pu for popping rocks and ^{238}U for the Eifel gas; Fig. 3).

The limited contribution from ^{244}Pu-derived Xe in Eifel gas (Fig. 3b) relative to popping rocks suggests either that (i) ^{244}Pu-derived Xe has been degassed early and therefore lost from the mantle reservoir, or that (ii) enhanced production of ^{238}U-derived Xe has overprinted the budget of fission-derived Xe isotopes. Given that the half-life of ^{129}I ($T_{1/2}$ = 15.7 Ma) is shorter than that of ^{244}Pu ($T_{1/2}$ = 80 Ma), ^{129}I would have been extinct before ^{244}Pu and so complete degassing of ^{244}Pu-derived Xe would also imply extensive degassing of ^{129}I-derived Xe, which is at odds with the preservation of radiogenic ^{129}Xe in the Eifel mantle source. Regarding the second hypothesis, a high contribution of ^{238}U-derived Xe in the Eifel magmatic gas could have several origins, including an HIMU-type source influence, or an additional input of radiogenic crustal derived noble gases as seen in well gases (Holland and Ballentine, 2006). Noble gas systematics in Eifel xenoliths are for example compatible with the addition of crustal material to a MORB-source signature (Dunai and Baur, 1995). However, from Ne isotopes, we see no evidence for extraneous crustal ^{21}Ne (Fig. 1). Concerning Xe isotopes, the composition of continental well gases deviates from the MORB and OIB trend toward lower ^{129}Xe/^{136}Xe because of crustal inputs of ^{238}U-derived ^{136}Xe and limited ex-

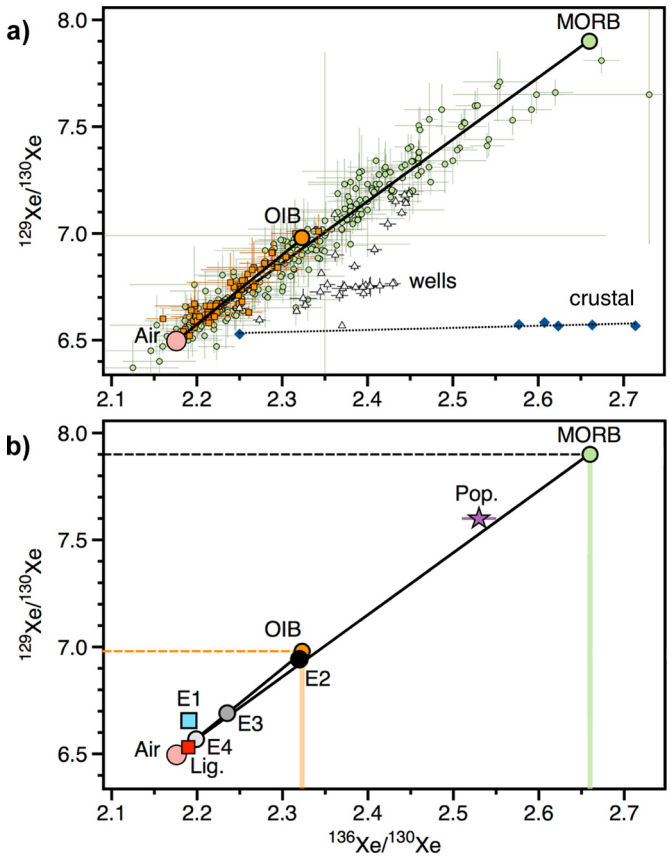

Fig. 7. $^{129}Xe/^{130}Xe$ vs. $^{136}Xe/^{130}Xe$ diagrams showing (a) air (Ozima and Podosek, 2002; pink circles), OIB (Iceland plume, DICE Mukhopadhyay, 2012; orange squares), MORBs (Kunz et al., 1998; Tucker et al., 2012; Parai and Mukhopadhyay, 2015; green circles), CO_2 well gases and thermal springs (diamonds; Caffee et al., 1999; Holland and Ballentine, 2006), as well as crustal fluids (blue diamonds; Holland et al., 2013). On panel (b), we also report the Lignat sample (Lig., red square; Moreira et al., 2018), popping rocks (Pop., purple star; Péron and Moreira, 2018), as well as the Eifel sample by Caracausi et al. (2016) (E1, blue square) and this study (grey circles). The known $^{129}Xe/^{130}Xe$ of OIB and MORB mantle sources (Mukhopadhyay, 2012) are used to determine the corresponding $^{136}Xe/^{130}Xe$.

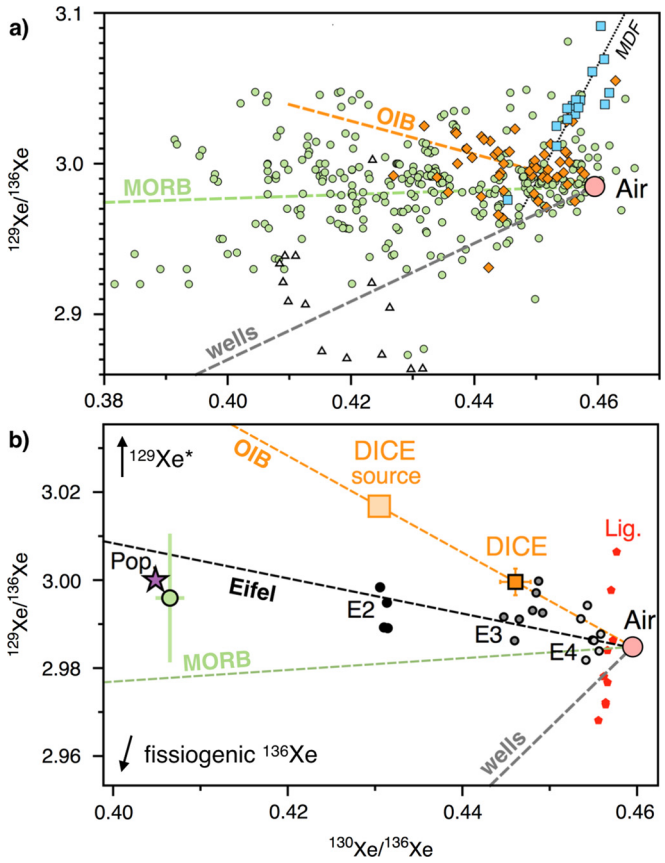

Fig. 8. $^{129}Xe/^{136}Xe$ vs. $^{130}Xe/^{136}Xe$ diagram showing (a) air (pink circle, Ozima and Podosek, 2002), OIB (Iceland plume, DICE Mukhopadhyay, 2012; orange diamonds), MORBs (green circles; Kunz et al., 1998; Tucker et al., 2012; Parai and Mukhopadhyay, 2015), CO_2 well gases (triangles; Caffee et al., 1999; Holland and Ballentine, 2006) and E1 sample from Eifel (blue squares, Caracausi et al., 2016). Fitting the respective datasets through atmosphere produces the wells, MORB and OIB lines. Mass dependent fractionation line is also represented as MDF. On panel (b), we report the wells, MORB and OIB lines along with E2, E3 and E4 Eifel samples (black, grey and white circles, respectively; this study) and Lignat measurements (red pentagons, labelled Lig.; Moreira et al., 2018). Popping rock sample (Pop., purple star) is from Péron and Moreira (2018). The green point is the average MORB composition compiled by Moreira et al. (2018). The OIB line defined by Iceland samples is distinct from that defined by MORB samples, with a lower $^{129}Xe/^{136}Xe$. Such differences cannot be related solely through recycling atmospheric Xe or by adding fissiogenic ^{136}Xe to MORB Xe (Mukhopadhyay, 2012). Given that the MORB reservoir has a higher I/Xe ratio, higher $^{129}Xe/^{136}Xe$ in OIB can only be accounted for by lower (Pu-U)/Xe in the OIB source. Irrespective of their degassing histories, the mantle sources of Eifel gas and popping rocks appear to have preserved similar $^{129}Xe/^{136}Xe$, although the main fissiogenic sources of ^{136}Xe excess are different (^{244}Pu for popping rocks and ^{238}U for the Eifel gas).

cesses of mantle-derived $^{129}Xe^*$ (Figs. 7–8). Such deviations are not observed for the Eifel gas, which plots exactly on the mantle-air mixing line in $^{129}Xe/^{130}Xe$-$^{136}Xe/^{130}Xe$ space (Fig. 7). Although we cannot rule out the potential for small crustal inputs, these data seem to exclude a significant crustal contribution in the Eifel gas. Likewise, relative abundances of the non-reactive components reported by Bräuer et al. (2013) together with the isotope signatures of the stable isotopes, especially of the major magmatic volatile CO_2, do not indicate any crustal contribution in the Victoriaquelle and Schwefelquelle wells, but seem to be characteristic for a MORB-like reservoir. Similarly, the low $^3He/^4He$ and high $^{40}Ar/^{36}Ar$ ratios in the Eifel region (Victoriaquelle and Schwefelquelle gases) have been suggested to be the result of magma ageing resulting in the continuous radioactive decay of U, Th and ^{40}K within the magmatic reservoir (Bräuer et al., 2013). However, once again this process cannot account for the observed excesses in ^{238}U-derived Xe given that these correlate with mantle-derived $^{129}Xe^*$ (Fig. 3) indicating that the low $^3He/^4He$, high $^{40}Ar/^{36}Ar$ and ^{238}U-derived Xe excesses all have a similar mantle origin.

Subduction recycling of altered oceanic crust with associated transport of U to the mantle over the last 2 billion years can make a significant contribution to U recycling into the mantle, potentially even dominating the total net U-addition to the post-Archean convecting mantle (Pettke et al., 2018). Portions of the mantle thought to derive from melting of these ancient sections of oceanic crust, referred to as HIMU, could have been significantly enriched in ^{238}U through this process. These are defined by He isotope ratios from 4.5 Ra to 12.8 Ra and Ne isotopic signatures that extend from the MORB range to compositions less nucleogenic than MORBs (Parai et al., 2009; Day and Hilton, 2011). Noble gases in mantle xenoliths from various European Cenozoic volcanic provinces depict mixtures between DMM-EM-HIMU end-members within the European sub-continental mantle source (e.g., Dunai and Baur, 1995). A HIMU-like source contribution in Eifel free gas samples could notably account for both the low $^3He/^4He$ (~4–5*Ra; Bräuer et al., 2013) and high contribution from ^{238}U fission derived Xe. The $^3He/^4He$ values of ultramafic xenoliths from the Eifel Quaternary volcanic field "Dreiser Weiher" (5.97 ± 0.49 Ra; Buikin et al., 2005) are in good agreement with the intrinsic signature of the subcontinental lithospheric mantle (SCLM; 6±1 Ra) although the authors acknowledge that there is also an obvious similarity to oceanic HIMU islands (Buikin et al., 2005). However, for the ^{238}U-derived

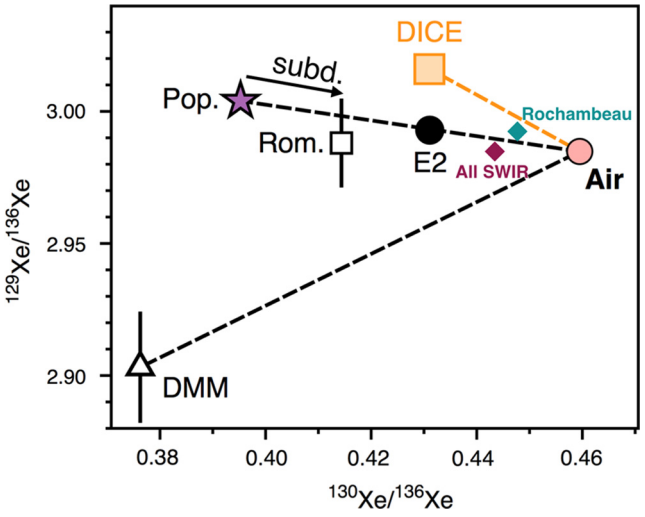

Fig. 9. $^{129}Xe/^{136}Xe$ vs. $^{130}Xe/^{136}Xe$ diagram showing air (Ozima and Podosek, 2002), mantle source compositions of OIB (DICE, Mukhopadhyay, 2012), popping rocks (Pop.; Péron and Moreira, 2018), the DMM (Tucker et al., 2012) and HIMU-type MORB from the north of the Romanche fracture zone (Rom.; Tucker et al., 2012). Also displayed are the error-weighted average compositions of the Rochambeau Rift (Pető et al., 2013) and SWIR Orthogonal Supersegment (Parai and Mukhopadhyay, 2015). The source of the HIMU-type MORB in the Romanche fracture zone is explained by addition of subducted air to the mantle source of popping rocks. The composition of Eifel sample E2 ($^{40}Ar/^{36}Ar \sim 8300$) also appears to plot on the MORB-air mixing line, which is at odds with the budget of fission-derived Xe isotopes being dominated by ^{238}U-derived Xe for Eifel, and by ^{244}Pu-derived Xe for popping rocks. A possibility is that the Eifel composition reflects a mixture between a HIMU-type source and a less degassed MORB reservoir, causing the resulting signature to fortuitously plot close to the popping rocks-air mixing line.

Xe in Eifel gas and $^{129}Xe^*$ to both have a HIMU-like origin would imply that transport of subducted crust in the mantle occurred at a time where ^{129}I was still extant, i.e. within 80 Myr after the start of Solar System formation, which is unlikely (Parai and Mukhopadhyay, 2018). The average time commonly postulated for ageing of a HIMU-type source component is 1.9 Ga (Pettke et al., 2018). We therefore conclude that at least two mantle sources, one of which being of HIMU-type and the other being little degassed, may be required to account for the geochemical signature of the Eifel gas.

Xenon isotopic measurements from equatorial Mid-Atlantic Ridge basalts previously indicated the mantle sources of DMMs, popping rocks and HIMU-influenced MORBs to have distinct $^{129}Xe/^{136}Xe$ (Tucker et al., 2012). The mantle source of North Mid-Atlantic Ridge samples (popping rock and HIMU-influenced MORBs) appears to have a $^{129}Xe/^{136}Xe$ that is intermediate between the DMM (low $^{129}Xe/^{136}Xe$) and OIB (high $^{129}Xe/^{136}Xe$) (Fig. 9). The lower $^{129}Xe/^{136}Xe$ of the DMM is consistent with a more degassed source than the mantle source of Mid-Atlantic Ridge samples. The high proportion of Pu-derived Xe in Romanche fracture zone samples (63^{+18}_{-18}%; labelled "HIMU-like MORB" in Tucker et al., 2012) was interpreted as requiring contribution from a less degassed mantle component to dominate over the ^{238}U-produced fission Xe in the recycled crust. More degassed sources will indeed have lower concentrations of primordial Xe isotopes, $^{129}Xe^*$ and Pu-derived Xe, such that adding ^{136}Xe from ^{238}U fission will produce lower $^{129}Xe/^{136}Xe$. Any addition of HIMU-like material to an OIB-like component would therefore lower the mantle source $^{129}Xe/^{136}Xe$ from high values akin to the Icelandic plume, toward MORB-like values. However, the recently determined Xe isotope composition of popping rocks (compilation from Moreira et al., 2018; Péron and Moreira, 2018) is different from that used by Tucker et al. (2012) to define the MORB end-member. This newly determined Xe isotope composition of the popping rock mantle source, representative of the convective mantle, has high Pu–Xe/(Pu+U)–Xe (99^{+1}_{-78}%, Table 1) and $^{129}Xe/^{136}Xe$ (similar to that of previously defined HIMU-influenced MORB mantle source at the Romanche fracture zone, Tucker et al., 2012; Fig. 9). HIMU-influenced MORBs defined by Tucker et al. (2012) might therefore represent the same MORB source as that of popping rocks, with a higher contribution from the atmospheric component (Fig. 9). The overlapping Pu–Xe/(Pu+U)–Xe of 99^{+1}_{-78}% for popping rocks (Péron and Moreira, 2018) and 63^{+18}_{-18}% for HIMU-influenced MORBs (Tucker et al., 2012) suggests that contribution of a deep undegassed source to the HIMU mantle defined by Tucker et al. (2012) may no longer be required.

As witnessed by its high $^{40}Ar/^{36}Ar$ and ^{238}U-derived Xe contribution, the Eifel gas has a large radiogenic contribution. However, the observation that the mantle sources of popping rocks and Eifel appear to have similar $^{129}Xe/^{136}Xe$ ratios indicates that the Eifel gas cannot be solely related to the DMM. To account for both the high $^{129}Xe/^{136}Xe$ relative to the DMM (Fig. 9) and low Pu- to U-derived fission Xe of the Eifel source may require contributions from both an undegassed reservoir with high $^{129}Xe/^{136}Xe$, and a highly degassed HIMU component primarily containing fissiogenic Xe continuously produced from the spontaneous decay of ^{238}U throughout its residence in the mantle. The undegassed reservoir with high $^{129}Xe/^{136}Xe$ is required to have a high I/Xe to account for the MORB-like $^{129}Xe/^{130}Xe$ of the Eifel mantle source (Fig. 4), and could not therefore correspond to a deep OIB-like reservoir akin to the Icelandic plume. Such a reservoir may have originated from a similar mantle source to that of MORB (popping rock and HIMU-like MORB) but with an even lower degree of degassing. The existence of this undegassed MORB reservoir remains to be proven although it is not inconceivable that sections of the mantle have remained less degassed than those currently expressed at mid ocean ridges. Addition of recycled, subduction-related material to such an undegassed source could have lowered the $^{129}Xe/^{136}Xe$ of the Eifel mantle source to produce intermediate $^{129}Xe/^{136}Xe$ values akin to that of the MORB mantle source. A promising avenue of investigation to further improve the deconvolution of mantle-derived signatures and better determine the $^{244}Pu/^{238}U$ of mantle reservoirs would be to better constrain the Xe fission spectrum of ^{244}Pu. Also note that the distribution of Pu in the early mantle is poorly constrained and often assumed to be similar to that of U. However, the potential for U and Pu to have been heterogeneously distributed in the early mantle, and for variations in the Pu- to U-derived fission Xe to not only be related to differences in degassing states, remains to be explored.

5. Conclusion

The origin of the CEVP has remained enigmatic given the potential for an OIB-like source to contribute to intraplate volcanism in the Eifel region. In this contribution, we show that the mantle source beneath Eifel, and by extension the CEVP, has a geochemical signature akin to the upper mantle reservoir sampled at mid ocean ridges. Accurate determination of $^{244}Pu/^{238}U$ ratios in mantle-derived samples has been commonly used to address the degassing states of corresponding mantle reservoirs. According to their Pu–Xe/(Pu+U)–Xe, the sources for Eifel volcanism and popping rocks would however have experienced extensive and limited degassing, respectively. The MORB reservoir therefore appears to exhibit variable Pu–Xe/(Pu+U)–Xe ratios which indicates that the presence of two mantle reservoirs (MORB and OIB) cannot be fully substantiated anymore solely by differences in Pu–Xe/(Pu+U)–Xe ratio. Differences between MORB and OIB sources would therefore only reside in the occurrence of solar-derived Ne, higher $^{20}Ne/^{21}Ne_E$ and higher $^{3}He/^{4}He$ in OIB, as well as higher $^{40}Ar/^{36}Ar$ and I/Xe in MORB relative to OIB. Interestingly, to account for both the high $^{129}Xe/^{136}Xe$ relative to the DMM and low Pu- to

U-derived fission Xe in the Eifel source may require contributions from both an undegassed MORB-like reservoir, with high $^{129}Xe/^{136}Xe$, and a deep HIMU-like mantle source also accounting for the low $^{3}He/^{4}He$ seen in Eifel gas. Although our results refute a deep plume OIB-like origin for volcanism in Eifel, Ne and Xe systematics therefore point toward contributions from multiple reservoirs with different degassing histories, originating from different depths in the mantle beneath the CEVP.

Author contributions

B.M, D.V.B, and M.W.B developed the Giggenbach sampling/storage method for noble gases. D.V.B, M.W.B, and B.M collected the samples. D.V.B. and M.W.B. did the noble gas analyses, discussed the results and their interpretations, and wrote the manuscript. B.M. and A.C. discussed the results and their interpretations, and contributed to writing the manuscript.

Data and materials availability

All data needed to evaluate the conclusions in the paper are present in the paper and/or the Supplementary Materials. Additional data related to this paper may be requested from the authors.

Competing interests

The authors declare that they have no competing interests.

Acknowledgements

We gratefully thank Rita Parai for providing us with the MATLAB code developed by Parai and Mukhopadhyay (2015). Sujoy Mukhopadhyay is thanked for his fruitful insights into how to improve our manuscript. We also thank Manuel Moreira for his review, and for having initiated this study by triggering insightful discussions about the origin of volcanism beneath Central Europe. This study was supported by the European Research Council (grant PHOTONIS 695618 to B.M.). This is CRPG contribution N° 2693.

Appendix A. Supplementary material

Supplementary material related to this article can be found online at https://doi.org/10.1016/j.epsl.2019.115766.

References

Allègre, C.J., Staudacher, T., Sarda, P., Kurz, M., 1983. Constraints on evolution of Earth's mantle from rare gas systematics. Nature 303 (5920), 762.
Avice, G., Marty, B., Burgess, R., Hofmann, A., Philippot, P., Zahnle, K., Zakharov, D., 2018. Evolution of atmospheric xenon and other noble gases inferred from Archean to Paleoproterozoic rocks. Geochim. Cosmochim. Acta 232, 82–100.
Azbel, I.Y., Tolstikhin, I.N., 1993. Accretion and early degassing of the Earth: constraints from Pu–U–I–Xe Isotopic systematics. Meteoritics 28 (5), 609–621.
Ballentine, C.J., Marty, B., Lollar, B.S., Cassidy, M., 2005. Neon isotopes constrain convection and volatile origin in the Earth's mantle. Nature 433 (7021), 33.
Bräuer, K., Kämpf, H., Niedermann, S., Strauch, G., 2013. Indications for the existence of different magmatic reservoirs beneath the Eifel area (Germany): a multi-isotope (C, N, He, Ne, Ar) approach. Chem. Geol. 356, 193–208.
Buikin, A., Trieloff, M., Hopp, J., Althaus, T., Korochantseva, E., Schwarz, W.H., Altherr, R., 2005. Noble gas isotopes suggest deep mantle plume source of late Cenozoic mafic alkaline volcanism in Europe. Earth Planet. Sci. Lett. 230 (1–2), 143–162.
Burnard, P., Graham, D., Turner, G., 1997. Vesicle-specific noble gas analyses of "popping rock": implications for primordial noble gases in Earth. Science 276 (5312), 568–571.
Caffee, M.W., Hudson, G.B., Velsko, C., Huss, G.R., Alexander, E.C., Chivas, A.R., 1999. Primordial noble gases from Earth's mantle: identification of a primitive volatile component. Science 285 (5436), 2115–2118.
Caracausi, A., Avice, G., Burnard, P.G., Füri, E., Marty, B., 2016. Chondritic xenon in the Earth's mantle. Nature 533 (7601), 82.
Clay, P.L., Burgess, R., Busemann, H., Ruzié-Hamilton, L., Joachim, B., Day, J.M., Ballentine, C.J., 2017. Halogens in chondritic meteorites and terrestrial accretion. Nature 551 (7682), 614.
Colin, A., Moreira, M., Gautheron, C., Burnard, P., 2015. Constraints on the noble gas composition of the deep mantle by bubble-by-bubble analysis of a volcanic glass sample from Iceland. Chem. Geol. 417, 173–183.
Craig, H., Lupton, J.E., 1976. Primordial neon, helium, and hydrogen in oceanic basalts. Earth Planet. Sci. Lett. 31 (3), 369–385.
Day, J.M., Hilton, D.R., 2011. Origin of $^{3}He/^{4}He$ ratios in HIMU-type basalts constrained from Canary Island lavas. Earth Planet. Sci. Lett. 305 (1–2), 226–234.
Dunai, T.J., Baur, H., 1995. Helium, neon, and argon systematics of the European subcontinental mantle: implications for its geochemical evolution. Geochim. Cosmochim. Acta 59 (13), 2767–2783.
Giggenbach, W.F., Goguel, R.L., 1989. Collection and Analysis of Geothermal and Volcanic Water and Gas Discharges. Chem. DIV. DSIR REPT. CD 2401, 81 pp.
Goes, S., Spakman, W., Bijwaard, H., 1999. A lower mantle source for central European volcanism. Science 286 (5446), 1928–1931.
Graham, D.W., 2002. Noble gas isotope geochemistry of mid-ocean ridge and ocean island basalts: characterization of mantle source reservoirs. Rev. Mineral. Geochem. 47 (1), 247–317.
Hallis, L.J., Huss, G.R., Nagashima, K., Taylor, G.J., Halldórsson, S.A., Hilton, D.R., Meech, K.J., 2015. Evidence for primordial water in Earth's deep mantle. Science 350 (6262), 795–797.
Hart, S.R., Hauri, E.H., Oschmann, L.A., Whitehead, J.A., 1992. Mantle plumes and entrainment—isotopic evidence. Science 256, 517–520.
Holland, G., Ballentine, C.J., 2006. Seawater subduction controls the heavy noble gas composition of the mantle. Nature 441 (7090), 186.
Holland, G., Cassidy, M., Ballentine, C.J., 2009. Meteorite Kr in Earth's mantle suggests a late accretionary source for the atmosphere. Science 326 (5959), 1522–1525.
Holland, G., Lollar, B.S., Li, L., Lacrampe-Couloume, G., Slater, G.F., Ballentine, C.J., 2013. Deep fracture fluids isolated in the crust since the Precambrian era. Nature 497 (7449), 357.
Honda, M., McDougall, I., Patterson, D.B., Doulgeris, A., Clague, D.A., 1993. Noble gases in submarine pillow basalt glasses from Loihi and Kilauea, Hawaii: a solar component in the Earth. Geochim. Cosmochim. Acta 57 (4), 859–874.
Jackson, C.R., Bennett, N.R., Du, Z., Cottrell, E., Fei, Y., 2018. Early episodes of high-pressure core formation preserved in plume mantle. Nature 553 (7689), 491.
Kellogg, L.H., Wasserburg, G.J., 1990. The role of plumes in mantle helium fluxes. Earth Planet. Sci. Lett. 99 (3), 276–289.
Kunz, J., Staudacher, T., Allegre, C.J., 1998. Plutonium-fission xenon found in Earth's mantle. Science 280 (5365), 877–880.
Loewen, M.W., Graham, D.W., Bindeman, I.N., Lupton, J.E., Garcia, M.O., 2019. Hydrogen isotopes in high $^{3}He/^{4}He$ submarine basalts: primordial vs. recycled water and the veil of mantle enrichment. Earth Planet. Sci. Lett. 508, 62–73.
Marty, B., 1989. Neon and xenon isotopes in MORB: implications for the earth-atmosphere evolution. Earth Planet. Sci. Lett. 94 (1–2), 45–56.
Meshik, A., Hohenberg, C., Pravdivtseva, O., Burnett, D., 2014. Heavy noble gases in solar wind delivered by Genesis mission. Geochim. Cosmochim. Acta 127, 326–347.
Moreira, M., Kunz, J., Allegre, C., 1998. Rare gas systematics in popping rock: isotopic and elemental compositions in the upper mantle. Science 279 (5354), 1178–1181.
Moreira, M., Rouchon, V., Muller, E., Noirez, S., 2018. The xenon isotopic signature of the mantle beneath Massif Central. Geochem. Perspect. Lett. 6, 28–32.
Mukhopadhyay, S., 2012. Early differentiation and volatile accretion recorded in deep-mantle neon and xenon. Nature 486 (7401), 101.
Mukhopadhyay, S., Parai, R., 2019. Noble gases: a record of Earth's evolution and mantle dynamics. Annu. Rev. Earth Planet. Sci. 47, 389–419.
Ozima, M., Podosek, F.A., 2002. Noble Gas Geochemistry. Cambridge University Press, Cambridge.
Parai, R., Mukhopadhyay, S., 2015. The evolution of MORB and plume mantle volatile budgets: constraints from fission Xe isotopes in Southwest Indian Ridge basalts. Geochem. Geophys. Geosyst. 16 (3), 719–735.
Parai, P., Mukhopadhyay, S., Lassiter, J.C., 2009. New constraints on the HIMU mantle from neon and helium isotopic compositions of basalts from the Cook–Austral Islands. Earth Planet. Sci. Lett. 277, 253–261.
Parai, R., Mukhopadhyay, S., 2018. Xenon isotopic constraints on the history of volatile recycling into the mantle. Nature 560 (7717), 223.
Péron, S., Moreira, M., Colin, A., Arbaret, L., Putlitz, B., Kurz, M.D., 2016. Neon isotopic composition of the mantle constrained by single vesicle analyses. Earth Planet. Sci. Lett. 449, 145–154.
Péron, S., Moreira, M., 2018. Onset of volatile recycling into the mantle determined by xenon anomalies. Geochem. Perspect. Lett. 9, 21–25.
Pető, M.K., Mukhopadhyay, S., Kelley, K.A., 2013. Heterogeneities from the first 100 million years recorded in deep mantle noble gases from the Northern Lau Back-arc Basin. Earth Planet. Sci. Lett. 369, 13–23.
Pettke, T., Kodolányi, J., Kamber, B.S., 2018. From ocean to mantle: new evidence for U-cycling with implications for the HIMU source and the secular Pb isotope evolution of Earth's mantle. Lithos 316, 66–76.

Porcelli, D., Ballentine, C.J., 2002. Models for distribution of terrestrial noble gases and evolution of the atmosphere. Rev. Mineral. Geochem. 47 (1), 411–480.
Porcelli, D., Wasserburg, G.J., 1995. Mass transfer of helium, neon, argon, and xenon through a steady-state upper mantle. Geochim. Cosmochim. Acta 59 (23), 4921–4937.
Press, W.H., Teukolsky, S.A., Vetterling, W.T., Flannery, B.P., 1992. Numerical Recipes in C: The Art of Scientific Computing, second edition. Cambridge University Press, New York.
Ritter, J.R.R., 2007. The seismic signature of the Eifel plume. In: Ritter, J.R.R., Christensen, U.R. (Eds.), Mantle Plumes: A Multidisciplinary Approach. Springer-Verlag, Berlin, Heidelberg, pp. 379–404.
Sarda, P., Staudacher, T., Allègre, C.J., 1985. $^{40}Ar/^{36}Ar$ in MORB glasses: constraints on atmosphere and mantle evolution. Earth Planet. Sci. Lett. 72 (4), 357–375.
Schmincke, H.U., 2007. The Quaternary volcanic fields of the east and west Eifel (Germany). In: Mantle Plumes. Springer, Berlin, Heidelberg, pp. 241–322.
Stuart, F.M., Lass-Evans, S., Fitton, J.G., Ellam, R.M., 2003. High $^{3}He/^{4}He$ ratios in picritic basalts from Baffin Island and the role of a mixed reservoir in mantle plumes. Nature 424 (6944), 57.
Tucker, J.M., Mukhopadhyay, S., Schilling, J.G., 2012. The heavy noble gas composition of the depleted MORB mantle (DMM) and its implications for the preservation of heterogeneities in the mantle. Earth Planet. Sci. Lett. 355, 244–254.
Weber, M., Bock, G., Budweg, M., 2007. Upper mantle structure beneath the Eifel from receiver functions. In: Ritter, J.R.R., Christensen, U.R. (Eds.), Mantle Plumes: A Multidisciplinary Approach. Springer-Verlag, Berlin, Heidelberg, pp. 405–415.
Williams, C.D., Mukhopadhyay, S., 2019. Capture of nebular gases during Earth's accretion is preserved in deep-mantle neon. Nature 565 (7737), 78.
Yokochi, R., Marty, B., 2004. A determination of the neon isotopic composition of the deep mantle. Earth Planet. Sci. Lett. 225 (1–2), 77–88.
Zindler, A., Hart, S., 1986. Chemical geodynamics. Annu. Rev. Earth Planet. Sci. 14, 493–571.

Precambrian Research 336 (2020) 105505

Appendix E

Contents lists available at ScienceDirect

Precambrian Research

journal homepage: www.elsevier.com/locate/precamres

Xenon isotopes in Archean and Proterozoic insoluble organic matter: A robust indicator of syngenecity?

D.V. Bekaert[a,*], M.W. Broadley[a], F. Delarue[b], Z. Druzhinina[c], G. Paris[a], F. Robert[b], K. Sugitani[d], B. Marty[a]

[a] Centre de Recherches Pétrographiques et Géochimiques, CRPG-CNRS, Université de Lorraine, UMR 7358, 15 rue Notre Dame des Pauvres, BP 20, 54501 Vandoeuvre-lès-Nancy, France
[b] IMPMC Sorbonne Universités—MNHN, UPMC Univ Paris 06, UMR CNRS 7590, IRD UMR 206, Paris, France
[c] California Institute of Technology, Division of Geological and Planetary Sciences, 1200 E. California Blvd, Pasadena CA91125, USA
[d] Department of Environmental Engineering and Architecture, Graduate School of Environmental Studies, Nagoya University, Nagoya 464-8601, Japan

A B S T R A C T

Insoluble organic materials (kerogens) isolated from ancient sedimentary rocks provide unique insights into the evolution of early life. However, establishing whether these kerogens are indeed syngenetic with the deposition of associated sedimentary host rocks, or contain contribution from episodes of secondary deposition, is not straightforward. Novel geochemical criterions are therefore required to test the syngenetic origin of Archean organic materials. On the one hand, the occurrence of mass-independent fractionation of sulphur isotopes (MIF-S) provides a tool to test the Archean origin of ancient sedimentary rocks. Determining the isotope composition of sulphur within kerogens whilst limiting the contribution from associated minerals (e.g., nano-pyrites) is however challenging. On the other hand, the Xe isotope composition of the Archean atmosphere has been shown to present enrichments in the light isotopes relative to its modern composition, together with a mono-isotopic deficit in ^{129}Xe. Given that the isotopic composition of atmospheric Xe evolved through time by mass dependent fractionation (MDF) until ~2.5 to 2.0 Ga, the degree of MDF of Xe isotopes trapped in kerogens could provide a time stamp for the last chemical equilibration between organic matter and the atmosphere. However, the extent to which geological processes could affect the signature of Xe trapped in ancient kerogen remains unclear. In this contribution, we present new Ar, Kr and Xe isotopic data for four kerogens isolated from 3.4 to 1.8 Gy-old cherts and confirm that Xe isotopes from the Archean atmosphere can be retained within kerogens. However, new Xe-derived model ages are lower than expected from the ages of host rocks, indicating that initially trapped Xe components were at least partially lost and/or mixed together with some Xe carried out by younger generations of organic materials, therefore complicating the Xe-based dating method. Whilst non-null Δ^{33}S values and ^{129}Xe deficits relative to modern atmosphere constitute reliable imprints from the Archean atmosphere, using Xe isotopes to provide information on the syngenetic origin of ancient organic matter appears to be a promising – but not unequivocal – tool that calls for further analytical development.

1. Introduction

Our understanding of the early Earth is limited by the scarcity of well-preserved ancient samples because of metamorphism and alteration (Kamber and Webb, 2001). The terrestrial rock record, which constitutes the primary source of record of primitive life, only extends to 4.0 Ga (Acasta gneisses; Bowring and Williams, 1999). Evidence for extensive water-rock interaction from the high δ^{18}O recorded in the Jack Hills zircons can further extend the evidence for crust and oceans on Earth to 4.4 Ga (Peck et al., 2001; Wilde et al., 2001). Jack Hills zircons may as well hold the oldest evidence (4.1 Gy-old) for biogenic organic carbon, as indicated by negative $\delta^{13}C_{PDB}$ anomalies measured from primary graphite inclusions (Bell et al., 2015). Interpreted as witness for autotrophic metabolisms such as photosynthesis, such light carbon isotope signatures were also determined in 3.95 Ga ($\delta^{13}C \sim -25.6$‰; Tashiro et al., 2017) and in 3.7 Ga ($\delta^{13}C_{PDB} \sim -19$‰; Rosing, 1999) early Archean rocks. However, various abiotic processes might as well produce isotopically light organic compounds during hydrocarbon formation by kinetically controlled polymerization reactions, such as the Fischer-Tropsch reaction or abiogenic CH_4 formation from HCO_3^- under hydrothermal conditions (Lollar et al., 2002; Horita, 2005). Likewise, we note that the Insoluble Organic Matter (IOM) in primitive carbonaceous meteorites is ^{13}C-poor, with $\delta^{13}C_{PDB}$ ranging from ≈ -34 to -8‰ (Alexander et al., 2007), so some of the light carbon isotope signatures in ancient rocks could as well be inherited from extra-terrestrial precursors. This implies that the assessment of biogenicity from isotopic measurements may require combination with additional analyses (e.g., morphology, population distributions, Raman spectroscopy, and/or elemental distributions) to be valuable (Oehler and Cady, 2014). Whilst 3.8 Gyr-old banded iron formations in Isua (Greenland) may be related to the microbial oxidation of ferrous iron (Konhauser et al., 2002), positive identifications of microfossils do not extend to more than 3.5 Ga (Walter et al., 1980; Allwood et al., 2006;

* Corresponding author.
E-mail address: dbekaert@crpg.cnrs-nancy.fr (D.V. Bekaert).

https://doi.org/10.1016/j.precamres.2019.105505
Received 17 August 2019; Received in revised form 15 October 2019; Accepted 16 October 2019
Available online 18 October 2019

Alleon et al., 2018). Older potential remnants of life (Mojzsis et al., 1996; McKeegan et al., 2007) are still debated (van Zuilen et al., 2002; Lepland et al., 2005). Ambiguities and controversies therefore persist regarding both their biogenicity and syngenecity, with the potential for organic matter (OM) from ancient biological sources to co-exist with organic matter or reduced carbon produced by non-biologic processes, or post-depositional organic contaminants (e.g., Marshall et al., 2012).

In order to unambiguously trace the evolution of early life on Earth, it is essential to show that organic materials recovered from ancient rocks, and often regarded as potential remnants of early life, are biogenic in origin, and syngenetic in age with their host rock. Biogenicity might be inferred from morphological observations if an ancient organic structure resembles recent organic remnants that are now well accepted to be of biological origin (Westall et al., 2001). However, non-biological processes may also produce morphologies similar to biologic structures and generate misinterpretation (e.g., García-Ruiz et al., 2003; Cosmidis and Templeton, 2016). Over the past decade, in-situ 2D and 3D techniques of spectroscopy, mass-spectrometry and microscopy have been developed for evaluating organic matter characteristics at the micrometer-to-sub-micrometer-scale (see Oehler and Cady (2014), for a review). New protocols for sample collection and analysis as well as novel insights into the importance of optimal depositional settings and geologic histories for the preservation of syngenetic biomarkers have therefore been achieved. However, the potential for secondary deposition of OM, younger than the host rocks, precludes non-ambiguous determination of the age of bulk ancient organic materials.

Assessment of OM spatial relationships to surrounding minerals, veins, and fractures provides information regarding the potential occurrence of post depositional organic materials (Oehler and Cady, 2014). In particular, for an ancient organic material to be considered syngenetic with its host rock requires its compositional and structural features to be homogeneous, and indicative of a level of maturity that is consistent with that of the host rock. For instance, investigations about the elemental ratios (H/C and N/C used as proxies for organic matter preservation; Delarue et al., 2018) and spectroscopic features (Delarue et al., 2016) provide information on the effect of thermal alteration and indirectly, of the syngenecity of organic materials. The occurrence of mass-independent fractionation of sulphur isotopes can also be used to confirm, to the first order, an Archean origin of ancient sedimentary rocks and organic materials, without however providing an accurate date of formation. Determining the S isotope composition of Archean kerogens is however challenging since it requires contribution from S-bearing mineral phases (e.g., pyrites) to be eliminated or at least corrected for (Bontognali et al., 2012). The origin of early Archean pyrite records is controversial, and whether they reflect microbial activities or fractionations introduced later in the complex history of sedimentary rocks is unknown (e.g., Watanabe et al., 2009; Farquhar et al., 2000). Wacey et al. (2011) notably identified that cellular microstructures from the 3.4-billion-year-old Strelley Pool Formation (Western Australia) were associated with micrometre-sized pyrite crystals interpreted as the metabolic by-products of these cells in a multicomponent sulphur-based bacterial ecosystem.

We recently showed that the isotopic composition of Xe trapped in Archean kerogens could be used to provide model-ages for Archean organic materials (Bekaert et al., 2018). This Xe-based dating method relies on the observation that the isotopic composition of Xe in the Archean atmosphere has evolved through time by MDF (Pujol et al., 2011; Avice et al., 2018) from a precursor comprising cometary and chondritic contributions (referred to as U-Xe; Marty et al., 2017). Assuming that the evolution of Xe isotopes in the terrestrial atmosphere was a global, continuous, and protracted process, Bekaert et al. (2018) utilized literature data from quartz and barite fluid inclusions (ages and degrees of mass dependent fractionation of trapped Xe) to compute a power law evolution curve for the isotopic composition of atmospheric Xe. The analysis of Ar, Kr and Xe isotopes in kerogen MGTKS3 isolated from the 3.0 Gyr-old Farrel Quartzite (Pilbara Craton, Western Australia) revealed that the trapped Xe component was mass-dependently fractionated in favour of the light isotopes relative to the modern day atmosphere composition, with a mono-isotopic deficit in ^{129}Xe, whereas lighter noble gases (Kr isotopes, ^{38}Ar/^{36}Ar) had a modern atmosphere-like signature (Bekaert et al., 2018). Such a mono-isotopic deficit in ^{129}Xe relative to the modern atmosphere composition is symptomatic of the Archean atmosphere, reflecting the fact that mantle degassing with high ^{129}Xe/^{130}Xe contributed ^{129}Xe (produced by the decay of extinct ^{129}I) to the atmosphere through geological periods of time (Avice et al., 2017). Thus, all observed features of Xe trapped in the Farrel Quartzite kerogen correspond to known properties of the Archean atmosphere, indicating that ancient atmospheric noble gases had been efficiently trapped and preserved over geological timescales within this sample (Bekaert et al., 2018). Reporting the degree of MDF of the trapped Xe component relative to modern atmospheric composition on the power law evolution curve of atmospheric Xe isotopic composition produced a model age of 2.98 ± 0.2 Gyr for the last chemical equilibration between the kerogen and the atmosphere (Bekaert et al., 2018). These concurrent ages of the host rock (3.0 Gyr) and of Xe trapped in kerogen constitute a reliable proof of concept for the Xe-based dating method, and for its ability to produce constraints on the syngenetic origin of ancient kerogens (Bekaert et al., 2018).

The ^{130}Xe enrichment factor (f) relative to ^{36}Ar in kerogen MGTKS3, compared to the modern air composition [$f = ([^{130}Xe]/[^{36}Ar])_{sample}/([^{130}Xe]/[^{36}Ar])_{ATM}$], was high ($f \sim 250$), in line with the efficient preservation of Xe relative to lighter noble gases (Bekaert et al., 2018). Strong retention of Xe in natural organic materials can have multiple causes, including the presence of labyrinth-with-constrictions (Torgersen et al., 2004), single-walled nanotube structures (Simonyan et al., 2001), or the presence of dangling functional groups (for example, −COOH) inside Xe diffusion paths (Kuznetsova et al., 2000). Unusually high retention of heavy noble gases in organic materials has even been experimentally documented (Wacker et al., 1985). However, how geological processes, potentially involving thermal processing and/or multicomponent mixing, could affect the signature of Xe trapped in ancient organic materials, and potentially hamper straightforward constraints to be set on their syngenecity and relation to the host rock, remains to be explored. In this contribution, we present new Ar, Kr and Xe isotopic data for four kerogens isolated from 3.4 to 1.8 Gy-old rocks to investigate the potential for the Xe-based dating method to provide information on the post depositional history of ancient organic matter. We also developed a sample preparation and analytical procedure to analyse the S isotope composition of kerogens with limited contribution from mineral S hosted by micro-pyrites. We tested this protocol on sample kerogen MGTKS3, which, from its Xe-based model age, had been shown to be syngenetic in origin (Bekaert et al., 2018).

2. Materials and methods

2.1. Samples

All kerogens analyzed as part of the present study were isolated from Archean to Proterozoic cherts (3.5 Ga to 1.88 Ga) and have been described by Delarue et al. (2016). The host rocks underwent limited metamorphism, ranging from prehnite-pumpellyite (≤250 °C) to greenschist facies (maximum temperature peak metamorphism of ~350 °C ± 50 °C). The Gunflint chert (hereafter PPRG134, 1.88 Gyr) was collected in the Gunflint Formation, at Port Arthur homocline (Ontario, Canada), which consists in an alternation of banded iron formations and cherts. Farrel Quartzite samples (MGTKS1 and MGTKS1up, 3.0 Gyr) were collected from the Goldsworthy greenstone belt in the Pilbara Craton (Western Australia). They originate from the same geological formation as kerogen MGTKS3 analyzed by Bekaert et al. (2018). MGTKS1up is a bedded black chert that contains microfossils (Sugitani et al., 2007, 2009; House et al., 2013 and references therein) and was most likely deposited in a shallow evaporitic basin influenced by inputs of hydrothermal fluids (Sugahara et al., 2010). The Middle Marker chert (hereafter 07SA22, 3472 ± 5 Myr; Armstrong et al., 1990) corresponds to silicified detrital sediments from the

Barberton greenstone belt (South Africa; Bourbin et al., 2012). The Panorama chert (hereafter PAN1, 3458 ± 1.9 Myr; Thorpe et al., 1992) is a laminated black chert sampled in the Panorama greenstone belt (Pilbara Craton, Western Australia), near the southern margin of the so-called "Trendall Ridge" (Lepot et al., 2013). It belongs to a sedimentary unit deposited in peritidal to inner platform environment (Sugitani et al., 2013). The REE + Y compositions of laterally equivalent cherts suggest precipitation from mixed marine-hydrothermal fluids (Allwood et al., 2010).

2.2. Noble gas analysis

Argon, krypton and xenon were extracted from kerogens by stepwise heating using a filament furnace and following the same extraction, purification and analysis procedure as described by Bekaert et al. (2018). We report here the general outlines of this method. Prior to loading the samples, each basket was degassed 3 times at ~1600 °C for 10 min in order to remove any adsorbed atmospheric noble gases. The samples were wrapped in tantalum foil and loaded into alumina-coated tungsten evaporation baskets (Ted Pella, Inc[@]) before baking the entire furnace at > 150 °C overnight under high vacuum. Kerogen aliquots, weighing between 2 and 14 mg, were heated separately over four temperature steps (~200 °C, ~500 °C, ~800 °C and ~1200 °C, respectively) with Ar, Kr and Xe isotopes systematically measured on the Helix MC Plus (Thermo Fisher[@]) mass spectrometer. Gases released from the kerogens were first passed through an in-line Ti and Ag getter at 650 °C to remove active gas species. Krypton and xenon were then condensed on to a quartz tube at liquid nitrogen temperature for 20 min. The quartz tube was then isolated, and the remaining Ar in the purification line was sequentially exposed to two hot (550 °C; 10 min) and two cold (room temperature; 10 min) Ti getters. Argon was then admitted to the mass spectrometer and measured using peak jumping mode on faraday (^{40}Ar) and compact dynode multiplier (^{36,38}Ar) collectors. Krypton and xenon were then released from the quartz cold finger and purified using the same procedure as Ar. Krypton and xenon were measured using the compact dynode multiplier, with Xe isotopes being measured first, followed by the measurement of Kr isotopes on the same fraction of gas. Blanks were measured at the same temperature as the samples using a basket loaded with empty tantalum foil packets. Aliquots of standards with atmospheric isotopic compositions were analyzed each day and between each sample for subsequent spectrometer mass discrimination corrections. Errors provided for each isotopic ratio of individual measurements correspond to the quadratic sum of the internal error (standard deviation σ_{int} of the given isotopic ratio over the ~20 cycles of sample analysis) and external reproducibility (standard deviation σ_{ext} of the given isotopic ratio over the series of standard analyses). For gas-rich samples (e.g., kerogen 07SA22), multiple analysis of the gas released at a given temperature step allowed computing standard errors (σ/sqrt(n − 1), where n is the number of repeat analyses and σ is the standard deviation of the given isotopic ratio over the repeat analyses). Total blanks over the full range of temperatures were 6×10^{-16}, 4×10^{-18} and 3×10^{-18} mol for ^{36}Ar, ^{84}Kr and ^{130}Xe, respectively, and had atmospheric isotopic compositions. Whereas blank contributions were potentially high for the 400 °C and 1100 °C temperature steps (from < 1% up to 50%), blank contributions associated with the release of potential trapped noble gas components at 600 °C and 800 °C were low, < 2%, so no correction was applied. Blank contributions are reported in Table S1. Isotopic fractionation of Xe relative to the modern atmosphere composition (which we note FXe) was computed by error-weighted correlations following the same procedure as that of Avice et al. (2018), that is, by using the stable, non-fissiogenic, nonradiogenic ^{126,128,130}Xe isotopes, in addition to ^{131}Xe (only negligibly contributed by the fission of ^{238}U).

2.3. Sample preparation and S isotopic analysis

We analyzed three organic samples from very different geological settings for their S isotope composition. The first sample is a S-rich organic matter from the bituminous laminites of Orbagnoux (France, upper Kimmeridgian; Mongenot et al. 1997) for which we analyzed 3 aliquots labelled r-d1 (5.8 mg), r-d2 (5.5 mg) and r-d3 (5.6 mg). These aliquots were first processed in HCl for dissolving carbonates, centrifuged and washed with MilliQ water before starting the common preparation process. The second sample corresponds to 5.0 mg of the Archean Kerogen MGTKS3 isolated from a black chert layer of the 3.0-Gy-old Farrel Quartzite (Pilbara Craton, Western Australia; Delarue et al. 2016; Bekaert et al. 2018). The third sample is 5.6 mg of Insoluble Organic Matter (IOM) from the meteorite GRO 95,502 (Grossman and Brearley, 2005).

The density of organic kerogens generally varies from 1.1 to 1.35 g/cm^3, whilst that of pyrite, and more generally sulphides, is 4.9 – 5.2 g/cm^3. Physical separation in sodium polytungstate heavy liquids (1.2 to 3.0 g/cm^3 depending on the water to sodium polytungstate powder ratio) was therefore chosen to isolate kerogens from potential micro-pyrites and other sulfides grains. Kerogens were first placed in 14 ml plastic tubes together with 4–8 ml of sodium polytungstate. Mixtures were repeatedly agitated before leaving them to settle for 48–72 h. Floating kerogens (hereafter "light fractions") were then collected into clean tubes. A few hours later, the powders sunk to the bottom of the plastic tubes (hereafter "heavy fractions") were also collected into clean tubes together with 1 to 4 ml of sodium polytungstate liquid. In order to reduce the mass fraction of Na in these two separates, we sequentially diluted them with 4–12 ml of MilliQ water, agitated the mixtures and centrifuged them for 5 min at 4400 rotations per min. The liquid phase was then removed, before adding another 4–12 ml of MilliQ water and repeating the process 5–15 times depending on the sample. Residues were placed into Teflon vials and heated at 90 °C for several hours in order to get rid of remaining water.

To extract sulfur from the light and heavy fractions of the kerogens, each residue was first mixed with 0.5 ml of hydrogen peroxide and heated in closed system for 48 h at 90 °C. Hydrogen peroxide was then evaporated and aqua regia (1 ml) was added to each vial, before heating them in closed system for 68 h at 150 °C. Aqua regia was then evaporated before dissolving each sample in 1 ml of MilliQ water at room temperature.

We purified the samples before analysis. We ran the samples on 0.6 ml of anionic resin Biorad AG1X8 (Paris et al., 2014). Each column with resin was rinsed with 10% V/V HNO3 (2 × 10CV), 33% V/V HCL (2x10CV), 0.5 N HCl (1 × 10CV) before loading a sample. After loading, each column was washed 5 times with MilliQ water (5 × 5CV) and eluted with 0.45 M HNO3 (3 × 2CV). Aliquots were dried down on hotplates with open lids (100 °C, 4 h) and diluted in 5% HNO3 and 2.5% NaOH. The samples were then analyzed on the ThermoScientific Neptune Plus MC-ICP-MS at the CRPG-CNRS using a standard-sample bracketing method (Paris et al., 2013). Samples are run at high resolution using an Aridus-II desolvating membrane to decrease oxide and hydride interferences. The plasma is run at 1000 W and data are acquired as 1 block of 50 cycles of 4.194 s each. The sequence consists of running as standard-sample-standard and measuring the instrumental blank inbetween each of them. After acquisition, raw data are processed offline using a Matlab script to identify and eliminate potential outliers (defined at the 3-sigma limit) within the fifty cycles. The sequence consists of running as standard-sample-standard and measuring the instrumental background inbetween each solution. The bracketing standard used here is a Na_2SO_4 solution, itself calibrated against international standard IAEA S1 and checked against IAEA S2 and S3. After being processed on Matlab, data are corrected for instrumental fractionation, drift and background following Paris et al. (2013) using an excel spreadsheet. $\Delta^{33}S$ is calculated as $\delta'^{33}S - 0.515 * \delta'^{34}S$ with $\delta'^{xx}S = \ln([^{xx}S/^{32}S]_{sample}/[^{xx}S/^{32}S]_{V\text{-}CDT})$.

3. Results

Noble gas abundances and blank contributions are reported in Table S1. Isotope ratios for Ar, Kr and Xe are reported in Tables S2–S4, respectively. Sulphur isotopic ratios are reported in Table S5.

3.1. Noble gas elemental ratios.

^{130}Xe enrichment factors ($f = ([^{130}Xe]/[^{36}Ar])_{sample}/([^{130}Xe]/[^{36}Ar])_{ATM}$) relative to ^{36}Ar and to the composition of modern air are reported in Table S1. The Gunflint kerogen (PPRG134, 1.88 Gyr), which was analyzed twice, shows the lowest f values (3 and 5, respectively), reflecting limited ^{130}Xe enrichment relative to ^{36}Ar and to the modern day atmospheric composition. Older samples show higher f values ($f_{PAN1} \sim 197$, $f_{075A22} \sim 194$ and $f_{MGTKS1up} \sim 388$) of the same order previously found for sample MGTKS3 ($f_{MGTKS3} \sim 250$; Bekaert et al., 2018). The f value for kerogen MGTKS1 is slightly higher ($f_{MGTKS1} \sim 495$). Kerogen PAN1 was reanalyzed, and we found a much higher f value ($f_{PAN1b} \sim 669$) potentially pointing towards a heterogeneous elemental distribution of noble gases in this sample.

Kerogen PPRG134 and 075A22 have the lowest ($\sim 4.10^{-15}$ mol ^{130}Xe/g) and highest ($\sim 1.6.10^{-13}$ mol ^{130}Xe/g) Xe concentrations, respectively, illustrating the fact that Xe concentrations in Archean kerogens can vary over orders of magnitude. The ^{84}Kr/^{130}Xe of kerogens upon stepwise heating (Fig. 1) are also variable and systematically lower than the air ratio. Taken together, these results are in good agreement with heavier noble gases being preferentially trapped/preserved compared to lighter ones, in line with Xe enrichment factors observed in sedimentary rocks (Torgersen et al. 2004).

3.2. Argon isotope data

Argon isotopic data are reported in Table S2 and displayed on Fig. 2. Radioactive decay of ^{40}K via electron capture produces ^{40}Ar. A high ^{40}Ar/^{36}Ar can therefore be considered as an indicator of the sample being ancient (i.e., enough time has elapsed to allow for the build-up of ^{40}Ar) and retentive for noble gases. In this framework, best samples for the Xe-based dating method would be expected to have high ^{40}Ar/^{36}Ar. Sample MGTKS3#2 (Bekaert et al., 2018), given here for comparison, shows increasing ^{40}Ar/^{36}Ar from 200 °C to 800 °C with a maximum ^{40}Ar/^{36}Ar reaching 2272.2 ± 44.5 at 800 °C. The ^{40}Ar/^{36}Ar then decreases at 1200 °C towards an atmospheric-like value (^{40}Ar/^{36}Ar$_{ATM}$ = 298.6; Lee et al., 2006). Among all samples analyzed in the present study, only 07SA22 and PAN1 reach such high ^{40}Ar/^{36}Ar ratios (7273.8 ± 114.5 at 800 °C and 3392.5 ± 21.6 at 500 °C, respectively). Kerogens MGTKS1 and MGTKS1up, although originating from the same geological formation as MGTKS3, exhibit maximum ^{40}Ar/^{36}Ar of ~750. Kerogen PPRG134 shows limited excess of radiogenic ^{40}Ar, with all ^{40}Ar/^{36}Ar ratios being < 320. All ^{38}Ar/^{36}Ar are within error of air composition (Table S2), except for sample MGTKS1up, which exhibits increasing ^{38}Ar/^{36}Ar with temperature (up to 0.2631 ± 0.0117 at 1200 °C) probably related to the release of cosmogenic noble gases trapped in residual mineral phases.

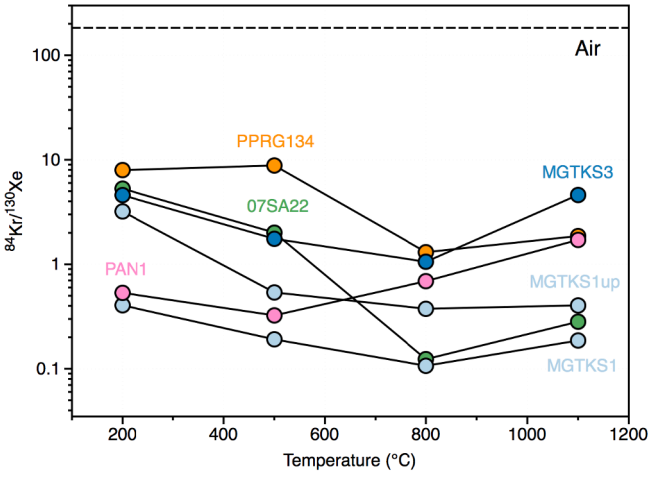

Fig. 1. ^{84}Kr/^{130}Xe in Archean kerogens as a function of temperature, consistent with the preferential retention of heavier noble gases in kerogens. Air composition (^{84}Kr/^{130}Xe = 183; Ozima and Podosek, 2002) is given for comparison.

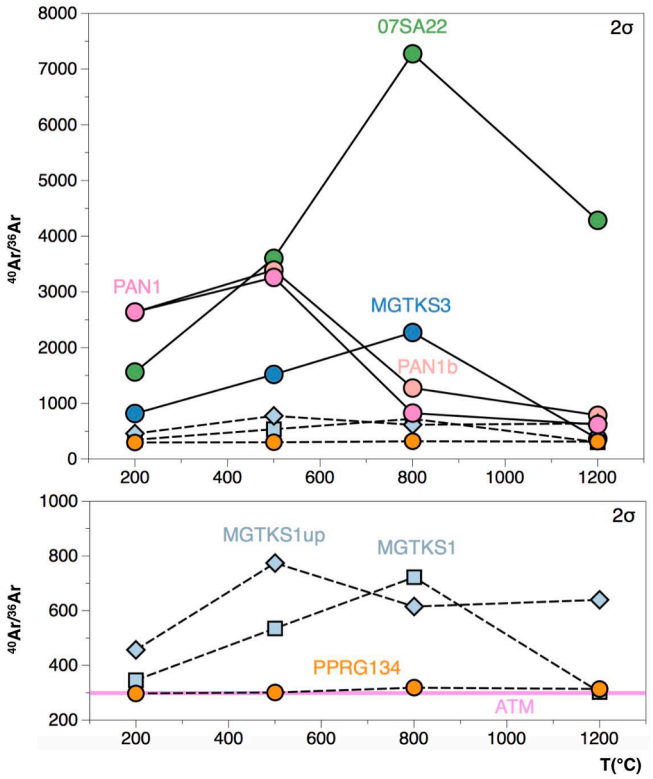

Fig. 2. ^{40}Ar/^{36}Ar in Archean kerogens as a function of temperature. Among all samples analyzed here, only 07SA22 and PAN1 reach ^{40}Ar/^{36}Ar values comparable to that of kerogen MGTKS3, indicating they potentially preserved an ancient noble gas component. Kerogens MGTKS1 and MGTKS1up, although originating from the same geological formation as MGTKS3, exhibit lower ^{40}Ar/^{36}Ar (≤750), suggesting their noble gas signature may have been disrupted and, hence, they might be less suited than kerogen MGTKS3 for the Xe-based dating tool.

3.3. Krypton and xenon isotope data

Krypton and xenon isotopic compositions in kerogens are given using the delta notations normalized to ^{84}Kr and ^{130}Xe, respectively, and to the isotopic composition of the modern atmosphere ($\delta^{i}A_{air}$ (sample) = $(([^{i}A/N)_{sample}/([^{i}A/N)_{air} - 1)*1000$, where A = Kr or Xe, N = ^{84}Kr or ^{130}Xe, and $\delta^{i}Xe_{air}$ (air) = $\delta^{i}Kr_{air}$ (air) = 0‰). Degrees of MDF (F, ‰.u^{-1}) of Kr and Xe isotopes released from the kerogens by stepwise heating are shown in Fig. 3. Apparent negative degrees of MDF for Kr at high temperature (e.g., MGTKS1up; Fig. 4) could be related to the occurrence of isobaric interferences with hydrocarbons at masses 78 (C_6H_6) and 80 (C_6H_8) (Fig. 4). At high temperature, cracking of the kerogen could indeed induce the production of gaseous hydrocarbons that, if not entirely purified during gas preparation, interfere with Kr light isotopes during analysis, therefore causing an overestimation of the corresponding isotopic ratios. For this reason, degrees of MDF reported Fig. 3 were computed using ^{82}Kr/^{84}Kr, ^{83}Kr/^{84}Kr and ^{86}Kr/^{84}Kr only. In addition, note that blank contributions at these temperatures are generally high (on the order of 50%; Table S1), supporting the idea that these signatures do not correspond to Archean atmosphere. The Kr isotopic data associated with the thermal cracking of Archean kerogens (~400 °C) show no significant deviation from the modern atmospheric composition, in line with previous measurements of Kr isotopes in Archean samples purported to have trapped ancient atmosphere (e.g., Pujol et al., 2011; Avice et al., 2017, 2018; Bekaert et al. 2018),

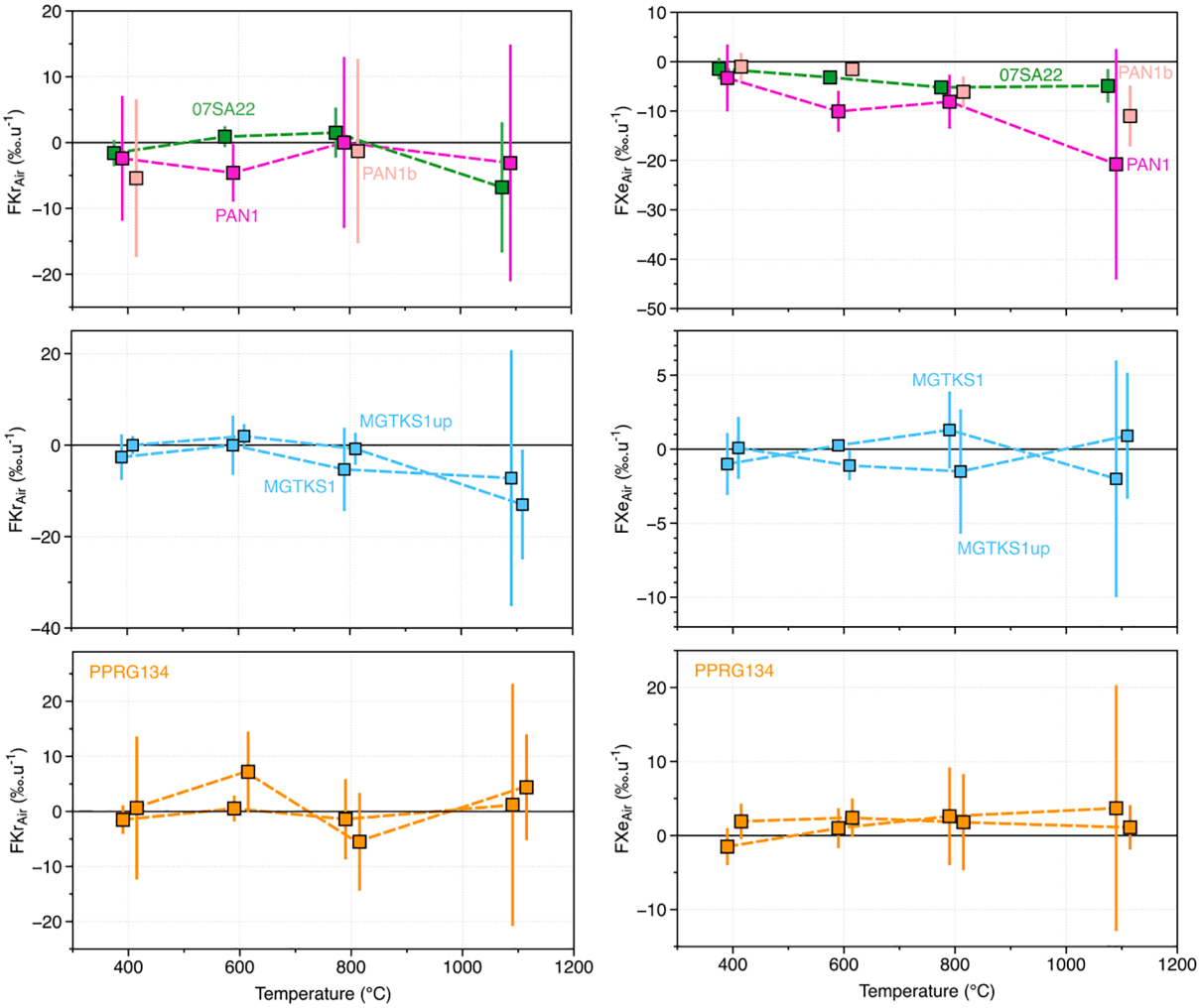

Fig. 3. Degrees of mass fractionation F (‰.u^{-1}) of Kr and Xe isotopes released from the kerogens by stepwise heating. Kr isotopic data for the Archean kerogens analyzed in the present study are similar to the modern day atmosphere composition. Xenon isotopes extracted from the kerogens are generally modern-like, except for samples PAN1 and 07SA22, which are discussed in the main text.

The Xe isotopic composition of the Gunflint kerogen PPRG134 and kerogen MGTKS1 for all heating extractions are indistinguishable from the modern atmospheric composition (Fig. 5). The presence, or not, of small isotopic deviations of Xe in kerogen MGTKS1up relative to the modern atmospheric composition is not clear (Fig. 5), and could be related to the contribution of cosmogenic Xe as suggested by increasing $^{38}Ar/^{36}Ar$ with temperature (Table S2). Conversely, isotopic spectra of Xe trapped in kerogen 07SA22 consistently exhibit excesses of the light isotopes ($^{124–129}Xe$) together with depletions of heavy isotopes ($^{131–136}Xe$) relative to the modern atmosphere (Fig. 6). The trapped Xe components extracted at 500 °C and 800 °C are consistently mass-dependently fractionated ($FXe_{07SA22} = -4.2 \pm 0.65$‰.u^{-1}). The isotopic spectrum of Xe released from kerogen PAN1 at 600 °C shows evidence for the presence of a trapped Xe component that is also mass-dependently fractionated (FXe_{PAN1} = -10.0 ± 4.2‰.u^{-1}), together with a mono-isotopic depletion of ^{129}Xe with respect to the mass-dependent fractionation trend (Fig. 7). Interestingly, Xe isotopes extracted at 600 °C from another aliquot of that kerogen (PAN1b) do not show any deviation from the present-day atmospheric composition, therefore pointing towards a heterogeneous composition of Xe isotopes in kerogen PAN1, in addition to the heterogeneous elemental distribution of noble gases in that sample as reported here above (Fig. 7). At last, once corrected for mass dependent fractionation relative to a starting composition similar to U-Xe, the $^{131–136}Xe$ excesses observed for kerogens 07SA22 and PAN1 are compatible with the presence of products of the spontaneous fission of ^{238}U - and not ^{244}Pu - as commonly observed for Archean sedimentary rocks (Fig. 8; Avice et al., 2017; Bekaert et al., 2018).

3.4. Sulphur isotope data

The S isotopic signatures of light and heavy separates from kerogen MGTKS3 are distinct from the modern atmosphere composition, with positive anomalies in $\Delta^{33}S$ and $\delta^{34}S$ (Fig. 9). Conversely, the Orbagnoux and GRO 95502 kerogens display close to zero $\Delta^{33}S$ values, with negative and positive $\delta^{34}S$ values, respectively (Fig. 9). Slightly negative $\delta^{34}S$ for the Orbagnoux samples are in agreement with values attributed to the microbial reduction of sulfates (Shen et al. 2009), and slightly positive $\delta^{34}S$ for the GRO 95502 IOM also fall within the range of previously reported values for extraterrestrial materials (Gao and Thiemens, 1993a,b).

4. Discussion

4.1. A Xe-based dating-tool for ancient organic matter.

An Archean atmospheric Xe signature associated with syngenetic organic matter corresponds to excesses of the light isotopes ($^{124–129}Xe$) together with depletions of heavy isotopes ($^{131–136}Xe$) relative to the modern atmosphere, with a possible mono-depletion in ^{129}Xe (Avice et al., 2017). The isotopic evolution of atmospheric Xe through

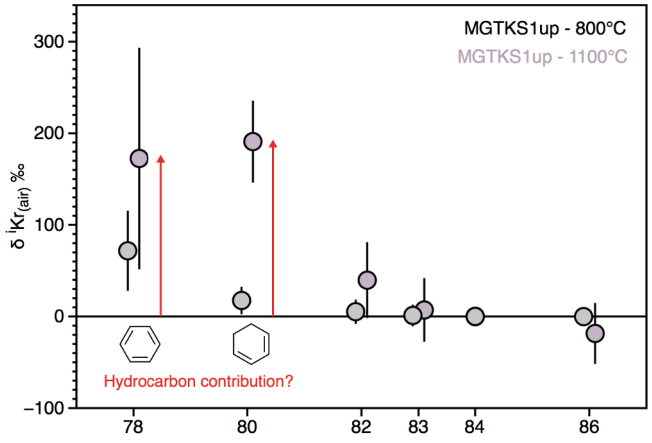

Fig. 4. Kr isotopic spectrum of kerogen MGTKS1up at 800 °C and 1100 °C, normalized to air composition. Although the light isotopes ($^{78,80}Kr/^{84}Kr$) appear to be in excess relative to the atmospheric composition, $^{86}Kr/^{84}Kr$ present no apparent deficits. At high temperature, cracking of the kerogen might induce the production of gaseous hydrocarbons that, if not entirely purified during gas preparation, could interfere with Kr light isotopes (e.g., benzene for ^{78}Kr, C_6H_8 for ^{80}Kr) during analysis, therefore causing an overestimation of the corresponding isotopic ratios. This could notably induce a potential bias in the determination of Kr degree of MDF. For this reason, degrees of Kr MDF (Fig. 3) were computed using $^{82}Kr/^{84}Kr$, $^{83}Kr/^{84}Kr$ and $^{86}Kr/^{84}Kr$ only.

geological times recently attracted broad interest, notably for setting time constraints on the history of surface volatile regassing into the mantle (e.g., Parai and Mukhopadhyay, 2018; Péron and Moreira, 2018). Although the exact driving mechanism behind this isotopic evolution remains debated (Hébrard and Marty, 2014; Zahnle et al., 2019), the MDF of U-Xe towards modern atmospheric values could have resulted from Xe ion-escape to space, a process that can also account for the depletion of Xe in air relative to other noble gases (see Bekaert et al., 2018 for more details). Although recently developed 1-D models of hydrodynamic diffusion-limited hydrogen escape from highly-irradiated CO_2-H_2-H atmospheres (Zahnle et al., 2019) concluded for the ion-escape model to provide the best explanation for Xe's protracted fractionation, at least one additional feature (e.g., limiting escape to narrow polar windows, or limiting Xe escape to brief episodes) is required to make the ion-escape model work over two billion years. Further work is therefore needed to elucidate on the exact conditions accounting for the progressive Xe MDF in the Archean atmosphere. Uncertainties regarding the driving mechanism behind this isotopic evolution do not however preclude the use of Xe isotopes as a paleochronometer. New data from Avice et al. (2018) support the choice of the power law evolution curve defined by Bekaert et al. (2018) as a good proxy for Xe isotopic evolution in the Archean atmosphere (Fig. 10), except for one data point (Fortescue Group, Hamersley Basin, Australia; 2.7 Ga, reported in light grey Fig. 10). This data point leaves the potential for the evolution of atmospheric Xe isotopes to have been discontinuous, but further work is needed to confirm this possibility.

The Xe-based dating method for ancient organic matter also relies on the potential for ancient organic materials to trap and preserve significant amounts of Xe from the Archean atmosphere. The syngenetic origin of organic material cracking below 350 °C is highly disputable since it can originate from several post-deposition contaminations and/or from residual bitumen (soluble fraction of organic matter) for which syngenecity is still an open issue (French et al., 2015). Using Rock-Eval Pyrolysis, thermal cracking of syngenetic Archean kerogens occurs at between 450 and 586 °C (Spangenberg and Frimmel, 2001; Delarue et al., 2018), as observed for kerogens MGTKS3 (Bekaert et al., 2018). Noble gases released in the 400–600 °C range (i.e. at ~500 °C in the present study) for these samples would therefore be closely related to the cracking of a syngenetic and thermorecalcitrant component.

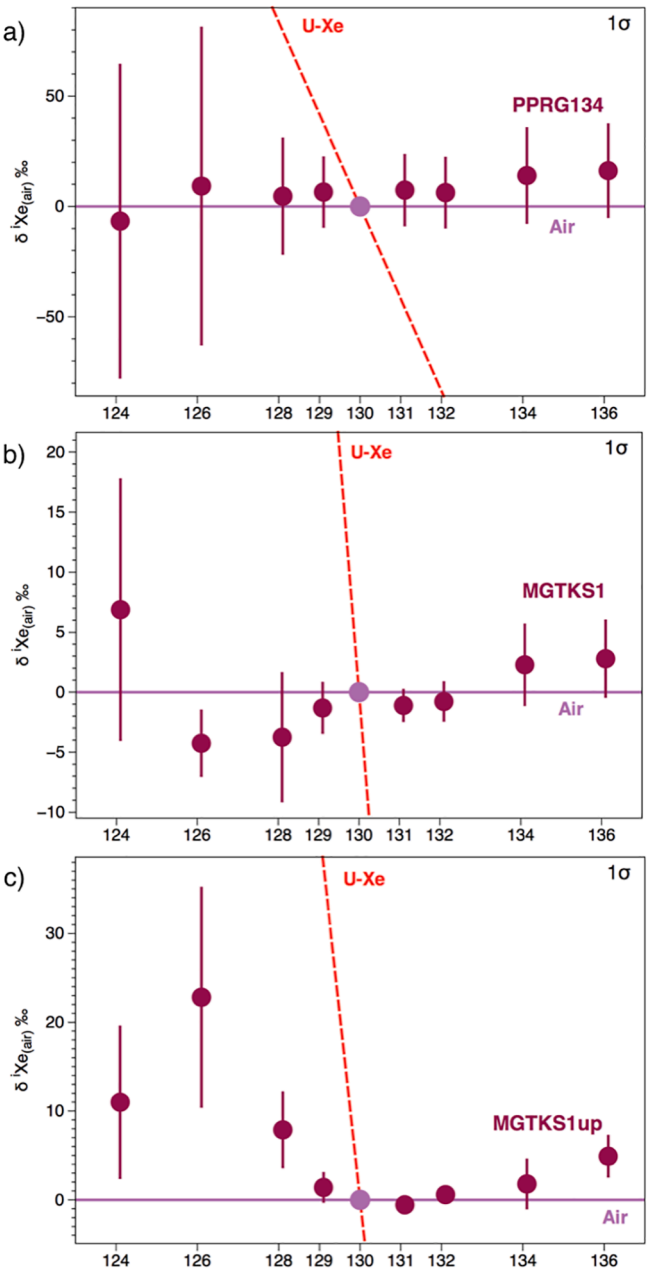

Fig. 5. Xe isotopic spectra of the trapped noble gas component in kerogen PPRG134 (a), MGTKS1 (b) and MGTKS1up (c), normalized to ^{130}Xe and to the modern atmosphere composition (Ozima and Podosek, 2002). Error bars are 1σ. The degree of MDF of U-Xe relative to modern atmosphere is given as a red dashed line for comparison. (For interpretation of the references to colour in this figure legend, the reader is referred to the web version of this article.)

To date, the most recent identification of ancient atmosphere has been proposed for mine fluids younger than 1.85 Ga (Warr et al., 2018). The youngest sample analyzed as part of the present study (1.88 Gyr old, kerogen PPRG134) has a Xe isotope composition that is indistinguishable from that of the modern atmosphere, in agreement with modern-like isotope compositions of the atmosphere being reached ~2 Ga (Bekaert et al. 2018). Sample PPRG134 released only limited amounts of Xe, implying that, if more material could be analyzed, a sufficient level of precision could be reached, allowing potential deviations from the modern atmospheric composition to be detected. In kerogen PPRG134, the low noble gas concentrations and very low ^{130}Xe enrichment factors relative to ^{36}Ar and to the composition of modern air (Table S1) might however indicate that noble gases released from

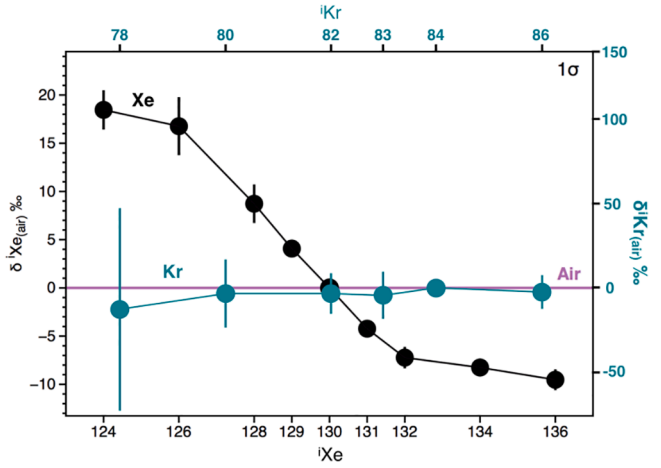

Fig. 6. Kr and Xe isotopic spectra of the trapped noble gas component in kerogen 07SA22, normalized to ^{84}Kr and ^{130}Xe, respectively, and to the modern atmosphere composition (Ozima and Podosek, 2002). Error bars are 1σ.

that sample correspond to adsorbed modern air (Wacker, 1989, Marrocchi and Marty, 2013), with no evidence for the occurrence of an ancient trapped Xe component.

Kerogens 07SA22 and PAN1 show evidence for ancient atmospheric Xe components akin to the one observed in kerogen MGTKS3 (Bekaert et al., 2018). However, as illustrated in Fig. 10, the degrees of MDF of trapped Xe within kerogens 07SA22 ($FXe_{07SA22} = -4.2 \pm 0.65‰.u^{-1}$) and PAN1 ($FXe_{PAN1} = -10.0 \pm 4.2‰.u^{-1}$) produce model ages ($2.32^{+0.10}_{-0.11}$ and $2.99^{+0.33}_{-0.44}$ Gyr-old, respectively) that are lower than those of the corresponding host rocks (3472 ± 5 Myr and 3458 ± 1.9 Myr, respectively; Armstrong et al., 1990; Thorpe et al., 1992) at the one sigma-level. At the two-sigma level, model ages for kerogens 07SA22 and PAN1 are $2.32^{+0.19}_{-0.22}$ and $2.99^{+0.59}_{-1.24}$ Gyr-old, respectively. Given the large uncertainty associated with the model age of kerogen PAN1, it potentially overlaps with the actual age of the host rock at the two-sigma level, although this clearly does not constitute a good match. For the rest of the discussion, the model age for kerogen PAN1 is therefore considered to be lower than that of its host rocks. Variable noble gas concentrations from one kerogen to another possibly reflect differences in the depositional environments of the host rocks, or variable efficiencies at trapping and/or preserving noble gases within organic materials. The next sections discuss the potential mechanisms accounting for lowering the degree of MDF of trapped Xe components during the post-depositional evolution of organic matter, including mixing with a more recent Xe-bearing organic generation and diffusive loss during thermal metamorphism or aqueous alteration.

4.2. Multi-component mixing

The low porosity of cherts is commonly advocated for making the syngenetic organic matter less prone to postdepositional contamination (Derenne et al., 2008). However, Raman spectroscopic data collected on the organic material present within the matrix of the Apex chert, one of the most well studied Archean deposits (e.g., Schopf, 1993; De Gregorio and Sharp, 2006), indicated the presence of two different phases of carbonaceous materials deposited as separate phases in the quartz matrix (Marshall et al., 2012). Hence, several generations of organic materials, of variable ages, could potentially coexist within a given kerogen. In this case, the final degree of MDF of the total trapped Xe component can be formulated as:

$$\delta Xe_{Tot} = \sum_{i=1}^{n} f_i * FXe_i * [Xe]_i$$

where δXe_{tot} is the degree of MDF of the total trapped Xe component, n is the number of coexisting generations of organic materials, f_i is the mass fraction of organic generation i, and FXe_i and $[Xe]_i$ are the degree of MDF and concentration of Xe associated with organic generation i, respectively. Accordingly, the weight a given generation of organic materials (with a given FXe) will have on the Xe isotopic signature of the total kerogen relies on both its mass fraction and Xe concentration. This implies that a generation of organic materials contributing limitedly to the total mass of the sample could have a significant effect on the final signature of the trapped Xe component if its Xe concentration were high. Conversely, an organic component carrying negligible amounts of Xe would have little influence on the final signature of the trapped Xe component, even at high mass fraction. This points towards a potential decoupling between the isotopic signature of the total Xe trapped component and the mass fractions of organic generations within a given kerogen. In addition, during isolation of organic materials from their host rocks, acid treatment with HF/HCl might induce the formation of neo-formed minerals such as fluorides (Garcette-Lepecq et al., 2000), which have to be removed before analysis of the Xe isotopes. These minerals would likely carry noble gases with modern atmosphere-like isotopic compositions, therefore inducing a potential

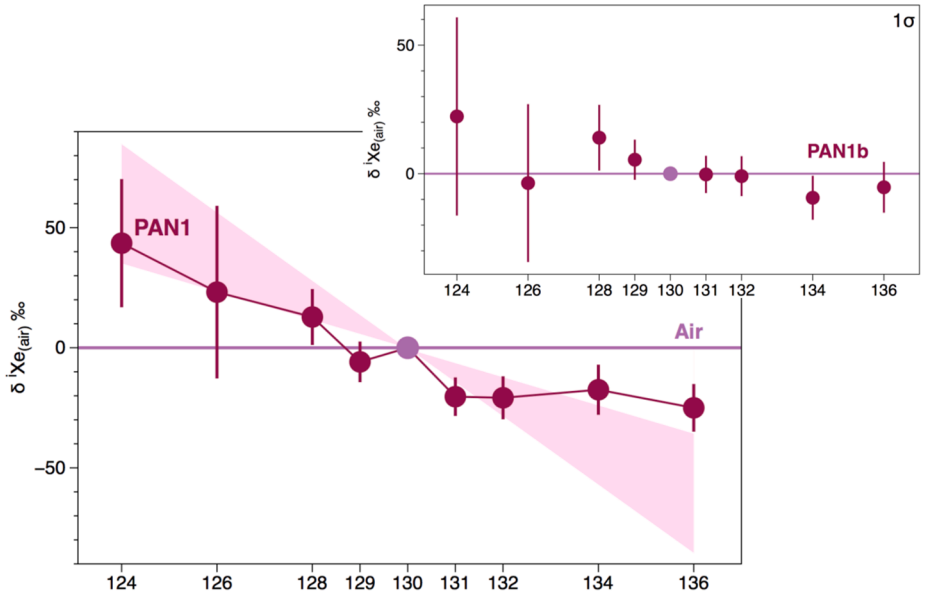

Fig. 7. Xe isotopic spectrum of the trapped noble gas component in kerogen PAN1 normalized to ^{130}Xe and to the modern atmosphere composition (Ozima and Podosek, 2002). The shaded area represents the uncertainties associated with the degree of MDF computed from the Xe isotopic spectrum of the kerogen PAN1. The Xe isotope spectrum of PAN1b is given for comparison. Error bars are 1σ.

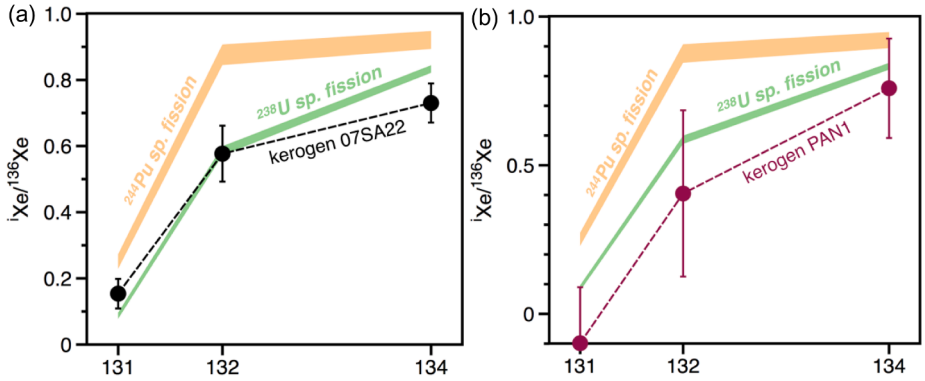

Fig. 8. Xenon fission spectra of kerogens 07SA22 (a) and PAN1 (b) corrected for mass dependent fractionation relative to a starting isotopic composition similar to U-Xe. Both spectra are in better agreement with spontaneous fission from ^{238}U and not ^{244}Pu. Fission spectra are from Porcelli and Ballentine (2002).

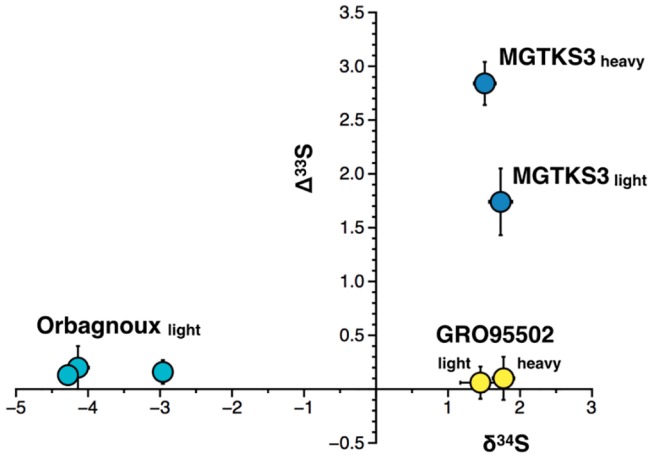

Fig. 9. Sulphur isotope composition of the S-rich organic matter from the bituminous laminites of Orbagnoux (France, upper Kimmeridgian; Mongenot et al., 1997; 3 aliquots), the Archean Kerogen MGTKS3 isolated from a black chert layer of the 3.0-Gy-old Farrel Quartzite (Pilbara Craton, Western Australia; Delarue et al., 2016; Bekaert et al., 2018), and IOM from the meteorite GRO 95,502 (Grossman and Brearley, 2005). The "light" and "heavy" fractions refer to the residues after separation in heavy liquid.

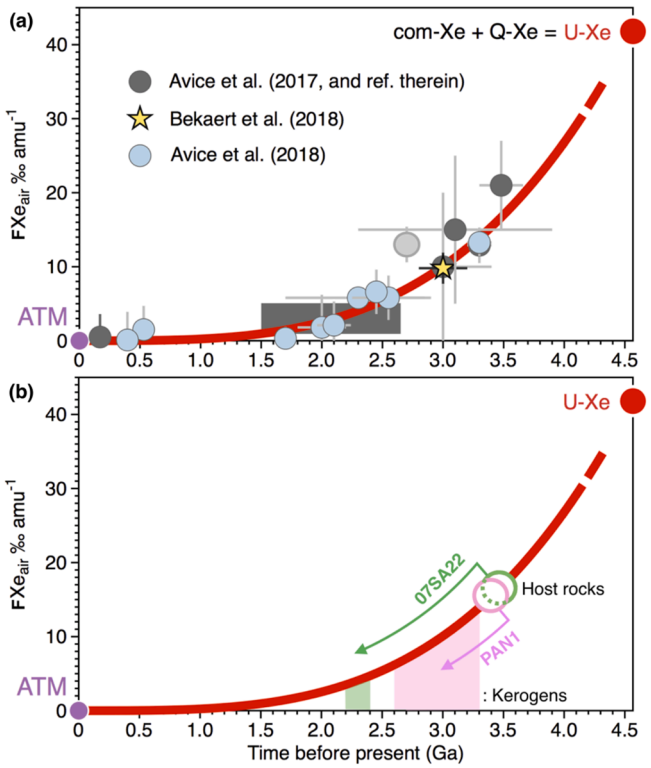

Fig. 10. MDF of atmospheric Xe with time relative to modern atmosphere (FXe). The red curve corresponds to the power law evolution ($y = 0.238*x^{3.41}$) computed by Bekaert et al. (2018) from data reported in Avice et al. (2017). (a) Novel data (Avice et al., 2018; reported at 2σ) support the use of this evolution curve, with however one "anomalous" point at 2.7 Ga (Fortescue Group, Hamersley Basin, Australia), reported here in light grey. (b) Two kerogens analyzed as part of this study (PAN1 and 07SA22) show the occurrence of ancient atmospheric Xe. However, the corresponding ages derived from Xe evolution curves (vertical shaded regions beneath the curve, with uncertainties at 1σ) are systematically lower than ages of the respective host rocks (open circles). The lowering of the MDF of the trapped Xe component relative to modern atmosphere might be interpreted in terms of post-depositional history of the related kerogens. (For interpretation of the references to colour in this figure legend, the reader is referred to the web version of this article.)

bias in the determination of the degree of MDF of the Xe trapped component if they were to still be present to some extent in the final kerogen.

Whilst the occurrence of mass-dependently fractionated Xe confirms the presence of Archean atmospheric Xe within the organic component (provided that lighter noble gases – e.g., ^{38}Ar/^{36}Ar, Kr isotopes - are not fractionated), only a good match between the Xe-based age and that of the host rock warrants the presence of a syngenetic organic component. If the degree of Xe MDF is lower than expected from the age of the host rock, no firm conclusion based on Xe isotopes solely can be drawn regarding the presence/absence of a syngenetic component. Indeed, such a signature could be accounted for by (i) mixing of a syngenetic component with a younger generation of organic materials that lowers the degree of MDF of the total Xe, or by (ii) the absence of a syngenetic component but occurrence of a unique generation of organic materials that is younger than the host rock. In case of a post-depositional organic contribution, assessment of organic matter spatial relationships to surrounding minerals, veins, and fractures, as well as comparison between Raman spectra determined on kerogens, on the mineral matrix, and on secondary hydrothermal veins (e.g., Marshall et al, 2012; Bekaert et al. 2018) can provide information regarding the multiplicity of organic sources.

The potential for multiple generations of CM to coexist in Archean kerogens illustrates the difficulty of searching for signs of life in Archean rocks. Rock-Eval pyrolysis of isolated OM from several Archean samples (Delarue et al., 2018) revealed the co-occurrence of various OM pools characterized by different thermal stabilities. Seven out of ten isolated Archean OM samples analyzed by Delarue et al. (2018) were characterized by the release of hydrocarbons in a narrow pyrolysis temperature range (576–586 °C) corresponding to the thermal cleavage of kerogen-bound hydrocarbon. However, multiple generations of hydrocarbons upon pyrolysis have also been observed in the MGTKS1up and

MGTKS3 isolated OM (Delarue et al., 2018), pointing towards the existence of several distinct pools of OM generating hydrocarbons at high pyrolysis temperature. The occurrence of distinct pools of OM does not necessary indicate the presence of distinct generations and, in the case of multiple generations of hydrocarbons, attributing a given Xe signature to a particular generation of OM appears unrealistic. Measuring the Xe isotopic composition of individual organic microstructures would require a high sensitivity that cannot be achieved using conventional static mass spectrometry. A promising avenue of investigation could be to couple *in situ* laser ablation techniques with an ultrasensitive, resonance ionization mass spectrometry (Gilmour and Turner, 1994).

4.3. Xenon mobility in organic materials

This section investigates the possibility for a syngenetic organic component to have lost – at least part of – its initially trapped Xe. Anomalous adsorption of heavy noble gases onto surface-associated defects, including those of mineral phases, has been experimentally documented (e.g., Yang et al., 1982). The mechanisms accounting for efficient trapping and preservation of atmospheric gases, especially Xe into organic materials, are not fully understood, but do not yield measurable isotopic fractionation without ionization ($-0.18‰ \pm 0.08‰$; Marrocchi and Marty, 2013). Elemental ratios and corresponding f factors indicate preferential incorporation and/or retention of Xe over lighter noble gases into organic materials. The natural occurrence of obstacles inside Xe's diffusion paths could delay/prevent its mobility within the organic matrix constrictions, therefore causing its preferential retention with respect to lighter noble gases (Kuznetsova et al., 2000). As we find in the present study, Xe concentrations in kerogens is highly variable, potentially reflecting differences in Xe concentrations within the depositional environments of the host rocks, or variable efficiencies at trapping and/or preserving noble gases over geological periods of time. Note that trapping of Xe atoms in organics does not yield measurable isotopic fractionation without ionization (Marrocchi and Marty, 2013). Under ionizing conditions, Xe trapping onto solids would favour the heavy isotopes (Marrocchi and Marty, 2013; Kuga et al., 2015) and not the light ones as observed here.

The very low diffusion coefficients for Xe resulting from its large radius, the structural changes of organic matter during carbonization (e.g. polyaromatic layer stacking), and the establishment of a closed system during silicification, would contribute together to preserving Xe in Archean kerogens over geological periods of time. One possibility is that a critical temperature (activation energy) has to be reached to allow Xe atoms to become mobile (e.g. if Xe is encapsulated in a cage-like molecular structure that would only be damaged at a high enough temperature). This has been studied in the framework of noble gas trapping in/releasing from fullerenes (C_{60} and larger), which present a closed central cavity that is large enough to accommodate noble gas atoms (including Xe; Saunders et al., 1996). Fullerenes are remarkably stable since several C–C bonds must be broken for the noble gas atoms to escape. Likewise, the loss of an initially trapped Xe component through cracking of the kerogen would indicate that the structure of the organic material has been modified, and that it is not retentive for Xe anymore. In this framework, a scenario where a syngenetic organic component would have lost its initially trapped Xe, which was then replaced by younger atmospheric Xe incorporated into the organic materials at a time corresponding to the Xe-based model age, would be unlikely.

Preferential loss of the lightest isotopes over to the heaviest ones during partial loss of an initially trapped Xe component could cause artificial decrease in the absolute degree of Xe MDF with respect to the modern atmosphere composition, therefore yielding underestimated Xe-based model ages. However, no sample has been found to exhibit a positive degree of MDF relative to the modern atmosphere composition, indicating that if this process was for instance the cause of null FXe in MGTKS1, increase in the degree of Xe MDF toward zero would have been coincidentally stopped at modern atmospheric composition. Likewise, diffusive loss should necessarily affect all noble gases in such a way that, if Xe isotopes were to have been fractionated during partial loss, then Kr isotopes should also be fractionated to at least the same extent, or more for a mass-dependent process, which is not observed. This is also valid for potential mass fractionation effects during the sample's maturation and/or partial filling/emptying of the sample's porosity by secondary fluid circulations (Torgersen et al., 2004). In addition, preferential loss of the lightest isotopes over to the heaviest ones during partial loss should yield a Xe component released at high temperature being enriched in the heaviest isotopes over to the lightest ones, which is never observed. All kerogens investigated in the present study show degrees of metamorphism that range from prehnite-pumpellyite to greenschist facies (Delarue et al., 2016), indicating the metamorphism maximum temperature did not exceed ~350 °C. Although samples were therefore held at 350 °C for potentially significant periods of time, trapped Xe components expected to be released within the 400–600 °C temperature window could have been limitedly affected. At last, kerogens MGTKS3 (Bekaert et al., 2018) and MGTKS1(up) originate from the same geological formation and were spatially separated by only a few tens of centimetres in the stratigraphic column (Delarue et al., 2016). One can therefore consider that they experienced similar thermal histories. Yet, it appears that kerogen MGTKS3 efficiently preserved its original trapped Xe component, whereas kerogen MGTKS1 and MGTKS1up lost their potential syngenetic Xe component.

Taken together, these considerations suggest that partial diffusive loss of an initially trapped, syngenetic Xe component during thermal metamorphism is unlikely to cause the observed lowering of Xe's degree of MDF relative to the modern atmosphere composition. Based on our noble gas data, we propose that mixing with younger generation(s) of organic material, with or without loss of an initial, syngenetic component, and/or contribution from neo-formed minerals alike to fluorides carrying atmospheric noble gases, would be the two most likely processes accounting for Xe-based model ages being lower than expected from the ages of the host rocks. Differences in the Xe isotope composition of samples originating from the same stratigraphic column may therefore arise from variable abilities at locally preserving closed systems and hampering mixing with more recent generations of organic materials. More work is however needed to better understand the mechanisms controlling Xe incorporation and mobility within kerogens.

4.4. Archean kerogens and early life: dating tools

The occurrence of mass-independently fractionated sulphur isotopes (MIF-S) can be used to confirm the Archean origin of ancient sedimentary rocks and potentially organic materials (e.g., Farquhar et al., 2000; Bontognali et al., 2012). The presence of MIF-S in sedimentary rocks older than ~2.4 Gyr, and the absence of MIF-S in younger rocks, has been considered the best evidence for a dramatic change from an anoxic to oxic atmosphere around 2.4 Gyr ago (e.g., Farquhar et al., 2000; Pavlov and Kasting, 2002). Reactions between reduced inorganic S and organic compounds are thought to substantially enhance the stabilization and burial of OM in anoxic environments (Boussafir et al., 1995; Damsté and De Leeuw, 1990), but the sulfurization process is poorly understood. Under certain conditions, S can be incorporated into OM on a timescale of days (Raven et al., 2016). In addition, determining the S isotope composition of Archean kerogens, excluding significant contribution from associated S-bearing mineral phases, is extremely challenging (Bontognali et al., 2012). Using our newly developed protocol to specifically separate by density kerogens (light fraction) from S-bearing minerals (concentrated in the heavy fraction), we find that, contrary to the extra-terrestrial IOM (GRO 95502) or the modern kerogen Orbagnoux, archean kerogen MGTKS3 has a positive MIF-S signature ($\Delta^{33}S = 2.84 \pm 0.20$ and 1.74 ± 0.31 for the heavy and light fractions, respectively) therefore supporting its Archean origin (> 2.4 Gyr). Although we cannot exclude that residual micro- to nano-pyrites still contribute to the S isotope composition determined for the

light fraction of the kerogen, this new data confirms that it is possible to measure Xe with an Archean signature (Bekaert et al., 2018) in kerogens with Archean geochemical characteristics. Sulphur isotopes do not however constitute a definitive tool for providing model ages of archean kerogen and testing their syngenetic origin.

Relative to cosmochemical precursors (solar or chondritic), atmospheric xenon presents a mono-isotopic excess of ^{129}Xe produced by the decay of extinct ^{129}I (Ozima and Podosek, 2002). This excess was mainly acquired during the Earth's formation and early evolution (Marty et al., 2017) but mantle degassing has also contributed ^{129}Xe to the atmosphere through geological time, most likely in a relatively short ($\approx$300 Myr) burst of mantle activity at the end of the Neo-Archean (Marty et al., in press). Trapped Archean atmospheric xenon shows a mono-isotopic excess of ^{129}Xe that is slightly less pronounced than in the present atmosphere (Avice et al., 2018; Marty et al., in press). The presence of a mono-isotopic deficit in ^{129}Xe is therefore symptomatic of the Archean atmosphere, prior to ~2.3 Ga (Marty et al., in press). The ^{129}Xe mono-isotopic deficit in kerogen PAN1 lends further credence to the conclusion of an Archean organic matter component being present in this sample. The absence of a ^{129}Xe mono-isotopic deficit and occurrence of a MDF signature in kerogen 07SA22 might indicate that influx of mantle-derived ^{129}Xe to the atmosphere was completed prior to the cessation of MDF of Xe isotopes in the atmosphere. According to the degree of MDF of Xe in 07SA22 relative to modern atmosphere (-4.2 ± 0.65‰.u^{-1}), the last chemical equilibration of the kerogen with the atmosphere could have occurred 2.3 ± 0.1 Ga. We speculate that the observation of a ^{129}Xe mono-isotopic deficit in ancient kerogens could also be used as Δ^{33}S values, to infer the presence of a trapped Archean Xe component.

As illustrated in the present study, the Xe-based dating tool for Archean kerogens requires conditions (kerogen homogeneity, uniqueness of the organic source, efficient preservation and non-disruption of the initially trapped Xe component) that may not be the rule in nature. Kerogen PAN1 is an ideal target given that it underwent a mild-thermal alteration in comparison to other studied Archean OM (Delarue et al., 2016). The degree of MDF of Xe trapped in kerogen PAN1 suggests that Archean organic materials at least 3.0 ± 0.3 Gy-old are present in this 3.46 Gyr-old sample. However, the analysis of another aliquot from the same sample (PAN1b) shows no evidence for the presence of an Archean Xe component, indicating that ancient Xe isotope signatures may be heterogeneously distributed within the sample. Such heterogeneity might be related to the handpicking aliquots for analysis, where more neo-formed minerals could for instance settle at the bottom of the sample holder and be concentrated when little material is left to be analyzed. This could also be in line with observed molecular and structural heterogeneities (Lepot et al., 2013) and heterogeneous elemental distribution of noble gases in this sample. Interestingly, the ^{40}Ar/^{36}Ar of bitumen cracking below 200 °C in this kerogen are very high (~2640; Fig. 1), indicating that thermolabile materials in PAN1 are probably ancient in line with Raman spectra determined on residual bitumen droplets (Delarue et al., 2018). However, providing accurate dating of these bituminous materials in PAN1 would require knowing their mass fraction in the sample and K contents, which is not the case.

One way of potentially circumventing issues related to the occurrence of multiple generations of OM within a given sample may be to separate them based on their thermal sensitivities, as illustrated by Rock Eval studies (Delarue et al., 2018). For instance, the Rock Eval signature of kerogen MGTKS1 is largely dominated by organic materials cracking before 400 °C (Delarue et al., 2018). This suggests that this kerogen manly comprises thermolabile components, in line with the high H/C (Delarue et al., 2018) and absence of Archean Xe signature (this study) in this sample. Yet, several studies have argued for the presence of syngenetic organic matter in kerogen MGTKS1, notably in the form of microfossils (Sugitani et al., 2007, 2009; House et al., 2013). But since cracking of kerogen MGTKS1 releases little amounts of hydrocarbons (with respect to thermolabile organic matter, Delarue et al., 2018) and no syngenetic Xe component, the Xe-based dating method cannot be applied. Other kerogens analyzed as part of the present study (especially 07SA22, MGTKS3 and MGTKS1up) show the release of hydrocarbons at high pyrolysis temperatures (Delarue et al., 2018), in line with the potential occurrence of ancient atmospheric Xe signatures. Whilst the multimodal release of hydrocarbons (MGTKS3 and MGTKS1up) could point towards the existence of several distinct pools of OM generating hydrocarbons at high pyrolysis temperature, the Gaussian shape of the high-temperature hydrocarbon peak detected for kerogen 07SA22 suggests a well-defined, unique generation of thermorecalcitrant organic matter in this sample. This is in line with the very consistent isotope composition of Xe extracted at 600 °C and 800 °C. In this case, Xe isotopes indicate that this component would not be syngenetic, but younger (2.3 ± 0.1 Gyr old) than the host rock (~3.47 Gyr old). Assuming kerogen 07SA22 contains a 3.47 Gyr old syngenetic component that was mixed with more recent organic materials having similar Xe concentrations but modern-like Xe isotopes would require that kerogen 07SA22 consists in 75 wt% syngenetic OM and 25 wt% modern OM. In future work, combining Rock Eval and noble gas analyses appears a promising avenue of investigation to ultimately differentiate noble gas signatures carried out by different organic components in kerogens.

5. Concluding remarks

The analysis of organic materials recovered from Archean rocks has the potential to elucidate on the origin of life and the timing of its emergence. Ambiguities and controversies however persist regarding the biogenetic and syngenetic origin of Archean organic materials. In particular, the potential for organic materials from ancient biological sources to co-exist with organic matter or reduced carbon produced by non-biologic processes, or post-depositional organic contaminants, suggests possible decoupling between the age of ancient organic materials and that of their host rock. Geochemical tools allowing the syngenetic origin of ancient organic materials to be tested are scarce and subject to limitations. The occurrence of non-null Δ^{33}S values and/or ^{129}Xe deficits relative to modern atmospheric composition constitute fingerprints of the Archean atmosphere. Their detection in ancient kerogens can therefore be used to validate their Archean origin. Determining the isotope composition of S within kerogens whilst limiting the contribution from associated minerals is however challenging. We recently proposed a Xe-based dating tool to potentially provide independent model ages for Archean kerogens (Bekaert et al., 2018). This method mainly relies on the combined observations that (i) atmospheric Xe evolved through time by MDFuntil ~2.5 Ga (Avice et al., 2018) and (ii) ancient organic materials can preserve significant amounts of Xe trapped from the atmosphere at the time of their formation. Here, we confirm that ancient atmospheric Xe can be preserved in Archean kerogens. However, we find trapped Xe components with lower degrees of MDF than expected from the ages of the respective host rocks, raising new questions regarding the conditions allowing Xe to be efficiently trapped and preserved within ancient organic materials. We suggest that partial diffusive loss of trapped Xe is unlikely to cause such lowering of Xe degree of MDF without affecting lighter noble gases, and that multiple component mixing could more likely account for Xe-based model ages being lower than expected from the ages of host rocks. In this case, deconvoluting Xe signals from the different generations of organic matter appears extremely challenging, potentially calling for new analytical developments coupling *in situ* laser ablation techniques with an ultrasensitive mass spectrometry, and/or investigations of the thermal sensitivity of organic materials through Rock Eval studies. Before being able to tackle the question of ancient organic material syngenecity based on the Xe dating tool, it appears that a better understanding of the mechanism(s)/conditions accounting for noble gas incorporation/mobility in organic materials is needed. Moreover, these might vary depending on the geological history of the samples (e.g., temperature, extent of hydrothermalism) as well as the nature and molecular/structural composition of the organic

materials. In other words, the degree of MDF of Xe isotopes constitutes a promising – but not unequivocal – geochemical tool for providing model ages for Archean kerogens.

Declaration of Competing Interest

The authors declare that they have no known competing financial interests or personal relationships that could have appeared to influence the work reported in this paper.

Acknowledgments

This study was supported by the European Research Council (grants PaleoNanoLife 2011-ADG_20110209 to F.R. and PHOTONIS 695618 to B.M.). We thank the two anonymous reviewers for their helpful comments, as well as Frances Westall for having provided the Middle Marker sample from the Barberton Greenstone Belt. We gratefully thank Raymond Michels and Laurette Piani for providing us with some bulk rock of the bituminous laminites of Orbagnoux, and some IOM from the meteorite GRO 95502, respectively. This is CRPG contribution n°2727.

Appendix A. Supplementary data

Supplementary data to this article can be found online at https://doi.org/10.1016/j.precamres.2019.105505.

References

Alexander, C.O.D., Fogel, M., Yabuta, H., Cody, G.D., 2007. The origin and evolution of chondrites recorded in the elemental and isotopic compositions of their macromolecular organic matter. Geochim. Cosmochim. Acta 71 (17), 4380–4403.
Alleon, J., Bernard, S., Le Guillou, C., Beyssac, O., Sugitani, K., Robert, F., 2018. Chemical nature of the 3.4 Ga Strelley Pool microfossils. Geochem. Perspect. Lett. 7, 37–42.
Allwood, A.C., Walter, M.R., Kamber, B.S., Marshall, C.P., Burch, I.W., 2006. Stromatolite reef from the Early Archaean era of Australia. Nature 441 (7094), 714.
Allwood, A.C., Kamber, B.S., Walter, M.R., Burch, I.W., Kanik, I., 2010. Trace elements record depositional history of an Early Archean stromatolitic carbonate platform. Chem. Geol. 270 (1–4), 148–163.
Armstrong, R.A., Compston, W., De Wit, M.J., Williams, I.S., 1990. The stratigraphy of the 3.5-3.2 Ga Barberton Greenstone Belt revisited: a single zircon ion microprobe study. Earth Planet. Sci. Lett. 101 (1), 90–106.
Avice, G., Marty, B., Burgess, R., 2017. The origin and degassing history of the Earth's atmosphere revealed by Archean xenon. Nat. Commun. 8, 15455.
Avice, G., Marty, B., Burgess, R., Hofmann, A., Philippot, P., Zahnle, K., Zakharov, D., 2018. Evolution of atmospheric xenon and other noble gases inferred from Archean to Paleoproterozoic rocks. Geochim. Cosmochim. Acta 232, 82–100.
Bekaert, D.V., Broadley, M.W., Delarue, F., Avice, G., Robert, F., Marty, B., 2018. Archean kerogen as a new tracer of atmospheric evolution: implications for dating the widespread nature of early life. Sci. Adv. 4 (2), eaar2091.
Bell, E.A., Boehnke, P., Harrison, T.M., Mao, W.L., 2015. Potentially biogenic carbon preserved in a 4.1 billion-year-old zircon. Proc. Natl. Acad. Sci. 112 (47), 14518–14521.
Bontognali, T.R., Sessions, A.L., Allwood, A.C., Fischer, W.W., Grotzinger, J.P., Summons, R.E., Eiler, J.M., 2012. Sulfur isotopes of organic matter preserved in 3.45-billion-year-old stromatolites reveal microbial metabolism. Proc. Natl. Acad. Sci. 109 (38), 15146–15151.
Bourbin, M., Derenne, S., Gourier, D., Rouzaud, J.N., Gautret, P., Westall, F., 2012. Electron paramagnetic resonance study of a photosynthetic microbial mat and comparison with Archean cherts. Orig. Life Evol. Biosph. 42, 569–585.
Boussafir, M., Gelin, F., Lallier-Verges, E., Derenne, S., Bertrand, P., Largeau, C., 1995. Electron microscopy and pyrolysis of kerogens from the Kimmeridge Clay Formation, UK: source organisms, preservation processes, and origin of microcycles. Geochim. Cosmochim. Acta 59 (18), 3731–3747.
Bowring, S.A., Williams, I.S., 1999. Priscoan (4.00–4.03 Ga) orthogneisses from northwestern Canada. Contrib. Miner. Petrol. 134 (1), 3–16.
Cosmidis, J., Templeton, A.S., 2016. Self-assembly of biomorphic carbon/sulfur microstructures in sulfidic environments. Nat. Commun. 7, 12812.
Damsté, J.S.S., De Leeuw, J.W., 1990. Analysis, structure and geochemical significance of organically-bound sulphur in the geosphere: state of the art and future research. Org. Geochem. 16 (4–6), 1077–1101.
De Gregorio, B.T., Sharp, T.G., 2006. The structure and distribution of carbon in 3.5 Ga Apex chert: implications for the biogenicity of Earth's oldest putative microfossils. Am. Mineral. 91 (5–6), 784–789.
Delarue, F., Rouzaud, J.N., Derenne, S., et al., 2016. The Raman-derived carbonization continuum: a tool to select the best preserved molecular structures in Archean kerogens. Astrobiology 16 (6), 407–417.
Delarue, F., Derenne, S., Sugitani, K., et al., 2018. What is the meaning of hydrogen-to-carbon ratio determined in Archean organic matter? Org. Geochem. 122, 140–146.
Derenne, S., Robert, F., Skrzypczak-Bonduelle, A., Gourier, D., Binet, L., Rouzaud, J.N., 2008. Molecular evidence for life in the 3.5 billion year old Warrawoona chert. Earth Planet. Sci. Lett. 272 (1–2), 476–480.
Farquhar, J., Bao, H., Thiemens, M., 2000. Atmospheric influence of Earth's earliest sulfur cycle. Science 289 (5480), 756–758.
French, K.L., Hallmann, C., Hope, J.M., et al., 2015. Reappraisal of hydrocarbon biomarkers in Archean rocks. Proc. Natl. Acad. Sci. 112 (19), 5915–5920.
Gao, X., Thiemens, M.H., 1993a. Isotopic composition and concentration of sulfur in carbonaceous chondrites. Geochim. Cosmochim. Acta 57 (13), 3159–3169.
Garcette-Lepecq, A., Derenne, S., Largeau, C., Bouloubassi, I., Saliot, A., 2000. Origin and formation pathways of kerogen-like organic matter in recent sediments off the Danube delta (northwestern Black Sea). Org Geochem. 31 (12), 1663–1683.
Gilmour, J.D., Turner, G., 1994. The RELAX mass spectrometer and its application to iodine-xenon dating. In: Noble Gas Geochemistry and Cosmochemistry. Terra Scientific Publishing, pp. 11–22.
Gao, X., Thiemens, M.H., 1993b. Variations of the isotopic composition of sulfur in enstatite and ordinary chondrites. Geochim. Cosmochim. Acta 57 (13), 3171–3176.
García-Ruiz, J.M., Hyde, S.T., Carnerup, A.M., Christy, A.G., Van Kranendonk, M.J., Welham, N.J., 2003. Self-assembled silica-carbonate structures and detection of ancient microfossils. Science 302 (5648), 1194–1197.
Grossman, J.N., Brearley, A.J., 2005. The onset of metamorphism in ordinary and carbonaceous chondrites. Meteorit. Planet. Sci. 40 (1), 87–122.
Hébrard, E., Marty, B., 2014. Coupled noble gas–hydrocarbon evolution of the early Earth atmosphere upon solar UV irradiation. Earth Planet. Sci. Lett. 385, 40–48.
Horita, J., 2005. Some perspectives on isotope biosignatures for early life. Chem. Geol. 218 (1–2), 171–186.
House, C.H., Oehler, D.Z., Sugitani, K., Mimura, K., 2013. Carbon isotopic analyses of ca. 3.0 Ga microstructures imply planktonic autotrophs inhabited Earth's early oceans. Geology 41 (6), 651–654.
Kamber, B.S., Webb, G.E., 2001. The geochemistry of late Archaean microbial carbonate: implications for ocean chemistry and continental erosion history. Geochim. Cosmochim. Acta 65 (15), 2509–2525.
Konhauser, K.O., Hamade, T., Raiswell, R., Morris, R.C., Ferris, F.G., Southam, G., Canfield, D.E., 2002. Could bacteria have formed the Precambrian banded iron formations? Geology 30 (12), 1079–1082.
Kuga, M., Marty, B., Marrocchi, Y., Tissandier, L., 2015. Synthesis of refractory organic matter in the ionized gas phase of the solar nebula. Proc. Natl. Acad. Sci. 112 (23), 7129–7134.
Kuznetsova, A., Yates Jr, J.T., Liu, J., Smalley, R.E., 2000. Physical adsorption of xenon in open single walled carbon nanotubes: observation of a quasi-one-dimensional confined Xe phase. J. Chem. Phys. 112 (21), 9590–9598.
Lee, J.Y., Marti, K., Severinghaus, J.P., Kawamura, K., Yoo, H.S., Lee, J.B., Kim, J.S., 2006. A redetermination of the isotopic abundances of atmospheric Ar. Geochim. Cosmochim. Acta 70 (17), 4507–4512.
Lepland, A., van Zuilen, M.A., Arrhenius, G., Whitehouse, M.J., Fedo, C.M., 2005. Questioning the evidence for Earth's earliest life—Akilia revisited. Geology 33 (1), 77–79.
Lepot, K., Williford, K.H., Ushikubo, T., Sugitani, K., Mimura, K., Spicuzza, M.J., Valley, J.W., 2013. Texture-specific isotopic compositions in 3.4 Gyr old organic matter support selective preservation in cell-like structures. Geochim. Cosmochim. Acta 112, 66–86.
Lollar, B.S., Westgate, T.D., Ward, J.A., Slater, G.F., Lacrampe-Couloume, G., 2002. Abiogenic formation of alkanes in the Earth's crust as a minor source for global hydrocarbon reservoirs. Nature 416 (6880), 522.
Marrocchi, Y., Marty, B., 2013. Experimental determination of the xenon isotopic fractionation during adsorption. Geophys. Res. Lett. 40, 4165–4170.
Marshall, A.O., Emry, J.R., Marshall, C.P., 2012. Multiple generations of carbon in the Apex chert and implications for preservation of microfossils. Astrobiology 12 (2), 160–166.
Marty, B., Altwegg, K., Balsiger, H., et al., 2017. Xenon isotopes in 67P/Churyumov-Gerasimenko show that comets contributed to Earth's atmosphere. Science 356 (6342), 1069–1072.
Marty, B., Bekaert, D.V., Broadley, M.W., Jaupart, C, in press. Geochemical evidence for high volatile fluxes from the mantle at the end of the Archean. Nature.
McKeegan, K.D., Kudryavtsev, A.B., Schopf, J.W., 2007. Raman and ion microscopic imagery of graphitic inclusions in apatite from older than 3830 Ma Akilia supracrustal rocks, west Greenland. Geology 35 (7), 591–594.
Mojzsis, S.J., Arrhenius, G., McKeegan, K.D., Harrison, T.M., Nutman, A.P., Friend, C.R.L., 1996. Evidence for life on Earth before 3,800 million years ago. Nature 384 (6604), 55.
Mongenot, T., Boussafir, M., Derenne, S., Lallier-Verges, E., Largeau, C., Tribovillard, N.P., 1997. Sulphur-rich organic matter from bituminous laminites of Orbagnoux (France, upper Kimmeridgian); the role of early vulcanization. Bulletin de la Société Géologique de France 168 (3), 331–341.
Oehler, D., Cady, S., 2014. Biogenicity and syngeneity of organic matter in ancient sedimentary rocks: recent advances in the search for evidence of past life. Challenges 5 (2), 260–283.
Ozima, M., Podosek, F.A., 2002. Noble gas geochemistry. Cambridge University Press.
Parai, R., Mukhopadhyay, S., 2018. Xenon isotopic constraints on the history of volatile recycling into the mantle. Nature 560 (7717), 223.
Paris, G., Sessions, A.L., Subhas, A.V., Adkins, J.F., 2013. MC-ICP-MS measurement of δ34S andΔ 33S in small amounts of dissolved sulfate. Chem. Geol. 345, 50–61.
Paris, G., Adkins, J.F., Sessions, A.L., Webb, S.M., Fischer, W.W., 2014. Neoarchean carbonate–associated sulfate records positive Δ33S anomalies. Science 346 (6210), 739–741.

Pavlov, A.A., Kasting, J.F., 2002. Mass-independent fractionation of sulfur isotopes in Archean sediments: strong evidence for an anoxic Archean atmosphere. Astrobiology 2 (1), 27–41.
Peck, W.H., Valley, J.W., Wilde, S.A., Graham, C.M., 2001. Oxygen isotope ratios and rare earth elements in 3.3 to 4.4 Ga zircons: ion microprobe evidence for high δ18O continental crust and oceans in the Early Archean. Geochim. Cosmochim. Acta 65 (22), 4215–4229.
Péron, S., Moreira, M., 2018. Onset of volatile recycling into the mantle determined by xenon anomalies. GPL 9, 21.
Porcelli, D., Ballentine, C.J., 2002. An overview of noble gas geochemistry and cosmochemistry. Rev. Mineral. Geochem. 47, 1–19.
Pujol, M., Marty, B., Burgess, R., 2011. Chondritic-like xenon trapped in Archean rocks: a possible signature of the ancient atmosphere. Earth Planet. Sci. Lett. 308 (3–4), 298–306.
Raven, M.R., Sessions, A.L., Adkins, J.F., Thunell, R.C., 2016. Rapid organic matter sulfurization in sinking particles from the Cariaco Basin water column. Geochim. Cosmochim. Acta 190, 175–190.
Rosing, M.T., 1999. 13C-depleted carbon microparticles in > 3700-Ma sea-floor sedimentary rocks from West Greenland. Science 283 (5402), 674–676.
Saunders, M., Cross, R.J., Jiménez-Vázquez, H.A., Shimshi, R., Khong, A., 1996. Noble gas atoms inside fullerenes. Science 271 (5256), 1693–1697.
Schopf, J.W., 1993. Microfossils of the Early Archean Apex chert: new evidence of the antiquity of life. Science 260 (5108), 640–646.
Shen, Y., Farquhar, J., Masterson, A., Kaufman, A.J., Buick, R., 2009. Evaluating the role of microbial sulfate reduction in the early Archean using quadruple isotope systematics. Earth Planet Sci. Lett. 279, 383–391.
Simonyan, V.V., Johnson, J.K., Kuznetsova, A., Yates Jr, J.T., 2001. Molecular simulation of xenon adsorption on single-walled carbon nanotubes. J. Chem. Phys. 114 (9), 4180–4185.
Spangenberg, J.E., Frimmel, H.E., 2001. Basin-internal derivation of hydrocarbons in the Witwatersrand Basin, South Africa: evidence from bulk and molecular δ13C data. Chem. Geol. 173 (4), 339–355.
Sugahara, H., Sugitani, K., Mimura, K., Yamashita, F., Yamamoto, K., 2010. A systematic rare-earth elements and yttrium study of Archean cherts at the Mount Goldsworthy greenstone belt in the Pilbara Craton: implications for the origin of microfossil-bearing black cherts. Precambr. Res. 177 (1–2), 73–87.
Sugitani, K., Grey, K., Allwood, A., et al., 2007. Diverse microstructures from Archaean chert from the Mount Goldsworthy-Mount Grant area, Pilbara Craton, Western Australia: microfossils, dubiofossils, or pseudofossils? Precambr. Res. 158 (3–4), 228–262.
Sugitani, K., Grey, K., Nagaoka, T., Mimura, K., Walter, M.R., 2009. Taxonomy and biogenicity of Archaean spheroidal microfossils (ca. 3.0 Ga) from the Mount Goldsworthy-Mount Grant area in the northeastern Pilbara Craton, Western Australia. Precambr. Res. 173 (1–4), 50–59.
Sugitani, K., Mimura, K., Nagaoka, T., Lepot, K., Takeuchi, M., 2013. Microfossil assemblage from the 3400 Ma Strelley Pool Formation in the Pilbara Craton, Western Australia: results form a new locality. Precambr. Res. 226, 59–74.
Tashiro, T., Ishida, A., Hori, M., et al., 2017. Early trace of life from 3.95 Ga sedimentary rocks in Labrador, Canada. Nature 549 (7673), 516.
Thorpe, R.I., Hickman, A.H., Davis, D.W., Mortensen, J.K., Trendall, A.F., 1992. Constraints to models for Archean lead evolution from precise zircon U-Pb geochronology for the Marble Bar region, Pilbara Craton, Western Australia. In: Glover, J.E., Ho, S.E. (Eds.), The Archean: Terrains, Processes and Metallogeny. Univ. West. Austral. Geol. Extens. Publ. 22, pp. 395–407.
Torgersen, T., Kennedy, B.M., van Soest, M.C., 2004. Diffusive separation of noble gases and noble gas abundance patterns in sedimentary rocks. Earth Planet. Sci. Lett. 226 (3–4), 477–489.
Van Zuilen, M.A., Lepland, A., Arrhenius, G., 2002. Reassessing the evidence for the earliest traces of life. Nature 418 (6898), 627.
Wacey, D., Kilburn, M.R., Saunders, M., Cliff, J., Brasier, M.D., 2011. Microfossils of sulphur-metabolizing cells in 3.4-billion-year-old rocks of Western Australia. Nat. Geosci. 4 (10), 698.
Wacker, J.F., Zadnik, M.G., Anders, E., 1985. Laboratory simulation of meteoritic noble gases. I. Sorption of xenon on carbon: trapping experiments. Geochim. Cosmochim. Acta 49 (4), 1035–1048.
Wacker, J.F., 1989. Laboratory simulation of meteoritic noble gases. III. Sorption of neon, argon, krypton, and xenon on carbon: elemental fractionation. Geochim. Cosmochim. Acta 53 (6), 1421–1433.
Walter, M.R., Buick, R., Dunlop, J.S.R., 1980. Stromatolites 3400–3500 Myr old from the North pole area, Western Australia. Nature 284 (5755), 443.
Warr, O., Lollar, B.S., Fellowes, J., et al., 2018. Tracing ancient hydrogeological fracture network age and compartmentalisation using noble gases. Geochim. Cosmochim. Acta 222, 340–362.
Watanabe, Y., Farquhar, J., Ohmoto, H., 2009. Anomalous fractionations of sulfur isotopes during thermochemical sulfate reduction. Science 324 (5925), 370–373.
Westall, F., de Wit, M.J., Dann, J., van der Gaast, S., de Ronde, C.E., Gerneke, D., 2001. Early Archean fossil bacteria and biofilms in hydrothermally-influenced sediments from the Barberton greenstone belt, South Africa. Precambr. Res. 106 (1–2), 93–116.
Wilde, S.A., Valley, J.W., Peck, W.H., Graham, C.M., 2001. Evidence from detrital zircons for the existence of continental crust and oceans on the Earth 4.4 Gyr ago. Nature 409 (6817), 175.
Yang, J., Lewis, R.S., Anders, E., 1982. Sorption of noble gases by solids, with reference to meteorites. I: magnetite and carbon. Geochim. Cosmochim. Acta 46, 841–860.
Zahnle, K.J., Gacesa, M., Catling, D.C., 2019. Strange messenger: a new history of hydrogen on Earth, as told by Xenon. Geochim. Cosmochim. Acta 244, 56–85.

General References

Adam, Z. R., Skidmore, M. L., Mogk, D. W., & Butterfield, N. J. (2017). A Laurentian record of the earliest fossil eukaryotes. *Geology*, *45*(5), 387-390.

Albarede, F. (2009). Volatile accretion history of the terrestrial planets and dynamic implications. *Nature*, *461*(7268), 1227.

Albarede, F., Ballhaus, C., Blichert-Toft, J., Lee, C. T., Marty, B., Moynier, F., & Yin, Q. Z. (2013). Asteroidal impacts and the origin of terrestrial and lunar volatiles. *Icarus*, *222*(1), 44-52.

Alexander, R. D., & Armitage, P. J. (2009). Giant planet migration, disk evolution, and the origin of transitional disks. *The Astrophysical Journal*, *704*(2), 989.

Alibert, Y., Venturini, J., Helled, R., Ataiee, S., Burn, R., Senecal, L., ... & Schönbächler, M. (2018). The formation of Jupiter by hybrid pebble–planetesimal accretion. *Nature astronomy*, *2*(11), 873.

Alleon, J., Bernard, S., Le Guillou, C., Beyssac, O., Sugitani, K., & Robert, F. (2018). Chemical nature of the 3.4 Ga Strelley Pool microfossils.

Allwood, A. C., Walter, M. R., Kamber, B. S., Marshall, C. P., & Burch, I. W. (2006). Stromatolite reef from the Early Archaean era of Australia. *Nature*, *441*(7094), 714.

Altwegg, K., Balsiger, H., Bar-Nun, A., Berthelier, J. J., Bieler, A., Bochsler, P., ... & Eberhardt, P. (2015). 67P/Churyumov-Gerasimenko, a Jupiter family comet with a high D/H ratio. *Science*, *347*(6220), 1261952.

Altwegg, K., Balsiger, H., Bar-Nun, A., Berthelier, J. J., Bieler, A., Bochsler, P., ... & De Keyser, J. (2016). Prebiotic chemicals—amino acid and phosphorus—in the coma of comet 67P/Churyumov-Gerasimenko. *Science advances*, *2*(5), e1600285.

Amari, S., Anders, E., Virag, A., & Zinner, E. (1990). Interstellar graphite in meteorites. *Nature*, *345*(6272), 238.

Amari, S., Matsuda, J. I., Stroud, R. M., & Chisholm, M. F. (2013). Highly concentrated nebular noble gases in porous nanocarbon separates from the Saratov (L4) meteorite. *The Astrophysical Journal*, *778*(1), 37.

Anbar, A. D., & Knoll, A., 2002. Proterozoic ocean chemistry and evolution: a bioinorganic bridge? Science, 297, 1137-1142.

Anbar, A. D., Duan, Y., Lyons, T. W., Arnold, G. L., Kendall, B., Creaser, R. A., ... & Buick, R. (2007). A whiff of oxygen before the great oxidation event?. *Science*, *317*(5846), 1903-1906.

Andersson, S., & Van Dishoeck, E. F. (2008). Photodesorption of water ice-A molecular dynamics study. *Astronomy & Astrophysics*, *491*(3), 907-916.

Anicich, V. G. (1993). Evaluated bimolecular ion-molecule gas phase kinetics of positive ions for use in modeling planetary atmospheres, cometary comae, and interstellar clouds. *Journal of Physical and Chemical Reference Data*, *22*(6), 1469-1569.

Aponte, J. C., Alexandre, M. R., Wang, Y., Brearley, A. J., Alexander, C. M. D., & Huang, Y. (2011). Effects of secondary alteration on the composition of free and IOM-derived monocarboxylic acids in carbonaceous chondrites. *Geochimica et Cosmochimica Acta*, *75*(9), 2309-2323.

Avice, G., & Marty, B. (2014). The iodine–plutonium–xenon age of the Moon–Earth system revisited. *Philosophical Transactions of the Royal Society A: Mathematical, Physical and Engineering Sciences*, *372*(2024), 20130260.

Avice, G., Marty, B., & Burgess, R. (2017). The origin and degassing history of the Earth's atmosphere revealed by Archean xenon. *Nature communications*, *8*, 15455.

Avice, G., Marty, B., Burgess, R., Hofmann, A., Philippot, P., Zahnle, K., & Zakharov, D. (2018). Evolution of atmospheric xenon and other noble gases inferred from Archean to Paleoproterozoic rocks. *Geochimica et Cosmochimica Acta*, *232*, 82-100.

Bada, J. L., Bigham, C., & Miller, S. L. (1994). Impact melting of frozen oceans on the early Earth: implications for the origin of life. *Proceedings of the National Academy of Sciences*, *91*(4), 1248-1250.

Bai, X. N. (2011). Magnetorotational-instability-driven accretion in protoplanetary disks. *The Astrophysical Journal*, *739*(1), 50.

Ballentine, C. J., Marty, B., Lollar, B. S., & Cassidy, M. (2005). Neon isotopes constrain convection and volatile origin in the Earth's mantle. *Nature*, *433*(7021), 33.

Ballentine, C. J., & Holland, G. (2008). What CO2 well gases tell us about the origin of noble gases in the mantle and their relationship to the atmosphere. *Philosophical Transactions of the Royal Society A: Mathematical, Physical and Engineering Sciences*, *366*(1883), 4183-4203.

Balsiger, H., Altwegg, K., Bochsler, P., Eberhardt, P., Fischer, J., Graf, S., ... & Müller, J. (2007). Rosina–Rosetta orbiter spectrometer for ion and neutral analysis. *Space Science Reviews*, *128*(1-4), 745-801.

Balsiger, H., Altwegg, K., Bar-Nun, A., Berthelier, J. J., Bieler, A., Bochsler, P., ... & Eberhardt, P. (2015). Detection of argon in the coma of comet 67P/Churyumov-Gerasimenko. *Science advances*, *1*(8), e1500377.

Bardin, N., Duprat, J., Slodzian, G., Wu, T. D., Baklouti, D., Dartois, E., ... & Guerquin-Kern, J. L. (2015). Hydrogen isotopic fractionation in secondary ion mass spectrometry using polyatomic ions. *International Journal of Mass Spectrometry*, *393*, 17-24.

Barfod, D. N., Ballentine, C. J., Halliday, A. N., & Fitton, J. G. (1999). Noble gases in the Cameroon line and the He, Ne, and Ar isotopic compositions of high μ (HIMU) mantle. *Journal of Geophysical Research: Solid Earth*, *104*(B12), 29509-29527.

Barnes JJ, Franchi IA, Anand M, Tartèse R, Starkey NA, et al. (2013). Accurate and precise measurements of the D/H ratio and hydroxyl content in lunar apatites using NanoSIMS. Chem. Geol. 337–38:48–55

Barnes, J. J., Tartèse, R., Anand, M., McCubbin, F. M., Franchi, I. A., Starkey, N. A., & Russell, S. S. (2014). The origin of water in the primitive Moon as revealed by the lunar highlands samples. *Earth and Planetary Science Letters*, *390*, 244-252.

Barnes, J. J., Kring, D. A., Tartese, R., Franchi, I. A., Anand, M., & Russell, S. S. (2016). An asteroidal origin for water in the Moon. *Nature communications*, *7*, 11684.

Bar-Nun, A., Herman, G., Laufer, D., & Rappaport, M. L. (1985). Trapping and release of gases by water ice and implications for icy bodies. *Icarus*, *63*(3), 317-332.

Basford, J. R., Dragon, J. C., Pepin, R. O., Coscio Jr, M. R. and Murthy, V. R. (1973). Krypton and xenon in lunar fines. In *Proc. Lunar Planet. Sci. Conf*, vol. **4**, p. 1915. Proc. Lunar Planet. Sci. Conf.

Bekaert, D. V., Avice, G., Marty, B., Henderson, B., & Gudipati, M. S. (2017). Stepwise heating of lunar anorthosites 60025, 60215, 65315 possibly reveals an indigenous noble gas component on the Moon. *Geochimica et Cosmochimica Acta*, *218*, 114-131.

Bekaert, D. V., Derenne, S., Tissandier, L., Marrocchi, Y., Charnoz, S., Anquetil, C., & Marty, B. (2018a). High-temperature ionization-induced synthesis of biologically relevant molecules in the protosolar nebula. *The Astrophysical Journal*, *859*(2), 142.

Bekaert, D. V., Avice, G., & Marty, B. (2018b). Origin and significance of cosmogenic signatures in vesicles of lunar basalt 15016. *Meteoritics & planetary science*, *53*(6), 1238-1251.

Bekaert, D. V., Broadley, M. W., Delarue, F., Avice, G., Robert, F., & Marty, B. (2018c). Archean kerogen as a new tracer of atmospheric evolution: Implications for dating the widespread nature of early life. *Science Advances*, *4*(2), eaar2091.

Bekaert, D. V., Marrocchi, Y., Meshik, A., Remusat, L., & Marty, B. (2019a). Primordial heavy noble gases in the pristine Paris carbonaceous chondrite. *Meteoritics & planetary science*, *54*(2), 395-414.

Bekaert, D. V., Gudipati, M. S., Henderson, B., & Marty, B. (2019b). Coulomb explosion of multiply ionized xenon in water ice. *Geochemical Journal*, *53*(1), 69-81.

Bekaert, D. V., Broadley, M. W., Caracausi, A., & Marty, B. (2019c). Novel insights into the degassing history of Earth's mantle from high precision noble gas analysis of magmatic gas. *Earth and Planetary Science Letters*, *525*, 115766.

Bekaert, D. V., Broadley, M. W., Delarue, F., Druzhinina, Z., Paris, G., Robert, F., ... & Marty, B. (2020). Xenon isotopes in Archean and Proterozoic insoluble organic matter: A robust indicator of syngenecity?. *Precambrian Research*, *336*, 105505.

Bernatowicz, T. J., Podosek, F. A., Honda, M. & Kramer F. E. (1984) The atmospheric inventory of xenon and noble gases in shales: The plastic bag experiment. J. Geophys. Res. Solid Earth 89, 4597–4611.

Bernatowicz, T., Fraundorf, G., Ming, T., Anders, E., Wopenka, B., Zinner, E., & Fraundorf, P. (1987). Evidence for interstellar SiC in the Murray carbonaceous meteorite. *Nature*, *330*(6150), 728.

Berndt, M. E., Allen, D. E., & Seyfried Jr, W. E. (1996). Reduction of CO2 during serpentinization of olivine at 300 C and 500 bar. *Geology*, *24*(4), 351-354.

Birnstiel, T., Dullemond, C. P., & Brauer, F. (2010). Gas-and dust evolution in protoplanetary disks. *Astronomy & Astrophysics*, *513*, A79.

Biron, K., Derenne, S., Robert, F., & Rouzaud, J. N. (2015). Toward an experimental synthesis of the chondritic insoluble organic matter. *Meteoritics & Planetary Science*, *50*(8), 1408-1422.

Bitsch, B., Johansen, A., Lambrechts, M., & Morbidelli, A. (2015). The structure of protoplanetary discs around evolving young stars. *Astronomy & Astrophysics*, *575*, A28.

Bitsch, B., Izidoro, A., Johansen, A., Raymond, S. N., Morbidelli, A., Lambrechts, M., & Jacobson, S. A. (2019). Formation of planetary systems by pebble accretion and migration: growth of gas giants. *Astronomy & Astrophysics*, *623*, A88.

Black, D. C., & Pepin, R. O. (1969). Trapped neon in meteorites—II. *Earth and Planetary Science Letters*, *6*(5), 395-405.

Black, D. C. (1972). On the origins of trapped helium, neon and argon isotopic variations in meteorites—II. Carbonaceous meteorites. *Geochimica et Cosmochimica Acta*, *36*(3), 377-394.

Blard, P. H., Bourles, D., Lave, J., & Pik, R. (2006). Applications of ancient cosmic-ray exposures: theory, techniques and limitations. *Quaternary Geochronology*, *1*(1), 59-73.

Bleeker, W. (2003). The late Archean record: a puzzle in ca. 35 pieces. *Lithos*, *71*(2-4), 99-134.

Blichert-Toft, J., & Albarède, F. (2008). Hafnium isotopes in Jack Hills zircons and the formation of the Hadean crust. *Earth and Planetary Science Letters*, *265*(3-4), 686-702.

Bockelée-Morvan, D., Crovisier, J., Mumma, M. J., & Weaver, H. A. (2004). The composition of cometary volatiles. *Comets II*, *1*, 391-423.

Bockelée-Morvan, D., Calmonte, U., Charnley, S., Duprat, J., Engrand, C., Gicquel, A., ... & Milam, S. (2015). Cometary isotopic measurements. *Space science reviews*, *197*(1-4), 47-83.

Boehnke, P., Caffee, M. W., & Harrison, T. M. (2015). Xenon isotopes in the MORB source, not distinctive of early global degassing. *Geophysical Research Letters*, *42*(11), 4367-4374.

Boehnke, P., & Harrison, T. M. (2016). Illusory late heavy bombardments. *Proceedings of the National Academy of Sciences*, *113*(39), 10802-10806.

Bollard, J., Connelly, J. N., & Bizzarro, M. (2015). Pb-Pb dating of individual chondrules from the CB a chondrite Gujba: Assessment of the impact plume formation model. *Meteoritics & planetary science*, *50*(7), 1197-1216.

Bollard, J., Connelly, J. N., Whitehouse, M. J., Pringle, E. A., Bonal, L., Jørgensen, J. K., ... & Bizzarro, M. (2017). Early formation of planetary building blocks inferred from Pb isotopic ages of chondrules. *Science advances*, *3*(8), e1700407.

Bosman, A. D., Walsh, C., & van Dishoeck, E. F. (2018). CO destruction in protoplanetary disk midplanes: Inside versus outside the CO snow surface. *Astronomy & Astrophysics*, *618*, A182.

Bottke, W. F. et al. Stochastic late accretion to Earth, the Moon, and Mars. Science 330, 1527–1530 (2010).

Boyce JW, Liu Y, Rossman GR, Guan Y, Eiler JM, et al. 2010. Lunar apatite with terrestrial volatile abundances. Nature 466:466–69

Boyce JW, Tomlinson SM, McCubbin FM. 2014. The lunar apatite paradox. Science 344:400–2

Brasser, R., & Morbidelli, A. (2013). Oort cloud and Scattered Disc formation during a late dynamical instability in the Solar System. *Icarus*, *225*(1), 40-49.

Brauer, F., Dullemond, C. P., & Henning, T. (2008). Coagulation, fragmentation and radial motion of solid particles in protoplanetary disks. *Astronomy & Astrophysics*, *480*(3), 859-877.

Bräuer, K., Kämpf, H., Niedermann, S., & Strauch, G. (2013). Indications for the existence of different magmatic reservoirs beneath the Eifel area (Germany): a multi-isotope (C, N, He, Ne, Ar) approach. *Chemical Geology*, *356*, 193-208.

Braukmüller, N., Wombacher, F., Funk, C., & Münker, C. (2019). Earth's volatile element depletion pattern inherited from a carbonaceous chondrite-like source. *Nature Geoscience*, 1.

Briani, G., Gounelle, M., Marrocchi, Y., Mostefaoui, S., Leroux, H., Quirico, E., & Meibom, A. (2009). Pristine extraterrestrial material with unprecedented nitrogen isotopic variation. *Proceedings of the National Academy of Sciences*, *106*(26), 10522-10527.

Broadley et al. 2019

Brown, M. (2006). Duality of thermal regimes is the distinctive characteristic of plate tectonics since the Neoarchean. *Geology*, *34*(11), 961-964.

Budde, G., Burkhardt, C., Brennecka, G. A., Fischer-Gödde, M., Kruijer, T. S., & Kleine, T. (2016). Molybdenum isotopic evidence for the origin of chondrules and a distinct genetic heritage of carbonaceous and non-carbonaceous meteorites. *Earth and Planetary Science Letters*, *454*, 293-303.

Budde, G., Burkhardt, C., & Kleine, T. (2019). Molybdenum isotopic evidence for the late accretion of outer Solar System material to Earth. *Nature Astronomy*, 1.

Buikin, A., Trieloff, M., Hopp, J., Althaus, T., Korochantseva, E., Schwarz, W.H. and Altherr, R., 2005. Noble gas isotopes suggest deep mantle plume source of late Cenozoic mafic alkaline volcanism in Europe. Earth and Planetary Science Letters, 230(1-2), pp.143-162.

Burkhardt, C., Dauphas, N., Hans, U., Bourdon, B., & Kleine, T. (2019). Elemental and isotopic variability in solar system materials by mixing and processing of primordial disk reservoirs. *Geochimica et Cosmochimica Acta*, *261*, 145-170.

Burnard, P., Zimmermann, L., & Sano, Y. (2013). The noble gases as geochemical tracers: History and background. In *The Noble Gases as Geochemical Tracers* (pp. 1-15). Springer, Berlin, Heidelberg.

Busemann, H., Baur, H., & Wieler, R. (2000). Primordial noble gases in "phase Q" in carbonaceous and ordinary chondrites studied by closed-system stepped etching. *Meteoritics & Planetary Science*, *35*(5), 949-973.

Busemann, H., Young, A. F., Alexander, C. M. D., Hoppe, P., Mukhopadhyay, S., & Nittler, L. R. (2006). Interstellar chemistry recorded in organic matter from primitive meteorites. *Science*, *312*(5774), 727-730.

Busemann, H., Nguyen, A. N., Cody, G. D., Hoppe, P., Kilcoyne, A. D., Stroud, R. M., ... & Nittler, L. R. (2009). Ultra-primitive interplanetary dust particles from the comet 26P/Grigg–Skjellerup dust stream collection. *Earth and Planetary Science Letters*, *288*(1-2), 44-57.

Cabral, R. A., Jackson, M. G., Rose-Koga, E. F., Koga, K. T., Whitehouse, M. J., Antonelli, M. A., ... & Hauri, E. H. (2013). Anomalous sulphur isotopes in plume lavas reveal deep mantle storage of Archaean crust. *Nature*, *496*(7446), 490.

Calmonte, U., Altwegg, K., Balsiger, H., Berthelier, J. J., Bieler, A., De Keyser, J., ... & Le Roy, L. (2017). Sulphur isotope mass-independent fractionation observed in comet 67P/Churyumov–Gerasimenko by Rosetta/ROSINA. *Monthly Notices of the Royal Astronomical Society*, *469*(Suppl_2), S787-S803.

Canup, R. M., & Asphaug, E. (2001). Origin of the Moon in a giant impact near the end of the Earth's formation. *Nature*, *412*(6848), 708.

Caracausi, A., Avice, G., Burnard, P. G., Füri, E., & Marty, B. (2016). Chondritic xenon in the Earth's mantle. *Nature*, *533*(7601), 82.

Cartier, C., & Wood, B. J. (2019). The role of reducing conditions in building Mercury. *Elements: An International Magazine of Mineralogy, Geochemistry, and Petrology*, *15*(1), 39-45.

Cartigny, P., & Ader, M. (2003). A comment on "The nitrogen record of crust–mantle interaction and mantle convection from Archean to Present" by B. Marty and N. Dauphas [Earth Planet. Sci. Lett. 206 (2003) 397–410]. *Earth and Planetary Science Letters*, *216*(3), 425-432.

Cavarroc, M., Alcouffe, G., Boufendi, L., Cernogora, G., & Szopa, C. (2007). Study of a radio frequency plasma for production of equivalents of Titan's aerosols. *Proc. ICPIG*, *28*, 2079-2082.

Chakraborty, S., Ahmed, M., Jackson, T. L., & Thiemens, M. H. (2008). Experimental test of self-shielding in vacuum ultraviolet photodissociation of CO. *Science*, *321*(5894), 1328-1331.

Chakraborty, S., Muskatel, B. H., Jackson, T. L., Ahmed, M., Levine, R. D., & Thiemens, M. H. (2014). Massive isotopic effect in vacuum UV photodissociation of N2 and implications for meteorite data. *Proceedings of the National Academy of Sciences*, *111*(41), 14704-14709.

Charnoz, S., Fouchet, L., Aleon, J., & Moreira, M. (2011). Three-dimensional lagrangian turbulent diffusion of dust grains in a protoplanetary disk: Method and first applications. *The Astrophysical Journal*, *737*(1), 33.

Charnoz, S., & Taillifet, E. (2012). A method for coupling dynamical and collisional evolution of dust in circumstellar disks: The effect of a dead zone. *The Astrophysical Journal*, *753*(2), 119.

Charnoz, S., Aléon, J., Chaumard, N., Baillié, K., & Taillifet, E. (2015). Growth of calcium–aluminum-rich inclusions by coagulation and fragmentation in a turbulent protoplanetary disk: Observations and simulations. *Icarus*, *252*, 440-453.

Charnoz, S., Pignatale, F. C., Hyodo, R., Mahan, B., Chaussidon, M., Siebert, J., & Moynier, F. (2019). Planetesimal formation in an evolving protoplanetary disk with a dead zone. *A&A* 627, A50.

Chatterjee, R., & Lassiter, J. C. (2016). 186Os/188Os variations in upper mantle peridotites: Constraints on the Pt/Os ratio of primitive upper mantle, and implications for late veneer accretion and mantle mixing timescales. *Chemical Geology*, *442*, 11-22.

Chen, Y., Zhang, Y., Liu, Y., Guan, Y., Eiler, J., & Stolper, E. M. (2015). Water, fluorine, and sulfur concentrations in the lunar mantle. *Earth and Planetary Science Letters*, *427*, 37-46.

Chyba, C., & Sagan, C. (1992). Endogenous production, exogenous delivery and impact-shock synthesis of organic molecules: an inventory for the origins of life. *Nature*, *355*(6356), 125.

Ciarniello, M., Capaccioni, F., Filacchione, G., Raponi, A., Tosi, F., De Sanctis, M. C., ... & Arnold, G. (2015). Photometric properties of comet 67P/Churyumov-Gerasimenko from VIRTIS-M onboard Rosetta. *Astronomy & Astrophysics*, *583*, A31.

Ciborowski, T. J. R., & Kerr, A. C. (2016). Did mantle plume magmatism help trigger the Great Oxidation Event?. *Lithos*, *246*, 128-133.

Ciesla, F. J., & Sandford, S. A. (2012). Organic synthesis via irradiation and warming of ice grains in the solar nebula. *Science*, *336*(6080), 452-454.

Ciesla, F. J., Krijt, S., Yokochi, R., & Sandford, S. (2018). The Efficiency of Noble Gas Trapping in Astrophysical Environments. *The Astrophysical Journal*, *867*(2), 146.

Claire, M. W., Sheets, J., Cohen, M., Ribas, I., MEADOwS, V. S., & Catling, D. C. (2012). The evolution of solar flux from 0.1 nm to 160 μm: quantitative estimates for planetary studies. *The Astrophysical Journal*, *757*(1), 95.

Clay, P. L., Burgess, R., Busemann, H., Ruzié-Hamilton, L., Joachim, B., Day, J. M., & Ballentine, C. J. (2017). Halogens in chondritic meteorites and terrestrial accretion. *Nature*, *551*(7682), 614.

Clayton, R. N., Grossman, L., & Mayeda, T. K. (1973). A component of primitive nuclear composition in carbonaceous meteorites. *Science*, *182*(4111), 485-488.

Clayton, D. D., & Ward, R. A. (1978). s-Process studies: Xenon and krypton isotopic abundances. *The Astrophysical Journal*.

Clayton, D. D. (1982). Cosmic chemical memory-a new astronomy. *Quarterly Journal of the Royal Astronomical Society*, *23*, 174.

Cleland, C. E., & Chyba, C. F. (2002). Defining 'life'. *Origins of Life and Evolution of the Biosphere*, *32*(4), 387-393.

Clement, M. S., Kaib, N. A., Raymond, S. N., Chambers, J. E., & Walsh, K. J. (2019). The early instability scenario: Terrestrial planet formation during the giant planet instability, and the effect of collisional fragmentation. *Icarus*, *321*, 778-790.

Cody, G.D. and Alexander, C.M.O.D. (2005) NMR studies of chemical and structural variation of insoluble organic matter from different carbonaceous chondrite groups. Geochimica et Cosmochimica Acta, 69,1085–1097.

Collings, M. P., Dever, J. W., Fraser, H. J., & McCoustra, M. R. (2003). Laboratory studies of the interaction of carbon monoxide with water ice. *Astrophysics and Space Science*, *285*(3-4), 633-659.

Connelly, J. N., Bollard, J., & Bizzarro, M. (2017). Pb–Pb chronometry and the early solar system. *Geochimica et Cosmochimica Acta*, *201*, 345-363.

Cosmidis, J., & Templeton, A. S. (2016). Self-assembly of biomorphic carbon/sulfur microstructures in sulfidic environments. *Nature communications*, *7*, 12812.

Ćuk, M., & Stewart, S. T. (2012). Making the Moon from a fast-spinning Earth: a giant impact followed by resonant despinning. *science*, *338*(6110), 1047-1052.

Dalai, P., Kaddour, H., & Sahai, N. (2016). Incubating life: prebiotic sources of organics for the origin of life. *Elements*, *12*(6), 401-406.

Dalou, C., Füri, E., Deligny, C., Piani, L., Caumon, M. C., Laumonier, M., ... & Edén, M. (2019). Redox control on nitrogen isotope fractionation during planetary core formation. *Proceedings of the National Academy of Sciences*, *116*(29), 14485-14494.

Danger, G., Orthous-Daunay, F. R., de Marcellus, P., Modica, P., Vuitton, V., Duvernay, F., ... & Chiavassa, T. (2013). Characterization of laboratory analogs of interstellar/cometary organic residues using very high resolution mass spectrometry. *Geochimica et Cosmochimica Acta*, *118*, 184-201.

Da Silva, L., Maurel, M. C., & Deamer, D. (2015). Salt-promoted synthesis of RNA-like molecules in simulated hydrothermal conditions. *Journal of molecular evolution*, *80*(2), 86-97.

Dauphas, N., & Marty, B. (1999). Heavy nitrogen in carbonatites of the Kola Peninsula: A possible signature of the deep mantle. *Science*, *286*(5449), 2488-2490.

Dauphas, N., Marty, B., & Reisberg, L. (2002). Molybdenum nucleosynthetic dichotomy revealed in primitive meteorites. *The Astrophysical Journal Letters*, *569*(2), L139.

Dauphas, N. (2003). The dual origin of the terrestrial atmosphere. *Icarus*, *165*(2), 326-339.

Dauphas, N., Davis, A. M., Marty, B., & Reisberg, L. (2004). The cosmic molybdenum–ruthenium isotope correlation. *Earth and Planetary Science Letters*, *226*(3-4), 465-475.

Dauphas, N., Remusat, L., Chen, J. H., Roskosz, M., Papanastassiou, D. A., Stodolna, J., ... & Eiler, J. M. (2010). Neutron-rich chromium isotope anomalies in supernova nanoparticles. *The Astrophysical Journal*, *720*(2), 1577.

Dauphas, N., & Chaussidon, M. (2011). A perspective from extinct radionuclides on a young stellar object: the Sun and its accretion disk. *Annual Review of Earth and Planetary Sciences*, *39*, 351-386.

Dauphas, N., & Pourmand, A. (2011). Hf–W–Th evidence for rapid growth of Mars and its status as a planetary embryo. *Nature*, *473*(7348), 489.

Dauphas, N., Burkhardt, C., Warren, P. H., & Fang-Zhen, T. (2014). Geochemical arguments for an Earth-like Moon-forming impactor. *Philosophical Transactions of the Royal Society A: Mathematical, Physical and Engineering Sciences*, *372*(2024), 20130244.

Dauphas, N. (2017). The isotopic nature of the Earth's accreting material through time. *Nature*, *541*(7638), 521.

Davis, A. M., Richter, F. M., Mendybaev, R. A., Janney, P. E., Wadhwa, M., & McKeegan, K. D. (2015). Isotopic mass fractionation laws for magnesium and their effects on 26Al–26Mg systematics in solar system materials. *Geochimica et Cosmochimica Acta*, *158*, 245-261.

Day, J. M., Pearson, D. G., & Taylor, L. A. (2007). Highly siderophile element constraints on accretion and differentiation of the Earth-Moon system. *Science*, *315*(5809), 217-219.

Deamer, D., Damer, B., & Kompanichenko, V. (2019). Hydrothermal chemistry and the origin of cellular life. *Astrobiology*.

De Hoffmann, E., Charette, J., Stroobant, V. (1994) Spéctrométrie de Masse, Masson, Paris, France. p178.

De Keyser, J., Dhooghe, F., Gibbons, A., Altwegg, K., Balsiger, H., Berthelier, J. J., ... & Fiethe, B. (2015). Correcting peak deformation in Rosetta's ROSINA/DFMS mass spectrometer. *International journal of mass spectrometry*, *393*, 41-51.

Delarue, F., Rouzaud, J. N., Derenne, S., Bourbin, M., Westall, F., Kremer, B., ... & Robert, F. (2016). The Raman-derived carbonization continuum: A tool to select the best preserved molecular structures in Archean kerogens. *Astrobiology*, *16*(6), 407-417.

Deloule, E., Albarede, F., & Sheppard, S. M. (1991). Hydrogen isotope heterogeneities in the mantle from ion probe analysis of amphiboles from ultramafic rocks. *Earth and Planetary Science Letters*, *105*(4), 543-553.

Deloule, E., & Robert, F. (1995). Interstellar water in meteorites?. *Geochimica et Cosmochimica Acta*, *59*(22), 4695-4706.

de Marcellus, P., Fresneau, A., Brunetto, R., Danger, G., Duvernay, F., Meinert, C., ... & Le Sergeant d'Hendecourt, L. (2016). Photo and thermochemical evolution of astrophysical ice analogues as a source for soluble and insoluble organic materials in solar system minor bodies. *Monthly Notices of the Royal Astronomical Society*, *464*(1), 114-120.

DeMeo, F. E., & Carry, B. (2013). The taxonomic distribution of asteroids from multi-filter all-sky photometric surveys. *Icarus*, *226*(1), 723-741.

Derenne, S., & Robert, F. (2010). Model of molecular structure of the insoluble organic matter isolated from Murchison meteorite. *Meteoritics & Planetary Science*, *45*(9), 1461-1475.

de Ronde, C.E.J., Channer, D.M. deR., Faure, K., Bray, C.J., Spooner, E.T.C., 1997. Fluid chemistry of Archean seafloor hydrothermal vents: Implications for the composition of circa 3.2 Ga seawater. Geochim. Cosmochim. Acta 61, 4025–4042.

Desch, S. J., Kalyaan, A., & Alexander, C. M. D. (2018). The effect of Jupiter's formation on the distribution of refractory elements and inclusions in meteorites. *The Astrophysical Journal Supplement Series*, *238*(1), 11.

d'Hendecourt, L. B., Allamandola, L. J., Baas, F., & Greenberg, J. M. (1982). Interstellar grain explosions-Molecule cycling between gas and dust. *Astronomy and Astrophysics*, *109*, L12-L14.

Dikov, Y. P., Ivanov, A. V., Wlotzka, F., Galimov, E. M., & Wänke, H. (1998). High enrichment of carbon and volatile elements in the surface layers of Luna 16 soil sample 1635: Result of comet or meteorite impact?. *Earth and planetary science letters*, *155*(3-4), 197-204.

DiSanti, M. A., Bonev, B. P., Gibb, E. L., Roth, N. X., Russo, N. D., & Vervack Jr, R. J. (2018). Comet C/2013 V5 (Oukaimeden): Evidence for Depleted Organic Volatiles and Compositional Heterogeneity as Revealed through Infrared Spectroscopy. *The Astronomical Journal*, *156*(6), 258.

Donati, J. F., Moutou, C., Malo, L., Baruteau, C., Yu, L., Hébrard, E., ... & Petit, P. (2016). A hot Jupiter orbiting a 2-million-year-old solar-mass T Tauri star. *Nature*, *534*(7609), 662.

Drake, M. J., & Righter, K. (2002). Determining the composition of the Earth. *Nature*, *416*(6876), 39.

Drążkowska, J., Alibert, Y., & Moore, B. (2016). Close-in planetesimal formation by pile-up of drifting pebbles. *Astronomy & Astrophysics*, *594*, A105.

Drążkowska, J., & Alibert, Y. (2017). Planetesimal formation starts at the snow line. *Astronomy & Astrophysics*, *608*, A92.

Dullemond, C. P. Theoretical Models of the Structure of Protoplanetary Disks Les Houches 2013.

Duprat, J., Dobrică, E., Engrand, C., Aléon, J., Marrocchi, Y., Mostefaoui, S., ... & Robert, F. (2010). Extreme deuterium excesses in ultracarbonaceous micrometeorites from central Antarctic snow. *Science*, *328*(5979), 742-745.

Durand, B., & Nicaise, G. (1980). Procedures for kerogen isolation. In *Kerogen* (pp. 35-53). Technip Paris.

Eberhardt, P., Eugster, O., & Marti, K. (1965). A redetermination of the isotopic composition of atmospheric neon. *Zeitschrift für Naturforschung A*, *20*(4), 623-624.

Ehrenfreund, P., & Fraser, H. (2003). Ice chemistry in space. In *Solid State Astrochemistry* (pp. 317-356). Springer, Dordrecht.

Ehrenfreund, P., Spaans, M., & Holm, N. G. (2011). The evolution of organic matter in space. *Philosophical Transactions of the Royal Society A: Mathematical, Physical and Engineering Sciences*, *369*(1936), 538-554.

Elkins-Tanton, L. T. Linked magma ocean solidification and atmospheric growth for Earth and Mars. *Earth and Planetary Science Letters*, *271*(1-4), 181-191 (2008).

Elkins-Tanton, L. T. Formation of early water oceans on rocky planets. *Astrophysics and Space Science*, *332*(2), 359-364 (2011).

Elkins-Tanton, L. T., Burgess, S., & Yin, Q. Z. (2011). The lunar magma ocean: Reconciling the solidification process with lunar petrology and geochronology. *Earth and Planetary Science Letters*, *304*(3-4), 326-336.

Elliott, T., Zindler, A., & Bourdon, B. (1999). Exploring the kappa conundrum: the role of recycling in the lead isotope evolution of the mantle. *Earth and Planetary Science Letters*, *169*(1-2), 129-145.

Engel, M. H., & Macko, S. A. (1997). Isotopic evidence for extraterrestrial non-racemic amino acids in the Murchison meteorite. *Nature*, *389*(6648), 265.

Epstein, S., & Taylor Jr, H. P. (1974). D/H and O-18/O-16 ratios of H2O in the'rusty'breccia 66095 and the origin of'lunar water'. In *Lunar and Planetary Science Conference Proceedings* (Vol. 5, pp. 1839-1854).

Eugster, O., Eberhardt, P., & Geiss, J. (1967b). Krypton and xenon isotopic composition in three carbonaceous chondrites. *Earth and Planetary Science Letters*, *3*, 249-257.

Eugster, O., Eberhardt, P., & Geiss, J. (1967a). The isotopic composition of krypton in unequilibrated and gas rich chondrites. *Earth and Planetary Science Letters*, *2*(5), 385-393.

Eugster, O., Eberhardt, P., Geiss, J., Grögler, N., Jungck, M., & Mörgeli, M. (1977). The cosmic-ray exposure history of Shorty Crater samples-The age of Shorty Crater. In *Lunar and Planetary Science Conference Proceedings* (Vol. 8, pp. 3059-3082).

Farquhar, J., Bao, H., & Thiemens, M. (2000). Atmospheric influence of Earth's earliest sulfur cycle. *Science*, *289*(5480), 756-758.

Farquhar, J., & Wing, B. A. (2003). Multiple sulfur isotopes and the evolution of the atmosphere. *Earth and Planetary Science Letters*, *213*(1-2), 1-13.

Favre, C., Fedele, D., Semenov, D., Parfenov, S., Codella, C., Ceccarelli, C., ... & Lefloch, B. (2018). First detection of the simplest organic acid in a protoplanetary disk. *The Astrophysical journal letters*, *862*(1), L2.

Fayolle, E. C., Öberg, K. I., Cuppen, H. M., Visser, R., & Linnartz, H. (2011). Laboratory H2O: CO2 ice desorption data: entrapment dependencies and its parameterization with an extended three-phase model. *Astronomy & Astrophysics*, *529*, A74.

Fehr, M. A., Hammond, S. J., & Parkinson, I. J. (2018). Tellurium stable isotope fractionation in chondritic meteorites and some terrestrial samples. *Geochimica et Cosmochimica Acta*, *222*, 17-33.

Ferris, J. P., Hill Jr, A. R., Liu, R., & Orgel, L. E. (1996). Synthesis of long prebiotic oligomers on mineral surfaces. *Nature*, *381*(6577), 59.

Feuillie, C., Daniel, I., Michot, L. J., & Pedreira-Segade, U. (2013). Adsorption of nucleotides onto Fe–Mg–Al rich swelling clays. *Geochimica et Cosmochimica Acta*, *120*, 97-108.

Feulner, G. (2012). The faint young Sun problem. *Reviews of Geophysics*, *50*(2).

Fischer-Gödde, M., Becker, H., & Wombacher, F. (2011). Rhodium, gold and other highly siderophile elements in orogenic peridotites and peridotite xenoliths. *Chemical Geology*, *280*(3-4), 365-383.

Fischer-Gödde, M., & Kleine, T. (2017). Ruthenium isotopic evidence for an inner Solar System origin of the late veneer. *Nature*, *541*(7638), 525.

Fitoussi, C., & Bourdon, B. (2012). Silicon isotope evidence against an enstatite chondrite Earth. *Science*, *335*(6075), 1477-1480.

Floss, C., Stadermann, F. J., Kearsley, A. T., Burchell, M. J., & Ong, W. J. (2013). The abundance of presolar grains in comet 81P/Wild 2. *The Astrophysical Journal*, *763*(2), 140.

Floss, C., & Haenecour, P. (2016). Presolar silicate grains: Abundances, isotopic and elemental compositions, and the effects of secondary processing. *Geochemical Journal*, *50*(1), 3-25.

Fray, N., & Schmitt, B. (2009). Sublimation of ices of astrophysical interest: A bibliographic review. *Planetary and Space Science*, *57*(14-15), 2053-2080.

Fray, N., Bardyn, A., Cottin, H., Altwegg, K., Baklouti, D., Briois, C., ... & Grün, E. (2016). High-molecular-weight organic matter in the particles of comet 67P/Churyumov–Gerasimenko. *Nature*, *538*(7623), 72.

Frick, U., Mack, R., & Chang, S. (1979). Noble gas trapping and fractionation during synthesis of carbonaceous matter. In *Lunar and Planetary Science Conference Proceedings* (Vol. 10, pp. 1961-1972).

Frick, U., & Pepin, R. O. (1981). On the distribution of noble gases in Allende: a differential oxidation study. *Earth and Planetary Science Letters*, *56*, 45-63.

Füri, E., Marty, B., & Assonov, S. S. (2012). Constraints on the flux of meteoritic and cometary water on the Moon from volatile element (N–Ar) analyses of single lunar soil grains, Luna 24 core. *Icarus*, *218*(1), 220-229.

Füri, E., Deloule, E., Gurenko, A., & Marty, B. (2014). New evidence for chondritic lunar water from combined D/H and noble gas analyses of single Apollo 17 volcanic glasses. *Icarus*, *229*, 109-120.

Füri, E., Barry, P. H., Taylor, L. A., & Marty, B. (2015). Indigenous nitrogen in the Moon: constraints from coupled nitrogen–noble gas analyses of mare basalts. *Earth and Planetary Science Letters*, *431*, 195-205.

Furukawa, Y., Sekine, T., Oba, M., Kakegawa, T., & Nakazawa, H. (2009). Biomolecule formation by oceanic impacts on early Earth. *Nature geoscience*, *2*(1), 62.

Gaillard, F., Scaillet, B., & Arndt, N. T. (2011). Atmospheric oxygenation caused by a change in volcanic degassing pressure. *Nature*, *478*(7368), 229.

García-Ruiz, J. M., Hyde, S. T., Carnerup, A. M., Christy, A. G., Van Kranendonk, M. J., & Welham, N. J. (2003). Self-assembled silica-carbonate structures and detection of ancient microfossils. *Science*, *302*(5648), 1194-1197.

Garrod, R. T., & Herbst, E. (2006). Formation of methyl formate and other organic species in the warm-up phase of hot molecular cores. *Astronomy & Astrophysics*, *457*(3), 927-936.

Garvie, L. A., & Buseck, P. R. (2007). Prebiotic carbon in clays from Orgueil and Ivuna (CI), and Tagish Lake (C2 ungrouped) meteorites. *Meteoritics & Planetary Science*, *42*(12), 2111-2117.

Genda, H., Brasser, R., & Mojzsis, S. J. (2017). The terrestrial late veneer from core disruption of a lunar-sized impactor. *Earth and Planetary Science Letters*, *480*, 25-32.

Gessmann, C. K., Rubie, D. C., & McCammon, C. A. (1999). Oxygen fugacity dependence of Ni, Co, Mn, Cr, V, and Si partitioning between liquid metal and magnesiowüstite at 9–18 GPa and 2200 C. *Geochimica et cosmochimica acta*, *63*(11-12), 1853-1863.

Gibson, E. K., & Moore, G. W. (1973). Volatile-rich lunar soil: evidence of possible cometary impact. *Science*, *179*(4068), 69-71.

Gilbert, W. (1986). Origin of life: The RNA world. *nature*, *319*(6055), 618.

Gilmour, J. D., & Turner, G. (2007). Constraints on nucleosynthesis from xenon isotopes in presolar material. *The Astrophysical Journal*, *657*(1), 600.

Gilmour, J. D. (2010). "Planetary" noble gas components and the nucleosynthetic history of solar system material. *Geochimica et Cosmochimica Acta*, *74*(1), 380-393.

Gilmour, J. D., & Filtness, M. J. (2019). Dissipation of the Solar System's debris disk recorded in primitive meteorites. *Nature Astronomy*, *3*(4), 326.

Gladman, B., Kavelaars, J. J., Petit, J. M., Morbidelli, A., Holman, M. J., & Loredo, T. (2001). The structure of the Kuiper belt: Size distribution and radial extent. *The Astronomical Journal*, *122*(2), 1051.

Gladman, B. (2005). The Kuiper belt and the solar system's comet disk. *Science*, *307*(5706), 71-75.

Glavin, D. P., & Dworkin, J. P. (2009). Enrichment of the amino acid L-isovaline by aqueous alteration on CI and CM meteorite parent bodies. *Proceedings of the National Academy of Sciences*, *106*(14), 5487-5492.

Göbel, R., Ott, U., & Begemann, F. (1978). On trapped noble gases in ureilites. *Journal of Geophysical Research: Solid Earth*, *83*(B2), 855-867.

Goldman, N., Reed, E. J., Fried, L. E., Kuo, I. F. W., & Maiti, A. (2010). Synthesis of glycine-containing complexes in impacts of comets on early Earth. *Nature Chemistry*, *2*(11), 949.

Gomes, R., Levison, H. F., Tsiganis, K., & Morbidelli, A. (2005). Origin of the cataclysmic Late Heavy Bombardment period of the terrestrial planets. *Nature*, *435*(7041), 466.

Gonzalez, J. F., Laibe, G., Maddison, S. T., Pinte, C., & Ménard, F. (2015). ALMA images of discs: are all gaps carved by planets?. *Monthly Notices of the Royal Astronomical Society: Letters*, *454*(1), L36-L40.

Goodrich, C. A., Jones, J. H., & Berkley, J. L. (1987). Origin and evolution of the ureilite parent magmas: Multi-stage igneous activity on a large parent body. *Geochimica et Cosmochimica Acta*, *51*(9), 2255-2273.

Gradie, J., & Tedesco, E. (1982). Compositional structure of the asteroid belt. *Science*, *216*(4553), 1405-1407.

Graham, D. W. (2002). Noble gas isotope geochemistry of mid-ocean ridge and ocean island basalts: Characterization of mantle source reservoirs. *Reviews in mineralogy and geochemistry*, *47*(1), 247-317.

Greber, N. D., Dauphas, N., Bekker, A., Ptáček, M. P., Bindeman, I. N., & Hofmann, A. (2017). Titanium isotopic evidence for felsic crust and plate tectonics 3.5 billion years ago. *Science*, *357*(6357), 1271-1274.

Greenwood, J. P., Itoh, S., Sakamoto, N., Warren, P., Taylor, L., & Yurimoto, H. (2011). Hydrogen isotope ratios in lunar rocks indicate delivery of cometary water to the Moon. *Nature Geoscience*, *4*(2), 79.

Greenwood, J. P., Karato, S. I., Vander Kaaden, K. E., Pahlevan, K., & Usui, T. (2018). Water and Volatile Inventories of Mercury, Venus, the Moon, and Mars. *Space Science Reviews*, *214*(5), 92.

Greenwood, R. C., Barrat, J. A., Miller, M. F., Anand, M., Dauphas, N., Franchi, I. A., ... & Starkey, N. A. (2018). Oxygen isotopic evidence for accretion of Earth's water before a high-energy Moon-forming giant impact. *Science advances*, *4*(3), eaao5928.

Grewal, D. S., Dasgupta, R., Sun, C., Tsuno, K., & Costin, G. (2019). Delivery of carbon, nitrogen, and sulfur to the silicate Earth by a giant impact. *Science advances*, *5*(1), eaau3669.

Gudipati, M. S., & Castillo-Rogez, J. (Eds.). (2012). *The science of solar system ices* (Vol. 356). Springer Science & Business Media.

Guilbert-Lepoutre, A., Rosenberg, E. D., Prialnik, D., & Besse, S. (2016). Modelling the evolution of a comet subsurface: Implications for 67P/Churyumov–Gerasimenko. *Monthly Notices of the Royal Astronomical Society*, *462*(Suppl_1), S146-S155.

Guzmán-Marmolejo, A., Segura, A., & Escobar-Briones, E. (2013). Abiotic production of methane in terrestrial planets. *Astrobiology*, *13*(6), 550-559.

Halliday, A. N. (2004). Mixing, volatile loss and compositional change during impact-driven accretion of the Earth. *Nature*, *427*(6974), 505.

Hallis, L. J., Huss, G. R., Nagashima, K., Taylor, G. J., Halldórsson, S. A., Hilton, D. R., ... & Meech, K. J. (2015). Evidence for primordial water in Earth's deep mantle. *Science*, *350*(6262), 795-797.

Hama, T., Yabushita, A., Yokoyama, M., Kawasaki, M., & Watanabe, N. (2009a). Formation mechanisms of oxygen atoms in the O (PJ 3) state from the 157 nm photoirradiation of amorphous water ice at 90 K. *The Journal of chemical physics*, *131*(11), 114511.

Hama, T., Yokoyama, M., Yabushita, A., Kawasaki, M., Wickramasinghe, P., Guo, W., ... & Western, C. M. (2009b). Translational and internal energy distributions of methyl and hydroxyl radicals produced by 157 nm photodissociation of amorphous solid methanol. *The Journal of chemical physics*, *131*(22), 224512.

Hama, T., Yokoyama, M., Yabushita, A., & Kawasaki, M. (2010). Role of OH radicals in the formation of oxygen molecules following vacuum ultraviolet photodissociation of amorphous solid water. *The Journal of chemical physics*, *133*(10), 104504.

Hamano, K., Abe, Y., & Genda, H. Emergence of two types of terrestrial planet on solidification of magma ocean. *Nature*, *497*(7451), 607 (2013)

Haner, J., & Schrobilgen, G. J. (2015). The chemistry of Xenon (IV). *Chemical reviews*, *115*(2), 1255-1295.

Hansen, B. M. (2009). Formation of the terrestrial planets from a narrow annulus. *The Astrophysical Journal*, *703*(1), 1131.

Haqq-Misra, J. D., Domagal-Goldman, S. D., Kasting, P. J., & Kasting, J. F. (2008). A revised, hazy methane greenhouse for the Archean Earth. *Astrobiology*, *8*(6), 1127-1137.

Hartmann, L., Calvet, N., Gullbring, E., & D'Alessio, P. (1998). Accretion and the evolution of T Tauri disks. *The Astrophysical Journal*, *495*(1), 385.

Hauri, E. H., Weinreich, T., Saal, A. E., Rutherford, M. C., & Van Orman, J. A. (2011). High pre-eruptive water contents preserved in lunar melt inclusions. *Science*, *333*(6039), 213-215.

Hauri, E. H., Saal, A. E., Rutherford, M. J., & Van Orman, J. A. (2015). Water in the Moon's interior: Truth and consequences. *Earth and Planetary Science Letters*, *409*, 252-264.

Hauri, E. H., Saal, A. E., Nakajima, M., Anand, M., Rutherford, M. J., Van Orman, J. A., & Le Voyer, M. (2017). Origin and evolution of water in the Moon's interior. *Annual Review of Earth and Planetary Sciences*, *45*, 89-111.

Hawkesworth, C., Cawood, P. A., & Dhuime, B. (2019). Rates of generation and growth of the continental crust. *Geoscience Frontiers*, *10*(1), 165-173.

Hay, W. W., Migdisov, A., Balukhovsky, A. N., Wold, C. N., Flögel, S., & Söding, E., 2006. Evaporites and the salinity of the ocean during the Phanerozoic: Implications for climate, ocean circulation and life. Palaeogeogr., Palaeoclim., Palaeoecol., 240, 3-46.

Heays, A. N., Bosman, A. D., & van Dishoeck, E. F. (2017). Photodissociation and photoionisation of atoms and molecules of astrophysical interest. *Astronomy & Astrophysics*, *602*, A105.

Heber, V. S., Baur, H., Bochsler, P., McKeegan, K. D., Neugebauer, M., Reisenfeld, D. B., ... & Wiens, R. C. (2012). Isotopic mass fractionation of solar wind: Evidence from fast and slow solar wind collected by the Genesis mission. *The Astrophysical Journal*, *759*(2), 121.

Herwartz, D., Pack, A., Friedrichs, B., & Bischoff, A. (2014). Identification of the giant impactor Theia in lunar rocks. *Science*, *344*(6188), 1146-1150.

Herzberg, C., Condie, K., & Korenaga, J. (2010). Thermal history of the Earth and its petrological expression. *Earth and Planetary Science Letters*, *292*(1-2), 79-88.

Hezel, D. C., & Palme, H. (2010). The chemical relationship between chondrules and matrix and the chondrule matrix complementarity. *Earth and Planetary Science Letters*, *294*(1-2), 85-93.

Hezel, D. C., Wilden, J. S., Becker, D., Steinbach, S., Wombacher, F., & Harak, M. (2018). Fe isotope composition of bulk chondrules from Murchison (CM2): Constraints for parent body alteration, nebula processes and chondrule-matrix complementarity. *Earth and Planetary Science Letters*, *490*, 31-39.

Hickman, A. H., & Van Kranendonk, M. J. (2012). Early Earth evolution: evidence from the 3.5-1.8 Ga geological history of the Pilbara region of Western Australia. *Episodes*, *35*(1), 283-297.

Hirschmann, M. M. (2016). Constraints on the early delivery and fractionation of Earth's major volatiles from C/H, C/N, and C/S ratios. *American Mineralogist*, *101*(3), 540-553.

Haugbølle, T., Weber, P., Wielandt, D. P., Benítez-Llambay, P., Bizzarro, M., Gressel, O., & Pessah, M. E. (2019). Probing the protosolar disk using dust filtering at gaps in the early Solar System. *arXiv preprint arXiv:1903.12274*.

Hohenberg, C. M., Thonnard, N., & Meshik, A. (2002). Active capture and anomalous adsorption: New mechanisms for the incorporation of heavy noble gases. *Meteoritics & Planetary Science*, *37*(2), 257-267.

Holland, G., & Ballentine, C. J. (2006). Seawater subduction controls the heavy noble gas composition of the mantle. *Nature*, *441*(7090), 186.

Holland, G., Cassidy, M., & Ballentine, C. J. (2009). Meteorite Kr in Earth's mantle suggests a late accretionary source for the atmosphere. *Science*, *326*(5959), 1522-1525.

Holland, H. D. (2006). The oxygenation of the atmosphere and oceans. *Philosophical Transactions of the Royal Society B: Biological Sciences*, *361*(1470), 903-915.

Hollenstein, U., Palm, H., & Merkt, F. (2000). A broadly tunable extreme ultraviolet laser source with a 0.008 cm− 1 bandwidth. *Review of Scientific Instruments*, *71*(11), 4023-4028.

Honda, M., Zhang, X., Phillips, D., Hamilton, D., Deerberg, M., & Schwieters, J. B. (2015). Redetermination of the 21Ne relative abundance of the atmosphere, using a high resolution, multi-collector noble gas mass spectrometer (HELIX-MC Plus). *International Journal of Mass Spectrometry*, *387*, 1-7.

Hoppe, P., Leitner, J., & Kodolányi, J. (2017). The stardust abundance in the local interstellar cloud at the birth of the solar system. *Nature Astronomy*, *1*(9), 617.

Hoppe, P., Rubin, M., & Altwegg, K. (2018). Presolar Isotopic Signatures in Meteorites and Comets: New Insights from the Rosetta Mission to Comet 67P/Churyumov–Gerasimenko. *Space science reviews*, *214*(6), 106.

Hosono, N., Karato, S. I., Makino, J., & Saitoh, T. R. (2019). Terrestrial magma ocean origin of the Moon. *Nature Geoscience*, 1.

Howard, K. T., Alexander, C. O. D., Schrader, D. L., & Dyl, K. A. (2015). Classification of hydrous meteorites (CR, CM and C2 ungrouped) by phyllosilicate fraction: PSD-XRD modal mineralogy and planetesimal environments. *Geochimica et Cosmochimica Acta*, *149*, 206-222.

Hui, H., Guan, Y., Chen, Y., Peslier, A. H., Zhang, Y., Liu, Y., ... & Osinski, G. R. (2017). A heterogeneous lunar interior for hydrogen isotopes as revealed by the lunar highlands samples. *Earth and Planetary Science Letters*, *473*, 14-23.

Humbert, F., Libourel, G., France-Lanord, C., Zimmermann, L., & Marty, B. (2000). CO2-laser extraction-static mass spectrometry analysis of ultra-low concentrations of nitrogen in silicates. *Geostandards Newsletter*, *24*(2), 255-260.

Hunten, D. M. (1993). Atmospheric evolution of the terrestrial planets. *Science*, 915-920.

Huss, G. R., & Lewis, R. S. (1994). Noble gases in presolar diamonds I: Three distinct components and their implications for diamond origins. *Meteoritics*, *29*(6), 791-810.

Huss, G. R., & Lewis, R. S. (1995). Presolar diamond, SiC, and graphite in primitive chondrites: Abundances as a function of meteorite class and petrologic type. *Geochimica et Cosmochimica Acta*, *59*(1), 115-160.

Huss, G. R., Lewis, R. S., & Hemkin, S. (1996). The "normal planetary" noble gas component in primitive chondrites: Compositions, carrier, and metamorphic history. *Geochimica et Cosmochimica Acta*, *60*(17), 3311-3340.

Hyodo, R., Ida, S., & Charnoz, S. (2019). Formation of rocky and icy planetesimals inside and outside the snow line: effects of diffusion, sublimation, and back-reaction. *Astronomy & Astrophysics*, *629*, A90.

Isella, A., Guidi, G., Testi, L., Liu, S., Li, H., Li, S., ... & Manara, C. F. (2016). Ringed structures of the HD 163296 protoplanetary disk revealed by ALMA. *Physical Review Letters*, *117*(25), 251101.

Ivanova, O. V., Picazzio, E., Luk'yanyk, I. V., Cavichia, O., & Andrievsky, S. M. (2018). Spectroscopic observations of the comet 29P/Schwassmann-Wachmann 1 at the SOAR telescope. *Planetary and Space Science*, *157*, 34-38.

Izidoro, A., Raymond, S. N., Pierens, A., Morbidelli, A., Winter, O. C., & Nesvorny, D. (2016). The asteroid belt as a relic from a chaotic early Solar System. *The Astrophysical Journal*, *833*(1), 40.

Jackson, M. G., & Dasgupta, R. (2008). Compositions of HIMU, EM1, and EM2 from global trends between radiogenic isotopes and major elements in ocean island basalts. *Earth and Planetary Science Letters*, *276*(1-2), 175-186.

Jackson, C. R., Bennett, N. R., Du, Z., Cottrell, E., & Fei, Y. (2018). Early episodes of high-pressure core formation preserved in plume mantle. *Nature*, *553*(7689), 491.

Javoy, M. (1995). The integral enstatite chondrite model of the Earth. *Geophysical Research Letters*, *22*(16), 2219-2222.

Javaux, E. J. (2019). Challenges in evidencing the earliest traces of life. *Nature*, *572*(7770), 451-460.

Johansen, A., & Lambrechts, M. (2017). Forming planets via pebble accretion. *Annual Review of Earth and Planetary Sciences*, *45*, 359-387.

Johnston, D. T. (2011). Multiple sulfur isotopes and the evolution of Earth's surface sulfur cycle. *Earth-Science Reviews*, *106*(1-2), 161-183.

Jessberger, E. K., & Kissel, J. (1991). Chemical properties of cometary dust and a note on carbon isotopes. In *International Astronomical Union Colloquium* (Vol. 116, No. 2, pp. 1075-1092). Cambridge University Press.

Jones, M. R., Wanless, V. D., Soule, S. A., Kurz, M. D., Mittelstaedt, E., Fornari, D. J., ... & Péron, S. (2019). New constraints on mantle carbon from Mid-Atlantic Ridge popping rocks. *Earth and Planetary Science Letters*, *511*, 67-75.

Kaddour, H., & Sahai, N. (2014). Synergism and mutualism in non-enzymatic RNA polymerization. *Life*, *4*(4), 598-620.

Kappler, A., Pasquero, C., Konhauser, K. O., & Newman, D. K. (2005). Deposition of banded iron formations by anoxygenic phototrophic Fe (II)-oxidizing bacteria. *Geology*, *33*(11), 865-868.

Kargel, J. S., & Lunine, J. I. (1998). Clathrate hydrates on Earth and in the solar system. In *Solar System Ices* (pp. 97-117). Springer, Dordrecht.

Kawamura, K., Nishi, T., & Sakiyama, T. (2005). Consecutive elongation of alanine oligopeptides at the second time range under hydrothermal conditions using a microflow reactor system. *Journal of the American Chemical Society*, *127*(2), 522-523.

Kebukawa, Y., Chan, Q. H., Tachibana, S., Kobayashi, K., & Zolensky, M. E. (2017). One-pot synthesis of amino acid precursors with insoluble organic matter in planetesimals with aqueous activity. *Science advances*, *3*(3), e1602093.

Keller, H. U., Mottola, S., Davidsson, B., Schröder, S. E., Skorov, Y., Kührt, E., ... & Scholten, F. (2015). Insolation, erosion, and morphology of comet 67P/Churyumov-Gerasimenko. *Astronomy & Astrophysics*, *583*, A34.

Kellogg, L. H., & Wasserburg, G. J. (1990). The role of plumes in mantle helium fluxes. *Earth and Planetary Science Letters*, *99*(3), 276-289.

Kendrick, M. A., Hémond, C., Kamenetsky, V. S., Danyushevsky, L., Devey, C. W., Rodemann, T., ... & Perfit, M. R. (2017). Seawater cycled throughout Earth's mantle in partially serpentinized lithosphere. *Nature Geoscience*, *10*(3), 222.

Kerrich, R., & Jia, Y. (2004). A comment on "The nitrogen record of crust–mantle interaction and mantle convection from Archean to Present" by B. Marty and N. Dauphas [Earth Planet. Sci. Lett. 206 (2003) 397–410]. *Earth and Planetary Science Letters*, *225*(3-4), 435-440.

Khriachtchev, L., Pettersson, M., Runeberg, N., Lundell, J., & Räsänen, M. (2000). A stable argon compound. *Nature*, *406*(6798), 874.

Khriachtchev, L., Isokoski, K., Cohen, A., Räsänen, M., & Gerber, R. B. (2008). A small neutral molecule with two noble-gas atoms: HXeOXeH. *Journal of the American Chemical Society*, *130*(19), 6114-6118.

Kimura, K., Lewis, R.S., Anders, E., Distribution of gold and rhenium between nickel–iron and silicate melts: implications for the abundance of siderophile elements on the Earth and Moon. *Geochim. Cosmochim. Acta* 38, 683–701. (1974).

Kleine, T., Münker, C., Mezger, K., & Palme, H. (2002). Rapid accretion and early core formation on asteroids and the terrestrial planets from Hf–W chronometry. *Nature*, *418*(6901), 952.

Kleine, T., Palme, H., Mezger, K., & Halliday, A. N. (2005). Hf-W chronometry of lunar metals and the age and early differentiation of the Moon. *Science*, *310*(5754), 1671-1674.

Kleine, T., Mezger, K., Palme, H., Scherer, E., & Münker, C. (2005). Early core formation in asteroids and late accretion of chondrite parent bodies: Evidence from 182Hf-182W in CAIs, metal-rich chondrites, and iron meteorites. *Geochimica et Cosmochimica Acta*, *69*(24), 5805-5818.

Knauth, L. P., 1998. Salinity history of the Earth's early ocean. Nature, 395, 554-555.

Knauth, L.P., 2005. Temperature and salinity history of the Precambrian ocean: Implications for the course of microbial evolution. Palaeogeogr. Palaeoclimatol. Palaeoecol. 219, 53–69.

Koeberl, C. (2006). Impact processes on the early Earth. *Elements*, *2*(4), 211-216.

Kokubo, E., & Ida, S. (2000). Formation of protoplanets from planetesimals in the solar nebula. *Icarus*, *143*(1), 15-27.

Komatsu, M., Fagan, T. J., Krot, A. N., Nagashima, K., Petaev, M. I., Kimura, M., & Yamaguchi, A. (2018). First evidence for silica condensation within the solar protoplanetary disk. *Proceedings of the National Academy of Sciences*, *115*(29), 7497-7502.

Konhauser, K. O., Hamade, T., Raiswell, R., Morris, R. C., Ferris, F. G., Southam, G., & Canfield, D. E. (2002). Could bacteria have formed the Precambrian banded iron formations?. *Geology*, *30*(12), 1079-1082.

Koonin, E. V. (2003). Comparative genomics, minimal gene-sets and the last universal common ancestor. *Nature Reviews Microbiology*, *1*(2), 127.

Korenaga, J. (2008). Urey ratio and the structure and evolution of Earth's mantle. *Reviews of Geophysics*, *46*(2).

Kouchi, A., & Yamamoto, T. (1995). Cosmoglaciology: Evolution of ice in interstellar space and the early solar system. *Progress in crystal growth and characterization of materials*, *30*(2-3), 83-107.

Krauss, O., & Wurm, G. (2005). Photophoresis and the pile-up of dust in young circumstellar disks. *The Astrophysical Journal*, *630*(2), 1088.

Krijt, S., Ciesla, F. J., & Bergin, E. A. (2016). Tracing water vapor and ice during dust growth. *The Astrophysical Journal*, *833*(2), 285.

Krishnamurthy, R. V., Epstein, S., Cronin, J. R., Pizzarello, S., & Yuen, G. U. (1992). Isotopic and molecular analyses of hydrocarbons and monocarboxylic acids of the Murchison meteorite. *Geochimica et Cosmochimica Acta*, *56*(11), 4045-4058.

Kruijer, T. S., Sprung, P., Kleine, T., Leya, I., Burkhardt, C., & Wieler, R. (2012). Hf–W chronometry of core formation in planetesimals inferred from weakly irradiated iron meteorites. *Geochimica et cosmochimica acta*, *99*, 287-304.

Kruijer, T. S., Burkhardt, C., Budde, G., & Kleine, T. (2017). Age of Jupiter inferred from the distinct genetics and formation times of meteorites. *Proceedings of the National Academy of Sciences*, *114*(26), 6712-6716.

Krummenacher, D., Merrihue, C. M., Pepin, R. O., & Reynolds, J. H. (1962). Meteoritic krypton and barium versus the general isotopic anomalies in meteoritic xenon. *Geochimica et Cosmochimica Acta*, *26*(2), 231-249.

Kuga, M., Marty, B., Marrocchi, Y., & Tissandier, L. (2015). Synthesis of refractory organic matter in the ionized gas phase of the solar nebula. *Proceedings of the National Academy of Sciences*, *112*(23), 7129-7134.

Kuga, M., Cernogora, G., Marrocchi, Y., Tissandier, L., & Marty, B. (2017). Processes of noble gas elemental and isotopic fractionations in plasma-produced organic solids: Cosmochemical implications. *Geochimica et Cosmochimica Acta*, *217*, 219-230.

Lambart, S., Koornneef, J. M., Millet, M. A., Davies, G. R., Cook, M., & Lissenberg, C. J. (2019). Highly heterogeneous depleted mantle recorded in the lower oceanic crust. *Nature Geoscience*, *12*(6), 482.

Lahav, N., White, D., & Chang, S. (1978). Peptide formation in the prebiotic era: thermal condensation of glycine in fluctuating clay environments. *Science*, *201*(4350), 67-69.

Larsen, K. K., Trinquier, A., Paton, C., Schiller, M., Wielandt, D., Ivanova, M. A., ... & Bizzarro, M. (2011). Evidence for magnesium isotope heterogeneity in the solar protoplanetary disk. *The Astrophysical Journal Letters*, *735*(2), L37.

Laurent, B., Roskosz, M., Remusat, L., Robert, F., Leroux, H., Vezin, H., ... & Lefebvre, J. M. (2015). The deuterium/hydrogen distribution in chondritic organic matter attests to early ionizing irradiation. *Nature communications*, *6*, 8567.

Lee, J. Y., Marti, K., Severinghaus, J. P., Kawamura, K., Yoo, H. S., Lee, J. B., & Kim, J. S. (2006). A redetermination of the isotopic abundances of atmospheric Ar. *Geochimica et Cosmochimica Acta*, *70*(17), 4507-4512.

Le Guillou, C., Bernard, S., Brearley, A. J., & Remusat, L. (2014). Evolution of organic matter in Orgueil, Murchison and Renazzo during parent body aqueous alteration: In situ investigations. *Geochimica et Cosmochimica Acta*, *131*, 368-392.

Leich, D. A., & Niemeyer, S. (1975). Trapped xenon in lunar anorthositic breccia 60015. In *Lunar and Planetary Science Conference Proceedings* (Vol. 6, pp. 1953-1965).

Leinhardt, Z. M., & Richardson, D. C. (2005). Planetesimals to protoplanets. I. Effect of fragmentation on terrestrial planet formation. *The Astrophysical Journal*, *625*(1), 427.

Leitner, J., Kodolányi, J., Hoppe, P., & Floss, C. (2012). Laboratory analysis of presolar silicate stardust from a nova. *The Astrophysical Journal Letters*, *754*(2), L41.

Lepland, A., van Zuilen, M. A., Arrhenius, G., Whitehouse, M. J., & Fedo, C. M. (2005). Questioning the evidence for Earth's earliest life—Akilia revisited. *Geology*, *33*(1), 77-79.

Leroy, C., Sanloup, C., Bureau, H., Schmidt, B. C., Konôpková, Z., & Raepsaet, C. (2018). Bonding of xenon to oxygen in magmas at depth. *Earth and Planetary Science Letters*, *484*, 103-110.

Lewis, R. S., Ming, T., Wacker, J. F., Anders, E., & Steel, E. (1987). Interstellar diamonds in meteorites. *Nature*, *326*(6109), 160.

Libourel, G., Marty, B., & Humbert, F. (2003). Nitrogen solubility in basaltic melt. Part I. Effect of oxygen fugacity. *Geochimica et Cosmochimica Acta*, *67*(21), 4123-4135.

Libourel, G., & Portail, M. (2018). Chondrules as direct thermochemical sensors of solar protoplanetary disk gas. *Science advances*, *4*(7), eaar3321.

Lichtenberg, T., Golabek, G. J., Burn, R., Meyer, M. R., Alibert, Y., Gerya, T. V., & Mordasini, C. (2019). A water budget dichotomy of rocky protoplanets from 26 Al-heating. *Nature Astronomy*, *3*(4), 307.

Lide, D. R. (1995). *CRC handbook of chemistry and physics: a ready-reference book of chemical and physical data*. CRC press.

Lightner, B. D., & Marti, K. (1974). Lunar trapped xenon. In *Lunar and Planetary Science Conference Proceedings* (Vol. 5, pp. 2023-2031).

Ligterink, N. F. W., Paardekooper, D. M., Chuang, K. J., Both, M. L., Cruz-Diaz, G. A., van Helden, J. H., & Linnartz, H. (2015). Controlling the emission profile of an H2 discharge lamp to simulate interstellar radiation fields. *Astronomy & Astrophysics*, *584*, A56.

Lin, Y., & van Westrenen, W. (2018). Isotopic evidence for volatile replenishment of the Moon during Late Accretion. *National Science Review*.

Lodders, K. (2000). An oxygen isotope mixing model for the accretion and composition of rocky planets. In *From Dust to Terrestrial Planets* (pp. 341-354). Springer, Dordrecht.

Lodders, K. (2004). Jupiter formed with more tar than ice. *The Astrophysical Journal*, *611*(1), 587.

Lollar, B. S., Westgate, T. D., Ward, J. A., Slater, G. F., & Lacrampe-Couloume, G. (2002). Abiogenic formation of alkanes in the Earth's crust as a minor source for global hydrocarbon reservoirs. *Nature*, *416*(6880), 522.

Lowe, D. R., & Knauth, L., 1977. Sedimentology of the Onverwacht Group (3.4 billion years), Transvaal, South Africa, and its bearing on the characteristics and evolution of the early earth. J. Geol., 85, 699-723.

Lunine, J. I. (2006). Physical conditions on the early Earth. *Philosophical Transactions of the Royal Society B: Biological Sciences*, *361*(1474), 1721-1731.

Luspay-Kuti, A., Mousis, O., Hässig, M., Fuselier, S. A., Lunine, J. I., Marty, B., ... & Rubin, M. (2016). The presence of clathrates in comet 67P/Churyumov-Gerasimenko. *Science advances*, *2*(4), e1501781.

Lyons, J. R., & Young, E. D. (2005). CO self-shielding as the origin of oxygen isotope anomalies in the early solar nebula. *Nature*, *435*(7040), 317.

Lyons, J R, R S Lewis, and R N Clayton. (2009). Comment on 'Experimental Test of Self- Shielding in Vacuum Ultraviolet Photodissociation of CO'. *Science* 324: 1516

Lyons, T. W., Reinhard, C. T., & Planavsky, N. J. (2014). The rise of oxygen in Earth's early ocean and atmosphere. *Nature*, *506*(7488), 307-315.

Luu, T. H., Hin, R. C., Coath, C. D., & Elliott, T. (2019). Bulk chondrite variability in mass independent magnesium isotope compositions–Implications for initial solar system 26Al/27Al and the timing of terrestrial accretion. *Earth and Planetary Science Letters*, *522*, 166-175.

Mabry, J., Burnard, P., Blard, P. H., & Zimmermann, L. (2012). Mapping changes in helium sensitivity and peak shape for varying parameters of a Nier-type noble gas ion source. *Journal of Analytical Atomic Spectrometry*, *27*(6), 1012-1017.

Madorsky, S. L. (1964). *Thermal degradation of organic polymers* (Vol. 7). Interscience Publishers.

Mahan, B., Siebert, J., Blanchard, I., Borensztajn, S., Badro, J., & Moynier, F. (2018). Constraining compositional proxies for Earth's accretion and core formation through high pressure and high temperature Zn and S metal-silicate partitioning. *Geochimica et Cosmochimica Acta*, *235*, 21-40.

Maher, K. A., & Stevenson, D. J. (1988). Impact frustration of the origin of life. *Nature*, *331*(6157), 612.

Maier, W. D., Barnes, S. J., Campbell, I. H., Fiorentini, M. L., Peltonen, P., Barnes, S. J., & Smithies, R. H. (2009). Progressive mixing of meteoritic veneer into the early Earth's deep mantle. *Nature*, *460*(7255), 620.

Marboeuf, U., Mousis, O., Petit, J. M., & Schmitt, B. (2009). Clathrate hydrates formation in short-period comets. *The Astrophysical Journal*, *708*(1), 812.

Marboeuf, U., Schmitt, B., Petit, J. M., Mousis, O., & Fray, N. (2012). A cometary nucleus model taking into account all phase changes of water ice: amorphous, crystalline, and clathrate. *Astronomy & Astrophysics*, *542*, A82.

Marchi, S., Canup, R. M., & Walker, R. J. (2018). Heterogeneous delivery of silicate and metal to the Earth by large planetesimals. *Nature geoscience*, *11*(1), 77.

Marrocchi, Y., Derenne, S., Marty, B., & Robert, F. (2005). Interlayer trapping of noble gases in insoluble organic matter of primitive meteorites. *Earth and Planetary Science Letters*, *236*(3-4), 569-578.

Marrocchi, Y., Marty, B., Reinhardt, P., & Robert, F. (2011). Adsorption of xenon ions onto defects in organic surfaces: Implications for the origin and the nature of organics in primitive meteorites. *Geochimica et Cosmochimica Acta*, *75*(20), 6255-6266.

Marrocchi, Y., & Marty, B. (2013). Experimental determination of the xenon isotopic fractionation during adsorption. *Geophysical Research Letters*, *40*(16), 4165-4170.

Marrocchi, Y., Avice, G., & Estrade, N. (2015). Multiple carriers of Q noble gases in primitive meteorites. *Geophysical Research Letters*, *42*(7), 2093-2099.

Marrocchi, Y., Bekaert, D. V., & Piani, L. (2018). Origin and abundance of water in carbonaceous asteroids. *Earth and Planetary Science Letters*, *482*, 23-32.

Marrocchi, Y., Villeneuve, J., Batanova, V., Piani, L., & Jacquet, E. (2018). Oxygen isotopic diversity of chondrule precursors and the nebular origin of chondrules. *Earth and Planetary Science Letters*, *496*, 132-141.

Marshall, W. L. (1994). Hydrothermal synthesis of amino acids. *Geochimica et Cosmochimica Acta*, *58*(9), 2099-2106.

Marshall, A. O., Emry, J. R., & Marshall, C. P. (2012). Multiple generations of carbon in the Apex chert and implications for preservation of microfossils. *Astrobiology*, *12*(2), 160-166.

Marti, K. (1967). Isotopic composition of trapped krypton and xenon in chondrites. *Earth and Planetary Science Letters*, *3*, 243-248.

Marty, B., & Dauphas, N. (2003). The nitrogen record of crust–mantle interaction and mantle convection from Archean to present. *Earth and Planetary Science Letters*, *206*(3-4), 397-410.

Marty, B., Palma, R. L., Pepin, R. O., Zimmermann, L., Schlutter, D. J., Burnard, P. G., ... & Simones, J. E. (2008). Helium and neon abundances and compositions in cometary matter. *Science*, *319*(5859), 75-78.

Marty, B. (2012). The origins and concentrations of water, carbon, nitrogen and noble gases on Earth. *Earth and Planetary Science Letters*, *313*, 56-66.

Marty, B., Zimmermann, L., Pujol, M., Burgess, R., & Philippot, P. (2013). Nitrogen isotopic composition and density of the Archean atmosphere. *Science*, *342*(6154), 101-104.

Marty, B., Avice, G., Sano, Y., Altwegg, K., Balsiger, H., Hässig, M., ... & Rubin, M. (2016). Origins of volatile elements (H, C, N, noble gases) on Earth and Mars in light of recent results from the ROSETTA cometary mission. *Earth and Planetary Science Letters*, *441*, 91-102.

Marty, B., Altwegg, K., Balsiger, H., Bar-Nun, A., Bekaert, D. V., Berthelier, J. J., ... & De Keyser, J. (2017). Xenon isotopes in 67P/Churyumov-Gerasimenko show that comets contributed to Earth's atmosphere. *Science*, *356*(6342), 1069-1072.

Marty, B., Avice, G., Bekaert, D. V., & Broadley, M. W. (2018). Salinity of the Archaean oceans from analysis of fluid inclusions in quartz. *Comptes Rendus Geoscience*, *350*(4), 154-163.

Marty, B., Bekaert, D. V., Broadley, M. W., & Jaupart, C. (2019). Geochemical evidence for high volatile fluxes from the mantle at the end of the Archaean. *Nature*, *575*(7783), 485-488.

Mastrapa, R. M., Sandford, S. A., Roush, T. L., Cruikshank, D. P., & Dalle Ore, C. M. (2009). Optical constants of amorphous and crystalline H_2O-ice: 2.5-22 μm (4000-455 cm–1) Optical constants of H_2O-ice. *The Astrophysical Journal*, *701*(2), 1347.

Mathew, K. J., & Marti, K. (2019). Lunar Xenon and the Origin of the Indigenous Component. *The Astrophysical Journal Letters*, *882*(2), L17.

Matsuda, J. I., & Maekawa, T. (1992). Noble gas implantation in glow discharge: Comparison between diamond and graphite. *Geochemical Journal*, *26*(5), 251-259.

Matsuda, J. I., Amari, S., Morishita, K., Nagashima, K., & Nara, M. (2010). The effect of pyridine treatment on phase Q: Orgueil and Allende. *Meteoritics & Planetary Science*, *45*(7), 1191-1205.

Matsumura, S., Thommes, E. W., Chatterjee, S., & Rasio, F. A. (2010). Unstable planetary systems emerging out of gas disks. *The Astrophysical Journal*, *714*(1), 194.

Matsumura, S., Brasser, R., & Ida, S. (2016). Effects of dynamical evolution of giant planets on the delivery of atmophile elements during terrestrial planet formation. *The Astrophysical Journal*, *818*(1), 15.

Mathew, K. J., & Marti, K. (2001). Early evolution of Martian volatiles: Nitrogen and noble gas components in ALH84001 and Chassigny. *Journal of Geophysical Research: Planets*, *106*(E1), 1401-1422.

Mauersberger, R., Ott, U., Henkel, C., Cernicharo, J., & Gallino, R. (2004). The abundance of S in IRC+ 10216 and its production in the Galaxy. *Astronomy & Astrophysics*, *426*(1), 219-227.

McCollom, T. M., & Seewald, J. S. (2001). A reassessment of the potential for reduction of dissolved CO_2 to hydrocarbons during serpentinization of olivine. *Geochimica et Cosmochimica Acta*, *65*(21), 3769-3778.

McCollom TM (2013) Miller-Urey and beyond: What have we learned about prebiotic organic synthesis reactions in the past 60 Years? Annual Review of Earth Planetary Sciences 41: 207-229

McCubbin, F. M., Steele, A., Hauri, E. H., Nekvasil, H., Yamashita, S., & Hemley, R. J. (2010). Nominally hydrous magmatism on the Moon. *Proceedings of the National Academy of Sciences*, *107*(25), 11223-11228.

McCubbin, F. M., & Barnes, J. J. (2019). Origin and abundances of H2O in the terrestrial planets, Moon, and asteroids. *Earth and Planetary Science Letters*, *526*, 115771.

McKeegan, K. D., Aléon, J., Bradley, J., Brownlee, D., Busemann, H., Butterworth, A., ... & Gounelle, M. (2006). Isotopic compositions of cometary matter returned by Stardust. *Science*, *314*(5806), 1724-1728.

McKeegan, K. D., Kudryavtsev, A. B., & Schopf, J. W. (2007). Raman and ion microscopic imagery of graphitic inclusions in apatite from older than 3830 Ma Akilia supracrustal rocks, west Greenland. *Geology*, *35*(7), 591-594.

McWilliam, A. (1997). Abundance ratios and galactic chemical evolution. *Annual Review of Astronomy and Astrophysics*, *35*(1), 503-556.

Meierhenrich, U. J., Filippi, J. J., Meinert, C., Bredehöft, J. H., Takahashi, J. I., Nahon, L., ... & Hoffmann, S. V. (2010). Circular dichroism of amino acids in the vacuum-ultraviolet region. *Angewandte Chemie International Edition*, *49*(42), 7799-7802.

Meisel, T., Walker, R. J., & Morgan, J. W. (1996). The osmium isotopic composition of the Earth's primitive upper mantle. *Nature*, *383*(6600), 517.

Meshik, A., Hohenberg, C., Pravdivtseva, O., & Burnett, D. (2014). Heavy noble gases in solar wind delivered by Genesis mission. *Geochimica et cosmochimica acta*, *127*, 326-347

Meshik, A. & Pravdivtseva, O. (2018) Precise Xenon Analyses of the Solar Wind: Implications for Indigenous Lunar Xenon. *Goldschmidt Conference*, Boston, USA.

Meyer, B. S. (1994). The r-, s-, and p-processes in nucleosynthesis. *Annual Review of Astronomy and Astrophysics*, *32*(1), 153-190.

Milićev, S. (1997). Badger and Herschbach-Laurie constants for the compounds of xenon and fluorine. In *Progress in Fourier Transform Spectroscopy* (pp. 539-541). Springer, Vienna.

Miller, S. L. (1953). A production of amino acids under possible primitive earth conditions. *Science*, *117*(3046), 528-529.

Miller, S. L., & Urey, H. C. (1959). Organic compound synthesis on the primitive earth. *Science*, *130*(3370), 245-251.

Miller, S. L., & Van Trump, J. E. (1981). The Strecker synthesis in the primitive ocean. In *Origin of life* (pp. 135-141). Springer, Dordrecht.

Misener, W., Krijt, S., & Ciesla, F. J. (2019). Tracking Dust Grains during Transport and Growth in Protoplanetary Disks. *The Astrophysical Journal*, *885*(2), 118.

Mizuno, H., Nakazawa, K., & Hayashi, C. (1980). Dissolution of the primordial rare gases into the molten Earth's material. *Earth and Planetary Science Letters*, *50*(1), 202-210.

Mojzsis, S. J., Arrhenius, G., McKeegan, K. D., Harrison, T. M., Nutman, A. P., & Friend, C. R. L. (1996). Evidence for life on Earth before 3,800 million years ago. *Nature*, *384*(6604), 55-59.

Mojzsis, S. J., Harrison, T. M., & Pidgeon, R. T. (2001). Oxygen-isotope evidence from ancient zircons for liquid water at the Earth's surface 4,300 Myr ago. *Nature*, *409*(6817), 178.

Molyarova, T., Akimkin, V., Semenov, D., Henning, T., Vasyunin, A., & Wiebe, D. (2017). Gas mass tracers in protoplanetary disks: CO is still the best. *The Astrophysical Journal*, *849*(2), 130.

Morbidelli, A., Crida, A., Masset, F., & Nelson, R. P. (2008). Building giant-planet cores at a planet trap. *Astronomy & Astrophysics*, *478*(3), 929-937.

Morbidelli, A., Marchi, S., Bottke, W. F., & Kring, D. A. (2012). A sawtooth-like timeline for the first billion years of lunar bombardment. *Earth and Planetary Science Letters*, *355*, 144-151.

Morbidelli, A., Lunine, J. I., O'Brien, D. P., Raymond, S. N., & Walsh, K. J. (2012). Building terrestrial planets. *Annual Review of Earth and Planetary Sciences*, *40*.

Morbidelli, A., & Wood, B. J. (2015). Late accretion and the late veneer. *The Early Earth: Accretion and Differentiation, Geophysical Monograph*, *212*, 71-82.

Morbidelli A, Walsh KJ, O'BrienDP, Minton DA, Bottke WF. (2015). The dynamical evolution of the asteroid belt. In Asteroids IV, ed. P Michel, F DeMeo, WF Bottke, pp. 493–508. Tucson: Univ. Ariz. Press.

Morbidelli, A., Bitsch, B., Crida, A., Gounelle, M., Guillot, T., Jacobson, S., ... & Lega, E. (2016). Fossilized condensation lines in the Solar System protoplanetary disk. *Icarus*, *267*, 368-376.

Moreira, M., Kunz, J., & Allegre, C. (1998). Rare gas systematics in popping rock: isotopic and elemental compositions in the upper mantle. *Science*, *279*(5354), 1178-1181.

Moreira, M., & Madureira, P. (2005). Cosmogenic helium and neon in 11 Myr old ultramafic xenoliths: consequences for mantle signatures in old samples. *Geochemistry, Geophysics, Geosystems*, *6*(8).

Moreira, M., & Charnoz, S. (2016). The origin of the neon isotopes in chondrites and on Earth. *Earth and Planetary Science Letters*, *433*, 249-256.

Moreira, M., Rouchon, V., Muller, E., Noirez, S. (2018) The xenon isotopic signature of the mantle beneath Massif Central. Geochemical Perspectives Letters 6, 28-32.

Mougel, B., Moynier, F., & Göpel, C. (2018). Chromium isotopic homogeneity between the Moon, the Earth, and enstatite chondrites. *Earth and Planetary Science Letters*, *481*, 1-8.

Mukhopadhyay, S. (2012). Early differentiation and volatile accretion recorded in deep-mantle neon and xenon. *Nature*, *486*(7401), 101.

Mukhopadhyay, S., & Parai, R. (2019). Noble gases: a record of Earth's evolution and mantle dynamics. *Annual Review of Earth and Planetary Sciences*, *47*, 389-419.

Muskatel, B. H., Remacle, F., Thiemens, M. H., & Levine, R. D. (2011). On the strong and selective isotope effect in the UV excitation of N2 with implications toward the nebula and Martian atmosphere. *Proceedings of the National Academy of Sciences*, *108*(15), 6020-6025.

Nagel, T. J., Hoffmann, J. E., & Münker, C. (2012). Generation of Eoarchean tonalite-trondhjemite-granodiorite series from thickened mafic arc crust. *Geology*, *40*(4), 375-378.

Nahon, L., de Oliveira, N., Garcia, G. A., Gil, J. F., Pilette, B., Marcouillé, O., ... & Polack, F. (2012). DESIRS: a state-of-the-art VUV beamline featuring high resolution and variable polarization for spectroscopy and dichroism at SOLEIL. *Journal of synchrotron radiation*, *19*(4), 508-520.

Nanne, J. A., Nimmo, F., Cuzzi, J. N., & Kleine, T. (2019). Origin of the non-carbonaceous–carbonaceous meteorite dichotomy. *Earth and Planetary Science Letters*, *511*, 44-54.

Néri, A., Guyot, F., Reynard, B., & Sotin, C. (2019). A carbonaceous chondrite and cometary origin for icy moons of Jupiter and Saturn. *Earth and Planetary Science Letters*, 115920.

Newman, M. J., & Rood, R. T. (1977). Implications of solar evolution for the Earth's early atmosphere. *Science*, *198*(4321), 1035-1037.

Niedermann, S., & Eugster, O. (1992). Noble gases in lunar anorthositic rocks 60018 and 65315: Acquisition of terrestrial krypton and xenon indicating an irreversible adsorption process. *Geochimica et cosmochimica acta*, *56*(1), 493-509.

Niemeyer, S., & Leich, D. A. (1976, April). Atmospheric rare gases in lunar rock 60015. In *Lunar and Planetary Science Conference Proceedings* (Vol. 7, pp. 587-597).

Nisbet, E. G., & Sleep, N. H. (2001). The habitat and nature of early life. *Nature*, *409*(6823), 1083.

Nittler, L. R., & Ciesla, F. (2016). Astrophysics with extraterrestrial materials. *Annual Review of Astronomy and Astrophysics*, *54*, 53-93.

Nittler, L. R., Stroud, R. M., Trigo-Rodríguez, J. M., De Gregorio, B. T., Alexander, C. M. D., Davidson, J., ... & Tanbakouei, S. (2019). A cometary building block in a primitive asteroidal meteorite. *Nature Astronomy*, 1.

Notesco, G., Bar-Nun, A., & Owen, T. (2003). Gas trapping in water ice at very low deposition rates and implications for comets. *Icarus*, *162*(1), 183-189.

Notesco, G., & Bar-Nun, A. (2005). A~ 25 K temperature of formation for the submicron ice grains which formed comets. *Icarus*, *175*(2), 546-550.

Nuevo, M. (2012). Laboratory astrochemistry: A powerful tool to understand the origin of organic molecules in the interstellar medium, comets, and meteorites. In *Frank N. Bash Symposium 2011: New Horizons in Astronomy* (Vol. 149, p. 004). SISSA Medialab.

Öberg, K. I., Linnartz, H., Visser, R., & Van Dishoeck, E. F. (2009). Photodesorption of ices. II. H2O and D2O. *The Astrophysical Journal*, *693*(2), 1209.

Öberg, K. I., & Bergin, E. A. (2016). Excess C/O and C/H in outer protoplanetary disk gas. *The Astrophysical Journal Letters*, *831*(2), L19.

Oehler, D., & Cady, S. (2014). Biogenicity and syngeneity of organic matter in ancient sedimentary rocks: recent advances in the search for evidence of past life. *Challenges*, *5*(2), 260-283.

Ohmoto, H., Watanabe, Y., Lasaga, A. C., Naraoka, H., Johnson, I., Brainard, J., & Chorney, A. (2014). Oxygen, iron, and sulfur geochemical cycles on early Earth: Paradigms and contradictions. *Geol. Soc. Am. Spec. Pap*, *504*, 55-95.

Oka, A., Nakamoto, T., & Ida, S. (2011). Evolution of snow line in optically thick protoplanetary disks: effects of water ice opacity and dust grain size. *The Astrophysical Journal*, *738*(2), 141.

Okazaki, R., Takaoka, N., Nagao, K., & Nakamura, T. (2010). Noble gases in enstatite chondrites released by stepped crushing and heating. *Meteoritics & Planetary Science*, *45*(3), 339-360.

Ong, L., Asphaug, E. I., Korycansky, D., & Coker, R. F. (2010). Volatile retention from cometary impacts on the Moon. *Icarus*, *207*(2), 578-589.

Oparin, A. I. (1936). Původ života (Origin of Life). *Dover Publications, NewYork*, *1953*, 196.

Oró, J., & Guidry, C. L. (1960). A novel synthesis of polypeptides. *Nature*, *186*(4719), 156-157.

Orthous-Daunay, F.R., Quirico, E., Lemelle, L., Beck, P., deAndrade, V., Simionovici, A. and Derenne, S. (2010) Speciation of sulfur in the insoluble organic matter from carbonaceous chondrites by XANES spectroscopy. Earth and Planetary Science Letters, 300, 321–328.

Orthous-Daunay, F.R., Quirico, E., Beck, P., Brissaud, O., Dartois, E., Pino, T. and Schmitt, B. (2013) Midinfrared study of the molecular structure variability of insoluble organic matter from primitive chondrites. Icarus, 223, 534–543.

Orthous-Daunay, F. R., Piani, L., Flandinet, L., Thissen, R., Wolters, C., Vuitton, V., ... & Tachibana, S. (2019). Ultraviolet-photon fingerprints on chondritic large organic molecules. *Geochemical Journal*, *53*(1), 21-32.

Ostrander, C. M., Nielsen, S. G., Owens, J. D., Kendall, B., Gordon, G. W., Romaniello, S. J., & Anbar, A. D. (2019). Fully oxygenated water columns over continental shelves before the Great Oxidation Event. *Nature geoscience*, *12*(3), 186.

Ott, U., Mack, R., & Sherwood, C. (1981). Noble-gas-rich separates from the Allende meteorite. *Geochimica et Cosmochimica Acta*, *45*(10), 1751-1788.

Ott, U. (2002). Noble gases in meteorites–trapped components. *Reviews in Mineralogy and Geochemistry*, *47*(1), 71-100.

Ott, U. (2014). Planetary and pre-solar noble gases in meteorites. *Geochemistry*, *74*(4), 519-544.

Owen, T., Bar-Nun, A., & Kleinfeld, I. (1992). Possible cometary origin of heavy noble gases in the atmospheres of Venus, Earth and Mars. *Nature*, *358*(6381), 43.

Ozima, M., & Podosek, F. A. (2002). *Noble gas geochemistry*. Cambridge University Press.

Ozima, M., Seki, K., Terada, N., Miura, Y. N., Podosek, F. A., & Shinagawa, H. (2005). Terrestrial nitrogen and noble gases in lunar soils. *Nature*, *436*(7051), 655.

Palme, H., & O'Neill, H. S. C. (2003). Cosmochemical estimates of mantle composition. *Treatise on geochemistry*, *2*, 568.

Parai, R., & Mukhopadhyay, S. (2015). The evolution of MORB and plume mantle volatile budgets: C onstraints from fission X e isotopes in Southwest Indian Ridge basalts. *Geochemistry, Geophysics, Geosystems*, *16*(3), 719-735.

Parai, R., & Mukhopadhyay, S. (2018). Xenon isotopic constraints on the history of volatile recycling into the mantle. *Nature*, *560*(7717), 223.

Parai, R., Mukhopadhyay, S., Tucker, J. M., & Pető, M. K. (2019). The emerging portrait of an ancient, heterogeneous and continuously evolving mantle plume source. *Lithos*, 105153.

Park, R.K., 1977. The preservation potential of some recent stromatolites. Sedimentology 24, 485-506.

Parnell-Turner, R., Sohn, R. A., Peirce, C., Reston, T. J., MacLeod, C. J., Searle, R. C., & Simão, N. M. (2017). Oceanic detachment faults generate compression in extension. *Geology*, *45*(10), 923-926.

Pasek, M., & Lauretta, D. (2008). Extraterrestrial flux of potentially prebiotic C, N, and P to the early Earth. Origins of Life and Evolution of Biospheres, 38(1), 5-21.

Patel, B. H., Percivalle, C., Ritson, D. J., Duffy, C. D., & Sutherland, J. D. (2015). Common origins of RNA, protein and lipid precursors in a cyanosulfidic protometabolism. Nature chemistry, 7(4), 301.

Pattou, L., Lorand, J. P., & Gros, M. (1996). Non-chondritic platinum-group element ratios in the Earth's mantle. Nature, 379(6567), 712.

Pearson, V. K., Sephton, M. A., Franchi, I. A., Gibson, J. M., & Gilmour, I. (2006). Carbon and nitrogen in carbonaceous chondrites: Elemental abundances and stable isotopic compositions. Meteoritics & Planetary Science, 41(12), 1899-1918.

Pepin, R. O. (1967). Trapped neon in meteorites. Earth and Planetary Science Letters, 2(1), 13-18.

Pepin, R. (1994). The hunt for U-Xenon. *Meteoritics*, *29*.

Pepin, R. O., Becker, R. H., & Rider, P. E. (1995). Xenon and krypton isotopes in extraterrestrial regolith soils and in the solar wind. *Geochimica et Cosmochimica Acta*, *59*(23), 4997-5022.

Pepin, R. O. (1998). Isotopic evidence for a solar argon component in the Earth's mantle. *Nature*, *394*(6694), 664.

Pepin, R. O. (2000). On the isotopic composition of primordial xenon in terrestrial planet atmospheres. In *From dust to terrestrial planets* (pp. 371-395). Springer, Dordrecht.

Pepin, R. O. (2003). On noble gas processing in the solar accretion disk. *Space science reviews*, *106*(1-4), 211-230.

Pepin, R. O., & Porcelli, D. (2006). Xenon isotope systematics, giant impacts, and mantle degassing on the early Earth. *Earth and Planetary Science Letters*, *250*(3-4), 470-485.

Pepin, R. O., Schlutter, D. J., Becker, R. H., & Reisenfeld, D. B. (2012). Helium, neon, and argon composition of the solar wind as recorded in gold and other Genesis collector materials. *Geochimica et Cosmochimica Acta*, *89*, 62-80.

Pernet-Fisher, J. F., & Joy, K. H. (2018, March). Noble-Gas Isotope Systematics of Lunar Anorthosites: Hunting for Indigenous Signatures. In *Lunar and Planetary Science Conference* (Vol. 49).

Péron, S., Moreira, M., Colin, A., Arbaret, L., Putlitz, B., & Kurz, M. D. (2016). Neon isotopic composition of the mantle constrained by single vesicle analyses. *Earth and Planetary Science Letters*, *449*, 145-154.

Péron, S., Moreira, M., Putlitz, B., & Kurz, M. D. (2017). Solar wind implantation supplied light volatiles during the first stage of Earth accretion. *Geochem. Perspect. Lett.*, *3*, 151-159.

Péron, S., & Moreira, M. (2018). Onset of volatile recycling into the mantle determined by xenon anomalies. *Geochemical Perspective Letters*, *9*, 21.

Pettersson, M, et al. 2000. Photochemistry of HNCO in solid xenon: Photoinduced and thermally activated formation of HXeNCO. J. Phys. Chem. A 104: 3579-3583.

Piani, L., Robert, F., Beyssac, O., Binet, L., Bourot-Denise, M., Derenne, S., ... & Thomen, A. (2012). Structure, composition, and location of organic matter in the enstatite chondrite Sahara 97096 (EH3). *Meteoritics & Planetary Science*, *47*(1), 8-29.

Piani, L., Robert, F., & Remusat, L. (2015). Micron-scale D/H heterogeneity in chondrite matrices: A signature of the pristine solar system water?. *Earth and Planetary Science Letters*, *415*, 154-164.

Pignatale, F. C., Charnoz, S., Chaussidon, M., & Jacquet, E. (2018). Making the Planetary Material Diversity during the Early Assembling of the Solar System. *The Astrophysical Journal Letters*, *867*(2), L23.

Pinte, C., Price, D. J., Ménard, F., Duchêne, G., Dent, W. R. F., Hill, T., ... & Mentiplay, D. (2018). Kinematic Evidence for an Embedded Protoplanet in a Circumstellar Disk. *The Astrophysical Journal Letters*, *860*(1), L13.

Pizzarello, S., & Cronin, J. R. (2000). Non-racemic amino acids in the Murray and Murchison meteorites. *Geochimica et Cosmochimica Acta*, *64*(2), 329-338.

Pizzarello, S., Cooper, G. W., & Flynn, G. J. (2006). The nature and distribution of the organic material in carbonaceous chondrites and interplanetary dust particles. *Meteorites and the early solar system II*, *1*, 625-651.

Pizzarello, S. (2006). The chemistry of life's origin: a carbonaceous meteorite perspective. *Accounts of Chemical Research*, *39*(4), 231-237.

Pizzarello, S., & Shock, E. (2010). The organic composition of carbonaceous meteorites: the evolutionary story ahead of biochemistry. *Cold Spring Harbor perspectives in biology*, *2*(3), a002105.

Podosek, F. A., Bernatowicz, T. J., Honda, M. & Kramer, F. E. (1982) The sedimentary inventory of atmospheric xenon, in Planetary Volatiles, vol. 488, p. 80. AQ29

Podosek, F. A., & Ozima, M. (2000). The xenon age of the Earth. *Origin of the Earth and Moon*, *1*, 63-72.

Poole, G. M., Rehkämper, M., Coles, B. J., Goldberg, T., & Smith, C. L. (2017). Nucleosynthetic molybdenum isotope anomalies in iron meteorites–new evidence for thermal processing of solar nebula material. *Earth and Planetary Science Letters*, *473*, 215-226.

Porcelli, D., & Ballentine, C. J. (2002). Models for distribution of terrestrial noble gases and evolution of the atmosphere. *Reviews in Mineralogy and Geochemistry*, *47*(1), 411-480.

Protin, M., Blard, P. H., Marrocchi, Y., & Mathon, F. (2016). Irreversible adsorption of atmospheric helium on olivine: A lobster pot analogy. *Geochimica et Cosmochimica Acta*, *179*, 76-88.

Pujol, M., Marty, B., & Burgess, R. (2011). Chondritic-like xenon trapped in Archean rocks: a possible signature of the ancient atmosphere. *Earth and Planetary Science Letters*, *308*(3-4), 298-306.

Quirico, E., Montagnac, G., Rouzaud, J. N., Bonal, L., Bourot-Denise, M., Duber, S., & Reynard, B. (2009). Precursor and metamorphic condition effects on Raman spectra of poorly ordered carbonaceous matter in chondrites and coals. *Earth and Planetary Science Letters*, *287*(1-2), 185-193.

Rai, V. K., Murty, S. V. S., & Ott, U. (2003). Noble gases in ureilites: cosmogenic, radiogenic, and trapped components. *Geochimica et Cosmochimica Acta*, *67*(22), 4435-4456.

Rapp, R. P., Irifune, T., Shimizu, N., Nishiyama, N., Norman, M. D., & Inoue, T. (2008). Subduction recycling of continental sediments and the origin of geochemically enriched reservoirs in the deep mantle. *Earth and Planetary Science Letters*, *271*(1-4), 14-23.

Raquin, A., & Moreira, M. (2009). Atmospheric 38Ar/36Ar in the mantle: implications for the nature of the terrestrial parent bodies. *Earth and Planetary Science Letters*, *287*(3-4), 551-558.

Raymond, S. N., & Morbidelli, A. (2014). The Grand Tack model: a critical review. *Proceedings of the International Astronomical Union*, *9*(S310), 194-203.

Raymond, S. N., & Izidoro, A. (2017). Origin of water in the inner Solar System: Planetesimals scattered inward during Jupiter and Saturn's rapid gas accretion. *Icarus*, *297*, 134-148.

Raymond, S. N., Izidoro, A., & Morbidelli, A. (2018). Solar System Formation in the Context of Extra-Solar Planets. *arXiv preprint arXiv:1812.01033*.

Regelous, M., Elliott, T., & Coath, C. D. (2008). Nickel isotope heterogeneity in the early Solar System. *Earth and Planetary Science Letters*, *272*(1-2), 330-338.

Reimold, W. U., & Koeberl, C. (2014). Impact structures in Africa: A review. *Journal of African Earth Sciences*, *93*, 57-175.

Remusat, L., Derenne, S., Robert, F., & Knicker, H. (2005). New pyrolytic and spectroscopic data on Orgueil and Murchison insoluble organic matter: A different origin than soluble?. *Geochimica et Cosmochimica Acta*, *69*(15), 3919-3932.

Remusat, L. (2015). Organics in primitive meteorites. *EMU Notes in Mineralogy*, *15*, 1-33.

Render, J., Fischer-Gödde, M., Burkhardt, C., & Kleine, T. (2017). The cosmic molybdenum-neodymium isotope correlation and the building material of the Earth. *Geochem Perspect Lett*, *3*, 170-178.

Reynolds, J. H., & Turner, G. (1964). Rare gases in the chondrite Renazzo. *Journal of Geophysical Research*, *69*(15), 3263-3281.

Ribas, I., Guinan, E. F., Güdel, M., & Audard, M. (2005). Evolution of the solar activity over time and effects on planetary atmospheres. I. High-energy irradiances (1-1700 Å). *The Astrophysical Journal*, *622*(1), 680.

Robert, F., Derenne, S., Lombardi, G., Hassouni, K., Michau, A., Reinhardt, P., ... & Biron, K. (2017). Hydrogen isotope fractionation in methane plasma. *Proceedings of the National Academy of Sciences*, *114*(5), 870-874.

Robinson, K. L., & Taylor, G. J. (2014). Heterogeneous distribution of water in the Moon. *Nature Geoscience*, *7*(6), 401-408.

Robinson, K. L., Barnes, J. J., Nagashima, K., Thomen, A., Franchi, I. A., Huss, G. R., ... & Taylor, G. J. (2016). Water in evolved lunar rocks: Evidence for multiple reservoirs. *Geochimica et Cosmochimica Acta*, *188*, 244-260.

Ros, K., & Johansen, A. (2013). Ice condensation as a planet formation mechanism. *Astronomy & Astrophysics*, *552*, A137.

Rosing, M. T. (1999). 13C-depleted carbon microparticles in> 3700-Ma sea-floor sedimentary rocks from West Greenland. *Science*, *283*(5402), 674-676.

Rosenfeld, K. A., Andrews, S. M., Hughes, A. M., Wilner, D. J., & Qi, C. (2013). A spatially resolved vertical temperature gradient in the HD 163296 disk. *The Astrophysical Journal*, *774*(1), 16.

Rubie, D. C., Frost, D. J., Mann, U., Asahara, Y., Nimmo, F., Tsuno, K., ... & Palme, H. (2011). Heterogeneous accretion, composition and core–mantle differentiation of the Earth. *Earth and Planetary Science Letters*, *301*(1-2), 31-42.

Rubie, D. C., Jacobson, S. A., Morbidelli, A., O'Brien, D. P., Young, E. D., de Vries, J., ... & Frost, D. J. (2015). Accretion and differentiation of the terrestrial planets with implications for the compositions of early-formed Solar System bodies and accretion of water. *Icarus*, *248*, 89-108.

Rubin, A. E., & Choi, B. G. (2009). Origin of halogens and nitrogen in enstatite chondrites. *Earth, Moon, and Planets*, *105*(1), 41-53.

Rubin, M., Altwegg, K., Balsiger, H., Bar-Nun, A., Berthelier, J. J., Bieler, A., ... & De Keyser, J. (2015). Molecular nitrogen in comet 67P/Churyumov-Gerasimenko indicates a low formation temperature. *Science*, *348*(6231), 232-235.

Rubin, M., Altwegg, K., Balsiger, H., Berthelier, J. J., Bieler, A., Calmonte, U., ... & Fuselier, S. A. (2017). Evidence for depletion of heavy silicon isotopes at comet 67P/Churyumov-Gerasimenko. *Astronomy & Astrophysics*, *601*, A123.

Rubin, M., Altwegg, K., Balsiger, H., Bar-Nun, A., Berthelier, J. J., Briois, C., ... & Fuselier, S. A. (2018). Krypton isotopes and noble gas abundances in the coma of comet 67P/Churyumov-Gerasimenko. *Science advances*, *4*(7), eaar6297.

Rubin, M., Bekaert, D. V., Broadley, M. W., Drozdovskaya, M. N., & Wampfler, S. F. (2019). Volatile Species in Comet 67P/Churyumov-Gerasimenko: Investigating the Link from the ISM to the Terrestrial Planets. *ACS earth and space chemistry*, *3*(9), 1792-1811.

Saal, A. E., Hauri, E. H., Cascio, M. L., Van Orman, J. A., Rutherford, M. C., & Cooper, R. F. (2008). Volatile content of lunar volcanic glasses and the presence of water in the Moon's interior. *Nature*, *454*(7201), 192.

Saal, A. E., Hauri, E. H., Van Orman, J. A., & Rutherford, M. J. (2013). Hydrogen isotopes in lunar volcanic glasses and melt inclusions reveal a carbonaceous chondrite heritage. *Science*, *340*(6138), 1317-1320.

Sakamoto, N., Seto, Y., Itoh, S., Kuramoto, K., Fujino, K., Nagashima, K., ... & Yurimoto, H. (2007). Remnants of the early solar system water enriched in heavy oxygen isotopes. *Science*, *317*(5835), 231-233.

Salinas, V. N., Hogerheijde, M. R., Bergin, E. A., Cleeves, L. I., Brinch, C., Blake, G. A., ... & Kristensen, L. (2016). First detection of gas-phase ammonia in a planet-forming disk-NH3, N2H+, and H2O in the disk around TW Hydrae. *Astronomy & Astrophysics*, *591*, A122.

Sandford, S. A., Aléon, J., Alexander, C. M. D., Araki, T., Bajt, S., Baratta, G. A., ... & Burchell, M. J. (2006). Organics captured from comet 81P/Wild 2 by the Stardust spacecraft. *Science*, *314*(5806), 1720-1724.

Sanloup, C., Schmidt, B. C., Perez, E. M. C., Jambon, A., Gregoryanz, E., & Mezouar, M. (2005). Retention of xenon in quartz and Earth's missing xenon. *Science*, *310*(5751), 1174-1177.

Sano, Y., Wakita, H., & Sheng, X. (1988). Atmospheric helium isotope ratio. *Geochemical Journal*, *22*(4), 177-181.

Sano, T., Miyama, S. M., Umebayashi, T., & Nakano, T. (2000). Magnetorotational instability in protoplanetary disks. II. Ionization state and unstable regions. *The Astrophysical Journal*, *543*(1), 486.

Schiller, M., Bizzarro, M., & Fernandes, V. A. (2018). Isotopic evolution of the protoplanetary disk and the building blocks of Earth and the Moon. *Nature*, *555*(7697), 507.

Schlichting, H. E., & Mukhopadhyay, S. (2018). Atmosphere impact losses. *Space Science Reviews*, *214*(1), 34.

Schmitt-Kopplin, P., Gabelica, Z., Gougeon, R. D., Fekete, A., Kanawati, B., Harir, M., ... & Hertkorn, N. (2010). High molecular diversity of extraterrestrial organic matter in Murchison meteorite revealed 40 years after its fall. *Proceedings of the National Academy of Sciences*, *107*(7), 2763-2768.

Schönbächler, M., Carlson, R. W., Horan, M. F., Mock, T. D., & Hauri, E. H. (2010). Heterogeneous accretion and the moderately volatile element budget of Earth. *Science*, *328*(5980), 884-887.

Schopf, J. W. (2006). The first billion years: When did life emerge?. *Elements*, *2*(4), 229-233.

Schopf, J. W., Kudryavtsev, A. B., Czaja, A. D., & Tripathi, A. B. (2007). Evidence of Archean life: stromatolites and microfossils. *Precambrian Research*, *158*(3-4), 141-155.

Schouren, F. (2001). Experimentelle und theoretische Untersuchungen an Edelgas-Sauerstoff-Verbindungen. (Doctoral dissertation).

Schwarz, K. R., Bergin, E. A., Cleeves, L. I., Zhang, K., Öberg, K. I., Blake, G. A., & Anderson, D. (2018). Unlocking CO depletion in protoplanetary disks. I. The warm molecular layer. *The Astrophysical Journal*, *856*(1), 85.

Scott, E. R. D., Barber, D. J., Alexander, C. M., Hutchinson, R., & Peck, J. A. (1988). Primitive material surviving in chondrites-Matrix. *Meteorites and the early solar system*, 718-745.

Sephton, M. A., Pillinger, C. T., & Gilmour, I. (1998). Small-scale hydrous pyrolysis of macromolecular material in meteorites. *Planetary and Space Science*, *47*(1-2), 181-187.

Shirey, S. B., & Richardson, S. H. (2011). Start of the Wilson cycle at 3 Ga shown by diamonds from subcontinental mantle. *Science*, *333*(6041), 434-436.

Shu, F. H., Shang, H., Gounelle, M., Glassgold, A. E., & Lee, T. (2001). The origin of chondrules and refractory inclusions in chondritic meteorites. *The Astrophysical Journal*, *548*(2), 1029.

Siebert, J., Badro, J., Antonangeli, D., & Ryerson, F. J. (2013). Terrestrial accretion under oxidizing conditions. *Science*, *339*(6124), 1194-1197.

Simon, J. B., Armitage, P. J., Li, R., & Youdin, A. N. (2016). The mass and size distribution of planetesimals formed by the streaming instability. I. The role of self-gravity. *The Astrophysical Journal*, *822*(1), 55.

Sleep, N. H., Zahnle, K. J., Kasting, J. F., & Morowitz, H. J. (1989). Annihilation of ecosystems by large asteroid impacts on the early Earth. *Nature*, *342*(6246), 139.

Sleep, N. H. (2017). Asteroid bombardment and the core of Theia as possible sources for the Earth's late veneer component. *Geochemistry, Geophysics, Geosystems*, *17*(7), 2623-2642.

Smit, M. A., & Mezger, K. (2017). Earth's early O 2 cycle suppressed by primitive continents. *Nature geoscience*, *10*(10), 788.

Snow, J. E., & Schmidt, G. (1998). Constraints on Earth accretion deduced from noble metals in the oceanic mantle. *Nature*, *391*(6663), 166.

Socrates, Infrared and Raman characteristics group frequencies – tables and charts, (3rd edn, 2001). Chichester, Wiley.

Staudacher, T., & Allègre, C. J. (1982). Terrestrial xenology. *Earth and Planetary Science Letters*, *60*(3), 389-406.

Stavrou, E., Yao, Y., Goncharov, A. F., Lobanov, S. S., Zaug, J. M., Liu, H., ... & Prakapenka, V. B. (2018). Synthesis of xenon and iron-nickel intermetallic compounds at Earth's core thermodynamic conditions. *Physical review letters*, *120*(9), 096001.

Stracke, A., Hofmann, A. W., & Hart, S. R. (2005). FOZO, HIMU, and the rest of the mantle zoo. *Geochemistry, Geophysics, Geosystems*, *6*(5).

Stuart, F. M., Lass-Evans, S., Fitton, J. G., & Ellam, R. M. (2003). High 3 He/4 He ratios in picritic basalts from Baffin Island and the role of a mixed reservoir in mantle plumes. *Nature*, *424*(6944), 57.

Sutherland JD (2016) The origin of life— out of the blue. Angewandte Chemie, International Edition 55: 104-121

Takeuchi, T., & Lin, D. N. C. (2002). Radial flow of dust particles in accretion disks. *The Astrophysical Journal*, *581*(2), 1344.

Tang, M., Chen, K., & Rudnick, R. L. (2016). Archean upper crust transition from mafic to felsic marks the onset of plate tectonics. *Science*, *351*(6271), 372-375.

Tartèse R, Anand M. (2013). Late delivery of chondritic hydrogen into the lunar mantle: insights from mare basalts. Earth Planet. Sci. Lett. 361:480–86

Tartèse R, Anand M, Barnes JJ, Starkey NA, Franchi IA, Sano Y. (2013). The abundance, distribution, and isotopic composition of hydrogen in the Moon as revealed by basaltic lunar samples: implications for the volatile inventory of the Moon. Geochim. Cosmochim. Acta 122:58–74

Tartèse R, Anand M, Joy KH, Franchi IA. (2014a). H and Cl isotope systematics of apatite in brecciated lunar meteorites Northwest Africa 4472, Northwest Africa 773, Sayh al Uhaymir 169, and Kalahari 009. Meteorit. Planet. Sci. 49:2266–89

Tartèse R, Anand M, McCubbin FM, Elardo SM, Shearer CK, Franchi IA. (2014b). Apatites in lunar KREEP basalts: the missing link to understanding the H isotope systematics of the Moon. Geology 42:363–66

Tartèse, R., Chaussidon, M., Gurenko, A., Delarue, F., & Robert, F. (2018). Insights into the origin of carbonaceous chondrite organics from their triple oxygen isotope composition. *Proceedings of the National Academy of Sciences*, *115*(34), 8535-8540

Taylor, M. G. G. T., Altobelli, N., Buratti, B. J., & Choukroun, M. (2017). The Rosetta mission orbiter science overview: the comet phase. *Philosophical Transactions of the Royal Society A: Mathematical, Physical and Engineering Sciences*, *375*(2097), 20160262.

Tera, F., Papanastassiou, D. A., & Wasserburg, G. J. (1974). Isotopic evidence for a terminal lunar cataclysm. *Earth and Planetary Science Letters*, *22*(1), 1-21.

Testi, L., Natta, A., Shepherd, D. S., & Wilner, D. J. (2003). Large grains in the disk of CQ Tau. *Astronomy & Astrophysics*, *403*(1), 323-328.

Testi, L., Birnstiel, T., Ricci, L., Andrews, S., Blum, J., Carpenter, J., ... & Wilner, D. J. (2014). Dust evolution in protoplanetary disks. *Protostars and Planets VI*, *914*, 339-61.

Thiemens, M. H., & Heidenreich, J. E. (1983). The mass-independent fractionation of oxygen: A novel isotope effect and its possible cosmochemical implications. *Science*, *219*(4588), 1073-1075.

Tielens, A. G. (2008). Interstellar polycyclic aromatic hydrocarbon molecules. *Annu. Rev. Astron. Astrophys.*, *46*, 289-337.

Tigrine, S., Carrasco, N., Vettier, L., Chitarra, O., & Cernogora, G. (2016). The APSIS experiment: Simulating the VUV Photochemistry of the Upper Atmosphere of Titan.

Tissandier, L., Libourel, G., & Robert, F. (2002). Gas-melt interactions and their bearing on chondrule formation. *Meteoritics & Planetary Science*, *37*(10), 1377-1389.

Touboul M, Puchtel IS, Walker RJ. 2012. 182W evidence for long-term preservation of early mantle differentiation products. Science 335:1065–69.

Trieloff, M., Kunz, J., & Allègre, C. J. (2002). Noble gas systematics of the Réunion mantle plume source and the origin of primordial noble gases in Earth's mantle. *Earth and Planetary Science Letters*, *200*(3-4), 297-313.

Trinquier, A., Elliott, T., Ulfbeck, D., Coath, C., Krot, A. N., & Bizzarro, M. (2009). Origin of nucleosynthetic isotope heterogeneity in the solar protoplanetary disk. *Science*, *324*(5925), 374-376.

Tucker, J. M., & Mukhopadhyay, S. (2014). Evidence for multiple magma ocean outgassing and atmospheric loss episodes from mantle noble gases. *Earth and Planetary Science Letters*, *393*, 254-265.

Turner, G. (1979). A Monte Carlo fragmentation model for the production of meteorites-Implications for gas retention ages. In *Lunar and Planetary Science Conference Proceedings* (Vol. 10, pp. 1917-1941).

Turner, G., Harrison, T. M., Holland, G., Mojzsis, S. J., & Gilmour, J. (2004). Extinct 244Pu in ancient zircons. *Science*, *306*(5693), 89-91.

Turner, G., Busfield, A., Crowther, S. A., Harrison, M., Mojzsis, S. J., & Gilmour, J. (2007). Pu–Xe, U–Xe, U–Pb chronology and isotope systematics of ancient zircons from Western Australia. *Earth and Planetary Science Letters*, *261*(3-4), 491-499.

Vacher, L. G., Marrocchi, Y., Verdier-Paoletti, M. J., Villeneuve, J., & Gounelle, M. (2016). Inward radial mixing of interstellar water ices in the solar protoplanetary disk. *The Astrophysical journal letters*, *827*(1), L1.

Vacher, L. G., Truche, L., Faure, F., Tissandier, L., Mosser-Ruck, R., & Marrocchi, Y. (2019). Deciphering the conditions of tochilinite and cronstedtite formation in CM chondrites from low temperature hydrothermal experiments. *Meteoritics & Planetary Science*.

Valdes, M. C., Moreira, M., Foriel, J., & Moynier, F. (2014). The nature of Earth's building blocks as revealed by calcium isotopes. *Earth and Planetary Science Letters*, *394*, 135-145.

Van der Hilst, R. D., Widiyantoro, S., & Engdahl, E. R. (1997). Evidence for deep mantle circulation from global tomography. *Nature*, *386*(6625), 578.

van Dishoeck, E. F., Jonkheid, B., & van Hemert, M. C. (2006). Photoprocesses in protoplanetary disks. *Faraday Discussions*, *133*, 231-243.

Van Kooten, E. M., Wielandt, D., Schiller, M., Nagashima, K., Thomen, A., Larsen, K. K., ... & Bizzarro, M. (2016). Isotopic evidence for primordial molecular cloud material in metal-rich carbonaceous chondrites. *Proceedings of the National Academy of Sciences*, *113*(8), 2011-2016.

Van Kooten, E. M., Moynier, F., & Agranier, A. (2019). A unifying model for the accretion of chondrules and matrix. *Proceedings of the National Academy of Sciences*, *116*(38), 18860-18866.

Van Zuilen, M. A., Lepland, A., & Arrhenius, G. (2002). Reassessing the evidence for the earliest traces of life. *Nature*, *418*(6898), 627.

Varas-Reus, M. I., König, S., Yierpan, A., Lorand, J. P., & Schoenberg, R. (2019). Selenium isotopes as tracers of a late volatile contribution to Earth from the outer Solar System. *Nature geoscience*, *12*(9), 779-782.

Vermeesch, P. (2015). Revised error propagation of 40 Ar/39 Ar data, including covariances. *Geochimica et Cosmochimica Acta*, **171**, 325-337.

Villeneuve, J., Chaussidon, M., & Libourel, G. (2009). Homogeneous distribution of 26Al in the solar system from the Mg isotopic composition of chondrules. *Science*, *325*(5943), 985-988.

Vinković, D. (2009). Radiation-pressure mixing of large dust grains in protoplanetary disks. *Nature*, *459*(7244), 227.

Vinogradoff, V., Bernard, S., Le Guillou, C., & Remusat, L. (2018). Evolution of interstellar organic compounds under asteroidal hydrothermal conditions. *Icarus*, *305*, 358-370.

Vogt, M., Hopp, J., Gail, H. P., Ott, U., & Trieloff, M. (2019). Acquisition of terrestrial neon during accretion–A mixture of solar wind and planetary components. *Geochimica et Cosmochimica Acta*, *264*, 141-164.

Wacey, D. (2010). Stromatolites in the~ 3400 Ma Strelley Pool Formation, Western Australia: examining biogenicity from the macro-to the nano-scale. *Astrobiology*, *10*(4), 381-395.

Wächtershäuser, G. (1990). The case for the chemoautotrophic origin of life in an iron-sulfur world. *Origins of Life and Evolution of the Biosphere*, *20*(2), 173-176.

Wacker, J. F. (1989). Laboratory simulation of meteoritic noble gases. III. Sorption of neon, argon, krypton, and xenon on carbon: Elemental fractionation. *Geochimica et Cosmochimica Acta*, *53*(6), 1421-1433.

98.Wade, J., & Wood, B. J. (2005). Core formation and the oxidation state of the Earth. *Earth and Planetary Science Letters*, *236*(1-2), 78-95.

Wade, J., Wood, B. J., & Tuff, J. (2012). Metal–silicate partitioning of Mo and W at high pressures and temperatures: evidence for late accretion of sulphur to the Earth. *Geochimica et Cosmochimica Acta*, *85*, 58-74.

Wade, J., & Wood, B. J. (2016). The oxidation state and mass of the Moon-forming impactor. *Earth and Planetary Science Letters*, *442*, 186-193.

Walsh, C., Nomura, H., Millar, T. J., & Aikawa, Y. (2012). Chemical processes in protoplanetary disks. II. On the importance of photochemistry and X-ray ionization. *The Astrophysical Journal*, *747*(2), 114.

Walter, M. R., Buick, R., & Dunlop, J. S. R. (1980). Stromatolites 3,400–3,500 Myr old from the North pole area, Western Australia. *Nature*, *284*(5755), 443.

Wänke, H. (1981). Constitution of terrestrial planets. *Philosophical Transactions of the Royal Society of London. Series A, Mathematical and Physical Sciences*, *303*(1477), 287-302.

Wang, Z., & Becker, H. (2013). Ratios of S, Se and Te in the silicate Earth require a volatile-rich late veneer. *Nature*, *499*(7458), 328.

Warren, P. H. (2011). Stable-isotopic anomalies and the accretionary assemblage of the Earth and Mars: A subordinate role for carbonaceous chondrites. *Earth and Planetary Science Letters*, *311*(1-2), 93-100.

Weber H. W., Hintenberger H., and Begemann F. (1971) Noble gases in the Haveröureilite. Earth and Planetary Science Letters 13, 205-209.

Weiss, R.F.,1970. The solubility of nitrogen, oxygen and argon in water and seawater. Deep Sea Res. Oceanogr.Abstr. 17, 721-735.

Weiss, Y., Class, C., Goldstein, S. L., & Hanyu, T. (2016). Key new pieces of the HIMU puzzle from olivines and diamond inclusions. *Nature*, *537*(7622), 666.

Wetherill, G. W. (1975). Radiometric chronology of the early solar system. *Annual Review of Nuclear Science*, *25*(1), 283-328.

Wetherill, G. W. (1992). An alternative model for the formation of the asteroids. *Icarus*, *100*(2), 307-325.

Werner, S.C., Ivanov, B.A., 2007 . Exogenic dynamics , cratering and surface ages. In : Treatise on Geophysics, vol.10, 2nd edition, pp.207–242.

Wesslau, V. H. (1956). Die molekulargewichtsverteilung einiger niederdruckpolyäthylene. *Die Makromolekulare Chemie: Macromolecular Chemistry and Physics*, *20*(1), 111-142.

White, W. M., & Duncan, R. A. (1996). Geochemistry and geochronology of the Society Islands: new evidence for deep mantle recycling. *Geophysical Monograph-American Geophysical Union*, *95*, 183-206.

Wielandt, D., & Storey, M. (2019). A new high precision determination of the atmospheric 21 Ne abundance. *Journal of Analytical Atomic Spectrometry*, *34*(3), 535-549.

Wieler, R., Anders, E., Baur, H., Lewis, R. S., & Signer, P. (1992). Characterisation of Q-gases and other noble gas components in the Murchison meteorite. *Geochimica et Cosmochimica Acta*, *56*(7), 2907-2921.

Wieler, R. (1994). Q-gases" as "local" primordial noble gas component in primitive meteorites. *Terra Scientific Publishing, Tokyo*, 31-41.

Wilde, S. A., Valley, J. W., Peck, W. H., & Graham, C. M. (2001). Evidence from detrital zircons for the existence of continental crust and oceans on the Earth 4.4 Gyr ago. *Nature*, *409*(6817), 175.

Willbold M, Elliott T, Moorbath S. 2011. The tungsten isotopic composition of the Earth's mantle before the terminal bombardment. Nature 477:195–98.

Williams, C. D., & Mukhopadhyay, S. (2019). Capture of nebular gases during Earth's accretion is preserved in deep-mantle neon. *Nature*, *565*(7737), 78.

Williams, J. P., & Cieza, L. A. (2011). Protoplanetary disks and their evolution. *Annual Review of Astronomy and Astrophysics*, *49*, 67-117.

Wilner, D. J., D'Alessio, P., Calvet, N., Claussen, M. J., & Hartmann, L. (2005). Toward planetesimals in the disk around TW Hydrae: 3.5 centimeter dust emission. *The Astrophysical Journal Letters*, *626*(2), L109.

Worsham, E. A., Bermingham, K. R., & Walker, R. J. (2017). Characterizing cosmochemical materials with genetic affinities to the Earth: genetic and chronological diversity within the IAB iron meteorite complex. *Earth and planetary science letters*, *467*, 157-166.

Worsham, E. A., Burkhardt, C., Budde, G., Fischer-Gödde, M., Kruijer, T. S., & Kleine, T. (2019). Distinct evolution of the carbonaceous and non-carbonaceous reservoirs: Insights from Ru, Mo, and W isotopes. *Earth and Planetary Science Letters*, *521*, 103-112.

Wurz, P., Rubin, M., Altwegg, K., Balsiger, H., Berthelier, J. J., Bieler, A., ... & Galli, A. (2015). Solar wind sputtering of dust on the surface of 67P/Churyumov-Gerasimenko. *Astronomy & Astrophysics*, *583*, A22.

Yabuta, H., Naraoka, H., Sakanishi, K. and Kawashima, H. (2005) Solid-state 13C NMR characterization of insoluble organic matter from Antarctic CM2 chondrites: Evaluation of the meteoritic alteration level. Meteoritics & Planetary Science, 40, 779–787.

Yang, L., & Ciesla, F. J. (2012). The effects of disk building on the distributions of refractory materials in the solar nebula. *Meteoritics & Planetary Science*, *47*(1), 99-119.

Yokochi, R., & Marty, B. (2004). A determination of the neon isotopic composition of the deep mantle. *Earth and Planetary Science Letters*, *225*(1-2), 77-88.

Yokochi, R., Marboeuf, U., Quirico, E., & Schmitt, B. (2012). Pressure dependent trace gas trapping in amorphous water ice at 77 K: Implications for determining conditions of comet formation. *Icarus*, *218*(2), 760-770.

Young, E. D., Galy, A., & Nagahara, H. (2002). Kinetic and equilibrium mass-dependent isotope fractionation laws in nature and their geochemical and cosmochemical significance. *Geochimica et Cosmochimica Acta*, *66*(6), 1095-1104.

Yurimoto, H., & Kuramoto, K. (2004). Molecular cloud origin for the oxygen isotope heterogeneity in the solar system. *Science*, *305*(5691), 1763-1766.

Zahnle, K. J. (2006). Earth's earliest atmosphere. *Elements*, *2*(4), 217-222.

Zahnle, K. J., Catling, D. C., & Claire, M. W. (2013). The rise of oxygen and the hydrogen hourglass. *Chemical Geology*, *362*, 26-34.

Zahnle K. J. (2015) Xenon fractionation and Archean hydrogen escape. In 46th Lunar and Planetary Science Conference. The Woodlands (Texas). pp. 1–2.

Zahnle, K. J., Gacesa, M., & Catling, D. C. (2019). Strange messenger: A new history of hydrogen on Earth, as told by Xenon. *Geochimica et Cosmochimica Acta*, *244*, 56-85.

Zaia, D. A. M. (2004). A review of adsorption of amino acids on minerals: was it important for origin of life?. *Amino acids*, *27*(1), 113-118.

Zaleski-Ejgierd, P., & Lata, P. M. (2016). Krypton oxides under pressure. *Scientific reports*, *6*, 18938.

Zanda, B., Humayun, M., Lewin, E., Pont, S., & Hewins, R. H. (2018). Mo-W Isotopic Evidence Against Chondrule-Matrix Complementarity. *LPI Contributions*, *2067*.

Zega, T. J., Alexander, C. M. D., Busemann, H., Nittler, L. R., Hoppe, P., Stroud, R. M., & Young, A. F. (2010). Mineral associations and character of isotopically anomalous organic material in the Tagish Lake carbonaceous chondrite. *Geochimica et Cosmochimica Acta*, *74*(20), 5966-5983.

Zellner, N. E. (2017). Cataclysm no more: new views on the timing and delivery of lunar impactors. *Origins of Life and Evolution of Biospheres*, *47*(3), 261-280.

Zhang, X., Honda, M., & Hamilton, D. (2016). Performance of the high resolution, multi-collector helix mc plus noble gas mass spectrometer at the Australian National University. *Journal of The American Society for Mass Spectrometry*, *27*(12), 1937-1943.

Zhang, K., Bergin, E. A., Schwarz, K., Krijt, S., & Ciesla, F. (2019). Systematic Variations of CO Gas Abundance with Radius in Gas-rich Protoplanetary Disks. *The Astrophysical Journal*, *883*(1),

Zhu, L., Liu, H., Pickard, C. J., Zou, G., & Ma, Y. (2014). Reactions of xenon with iron and nickel are predicted in the Earth's inner core. *Nature chemistry*, *6*(7), 644.

Zhu, M. H., Artemieva, N., Morbidelli, A., Yin, Q. Z., Becker, H., & Wünnemann, K. (2019). Reconstructing the late-accretion history of the Moon. *Nature*, *571*(7764), 226-229.

Zimmermann, L., & Marty, B. (2014). Méthodes d'extraction des gaz rares sous ultravide. *Techniques de l'ingénieur, j6632*.

Zimmermann, L., Füri, E., and Burnard, P. (2015). Purification des gaz rares sous ultravide - Méthodes de purification. Techniques de l'ingénieur , (J6635):1–23.

Résumé en français

La Terre s'est formée il y a 4,5 milliards d'années par accumulation de poussières, de roches et de gaz. La composition de ces matériaux primitifs est aujourd'hui enregistrée dans les météorites. Cependant, l'origine des éléments volatils présents dans l'atmosphère (e.g., H, C, N, O) reste incomprise. En combinant des approches expérimentales à l'étude d'échantillons naturels, je me suis intéressé aux objets célestes contenant les ingrédients nécessaires à la formation de l'atmosphère terrestre. Il s'agit principalement des éléments volatils contenus dans la matière organique des météorites et dans la glace des corps cométaires. Afin de reconstituer l'histoire de formation de la Terre et de son atmosphère, j'ai utilisé les gaz nobles (He, Ne, Ar, Kr, Xe) comme traceurs des processus physiques ayant eu lieu dans le Système Solaire jeune et sur la Terre primitive. Bien que les comètes aient significativement contribué à l'apport des gaz nobles lourds de l'atmosphère (~20%), la majorité des autres éléments volatils terrestres (incluant l'eau, le carbone et l'azote) aurait été apportée par des corps dits "chondritiques", similaires aux météorites. Une fois formée, l'atmosphère a évolué au cours des temps géologiques, conduisant à l'établissement des conditions environnementales propices au développement de la vie. Les processus majeurs ayant affecté la masse et la composition de l'atmosphère ancienne se reflètent dans l'évolution isotopique du Xe atmosphérique, de 4.5 Ga à ~2 Ga. Nous étudions la possibilité d'apporter des contraintes sur l'âge des matériaux organiques retrouvés dans les roches sédimentaires plus anciennes que 2 Ga, en utilisant la signature isotopique du Xe qu'ils ont piégé au moment de leur formation. Cette méthode pourrait avoir des implications vis-à-vis de l'âge présumé des plus anciennes traces de vie organique.

English abstract

The Earth formed some 4.5 Ga from the accumulation of dust, rocks and gas. The composition of these primitive materials is today recorded in meteorites. However, the origin of volatile elements within the atmosphere (e.g., H, C, N, O) remains poorly understood. By combining experimental approaches and the analysis of natural samples, I studied the composition of celestial objects comprising the ingredients required for the formation of the terrestrial atmosphere. These mainly correspond to volatile elements trapped in meteoritic organic materials and in the ice of cometary bodies. In order to better understand the timeline of Earth's formation and volatile accretion, I used noble gases (He, Ne, Ar, Kr, Xe) as tracers of the physical processes that occurred in the early Solar System and on primitive Earth. Whilst comets significantly contributed to the heavy noble gas budget of the terrestrial atmosphere (~20%), most of the other terrestrial volatile elements (including water, carbon and nitrogen) would have been supplied to Earth by chondrtitic bodies similar to meteorites. Once formed, the atmosphere evolved over geological periods of time, leading to the establishment of suitable environmental conditions for life to develop. The major processes that affected the mass and composition of the ancient atmosphere can be studied by investigating the isotopic evolution of atmospheric Xe, from 4.5 Ga to ~2 Ga. We investigate the possibility to bring constraints on the age of organic materials isolated from sedimentary ricks older than 2 Ga, using the isotopic signature of the Xe component that was trapped at the time of their formation. This method could have implications regarding the presumed age of the earliest remnants of organic life.

General References

Adam, Z. R., Skidmore, M. L., Mogk, D. W., & Butterfield, N. J. (2017). A Laurentian record of the earliest fossil eukaryotes. *Geology*, *45*(5), 387-390.

Albarede, F. (2009). Volatile accretion history of the terrestrial planets and dynamic implications. *Nature*, *461*(7268), 1227.

Albarede, F., Ballhaus, C., Blichert-Toft, J., Lee, C. T., Marty, B., Moynier, F., & Yin, Q. Z. (2013). Asteroidal impacts and the origin of terrestrial and lunar volatiles. *Icarus*, *222*(1), 44-52.

Alexander, R. D., & Armitage, P. J. (2009). Giant planet migration, disk evolution, and the origin of transitional disks. *The Astrophysical Journal*, *704*(2), 989.

Alibert, Y., Venturini, J., Helled, R., Ataiee, S., Burn, R., Senecal, L., ... & Schönbächler, M. (2018). The formation of Jupiter by hybrid pebble–planetesimal accretion. *Nature astronomy*, *2*(11), 873.

Alleon, J., Bernard, S., Le Guillou, C., Beyssac, O., Sugitani, K., & Robert, F. (2018). Chemical nature of the 3.4 Ga Strelley Pool microfossils.

Allwood, A. C., Walter, M. R., Kamber, B. S., Marshall, C. P., & Burch, I. W. (2006). Stromatolite reef from the Early Archaean era of Australia. *Nature*, *441*(7094), 714.

Altwegg, K., Balsiger, H., Bar-Nun, A., Berthelier, J. J., Bieler, A., Bochsler, P., ... & Eberhardt, P. (2015). 67P/Churyumov-Gerasimenko, a Jupiter family comet with a high D/H ratio. *Science*, *347*(6220), 1261952.

Altwegg, K., Balsiger, H., Bar-Nun, A., Berthelier, J. J., Bieler, A., Bochsler, P., ... & De Keyser, J. (2016). Prebiotic chemicals—amino acid and phosphorus—in the coma of comet 67P/Churyumov-Gerasimenko. *Science advances*, *2*(5), e1600285.

Amari, S., Anders, E., Virag, A., & Zinner, E. (1990). Interstellar graphite in meteorites. *Nature*, *345*(6272), 238.

Amari, S., Matsuda, J. I., Stroud, R. M., & Chisholm, M. F. (2013). Highly concentrated nebular noble gases in porous nanocarbon separates from the Saratov (L4) meteorite. *The Astrophysical Journal*, *778*(1), 37.

Anbar, A. D., & Knoll, A., 2002. Proterozoic ocean chemistry and evolution: a bioinorganic bridge? Science, 297, 1137-1142.

Anbar, A. D., Duan, Y., Lyons, T. W., Arnold, G. L., Kendall, B., Creaser, R. A., ... & Buick, R. (2007). A whiff of oxygen before the great oxidation event?. *Science*, *317*(5846), 1903-1906.

Andersson, S., & Van Dishoeck, E. F. (2008). Photodesorption of water ice-A molecular dynamics study. *Astronomy & Astrophysics*, *491*(3), 907-916.

Anicich, V. G. (1993). Evaluated bimolecular ion-molecule gas phase kinetics of positive ions for use in modeling planetary atmospheres, cometary comae, and interstellar clouds. *Journal of Physical and Chemical Reference Data*, *22*(6), 1469-1569.

Aponte, J. C., Alexandre, M. R., Wang, Y., Brearley, A. J., Alexander, C. M. D., & Huang, Y. (2011). Effects of secondary alteration on the composition of free and IOM-derived monocarboxylic acids in carbonaceous chondrites. *Geochimica et Cosmochimica Acta*, *75*(9), 2309-2323.

Avice, G., & Marty, B. (2014). The iodine–plutonium–xenon age of the Moon–Earth system revisited. *Philosophical Transactions of the Royal Society A: Mathematical, Physical and Engineering Sciences*, *372*(2024), 20130260.

Avice, G., Marty, B., & Burgess, R. (2017). The origin and degassing history of the Earth's atmosphere revealed by Archean xenon. *Nature communications*, *8*, 15455.

Avice, G., Marty, B., Burgess, R., Hofmann, A., Philippot, P., Zahnle, K., & Zakharov, D. (2018). Evolution of atmospheric xenon and other noble gases inferred from Archean to Paleoproterozoic rocks. *Geochimica et Cosmochimica Acta*, *232*, 82-100.

Bada, J. L., Bigham, C., & Miller, S. L. (1994). Impact melting of frozen oceans on the early Earth: implications for the origin of life. *Proceedings of the National Academy of Sciences*, *91*(4), 1248-1250.

Bai, X. N. (2011). Magnetorotational-instability-driven accretion in protoplanetary disks. *The Astrophysical Journal*, *739*(1), 50.

Ballentine, C. J., Marty, B., Lollar, B. S., & Cassidy, M. (2005). Neon isotopes constrain convection and volatile origin in the Earth's mantle. *Nature*, *433*(7021), 33.

Ballentine, C. J., & Holland, G. (2008). What CO2 well gases tell us about the origin of noble gases in the mantle and their relationship to the atmosphere. *Philosophical Transactions of the Royal Society A: Mathematical, Physical and Engineering Sciences*, *366*(1883), 4183-4203.

Balsiger, H., Altwegg, K., Bochsler, P., Eberhardt, P., Fischer, J., Graf, S., ... & Müller, J. (2007). Rosina–Rosetta orbiter spectrometer for ion and neutral analysis. *Space Science Reviews*, *128*(1-4), 745-801.

Balsiger, H., Altwegg, K., Bar-Nun, A., Berthelier, J. J., Bieler, A., Bochsler, P., ... & Eberhardt, P. (2015). Detection of argon in the coma of comet 67P/Churyumov-Gerasimenko. *Science advances*, *1*(8), e1500377.

Bardin, N., Duprat, J., Slodzian, G., Wu, T. D., Baklouti, D., Dartois, E., ... & Guerquin-Kern, J. L. (2015). Hydrogen isotopic fractionation in secondary ion mass spectrometry using polyatomic ions. *International Journal of Mass Spectrometry*, *393*, 17-24.

Barfod, D. N., Ballentine, C. J., Halliday, A. N., & Fitton, J. G. (1999). Noble gases in the Cameroon line and the He, Ne, and Ar isotopic compositions of high μ (HIMU) mantle. *Journal of Geophysical Research: Solid Earth*, *104*(B12), 29509-29527.

Barnes JJ, Franchi IA, Anand M, Tartèse R, Starkey NA, et al. (2013). Accurate and precise measurements of the D/H ratio and hydroxyl content in lunar apatites using NanoSIMS. Chem. Geol. 337–38:48–55

Barnes, J. J., Tartèse, R., Anand, M., McCubbin, F. M., Franchi, I. A., Starkey, N. A., & Russell, S. S. (2014). The origin of water in the primitive Moon as revealed by the lunar highlands samples. *Earth and Planetary Science Letters*, *390*, 244-252.

Barnes, J. J., Kring, D. A., Tartese, R., Franchi, I. A., Anand, M., & Russell, S. S. (2016). An asteroidal origin for water in the Moon. *Nature communications*, *7*, 11684.

Bar-Nun, A., Herman, G., Laufer, D., & Rappaport, M. L. (1985). Trapping and release of gases by water ice and implications for icy bodies. *Icarus*, *63*(3), 317-332.

Basford, J. R., Dragon, J. C., Pepin, R. O., Coscio Jr, M. R. and Murthy, V. R. (1973). Krypton and xenon in lunar fines. In *Proc. Lunar Planet. Sci. Conf*, vol. **4**, p. 1915. Proc. Lunar Planet. Sci. Conf.

Bekaert, D. V., Avice, G., Marty, B., Henderson, B., & Gudipati, M. S. (2017). Stepwise heating of lunar anorthosites 60025, 60215, 65315 possibly reveals an indigenous noble gas component on the Moon. *Geochimica et Cosmochimica Acta*, *218*, 114-131.

Bekaert, D. V., Derenne, S., Tissandier, L., Marrocchi, Y., Charnoz, S., Anquetil, C., & Marty, B. (2018a). High-temperature ionization-induced synthesis of biologically relevant molecules in the protosolar nebula. *The Astrophysical Journal*, *859*(2), 142.

Bekaert, D. V., Avice, G., & Marty, B. (2018b). Origin and significance of cosmogenic signatures in vesicles of lunar basalt 15016. *Meteoritics & planetary science*, *53*(6), 1238-1251.

Bekaert, D. V., Broadley, M. W., Delarue, F., Avice, G., Robert, F., & Marty, B. (2018c). Archean kerogen as a new tracer of atmospheric evolution: Implications for dating the widespread nature of early life. *Science Advances*, *4*(2), eaar2091.

Bekaert, D. V., Marrocchi, Y., Meshik, A., Remusat, L., & Marty, B. (2019a). Primordial heavy noble gases in the pristine Paris carbonaceous chondrite. *Meteoritics & planetary science*, *54*(2), 395-414.

Bekaert, D. V., Gudipati, M. S., Henderson, B., & Marty, B. (2019b). Coulomb explosion of multiply ionized xenon in water ice. *Geochemical Journal*, *53*(1), 69-81.

Bekaert, D. V., Broadley, M. W., Caracausi, A., & Marty, B. (2019c). Novel insights into the degassing history of Earth's mantle from high precision noble gas analysis of magmatic gas. *Earth and Planetary Science Letters*, *525*, 115766.

Bekaert, D. V., Broadley, M. W., Delarue, F., Druzhinina, Z., Paris, G., Robert, F., ... & Marty, B. (2020). Xenon isotopes in Archean and Proterozoic insoluble organic matter: A robust indicator of syngenecity?. *Precambrian Research*, *336*, 105505.

Bernatowicz, T. J., Podosek, F. A., Honda, M. & Kramer F. E. (1984) The atmospheric inventory of xenon and noble gases in shales: The plastic bag experiment. J. Geophys. Res. Solid Earth 89, 4597–4611.

Bernatowicz, T., Fraundorf, G., Ming, T., Anders, E., Wopenka, B., Zinner, E., & Fraundorf, P. (1987). Evidence for interstellar SiC in the Murray carbonaceous meteorite. *Nature*, *330*(6150), 728.

Berndt, M. E., Allen, D. E., & Seyfried Jr, W. E. (1996). Reduction of CO2 during serpentinization of olivine at 300 C and 500 bar. *Geology*, *24*(4), 351-354.

Birnstiel, T., Dullemond, C. P., & Brauer, F. (2010). Gas-and dust evolution in protoplanetary disks. *Astronomy & Astrophysics*, *513*, A79.

Biron, K., Derenne, S., Robert, F., & Rouzaud, J. N. (2015). Toward an experimental synthesis of the chondritic insoluble organic matter. *Meteoritics & Planetary Science*, *50*(8), 1408-1422.

Bitsch, B., Johansen, A., Lambrechts, M., & Morbidelli, A. (2015). The structure of protoplanetary discs around evolving young stars. *Astronomy & Astrophysics*, *575*, A28.

Bitsch, B., Izidoro, A., Johansen, A., Raymond, S. N., Morbidelli, A., Lambrechts, M., & Jacobson, S. A. (2019). Formation of planetary systems by pebble accretion and migration: growth of gas giants. *Astronomy & Astrophysics*, *623*, A88.

Black, D. C., & Pepin, R. O. (1969). Trapped neon in meteorites—II. *Earth and Planetary Science Letters*, *6*(5), 395-405.

Black, D. C. (1972). On the origins of trapped helium, neon and argon isotopic variations in meteorites—II. Carbonaceous meteorites. *Geochimica et Cosmochimica Acta*, *36*(3), 377-394.

Blard, P. H., Bourles, D., Lave, J., & Pik, R. (2006). Applications of ancient cosmic-ray exposures: theory, techniques and limitations. *Quaternary Geochronology*, *1*(1), 59-73.

Bleeker, W. (2003). The late Archean record: a puzzle in ca. 35 pieces. *Lithos*, *71*(2-4), 99-134.

Blichert-Toft, J., & Albarède, F. (2008). Hafnium isotopes in Jack Hills zircons and the formation of the Hadean crust. *Earth and Planetary Science Letters*, *265*(3-4), 686-702.

Bockelée-Morvan, D., Crovisier, J., Mumma, M. J., & Weaver, H. A. (2004). The composition of cometary volatiles. *Comets II*, *1*, 391-423.

Bockelée-Morvan, D., Calmonte, U., Charnley, S., Duprat, J., Engrand, C., Gicquel, A., ... & Milam, S. (2015). Cometary isotopic measurements. *Space science reviews*, *197*(1-4), 47-83.

Boehnke, P., Caffee, M. W., & Harrison, T. M. (2015). Xenon isotopes in the MORB source, not distinctive of early global degassing. *Geophysical Research Letters*, *42*(11), 4367-4374.

Boehnke, P., & Harrison, T. M. (2016). Illusory late heavy bombardments. *Proceedings of the National Academy of Sciences*, *113*(39), 10802-10806.

Bollard, J., Connelly, J. N., & Bizzarro, M. (2015). Pb-Pb dating of individual chondrules from the CB a chondrite Gujba: Assessment of the impact plume formation model. *Meteoritics & planetary science*, *50*(7), 1197-1216.

Bollard, J., Connelly, J. N., Whitehouse, M. J., Pringle, E. A., Bonal, L., Jørgensen, J. K., ... & Bizzarro, M. (2017). Early formation of planetary building blocks inferred from Pb isotopic ages of chondrules. *Science advances*, *3*(8), e1700407.

Bosman, A. D., Walsh, C., & van Dishoeck, E. F. (2018). CO destruction in protoplanetary disk midplanes: Inside versus outside the CO snow surface. *Astronomy & Astrophysics*, *618*, A182.

Bottke, W. F. et al. Stochastic late accretion to Earth, the Moon, and Mars. Science 330, 1527–1530 (2010).

Boyce JW, Liu Y, Rossman GR, Guan Y, Eiler JM, et al. 2010. Lunar apatite with terrestrial volatile abundances. Nature 466:466–69

Boyce JW, Tomlinson SM, McCubbin FM. 2014. The lunar apatite paradox. Science 344:400–2

Brasser, R., & Morbidelli, A. (2013). Oort cloud and Scattered Disc formation during a late dynamical instability in the Solar System. *Icarus*, *225*(1), 40-49.

Brauer, F., Dullemond, C. P., & Henning, T. (2008). Coagulation, fragmentation and radial motion of solid particles in protoplanetary disks. *Astronomy & Astrophysics*, *480*(3), 859-877.

Bräuer, K., Kämpf, H., Niedermann, S., & Strauch, G. (2013). Indications for the existence of different magmatic reservoirs beneath the Eifel area (Germany): a multi-isotope (C, N, He, Ne, Ar) approach. *Chemical Geology*, *356*, 193-208.

Braukmüller, N., Wombacher, F., Funk, C., & Münker, C. (2019). Earth's volatile element depletion pattern inherited from a carbonaceous chondrite-like source. *Nature Geoscience*, 1.

Briani, G., Gounelle, M., Marrocchi, Y., Mostefaoui, S., Leroux, H., Quirico, E., & Meibom, A. (2009). Pristine extraterrestrial material with unprecedented nitrogen isotopic variation. *Proceedings of the National Academy of Sciences*, *106*(26), 10522-10527.

Broadley et al. 2019

Brown, M. (2006). Duality of thermal regimes is the distinctive characteristic of plate tectonics since the Neoarchean. *Geology*, *34*(11), 961-964.

Budde, G., Burkhardt, C., Brennecka, G. A., Fischer-Gödde, M., Kruijer, T. S., & Kleine, T. (2016). Molybdenum isotopic evidence for the origin of chondrules and a distinct genetic heritage of carbonaceous and non-carbonaceous meteorites. *Earth and Planetary Science Letters*, *454*, 293-303.

Budde, G., Burkhardt, C., & Kleine, T. (2019). Molybdenum isotopic evidence for the late accretion of outer Solar System material to Earth. *Nature Astronomy*, 1.

Buikin, A., Trieloff, M., Hopp, J., Althaus, T., Korochantseva, E., Schwarz, W.H. and Altherr, R., 2005. Noble gas isotopes suggest deep mantle plume source of late Cenozoic mafic alkaline volcanism in Europe. Earth and Planetary Science Letters, 230(1-2), pp.143-162.

Burkhardt, C., Dauphas, N., Hans, U., Bourdon, B., & Kleine, T. (2019). Elemental and isotopic variability in solar system materials by mixing and processing of primordial disk reservoirs. *Geochimica et Cosmochimica Acta*, *261*, 145-170.

Burnard, P., Zimmermann, L., & Sano, Y. (2013). The noble gases as geochemical tracers: History and background. In *The Noble Gases as Geochemical Tracers* (pp. 1-15). Springer, Berlin, Heidelberg.

Busemann, H., Baur, H., & Wieler, R. (2000). Primordial noble gases in "phase Q" in carbonaceous and ordinary chondrites studied by closed-system stepped etching. *Meteoritics & Planetary Science*, *35*(5), 949-973.

Busemann, H., Young, A. F., Alexander, C. M. D., Hoppe, P., Mukhopadhyay, S., & Nittler, L. R. (2006). Interstellar chemistry recorded in organic matter from primitive meteorites. *Science*, *312*(5774), 727-730.

Busemann, H., Nguyen, A. N., Cody, G. D., Hoppe, P., Kilcoyne, A. D., Stroud, R. M., ... & Nittler, L. R. (2009). Ultra-primitive interplanetary dust particles from the comet 26P/Grigg–Skjellerup dust stream collection. *Earth and Planetary Science Letters*, *288*(1-2), 44-57.

Cabral, R. A., Jackson, M. G., Rose-Koga, E. F., Koga, K. T., Whitehouse, M. J., Antonelli, M. A., ... & Hauri, E. H. (2013). Anomalous sulphur isotopes in plume lavas reveal deep mantle storage of Archaean crust. *Nature*, *496*(7446), 490.

Calmonte, U., Altwegg, K., Balsiger, H., Berthelier, J. J., Bieler, A., De Keyser, J., ... & Le Roy, L. (2017). Sulphur isotope mass-independent fractionation observed in comet 67P/Churyumov–Gerasimenko by Rosetta/ROSINA. *Monthly Notices of the Royal Astronomical Society*, *469*(Suppl_2), S787-S803.

Canup, R. M., & Asphaug, E. (2001). Origin of the Moon in a giant impact near the end of the Earth's formation. *Nature*, *412*(6848), 708.

Caracausi, A., Avice, G., Burnard, P. G., Füri, E., & Marty, B. (2016). Chondritic xenon in the Earth's mantle. *Nature*, *533*(7601), 82.

Cartier, C., & Wood, B. J. (2019). The role of reducing conditions in building Mercury. *Elements: An International Magazine of Mineralogy, Geochemistry, and Petrology*, *15*(1), 39-45.

Cartigny, P., & Ader, M. (2003). A comment on "The nitrogen record of crust–mantle interaction and mantle convection from Archean to Present" by B. Marty and N. Dauphas [Earth Planet. Sci. Lett. 206 (2003) 397–410]. *Earth and Planetary Science Letters*, *216*(3), 425-432.

Cavarroc, M., Alcouffe, G., Boufendi, L., Cernogora, G., & Szopa, C. (2007). Study of a radio frequency plasma for production of equivalents of Titan's aerosols. *Proc. ICPIG*, *28*, 2079-2082.

Chakraborty, S., Ahmed, M., Jackson, T. L., & Thiemens, M. H. (2008). Experimental test of self-shielding in vacuum ultraviolet photodissociation of CO. *Science*, *321*(5894), 1328-1331.

Chakraborty, S., Muskatel, B. H., Jackson, T. L., Ahmed, M., Levine, R. D., & Thiemens, M. H. (2014). Massive isotopic effect in vacuum UV photodissociation of N2 and implications for meteorite data. *Proceedings of the National Academy of Sciences*, *111*(41), 14704-14709.

Charnoz, S., Fouchet, L., Aleon, J., & Moreira, M. (2011). Three-dimensional lagrangian turbulent diffusion of dust grains in a protoplanetary disk: Method and first applications. *The Astrophysical Journal*, *737*(1), 33.

Charnoz, S., & Taillifet, E. (2012). A method for coupling dynamical and collisional evolution of dust in circumstellar disks: The effect of a dead zone. *The Astrophysical Journal*, *753*(2), 119.

Charnoz, S., Aléon, J., Chaumard, N., Baillié, K., & Taillifet, E. (2015). Growth of calcium–aluminum-rich inclusions by coagulation and fragmentation in a turbulent protoplanetary disk: Observations and simulations. *Icarus*, *252*, 440-453.

Charnoz, S., Pignatale, F. C., Hyodo, R., Mahan, B., Chaussidon, M., Siebert, J., & Moynier, F. (2019). Planetesimal formation in an evolving protoplanetary disk with a dead zone. *A&A* 627, A50.

Chatterjee, R., & Lassiter, J. C. (2016). 186Os/188Os variations in upper mantle peridotites: Constraints on the Pt/Os ratio of primitive upper mantle, and implications for late veneer accretion and mantle mixing timescales. *Chemical Geology*, *442*, 11-22.

Chen, Y., Zhang, Y., Liu, Y., Guan, Y., Eiler, J., & Stolper, E. M. (2015). Water, fluorine, and sulfur concentrations in the lunar mantle. *Earth and Planetary Science Letters*, *427*, 37-46.

Chyba, C., & Sagan, C. (1992). Endogenous production, exogenous delivery and impact-shock synthesis of organic molecules: an inventory for the origins of life. *Nature*, *355*(6356), 125.

Ciarniello, M., Capaccioni, F., Filacchione, G., Raponi, A., Tosi, F., De Sanctis, M. C., ... & Arnold, G. (2015). Photometric properties of comet 67P/Churyumov-Gerasimenko from VIRTIS-M onboard Rosetta. *Astronomy & Astrophysics*, *583*, A31.

Ciborowski, T. J. R., & Kerr, A. C. (2016). Did mantle plume magmatism help trigger the Great Oxidation Event?. *Lithos*, *246*, 128-133.

Ciesla, F. J., & Sandford, S. A. (2012). Organic synthesis via irradiation and warming of ice grains in the solar nebula. *Science*, *336*(6080), 452-454.

Ciesla, F. J., Krijt, S., Yokochi, R., & Sandford, S. (2018). The Efficiency of Noble Gas Trapping in Astrophysical Environments. *The Astrophysical Journal*, *867*(2), 146.

Claire, M. W., Sheets, J., Cohen, M., Ribas, I., MEADOwS, V. S., & Catling, D. C. (2012). The evolution of solar flux from 0.1 nm to 160 μm: quantitative estimates for planetary studies. *The Astrophysical Journal*, *757*(1), 95.

Clay, P. L., Burgess, R., Busemann, H., Ruzié-Hamilton, L., Joachim, B., Day, J. M., & Ballentine, C. J. (2017). Halogens in chondritic meteorites and terrestrial accretion. *Nature*, *551*(7682), 614.

Clayton, R. N., Grossman, L., & Mayeda, T. K. (1973). A component of primitive nuclear composition in carbonaceous meteorites. *Science*, *182*(4111), 485-488.

Clayton, D. D., & Ward, R. A. (1978). s-Process studies: Xenon and krypton isotopic abundances. *The Astrophysical Journal*.

Clayton, D. D. (1982). Cosmic chemical memory-a new astronomy. *Quarterly Journal of the Royal Astronomical Society*, *23*, 174.

Cleland, C. E., & Chyba, C. F. (2002). Defining 'life'. *Origins of Life and Evolution of the Biosphere*, *32*(4), 387-393.

Clement, M. S., Kaib, N. A., Raymond, S. N., Chambers, J. E., & Walsh, K. J. (2019). The early instability scenario: Terrestrial planet formation during the giant planet instability, and the effect of collisional fragmentation. *Icarus*, *321*, 778-790.

Cody, G.D. and Alexander, C.M.O.D. (2005) NMR studies of chemical and structural variation of insoluble organic matter from different carbonaceous chondrite groups. Geochimica et Cosmochimica Acta, 69,1085–1097.

Collings, M. P., Dever, J. W., Fraser, H. J., & McCoustra, M. R. (2003). Laboratory studies of the interaction of carbon monoxide with water ice. *Astrophysics and Space Science*, *285*(3-4), 633-659.

Connelly, J. N., Bollard, J., & Bizzarro, M. (2017). Pb–Pb chronometry and the early solar system. *Geochimica et Cosmochimica Acta*, *201*, 345-363.

Cosmidis, J., & Templeton, A. S. (2016). Self-assembly of biomorphic carbon/sulfur microstructures in sulfidic environments. *Nature communications*, *7*, 12812.

Ćuk, M., & Stewart, S. T. (2012). Making the Moon from a fast-spinning Earth: a giant impact followed by resonant despinning. *science*, *338*(6110), 1047-1052.

Dalai, P., Kaddour, H., & Sahai, N. (2016). Incubating life: prebiotic sources of organics for the origin of life. *Elements*, *12*(6), 401-406.

Dalou, C., Füri, E., Deligny, C., Piani, L., Caumon, M. C., Laumonier, M., ... & Edén, M. (2019). Redox control on nitrogen isotope fractionation during planetary core formation. *Proceedings of the National Academy of Sciences*, *116*(29), 14485-14494.

Danger, G., Orthous-Daunay, F. R., de Marcellus, P., Modica, P., Vuitton, V., Duvernay, F., ... & Chiavassa, T. (2013). Characterization of laboratory analogs of interstellar/cometary organic residues using very high resolution mass spectrometry. *Geochimica et Cosmochimica Acta*, *118*, 184-201.

Da Silva, L., Maurel, M. C., & Deamer, D. (2015). Salt-promoted synthesis of RNA-like molecules in simulated hydrothermal conditions. *Journal of molecular evolution*, *80*(2), 86-97.

Dauphas, N., & Marty, B. (1999). Heavy nitrogen in carbonatites of the Kola Peninsula: A possible signature of the deep mantle. *Science*, *286*(5449), 2488-2490.

Dauphas, N., Marty, B., & Reisberg, L. (2002). Molybdenum nucleosynthetic dichotomy revealed in primitive meteorites. *The Astrophysical Journal Letters*, *569*(2), L139.

Dauphas, N. (2003). The dual origin of the terrestrial atmosphere. *Icarus*, *165*(2), 326-339.

Dauphas, N., Davis, A. M., Marty, B., & Reisberg, L. (2004). The cosmic molybdenum–ruthenium isotope correlation. *Earth and Planetary Science Letters*, *226*(3-4), 465-475.

Dauphas, N., Remusat, L., Chen, J. H., Roskosz, M., Papanastassiou, D. A., Stodolna, J., ... & Eiler, J. M. (2010). Neutron-rich chromium isotope anomalies in supernova nanoparticles. *The Astrophysical Journal*, *720*(2), 1577.

Dauphas, N., & Chaussidon, M. (2011). A perspective from extinct radionuclides on a young stellar object: the Sun and its accretion disk. *Annual Review of Earth and Planetary Sciences*, *39*, 351-386.

Dauphas, N., & Pourmand, A. (2011). Hf–W–Th evidence for rapid growth of Mars and its status as a planetary embryo. *Nature*, *473*(7348), 489.

Dauphas, N., Burkhardt, C., Warren, P. H., & Fang-Zhen, T. (2014). Geochemical arguments for an Earth-like Moon-forming impactor. *Philosophical Transactions of the Royal Society A: Mathematical, Physical and Engineering Sciences*, *372*(2024), 20130244.

Dauphas, N. (2017). The isotopic nature of the Earth's accreting material through time. *Nature*, *541*(7638), 521.

Davis, A. M., Richter, F. M., Mendybaev, R. A., Janney, P. E., Wadhwa, M., & McKeegan, K. D. (2015). Isotopic mass fractionation laws for magnesium and their effects on 26Al–26Mg systematics in solar system materials. *Geochimica et Cosmochimica Acta*, *158*, 245-261.

Day, J. M., Pearson, D. G., & Taylor, L. A. (2007). Highly siderophile element constraints on accretion and differentiation of the Earth-Moon system. *Science*, *315*(5809), 217-219.

Deamer, D., Damer, B., & Kompanichenko, V. (2019). Hydrothermal chemistry and the origin of cellular life. *Astrobiology*.

De Hoffmann, E., Charette, J., Stroobant, V. (1994) Spéctrométrie de Masse, Masson, Paris, France. p178.

De Keyser, J., Dhooghe, F., Gibbons, A., Altwegg, K., Balsiger, H., Berthelier, J. J., ... & Fiethe, B. (2015). Correcting peak deformation in Rosetta's ROSINA/DFMS mass spectrometer. *International journal of mass spectrometry*, *393*, 41-51.

Delarue, F., Rouzaud, J. N., Derenne, S., Bourbin, M., Westall, F., Kremer, B., ... & Robert, F. (2016). The Raman-derived carbonization continuum: A tool to select the best preserved molecular structures in Archean kerogens. *Astrobiology*, *16*(6), 407-417.

Deloule, E., Albarede, F., & Sheppard, S. M. (1991). Hydrogen isotope heterogeneities in the mantle from ion probe analysis of amphiboles from ultramafic rocks. *Earth and Planetary Science Letters*, *105*(4), 543-553.

Deloule, E., & Robert, F. (1995). Interstellar water in meteorites?. *Geochimica et Cosmochimica Acta*, *59*(22), 4695-4706.

de Marcellus, P., Fresneau, A., Brunetto, R., Danger, G., Duvernay, F., Meinert, C., ... & Le Sergeant d'Hendecourt, L. (2016). Photo and thermochemical evolution of astrophysical ice analogues as a source for soluble and insoluble organic materials in solar system minor bodies. *Monthly Notices of the Royal Astronomical Society*, *464*(1), 114-120.

DeMeo, F. E., & Carry, B. (2013). The taxonomic distribution of asteroids from multi-filter all-sky photometric surveys. *Icarus*, *226*(1), 723-741.

Derenne, S., & Robert, F. (2010). Model of molecular structure of the insoluble organic matter isolated from Murchison meteorite. *Meteoritics & Planetary Science*, *45*(9), 1461-1475.

de Ronde, C.E.J., Channer, D.M. deR., Faure, K., Bray, C.J., Spooner, E.T.C., 1997. Fluid chemistry of Archean seafloor hydrothermal vents: Implications for the composition of circa 3.2 Ga seawater. Geochim. Cosmochim. Acta 61, 4025–4042.

Desch, S. J., Kalyaan, A., & Alexander, C. M. D. (2018). The effect of Jupiter's formation on the distribution of refractory elements and inclusions in meteorites. *The Astrophysical Journal Supplement Series*, *238*(1), 11.

d'Hendecourt, L. B., Allamandola, L. J., Baas, F., & Greenberg, J. M. (1982). Interstellar grain explosions-Molecule cycling between gas and dust. *Astronomy and Astrophysics*, *109*, L12-L14.

Dikov, Y. P., Ivanov, A. V., Wlotzka, F., Galimov, E. M., & Wänke, H. (1998). High enrichment of carbon and volatile elements in the surface layers of Luna 16 soil sample 1635: Result of comet or meteorite impact?. *Earth and planetary science letters*, *155*(3-4), 197-204.

DiSanti, M. A., Bonev, B. P., Gibb, E. L., Roth, N. X., Russo, N. D., & Vervack Jr, R. J. (2018). Comet C/2013 V5 (Oukaimeden): Evidence for Depleted Organic Volatiles and Compositional Heterogeneity as Revealed through Infrared Spectroscopy. *The Astronomical Journal*, *156*(6), 258.

Donati, J. F., Moutou, C., Malo, L., Baruteau, C., Yu, L., Hébrard, E., ... & Petit, P. (2016). A hot Jupiter orbiting a 2-million-year-old solar-mass T Tauri star. *Nature*, *534*(7609), 662.

Drake, M. J., & Righter, K. (2002). Determining the composition of the Earth. *Nature*, *416*(6876), 39.

Drążkowska, J., Alibert, Y., & Moore, B. (2016). Close-in planetesimal formation by pile-up of drifting pebbles. *Astronomy & Astrophysics*, *594*, A105.

Drążkowska, J., & Alibert, Y. (2017). Planetesimal formation starts at the snow line. *Astronomy & Astrophysics*, *608*, A92.

Dullemond, C. P. Theoretical Models of the Structure of Protoplanetary Disks Les Houches 2013.

Duprat, J., Dobrică, E., Engrand, C., Aléon, J., Marrocchi, Y., Mostefaoui, S., ... & Robert, F. (2010). Extreme deuterium excesses in ultracarbonaceous micrometeorites from central Antarctic snow. *Science*, *328*(5979), 742-745.

Durand, B., & Nicaise, G. (1980). Procedures for kerogen isolation. In *Kerogen* (pp. 35-53). Technip Paris.

Eberhardt, P., Eugster, O., & Marti, K. (1965). A redetermination of the isotopic composition of atmospheric neon. *Zeitschrift für Naturforschung A*, *20*(4), 623-624.

Ehrenfreund, P., & Fraser, H. (2003). Ice chemistry in space. In *Solid State Astrochemistry* (pp. 317-356). Springer, Dordrecht.

Ehrenfreund, P., Spaans, M., & Holm, N. G. (2011). The evolution of organic matter in space. *Philosophical Transactions of the Royal Society A: Mathematical, Physical and Engineering Sciences*, *369*(1936), 538-554.

Elkins-Tanton, L. T. Linked magma ocean solidification and atmospheric growth for Earth and Mars. *Earth and Planetary Science Letters*, *271*(1-4), 181-191 (2008).

Elkins-Tanton, L. T. Formation of early water oceans on rocky planets. *Astrophysics and Space Science*, *332*(2), 359-364 (2011).

Elkins-Tanton, L. T., Burgess, S., & Yin, Q. Z. (2011). The lunar magma ocean: Reconciling the solidification process with lunar petrology and geochronology. *Earth and Planetary Science Letters*, *304*(3-4), 326-336.

Elliott, T., Zindler, A., & Bourdon, B. (1999). Exploring the kappa conundrum: the role of recycling in the lead isotope evolution of the mantle. *Earth and Planetary Science Letters*, *169*(1-2), 129-145.

Engel, M. H., & Macko, S. A. (1997). Isotopic evidence for extraterrestrial non-racemic amino acids in the Murchison meteorite. *Nature*, *389*(6648), 265.

Epstein, S., & Taylor Jr, H. P. (1974). D/H and O-18/O-16 ratios of H2O in the'rusty'breccia 66095 and the origin of'lunar water'. In *Lunar and Planetary Science Conference Proceedings* (Vol. 5, pp. 1839-1854).

Eugster, O., Eberhardt, P., & Geiss, J. (1967b). Krypton and xenon isotopic composition in three carbonaceous chondrites. *Earth and Planetary Science Letters*, *3*, 249-257.

Eugster, O., Eberhardt, P., & Geiss, J. (1967a). The isotopic composition of krypton in unequilibrated and gas rich chondrites. *Earth and Planetary Science Letters*, *2*(5), 385-393.

Eugster, O., Eberhardt, P., Geiss, J., Grögler, N., Jungck, M., & Mörgeli, M. (1977). The cosmic-ray exposure history of Shorty Crater samples-The age of Shorty Crater. In *Lunar and Planetary Science Conference Proceedings* (Vol. 8, pp. 3059-3082).

Farquhar, J., Bao, H., & Thiemens, M. (2000). Atmospheric influence of Earth's earliest sulfur cycle. *Science*, *289*(5480), 756-758.

Farquhar, J., & Wing, B. A. (2003). Multiple sulfur isotopes and the evolution of the atmosphere. *Earth and Planetary Science Letters*, *213*(1-2), 1-13.

Favre, C., Fedele, D., Semenov, D., Parfenov, S., Codella, C., Ceccarelli, C., ... & Lefloch, B. (2018). First detection of the simplest organic acid in a protoplanetary disk. *The Astrophysical journal letters*, *862*(1), L2.

Fayolle, E. C., Öberg, K. I., Cuppen, H. M., Visser, R., & Linnartz, H. (2011). Laboratory H2O: CO2 ice desorption data: entrapment dependencies and its parameterization with an extended three-phase model. *Astronomy & Astrophysics*, *529*, A74.

Fehr, M. A., Hammond, S. J., & Parkinson, I. J. (2018). Tellurium stable isotope fractionation in chondritic meteorites and some terrestrial samples. *Geochimica et Cosmochimica Acta*, *222*, 17-33.

Ferris, J. P., Hill Jr, A. R., Liu, R., & Orgel, L. E. (1996). Synthesis of long prebiotic oligomers on mineral surfaces. *Nature*, *381*(6577), 59.

Feuillie, C., Daniel, I., Michot, L. J., & Pedreira-Segade, U. (2013). Adsorption of nucleotides onto Fe–Mg–Al rich swelling clays. *Geochimica et Cosmochimica Acta*, *120*, 97-108.

Feulner, G. (2012). The faint young Sun problem. *Reviews of Geophysics*, *50*(2).

Fischer-Gödde, M., Becker, H., & Wombacher, F. (2011). Rhodium, gold and other highly siderophile elements in orogenic peridotites and peridotite xenoliths. *Chemical Geology*, *280*(3-4), 365-383.

Fischer-Gödde, M., & Kleine, T. (2017). Ruthenium isotopic evidence for an inner Solar System origin of the late veneer. *Nature*, *541*(7638), 525.

Fitoussi, C., & Bourdon, B. (2012). Silicon isotope evidence against an enstatite chondrite Earth. *Science*, *335*(6075), 1477-1480.

Floss, C., Stadermann, F. J., Kearsley, A. T., Burchell, M. J., & Ong, W. J. (2013). The abundance of presolar grains in comet 81P/Wild 2. *The Astrophysical Journal*, *763*(2), 140.

Floss, C., & Haenecour, P. (2016). Presolar silicate grains: Abundances, isotopic and elemental compositions, and the effects of secondary processing. *Geochemical Journal*, *50*(1), 3-25.

Fray, N., & Schmitt, B. (2009). Sublimation of ices of astrophysical interest: A bibliographic review. *Planetary and Space Science*, *57*(14-15), 2053-2080.

Fray, N., Bardyn, A., Cottin, H., Altwegg, K., Baklouti, D., Briois, C., ... & Grün, E. (2016). High-molecular-weight organic matter in the particles of comet 67P/Churyumov–Gerasimenko. *Nature*, *538*(7623), 72.

Frick, U., Mack, R., & Chang, S. (1979). Noble gas trapping and fractionation during synthesis of carbonaceous matter. In *Lunar and Planetary Science Conference Proceedings* (Vol. 10, pp. 1961-1972).

Frick, U., & Pepin, R. O. (1981). On the distribution of noble gases in Allende: a differential oxidation study. *Earth and Planetary Science Letters*, *56*, 45-63.

Füri, E., Marty, B., & Assonov, S. S. (2012). Constraints on the flux of meteoritic and cometary water on the Moon from volatile element (N–Ar) analyses of single lunar soil grains, Luna 24 core. *Icarus*, *218*(1), 220-229.

Füri, E., Deloule, E., Gurenko, A., & Marty, B. (2014). New evidence for chondritic lunar water from combined D/H and noble gas analyses of single Apollo 17 volcanic glasses. *Icarus*, *229*, 109-120.

Füri, E., Barry, P. H., Taylor, L. A., & Marty, B. (2015). Indigenous nitrogen in the Moon: constraints from coupled nitrogen–noble gas analyses of mare basalts. *Earth and Planetary Science Letters*, *431*, 195-205.

Furukawa, Y., Sekine, T., Oba, M., Kakegawa, T., & Nakazawa, H. (2009). Biomolecule formation by oceanic impacts on early Earth. *Nature geoscience*, *2*(1), 62.

Gaillard, F., Scaillet, B., & Arndt, N. T. (2011). Atmospheric oxygenation caused by a change in volcanic degassing pressure. *Nature*, *478*(7368), 229.

García-Ruiz, J. M., Hyde, S. T., Carnerup, A. M., Christy, A. G., Van Kranendonk, M. J., & Welham, N. J. (2003). Self-assembled silica-carbonate structures and detection of ancient microfossils. *Science*, *302*(5648), 1194-1197.

Garrod, R. T., & Herbst, E. (2006). Formation of methyl formate and other organic species in the warm-up phase of hot molecular cores. *Astronomy & Astrophysics*, *457*(3), 927-936.

Garvie, L. A., & Buseck, P. R. (2007). Prebiotic carbon in clays from Orgueil and Ivuna (CI), and Tagish Lake (C2 ungrouped) meteorites. *Meteoritics & Planetary Science*, *42*(12), 2111-2117.

Genda, H., Brasser, R., & Mojzsis, S. J. (2017). The terrestrial late veneer from core disruption of a lunar-sized impactor. *Earth and Planetary Science Letters*, *480*, 25-32.

Gessmann, C. K., Rubie, D. C., & McCammon, C. A. (1999). Oxygen fugacity dependence of Ni, Co, Mn, Cr, V, and Si partitioning between liquid metal and magnesiowüstite at 9–18 GPa and 2200 C. *Geochimica et cosmochimica acta*, *63*(11-12), 1853-1863.

Gibson, E. K., & Moore, G. W. (1973). Volatile-rich lunar soil: evidence of possible cometary impact. *Science*, *179*(4068), 69-71.

Gilbert, W. (1986). Origin of life: The RNA world. *nature*, *319*(6055), 618.

Gilmour, J. D., & Turner, G. (2007). Constraints on nucleosynthesis from xenon isotopes in presolar material. *The Astrophysical Journal*, *657*(1), 600.

Gilmour, J. D. (2010). "Planetary" noble gas components and the nucleosynthetic history of solar system material. *Geochimica et Cosmochimica Acta*, *74*(1), 380-393.

Gilmour, J. D., & Filtness, M. J. (2019). Dissipation of the Solar System's debris disk recorded in primitive meteorites. *Nature Astronomy*, *3*(4), 326.

Gladman, B., Kavelaars, J. J., Petit, J. M., Morbidelli, A., Holman, M. J., & Loredo, T. (2001). The structure of the Kuiper belt: Size distribution and radial extent. *The Astronomical Journal*, *122*(2), 1051.

Gladman, B. (2005). The Kuiper belt and the solar system's comet disk. *Science*, *307*(5706), 71-75.

Glavin, D. P., & Dworkin, J. P. (2009). Enrichment of the amino acid L-isovaline by aqueous alteration on CI and CM meteorite parent bodies. *Proceedings of the National Academy of Sciences*, *106*(14), 5487-5492.

Göbel, R., Ott, U., & Begemann, F. (1978). On trapped noble gases in ureilites. *Journal of Geophysical Research: Solid Earth*, *83*(B2), 855-867.

Goldman, N., Reed, E. J., Fried, L. E., Kuo, I. F. W., & Maiti, A. (2010). Synthesis of glycine-containing complexes in impacts of comets on early Earth. *Nature Chemistry*, *2*(11), 949.

Gomes, R., Levison, H. F., Tsiganis, K., & Morbidelli, A. (2005). Origin of the cataclysmic Late Heavy Bombardment period of the terrestrial planets. *Nature*, *435*(7041), 466.

Gonzalez, J. F., Laibe, G., Maddison, S. T., Pinte, C., & Ménard, F. (2015). ALMA images of discs: are all gaps carved by planets?. *Monthly Notices of the Royal Astronomical Society: Letters*, *454*(1), L36-L40.

Goodrich, C. A., Jones, J. H., & Berkley, J. L. (1987). Origin and evolution of the ureilite parent magmas: Multi-stage igneous activity on a large parent body. *Geochimica et Cosmochimica Acta*, *51*(9), 2255-2273.

Gradie, J., & Tedesco, E. (1982). Compositional structure of the asteroid belt. *Science*, *216*(4553), 1405-1407.

Graham, D. W. (2002). Noble gas isotope geochemistry of mid-ocean ridge and ocean island basalts: Characterization of mantle source reservoirs. *Reviews in mineralogy and geochemistry*, *47*(1), 247-317.

Greber, N. D., Dauphas, N., Bekker, A., Ptáček, M. P., Bindeman, I. N., & Hofmann, A. (2017). Titanium isotopic evidence for felsic crust and plate tectonics 3.5 billion years ago. *Science*, *357*(6357), 1271-1274.

Greenwood, J. P., Itoh, S., Sakamoto, N., Warren, P., Taylor, L., & Yurimoto, H. (2011). Hydrogen isotope ratios in lunar rocks indicate delivery of cometary water to the Moon. *Nature Geoscience*, *4*(2), 79.

Greenwood, J. P., Karato, S. I., Vander Kaaden, K. E., Pahlevan, K., & Usui, T. (2018). Water and Volatile Inventories of Mercury, Venus, the Moon, and Mars. *Space Science Reviews*, *214*(5), 92.

Greenwood, R. C., Barrat, J. A., Miller, M. F., Anand, M., Dauphas, N., Franchi, I. A., ... & Starkey, N. A. (2018). Oxygen isotopic evidence for accretion of Earth's water before a high-energy Moon-forming giant impact. *Science advances*, *4*(3), eaao5928.

Grewal, D. S., Dasgupta, R., Sun, C., Tsuno, K., & Costin, G. (2019). Delivery of carbon, nitrogen, and sulfur to the silicate Earth by a giant impact. *Science advances*, *5*(1), eaau3669.

Gudipati, M. S., & Castillo-Rogez, J. (Eds.). (2012). *The science of solar system ices* (Vol. 356). Springer Science & Business Media.

Guilbert-Lepoutre, A., Rosenberg, E. D., Prialnik, D., & Besse, S. (2016). Modelling the evolution of a comet subsurface: Implications for 67P/Churyumov–Gerasimenko. *Monthly Notices of the Royal Astronomical Society*, *462*(Suppl_1), S146-S155.

Guzmán-Marmolejo, A., Segura, A., & Escobar-Briones, E. (2013). Abiotic production of methane in terrestrial planets. *Astrobiology*, *13*(6), 550-559.

Halliday, A. N. (2004). Mixing, volatile loss and compositional change during impact-driven accretion of the Earth. *Nature*, *427*(6974), 505.

Hallis, L. J., Huss, G. R., Nagashima, K., Taylor, G. J., Halldórsson, S. A., Hilton, D. R., ... & Meech, K. J. (2015). Evidence for primordial water in Earth's deep mantle. *Science*, *350*(6262), 795-797.

Hama, T., Yabushita, A., Yokoyama, M., Kawasaki, M., & Watanabe, N. (2009a). Formation mechanisms of oxygen atoms in the O (PJ 3) state from the 157 nm photoirradiation of amorphous water ice at 90 K. *The Journal of chemical physics*, *131*(11), 114511.

Hama, T., Yokoyama, M., Yabushita, A., Kawasaki, M., Wickramasinghe, P., Guo, W., ... & Western, C. M. (2009b). Translational and internal energy distributions of methyl and hydroxyl radicals produced by 157 nm photodissociation of amorphous solid methanol. *The Journal of chemical physics*, *131*(22), 224512.

Hama, T., Yokoyama, M., Yabushita, A., & Kawasaki, M. (2010). Role of OH radicals in the formation of oxygen molecules following vacuum ultraviolet photodissociation of amorphous solid water. *The Journal of chemical physics*, *133*(10), 104504.

Hamano, K., Abe, Y., & Genda, H. Emergence of two types of terrestrial planet on solidification of magma ocean. *Nature*, *497*(7451), 607 (2013)

Haner, J., & Schrobilgen, G. J. (2015). The chemistry of Xenon (IV). *Chemical reviews*, *115*(2), 1255-1295.

Hansen, B. M. (2009). Formation of the terrestrial planets from a narrow annulus. *The Astrophysical Journal*, *703*(1), 1131.

Haqq-Misra, J. D., Domagal-Goldman, S. D., Kasting, P. J., & Kasting, J. F. (2008). A revised, hazy methane greenhouse for the Archean Earth. *Astrobiology*, *8*(6), 1127-1137.

Hartmann, L., Calvet, N., Gullbring, E., & D'Alessio, P. (1998). Accretion and the evolution of T Tauri disks. *The Astrophysical Journal*, *495*(1), 385.

Hauri, E. H., Weinreich, T., Saal, A. E., Rutherford, M. C., & Van Orman, J. A. (2011). High pre-eruptive water contents preserved in lunar melt inclusions. *Science*, *333*(6039), 213-215.

Hauri, E. H., Saal, A. E., Rutherford, M. J., & Van Orman, J. A. (2015). Water in the Moon's interior: Truth and consequences. *Earth and Planetary Science Letters*, *409*, 252-264.

Hauri, E. H., Saal, A. E., Nakajima, M., Anand, M., Rutherford, M. J., Van Orman, J. A., & Le Voyer, M. (2017). Origin and evolution of water in the Moon's interior. *Annual Review of Earth and Planetary Sciences*, *45*, 89-111.

Hawkesworth, C., Cawood, P. A., & Dhuime, B. (2019). Rates of generation and growth of the continental crust. *Geoscience Frontiers*, *10*(1), 165-173.

Hay, W. W., Migdisov, A., Balukhovsky, A. N., Wold, C. N., Flögel, S., & Söding, E., 2006. Evaporites and the salinity of the ocean during the Phanerozoic: Implications for climate, ocean circulation and life. Palaeogeogr., Palaeoclim., Palaeoecol., 240, 3-46.

Heays, A. N., Bosman, A. D., & van Dishoeck, E. F. (2017). Photodissociation and photoionisation of atoms and molecules of astrophysical interest. *Astronomy & Astrophysics*, *602*, A105.

Heber, V. S., Baur, H., Bochsler, P., McKeegan, K. D., Neugebauer, M., Reisenfeld, D. B., ... & Wiens, R. C. (2012). Isotopic mass fractionation of solar wind: Evidence from fast and slow solar wind collected by the Genesis mission. *The Astrophysical Journal*, *759*(2), 121.

Herwartz, D., Pack, A., Friedrichs, B., & Bischoff, A. (2014). Identification of the giant impactor Theia in lunar rocks. *Science*, *344*(6188), 1146-1150.

Herzberg, C., Condie, K., & Korenaga, J. (2010). Thermal history of the Earth and its petrological expression. *Earth and Planetary Science Letters*, *292*(1-2), 79-88.

Hezel, D. C., & Palme, H. (2010). The chemical relationship between chondrules and matrix and the chondrule matrix complementarity. *Earth and Planetary Science Letters*, *294*(1-2), 85-93.

Hezel, D. C., Wilden, J. S., Becker, D., Steinbach, S., Wombacher, F., & Harak, M. (2018). Fe isotope composition of bulk chondrules from Murchison (CM2): Constraints for parent body alteration, nebula processes and chondrule-matrix complementarity. *Earth and Planetary Science Letters*, *490*, 31-39.

Hickman, A. H., & Van Kranendonk, M. J. (2012). Early Earth evolution: evidence from the 3.5-1.8 Ga geological history of the Pilbara region of Western Australia. *Episodes*, *35*(1), 283-297.

Hirschmann, M. M. (2016). Constraints on the early delivery and fractionation of Earth's major volatiles from C/H, C/N, and C/S ratios. *American Mineralogist*, *101*(3), 540-553.

Haugbølle, T., Weber, P., Wielandt, D. P., Benítez-Llambay, P., Bizzarro, M., Gressel, O., & Pessah, M. E. (2019). Probing the protosolar disk using dust filtering at gaps in the early Solar System. *arXiv preprint arXiv:1903.12274*.

Hohenberg, C. M., Thonnard, N., & Meshik, A. (2002). Active capture and anomalous adsorption: New mechanisms for the incorporation of heavy noble gases. *Meteoritics & Planetary Science*, *37*(2), 257-267.

Holland, G., & Ballentine, C. J. (2006). Seawater subduction controls the heavy noble gas composition of the mantle. *Nature*, *441*(7090), 186.

Holland, G., Cassidy, M., & Ballentine, C. J. (2009). Meteorite Kr in Earth's mantle suggests a late accretionary source for the atmosphere. *Science*, *326*(5959), 1522-1525.

Holland, H. D. (2006). The oxygenation of the atmosphere and oceans. *Philosophical Transactions of the Royal Society B: Biological Sciences*, *361*(1470), 903-915.

Hollenstein, U., Palm, H., & Merkt, F. (2000). A broadly tunable extreme ultraviolet laser source with a 0.008 cm− 1 bandwidth. *Review of Scientific Instruments*, *71*(11), 4023-4028.

Honda, M., Zhang, X., Phillips, D., Hamilton, D., Deerberg, M., & Schwieters, J. B. (2015). Redetermination of the 21Ne relative abundance of the atmosphere, using a high resolution, multi-collector noble gas mass spectrometer (HELIX-MC Plus). *International Journal of Mass Spectrometry*, *387*, 1-7.

Hoppe, P., Leitner, J., & Kodolányi, J. (2017). The stardust abundance in the local interstellar cloud at the birth of the solar system. *Nature Astronomy*, *1*(9), 617.

Hoppe, P., Rubin, M., & Altwegg, K. (2018). Presolar Isotopic Signatures in Meteorites and Comets: New Insights from the Rosetta Mission to Comet 67P/Churyumov–Gerasimenko. *Space science reviews*, *214*(6), 106.

Hosono, N., Karato, S. I., Makino, J., & Saitoh, T. R. (2019). Terrestrial magma ocean origin of the Moon. *Nature Geoscience*, 1.

Howard, K. T., Alexander, C. O. D., Schrader, D. L., & Dyl, K. A. (2015). Classification of hydrous meteorites (CR, CM and C2 ungrouped) by phyllosilicate fraction: PSD-XRD modal mineralogy and planetesimal environments. *Geochimica et Cosmochimica Acta*, *149*, 206-222.

Hui, H., Guan, Y., Chen, Y., Peslier, A. H., Zhang, Y., Liu, Y., ... & Osinski, G. R. (2017). A heterogeneous lunar interior for hydrogen isotopes as revealed by the lunar highlands samples. *Earth and Planetary Science Letters*, *473*, 14-23.

Humbert, F., Libourel, G., France-Lanord, C., Zimmermann, L., & Marty, B. (2000). CO2-laser extraction-static mass spectrometry analysis of ultra-low concentrations of nitrogen in silicates. *Geostandards Newsletter*, *24*(2), 255-260.

Hunten, D. M. (1993). Atmospheric evolution of the terrestrial planets. *Science*, 915-920.

Huss, G. R., & Lewis, R. S. (1994). Noble gases in presolar diamonds I: Three distinct components and their implications for diamond origins. *Meteoritics*, *29*(6), 791-810.

Huss, G. R., & Lewis, R. S. (1995). Presolar diamond, SiC, and graphite in primitive chondrites: Abundances as a function of meteorite class and petrologic type. *Geochimica et Cosmochimica Acta*, *59*(1), 115-160.

Huss, G. R., Lewis, R. S., & Hemkin, S. (1996). The "normal planetary" noble gas component in primitive chondrites: Compositions, carrier, and metamorphic history. *Geochimica et Cosmochimica Acta*, *60*(17), 3311-3340.

Hyodo, R., Ida, S., & Charnoz, S. (2019). Formation of rocky and icy planetesimals inside and outside the snow line: effects of diffusion, sublimation, and back-reaction. *Astronomy & Astrophysics*, *629*, A90.

Isella, A., Guidi, G., Testi, L., Liu, S., Li, H., Li, S., ... & Manara, C. F. (2016). Ringed structures of the HD 163296 protoplanetary disk revealed by ALMA. *Physical Review Letters*, *117*(25), 251101.

Ivanova, O. V., Picazzio, E., Luk'yanyk, I. V., Cavichia, O., & Andrievsky, S. M. (2018). Spectroscopic observations of the comet 29P/Schwassmann-Wachmann 1 at the SOAR telescope. *Planetary and Space Science*, *157*, 34-38.

Izidoro, A., Raymond, S. N., Pierens, A., Morbidelli, A., Winter, O. C., & Nesvorny, D. (2016). The asteroid belt as a relic from a chaotic early Solar System. *The Astrophysical Journal*, *833*(1), 40.

Jackson, M. G., & Dasgupta, R. (2008). Compositions of HIMU, EM1, and EM2 from global trends between radiogenic isotopes and major elements in ocean island basalts. *Earth and Planetary Science Letters*, *276*(1-2), 175-186.

Jackson, C. R., Bennett, N. R., Du, Z., Cottrell, E., & Fei, Y. (2018). Early episodes of high-pressure core formation preserved in plume mantle. *Nature*, *553*(7689), 491.

Javoy, M. (1995). The integral enstatite chondrite model of the Earth. *Geophysical Research Letters*, *22*(16), 2219-2222.

Javaux, E. J. (2019). Challenges in evidencing the earliest traces of life. *Nature*, *572*(7770), 451-460.

Johansen, A., & Lambrechts, M. (2017). Forming planets via pebble accretion. *Annual Review of Earth and Planetary Sciences*, *45*, 359-387.

Johnston, D. T. (2011). Multiple sulfur isotopes and the evolution of Earth's surface sulfur cycle. *Earth-Science Reviews*, *106*(1-2), 161-183.

Jessberger, E. K., & Kissel, J. (1991). Chemical properties of cometary dust and a note on carbon isotopes. In *International Astronomical Union Colloquium* (Vol. 116, No. 2, pp. 1075-1092). Cambridge University Press.

Jones, M. R., Wanless, V. D., Soule, S. A., Kurz, M. D., Mittelstaedt, E., Fornari, D. J., ... & Péron, S. (2019). New constraints on mantle carbon from Mid-Atlantic Ridge popping rocks. *Earth and Planetary Science Letters*, *511*, 67-75.

Kaddour, H., & Sahai, N. (2014). Synergism and mutualism in non-enzymatic RNA polymerization. *Life*, *4*(4), 598-620.

Kappler, A., Pasquero, C., Konhauser, K. O., & Newman, D. K. (2005). Deposition of banded iron formations by anoxygenic phototrophic Fe (II)-oxidizing bacteria. *Geology*, *33*(11), 865-868.

Kargel, J. S., & Lunine, J. I. (1998). Clathrate hydrates on Earth and in the solar system. In *Solar System Ices* (pp. 97-117). Springer, Dordrecht.

Kawamura, K., Nishi, T., & Sakiyama, T. (2005). Consecutive elongation of alanine oligopeptides at the second time range under hydrothermal conditions using a microflow reactor system. *Journal of the American Chemical Society*, *127*(2), 522-523.

Kebukawa, Y., Chan, Q. H., Tachibana, S., Kobayashi, K., & Zolensky, M. E. (2017). One-pot synthesis of amino acid precursors with insoluble organic matter in planetesimals with aqueous activity. *Science advances*, *3*(3), e1602093.

Keller, H. U., Mottola, S., Davidsson, B., Schröder, S. E., Skorov, Y., Kührt, E., ... & Scholten, F. (2015). Insolation, erosion, and morphology of comet 67P/Churyumov-Gerasimenko. *Astronomy & Astrophysics*, *583*, A34.

Kellogg, L. H., & Wasserburg, G. J. (1990). The role of plumes in mantle helium fluxes. *Earth and Planetary Science Letters*, *99*(3), 276-289.

Kendrick, M. A., Hémond, C., Kamenetsky, V. S., Danyushevsky, L., Devey, C. W., Rodemann, T., ... & Perfit, M. R. (2017). Seawater cycled throughout Earth's mantle in partially serpentinized lithosphere. *Nature Geoscience*, *10*(3), 222.

Kerrich, R., & Jia, Y. (2004). A comment on "The nitrogen record of crust–mantle interaction and mantle convection from Archean to Present" by B. Marty and N. Dauphas [Earth Planet. Sci. Lett. 206 (2003) 397–410]. *Earth and Planetary Science Letters*, *225*(3-4), 435-440.

Khriachtchev, L., Pettersson, M., Runeberg, N., Lundell, J., & Räsänen, M. (2000). A stable argon compound. *Nature*, *406*(6798), 874.

Khriachtchev, L., Isokoski, K., Cohen, A., Räsänen, M., & Gerber, R. B. (2008). A small neutral molecule with two noble-gas atoms: HXeOXeH. *Journal of the American Chemical Society*, *130*(19), 6114-6118.

Kimura, K., Lewis, R.S., Anders, E., Distribution of gold and rhenium between nickel–iron and silicate melts: implications for the abundance of siderophile elements on the Earth and Moon. *Geochim. Cosmochim. Acta* 38, 683–701. (1974).

Kleine, T., Münker, C., Mezger, K., & Palme, H. (2002). Rapid accretion and early core formation on asteroids and the terrestrial planets from Hf–W chronometry. *Nature*, *418*(6901), 952.

Kleine, T., Palme, H., Mezger, K., & Halliday, A. N. (2005). Hf-W chronometry of lunar metals and the age and early differentiation of the Moon. *Science*, *310*(5754), 1671-1674.

Kleine, T., Mezger, K., Palme, H., Scherer, E., & Münker, C. (2005). Early core formation in asteroids and late accretion of chondrite parent bodies: Evidence from 182Hf-182W in CAIs, metal-rich chondrites, and iron meteorites. *Geochimica et Cosmochimica Acta*, *69*(24), 5805-5818.

Knauth, L. P., 1998. Salinity history of the Earth's early ocean. Nature, 395, 554-555.

Knauth, L.P., 2005. Temperature and salinity history of the Precambrian ocean: Implications for the course of microbial evolution. Palaeogeogr. Palaeoclimatol. Palaeoecol. 219, 53–69.

Koeberl, C. (2006). Impact processes on the early Earth. *Elements*, *2*(4), 211-216.

Kokubo, E., & Ida, S. (2000). Formation of protoplanets from planetesimals in the solar nebula. *Icarus*, *143*(1), 15-27.

Komatsu, M., Fagan, T. J., Krot, A. N., Nagashima, K., Petaev, M. I., Kimura, M., & Yamaguchi, A. (2018). First evidence for silica condensation within the solar protoplanetary disk. *Proceedings of the National Academy of Sciences*, *115*(29), 7497-7502.

Konhauser, K. O., Hamade, T., Raiswell, R., Morris, R. C., Ferris, F. G., Southam, G., & Canfield, D. E. (2002). Could bacteria have formed the Precambrian banded iron formations?. *Geology*, *30*(12), 1079-1082.

Koonin, E. V. (2003). Comparative genomics, minimal gene-sets and the last universal common ancestor. *Nature Reviews Microbiology*, *1*(2), 127.

Korenaga, J. (2008). Urey ratio and the structure and evolution of Earth's mantle. *Reviews of Geophysics*, *46*(2).

Kouchi, A., & Yamamoto, T. (1995). Cosmoglaciology: Evolution of ice in interstellar space and the early solar system. *Progress in crystal growth and characterization of materials*, *30*(2-3), 83-107.

Krauss, O., & Wurm, G. (2005). Photophoresis and the pile-up of dust in young circumstellar disks. *The Astrophysical Journal*, *630*(2), 1088.

Krijt, S., Ciesla, F. J., & Bergin, E. A. (2016). Tracing water vapor and ice during dust growth. *The Astrophysical Journal*, *833*(2), 285.

Krishnamurthy, R. V., Epstein, S., Cronin, J. R., Pizzarello, S., & Yuen, G. U. (1992). Isotopic and molecular analyses of hydrocarbons and monocarboxylic acids of the Murchison meteorite. *Geochimica et Cosmochimica Acta*, *56*(11), 4045-4058.

Kruijer, T. S., Sprung, P., Kleine, T., Leya, I., Burkhardt, C., & Wieler, R. (2012). Hf–W chronometry of core formation in planetesimals inferred from weakly irradiated iron meteorites. *Geochimica et cosmochimica acta*, *99*, 287-304.

Kruijer, T. S., Burkhardt, C., Budde, G., & Kleine, T. (2017). Age of Jupiter inferred from the distinct genetics and formation times of meteorites. *Proceedings of the National Academy of Sciences*, *114*(26), 6712-6716.

Krummenacher, D., Merrihue, C. M., Pepin, R. O., & Reynolds, J. H. (1962). Meteoritic krypton and barium versus the general isotopic anomalies in meteoritic xenon. *Geochimica et Cosmochimica Acta*, *26*(2), 231-249.

Kuga, M., Marty, B., Marrocchi, Y., & Tissandier, L. (2015). Synthesis of refractory organic matter in the ionized gas phase of the solar nebula. *Proceedings of the National Academy of Sciences*, *112*(23), 7129-7134.

Kuga, M., Cernogora, G., Marrocchi, Y., Tissandier, L., & Marty, B. (2017). Processes of noble gas elemental and isotopic fractionations in plasma-produced organic solids: Cosmochemical implications. *Geochimica et Cosmochimica Acta*, *217*, 219-230.

Lambart, S., Koornneef, J. M., Millet, M. A., Davies, G. R., Cook, M., & Lissenberg, C. J. (2019). Highly heterogeneous depleted mantle recorded in the lower oceanic crust. *Nature Geoscience*, *12*(6), 482.

Lahav, N., White, D., & Chang, S. (1978). Peptide formation in the prebiotic era: thermal condensation of glycine in fluctuating clay environments. *Science*, *201*(4350), 67-69.

Larsen, K. K., Trinquier, A., Paton, C., Schiller, M., Wielandt, D., Ivanova, M. A., ... & Bizzarro, M. (2011). Evidence for magnesium isotope heterogeneity in the solar protoplanetary disk. *The Astrophysical Journal Letters*, *735*(2), L37.

Laurent, B., Roskosz, M., Remusat, L., Robert, F., Leroux, H., Vezin, H., ... & Lefebvre, J. M. (2015). The deuterium/hydrogen distribution in chondritic organic matter attests to early ionizing irradiation. *Nature communications*, *6*, 8567.

Lee, J. Y., Marti, K., Severinghaus, J. P., Kawamura, K., Yoo, H. S., Lee, J. B., & Kim, J. S. (2006). A redetermination of the isotopic abundances of atmospheric Ar. *Geochimica et Cosmochimica Acta*, *70*(17), 4507-4512.

Le Guillou, C., Bernard, S., Brearley, A. J., & Remusat, L. (2014). Evolution of organic matter in Orgueil, Murchison and Renazzo during parent body aqueous alteration: In situ investigations. *Geochimica et Cosmochimica Acta*, *131*, 368-392.

Leich, D. A., & Niemeyer, S. (1975). Trapped xenon in lunar anorthositic breccia 60015. In *Lunar and Planetary Science Conference Proceedings* (Vol. 6, pp. 1953-1965).

Leinhardt, Z. M., & Richardson, D. C. (2005). Planetesimals to protoplanets. I. Effect of fragmentation on terrestrial planet formation. *The Astrophysical Journal*, *625*(1), 427.

Leitner, J., Kodolányi, J., Hoppe, P., & Floss, C. (2012). Laboratory analysis of presolar silicate stardust from a nova. *The Astrophysical Journal Letters*, *754*(2), L41.

Lepland, A., van Zuilen, M. A., Arrhenius, G., Whitehouse, M. J., & Fedo, C. M. (2005). Questioning the evidence for Earth's earliest life—Akilia revisited. *Geology*, *33*(1), 77-79.

Leroy, C., Sanloup, C., Bureau, H., Schmidt, B. C., Konôpková, Z., & Raepsaet, C. (2018). Bonding of xenon to oxygen in magmas at depth. *Earth and Planetary Science Letters*, *484*, 103-110.

Lewis, R. S., Ming, T., Wacker, J. F., Anders, E., & Steel, E. (1987). Interstellar diamonds in meteorites. *Nature*, *326*(6109), 160.

Libourel, G., Marty, B., & Humbert, F. (2003). Nitrogen solubility in basaltic melt. Part I. Effect of oxygen fugacity. *Geochimica et Cosmochimica Acta*, *67*(21), 4123-4135.

Libourel, G., & Portail, M. (2018). Chondrules as direct thermochemical sensors of solar protoplanetary disk gas. *Science advances*, *4*(7), eaar3321.

Lichtenberg, T., Golabek, G. J., Burn, R., Meyer, M. R., Alibert, Y., Gerya, T. V., & Mordasini, C. (2019). A water budget dichotomy of rocky protoplanets from 26 Al-heating. *Nature Astronomy*, *3*(4), 307.

Lide, D. R. (1995). *CRC handbook of chemistry and physics: a ready-reference book of chemical and physical data*. CRC press.

Lightner, B. D., & Marti, K. (1974). Lunar trapped xenon. In *Lunar and Planetary Science Conference Proceedings* (Vol. 5, pp. 2023-2031).

Ligterink, N. F. W., Paardekooper, D. M., Chuang, K. J., Both, M. L., Cruz-Diaz, G. A., van Helden, J. H., & Linnartz, H. (2015). Controlling the emission profile of an H2 discharge lamp to simulate interstellar radiation fields. *Astronomy & Astrophysics*, *584*, A56.

Lin, Y., & van Westrenen, W. (2018). Isotopic evidence for volatile replenishment of the Moon during Late Accretion. *National Science Review*.

Lodders, K. (2000). An oxygen isotope mixing model for the accretion and composition of rocky planets. In *From Dust to Terrestrial Planets* (pp. 341-354). Springer, Dordrecht.

Lodders, K. (2004). Jupiter formed with more tar than ice. *The Astrophysical Journal*, *611*(1), 587.

Lollar, B. S., Westgate, T. D., Ward, J. A., Slater, G. F., & Lacrampe-Couloume, G. (2002). Abiogenic formation of alkanes in the Earth's crust as a minor source for global hydrocarbon reservoirs. *Nature*, *416*(6880), 522.

Lowe, D. R., & Knauth, L., 1977. Sedimentology of the Onverwacht Group (3.4 billion years), Transvaal, South Africa, and its bearing on the characteristics and evolution of the early earth. J. Geol., 85, 699-723.

Lunine, J. I. (2006). Physical conditions on the early Earth. *Philosophical Transactions of the Royal Society B: Biological Sciences*, *361*(1474), 1721-1731.

Luspay-Kuti, A., Mousis, O., Hässig, M., Fuselier, S. A., Lunine, J. I., Marty, B., ... & Rubin, M. (2016). The presence of clathrates in comet 67P/Churyumov-Gerasimenko. *Science advances*, *2*(4), e1501781.

Lyons, J. R., & Young, E. D. (2005). CO self-shielding as the origin of oxygen isotope anomalies in the early solar nebula. *Nature*, *435*(7040), 317.

Lyons, J R, R S Lewis, and R N Clayton. (2009). Comment on 'Experimental Test of Self- Shielding in Vacuum Ultraviolet Photodissociation of CO'. *Science* 324: 1516

Lyons, T. W., Reinhard, C. T., & Planavsky, N. J. (2014). The rise of oxygen in Earth's early ocean and atmosphere. *Nature*, *506*(7488), 307-315.

Luu, T. H., Hin, R. C., Coath, C. D., & Elliott, T. (2019). Bulk chondrite variability in mass independent magnesium isotope compositions–Implications for initial solar system 26Al/27Al and the timing of terrestrial accretion. *Earth and Planetary Science Letters*, *522*, 166-175.

Mabry, J., Burnard, P., Blard, P. H., & Zimmermann, L. (2012). Mapping changes in helium sensitivity and peak shape for varying parameters of a Nier-type noble gas ion source. *Journal of Analytical Atomic Spectrometry*, *27*(6), 1012-1017.

Madorsky, S. L. (1964). *Thermal degradation of organic polymers* (Vol. 7). Interscience Publishers.

Mahan, B., Siebert, J., Blanchard, I., Borensztajn, S., Badro, J., & Moynier, F. (2018). Constraining compositional proxies for Earth's accretion and core formation through high pressure and high temperature Zn and S metal-silicate partitioning. *Geochimica et Cosmochimica Acta*, *235*, 21-40.

Maher, K. A., & Stevenson, D. J. (1988). Impact frustration of the origin of life. *Nature*, *331*(6157), 612.

Maier, W. D., Barnes, S. J., Campbell, I. H., Fiorentini, M. L., Peltonen, P., Barnes, S. J., & Smithies, R. H. (2009). Progressive mixing of meteoritic veneer into the early Earth's deep mantle. *Nature*, *460*(7255), 620.

Marboeuf, U., Mousis, O., Petit, J. M., & Schmitt, B. (2009). Clathrate hydrates formation in short-period comets. *The Astrophysical Journal*, *708*(1), 812.

Marboeuf, U., Schmitt, B., Petit, J. M., Mousis, O., & Fray, N. (2012). A cometary nucleus model taking into account all phase changes of water ice: amorphous, crystalline, and clathrate. *Astronomy & Astrophysics*, *542*, A82.

Marchi, S., Canup, R. M., & Walker, R. J. (2018). Heterogeneous delivery of silicate and metal to the Earth by large planetesimals. *Nature geoscience*, *11*(1), 77.

Marrocchi, Y., Derenne, S., Marty, B., & Robert, F. (2005). Interlayer trapping of noble gases in insoluble organic matter of primitive meteorites. *Earth and Planetary Science Letters*, *236*(3-4), 569-578.

Marrocchi, Y., Marty, B., Reinhardt, P., & Robert, F. (2011). Adsorption of xenon ions onto defects in organic surfaces: Implications for the origin and the nature of organics in primitive meteorites. *Geochimica et Cosmochimica Acta*, *75*(20), 6255-6266.

Marrocchi, Y., & Marty, B. (2013). Experimental determination of the xenon isotopic fractionation during adsorption. *Geophysical Research Letters*, *40*(16), 4165-4170.

Marrocchi, Y., Avice, G., & Estrade, N. (2015). Multiple carriers of Q noble gases in primitive meteorites. *Geophysical Research Letters*, *42*(7), 2093-2099.

Marrocchi, Y., Bekaert, D. V., & Piani, L. (2018). Origin and abundance of water in carbonaceous asteroids. *Earth and Planetary Science Letters*, *482*, 23-32.

Marrocchi, Y., Villeneuve, J., Batanova, V., Piani, L., & Jacquet, E. (2018). Oxygen isotopic diversity of chondrule precursors and the nebular origin of chondrules. *Earth and Planetary Science Letters*, *496*, 132-141.

Marshall, W. L. (1994). Hydrothermal synthesis of amino acids. *Geochimica et Cosmochimica Acta*, *58*(9), 2099-2106.

Marshall, A. O., Emry, J. R., & Marshall, C. P. (2012). Multiple generations of carbon in the Apex chert and implications for preservation of microfossils. *Astrobiology*, *12*(2), 160-166.

Marti, K. (1967). Isotopic composition of trapped krypton and xenon in chondrites. *Earth and Planetary Science Letters*, *3*, 243-248.

Marty, B., & Dauphas, N. (2003). The nitrogen record of crust–mantle interaction and mantle convection from Archean to present. *Earth and Planetary Science Letters*, *206*(3-4), 397-410.

Marty, B., Palma, R. L., Pepin, R. O., Zimmermann, L., Schlutter, D. J., Burnard, P. G., ... & Simones, J. E. (2008). Helium and neon abundances and compositions in cometary matter. *Science*, *319*(5859), 75-78.

Marty, B. (2012). The origins and concentrations of water, carbon, nitrogen and noble gases on Earth. *Earth and Planetary Science Letters*, *313*, 56-66.

Marty, B., Zimmermann, L., Pujol, M., Burgess, R., & Philippot, P. (2013). Nitrogen isotopic composition and density of the Archean atmosphere. *Science*, *342*(6154), 101-104.

Marty, B., Avice, G., Sano, Y., Altwegg, K., Balsiger, H., Hässig, M., ... & Rubin, M. (2016). Origins of volatile elements (H, C, N, noble gases) on Earth and Mars in light of recent results from the ROSETTA cometary mission. *Earth and Planetary Science Letters*, *441*, 91-102.

Marty, B., Altwegg, K., Balsiger, H., Bar-Nun, A., Bekaert, D. V., Berthelier, J. J., ... & De Keyser, J. (2017). Xenon isotopes in 67P/Churyumov-Gerasimenko show that comets contributed to Earth's atmosphere. *Science*, *356*(6342), 1069-1072.

Marty, B., Avice, G., Bekaert, D. V., & Broadley, M. W. (2018). Salinity of the Archaean oceans from analysis of fluid inclusions in quartz. *Comptes Rendus Geoscience*, *350*(4), 154-163.

Marty, B., Bekaert, D. V., Broadley, M. W., & Jaupart, C. (2019). Geochemical evidence for high volatile fluxes from the mantle at the end of the Archaean. *Nature*, *575*(7783), 485-488.

Mastrapa, R. M., Sandford, S. A., Roush, T. L., Cruikshank, D. P., & Dalle Ore, C. M. (2009). Optical constants of amorphous and crystalline H_2O-ice: 2.5-22 μm (4000-455 cm–1) Optical constants of H_2O-ice. *The Astrophysical Journal*, *701*(2), 1347.

Mathew, K. J., & Marti, K. (2019). Lunar Xenon and the Origin of the Indigenous Component. *The Astrophysical Journal Letters*, *882*(2), L17.

Matsuda, J. I., & Maekawa, T. (1992). Noble gas implantation in glow discharge: Comparison between diamond and graphite. *Geochemical Journal*, *26*(5), 251-259.

Matsuda, J. I., Amari, S., Morishita, K., Nagashima, K., & Nara, M. (2010). The effect of pyridine treatment on phase Q: Orgueil and Allende. *Meteoritics & Planetary Science*, *45*(7), 1191-1205.

Matsumura, S., Thommes, E. W., Chatterjee, S., & Rasio, F. A. (2010). Unstable planetary systems emerging out of gas disks. *The Astrophysical Journal*, *714*(1), 194.

Matsumura, S., Brasser, R., & Ida, S. (2016). Effects of dynamical evolution of giant planets on the delivery of atmophile elements during terrestrial planet formation. *The Astrophysical Journal*, *818*(1), 15.

Mathew, K. J., & Marti, K. (2001). Early evolution of Martian volatiles: Nitrogen and noble gas components in ALH84001 and Chassigny. *Journal of Geophysical Research: Planets*, *106*(E1), 1401-1422.

Mauersberger, R., Ott, U., Henkel, C., Cernicharo, J., & Gallino, R. (2004). The abundance of S in IRC+ 10216 and its production in the Galaxy. *Astronomy & Astrophysics*, *426*(1), 219-227.

McCollom, T. M., & Seewald, J. S. (2001). A reassessment of the potential for reduction of dissolved CO_2 to hydrocarbons during serpentinization of olivine. *Geochimica et Cosmochimica Acta*, *65*(21), 3769-3778.

McCollom TM (2013) Miller-Urey and beyond: What have we learned about prebiotic organic synthesis reactions in the past 60 Years? Annual Review of Earth Planetary Sciences 41: 207-229

McCubbin, F. M., Steele, A., Hauri, E. H., Nekvasil, H., Yamashita, S., & Hemley, R. J. (2010). Nominally hydrous magmatism on the Moon. *Proceedings of the National Academy of Sciences*, *107*(25), 11223-11228.

McCubbin, F. M., & Barnes, J. J. (2019). Origin and abundances of H2O in the terrestrial planets, Moon, and asteroids. *Earth and Planetary Science Letters*, *526*, 115771.

McKeegan, K. D., Aléon, J., Bradley, J., Brownlee, D., Busemann, H., Butterworth, A., ... & Gounelle, M. (2006). Isotopic compositions of cometary matter returned by Stardust. *Science*, *314*(5806), 1724-1728.

McKeegan, K. D., Kudryavtsev, A. B., & Schopf, J. W. (2007). Raman and ion microscopic imagery of graphitic inclusions in apatite from older than 3830 Ma Akilia supracrustal rocks, west Greenland. *Geology*, *35*(7), 591-594.

McWilliam, A. (1997). Abundance ratios and galactic chemical evolution. *Annual Review of Astronomy and Astrophysics*, *35*(1), 503-556.

Meierhenrich, U. J., Filippi, J. J., Meinert, C., Bredehöft, J. H., Takahashi, J. I., Nahon, L., ... & Hoffmann, S. V. (2010). Circular dichroism of amino acids in the vacuum-ultraviolet region. *Angewandte Chemie International Edition*, *49*(42), 7799-7802.

Meisel, T., Walker, R. J., & Morgan, J. W. (1996). The osmium isotopic composition of the Earth's primitive upper mantle. *Nature*, *383*(6600), 517.

Meshik, A., Hohenberg, C., Pravdivtseva, O., & Burnett, D. (2014). Heavy noble gases in solar wind delivered by Genesis mission. *Geochimica et cosmochimica acta*, *127*, 326-347

Meshik, A. & Pravdivtseva, O. (2018) Precise Xenon Analyses of the Solar Wind: Implications for Indigenous Lunar Xenon. *Goldschmidt Conference*, Boston, USA.

Meyer, B. S. (1994). The r-, s-, and p-processes in nucleosynthesis. *Annual Review of Astronomy and Astrophysics*, *32*(1), 153-190.

Milićev, S. (1997). Badger and Herschbach-Laurie constants for the compounds of xenon and fluorine. In *Progress in Fourier Transform Spectroscopy* (pp. 539-541). Springer, Vienna.

Miller, S. L. (1953). A production of amino acids under possible primitive earth conditions. *Science*, *117*(3046), 528-529.

Miller, S. L., & Urey, H. C. (1959). Organic compound synthesis on the primitive earth. *Science*, *130*(3370), 245-251.

Miller, S. L., & Van Trump, J. E. (1981). The Strecker synthesis in the primitive ocean. In *Origin of life* (pp. 135-141). Springer, Dordrecht.

Misener, W., Krijt, S., & Ciesla, F. J. (2019). Tracking Dust Grains during Transport and Growth in Protoplanetary Disks. *The Astrophysical Journal*, *885*(2), 118.

Mizuno, H., Nakazawa, K., & Hayashi, C. (1980). Dissolution of the primordial rare gases into the molten Earth's material. *Earth and Planetary Science Letters*, *50*(1), 202-210.

Mojzsis, S. J., Arrhenius, G., McKeegan, K. D., Harrison, T. M., Nutman, A. P., & Friend, C. R. L. (1996). Evidence for life on Earth before 3,800 million years ago. *Nature*, *384*(6604), 55-59.

Mojzsis, S. J., Harrison, T. M., & Pidgeon, R. T. (2001). Oxygen-isotope evidence from ancient zircons for liquid water at the Earth's surface 4,300 Myr ago. *Nature*, *409*(6817), 178.

Molyarova, T., Akimkin, V., Semenov, D., Henning, T., Vasyunin, A., & Wiebe, D. (2017). Gas mass tracers in protoplanetary disks: CO is still the best. *The Astrophysical Journal*, *849*(2), 130.

Morbidelli, A., Crida, A., Masset, F., & Nelson, R. P. (2008). Building giant-planet cores at a planet trap. *Astronomy & Astrophysics*, *478*(3), 929-937.

Morbidelli, A., Marchi, S., Bottke, W. F., & Kring, D. A. (2012). A sawtooth-like timeline for the first billion years of lunar bombardment. *Earth and Planetary Science Letters*, *355*, 144-151.

Morbidelli, A., Lunine, J. I., O'Brien, D. P., Raymond, S. N., & Walsh, K. J. (2012). Building terrestrial planets. *Annual Review of Earth and Planetary Sciences*, *40*.

Morbidelli, A., & Wood, B. J. (2015). Late accretion and the late veneer. *The Early Earth: Accretion and Differentiation, Geophysical Monograph*, *212*, 71-82.

Morbidelli A, Walsh KJ, O'BrienDP, Minton DA, Bottke WF. (2015). The dynamical evolution of the asteroid belt. In Asteroids IV, ed. P Michel, F DeMeo, WF Bottke, pp. 493–508. Tucson: Univ. Ariz. Press.

Morbidelli, A., Bitsch, B., Crida, A., Gounelle, M., Guillot, T., Jacobson, S., ... & Lega, E. (2016). Fossilized condensation lines in the Solar System protoplanetary disk. *Icarus*, *267*, 368-376.

Moreira, M., Kunz, J., & Allegre, C. (1998). Rare gas systematics in popping rock: isotopic and elemental compositions in the upper mantle. *Science*, *279*(5354), 1178-1181.

Moreira, M., & Madureira, P. (2005). Cosmogenic helium and neon in 11 Myr old ultramafic xenoliths: consequences for mantle signatures in old samples. *Geochemistry, Geophysics, Geosystems*, *6*(8).

Moreira, M., & Charnoz, S. (2016). The origin of the neon isotopes in chondrites and on Earth. *Earth and Planetary Science Letters*, *433*, 249-256.

Moreira, M., Rouchon, V., Muller, E., Noirez, S. (2018) The xenon isotopic signature of the mantle beneath Massif Central. Geochemical Perspectives Letters 6, 28-32.

Mougel, B., Moynier, F., & Göpel, C. (2018). Chromium isotopic homogeneity between the Moon, the Earth, and enstatite chondrites. *Earth and Planetary Science Letters*, *481*, 1-8.

Mukhopadhyay, S. (2012). Early differentiation and volatile accretion recorded in deep-mantle neon and xenon. *Nature*, *486*(7401), 101.

Mukhopadhyay, S., & Parai, R. (2019). Noble gases: a record of Earth's evolution and mantle dynamics. *Annual Review of Earth and Planetary Sciences*, *47*, 389-419.

Muskatel, B. H., Remacle, F., Thiemens, M. H., & Levine, R. D. (2011). On the strong and selective isotope effect in the UV excitation of N2 with implications toward the nebula and Martian atmosphere. *Proceedings of the National Academy of Sciences*, *108*(15), 6020-6025.

Nagel, T. J., Hoffmann, J. E., & Münker, C. (2012). Generation of Eoarchean tonalite-trondhjemite-granodiorite series from thickened mafic arc crust. *Geology*, *40*(4), 375-378.

Nahon, L., de Oliveira, N., Garcia, G. A., Gil, J. F., Pilette, B., Marcouillé, O., ... & Polack, F. (2012). DESIRS: a state-of-the-art VUV beamline featuring high resolution and variable polarization for spectroscopy and dichroism at SOLEIL. *Journal of synchrotron radiation*, *19*(4), 508-520.

Nanne, J. A., Nimmo, F., Cuzzi, J. N., & Kleine, T. (2019). Origin of the non-carbonaceous–carbonaceous meteorite dichotomy. *Earth and Planetary Science Letters*, *511*, 44-54.

Néri, A., Guyot, F., Reynard, B., & Sotin, C. (2019). A carbonaceous chondrite and cometary origin for icy moons of Jupiter and Saturn. *Earth and Planetary Science Letters*, 115920.

Newman, M. J., & Rood, R. T. (1977). Implications of solar evolution for the Earth's early atmosphere. *Science*, *198*(4321), 1035-1037.

Niedermann, S., & Eugster, O. (1992). Noble gases in lunar anorthositic rocks 60018 and 65315: Acquisition of terrestrial krypton and xenon indicating an irreversible adsorption process. *Geochimica et cosmochimica acta*, *56*(1), 493-509.

Niemeyer, S., & Leich, D. A. (1976, April). Atmospheric rare gases in lunar rock 60015. In *Lunar and Planetary Science Conference Proceedings* (Vol. 7, pp. 587-597).

Nisbet, E. G., & Sleep, N. H. (2001). The habitat and nature of early life. *Nature*, *409*(6823), 1083.

Nittler, L. R., & Ciesla, F. (2016). Astrophysics with extraterrestrial materials. *Annual Review of Astronomy and Astrophysics*, *54*, 53-93.

Nittler, L. R., Stroud, R. M., Trigo-Rodríguez, J. M., De Gregorio, B. T., Alexander, C. M. D., Davidson, J., ... & Tanbakouei, S. (2019). A cometary building block in a primitive asteroidal meteorite. *Nature Astronomy*, 1.

Notesco, G., Bar-Nun, A., & Owen, T. (2003). Gas trapping in water ice at very low deposition rates and implications for comets. *Icarus*, *162*(1), 183-189.

Notesco, G., & Bar-Nun, A. (2005). A~ 25 K temperature of formation for the submicron ice grains which formed comets. *Icarus*, *175*(2), 546-550.

Nuevo, M. (2012). Laboratory astrochemistry: A powerful tool to understand the origin of organic molecules in the interstellar medium, comets, and meteorites. In *Frank N. Bash Symposium 2011: New Horizons in Astronomy* (Vol. 149, p. 004). SISSA Medialab.

Öberg, K. I., Linnartz, H., Visser, R., & Van Dishoeck, E. F. (2009). Photodesorption of ices. II. H2O and D2O. *The Astrophysical Journal*, *693*(2), 1209.

Öberg, K. I., & Bergin, E. A. (2016). Excess C/O and C/H in outer protoplanetary disk gas. *The Astrophysical Journal Letters*, *831*(2), L19.

Oehler, D., & Cady, S. (2014). Biogenicity and syngeneity of organic matter in ancient sedimentary rocks: recent advances in the search for evidence of past life. *Challenges*, *5*(2), 260-283.

Ohmoto, H., Watanabe, Y., Lasaga, A. C., Naraoka, H., Johnson, I., Brainard, J., & Chorney, A. (2014). Oxygen, iron, and sulfur geochemical cycles on early Earth: Paradigms and contradictions. *Geol. Soc. Am. Spec. Pap*, *504*, 55-95.

Oka, A., Nakamoto, T., & Ida, S. (2011). Evolution of snow line in optically thick protoplanetary disks: effects of water ice opacity and dust grain size. *The Astrophysical Journal*, *738*(2), 141.

Okazaki, R., Takaoka, N., Nagao, K., & Nakamura, T. (2010). Noble gases in enstatite chondrites released by stepped crushing and heating. *Meteoritics & Planetary Science*, *45*(3), 339-360.

Ong, L., Asphaug, E. I., Korycansky, D., & Coker, R. F. (2010). Volatile retention from cometary impacts on the Moon. *Icarus*, *207*(2), 578-589.

Oparin, A. I. (1936). Původ života (Origin of Life). *Dover Publications, NewYork*, *1953*, 196.

Oró, J., & Guidry, C. L. (1960). A novel synthesis of polypeptides. *Nature*, *186*(4719), 156-157.

Orthous-Daunay, F.R., Quirico, E., Lemelle, L., Beck, P., deAndrade, V., Simionovici, A. and Derenne, S. (2010) Speciation of sulfur in the insoluble organic matter from carbonaceous chondrites by XANES spectroscopy. Earth and Planetary Science Letters, 300, 321–328.

Orthous-Daunay, F.R., Quirico, E., Beck, P., Brissaud, O., Dartois, E., Pino, T. and Schmitt, B. (2013) Midinfrared study of the molecular structure variability of insoluble organic matter from primitive chondrites. Icarus, 223, 534–543.

Orthous-Daunay, F. R., Piani, L., Flandinet, L., Thissen, R., Wolters, C., Vuitton, V., ... & Tachibana, S. (2019). Ultraviolet-photon fingerprints on chondritic large organic molecules. *Geochemical Journal*, *53*(1), 21-32.

Ostrander, C. M., Nielsen, S. G., Owens, J. D., Kendall, B., Gordon, G. W., Romaniello, S. J., & Anbar, A. D. (2019). Fully oxygenated water columns over continental shelves before the Great Oxidation Event. *Nature geoscience*, *12*(3), 186.

Ott, U., Mack, R., & Sherwood, C. (1981). Noble-gas-rich separates from the Allende meteorite. *Geochimica et Cosmochimica Acta*, *45*(10), 1751-1788.

Ott, U. (2002). Noble gases in meteorites–trapped components. *Reviews in Mineralogy and Geochemistry*, *47*(1), 71-100.

Ott, U. (2014). Planetary and pre-solar noble gases in meteorites. *Geochemistry*, *74*(4), 519-544.

Owen, T., Bar-Nun, A., & Kleinfeld, I. (1992). Possible cometary origin of heavy noble gases in the atmospheres of Venus, Earth and Mars. *Nature*, *358*(6381), 43.

Ozima, M., & Podosek, F. A. (2002). *Noble gas geochemistry*. Cambridge University Press.

Ozima, M., Seki, K., Terada, N., Miura, Y. N., Podosek, F. A., & Shinagawa, H. (2005). Terrestrial nitrogen and noble gases in lunar soils. *Nature*, *436*(7051), 655.

Palme, H., & O'Neill, H. S. C. (2003). Cosmochemical estimates of mantle composition. *Treatise on geochemistry*, *2*, 568.

Parai, R., & Mukhopadhyay, S. (2015). The evolution of MORB and plume mantle volatile budgets: C onstraints from fission X e isotopes in Southwest Indian Ridge basalts. *Geochemistry, Geophysics, Geosystems*, *16*(3), 719-735.

Parai, R., & Mukhopadhyay, S. (2018). Xenon isotopic constraints on the history of volatile recycling into the mantle. *Nature*, *560*(7717), 223.

Parai, R., Mukhopadhyay, S., Tucker, J. M., & Pető, M. K. (2019). The emerging portrait of an ancient, heterogeneous and continuously evolving mantle plume source. *Lithos*, 105153.

Park, R.K., 1977. The preservation potential of some recent stromatolites. Sedimentology 24, 485-506.

Parnell-Turner, R., Sohn, R. A., Peirce, C., Reston, T. J., MacLeod, C. J., Searle, R. C., & Simão, N. M. (2017). Oceanic detachment faults generate compression in extension. *Geology*, *45*(10), 923-926.

Pasek, M., & Lauretta, D. (2008). Extraterrestrial flux of potentially prebiotic C, N, and P to the early Earth. Origins of Life and Evolution of Biospheres, 38(1), 5-21.

Patel, B. H., Percivalle, C., Ritson, D. J., Duffy, C. D., & Sutherland, J. D. (2015). Common origins of RNA, protein and lipid precursors in a cyanosulfidic protometabolism. Nature chemistry, 7(4), 301.

Pattou, L., Lorand, J. P., & Gros, M. (1996). Non-chondritic platinum-group element ratios in the Earth's mantle. Nature, 379(6567), 712.

Pearson, V. K., Sephton, M. A., Franchi, I. A., Gibson, J. M., & Gilmour, I. (2006). Carbon and nitrogen in carbonaceous chondrites: Elemental abundances and stable isotopic compositions. Meteoritics & Planetary Science, 41(12), 1899-1918.

Pepin, R. O. (1967). Trapped neon in meteorites. Earth and Planetary Science Letters, 2(1), 13-18.

Pepin, R. (1994). The hunt for U-Xenon. *Meteoritics*, *29*.

Pepin, R. O., Becker, R. H., & Rider, P. E. (1995). Xenon and krypton isotopes in extraterrestrial regolith soils and in the solar wind. *Geochimica et Cosmochimica Acta*, *59*(23), 4997-5022.

Pepin, R. O. (1998). Isotopic evidence for a solar argon component in the Earth's mantle. *Nature*, *394*(6694), 664.

Pepin, R. O. (2000). On the isotopic composition of primordial xenon in terrestrial planet atmospheres. In *From dust to terrestrial planets* (pp. 371-395). Springer, Dordrecht.

Pepin, R. O. (2003). On noble gas processing in the solar accretion disk. *Space science reviews*, *106*(1-4), 211-230.

Pepin, R. O., & Porcelli, D. (2006). Xenon isotope systematics, giant impacts, and mantle degassing on the early Earth. *Earth and Planetary Science Letters*, *250*(3-4), 470-485.

Pepin, R. O., Schlutter, D. J., Becker, R. H., & Reisenfeld, D. B. (2012). Helium, neon, and argon composition of the solar wind as recorded in gold and other Genesis collector materials. *Geochimica et Cosmochimica Acta*, *89*, 62-80.

Pernet-Fisher, J. F., & Joy, K. H. (2018, March). Noble-Gas Isotope Systematics of Lunar Anorthosites: Hunting for Indigenous Signatures. In *Lunar and Planetary Science Conference* (Vol. 49).

Péron, S., Moreira, M., Colin, A., Arbaret, L., Putlitz, B., & Kurz, M. D. (2016). Neon isotopic composition of the mantle constrained by single vesicle analyses. *Earth and Planetary Science Letters*, *449*, 145-154.

Péron, S., Moreira, M., Putlitz, B., & Kurz, M. D. (2017). Solar wind implantation supplied light volatiles during the first stage of Earth accretion. *Geochem. Perspect. Lett.*, *3*, 151-159.

Péron, S., & Moreira, M. (2018). Onset of volatile recycling into the mantle determined by xenon anomalies. *Geochemical Perspective Letters*, *9*, 21.

Pettersson, M, et al. 2000. Photochemistry of HNCO in solid xenon: Photoinduced and thermally activated formation of HXeNCO. J. Phys. Chem. A 104: 3579-3583.

Piani, L., Robert, F., Beyssac, O., Binet, L., Bourot-Denise, M., Derenne, S., ... & Thomen, A. (2012). Structure, composition, and location of organic matter in the enstatite chondrite Sahara 97096 (EH3). *Meteoritics & Planetary Science*, *47*(1), 8-29.

Piani, L., Robert, F., & Remusat, L. (2015). Micron-scale D/H heterogeneity in chondrite matrices: A signature of the pristine solar system water?. *Earth and Planetary Science Letters*, *415*, 154-164.

Pignatale, F. C., Charnoz, S., Chaussidon, M., & Jacquet, E. (2018). Making the Planetary Material Diversity during the Early Assembling of the Solar System. *The Astrophysical Journal Letters*, *867*(2), L23.

Pinte, C., Price, D. J., Ménard, F., Duchêne, G., Dent, W. R. F., Hill, T., ... & Mentiplay, D. (2018). Kinematic Evidence for an Embedded Protoplanet in a Circumstellar Disk. *The Astrophysical Journal Letters*, *860*(1), L13.

Pizzarello, S., & Cronin, J. R. (2000). Non-racemic amino acids in the Murray and Murchison meteorites. *Geochimica et Cosmochimica Acta*, *64*(2), 329-338.

Pizzarello, S., Cooper, G. W., & Flynn, G. J. (2006). The nature and distribution of the organic material in carbonaceous chondrites and interplanetary dust particles. *Meteorites and the early solar system II*, *1*, 625-651.

Pizzarello, S. (2006). The chemistry of life's origin: a carbonaceous meteorite perspective. *Accounts of Chemical Research*, *39*(4), 231-237.

Pizzarello, S., & Shock, E. (2010). The organic composition of carbonaceous meteorites: the evolutionary story ahead of biochemistry. *Cold Spring Harbor perspectives in biology*, *2*(3), a002105.

Podosek, F. A., Bernatowicz, T. J., Honda, M. & Kramer, F. E. (1982) The sedimentary inventory of atmospheric xenon, in Planetary Volatiles, vol. 488, p. 80. AQ29

Podosek, F. A., & Ozima, M. (2000). The xenon age of the Earth. *Origin of the Earth and Moon*, *1*, 63-72.

Poole, G. M., Rehkämper, M., Coles, B. J., Goldberg, T., & Smith, C. L. (2017). Nucleosynthetic molybdenum isotope anomalies in iron meteorites–new evidence for thermal processing of solar nebula material. *Earth and Planetary Science Letters*, *473*, 215-226.

Porcelli, D., & Ballentine, C. J. (2002). Models for distribution of terrestrial noble gases and evolution of the atmosphere. *Reviews in Mineralogy and Geochemistry*, *47*(1), 411-480.

Protin, M., Blard, P. H., Marrocchi, Y., & Mathon, F. (2016). Irreversible adsorption of atmospheric helium on olivine: A lobster pot analogy. *Geochimica et Cosmochimica Acta*, *179*, 76-88.

Pujol, M., Marty, B., & Burgess, R. (2011). Chondritic-like xenon trapped in Archean rocks: a possible signature of the ancient atmosphere. *Earth and Planetary Science Letters*, *308*(3-4), 298-306.

Quirico, E., Montagnac, G., Rouzaud, J. N., Bonal, L., Bourot-Denise, M., Duber, S., & Reynard, B. (2009). Precursor and metamorphic condition effects on Raman spectra of poorly ordered carbonaceous matter in chondrites and coals. *Earth and Planetary Science Letters*, *287*(1-2), 185-193.

Rai, V. K., Murty, S. V. S., & Ott, U. (2003). Noble gases in ureilites: cosmogenic, radiogenic, and trapped components. *Geochimica et Cosmochimica Acta*, *67*(22), 4435-4456.

Rapp, R. P., Irifune, T., Shimizu, N., Nishiyama, N., Norman, M. D., & Inoue, T. (2008). Subduction recycling of continental sediments and the origin of geochemically enriched reservoirs in the deep mantle. *Earth and Planetary Science Letters*, *271*(1-4), 14-23.

Raquin, A., & Moreira, M. (2009). Atmospheric 38Ar/36Ar in the mantle: implications for the nature of the terrestrial parent bodies. *Earth and Planetary Science Letters*, *287*(3-4), 551-558.

Raymond, S. N., & Morbidelli, A. (2014). The Grand Tack model: a critical review. *Proceedings of the International Astronomical Union*, *9*(S310), 194-203.

Raymond, S. N., & Izidoro, A. (2017). Origin of water in the inner Solar System: Planetesimals scattered inward during Jupiter and Saturn's rapid gas accretion. *Icarus*, *297*, 134-148.

Raymond, S. N., Izidoro, A., & Morbidelli, A. (2018). Solar System Formation in the Context of Extra-Solar Planets. *arXiv preprint arXiv:1812.01033*.

Regelous, M., Elliott, T., & Coath, C. D. (2008). Nickel isotope heterogeneity in the early Solar System. *Earth and Planetary Science Letters*, *272*(1-2), 330-338.

Reimold, W. U., & Koeberl, C. (2014). Impact structures in Africa: A review. *Journal of African Earth Sciences*, *93*, 57-175.

Remusat, L., Derenne, S., Robert, F., & Knicker, H. (2005). New pyrolytic and spectroscopic data on Orgueil and Murchison insoluble organic matter: A different origin than soluble?. *Geochimica et Cosmochimica Acta*, *69*(15), 3919-3932.

Remusat, L. (2015). Organics in primitive meteorites. *EMU Notes in Mineralogy*, *15*, 1-33.

Render, J., Fischer-Gödde, M., Burkhardt, C., & Kleine, T. (2017). The cosmic molybdenum-neodymium isotope correlation and the building material of the Earth. *Geochem Perspect Lett*, *3*, 170-178.

Reynolds, J. H., & Turner, G. (1964). Rare gases in the chondrite Renazzo. *Journal of Geophysical Research*, *69*(15), 3263-3281.

Ribas, I., Guinan, E. F., Güdel, M., & Audard, M. (2005). Evolution of the solar activity over time and effects on planetary atmospheres. I. High-energy irradiances (1-1700 Å). *The Astrophysical Journal*, *622*(1), 680.

Robert, F., Derenne, S., Lombardi, G., Hassouni, K., Michau, A., Reinhardt, P., ... & Biron, K. (2017). Hydrogen isotope fractionation in methane plasma. *Proceedings of the National Academy of Sciences*, *114*(5), 870-874.

Robinson, K. L., & Taylor, G. J. (2014). Heterogeneous distribution of water in the Moon. *Nature Geoscience*, *7*(6), 401-408.

Robinson, K. L., Barnes, J. J., Nagashima, K., Thomen, A., Franchi, I. A., Huss, G. R., ... & Taylor, G. J. (2016). Water in evolved lunar rocks: Evidence for multiple reservoirs. *Geochimica et Cosmochimica Acta*, *188*, 244-260.

Ros, K., & Johansen, A. (2013). Ice condensation as a planet formation mechanism. *Astronomy & Astrophysics*, *552*, A137.

Rosing, M. T. (1999). 13C-depleted carbon microparticles in> 3700-Ma sea-floor sedimentary rocks from West Greenland. *Science*, *283*(5402), 674-676.

Rosenfeld, K. A., Andrews, S. M., Hughes, A. M., Wilner, D. J., & Qi, C. (2013). A spatially resolved vertical temperature gradient in the HD 163296 disk. *The Astrophysical Journal*, *774*(1), 16.

Rubie, D. C., Frost, D. J., Mann, U., Asahara, Y., Nimmo, F., Tsuno, K., ... & Palme, H. (2011). Heterogeneous accretion, composition and core–mantle differentiation of the Earth. *Earth and Planetary Science Letters*, *301*(1-2), 31-42.

Rubie, D. C., Jacobson, S. A., Morbidelli, A., O'Brien, D. P., Young, E. D., de Vries, J., ... & Frost, D. J. (2015). Accretion and differentiation of the terrestrial planets with implications for the compositions of early-formed Solar System bodies and accretion of water. *Icarus*, *248*, 89-108.

Rubin, A. E., & Choi, B. G. (2009). Origin of halogens and nitrogen in enstatite chondrites. *Earth, Moon, and Planets*, *105*(1), 41-53.

Rubin, M., Altwegg, K., Balsiger, H., Bar-Nun, A., Berthelier, J. J., Bieler, A., ... & De Keyser, J. (2015). Molecular nitrogen in comet 67P/Churyumov-Gerasimenko indicates a low formation temperature. *Science*, *348*(6231), 232-235.

Rubin, M., Altwegg, K., Balsiger, H., Berthelier, J. J., Bieler, A., Calmonte, U., ... & Fuselier, S. A. (2017). Evidence for depletion of heavy silicon isotopes at comet 67P/Churyumov-Gerasimenko. *Astronomy & Astrophysics*, *601*, A123.

Rubin, M., Altwegg, K., Balsiger, H., Bar-Nun, A., Berthelier, J. J., Briois, C., ... & Fuselier, S. A. (2018). Krypton isotopes and noble gas abundances in the coma of comet 67P/Churyumov-Gerasimenko. *Science advances*, *4*(7), eaar6297.

Rubin, M., Bekaert, D. V., Broadley, M. W., Drozdovskaya, M. N., & Wampfler, S. F. (2019). Volatile Species in Comet 67P/Churyumov-Gerasimenko: Investigating the Link from the ISM to the Terrestrial Planets. *ACS earth and space chemistry*, *3*(9), 1792-1811.

Saal, A. E., Hauri, E. H., Cascio, M. L., Van Orman, J. A., Rutherford, M. C., & Cooper, R. F. (2008). Volatile content of lunar volcanic glasses and the presence of water in the Moon's interior. *Nature*, *454*(7201), 192.

Saal, A. E., Hauri, E. H., Van Orman, J. A., & Rutherford, M. J. (2013). Hydrogen isotopes in lunar volcanic glasses and melt inclusions reveal a carbonaceous chondrite heritage. *Science*, *340*(6138), 1317-1320.

Sakamoto, N., Seto, Y., Itoh, S., Kuramoto, K., Fujino, K., Nagashima, K., ... & Yurimoto, H. (2007). Remnants of the early solar system water enriched in heavy oxygen isotopes. *Science*, *317*(5835), 231-233.

Salinas, V. N., Hogerheijde, M. R., Bergin, E. A., Cleeves, L. I., Brinch, C., Blake, G. A., ... & Kristensen, L. (2016). First detection of gas-phase ammonia in a planet-forming disk-NH3, N2H+, and H2O in the disk around TW Hydrae. *Astronomy & Astrophysics*, *591*, A122.

Sandford, S. A., Aléon, J., Alexander, C. M. D., Araki, T., Bajt, S., Baratta, G. A., ... & Burchell, M. J. (2006). Organics captured from comet 81P/Wild 2 by the Stardust spacecraft. *Science*, *314*(5806), 1720-1724.

Sanloup, C., Schmidt, B. C., Perez, E. M. C., Jambon, A., Gregoryanz, E., & Mezouar, M. (2005). Retention of xenon in quartz and Earth's missing xenon. *Science*, *310*(5751), 1174-1177.

Sano, Y., Wakita, H., & Sheng, X. (1988). Atmospheric helium isotope ratio. *Geochemical Journal*, *22*(4), 177-181.

Sano, T., Miyama, S. M., Umebayashi, T., & Nakano, T. (2000). Magnetorotational instability in protoplanetary disks. II. Ionization state and unstable regions. *The Astrophysical Journal*, *543*(1), 486.

Schiller, M., Bizzarro, M., & Fernandes, V. A. (2018). Isotopic evolution of the protoplanetary disk and the building blocks of Earth and the Moon. *Nature*, *555*(7697), 507.

Schlichting, H. E., & Mukhopadhyay, S. (2018). Atmosphere impact losses. *Space Science Reviews*, *214*(1), 34.

Schmitt-Kopplin, P., Gabelica, Z., Gougeon, R. D., Fekete, A., Kanawati, B., Harir, M., ... & Hertkorn, N. (2010). High molecular diversity of extraterrestrial organic matter in Murchison meteorite revealed 40 years after its fall. *Proceedings of the National Academy of Sciences*, *107*(7), 2763-2768.

Schönbächler, M., Carlson, R. W., Horan, M. F., Mock, T. D., & Hauri, E. H. (2010). Heterogeneous accretion and the moderately volatile element budget of Earth. *Science*, *328*(5980), 884-887.

Schopf, J. W. (2006). The first billion years: When did life emerge?. *Elements*, *2*(4), 229-233.

Schopf, J. W., Kudryavtsev, A. B., Czaja, A. D., & Tripathi, A. B. (2007). Evidence of Archean life: stromatolites and microfossils. *Precambrian Research*, *158*(3-4), 141-155.

Schouren, F. (2001). Experimentelle und theoretische Untersuchungen an Edelgas-Sauerstoff-Verbindungen. (Doctoral dissertation).

Schwarz, K. R., Bergin, E. A., Cleeves, L. I., Zhang, K., Öberg, K. I., Blake, G. A., & Anderson, D. (2018). Unlocking CO depletion in protoplanetary disks. I. The warm molecular layer. *The Astrophysical Journal*, *856*(1), 85.

Scott, E. R. D., Barber, D. J., Alexander, C. M., Hutchinson, R., & Peck, J. A. (1988). Primitive material surviving in chondrites-Matrix. *Meteorites and the early solar system*, 718-745.

Sephton, M. A., Pillinger, C. T., & Gilmour, I. (1998). Small-scale hydrous pyrolysis of macromolecular material in meteorites. *Planetary and Space Science*, *47*(1-2), 181-187.

Shirey, S. B., & Richardson, S. H. (2011). Start of the Wilson cycle at 3 Ga shown by diamonds from subcontinental mantle. *Science*, *333*(6041), 434-436.

Shu, F. H., Shang, H., Gounelle, M., Glassgold, A. E., & Lee, T. (2001). The origin of chondrules and refractory inclusions in chondritic meteorites. *The Astrophysical Journal*, *548*(2), 1029.

Siebert, J., Badro, J., Antonangeli, D., & Ryerson, F. J. (2013). Terrestrial accretion under oxidizing conditions. *Science*, *339*(6124), 1194-1197.

Simon, J. B., Armitage, P. J., Li, R., & Youdin, A. N. (2016). The mass and size distribution of planetesimals formed by the streaming instability. I. The role of self-gravity. *The Astrophysical Journal*, *822*(1), 55.

Sleep, N. H., Zahnle, K. J., Kasting, J. F., & Morowitz, H. J. (1989). Annihilation of ecosystems by large asteroid impacts on the early Earth. *Nature*, *342*(6246), 139.

Sleep, N. H. (2017). Asteroid bombardment and the core of Theia as possible sources for the Earth's late veneer component. *Geochemistry, Geophysics, Geosystems*, *17*(7), 2623-2642.

Smit, M. A., & Mezger, K. (2017). Earth's early O 2 cycle suppressed by primitive continents. *Nature geoscience*, *10*(10), 788.

Snow, J. E., & Schmidt, G. (1998). Constraints on Earth accretion deduced from noble metals in the oceanic mantle. *Nature*, *391*(6663), 166.

Socrates, Infrared and Raman characteristics group frequencies – tables and charts, (3rd edn, 2001). Chichester, Wiley.

Staudacher, T., & Allègre, C. J. (1982). Terrestrial xenology. *Earth and Planetary Science Letters*, *60*(3), 389-406.

Stavrou, E., Yao, Y., Goncharov, A. F., Lobanov, S. S., Zaug, J. M., Liu, H., ... & Prakapenka, V. B. (2018). Synthesis of xenon and iron-nickel intermetallic compounds at Earth's core thermodynamic conditions. *Physical review letters*, *120*(9), 096001.

Stracke, A., Hofmann, A. W., & Hart, S. R. (2005). FOZO, HIMU, and the rest of the mantle zoo. *Geochemistry, Geophysics, Geosystems*, *6*(5).

Stuart, F. M., Lass-Evans, S., Fitton, J. G., & Ellam, R. M. (2003). High 3 He/4 He ratios in picritic basalts from Baffin Island and the role of a mixed reservoir in mantle plumes. *Nature*, *424*(6944), 57.

Sutherland JD (2016) The origin of life— out of the blue. Angewandte Chemie, International Edition 55: 104-121

Takeuchi, T., & Lin, D. N. C. (2002). Radial flow of dust particles in accretion disks. *The Astrophysical Journal*, *581*(2), 1344.

Tang, M., Chen, K., & Rudnick, R. L. (2016). Archean upper crust transition from mafic to felsic marks the onset of plate tectonics. *Science*, *351*(6271), 372-375.

Tartèse R, Anand M. (2013). Late delivery of chondritic hydrogen into the lunar mantle: insights from mare basalts. Earth Planet. Sci. Lett. 361:480–86

Tartèse R, Anand M, Barnes JJ, Starkey NA, Franchi IA, Sano Y. (2013). The abundance, distribution, and isotopic composition of hydrogen in the Moon as revealed by basaltic lunar samples: implications for the volatile inventory of the Moon. Geochim. Cosmochim. Acta 122:58–74

Tartèse R, Anand M, Joy KH, Franchi IA. (2014a). H and Cl isotope systematics of apatite in brecciated lunar meteorites Northwest Africa 4472, Northwest Africa 773, Sayh al Uhaymir 169, and Kalahari 009. Meteorit. Planet. Sci. 49:2266–89

Tartèse R, Anand M, McCubbin FM, Elardo SM, Shearer CK, Franchi IA. (2014b). Apatites in lunar KREEP basalts: the missing link to understanding the H isotope systematics of the Moon. Geology 42:363–66

Tartèse, R., Chaussidon, M., Gurenko, A., Delarue, F., & Robert, F. (2018). Insights into the origin of carbonaceous chondrite organics from their triple oxygen isotope composition. *Proceedings of the National Academy of Sciences*, *115*(34), 8535-8540

Taylor, M. G. G. T., Altobelli, N., Buratti, B. J., & Choukroun, M. (2017). The Rosetta mission orbiter science overview: the comet phase. *Philosophical Transactions of the Royal Society A: Mathematical, Physical and Engineering Sciences*, *375*(2097), 20160262.

Tera, F., Papanastassiou, D. A., & Wasserburg, G. J. (1974). Isotopic evidence for a terminal lunar cataclysm. *Earth and Planetary Science Letters*, *22*(1), 1-21.

Testi, L., Natta, A., Shepherd, D. S., & Wilner, D. J. (2003). Large grains in the disk of CQ Tau. *Astronomy & Astrophysics*, *403*(1), 323-328.

Testi, L., Birnstiel, T., Ricci, L., Andrews, S., Blum, J., Carpenter, J., ... & Wilner, D. J. (2014). Dust evolution in protoplanetary disks. *Protostars and Planets VI*, *914*, 339-61.

Thiemens, M. H., & Heidenreich, J. E. (1983). The mass-independent fractionation of oxygen: A novel isotope effect and its possible cosmochemical implications. *Science*, *219*(4588), 1073-1075.

Tielens, A. G. (2008). Interstellar polycyclic aromatic hydrocarbon molecules. *Annu. Rev. Astron. Astrophys.*, *46*, 289-337.

Tigrine, S., Carrasco, N., Vettier, L., Chitarra, O., & Cernogora, G. (2016). The APSIS experiment: Simulating the VUV Photochemistry of the Upper Atmosphere of Titan.

Tissandier, L., Libourel, G., & Robert, F. (2002). Gas-melt interactions and their bearing on chondrule formation. *Meteoritics & Planetary Science*, *37*(10), 1377-1389.

Touboul M, Puchtel IS, Walker RJ. 2012. 182W evidence for long-term preservation of early mantle differentiation products. Science 335:1065–69.

Trieloff, M., Kunz, J., & Allègre, C. J. (2002). Noble gas systematics of the Réunion mantle plume source and the origin of primordial noble gases in Earth's mantle. *Earth and Planetary Science Letters*, *200*(3-4), 297-313.

Trinquier, A., Elliott, T., Ulfbeck, D., Coath, C., Krot, A. N., & Bizzarro, M. (2009). Origin of nucleosynthetic isotope heterogeneity in the solar protoplanetary disk. *Science*, *324*(5925), 374-376.

Tucker, J. M., & Mukhopadhyay, S. (2014). Evidence for multiple magma ocean outgassing and atmospheric loss episodes from mantle noble gases. *Earth and Planetary Science Letters*, *393*, 254-265.

Turner, G. (1979). A Monte Carlo fragmentation model for the production of meteorites-Implications for gas retention ages. In *Lunar and Planetary Science Conference Proceedings* (Vol. 10, pp. 1917-1941).

Turner, G., Harrison, T. M., Holland, G., Mojzsis, S. J., & Gilmour, J. (2004). Extinct 244Pu in ancient zircons. *Science*, *306*(5693), 89-91.

Turner, G., Busfield, A., Crowther, S. A., Harrison, M., Mojzsis, S. J., & Gilmour, J. (2007). Pu–Xe, U–Xe, U–Pb chronology and isotope systematics of ancient zircons from Western Australia. *Earth and Planetary Science Letters*, *261*(3-4), 491-499.

Vacher, L. G., Marrocchi, Y., Verdier-Paoletti, M. J., Villeneuve, J., & Gounelle, M. (2016). Inward radial mixing of interstellar water ices in the solar protoplanetary disk. *The Astrophysical journal letters*, *827*(1), L1.

Vacher, L. G., Truche, L., Faure, F., Tissandier, L., Mosser-Ruck, R., & Marrocchi, Y. (2019). Deciphering the conditions of tochilinite and cronstedtite formation in CM chondrites from low temperature hydrothermal experiments. *Meteoritics & Planetary Science*.

Valdes, M. C., Moreira, M., Foriel, J., & Moynier, F. (2014). The nature of Earth's building blocks as revealed by calcium isotopes. *Earth and Planetary Science Letters*, *394*, 135-145.

Van der Hilst, R. D., Widiyantoro, S., & Engdahl, E. R. (1997). Evidence for deep mantle circulation from global tomography. *Nature*, *386*(6625), 578.

van Dishoeck, E. F., Jonkheid, B., & van Hemert, M. C. (2006). Photoprocesses in protoplanetary disks. *Faraday Discussions*, *133*, 231-243.

Van Kooten, E. M., Wielandt, D., Schiller, M., Nagashima, K., Thomen, A., Larsen, K. K., ... & Bizzarro, M. (2016). Isotopic evidence for primordial molecular cloud material in metal-rich carbonaceous chondrites. *Proceedings of the National Academy of Sciences*, *113*(8), 2011-2016.

Van Kooten, E. M., Moynier, F., & Agranier, A. (2019). A unifying model for the accretion of chondrules and matrix. *Proceedings of the National Academy of Sciences*, *116*(38), 18860-18866.

Van Zuilen, M. A., Lepland, A., & Arrhenius, G. (2002). Reassessing the evidence for the earliest traces of life. *Nature*, *418*(6898), 627.

Varas-Reus, M. I., König, S., Yierpan, A., Lorand, J. P., & Schoenberg, R. (2019). Selenium isotopes as tracers of a late volatile contribution to Earth from the outer Solar System. *Nature geoscience*, *12*(9), 779-782.

Vermeesch, P. (2015). Revised error propagation of 40 Ar/39 Ar data, including covariances. *Geochimica et Cosmochimica Acta*, **171**, 325-337.

Villeneuve, J., Chaussidon, M., & Libourel, G. (2009). Homogeneous distribution of 26Al in the solar system from the Mg isotopic composition of chondrules. *Science*, *325*(5943), 985-988.

Vinković, D. (2009). Radiation-pressure mixing of large dust grains in protoplanetary disks. *Nature*, *459*(7244), 227.

Vinogradoff, V., Bernard, S., Le Guillou, C., & Remusat, L. (2018). Evolution of interstellar organic compounds under asteroidal hydrothermal conditions. *Icarus*, *305*, 358-370.

Vogt, M., Hopp, J., Gail, H. P., Ott, U., & Trieloff, M. (2019). Acquisition of terrestrial neon during accretion–A mixture of solar wind and planetary components. *Geochimica et Cosmochimica Acta*, *264*, 141-164.

Wacey, D. (2010). Stromatolites in the~ 3400 Ma Strelley Pool Formation, Western Australia: examining biogenicity from the macro-to the nano-scale. *Astrobiology*, *10*(4), 381-395.

Wächtershäuser, G. (1990). The case for the chemoautotrophic origin of life in an iron-sulfur world. *Origins of Life and Evolution of the Biosphere*, *20*(2), 173-176.

Wacker, J. F. (1989). Laboratory simulation of meteoritic noble gases. III. Sorption of neon, argon, krypton, and xenon on carbon: Elemental fractionation. *Geochimica et Cosmochimica Acta*, *53*(6), 1421-1433.

98.Wade, J., & Wood, B. J. (2005). Core formation and the oxidation state of the Earth. *Earth and Planetary Science Letters*, *236*(1-2), 78-95.

Wade, J., Wood, B. J., & Tuff, J. (2012). Metal–silicate partitioning of Mo and W at high pressures and temperatures: evidence for late accretion of sulphur to the Earth. *Geochimica et Cosmochimica Acta*, *85*, 58-74.

Wade, J., & Wood, B. J. (2016). The oxidation state and mass of the Moon-forming impactor. *Earth and Planetary Science Letters*, *442*, 186-193.

Walsh, C., Nomura, H., Millar, T. J., & Aikawa, Y. (2012). Chemical processes in protoplanetary disks. II. On the importance of photochemistry and X-ray ionization. *The Astrophysical Journal*, *747*(2), 114.

Walter, M. R., Buick, R., & Dunlop, J. S. R. (1980). Stromatolites 3,400–3,500 Myr old from the North pole area, Western Australia. *Nature*, *284*(5755), 443.

Wänke, H. (1981). Constitution of terrestrial planets. *Philosophical Transactions of the Royal Society of London. Series A, Mathematical and Physical Sciences*, *303*(1477), 287-302.

Wang, Z., & Becker, H. (2013). Ratios of S, Se and Te in the silicate Earth require a volatile-rich late veneer. *Nature*, *499*(7458), 328.

Warren, P. H. (2011). Stable-isotopic anomalies and the accretionary assemblage of the Earth and Mars: A subordinate role for carbonaceous chondrites. *Earth and Planetary Science Letters*, *311*(1-2), 93-100.

Weber H. W., Hintenberger H., and Begemann F. (1971) Noble gases in the Haveröureilite. Earth and Planetary Science Letters 13, 205-209.

Weiss, R.F.,1970. The solubility of nitrogen, oxygen and argon in water and seawater. Deep Sea Res. Oceanogr.Abstr. 17, 721-735.

Weiss, Y., Class, C., Goldstein, S. L., & Hanyu, T. (2016). Key new pieces of the HIMU puzzle from olivines and diamond inclusions. *Nature*, *537*(7622), 666.

Wetherill, G. W. (1975). Radiometric chronology of the early solar system. *Annual Review of Nuclear Science*, *25*(1), 283-328.

Wetherill, G. W. (1992). An alternative model for the formation of the asteroids. *Icarus*, *100*(2), 307-325.

Werner, S.C., Ivanov, B.A., 2007 . Exogenic dynamics , cratering and surface ages. In : Treatise on Geophysics, vol.10, 2nd edition, pp.207–242.

Wesslau, V. H. (1956). Die molekulargewichtsverteilung einiger niederdruckpolyäthylene. *Die Makromolekulare Chemie: Macromolecular Chemistry and Physics*, *20*(1), 111-142.

White, W. M., & Duncan, R. A. (1996). Geochemistry and geochronology of the Society Islands: new evidence for deep mantle recycling. *Geophysical Monograph-American Geophysical Union*, *95*, 183-206.

Wielandt, D., & Storey, M. (2019). A new high precision determination of the atmospheric 21 Ne abundance. *Journal of Analytical Atomic Spectrometry*, *34*(3), 535-549.

Wieler, R., Anders, E., Baur, H., Lewis, R. S., & Signer, P. (1992). Characterisation of Q-gases and other noble gas components in the Murchison meteorite. *Geochimica et Cosmochimica Acta*, *56*(7), 2907-2921.

Wieler, R. (1994). Q-gases" as "local" primordial noble gas component in primitive meteorites. *Terra Scientific Publishing, Tokyo*, 31-41.

Wilde, S. A., Valley, J. W., Peck, W. H., & Graham, C. M. (2001). Evidence from detrital zircons for the existence of continental crust and oceans on the Earth 4.4 Gyr ago. *Nature*, *409*(6817), 175.

Willbold M, Elliott T, Moorbath S. 2011. The tungsten isotopic composition of the Earth's mantle before the terminal bombardment. Nature 477:195–98.

Williams, C. D., & Mukhopadhyay, S. (2019). Capture of nebular gases during Earth's accretion is preserved in deep-mantle neon. *Nature*, *565*(7737), 78.

Williams, J. P., & Cieza, L. A. (2011). Protoplanetary disks and their evolution. *Annual Review of Astronomy and Astrophysics*, *49*, 67-117.

Wilner, D. J., D'Alessio, P., Calvet, N., Claussen, M. J., & Hartmann, L. (2005). Toward planetesimals in the disk around TW Hydrae: 3.5 centimeter dust emission. *The Astrophysical Journal Letters*, *626*(2), L109.

Worsham, E. A., Bermingham, K. R., & Walker, R. J. (2017). Characterizing cosmochemical materials with genetic affinities to the Earth: genetic and chronological diversity within the IAB iron meteorite complex. *Earth and planetary science letters*, *467*, 157-166.

Worsham, E. A., Burkhardt, C., Budde, G., Fischer-Gödde, M., Kruijer, T. S., & Kleine, T. (2019). Distinct evolution of the carbonaceous and non-carbonaceous reservoirs: Insights from Ru, Mo, and W isotopes. *Earth and Planetary Science Letters*, *521*, 103-112.

Wurz, P., Rubin, M., Altwegg, K., Balsiger, H., Berthelier, J. J., Bieler, A., ... & Galli, A. (2015). Solar wind sputtering of dust on the surface of 67P/Churyumov-Gerasimenko. *Astronomy & Astrophysics*, *583*, A22.

Yabuta, H., Naraoka, H., Sakanishi, K. and Kawashima, H. (2005) Solid-state 13C NMR characterization of insoluble organic matter from Antarctic CM2 chondrites: Evaluation of the meteoritic alteration level. Meteoritics & Planetary Science, 40, 779–787.

Yang, L., & Ciesla, F. J. (2012). The effects of disk building on the distributions of refractory materials in the solar nebula. *Meteoritics & Planetary Science*, *47*(1), 99-119.

Yokochi, R., & Marty, B. (2004). A determination of the neon isotopic composition of the deep mantle. *Earth and Planetary Science Letters*, *225*(1-2), 77-88.

Yokochi, R., Marboeuf, U., Quirico, E., & Schmitt, B. (2012). Pressure dependent trace gas trapping in amorphous water ice at 77 K: Implications for determining conditions of comet formation. *Icarus*, *218*(2), 760-770.

Young, E. D., Galy, A., & Nagahara, H. (2002). Kinetic and equilibrium mass-dependent isotope fractionation laws in nature and their geochemical and cosmochemical significance. *Geochimica et Cosmochimica Acta*, *66*(6), 1095-1104.

Yurimoto, H., & Kuramoto, K. (2004). Molecular cloud origin for the oxygen isotope heterogeneity in the solar system. *Science*, *305*(5691), 1763-1766.

Zahnle, K. J. (2006). Earth's earliest atmosphere. *Elements*, *2*(4), 217-222.

Zahnle, K. J., Catling, D. C., & Claire, M. W. (2013). The rise of oxygen and the hydrogen hourglass. *Chemical Geology*, *362*, 26-34.

Zahnle K. J. (2015) Xenon fractionation and Archean hydrogen escape. In 46th Lunar and Planetary Science Conference. The Woodlands (Texas). pp. 1–2.

Zahnle, K. J., Gacesa, M., & Catling, D. C. (2019). Strange messenger: A new history of hydrogen on Earth, as told by Xenon. *Geochimica et Cosmochimica Acta*, *244*, 56-85.

Zaia, D. A. M. (2004). A review of adsorption of amino acids on minerals: was it important for origin of life?. *Amino acids*, *27*(1), 113-118.

Zaleski-Ejgierd, P., & Lata, P. M. (2016). Krypton oxides under pressure. *Scientific reports*, *6*, 18938.

Zanda, B., Humayun, M., Lewin, E., Pont, S., & Hewins, R. H. (2018). Mo-W Isotopic Evidence Against Chondrule-Matrix Complementarity. *LPI Contributions*, *2067*.

Zega, T. J., Alexander, C. M. D., Busemann, H., Nittler, L. R., Hoppe, P., Stroud, R. M., & Young, A. F. (2010). Mineral associations and character of isotopically anomalous organic material in the Tagish Lake carbonaceous chondrite. *Geochimica et Cosmochimica Acta*, *74*(20), 5966-5983.

Zellner, N. E. (2017). Cataclysm no more: new views on the timing and delivery of lunar impactors. *Origins of Life and Evolution of Biospheres*, *47*(3), 261-280.

Zhang, X., Honda, M., & Hamilton, D. (2016). Performance of the high resolution, multi-collector helix mc plus noble gas mass spectrometer at the Australian National University. *Journal of The American Society for Mass Spectrometry*, *27*(12), 1937-1943.

Zhang, K., Bergin, E. A., Schwarz, K., Krijt, S., & Ciesla, F. (2019). Systematic Variations of CO Gas Abundance with Radius in Gas-rich Protoplanetary Disks. *The Astrophysical Journal*, *883*(1),

Zhu, L., Liu, H., Pickard, C. J., Zou, G., & Ma, Y. (2014). Reactions of xenon with iron and nickel are predicted in the Earth's inner core. *Nature chemistry*, *6*(7), 644.

Zhu, M. H., Artemieva, N., Morbidelli, A., Yin, Q. Z., Becker, H., & Wünnemann, K. (2019). Reconstructing the late-accretion history of the Moon. *Nature*, *571*(7764), 226-229.

Zimmermann, L., & Marty, B. (2014). Méthodes d'extraction des gaz rares sous ultravide. *Techniques de l'ingénieur, j6632*.

Zimmermann, L., Füri, E., and Burnard, P. (2015). Purification des gaz rares sous ultravide - Méthodes de purification. Techniques de l'ingénieur , (J6635):1–23.

Résumé en français

La Terre s'est formée il y a 4,5 milliards d'années par accumulation de poussières, de roches et de gaz. La composition de ces matériaux primitifs est aujourd'hui enregistrée dans les météorites. Cependant, l'origine des éléments volatils présents dans l'atmosphère (e.g., H, C, N, O) reste incomprise. En combinant des approches expérimentales à l'étude d'échantillons naturels, je me suis intéressé aux objets célestes contenant les ingrédients nécessaires à la formation de l'atmosphère terrestre. Il s'agit principalement des éléments volatils contenus dans la matière organique des météorites et dans la glace des corps cométaires. Afin de reconstituer l'histoire de formation de la Terre et de son atmosphère, j'ai utilisé les gaz nobles (He, Ne, Ar, Kr, Xe) comme traceurs des processus physiques ayant eu lieu dans le Système Solaire jeune et sur la Terre primitive. Bien que les comètes aient significativement contribué à l'apport des gaz nobles lourds de l'atmosphère (~20%), la majorité des autres éléments volatils terrestres (incluant l'eau, le carbone et l'azote) aurait été apportée par des corps dits "chondritiques", similaires aux météorites. Une fois formée, l'atmosphère a évolué au cours des temps géologiques, conduisant à l'établissement des conditions environnementales propices au développement de la vie. Les processus majeurs ayant affecté la masse et la composition de l'atmosphère ancienne se reflètent dans l'évolution isotopique du Xe atmosphérique, de 4.5 Ga à ~2 Ga. Nous étudions la possibilité d'apporter des contraintes sur l'âge des matériaux organiques retrouvés dans les roches sédimentaires plus anciennes que 2 Ga, en utilisant la signature isotopique du Xe qu'ils ont piégé au moment de leur formation. Cette méthode pourrait avoir des implications vis-à-vis de l'âge présumé des plus anciennes traces de vie organique.

English abstract

The Earth formed some 4.5 Ga from the accumulation of dust, rocks and gas. The composition of these primitive materials is today recorded in meteorites. However, the origin of volatile elements within the atmosphere (e.g., H, C, N, O) remains poorly understood. By combining experimental approaches and the analysis of natural samples, I studied the composition of celestial objects comprising the ingredients required for the formation of the terrestrial atmosphere. These mainly correspond to volatile elements trapped in meteoritic organic materials and in the ice of cometary bodies. In order to better understand the timeline of Earth's formation and volatile accretion, I used noble gases (He, Ne, Ar, Kr, Xe) as tracers of the physical processes that occurred in the early Solar System and on primitive Earth. Whilst comets significantly contributed to the heavy noble gas budget of the terrestrial atmosphere (~20%), most of the other terrestrial volatile elements (including water, carbon and nitrogen) would have been supplied to Earth by chondrtitic bodies similar to meteorites. Once formed, the atmosphere evolved over geological periods of time, leading to the establishment of suitable environmental conditions for life to develop. The major processes that affected the mass and composition of the ancient atmosphere can be studied by investigating the isotopic evolution of atmospheric Xe, from 4.5 Ga to ~2 Ga. We investigate the possibility to bring constraints on the age of organic materials isolated from sedimentary ricks older than 2 Ga, using the isotopic signature of the Xe component that was trapped at the time of their formation. This method could have implications regarding the presumed age of the earliest remnants of organic life.